11-3-2016 12:00 AM

Evolution of Mafic Impact Melt Bodies at the Crater Floor Interfaces of the Vredefort and Sudbury Impact Structures

Carmela Lisa Cupelli, *The University of Western Ontario*

Supervisor: Desmond Moser, *The University of Western Ontario*
A thesis submitted in partial fulfillment of the requirements for the Doctor of Philosophy degree in Geology

Abstract

The Vredefort and Sudbury impact basins in South Africa and Canada, respectively, are currently the world's oldest and largest impact structures. Over a hundred years of study on both impacts has still not answered all the questions surrounding these sites. The 2019 Ma Vredefort structure is thought to have an original diameter of 300 km, however, due to erosion all that is left of the structure is the basement of the central uplift. Small pockets and dykes of melt rock still remain but in the case of the gabbronorite its origin remains to be proven. The Sudbury structure is 1850 Ma, with an original diameter of approximately 250 km, orogenic deformation has preserved the impact melt, including mafic-ultramafic inclusions found at the base of the melt sheet. The origin of these inclusions are still not fully understood. In this work, new light is shed on impact melting through detailed field mapping and application of new geochemical and micro-imaging techniques (e.g. FEG-SEM Electron Backscatter Diffraction, colour cathodoluminescence, SIMS and Laser ablation ICP-MS) to evaluate mineral assemblages and U-Pb dating minerals from both sites. At Vredefort, dykes and lenses of a gabbronorite body were studied and determined to be the age of the impact as well as Lu-Hf values in concordance with zircons formed from melting of the target material, however, the whole rock chemistry suggests a mantle origin for the melt. Zircons from the mafic-ultramafic inclusions in the Sudbury Sublayer were analysed for evidence of shock and found to have igneous-like textures and no planer or remodeling features. This suggests that the mafic-ultramafic inclusions formed at the time of impact. Both sites show strong evidence for late modification stage adjustment in the central uplift and crater floor, and raises questions about the crystallization and modification of impact basins. Further understanding of these processes and the microstructures formed during these events could lead to new bench marks for identifying old impact craters on Earth and for understanding crater dynamics on other stony bodies in the solar system.

Keywords

Vredefort, Sudbury, Impact Melt, Large Scale Impacts, Zircons, Accessory Phases, EBSD, U-Pb Dating, Shocked Zircons.

Co-Authorship Statement

Chapter 2: The samples in this study were collected by Lisa Cupelli and Desmond Moser. SHRIMP analysis was carried out by Desmond Moser and John Bowman at the Stanford/ U.S.G.S SHRIMP-RG facility. SEM analysis was conducted by Lisa Cupelli with support by Ivan Barker. Lu-Hf analysis was conducted by Bruno Dhuime and James Darling at the University of Bristol. Lisa Cupelli analysed and interpreted the data and wrote the manuscript, with comments and editing by the co-authors.

Chapter 3: The samples in this study were collected by Lisa Cupelli and Desmond Moser. Sample preparation, analysis and interpretation was conducted by Lisa Cupelli, with SEM support provided by Ivan Barker and EBSD support from Desmond Moser. Desmond Moser and Peter Lightfoot assisted with the chemistry interpretation. The manuscript was written by Lisa Cupelli and editing and comments were provided by the co-authors.

Chapter 4: Samples for this study were collected by Peter Lightfoot in 1993 with the OGS. Sample preparation and SEM analysis were conducted by Lisa Cupelli with SEM support by Ivan Barker and EBSD support by Desmond Moser. The manuscript was written by Lisa Cupelli and editing and comments were provided by the co-authors.

Acknowledgments

I would like to start by thanking Desmond Moser for introducing me to the Vredefort Impact Structure, and for all his guidance and encouragement over the years. I would also like to extend my sincerest thanks to Peter Lightfoot and Norm Duke, for always taking the time out of their busy schedules to talk with me about the many puzzles that Vredefort and Sudbury provided.

This work could not have been possible without the help of many technicians, particularly Ivan Barker, whose constant patience and support over the years has been greatly appreciated. I would also like to thank, Joe Wooden, Bruno Dhuime, Steve and Gordon Wood, Ian Craig, Judy Weaver, and the team at the Jack Satterly Geochronology Lab at U of T. I wish to acknowledge support from NSERC and NSF for providing funding and Vale for providing samples.

Thank you to my colleagues and the staff in the Earth Sciences Department for all their support and encouragement, and for making Western feel like home for the past decade: James Darling, Nik Ganderton, Connor Davis, Brendt Hyde, Laura Sanchez, Andrea Prentice, Rachel Schwartz-Narbonne, Cassandra Marion-Beauchamp, Louisa Preston, Ryan Hladyniuk, Jessica Flynn, Jeremiah Shuster, Bhairavi Shankar, Caitlin Latimar, Jessica Stromberg, Marie and Miguel Gill, Matt Izawa, Melissa Battler, my office mates in 1031, Roberta Flemming, Gordon Osinski, Phil McCausland, Steve Hicock, Dazhi Jiang, Sean Shieh, Robert Schincariol, Cam Tsujita, Elizabeth Webb, Marie Schell, Jen Heidenheim. Thank you to Rodger Hart for his guidance and thought provoking discussions in the field, and Julie Vizza, Debbie Payette, Kaitlin Brennen, Zac Brown, AJ Harkness, Dave Skelton and Christan Mariyanayagam for being there whenever I needed that little extra help staying sane.

Finally I would like to thank my family; my parents Luigi and Carmela Cupelli, and my brothers Carmine and Frank for their unwavering love and encouragement, thank you for supporting me regardless of how far or how crazy the journey may have seemed.

Table of Contents

List of Tables

List of Figures

List of Appendices

List of Abbreviations

BSE	Back Scattered Electron
BIF	Banded Iron Formation
Ga	Billion years ago
CL	Cathodoluminescence
CAG	Central Anatectic Granite
CPX	Clinopyroxene
DM	Depleted mantle
EBSD	Electron Backscatter Diffraction
EDS	Energy Dispersive Spectroscopy
FEG-SEM	Field Emission Gun-Scanning Electron Microscope
GIS	Geographic Information System
GPS	Global Positioning System
HREE	Heavy Rare Earth Elements
IBNR	Inclusion Basic Norite
ILG	Inlandsee Leucogranofels
kV	Kilovolts
LA ICP-MS	Laser Ablation Multi-collector Inductively Coupled Plasma Mass Spectrometer
LREE	Light Rare Earth Elements
Ma	Million Years Ago
OGS	Ontario Geological Survey
OPX	Orthopyroxene
PPB	Parts Per Billion
PPM	Parts Per Million
PDF	Planner Deformation Features
PF	Planner Features
PGE	Platnum Group Elements
REE	Rare Earth Element
SEM	Scanning Electron Microscope
SE	Secondary Electron
SIMS	Secondary Ion Mass Spectrometer
SHRIMP-RG	Sensitive High Resolution Ion Microprobe- Reverse Geometry
SIC	Sudbury Igneous Complex
TIMS	Thermal Ionization Mass Spectrometry
USGS	United Stated Geological Survey
wt%	Weight Percent
ZAPLab	Zircon and Accessory Phase Laboratory

Chapter 1: Introduction

Meteorite impact-related processes are an important component of the evolution of planetary crusts particularly early in the habitable stages of planets (e.g. Marchi et al. 2014) however, the detailed interactions between impactites such as large melt sheets and the subjacent impacted crust are poorly understood. Much of the lack of understanding is due to the obliterating effects of erosion and plate tectonics that make it difficult for geologists to study ancient impacts (Grieve and Pesonen 1992), which were thought to be abundant on Earth during the late heavy bombardment at 4.2 to 3.8 Ga (Tera et al. 1974; Sleep et al. 1989; Kring and Cohen 2002). The focus of this thesis is to compare the petrogenesis of impact-generated magmas and their relationship to Archean continental crust at the Vredefort and Sudbury impact structures of South Africa and Canada, respectively. These two impacts were chosen based on their similar age, original diameter, target lithology, and because they display two very different ends of the preservation spectrum. Vredefort is a unique location for studying the effects an impact has on target rocks beneath the melt sheet due to approximately 8 to 10 km of erosion (Gibson et al. 1998), whereas Sudbury has undergone folding during the Penokean orogeny to preserve the contact between the layers of impact melt and the basement (Szabo and Hall 2006). This preservation allows us to use Sudbury as an analogue for the types of impact melting features we would expect to find at Vredefort pre-erosion, whereas the central uplift environment at Vredefort can be used to predict phenomena in the unexposed corollary at Sudbury. The larger scale implications for this work include a better understanding of the crater-contact zone and the effects of impacts on the early crust, as well as increasing the scientific community's tools for identifying ancient, heavily eroded impacts.

1.1 Impact Melts

The formation of melt sheets is a unique process that differs drastically from other magmatic events. Melts form by rapid and total melting of near surface target rocks located directly below the impact (French 1998). Impact melt bodies can be divided into two types based on time and conditions of formation. The first type are penetration phase melts which occur at the time of impact. These melts are compositionally similar to the target rock and do not involve much large-scale mixing. The second type are bottom melts which occur later and represent a well-mixed average melt of the target rocks (Feldman et al. 2006).

Post shock temperatures in the target rock can reach ≥ 2000°C, which are much greater than the temperatures needed to melt the target rocks and the minerals that comprise them, causing spontaneous and instantaneous melting. The kinetic energy provided by the shock waves allows for the melt to flow (French 1998). The melt is driven down and outwards at velocities of a few kilometers per second, eventually reaching the crater floor and moving along the crater rim (Grieve et al. 1977). The melt can collect clasts as it moves, which can cause the melt to cool rapidly if the clasts are abundant (Simonds et al. 1976).

1.2 Size of Melt Sheets

An impact structure with a diameter of 25 km or more has the potential to produce hundreds of cubic kilometers of impact melt, which can form dyke and sill-like bodies. (French 1998). In small impacts, the melts are found as small suevite (a type of breccia with impact melt matrix) bodies and as matrix material in clast-rich breccias.

Theoretical studies have estimated that typical impact velocities are between 15 to 30 km/s, and that anywhere from 40 to 60% of the kinetic energy can be transferred into the target rocks as thermal energy. The process is not completely efficient and, therefore, not all of this energy is used to create the melt sheet, but an impact of that speed has the potential to form an impact melt greater than 100 times the volume of the original projectile (O'Keefe and Ahrens 1977).

Grieve and Cintala (1992) have formulated an equation to determine the volume of melt produced by an impact. They believed that the volume of melt will increase exponentially with crater diameter. The equation is

$$V_m = cD^d_{tc}, \qquad (1)$$

where V_m is the volume of the melt in cubic kilometers, D_{tc} is the transient crater diameter in kilometers and c and d are constants resulting from the regression. In their theoretical and experimental studies, they found an approximate value for c to be 0.0004 and d to be 3.84.

The ability to use modeling and theoretical studies is important to the study of impact melt sheets because there are often uncertainties associated with such a heterogeneous, large-scale process. For example, it is difficult to estimate the original volume of melt in older eroded structures, and it is also difficult to estimate the volume of a melt sheet in poorly exposed structures. These reservations are the reason that theoretical and experimental values do not always match those found in the field (French 1998).

1.3 Types of melts

The types of impact melts are categorized based on the time of formation during and after the impact. However, melts can also be categorized based on texture and size (French 1998). When an impact melt forms, it is deposited within or just outside of the crater rim. There are three types of melts that can be found in this area, including small glassy bodies, impact melt breccias, and large crystalline bodies. During crater formation, a portion of the material that makes up the original target rocks is ejected from the crater, and this ejecta material can also contain some of the impact melt. In this study the focus is on large crystalline bodies which are less common in the rock record than the smaller glasses and breccia melts. Large crystalline melt bodies range in volume from several hundred to a few thousand cubic kilometers. The two basic forms for these melts include sill like bodies such as those seen in Sudbury, Ontario, Canada, or as dyke-like bodies that penetrate the basement rocks of a crater (French 1998).

1.4 Vredefort

1.4.1 Vredefort Geology

At the centre of the Vredefort impact basin, the Vredefort dome consists of Archean crystalline basement centred at 27°S, 27°30'E, 120 km southwest of Johannesburg, South Africa. The physiographic expression of the structure, previously 250 to 260 km in diameter, is now a semiannular exposure of upturned sedimentary strata 80 km in diameter (Gibson et al. 1998). The exposed, predominantly granitic and gneissic, basement rocks are dome shaped masses localized at the intersection of two sets of anticlines (Truswell 1970). The dome, often referred to as the Central Dome or Central Uplift, is 43 km in diameter along its north-east axis, and approximately 55 to 56 km along its northwest axis (Bischoff 1988). The dome is surrounded by approximately 12,350 m of younger volcanics and sediments from the Witwatersrand (comprised of the West Rand and Central Rand Groups), Ventersdorp and Transvaal systems (Truswell 1970), which are Late Archean to Early Proterozoic in age (Gibson et al. 1998). The diameter of the outer dome is approximately 100 km along the northeast axis and 120 km along the northwest axis (Bischoff 1988). These younger units have been overturned against the granites that were once below them (Truswell 1970) and the dips change outward from the central dome. The lower portion of the collar of the West Rand Group is overturned at 100 to 110°, which is less than the Central Rand Group formations which are overturned between 120 to 130°

(Bischoff 1988). The Ventersdorp Supergroup and the Transvaal Sequences are closer to vertical dip near the lower Transvaal strata and once you reach the Pretoria Subgroup, the dip becomes normal again (20 to 40°) (Bisschoff 1988). The southern parts of the second ring, along with other portions of the structure beyond the second ring, were then eroded, allowing for the deposition of the Karoo Supergroup (Brink et al. 2000) in the Phanerozoic (Gibson et al. 1998). Breccia zones are seen in almost all of the concentric ramps of thrust faults that accompany the Vredefort event and are visible in a number of chert beds in both the Malmani subgroup and Monte Christo Formation (Brink et al. 2000).

The surficial record at Vredefort, which is thought to have been between 250 to 300 km wide (Reimold and Gibson 1996), has been greatly minimized by erosion over the past 2020 m.y. (Brink et al. 2000). Although it is postulated that spherule beds recently found in Russia are a result of impact ejecta from the Vredefort impact event (Huber et al. 2014), crustal material that was ejected away from the centre of the impact during the collision has now been dominantly eroded (Brink et al. 2000). Away from the central dome an ordered structure of folds and faults with concentric shapes is visible (Brink et al. 2000).

When the impact occurred, many of the rocks in the surrounding area were deformed, up to and including the Transvaal Supergroup (Bischoff 1988). The Vredefort Structure has a metamorphic aureole associated with it. It is roughly elliptical at surface and the northernmost boundary is near the contact between the Ventersdorp and Witwatersrand rocks (Bisschoff 1988). There is an increase in metamorphic grade towards the centre of the dome and tangentially around the dome to the northwestern region. In that region of the collar, metamorphic grades increase from greenschist facies in the Ventersdorp and Upper

Witwatersrand Supergroups to mid-amphibolite facies in the lower zones of the Witwatersrand and Dominion Group (Reimold and Gibson 1996).

Bischoff (1988) discovered that there are many locations in the Vredefort Structure in which pseudotachylite and shatter cones are present, from the Archean basement rocks to the igneous rocks of the Bushveld (2.055 Ga). The granulitic rocks in the central dome appear to contain little to no pseudotachylite. However, the presence of pseudotachylite is greatest in the amphibolites faces of the rocks and in the collar rocks that are encompassed in the thermal metamorphic aureole (Bischoff 1988). Outside of the thermal metamorphic aureole the pseudotachylites begins to diminish in abundance and where it is seen, the veins are smaller. The hornfelses in the collar rocks are cut by the pseudotachylite indicating that the latter must be younger then the thermal metamorphic event or were formed towards the end of metamorphism (Bischoff 1988).

1.4.2 Identification history of impact melt bodies at Vredefort

No previously recognized impact melt sheet has been found at the Vredefort impact structure. There are only three types of impact generated melts that are widely accepted: the pseudotachylite first discovered by Dietz (1961a), the radially distributed granophyre dykes (Walraven 1990; Kamo et al. 1996) and a body of Vredefort Central Anatectic Granite, dated at 2017 ± 5 Ma (Gibson et al. 1997), which occurs as m-scale pods of partial melt of Archean gneiss in the central uplift. A third unit, a 0.5 m wide foliated norite dyke (following petrographic analysis in this study, the unit was reclassified as gabbronorite), with a zircon age of 2019 ± 2 Ma has also been reported (Moser 1997). It has since been proposed that this gabbronorite unit be reclassified as a mafic pseudotachylite, and that the impact age zircons are the result of post impact metamorphism (Gibson et al. 1997). This is due to the presence of inclusions of Archean felsic gneiss (ILG) (Gibson and Reimold 2008), which our mapping has found only at the margins of the gabbronorite bodies. It has also been suggested that the impact U-Pb age of zircons from this unit are a consequence of shock and thermal resetting of Archean pre-impact grains, and does not correspond to primary crystallization (Gibson et al. 1998).

1.4.3 Other mafic units associated with the Bushveld Igneous Complex

Other mafic units have been found in the Vredefort structure that are not associated with the impact, primarily including mafic intrusions of possible Bushveld age. Coetzee et al. (2006) conducted a geochemistry and petrogenesis of tholeiitic intrusions found in the Vredefort dome, and consider these units to be derived from an olivine fractionation of an ultramafic Bushveld-type magma from the same magmatic event. de Waal et al. (2006), discussed a number of km-sized mafic bodies along the northern rim of the Vredefort impact structure and east toward the town of Heidelberg including; the Roodekraal Complex, the Lindeques drift intrusion, the Reitfontein Complex, the Heidelberg Intrusion, the Kaffirskraal Complex, and the Losberg Intrusion. These bodies, excluding the Losberg Intrusion, are syn-Bushveld high-Ti igneous suites. de Waal et al. (2006), concluded that the units are derived from a ferrobasaltic magma with alkaline affinities. Ultramafic rocks were also found in the centre of the dome and believed by Hart et al. (1995), to be carrying remnant magnetization acquired syn- or post-uplift. Merkle and Wallmach (1997) disagree with Hart et al.'s theory that the samples originate from the upper mantle but they cannot verifiably prove that the unit is of Bushveld age.

1.5 Sudbury

1.5.1 Sudbury Regional Geology

Located in central Ontario, Canada, the Sudbury impact structure occurs at the intersection of two provinces of the Canadian Shield; to the north are the Archean plutonic rocks of the Superior province, and to the south, Early Proterozoic Huronian supracrustal rocks of the

Southern province (Card et al. 1984). The Levack Gneiss Complex, thought to have a primary age of 2711 ± 7 Ma and a secondary age of metamorphism at ~2640 Ma, is 0.5 to 5.0 km wide and borders the Sudbury structure to the north (Krogh et al. 1984). The granodioritic Cartier Batholith intruded the Levack Gneiss at 2642 ± 1 Ma (Szabo and Hall 2006). The Early Proterozoic supracrustal sequence of the Southern Province, the Huronian Supergroup in the east and the Marquette Range Supergroup, Animikie Group and correlative rocks in the west, were deposited between 2500 Ma and 1900 Ma and thicken southward from an erosional edge to over 10 km. This sequence forms a discontinuous linear fold belt approximately 1,300 km in length along the southern margin of the Superior Province. The clastic sedimentary rocks were derived mainly from the Superior Province Archean craton to the north (Card et al. 1984). Fe-rich quartz tholeiites that trend NNW, make up the Matachewan dyke swarm that intruded into the Archean rocks to the north at ~ 2473 +16/-9 Ma (Heaman 1997) and the pyroxene and hornblende gabbro Nipissing dykes were emplaced at 2219 ± 4 Ma (Corfu and Andrews, 1986; Noble and Lightfoot 1992; Sproule et al. 2007). The elliptical form of the Sudbury basin seen today is a result of multiple orogenic events. It is theorised that during the Penokean and Mazatzal orogenies the structure was displaced 8 km to the northwest, resulting in the deformation of its original circular form to the ellipse we see today (Szabo and Hall, 2006; Riller 2005; Raharimahefa et al. 2014).

1.5.2 Sudbury Igneous Complex Sublayer

The Sudbury Igneous Complex (SIC) Sublayer occurs as laterally extensive sheets, flat irregular lenses, small bodies in embayments or troughs in the footwall, and in offset dykes. From top to bottom, an idealized Sublayer occurrence would consist of contaminated hybrid basal irruptive (similar to the North Range mafic norite), a sub-poikilitic igneous Sublayer, metamorphic-textured leucocratic breccias, mega-breccia, and Sudbury brecciated footwall

(Pattison 1979). The SIC Sublayer was first defined by Souch et al. (1969) as a sulfide- and inclusion-bearing silicate magma. Souch et al. (1969), attempted to radiometrically date the Sublayer using Rb-Sr analysis, however they determined that none of the three samples analyzed from the South Range fell on previously defined Rb-Sr isochrons and did not define a single isochron. Naldrett et al. (1972) defined the two fundamental facies of the Sublayer as 1) igneous Sublayer; a group of igneous-textured gabbroic, noritic and dioritic rocks and 2) leucocratic breccias consisting of a group of metamorphic-textured felsic to mafic breccias. Both the North and South range igneous Sublayer have a matrix that consists of zoned plagioclase laths, prismatic to subophitic clino- and orthopyroxenes, minor amounts of primary biotite and hornblende, highly variable quantities of interstitial quartz, micrographic quartz-feldspar intergrowth and microcline, and Cu-Ni-Fe sulphides. Only at the Whistle embayment is rare olivine reported to occur in the igneous Sublayer (Pattison 1979).

A major component of the SIC Sublayer is its subrounded inclusions which range from 8 cm to 1.5 m in diameter (Scribbins et al. 1984), and can be divided into two types. The first are those clearly derived from the local footwall rocks and their metamorphic counterparts. The second consists of a mafic to ultramafic rock with the mineral assemblage olivine, orthopyroxene, clinopyroxene and calcic plagioclase and some primary hornblende and biotite (Pattison 1979). Scribbins et al. (1984) analyzed 390 inclusions from the igneous Sublayer, 264 from the Strathcona mine in the North Range and 126 from the South Range. The inclusions found in the Strathcona samples varied from dunite composition through harzburgite, wehrlite and clinopyroxenite to norite and gabbro. The samples analyzed from the South Range only contained rock types that are orthopyroxene dominant, such as harzburgite and melanorite and there appears to be more recrystallization and alteration in the South Range xenoliths although recrystallization is still common in the Strathcona samples. The olivine composition from the inclusions in the South Range varies from $Fo_{74.4}$ to $Fo_{85.6}$, whereas the compositions from the inclusions in the Strathcona samples range from $Fo_{73.4}$ to $Fo_{84.4}$

1.5.3 Whistle Embayment

The Whistle embayment is located in the northeast corner of the Sudbury structure and consists of a zone of Sublayer (radially up to 1 km thick) that occupies an embayment structure at the base of the Main Mass, and an offset dyke hosted in Archean granitoid rocks and amphibolite (Lightfoot et al. 1997c). The embayment is a funnel-shaped norite body (Giroux and Benn 2005), consisting of Sublayer rocks overlain to the southwest by basal irruptive mafic and felsic norites (Pattison 1979). The Whistle offset dyke stretches 12 km north-northeast of the SIC (Murphy and Spray 2002) and is 100 to 150 m wide narrowing away from the SIC to about 15 to 20 m (Giroux and Benn 2005). The Whistle embayment rocks are comprised of an orthopyroxene-rich Sublayer and inclusions of olivine-bearing norite and melanorite. The Sublayer becomes more siliceous as it nears the footwall. Leucocratic breccias from the contact of the embayment are gradational in contact with the igneous Sublayer (Pattison 1979). The rest of the offset consists of radial breccias, mafic-sulphide bearing igneous breccias, inclusion-bearing quartz diorite and inclusion-poor quartz diorite. The inclusions in the Sublayer at the Whistle embayment are composed of melanorite, diabase and pyroxenite (Murphy and Spray 2002). The main mass norite bodies at the Whistle embayment consist of mafic norite at the base which gradationally transitions over a range of 1 to 5 cm to a basal felsic norite above. At the Whistle mine, this unit has a hypidiomorphic-granular texture with $< 5\%$ cumulus orthopyroxene. Located between the basal felsic norite and the mafic norite is a zone of orthopyroxene-rich poikilitic melanorite that when present can be ≤ 15 m in width. This unit is composed of interstitial sulphide (1 to 10%), cumulus orthopyroxene (20 to 40%), intercumulus plagioclase (40 to 50%), and intercumulus biotite (1 to 10%) (Lightfoot et al. 1997c).

The contact between the main mass and the Sublayer of the Whistle embayment is defined by a sharp contact between the orthopyroxene-poor felsic norite and the porphyritic-textured inclusions and sulphide-bearing Sublayer norite matrix (Corfu and Lightfoot 1996). Compared to the main mass felsic norite there is an increase in heavy rare earth elements (REE) and a decrease in light REE in both the intermediate and igneous-textured Sublayer matrix norites at the Whistle embayment (Lightfoot et al. 1997c). There is iron enrichment in both ortho- and clinopyroxene as you approach the footwall (or base of the funnel), which appears to be the typical trend of the igneous Sublayer (Pattison 1979). Lightfoot et al. (1997a) proposes that the igneous Sublayer matrix at Whistle is a compositional mixture of 20% mafic norite magma, 70% diabase inclusions and 10% footwall granitoid. The problem with this model is that a typical mafic magma having this relatively low volume could not assimilate a 70% volume of diabase inclusions unless it was superheated. It is possible, however, that volatiles played a significant role in superheating the magma.

1.5.4 Source of the inclusions

The Sudbury literature is full of theories on sources for the mafic to ultramafic inclusions in the Sublayer, however to date none have met the age, compositional or textural requirements to fully satisfy a complete theory. Many mafic footwall units have been proposed including: mafic components of the Levack complex (Pattison 1979; Farrell et al. 1995), Nipissing diabase (Card and Pattison 1973), and a Huronian intrusive suite which consists of the East Bull Lake and Shakespeare-Dunlop intrusions to the west and the River Valley intrusion in the east. A number of smaller sills that occur in between these major bodies have also been considered

(Prevec and Baadsgaard 2005). Lightfoot et al. (1997c) found that compositionally the Matachewan diabase dykes are a better fit for the diabase inclusions at Whistle than the Nipissing dykes, however they do not match the 1848.1 to 1849.8 Ma zircon and baddeleyite ages determined for the inclusions (Corfu and Lightfoot 1996).

A second hypothesis is that the inclusions came from the SIC itself due to disruption of an early cumulate layer (Morrison et al. 1994). Lightfoot et al. (1997c) argued that the mineral chemistry did not support this hypothesis and that the thermal conditions would have been too hot to allow for the melt to become brittle. However, Ivanov (2005) proposed that post-impact thermal conditions vary considerably with radial distance from the centre of the impact (Ivanov 2005). Due to the uncertainty regarding the radial distance of the Whistle embayment from the centre of the impact due to basin collapse, this allows for a range of possible thermal conditions in the crater floor when the embayment formed.

Corfu and Lightfoot (1996) analyzed five samples from the Whistle embayment for U/Pb geochronology and found that the ages ranged between 1848.1 to 1849.8 Ma. The samples consisted of an olivine bearing two-pyroxene norite representing the Sublayer matrix, an olivine melanorite from a pod, melanorite pods in Sublayer norite next to a sulphide zone, metapyroxenite inclusion from the sulphide zone, and a glomero-porphyritic-plagioclase-bearing diabase. Four zircons and one baddeleyite were analyzed from five samples and it was suggested that the minerals crystallized from one mafic magma enriched in light REE and large ion lithophile elements. It has been suggested that the zircon ages were reset due to metasomatic overprinting, and that the age data for the zircons correspond to a metamorphic igneous event rather than the primary age of the inclusions; however, the zircon crystal morphology suggests a magmatic origin (Lightfoot et al. 1997c).

1.6 Purpose of Study and Thesis Structure

In order to increase our knowledge of impact melting effects on ancient crust using scanning electron microscope (SEM) techniques such as: secondary and backscatter electron, cathodoluminescence, energy dispersion spectroscopy and electron backscatter diffraction, accessory phases were examined for micro-structures which allow for a better understanding of formation history. The research objectives varied with field area, however the same methodology was applied. At Vredefort, the existence of crystalline melt bodies was in question so mapping was carried out to discover any further exposures of a m-scale norite dyke reported in the area by Moser (1997). At Sudbury, the impact melt sheet has long been accepted, however, the early history of the melt sheet was in contention with regard to ultramafic inclusions that appeared to have formed the basis of the early melt sheet. In both cases, the intense heating associated with post-impact crater recovery has removed many of the microscopic mineral features commonly used to distinguish pre-impact rocks from those genetically related to the shock wave. Consequently, this study has utilized the accessory zirconium and phosphate mineral phases as they retain a record of shock processes while surrounding minerals are completely recrystallized. At Vredefort the goal was to understand the origin of the melt source and map the formation history of the gabbronorite unit. Along with SEM imaging, zircon and whole rock chemistry were also analyzed by SHRIMP-RG and LA-ICP-MS. At Sudbury, the goal was to progress the debate regarding isotopic age-resetting in zircon. This was accomplished using the aforementioned SEM techniques to show that no evidence of shock occurred in the accessory phases to cause resetting. The work done at both sites provides the scientific community with new methods for studying impacts, and it is anticipated that these methods will progress to the discovery of new ancient impact craters.

This thesis has been presented in three main chapters. Chapter 2 considers the zircon microstructural, trace element and isotopic analyses (U-Pb, Lu-Hf) of the gabbronorite in Vredefort to determine if the unit is indeed an impact related melt. Chapter 3 takes a closer look at the whole rock chemistry, mineralogy and textures of the gabbronorite in Vredefort and draws comparisons with the surrounding country rock and units found in the literature to distinguish the source and emplacement history of the gabbronorite. Finally Chapter 4 addresses the question of zircon and baddeleyite resetting in the mafic to ultramafic inclusions of the Whistle embayment at Sudbury and considers their possible emplacement histories.

1.7 References

Bisschoff, A.A. 1988. The history and origin of the Vredefort Dome. Suid-Afrikaanse Tydskrif vir Wetenskap, **84**: 413-417.

Brink, M.C., Waanders, F.B. and Bisschoff, A.A. 2000. The Katdoornbosch- Witpoortjie Fault: A ring thrust of Vredefort event age. South African Journal of Geology, **103**: 15-31.

Card, K.D., Gupta, V.K., McGrath, P.H. and Grant, F.S. 1984. The Sudbury Structure: Its regional geological and geophysical setting *In* The Geology and Ore Deposits of the Sudbury Structure. *Edited by* Pye, E.G., Naldrett, A.J., and Giblin, P.E. Ontario Geological Survey, Special Volume **1**: 25-43.

Card, K.D. & Pattison, E.F. 1973. Nipissing diabase of the Southern province Ontario. *In* Huronian Stratigraphy and Sedimentation. *Edited by* Young, G.M. Geological Association of Canada, Special Paper **L2**: 7-30.

Coetzee, M.S., Beukes, G.J., de Bruiyn, H. and Bisschoff, A.A. 2006. Geochemistry and petrogenesis of tholeiitic intrusions of possible Bushveld-age in the Vredefort Dome, South Africa. Journal of African Earth Sciences, **45:** 213-235.

Corfu, F. and Andrews, A. 1986. A U-Pb age for mineralized Nipissing diabase, Gowganda, Ontario. Canadian Journal of Earth Science, **23**: 107-112.

Corfu, F. and Lightfoot, P.C. 1996. U-Pb geochronology of the sublayer environment, Sudbury Igneous Complex, Ontario. Economic Geology, **91**: 1263-1269.

Dietz, R.S. 1961a. Vredefort Ring Structure: Meteorite impact scar? Journal of Geology, 69: 499-516.

de Waal, S.A., Graham, I.T. and Armstrong, R.A. 2006. The Lindeques Drift and Heidelberg Intrusions and the Roodekraal Complex, Vredefort South Africa: comagmatic plutonic and volcanic products of a 2055Ma ferrobasaltic magma. South African Journal of Geology, **109:** 279-300.

Farrell, K.P.J., Lightfoot, P.C. and Keays, R.R. 1995. Mafic-ultramafic inclusions in the Sublayer of the Sudbury Igneous Complex, Whistle mine, Sudbury, Ontario. Ontario Geological Survey Miscellaneous Paper, **164**: 126-128.

Feldman, V.I., Sazonova, L.V. and Kozlov, E.A. 2006. Some Peculiaritias of Impact Melts (Natural and Experimental Data). Lunar and Planetary Science XXXVII.

French B.M. 1998. Traces of catastrophe: A handbook of shock-metamorphic effects in terrestrial meteorite impact structures. LPI Contribution No. **954**, Lunar and Planetary Institute, Huston.

Gibson, R.L., Armstrong, R.A. and Reimold, W.U. 1997. W.U. The age and thermal evolution of the Vredefort impact structure: A single-grain U-Pb zircon study. Geochimica et Cosrnochimica Acta, **61**: 1531-1540.

Gibson, R.L. and Reimold, W.U. 2008. Geology of the Vredefort impact structure, a guide to sites of interest. Council of Geoscience, Memoir **97**, Pretoria, 181 p.

Gibson, R.L., Reimold, W.U. and Stevens, G., 1998. Thermal-metamorphic signature of an impact event in the Vredefort Dome, South Africa. Geology, **26**(9): 787-790.

Giroux, L.A. and Benn, K. 2005. Emplacement of the Whistle Dke, the Whistle Embayment and hosted sulphides, Sudbury Impact Structure, based on anisotropies of magnetic susceptibility and magnetic remanence. Economic Geology, **100**: 1207-1227.

Grieve, R.A.F., and Cintala M.J. 1992. An analysis of differential impact melt-crater scaling and implications for the terrestrial impact record. Meteorites, **27**: 526-538.

Grieve, R.A.F., Dence M.R. and Robertson P.B. 1977. Cratering processes: As interpreted from the occurrence of impact melts. *In* Impact and Explosion Cratering: Planetary and Terrestrial Implications. *Edited by* Roddy, D.J., Pepin, R.O., and Merrill, R.B. pp. 791-814. Pergamon, New York.

Grieve, R.A.F. and Pesonen, L.J. 1992. The terrestrial impact cratering record. Tectonophysics, **216**: 1-30.

Hart, R.J., Hargraves, R.B., Andreoli, M.A.G., Tredoux, M. and Doucoure, C.M. 1995. Magnetic anomaly near the center of the Vredefort structure: Implications for impact-related magnetic signatures. Geology, **23:** 277-280.

Heaman, L.M. 1997. Global mafic magmatism at 2.45Ga: remnants of an ancient large igneous province? Geology, **25**(4): 299-302.

Huber, M.S., Crne, A.E., McDonald, I., Hecht, L., Melezhik, V.A., and Koeberl, C. 2014. Impact spherules from Karelia, Russia: Possible ejecta from the 2.02 Ga Vredefort impact event. Geology, **42**(5): 375-378.

Ivanov, B.A. 2005. Modeling of the largest terrestrial meteoritecraters. Solar System Research, **39**: 381–409.

Kamo, S.L., Reimold, W.U., Krogh, T.E. and Colliston, W.P. 1996. A 2.023 Ga age for the Vredefort impact event and a first report of shock metamorphosed zircons in pseudotachylitic breccias and granophyres. Earth and Planetary Science Letters, **144**: 369-388.

Kring D.A. and Cohen B.A. 2002. Cataclysmic bombardment throughout the inner solar system 3.9-4.0 Ga. Journal of Geophysical Research, **107**: 4-6.

Krogh, T.E., Davis, D.W. and Corfu, F. 1984. Precise U-Pb zircon and baddeleyite ages for the Sudbury area. *In* The Geology and Ore Deposits of the Sudbury Structure. *Edited by* Pye, E.G., Naldrett, A.J., and Giblin, P.E. Ontario Geological Survey, Special Volume **1**: 431-446.

Lightfoot, P.C., Doherty, W., Farrell, K., Keays, R.R., Moore, M. and Peleski, D. 1997a. Geochemistry of the main mass, sublayer, offsets, and inclusions from the Sudbury Igneous Complex, Ontario. Ontario Geological Survey, Open File Report **5959:** 231p

Lightfoot, P.C., Keays, R.R., Morrisson, G.G., Bite, A. and Farrell, K.P. 1997c. Geologic and geochemical relationships between the contact sublayer, inclusions and main mass of the Sudbury Igneous Complex: A case study of the Whistle mine embayment. Economic Geology, **92**: 647-672.

Merkle, R.K.W. and Wallmach, T. 1997. Ultramafic rocks in the centre of the Vredefort Structure (South Africa): Geochemical affinity to Bushveld rocks. Chemical Geology, **143:** 43-64.

Morrison, G. G., Jago, B. C. and White, T.L. 1994. Footwall mineralization of the Sudbury igneous Complex. Ontario Geological Survey, Special Volume, **5**: 57-64.

Moser, D.E. 1997. Dating the shock wave and thermal imprint of the giant Vredefort impact, South Africa. Geology, **25**: 7-10.

Murphy, A.J. and Spray, J.G. 2002. Geology, mineralization, and emplacement of the Whistle-Parkin offset dike, Sudbury. Economic Geology, **97**: 1399-1418.

Naldrett, A.J., Gneenman, L. and Hewins, R.H. 1972. The main Irruptive and the sub-layer at Sudbury, Ontario. International Geological Congress, 24th **4**:206-214.

Noble, S.R. and Lightfoot, P.C. 1992. U-Pb baddeleyite ages of the Kerns and Triangle Mountain intrusions, Nipissing Diabase, Ontario. Canadian Journal of Earth Science **29**: 1424-1429.

O'Keefe, J.A. and Ahrens, T.J. 1977. Impact-induced energy partitioning, melting and vaporizarion on terrestrial planets. Proc. Lunar Science Conference. 8th, pp. 3357-3374.

Pattison, E.F. 1979. The Sudbury Sublayer: its characteristics and relationships with the Main Mass of the Sudbury Irruptive. Canadian Mineralogist, **17**: 257-274.

Prevec, S.A. and Baadsgaard, H. 2005. Evolution of Palaeoproterozoic mafic intrusions located within the thermal aureole of the Sudbury Igneous Complex, Canada: Isotopic, geochronological and geochemical evidence. Geochemica et Cosmochimica Acta, **69**(14): 3653-3669.

Raharimahefa, T., Lafrance, B. and Tinkham, D.K. 2014. New structural, metamorphic, and U–Pb geochronological constraints on the Blezardian Orogeny and Yavapai Orogeny in the Southern Province, Sudbury, Canada. Canadian Journal of Earth Science, **51**: 750-774.

Reimold, W.U. and Gibson, R.L. 1996. Geology and evolution of the Vredefort Impact Structure, South Africa. Journal of African Earth Science, **23**(2): 125-162.

Riller, U. 2005. Structural characteristics of the Sudbury Impact Structure, Canada: Impact-induced versus orogenic deformation-A review. Meteoritics & Planetary Science, **40**(11): 1723-1740.

Scribbins, B., Rae, D.R. and Naldrett, A.J. 1984. Mafic and ultramafic inclusions in the Sublayer of the Sudbury Igneous Complex. Canadian Mineralogist, **22**: 67-75.

Simonds C.H., Warner J.L., Phinney W.C. and McGee P.E. 1976. Thermal model for impact breccia lithification: Manicouagan and the Moon. Proc. Lunar Science Conference 7th, pp 2509-2528.

Sleep, N. H., Zahnle, K. J., Kasting, J. F. and Morowitz, H. J. 1989. Annihilation of ecosystems by large asteroid impacts on the early Earth. Nature, **342**:139–142.

Souch, B.E., Podolsky, T. and the Inco Ltd. Geological staff. 1969. The sulphide ores at Sudbury. Their particular relationship to inclusion-bearing facies of the nickel irruptive. Economic Geology Monograph, **4**: 252-261.

Sproule, R.A., Sutcliffe, R., Tracanelli, H., and Lesher, C.M. 2007. Palaeoproterozoic Ni–Cu–PGE mineralisation in the Shakespeare intrusion, Ontario, Canada: a new style of Nipissing gabbro-hosted mineralisation. Applied Earth Science (Trans. Inst. Min. Metall. B), **116**(4):188-200.

Szabo, E. and Hall, H.C. 2006. Deformation of the Sudbury Structure: paleomagnetic evidence from the Sudbury breccias. Precambrian Research, **150**: 27-48.

Tera, F., Papanastassiou, D.A., Wasserburg, G.J. 1974. Isotopic evidence for a terminal lunar cataclysm. Earth and Planetary Science Letters, **22**: 1–21.

Truswell, J.F. 1970. An introduction to the historical geology of South Africa, Purnell & Sons (S.A.) PTY., LTD. Cape Town, South Africa. p. 70-71.

Walraven, F., Armstrong, R.A. and Kruger, F.J. 1990. A chronostratigraphic framework for the north-central Kaapvaal craton, the Bushveld Complex and the Vredefort structure. Tectonophysics, **171**: 23-48.

Chapter 2: Discovery of Mafic Impact Melt in the Center of the Vredefort Dome; Archetype for Continental Residua of Early Earth Cratering?

C. L. Cupelli[1*], D.E. Moser[1], I.R. Barker[1], J.R. Darling[2], J.R. Bowman[3], and B. Dhuime[4]

[1]*Earth Science, Western University, 1151 Richmond Street, London, Ontario N6A 5B7, Canada.*

[2]*University of Portsmouth, Burnaby Building, Burnaby Road, Portsmouth P01 3QL, UK*

[3]*Geology and Geophysics, University of Utah, 115 S 1460E, Salt Lake City, Utah 84112, USA.*

[4]*Earth Sciences, University of Bristol, Wills Memorial Building, Queens Road, Bristol BS8 1RJ, UK.*

2.1 Introduction

Large-scale impact heating and melting of crust is thought to have been important on the Early Earth (Kring and Cohen 2002), yet interactions at melt-lithosphere contacts in the central uplift of large craters are rarely exposed in terrestrial targets and remain poorly understood (Grieve and Cintala 1992; Wielicki et al. 2012). The question is; what do the deep levels of large, deeply eroded impact structures look like (Garde et al. 2012)? The 2.020 Ga Vredefort impact structure of South Africa (Spray et al. 1995; Kamo et al. 1996; Moser 1997) is an ideal site to address such questions. It is among the largest of the known terrestrial impact structures, with a rim-to-rim diameter of the collapsed transient cavity of ~160 km (Bishopp 1962), and the structure extends vertically ~20 km into the Mesoarchean Kaapvaal craton (Henkel and Reimold 1998). The Vredefort crater, like Sudbury, would have been filled by an extensive melt sheet several kilometers thick derived from the Archean and Proterozoic target rocks (Ivanov 2005). However, only three impact-related igneous units have so far been widely accepted:

[1]This chapter was previously published: Cupelli, C.L., Moser, D.E., Barker, I.R., Darling, J.R., Bowman, J.R. and Dhuime, B. 2014. Discovery of mafic impact melt in the center of the Vredefort dome: Archetype for continental residua of early Earth cratering? Geology, **42**(5): 403-406.

pseudotachyllite dykes and allochthonous radially distributed granophyre dykes (Walraven et al. 1990; Kamo et al. 1996) that intrude the outer Archean crystalline bedrock of the central uplift, and an autochthonous dm-scale granitic body at the center of the uplift, referred to as the Central Anatectic Granite, dated at 2017 ± 5 Ma (Gibson et al. 1997) and considered to be a partial melt of a ~300 km^2 area of recrystallized felsic Archean gneiss, the Inlandsee Leucogranofels (ILG). No vestiges of the impact melt sheet have been recognized with the possible exception of a 0.5 m wide, foliated mafic dyke with a zircon age of 2019 ± 2 Ma (Moser 1997). Other works have since proposed that this unit is instead a recrystallized mafic pseudotachyllite, due to the presence of inclusions of Archean felsic gneiss (ILG) in drill core (Gibson and Reimold 2008), and that its impact-age zircons are the result of post impact metamorphism (Gibson et al. 1998). We present regional and detailed mapping in a ~2 km^2 area of ILG bedrock in the vicinity of the foliated mafic dyke near the center of the Vredefort structure that reveals additional, larger occurrences of the mafic unit, and test for its impact origin with detailed mapping of contact relationships and analyses of zircon U-Pb and Lu-Hf isotopic composition, microstructure and Ti abundance for the purpose of thermometry.

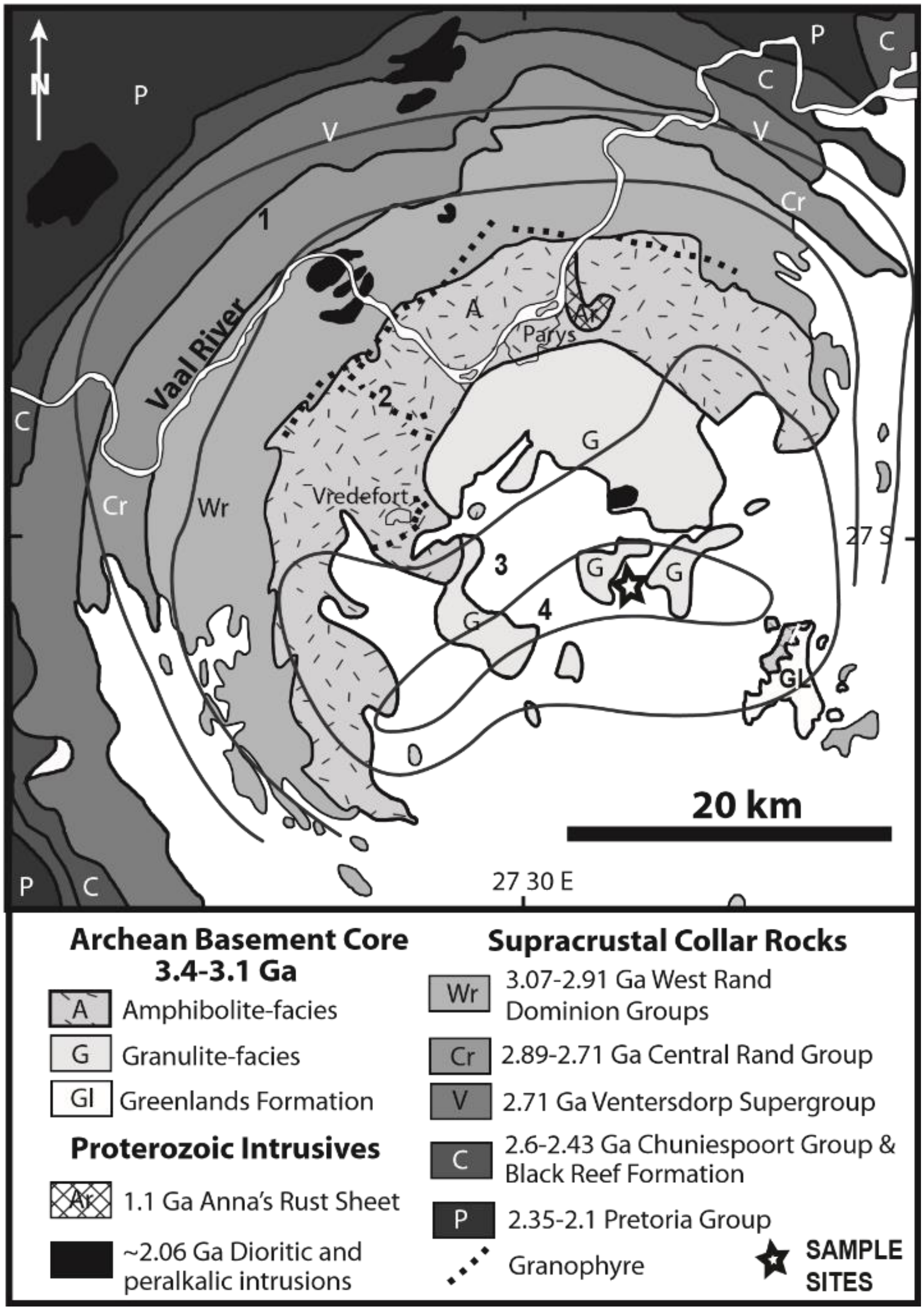

Figure 2-1. Generalized bedrock geology map of the Vredefort Dome (after Gibson and Reimold 2008). Grey contours represent degree of post-shock thermal annealing of planar deformation features in quartz (Grieve et al. 1990), with zone 4 representing complete annealing and 1 representing the least annealing. Location of study area indicated with a star.

2.2 Methods

Bedrock exposure in the central uplift region (Figure 2-1) is very low (<1%) and reconnaissance mapping of a 2 km^2 area north of the Inlandsee Pan revealed two areas of outcrop of mafic rock similar to the 'type' mafic dyke (Moser 1997). Sites (1 and 2) were subsequently mapped at a 10 m grid spacing to define the contact relationships and extent of the mafic bodies prior to sampling. Optical and electron microscopy (secondary and backscatter electron imaging (SE and BSE), energy dispersive spectroscopy (EDS), cathodoluminescence (CL) and electron backscatter diffraction (EBSD)) of petrographic thin sections was carried out, using a Hitachi SU6600 Field Emission Gun-Scanning Electron Microscope (FEG-SEM) at the Western University Zircon and Accessory Phase Laboratory (ZAPLab). Zircon separation for geochronology was conducted at the Jack Satterly Geochronology lab at the University of Toronto using standard procedures. Secondary Ion Mass Spectrometer (SIMS) U-Pb isotopic analysis and Ti-thermometry was conducted at the Stanford/ U.S.G.S. SHRIMP-RG facility according to previously published procedures (Mazdab and Wooden 2006), and referenced to internal zircon geochronology standard VP-10 (Bowman et al. 2011). Lu-Hf isotope measurements of zircon were made by LA-MC-ICP-MS at the University of Bristol according to previously published procedures (Hawkesworth and Kemp 2006; Fisher et al. 2011). The standards used were Plešovice (Sláma et al. 2008) which had an average $^{176}Hf/^{177}Hf$ of 0.282487 ± 0.000023 (n = 20), Mud Tank (Woodhead and Hergt 2005) with an average of 0.282523 ± 0.000021 (n = 19) and Temora-2 (Woodhead and Hergt 2005) which had an average of 0.282700 ± 0.000044 (n = 9).

2.3 Results

2.3.1 Field Relationships and Mineral Textures

The bedrock at Sites 1 and 2 consists of polydeformed Archean ILG (granodioritic gneiss) with minor meta-ironstone inclusions, as is typical of the region (Stepto 1990). We report that within this are lenticular to dyke-like bodies of mafic composition that exhibit rubbly, spheroidal weathering surfaces and sharp contacts with the Mesoarchean granitoid gneiss (Figure 2-2).

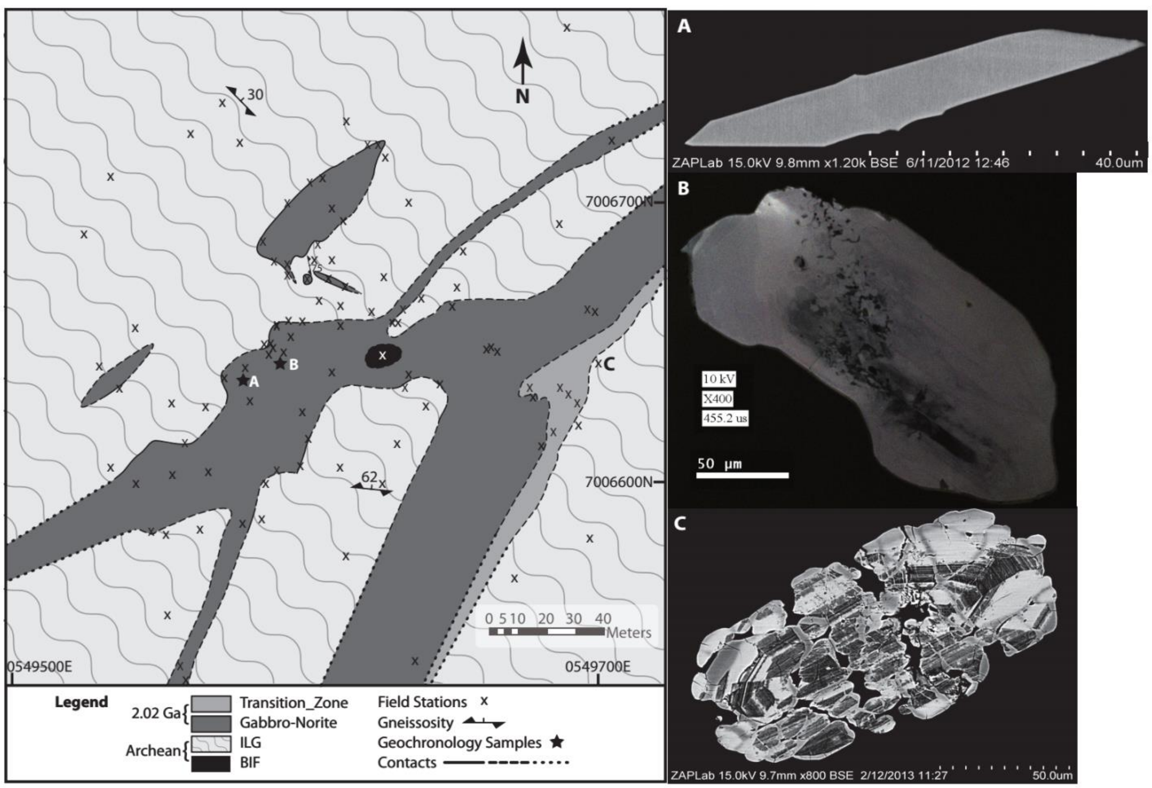

Figure 2-2. Geological map of Site 2 showing dykes and pods of gabbronorite within Mesoarchean ILG gneiss. The southeastern margin is referred to as the transition zone as it consists of a mixture of fine-grained gabbronorite and ILG units inter-fingered at the scale of meters to centimeters. Igneous zircon was analyzed from two Site 2 samples in the main body (A: V232 and B: V235). The BSE and CL images on the right show the typical zircon morphology for (A) prismatic igneous zircon from gabbronorite sample V235, (B) zircon with recrystallized xenocrystic core from gabbronorite sample V232 (see also Moser et al. 2011) and (C) shocked recrystallized Archean zircon from ILG, proximal to the transition zone (location indicated by “C”).

The map pattern is either a bifurcating or stockwork distribution, or trains of amoeboid-shaped bodies. Variations of mineral abundances determined using energy dispersive spectroscopy (EDS) analysis place the rock type at the boundary of gabbroic and noritic classification fields, and for simplicity is referred to here as gabbronorite. The pyroxenes have inverted pigeonite exsolution lamellae and subhedral to anhedral grain boundaries indicate some recrystallization. Similar textures were described for units interpreted as Archean mafic granulite by early workers (Schreyer et al. 1978; Stepto 1990). Gabbronorite bodies display a range of mineral textures from medium-grained and massive to weakly foliated at the center, to strongly foliated and finer grained near contacts with ILG. The fabric is defined by alignment of mafic and oxide minerals (Figure 2-3) but no evidence of shock microstructures or metamorphism was observed in the rock-forming minerals of the gabbronorite at either site.

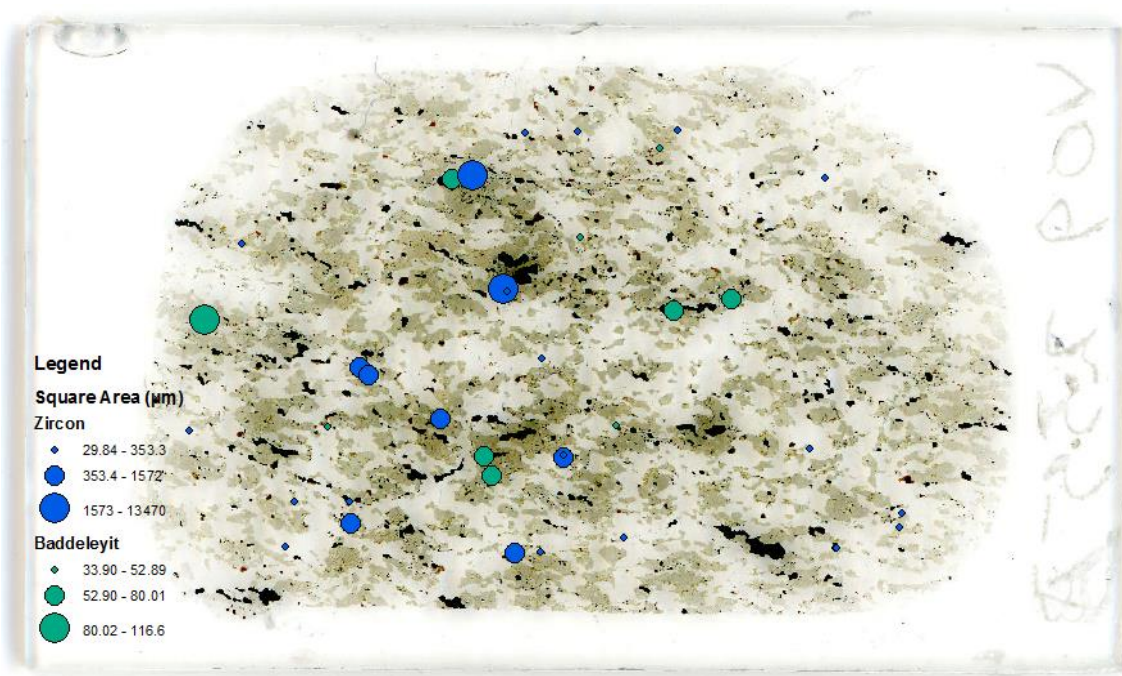

Figure. 2-3: MicroGIS of thin section V235 with distribution of zircons and baddeleyites, grain size is indicated by spot size.

2.3.2 Zircon Microstructure, Thermometry and U-Pb Geochronology

Zircon imaging CL and BSE, geochronology (U-Pb), and Ti thermometry were performed on zircon separates from samples of the ‘type’ mafic dyke at Site 1 (V250), and two samples from Site 2. Site 2 samples are of a fine grained (V235) and coarse grained (V232) massive gabbronorite. Lu-Hf analysis was also performed on zircons from samples V250 and V235. The CL reveals dominantly unshocked euhedral to subhedral grains with sharp oscillatory concentric planar growth bands (Figure 2-4) typical of igneous zircon (Corfu et al. 2003); likewise the co-existing baddeleyite is euhedral and shows no evidence of shock (Moser et al. 2013). Mapping and imaging of zircon type and location in thin section (Figure 2-3) reveals a random distribution relative to mineralogy, consistent with an igneous paragenesis. This is in sharp contrast with the neighboring ILG gneiss in which CL and EBSD analyses shows that zircons contain shock features such as microtwins over-printed by post-shock recrystallization (Figure 2-2C) (Moser et al. 2011). A subpopulation of gabbronorite zircons exhibits

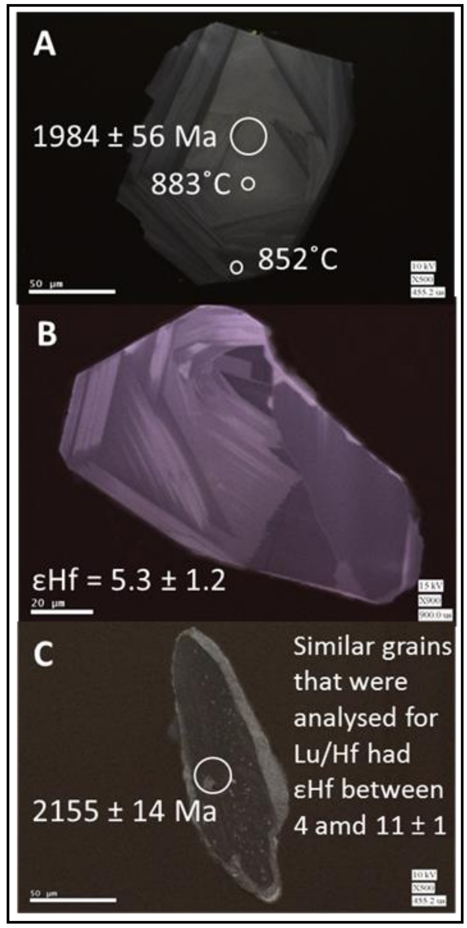

Figure 2-4: CL images of zircons from the gabbronorite body, polished to mid-plane and imaged by FEG-SEM.: (A) CL image of unshocked, igneous grain with typical oscillatory planar growth banding and sector zoning are from sample V232 at Site 2. Note the clearly different CL zoning patterns in the shocked and unshocked grains. This grain has a U-Pb age of 1984 ± 56 Ma and has a core temperature of 883˚C and a rim temperature of 852˚C. (B) CL image of an unshocked, igneous grain from V250 that was analyzed for Lu/Hf and has a εHf value of -5.3 ± 1.2. (C) CL image illustrates a shocked and recrystallized xenocrystic grain from sample V250 from Site 1, this grain has a U-Pb age of 2155 ± 14 Ma. Similar grains from this sample were analyzed for Lu/Hf ratios and have εHf values between 4 and 11 ± 1.

irregular to chaotic CL patterns, planar features, and a higher abundance of inclusions similar to ILG zircons and these are interpreted as xenocrysts from the host felsic gneiss (Figure 2-2B) (Moser 1997; Moser et al. 2011). Based on thin section analysis, xenocrysts are slightly more abundant (~60%) than igneous grains in the narrow gabbronorite dyke from Site 1 suggesting significant crustal contamination, whereas in samples V232 and V235 of the larger body at Site 2, igneous grains are dominant (>90%). SHRIMP U-Pb data from the igneous zircons are generally concordant, with evidence of weak discordance due to a minor 1.1 Ga Pb-loss event known in the region (Moser et al. 2011). The upper intercept age for igneous zircons from V250 is 2036 ± 45 Ma, in agreement with the ID-TIMS age of 2019 ± 2 Ma for this sample (Moser 1997). Data for igneous zircons from samples V232 and V235 have a combined upper intercept age of 2039 ± 33 Ma, also overlapping the 2020 ± 3 Ma age of impact (Table 1).

Ti-in-zircon thermometry of igneous zircons from V250, V232 and V235, was calculated using a TiO_2 activity = 0.7 due to the presence of ilmenite in all the samples (Ghent and Stout 1984; Ferry and Watson 2007). The apparent (Fu et al. 2008) Ti-in-zircon crystallization temperatures range from 928 ± 10˚C to 795 ± 8.7˚C (See Table 2-2). One grain from V235 shows core to rim apparent temperature decrease of ~ 40˚C and three zircons from sample V232 show an average core to rim decrease of ~ 50˚C.

2.3.3 Lu-Hf Isotope Composition

Six igneous grains and two xenocrysts from sample V250 (Site 1) and eight igneous grains from sample V235 (Site 2) were analyzed. The igneous grains from Site 1 have εHf of -1.4 to -5.3, and the grains from Site 2 have εHf of -5.4 to -7.9 (Table 3 and Figure 2-5). The two xenocrysts from V250 were not analyzed for U-Pb age, but are assumed to have had a primary age between 2.7 and 3.2 Ga based on xenocryst dating in this unit (Moser 1997; Moser et al.

2011). When modeled at these ages, the xenocryst εHf values are +0.4 and +11, respectively. The depleted mantle age of the source of the gabbronorite magma is also between 2.7 Ga and 3.2 Ga assuming a 176Lu/177Hf reservoir value of 0.021 for crust derived from melting of mafic crust (Kemp et al. 2006).

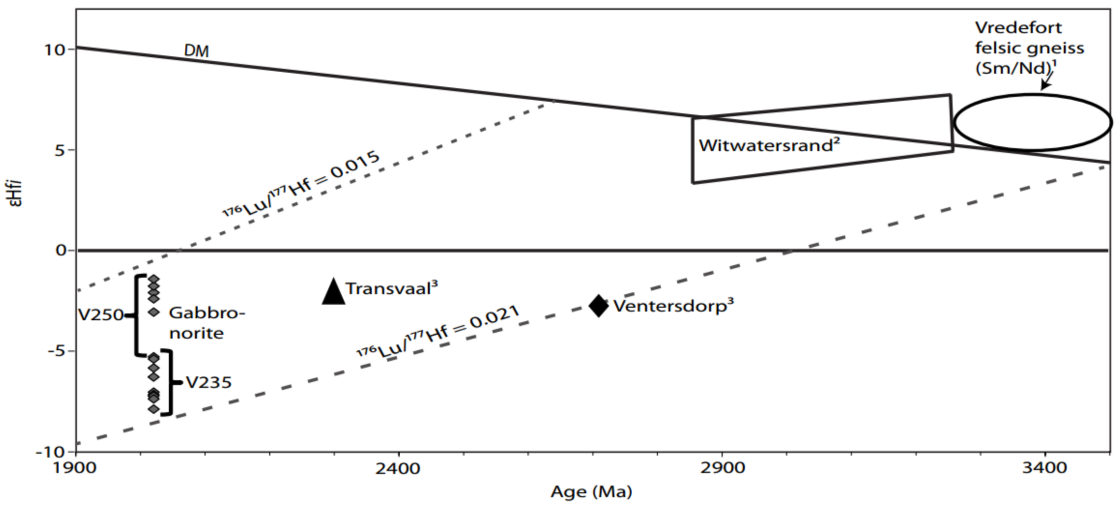

Figure 2-5. Plot of εHf of gabbronorite zircon at 2020 ± 3 Ma age of the impact compared to values for target lithologies. Samples from this study are shown as small gray diamonds. We use a Lu/Hf model ratio of 0.021 to determine the TDM range of 3.2 to 2.7 Ga for the gabbronorite source. The evolution path for the average continental crust with 176Lu/177Hf = 0.015 is shown for comparison. The range of gabbronorite TDM overlaps the Sm/Nd model age for gneisses half way from the center of the Vredefort dome (oval, from Hart et al. 1990)[1]; as well as zircon Hf TDM for the Witwatersrand (box) (Zeh and Gerdes 2012)[2], Ventersdorp (diamond) and Transvaal (triangle) (Stevenson and Patchett 1990)[3].

Table 2-1: U-Pb Data for V250, V232 and V235

Sample #	**207/206 age**	**2sd error**	**Conc (%)**	**204 cts/ sec**	**204 /206**	**Pb/U: UO/U²**	**% error**	**Pb²⁰⁴ Corr 207r/ 206r**	**% error**
V09_232									
V09_232_ 1.1	1993	46	2	0.06	8.5E-5	.02779	1.1	.1225	1.3
V09_232_ 2.1	1984	56	0	0.07	1.3E-4	.02828	1.3	.1219	1.6
V09_232_ 3.1	2000	40	0	0.05	5.0E-5	.02845	1.0	.1230	1.1
V09_232_ 4.1	2013	40	0	-0.07	-7.1E-5	.02874	1.0	.1239	1.1
V09_232_ 5.1	1995	60	1	0.05	1.0E-4	.02822	1.3	.1227	1.7
V09_232_ 7.1	2035	44	2	0.06	8.1E-5	.02830	1.1	.1255	1.3
V09_232_ 8.1	2003	36	1	-0.13	-9.3E-5	.02807	0.8	.1232	1.0
V09_235									
V09_235_ 1.1	1994	30	-1	0.10	5.5E-5	.02888	0.7	.1225	0.9
V09_235_ 2.1	2015	28	1	0.07	3.8E-5	.02839	0.7	.1240	0.8
V09_235_ 3.1	2089	74	3	-0.21	-3.6E-4	.02885	1.4	.1293	2.1
V09_235_ 4.1	2025	34	4	0.03	2.5E-5	.02747	0.9	.1248	1.0
V09_235_ 5.1	2018	52	8	0.04	7.2E-5	.02628	1.2	.1243	1.4
V09_235_ 6.1	2003	32	2	0.06	4.1E-5	.02787	0.8	.1232	0.9
V09_235_ 7.1	2015	26	3	0.00	---	.02783	0.7	.1240	0.7
V09_235_ 8.1	2015	30	3	0.09	5.6E-5	.02773	0.7	.1240	0.8
V09_235_ 9.1	2005	40	8	0.08	8.3E-5	.02628	0.9	.1234	1.1
V09_250									
V09_250_ 1.1	2009	48	2	0.06	7.1E-5	.02802	1.0	.1236	1.4
V09_250_ 4.1	2030	50	1	0.00	---	.02864	1.3	.1251	1.4
V09_250_ 5.1	2016	38	1	0.00	---	0.2843	1.0	.1241	1.1

Table 2-1: U-Pb Data for V250, V232 and V235 Continued

Sample #	**Pb^{204} Corr 207r/235r**	**% error**	**Pb^{204} Corr 207r/238**	**% error**	**Err corr**	**U (ppm)**	**Th (ppm)**	**Th/U**
V09_232								
V09_232 _1.1	5.99	1.7	.3547	1.1	.653	37	17	0.49
V09_232 _2.1	6.06	2.1	.3606	1.3	.637	27	10	0.38
V09_232 _3.1	6.16	1.5	.3632	1.0	.670	53	27	0.53
V09_232 _4.1	6.28	1.5	.3676	1.0	.649	51	26	0.52
V09_232 _5.1	6.09	2.1	.3600	1.3	.621	33	11	0.35
V09_232 _ 7.1	6.25	1.7	.3611	1.1	.661	48	38	0.82
V09_232 _8.1	6.10	1.3	.3591	0.8	.633	81	41	0.51
V09_235								
V09_235 _1.1	6.23	1.1	.3687	0.7	.630	111	49	0.46
V09_235 _2.1	6.20	1.1	.3625	0.7	.666	106	48	0.46
V09_235 _3.1	6.61	2.6	.3706	1.5	.570	34	14	0.42
V09_235 _4.1	6.04	1.3	.3509	0.9	.655	90	54	0.62
V09_235 _5.1	5.75	1.9	.3355	1.2	.643	48	21	0.45
V09_235 _6.1	6.04	1.2	.3558	0.8	.655	106	62	0.61
V09_235 _7.1	6.08	1.0	.3556	0.7	.681	140	81	0.60
V09_235 _8.1	6.05	1.1	.3541	0.7	.653	117	46	0.40
V09_235 _9.1	5.70	1.5	.3353	0.9	.636	93	54	0.60
V09_250								
V09_250 _1.1	6.10	1.7	.3576	1.0	.613	50	17	0.36
V09_250 _4.1	6.31	1.9	3659	1.3	.691	29	7	0.24
V09_250 _5.1	6.22	1.5	.3633	1.0	.685	59	17	0.30

Table 2-2: Ti-in-zircon data

Sample	Ti 48(ppm)	Ti 49(ppm)	T (˚C)
V09-232-1.3TE	19.1	19.2	833
V09-232-2.2TE	30.1	30.3	883
V09-232-2.3TE	22.7	22.9	852
V09-232-3.2TE	27.1	27.8	873
V09-232-3.3TE	17.8	19.0	832
V09-232-4.2TE	32.5	32.2	890
V09-232-5.2TE	24.0	23.9	857
V09-232-5.3TE	13.2	13.2	795
V09-232-6.2TE	38.4	38.2	910
V09-232-6.3TE	30.8	31.9	889
V09-232-7.2TE	29.4	27.8	874
V09-232-7.3TE	18.2	17.5	824
V09-232-8.2TE	15.2	14.4	804
V09-232-9.4TE	31.5	31.2	887
V09-232-9.5TE	30.5	30.8	885
V09-232-9.6TE	32.7	34.0	897
V09-235-1.2TE	18.6	18.9	832
V09-235-2.2TE	15.8	15.6	812
V09-235-3.2TE	44.9	44.1	928
V09-235-4.2TE	18.7	18.3	828
V09-235-5.2TE	26.8	27.2	871
V09-235-6.2TE	22.7	21.9	847
V09-235-7.2TE	19.0	19.0	832
V09-235-8.2TE	18.0	17.5	824
V09-235-9.2TE	20.8	20.9	842
V09-235-9.3TE	29.4	29.6	880
V09-235-10.2TE	18.0	17.5	824
V09-250-1.2TE	22.7	22.3	849
V09-250-2.2TE	19.1	19.9	837
V09-250-3.2TE	45.0	42.9	924
V09-250-4.2TE	18.3	17.9	826
V09-250-5.2TE	23.4	22.5	850
V09-250-6.2TE	27.1	26.3	867
V09-250-6.3TE	24.0	24.2	858

Table 2-3: Lu-Hf data

Name	Age Ma ±1σ	$^{176}Lu/^{177}Hf$	$^{176}Yb/^{177}Hf$	$^{176}Hf/^{177}Hf$	±1σ	εHfT ±2σ	T(DM)[c] Ma
V250- Z1	2020	0.000595	0.025532	0.281345	0.000017	-5.3 1.2	2993
V250- Z2	2020	0.000858	0.032652	0.281435	0.000019	-2.1 1.3	2791
V250- Z6	2020	0.000549	0.023084	0.281407	0.000014	-3.1 1.0	2853
V250- Z9	2020	0.000439	0.017480	0.281426	0.000011	-2.4 0.8	2811
V250- Z10	2020	0.000556	0.023501	0.281454	0.000016	-1.4 1.1	2748
V250- Z11	2020	0.000389	0.015887	0.281443	0.000012	-1.8 0.9	2772
V250- Z12	2700	0.001548	0.064351	0.281060	0.000015	0.4 1.1	3166
V250- Z13	3200	0.001188	0.048438	0.281036	0.000013	11.4 1.0	2855
V235- Z15	2020	0.000689	0.027850	0.281296	0.000011	-7.0 0.8	3104
V235- Z16	2020	0.000560	0.022015	0.281290	0.000015	-7.2 1.0	3116
V235- Z20	2020	0.000398	0.015387	0.281342	0.000020	-5.4 1.4	3000
V235- Z21	2020	0.000445	0.016924	0.281317	0.000016	-6.3 1.2	3057
V235- Z25	2020	0.000281	0.010548	0.281292	0.000015	-7.2 1.1	3112
V235- Z26	2020	0.000652	0.024328	0.281329	0.000013	-5.8 0.9	3028
V235- Z27	2020	0.000529	0.020668	0.281286	0.000015	-7.4 1.0	3126
V235- Z30	2020	0.000418	0.016673	0.281272	0.000020	-7.9 1.4	3158

[c] Stands for crustal source.

2.4 Discussion

Our new mapping, petrologic, and zircon geochronology and geochemistry data reveal properties of the Vredefort gabbronorite bodies that are consistent with an origin through impact melting of the Kaapvaal craton, with implications for ancient crustal and mineral residua (e.g. Cavosie et al. 2010). Pyroxene exsolution textures are typical of rapidly cooled gabbroic bodies and show no evidence of shock metamorphism. The cogenetic spatial relationship of igneous-zoned zircon and coexisting baddeleyite with primary minerals, and the consistency of their ages with the previous ID-TIMS U-Pb zircon age of 2019 ± 2 Ma for this rock type (Moser 1997), indicate crystallization shortly after the Vredefort impact event. An intrusive process is supported by the presence of ILG inclusions and the map pattern of the gabbronorite, which is reminiscent of basal melt sheet embayments on the original crater floor at Sudbury (Morrison 1984). The temperature range for the crystallization of Vredefort impact melt zircons is between

795 and 928˚C, high for tectonically generated crustal melts (Wei et al. 2008) but in concordance with Ti-in-zircon temperatures of mafic basal units of the Sudbury Igneous Complex (Darling et al. 2009) and zircon saturation modeling (Wielicki et al. 2012). At the lower end of the temperature range, our values overlap those of 750 and 810˚C unshocked zircon from "mafic pseudotachylite breccias" (Wielicki et al. 2012) that are more likely a xenolithic transitional contact to gabbronorite. Zircons from the ILG gneiss, however, are distinctively shocked and partially recrystallized with disturbed Archean U-Pb ages (Moser 1997; Moser et al. 2011). Similar microstructures are observed in SEM analyses of the 5 to 10 cm long felsic inclusions in the transition zone at Site 2, most simply interpreted as incomplete assimilation of ILG country rock into rapidly emplaced mafic melt.

The locally developed grain fabric within the gabbronorite bodies is the basis for their longstanding interpretation as pre-impact Archean rocks, however, the geochronology data dictate that this is a post-impact fabric restricted to this unit and its contacts and hence we call on its genesis by either flow and/or localized deformation during the crater modification stage. Numerical modeling by Ivanov (2005) points to an original melt sheet volume for the Vredefort impact structure of ~13,000 km^3 that took ~10 Myr to cool at the base, in the aftermath of ~20 km of central crater excavation and rebound (Henkel and Reimold 1996). Localized downward intrusion and deformation during subsequent isostatic readjustment of the crater floor, while the deep melt sheet remained molten, could explain the gabbronorite field and textural characteristics. This would have occurred after intrusion of the granophyre dykes in the outer regions of the central uplift, thought to be similar to the Sudbury offset dykes that formed before melt sheet differentiation (Lightfoot and Farrow 2002).

The highly negative εHf values for igneous zircon from the gabbronorite (Figure 2-5) indicate that it crystallized from either a crustally-contaminated mantle melt, or a melt derived from Archean crust and/or derivative sediments. The highest εHf values, from Site 1, could be interpreted as reflecting impact triggered mafic magmatism, which would bring into question how deeply the impact affected the crust and underlying mantle beyond impact-triggered flow at the crust-mantle boundary (Moser et al. 2009). However, the Hf model (depleted mantle) age for the gabbronorite source, which falls between 3.16 to 2.68 Ga (Figure 2-5), also overlaps the Hf model age of zircons from the Witwatersrand supergroup (Zeh and Gerdes 2012) and Ventersdorp and Transvaal units (Stevenson and Patchett 1990) that would have melted to form the Vredefort melt sheet. As a similar 3.2 Ga Sm-Nd model age is exhibited by the 2.02 Ga bronzite granophyre dykes that have crustal and meteoritic composition (Koeberl et al. 1996), a melt sheet origin for the gabbronorite is favoured. Taken together, we hypothesize an origin for the gabbronorite by downward injection from a large overlying differentiated melt sheet, similar to those at the Sudbury and Manicouagan (O'Connell-Cooper and Spray 2011) impact structures, at some point during the crater modification stage. The large variation in εHf values of V250 and V235, is similar to that seen in Sm-Nd compositions of the Sudbury Sublayer (Prevec et al. 2000) and at this point are attributed to isotopic variation in local, upper crustal target lithology.

The archetypal Archean cratonic crust is composed of multiply deformed granitoid gneisses, containing subordinate supra-crustal and mafic meta-igneous units, which exhibit one or more generations of mineral fabric (Kusky and Polat 1999). Our evidence demonstrates that a ~300 km^2 crustal assemblage with similar macroscopic features can also be created through ancient impact processes, and mistaken as tectonic in origin. Zircon igneous and shock microstructures, high Ti-in zircon crystallization temperatures and perhaps highly negative εHf values allow discrimination of relic impact-generated igneous units, or their residual zircon, and are a useful guide in the search for surviving continental residua of the large impacts that almost certainly affected the early crust of our planet.

2.5 Conclusions

Detailed field mapping and petrographic analysis, along with zircon microstructural, trace element and isotopic data, indicate an impact melting origin for gabbronorite bodies within the Archean gneisses of the Vredefort Dome or central uplift. We interpret these bodies to be relics of the Vredefort impact melt sheet, injected into the basement during crater modification. Long mistaken as part of the deep crustal Archean gneiss assemblage, the discovery of this impactite provides an opportunity to study the relationship of the deep melt sheet and dynamic central crater floor in a large impact environment that is rarely accessible but perhaps more common on Early Earth continental crust. One may ask: how many more such impact-generated assemblages exist in today's cratonic fragments? Further characterization of the petrogenesis and fabric development of the Vredefort gabbronorite bodies is under way. Their recognition makes the central region of the Earth's largest known impact an analogue site that is uniquely important in understanding crustal modification by impact processes.

2.6 References

Bishopp, D.W. 1962. The Vredefort Ring: A further consideration. Geology, **70**: 500-502.

Bowman, J.R., Moser, D.E., Valley, J.W., Wooden, J.L., Kita, N.T. and Mazdab, F.K. 2011. Zircon U-Pb isotopic, $\delta^{18}O$ and trace element response to 80 m.y. of high temperature metamorphism in the lower crust: sluggish diffusion and new records of Archean craton formation. American Journal of Science, **311**:719-772. DOI 10.2475/09.2011.01.

Cavosie, A.J., Quintero, R.R., Radovan, H.A. and Moser, D.E. 2010. A record of ancient cataclysm in modern sand: Shock microstructures in detrital minerals from the Vaal River, Vredefort Dome, South Africa. GSA Bulletin, **122**: 1968-1980. doi: 10.1130/B30187.1.

Corfu, F., Hanchar, J.M., Hoskin, P.W.O. and Kinny, P. 2003. Atlas of Zircon Textures. *In* Zircon. *Edited by* Hanchar, J.M., and Hoskin, P.W.O. Reviews in Mineralogy and Geochronology, **53**: 469–500.

Darling, J., Storey, C. and Hawkesworth, C. 2009. Impact melt sheet zircons and their implications for the Hadean crust. Geology, **37**: 927–930. doi:10.1130/G30251A.1.

Ferry, J.M. and Watson, E.B. 2007. New thermodynamic models and revised calibrations for the Ti-in-zircon and Zr-in-rutile thermometers: Contributions to Mineralogy and Petrology. **154**: 429–437. doi:10.1007/s00410-007-0201-0.

Fisher, C.M., Hanchar, J.M., Samson, S.D., Dhuime, B., Blichert-Toft, J., Vervoort, J.D. and Lam, R. 2011. Synthetic zircon doped with hafnium and rare earth elements: A reference material for in situ hafnium isotope analysis. Chemical Geology, **286**: 32-47.

Fu, B., Page, F.Z., Cavosie, A.J., Fournelle, J., Kita, N.T., Lackey, J.S., Wilde, S.A. and Valley, J.W. 2008. Ti-in-zircon thermometry: applications and limitations. Contributions to Mineralogy and Petrology, **156**: 197-215.

Ghent, E.D. and Stout, M.Z. 1984. TiO2 activity in metamorphosed pelitic and basic rocks: Principles and applications to metamorphism in southeastern Canadian Cordillera. Contributions to Mineralogy and Petrology, **86**: 248–255. doi:10.1007/BF00373670.

Gibson, R.L., Armstrong, R.A. and Reimold, W.U. 1997. The age and thermal evolution of the Vredefort impact structure: A single-grain U-Pb zircon study. Geochimica et Cosmochimica Acta, **61**: 1531–1540. doi:10.1016/S0016-7037(97)00013-6.

Gibson, R.L., Reimold, W.U. and Stevens, G. 1998. Thermal-metamorphic signature of an impact event in the Vredefort Dome, South Africa. Geology, **26**:787–790, doi:10.1130/0091-7613(1998)026<0787:TMSOAI>2.3.CO;2.

Gibson, R.L. and Reimold, W.U. 2008. Geology of the Vredefort impact structure, a guide to sites of interest. Council of Geoscience, Memoir 97, Pretoria, 181 p.

Garde, A.A., McDonald, I., Dyck, B. and Keulen, N. 2012. Searching for giant, ancient impact structures on Earth: The Mesoarchean Maniitsoq structure, West Greenland. Earth and Planetary Science Letters, **337–338**: 197–210. doi:10.1016/j.epsl.2012.04.026.

Grieve, R.A.F. and Cintala, M.J. 1992. An analysis of differential impact melt-crater scaling and implications for the terrestrial impact record. Meteoritics, **27**: 526–538. doi:10.1111/j.1945-5100.1992.tb01074.x.

Grieve, R.A.F., Coderre, J.M., Robertson, P.B. and Alexopoulos, J. 1990. Microscopic planar deformation features in quartz of the Vredefort structure: Anomalous but still suggestive of an impact origin. Tectonophysics, **171**: 185-200. doi:10.1016/0040-1951(90)90098-S.

Hart, R.J., Andreoli, M.A.G., Tredoux, M. and DeWit, M.J. 1990. Geochemistry across an exposed section of Archaean crust at Vredefort, South Africa: With implications for mid-crustal discontinuities. Chemical Geology, **82**: 21–50. doi:10.1016/0009-2541(90)90072-F.

Hawkesworth, C.J., and Kemp, A.I.S. 2006. Using hafnium and oxygen isotopes in zircons to unravel the record of crustal evolution. Chemical Geology, **226**:144–162. doi:10.1016/j.chemgeo.2005.09.018 13.

Henkel, H. and Reimold, W.U. 1996. Geophysical modeling and reconstruction of the Vredefort Impact Structure, South Africa. Meteoritics & Planetary Science, **31**: 59.

Henkel, H. and Reimold, W.U. 1998. Integrated geophysical modelling of a giant, complex impact structure: Anatomy of the Vredefort Structure, South Africa. Tectonophysics, **287**:1–20, doi:10.1016/S0040-1951(98)80058-9.
Ivanov, B.A. 2005. Modeling of the largest terrestrial meteoritecraters. Solar System Research, **39**: 381–409. doi:10.1007/s11208-005-0051-0.

Kamo, S.L., Reimold, W.U., Krogh, T.E. and Colliston, W.P. 1996. A 2.023 Ga age for the Vredefort impact event and a first report of shock metamorphosed zircons in pseudotachylitic breccias and granophyres. Earth and Planetary Science Letters, **144**: 369–387. doi:10.1016/S0012-821X(96)00180-X.

Kemp, A.I.S., Hawkesworth, C.J., Paterson, B.A. and Kinny, P.D. 2006. Episodic growth of the Gondwana supercontinent from hafnium and oxygen isotopes in zircon. Nature, **439**: 580-583, doi:10.1038/nature04505.

Koeberl, C., Reimold, W.U. and Shirey, S.B. 1996. Re-Os isotope and geochemical study of the Vredefort Granophyre: Clues to the origin of the Vredefort structure, South Africa. Geology, **24**: 913–916. doi:10.1130/0091-7613(1996)024<0913:ROIAGS>2.3.CO;2.

Kring, D.A. and Cohen, B.A. 2002. Cataclysmic bombardment throughout the inner solar system 3.9–4.0 Ga. Journal of Geophysical Research, **107**: 4–6, doi:10.1029/2001JE001529.

Kusky, T.M. and Polat, A. 1999 Growth of granite-greenstone terranes at convergent margins, and stabilization of Archean cratons. Tectonophysics, **305**: 43–73. doi:10.1016/S0040-1951(99)00014-1.

Lightfoot, P.C. and Farrow, C.E.G. 2002. Geology, Geochemistry, and Mineralogy of the Worthington Offset Dike: A Genetic Model for Offset Dike Mineralization in the Sudbury Igneous Complex. Economic Geology, **97**: 1419-1446.

Mazdab, F.M. and Wooden, J.L. 2006. Trace element analysis in zircon by ion microprobe (SHRIMP-RG); technique and applications. Geochimica et Cosmochimica Acta, **70**(Supp.1): A405, doi:10.1016/j.gca.2006.06.817.

Morrison, G.G. 1984. Morphology of the Sudbury Structure in relation to an Impact Origin. *In* The Geology and Ore Deposits of the Sudbury Structure. *Edited by* Pye, E.G., Naldrett, A.J., and Giblin, P.E. Ontario Geological Survey, Special Volume **1**: 513–520.

Moser, D.E. 1997. Dating the shock wave and thermal imprint of the giant Vredefort impact, South Africa. Geology. **25**: 7–10. doi:10.1130/0091-7613(1997)025<0007:DTSWAT>2.3.CO;2.

Moser, D.E., Davis, W.J., Reddy, S.M., Flemming, R.L. and Hart, R.J. 2009. Zircon U-Pb strain chronometry reveals deep impact-triggered flow. Earth and Planetary Science Letters, **277**:73–79. doi:10.1016/j.epsl.2008.09.036.

Moser, D.E., Cupelli, C.L., Barker, I.R., Flowers, R.M., Bowman, J.R., Wooden, J. and Hart, J.R. 2011. New Zircon Shock Phenomenon and their use for Dating and Reconstruction of Large Impact Structures Revealed by Electron Nanobeam (EBSD, CL, EDS), and Isotopic U-Pb, and (U-Th)/He Analysis of the Vredefort dome. Canadian Journal of Earth Sciences, **4**: 117–139.

Moser, D.E., Chamberlain, K.R., Tait, K.T., Schmitt, A.K., Darling, J.R., Barker, I.R. and Hyde, B.C. 2013. Solving the Martian meteorite age conundrum using micro-baddeleyite and launch-generated zircon. Nature, **499**: 454–457. doi:10.1038/nature12341.

O'Connell-Cooper, C.D. and Spray, J.G. 2011. Geochemistry of the impact-generated melt sheet at Manicouagan: Evidence for fractional crystallization. Journal of Geophysical Research (Solid Earth), **116**: B06204. doi:10.1029/2010JB008084.

Prevec, S.A., Lightfoot, P.C. and Keays, R.R. 2000. Evolution of the Sublayer of the Sudbury Igneous Complex: Geochemical, Sm-Nd isotopic and petrologic evidence. Lithos, **51**: 271–292. doi:10.1016/S0024-4937(00)00005-0.

Schreyer, W., Stepto, D., Abraham, K. and Muller, W.F. 1978. Clinoeulite (Magnesian Clinoferrosilite) in a Eulysite of a Metamorphosed Iron Formation in the Vredefort Structure, South Africa. Contributions to Mineralogy and Petrology, **65**: 351–361. doi:10.1007/BF00372283.

Sláma, J., Košler, J., Condon, D. J., Crowley, J. L., Gerdes, A., Hanchar, J. M., Horstwood, M. S. A., Morris, G. A., Nasdala, L., Norberg, N., Schaltegger, U., Schoene, B., Tubrett, M. N. and Whitehouse, M. J. 2008. Plešovice zircon — A new natural reference material for U–Pb and Hf isotopic microanalysis. Chemical Geology, **249**:1-35.

Spray, J.G., Kelley, S.P. and Reimold, W.U. 1995. Laser probe argon-40/argon-39 dating of coesite and stishovite-bearing pseudotachylytes and the age of the Vredefort impact event. Meteoritics, **30**: 335–343. doi:10.1111/j.1945-5100.1995.tb01132.x.

Stepto, D. 1990. The geology and gravity field in the central core of the Vredefort structure. Tectonophysics, **171**: 75–103. doi:10.1016/0040-1951(90)90091-L.

Stevenson, R.K. and Patchett, P.J. 1990. Implications for the evolution of continental crust from Hf isotope systematic of Archean detrital zircons. Geochimica et Cosmochimica Acta, **54**: 1683–1697. doi:10.1016/0016-7037(90)90400-F.

Walraven, F., Armstrong, R.A. and Kruger, F.J. 1990. A chronostratigraphic framework for the north-central Kaapvaal craton, the Bushveld Complex and the Vredefort structure. Tectonophysics, **171**: 23–48. doi:10.1016/0040-1951(90)90088-P.

Wei, C.S., Zhao, Z.F. and Spicuzza, M.J. 2008. Zircon oxygen isotopic constraint on the sources of late Mesozoic A-type granites in eastern China. Chemical Geology, **250**: 1–15. doi:10.1016/j.chemgeo.2008.01.004.

Wielicki, M.M., Harrison, T.M. and Schmitt, A.K. 2012. Geochemical signatures and magmatic stability of terrestrial impact produced zircon. Earth and Planetary Science Letters, **321–322**: 20–31. doi:10.1016/j.epsl.2012.01.009.

Woodhead, J. D. and Hergt, J. M. 2005. A Preliminary Appraisal of Seven Natural Zircon Reference Materials for In Situ Hf Isotope Determination. Geostandards and Geoanalytical Research, **29**: 183-195.

Zeh, A. and Gerdes, A. 2012. U-Pb and Hf isotope record of detrital zircons from gold-bearing sediments of the Pietersburg Greenstone Belt (South Africa)—Is there a common provenance with the Witwatersrand Basin. Precambrian Research, **204–205**: 46–56. doi:10.1016/j.precamres.2012.02.013.

Chapter 3: Petrogenesis of a Gabbronorite Impact Melt Body in the Central Uplift of the Vredefort Impact Structure: South Africa

***Cupelli, C.L.[1], Moser, D.E.[1], Barker, I.R.[1], Lightfoot, P.C.[2,3]**

[1]*Earth Science, University of Western University, 1151 Richmond Street, London, Ontario, N6A 5B7, Canada.*

[2]*Department of Earth Sciences, Laurentian University, Sudbury, Ontario, P3E 2C6, Canada.*

3.1 Introduction

Meteorite impact cratering is a ubiquitous process within the solar system, and has had a significant effect on the Earth's crust and habitability during the early bombardment period between 3.9 to 4.5 Ga (Grieve 1980; Kring and Cohen 2002; Marchi et al. 2014). Beyond the initial few minutes of impact, the geological effects of large scale meteorite impacts, particularly on early continental crustal targets, are poorly understood due to a lack of preservation. The exposed country rocks of the 2.02 Ga Vredefort impact structure, from extensive erosion, is one of the best studied analogues, which demonstrates the effects of impacts on early terrestrial and lunar crust (Gibson et al. 2002). The depth of erosion offers a rare opportunity to explore large scale impact processes in detail at the crater-crust interface.

As a result of extensive erosion, occurring over the past 2.02 Ga, the Vredefort Impact Structure, in Gauteng Province, South Africa, (See Chapter 2, Figure 2-1) allows an opportunity to observe basement rocks that are located at the centre of Earth's oldest and largest known impact structure. Vredefort was first recognized as an impact structure in 1961, when Dietz (1961a) proposed that the pseudotachylites found in the area were a product of an impact event. However, the strongest piece of evidence that a much larger structure was originally present is the central uplift, or dome. The original impact basin is thought to have been ~300 km in diameter and many scientists have considered that, much like its sister impact in Sudbury, it once had a large, possibly differentiated, melt sheet (French and Nielsen 1990; Cupelli et al. 2014). Vredefort and Sudbury, are both multi-ring impact structures with relatively similar ages (Sudbury is dated at 1850.5 ± 3 Ma (Krogh et al. 1984)) and similar sizes (Sudbury has an original diameter of 250 km (Spray et al. 2004)). One major difference between the two structures is their degree of preservation, while the Vredefort impact has been eroded to expose the 3.1 Ga target rocks, the Sudbury impact has been preserved by deformation. The Sudbury Igneous Complex (SIC), is now an elliptical body, approximately 27 km by 60 km in size (Murphy and Spray 2002), and ~2.5 km thick (Tuchscherer and Spray 2002). The SIC is the best known example of a differentiated impact melt sheet, which includes noritic rocks with ultramafic to mafic inclusions at the bottom of the sheet and granophyre at the top, however, it is not the only impact structure with a differentiated melt sheet nor the only one to contain mafic rocks. The younger and smaller Morokweng impact structure, located in North West Provence, South Africa, has some degree of differentiation in its melt sheet, which is composed of quartz rich norite (Andreoli et al. 1999). Melts found within impact craters on the Moon also contain mafic components (Gibson et al. 2002). A common unit is impact derived mafic breccias, which obscure the identification of the protolith rock. Since large melt sheets are thought to have more time to differentiate, creating mafic units on the bottom and progressively more felsic units upwards, it is probable that any remaining unit of the Vredefort impact melt would be a mafic unit located at the base of the original melt sheet.

The size of the Vredefort impact structure was larger than Sudbury and both targets were composed of Archean granofels and Proterozoic volcanics and sediments, then Vredefort must have also once hosted a melt body as large as or larger than that developed at Sudbury. Only a few confirmed rock types have been found at Vredefort that are directly linked to a melt sheet or impact melting, which includes granophyre dykes, a biotite rich granite, and a gabbronorite body. The most widely accepted impact melt bodies at Vredefort are the granophyre dykes that constrain the age of the impact event (Walraven et al. 1990) and are thought to have been injected into the target rock by a similar process to that forming the offset dykes at Sudbury (Therriault et al 1996). French et al. (1989) found that the Ir signature of the granophyre was too small to accurately confirm an extraterrestrial contribution to Vredefort, but compositional analysis supports the idea that the dykes were produced by mixing the target rocks. This implies that the Vredefort granophyres were produced by crustal melting. Further evidence of an impact origin of Vredefort was provided by Koeberl et al. (1996) who discovered that the bodies have a Re-Os isotope composition indicative of a meteorite contribution. The second impact related body at Vredefort is a biotite rich granite termed the Central Anatectic Granite (CAG), and based on its granitic composition, and age (2017 ± 5 Ma (Gibson et al. 1997)), it is believed to have been derived through partial melting due to impact, from the host Archean Inlandsee Leucogranofels (ILG) (Gibson et al. 1997). In an outcrop ~1.5 km away from the CAG, Moser (1997) reported the presence of a 0.5 m wide dyke-like body in the centre of the uplift, which was shown to be a gabbronorite, formed from an impact melt related to the Vredefort event (Chapter 2: Cupelli et al. 2014). The relative contribution of mantle versus crustal material to the parent magma of the gabbronorite are equivocal and the timing and conditions of its emplacement are not fully understood. This paper contains a multi-scale analysis of the mineralogy, texture and strain history of the gabbronorite and its accessory minerals; it draws comparisons to the ILG, CAG, and other units like the granophye dykes (Koeberl et al. 1996) to establish the source of the gabbronorite melt. This research offers an opportunity to better understand deep level processes in impact craters that may not be preserved at accessible levels of erosion at other structures such as the Sudbury impact structure. These rocks also record evidence of mantle versus crustal contributions, constrain impactor composition, and help investigate crater modification process during stabilization.

3.2 Background Geology

The Vredefort impact structure is located in the deeply eroded Kaapvaal Craton, and based on the 'Crust on Edge Model' (Hart et al. 1981), the Vredefort dome is believed to represent a cross section of the craton's continental crust. Prior to the impact event, the now exposed Archean basement rocks were overlain by: the Dominion Group and the Witwatersrand, Ventersdorp and Transvaal Supergroups; these units were deposited between 3.07 and approximately 2.25 Ga ago, and consist of a mix of volcanics and sediments (Armstrong et al. 1991). Due to the formation of the central uplift, these units make up the collar rocks of the Vredefort dome (Reimold and Gibson 1996). The Outer Granite Gneiss dated at 3.08 Ga by U-Pb methods (Hart et al. 1981) represents the exposed upper continental crust, while the ILG, which is the dominant rock unit surrounding the gabbronorite in the Vredefort central uplift, represents the deeper continental crust and has a U-Pb age of 3.29 Ga (Moser 1997).

The ILG is a multiply deformed unit that has undergone four Archean deformation events. The oldest fabric (S1) is defined by gneissic foliation, this fabric was later transposed by S2 and S3 fabrics, the degree of which varies throughout the dome. S4 deformation consists of a mylonitic sheer zone in the north and central parts of the dome (Lana et al. 2003). The observed textures, which are supported by the mineralogy, are attributed to two different events, a long period of static metamorphism with extreme heat and the impact event which caused dynamic metamorphism (Schreyer 1983). At the centre of the dome (within a <7 km radius) the ILG appears to have preserved Archean structures and gneissosity at the meter scale. When the ILG is observed in thin section however distinct fine scale texture is observed and often varies from one location to another. The texture of the ILG in the center of the Vredefort dome consists of granoblastic feldspar and quartz, which includes elongated domains of quartz that are coarse in the centre and have edges that display intergrowths with feldspar. Gibson and Reimold (2005), described the quartz rich patches as glomerogranular, and interpreted them to be the product of local shock melting followed by rapid cooling in a ductile strain environment. It is widely accepted that distinctive glomerogranular aggregates of fine-grained quartz and overall granofels texture are a product of impact-induced melting and recrystallization (Stepto 1979; Stepto 1990; Hart et al 1990; Gibson et al. 2002).

There are many mafic rock units in the Kaapvaal Craton that pre- and post-date the Vredefort impact event. These units provide an opportunity to compare the gabbronorite to mafic bodies formed throughout the development of the underlying mantle. In this study the Bushveld Igneous Complex (BIC) which predates the impact event and the Anna's Rust Sheet and its associated mafic units that postdate the impact event, are compared to the gabbronorite. The Bushveld Igneous Complex was emplaced between 2.05 to 2.06 Ga (Walraven et al. 1990) and consists of layered mafic and felsic intrusions. It is located 150 km north of the Vredefort structure but some researchers believe it could have extended further south (Stevens et al. 1997). The Anna's Rust Sheet is a high-Ti, tholeiitic gabbro that occurs as a sub-horizontal sheet intrusion and is best observed in outcrop to the east of the Vaal River in the Vredefort structure (Gibson and Reimold 2008). It cross cuts the granophyre dykes and pseudotacytlites and is dated at 1.10 Ga (Riemold et al. 2000). Both of these units provide a comparison for the Gabbronorite melt source. The Bushveld is an obvious unit of comparison but the Anna's Rust Sheet is equally as useful in studying the potential for pockets of melt in the crust that may have been remobilized during the impact event.

Information on the petrogenesis of igneous and metamorphic rocks can often be deduced using the distribution, paragenesis and microstructure of the dominant minerals. However in shock metamorphic rocks, particularly at the Vredefort structure, accessory minerals can retain information that is otherwise lost to recrystallization in other shock indicator minerals such as quartz (e.g. Grieve et al. 1990). Zircon and baddeleyite in particular, are known to be resistant to complete destruction by shock metamorphism and provide useful isotopic, geochemical and microstructural markers for pre- and post-shock history (eg. Moser et al. 2011). Together with field mapping and bulk geochemical analysis, the main and accessory minerals were studied in the gabbronorite and ILG samples, as well as with the bulk chemistry of the CAG, to provide an accurate history of the melt provenance, crystallization and post-impact modification. This was done to better understand the effects of impact process on early crust as well as the petrogenesis of impact melt sheets in large impacts.

3.3 Methods

Detailed field mapping at a 10 m grid spacing with a handheld GPS unit (datum WGS84) was carried out in the area of the ‘type norite’ dyke (Moser, 1997). Field identification of mineralogy and textures were confirmed through petrographic thin section analysis and electron beam microanalysis. Representative samples were analyzed for major, minor and trace element composition using bulk inductively coupled plasma mass spectrometry (ICP-MS), at Actlabs in Ancaster, Ontario (using the 4Litho research package). Mineral separation for geochronology was conducted at the Jack Satterly Geochronology lab at the University of Toronto using standard procedures. Electron nanobeam techniques including Cathodoluminescence (CL), Energy Dispersive Spectroscopy (EDS), and Electron Backscatter Diffraction (EBSD) were performed with a Hitachi SU6600 Field Emission Gun-Scanning Electron Microscope (FEG-SEM) at the University of Western Ontario, Zircon and Accessory Phase Laboratory (ZAPLab), on full thin sections and in-situ grains. CL was conducted at an acceleration voltage of 10 kV, and EDS analysis was conducted with an acceleration voltage of 15 kV. EBSD analysis required the sample to be mounted at a 70° tilt, and the accelerating voltage was set to 20 kV. Mineralogical composition was determined by optical microscopy and quantitative EDS elemental analyses of petrographic thin sections. Zircon chemistry was conducted at the Stanford/U.S.G.S. SHRIMP-RG facility according to previously published procedures (Mazdab and Wooden 2006), and referenced to internal zircon geochronology standard VP-10.

3.4 Results

3.4.1 Field Relationships and Bulk Geochemical Composition

Mapping was conducted on two adjacent localities, ~1.23 km apart in the rangeland immediately north of the Inlandsee Pan, which is ~4 km south of the geographic centre of the impact structure. Bedrock exposure is poor to absent in the Inlandsee Pan region, and two areas of ~5% exposure were selected for detailed mapping based on known or new gabbronorite occurrences. The UTM coordinates at the centres of the two map areas are 548348E/7007533N at Site 1 (Figure 3-1) and 549618E/7006641N at Site 2 (Figure 3-2). The two main rock types in the two map areas are the intrusive gabbronorite (V232, V234, V235, and V250) and its country rock unit the ILG (V234-2, V245, V252 and V262). Subordinate rock types include m-scale inclusions of metasupracrustals such as meta-ironstone in the ILG, as well as a thin diabase dyke at Site 1. At the eastern side of the gabbronorite body at Site 2 a transition zone was mapped, this zone contains gabbronorites with inclusions of ILG (V241 and V249) and a fine grained gabbronorite (V246). A sample of the CAG (V111) was also collected from an exposure east of the area mapped at Site 2 (see Table 3-1 for sample numbers and general locations).

3.4.1.1 Gabbronorite

In outcrop, the weathered surface of the gabbronorite unit is reddish to dark brown, and its fresh surface is black to dark grey. At Site 1 (Figure 3-1), which encompasses the ‘type norite’ dyke reported by Moser (1997), the exposed surface is very weathered, as are the contacts with the country rock, which are rarely clearly exposed. Contacts with ILG were mapped using a combination of adjacent (within 5 cm of the gabbronorite) outcrop exposures, which show a change in rock type from ILG to gabbronorite, and/or accompanying soil colour changes from sandy brown to dark red (gabbronorite); both vary in nature between Sites 1 and 2. The map pattern of the gabbronorite at Site 1 varies from dykes with straight sided margins, 10 m diameter lenses with curved boundaries, and occasional 10 cm apophyses into the ILG (Figure 3-1).

Table 3-1: List of Samples and Their Relative Locations

Sample #	**Rock Type**	**Site Location**
V111	CAG	East of Site 2, outside of the map area
V232	Massive Gabbronorite	Site 2
V234	Foliated Gabbronorite	Site 2
V234-2	ILG	Site 2: Proximal to the gabbronorite
V235	Massive Gabbronorite	Site 2
V238	ILG	Site 2: 35 m from the gabbronorite
V241	Gabbronorite with ILG inclusions	Site 2: Transition Zone
V245	ILG	Site 2: Proximal to the Transition Zone
V246	Massive Gabbronorite	Site 2: Transition Zone
V249	Gabbronorite with ILG inclusions	Site 2: Transition Zone
V250	Foliated Gabbronorite	Site 1: Same location as ‘type norite’ from Moser (1997)
V252	ILG	Site 1: Proximal to the gabbronorite
V262	ILG	Site 1: 95 m from the gabbronorite

Note: Proximal is used to describe any outcrop within 5 meters of the gabbronorite.

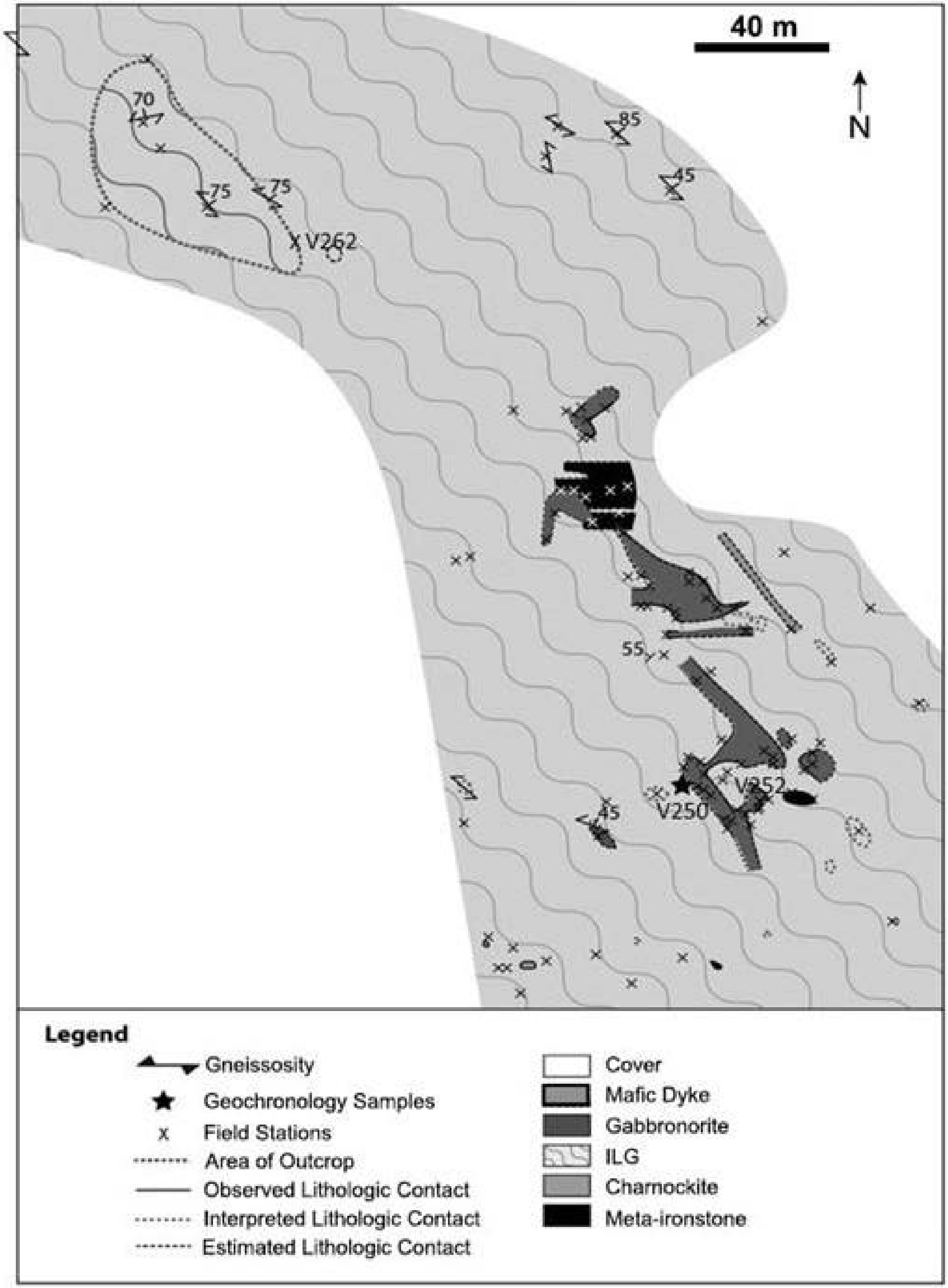

Figure 3-1: Bedrock geology map of Site 1 north of the Inlandsee Pan, ~4 km south of the center of the impact structure. Note the discontinuous nature of gabbronorite distribution as well as the lack of consistent orientation relative to the NW trend of the host ILG gneissosity.

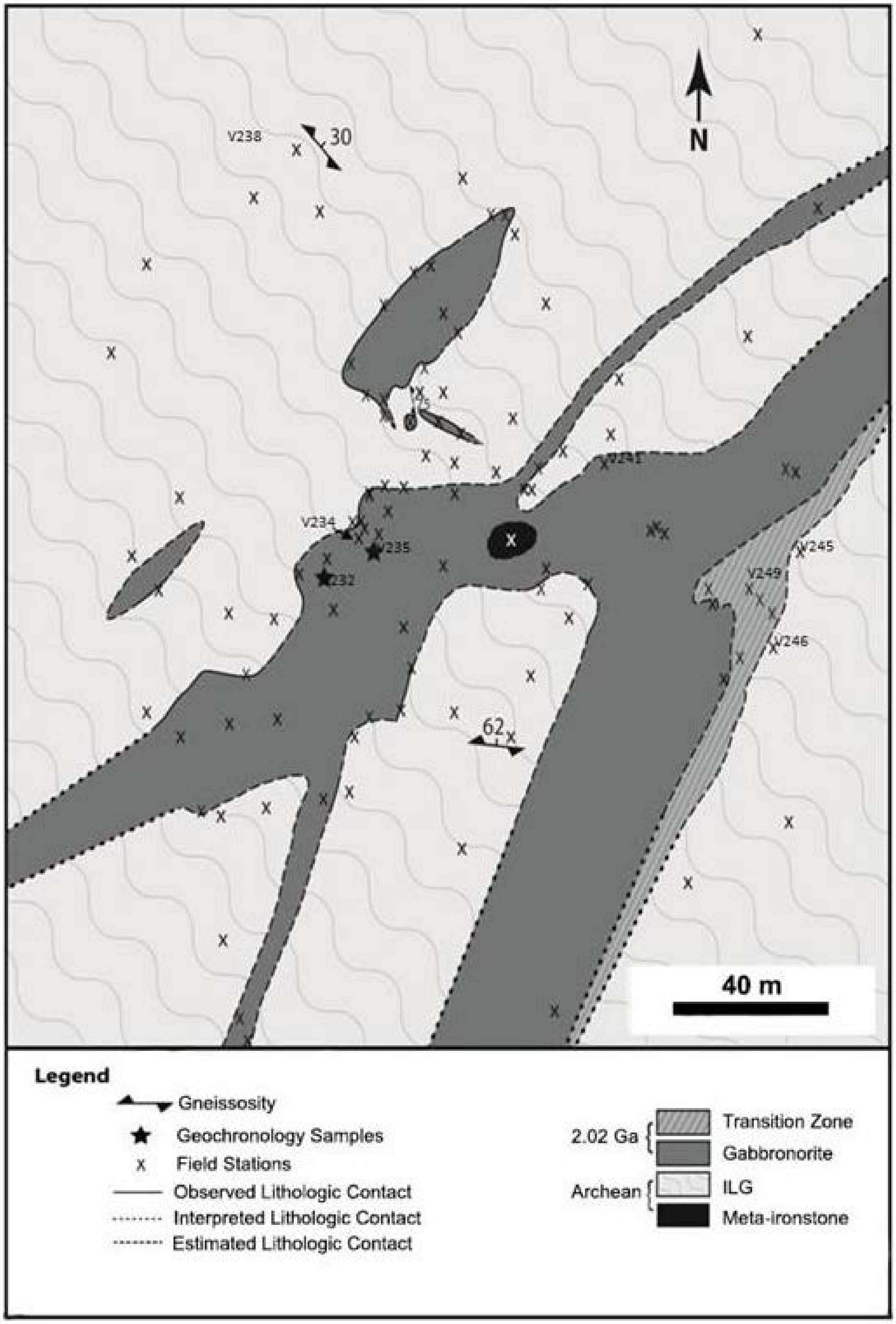

Figure 3-2: Bedrock geology map of Site 2 north of the Inlandsee Pan, ~4 km south of the center of the impact structure. Note the transition zone on the east side of the gabbronorite.

Figure 3-3: Field area photographs showing nature of exposure and main lithologies; A) the center of the large gabbronorite body at Site 2, B) Gabbronorite sample V234 at western contact with ILG, C) Transition zone sample V241 from eastern fine-grained zone showing tabular xenolith of ILG gneiss, and D) typical ILG gneiss showing Archean pre-impact gneissosity.

The gabbronorite is best exposed at Site 2 (Figure 3-2 and 3-3) providing the best location to describe it in detail. Exposures occur in outcrops as much as 15 m across with evidence for thickness of up to 40 m. 10 m grid mapping revealed that the gabbronorite unit is irregular in shape and forms a large discontinuous north-south trending, steeply dipping body approximately 209 m long by 34 m wide. There is a variation in grain size and texture within the gabbronorite unit at both Site 1 and Site 2 that is discernible at the scale of field exposures and in hand samples. The greatest variation is seen at Site 2 with grain size varying from medium to fine from west to east across the strike of the body. Since this is also the best exposed gabbronorite, Site 2 is here described in detail beginning on the west side with the coarser-grained sample V232. Gabbronorite V232 (similar to V250 at the west side of Site 1) consists of medium-grained domains of pyroxene ± fresh olivine which form elongate aggregates (L:W = ~2) several mm's long, each consisting of dozens of anhedral grains. The grain boundaries sometimes form triple-junctions but are irregular, presenting a granoblastic interlobate texture (Streckeisen, 1975) (Figure 3-4). The pyroxene domains and concentrations of oxide minerals, ilmenite and magnetite, are aligned such that they define a mineral shape fabric in a matrix of subhedral plagioclase. There is no sign of deformation of the exsolution lamellae or other grain features (Figure 3-4). Located a few metres to the east is sample V234 which is finer grained and likewise has a visible grain fabric and no evidence of deformation. There is a weak north-striking and steeply dipping planar grain fabric of variable intensity throughout the east and west margins of the unit that is defined by elongate, subhedral aggregates of pyroxene and ilmenite.

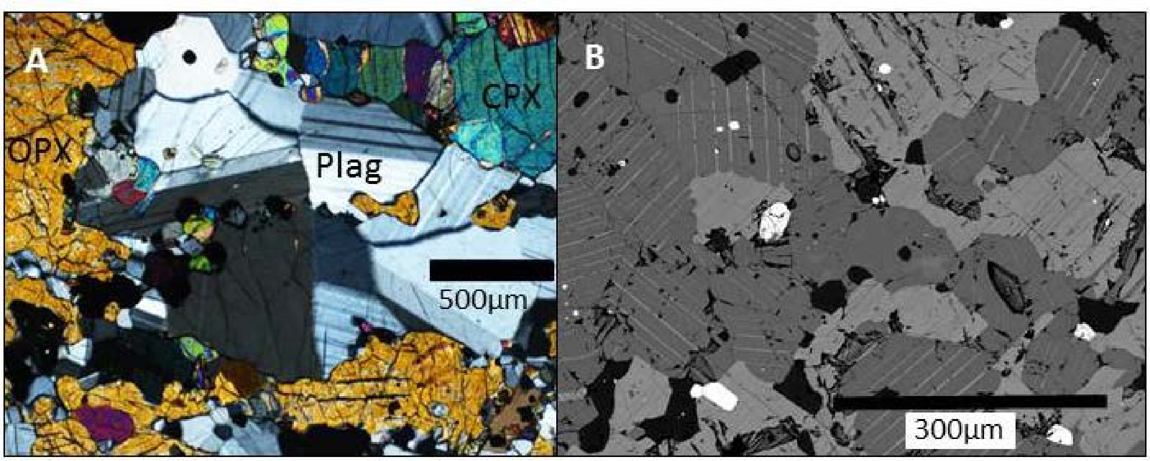

Figure. 3-4: Gabbronorite textures; A) optical photomicrograph of most representative gabbronorite sample V235 from center of Site 2 (phases labeled; clinopyroxene (cpx), orthopyroxene (opx) and plagioclase (plag)) showing plagioclase twins and pyroxene association. B: BSE image of pyroxene textures in sample V232 showing undeformed exsolution lamellae.

Four gabbronorite samples, one from Site 1 (V250) and three from Site 2 (V232, V234, V235), representing a range in grain sizes, fabric development and proximity to ILG contacts were selected for bulk geochemical analyses of major, minor and trace elements. Sample V235 has the best outcrop exposure and is most representative of the predominant texture seen in the gabbronorite. The average major element composition is 46.4% SiO_2, 12.3% Al_2O_3, 21.4% Fe_2O_3, 9.1% CaO, 5.2% MgO and 2.4 % Na_2O (Table 3-2).

Table 3-2: Vredefort Major Element Bulk Chemistry

Analyte Symbol	GN V232	GN V234	GN V235	GN V250	CAG V111	ILG V238
SiO_2	40.38	49.45	49.66	45.97	71.27	75.63
Al_2O_3	8.67	13.89	14.44	12.30	15.85	12.68
Fe_2O_3(T)	30.54	16.62	16.63	21.79	2.06	0.75
CaO	7.79	9.75	9.92	8.98	2.13	0.66
Na_2O	1.74	2.76	2.77	2.53	4.28	2.82
K_2O	0.28	0.34	0.32	0.42	3.83	6.00
TiO_2	5.23	1.66	1.72	3.13	0.25	0.06
P_2O_5	0.19	0.22	0.20	0.32	0.04	0.02
LOI	-0.72	-0.58	-0.69	-0.43	0.86	0.59
Total	99.55	99.88	100.80	99.73	101.00	99.33

Note: The analysis method used for all major oxides was ICP, all values are reported in wt%, and with the exception of MnO and TiO_2 which have detection limits of 0.001%, all major oxides have a detection limit of 0.01% and an average error range of ± 0.09%.

When the samples are plotted on an AFM plot (Figure 3-5) there is a spread in the data with V235 and V234 being more alkali and MgO rich. The coarser grained sample, V232, has noticeably different bulk chemistry, as it contains less SiO_2 and Al_2O_3 (40.38% and 8.67% respectively) and a higher Fe_2O_3 composition (30.54%). There is also a higher level of Fe_2O_3 in the finer grained dyke sample V250 than in V234 and V235, which can be explained by a greater abundance of ilmenite in both the V232 and V250 samples.

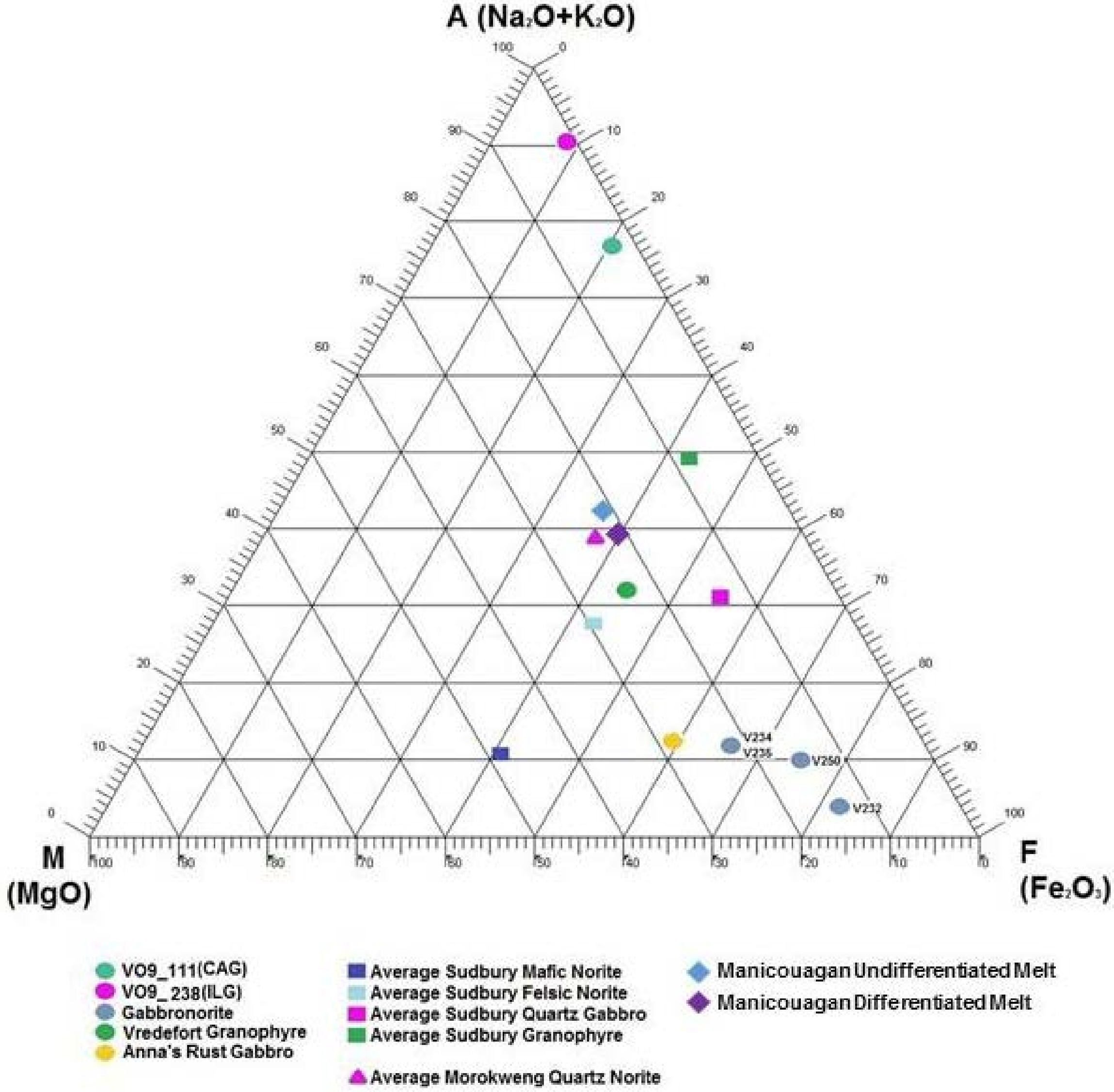

Figure 3-5: AFM plot comparing whole rock compositions of Vredefort rock types and known impact melts from other craters. Vredefort samples are: Central Anatectic Granite (CAG), Inlandsee Leucogranofels (ILG), Gabbronorite (V250 from Site 1, the type locality, and three others from Site 2), and Vredefort Granophyre (Koeberl et al. 1996). Compositions from the Sudbury melt sheet (Lightfoot et al. 2001), Morokweng melt sheet (Andreoli et al. 1999) and Manicouagan (O'Connell-Cooper and Spray 2011) are also shown. Note the Fe-rich composition of Vredefort gabbronorite, with coarsest grained and most ilmenite- rich gabbronorite sample V232 plotting closest to the Fe apex. V235 is most representative but is still more Fe-rich than intracontinental basaltic intrusions such as the nearby 1.1 Ga Anna's Rust sheet (Reimold et al. 2000).

Table 3-3: Vredefort Minor and Trace Element Bulk Chemistry

Analyte Symbol	Detection Limit	Error (±)	GN V232	GN V234	GN V235	GN V250	CAG V111	ILG V238
Sc	1.0	0.2	42.0	33.0	32.0	38.0	2.0	< 1.0
Be	1.0	3.8	2.0	< 1.0	< 1.0	1.0	2.0	< 1.0
V	5	16	1507	331	332	483	12	8
Cr	20	6	50	110	120	< 20	< 20	< 20
Co	1	2	77	51	54	56	3	2
Ni	20	6	130	100	110	70	< 20	20
Cu	10	18	270	210	270	210	< 10	< 10
Zn	30.0	0.2	270.0	130.0	140.0	190.0	< 30.0	< 30.0
Ga	1.0	0.2	23.0	17.0	18.0	22.0	18.0	10.0
Ge	0.5	0.4	2.0	1.8	1.6	2.0	1.0	0.7
Rb	1	3	1	< 1	< 1	1	151	126
Sr	2	7	116	174	183	182	349	395
Y	0.5	4.8	38.3	32.9	31.8	44.9	10.0	0.8
Zr	1	2	146	93	72	206	241	14
Nb	0.2	1.1	13.4	8.2	8.4	13.8	11.8	1.4
Ag	0.5	0.4	0.6	< 0.5	< 0.5	0.8	0.9	< 0.5
Sn	1.0	0.3	3.0	< 1.0	< 1.0	2.0	5.0	< 1.0
Cs	0.1	0.9	< 0.1	< 0.1	< 0.1	< 0.1	2.7	0.4
Ba	3	19	164	133	121	215	566	1553
La	0.1	8.4	19.0	13.1	11.7	16.4	37.7	8.7
Ce	0.05	4.21	38.60	29.00	25.60	36.60	63.70	10.20
Pr	0.01	9.48	4.88	3.94	3.42	5.11	6.35	0.93
Nd	0.05	0.65	22.50	19.10	16.70	24.80	20.80	2.77
Sm	0.01	0.10	5.77	5.07	4.55	6.82	3.03	0.35

Table 3-3: Vredefort Minor and Trace Element Bulk Chemistry Continued

Analyte Symbol	Detection Limit	Error (±)	GN V232	GN V234	GN V235	GN V250	CAG V111	ILG V238
Eu	0.005	0.08	1.73	1.68	1.62	2.15	0.91	0.86
Gd	0.01	0.16	6.63	5.97	5.58	8.02	2.40	0.27
Tb	0.01	1.78	1.19	1.06	1.02	1.43	0.34	0.04
Dy	0.01	0.23	7.28	6.32	6.06	8.67	1.94	0.16
Ho	0.01	0.29	1.45	1.25	1.21	1.71	0.38	0.03
Er	0.01	0.39	4.38	3.73	3.53	5.00	1.14	0.07
Tm	0.005	1.31	0.72	0.59	0.56	0.78	0.19	0.01
Yb	0.01	0.438	4.90	3.85	3.54	4.94	1.27	0.06
Lu	0.002	0.07	0.75	0.59	0.51	0.71	0.20	0.01
Hf	0.1	9.43	3.80	2.50	2.00	5.10	5.60	0.30
Ta	0.01	0.04	0.64	0.42	0.39	0.80	0.49	< 0.01
Tl	0.05	0.16	< 0.05	< 0.05	< 0.05	< 0.05	0.68	0.60
Pb	5	1	< 5	< 5	< 5	< 5	14	16
Th	0.05	0.87	0.40	0.41	0.24	0.29	12.90	0.32
U	0.01	0.01	0.10	0.08	0.05	0.16	0.94	0.04

Note all elements are reported in ppm, and the analysis methods used was FUS-MS, with the exception of Sc Be, V, Sr and Ba which was analyzed with FUS-ICP.

With regard to trace elements (Table 3-3), sample V232 has the most variation compared to the other three samples, this is likely due to its higher ilmenite content. Cu/Zr (< 0.7 ppm) and Cr (<100 ppm) values also vary among the gabbronorite samples. (See Appendix B-1 for plots). The chondrite normalized REE values show an order of magnitude light REE enrichment relative to the ILG and two orders with respect to the heavy REE, to give an overall slope that is slightly negative (Figure 3-6). The gabbronorite compositions were also normalized to the granophyre using analysis done by Peter Lightfoot. The gabbronorite was normalized to the granophyre, because it represents the earliest known phase of the impact melt and can be used to determine if the units were derived from the same melt body. Similar comparisons are made at Sudbury between the offset dykes and the main mass to study the evolution of the SIC. It was found that the granophyre REE slope is steeper such that the La and Ce values are much higher than those of the gabbronorite, whereas Sm to Yb values are much lower, with a crossover at Nd. The gabbronorite sample V250 has the highest REE values and V235 has the lowest, but the spread between the samples is relatively small; ~2 ppm when normalized to granophyre and ~20 ppm when normalized to chondritic values.

Figure 6: REE Plot of Units from the Vredefort Dome

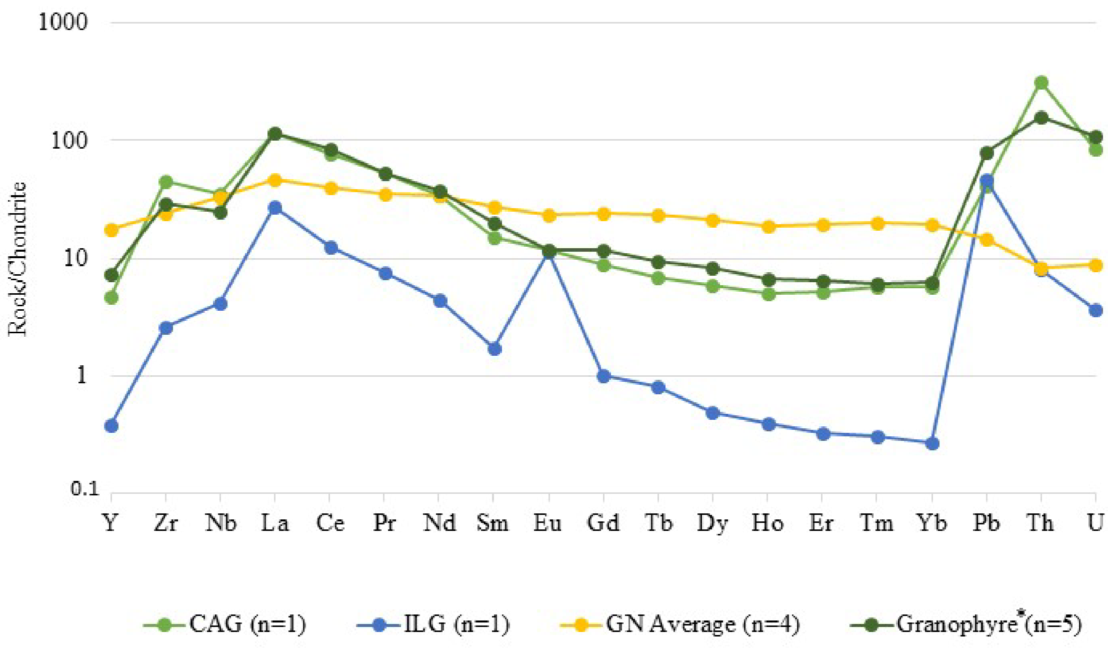

Figure 3-6: REE plot of melt and footwall rocks in the Vredefort Dome. The average composition of gabbronorite (type sample at Site 1 and three samples from Site 2) is shown. Note the remarkably gentle slope of the gabbronorite pattern relative to other impact melts and basement ILG, and the strong gabbronorite REE enrichment in heavy REE. There is also a marked similarity between the Central Anatectic Granite and the Granophyre Dykes (chemistry provided by Peter Lightfoot*) that are similarly enriched relative to the ILG.

3.4.1.2 Transition Zone

The transition zone is located at the north-east edge of the gabbronorite body at Site 2. It consists of fine grained, massive varieties of gabbronorite (V246) on the far eastern margin of the transition zone, and gabbronorite with cm to dm-scale bodies of ILG composition occur within (Figure 3-3C). The ILG found in the gabbronorite is consistent with a xenolithic origin. In hand samples V249 and V241, the contacts between the ILG gnessic xenoliths and the massive gabbronorite are sharp and bear the distinctive glomerogranular quartz texture of the ILG with the shape of the quartz domains oriented parallel to the gabbronorite fabric (Figure 3-10 and Appendix E-3).

3.4.1.3 Inlandsee Leucogranofels (ILG)

The ILG's exposure ranges from low m-scale ridges and rare mounds to m-scale patches of 'pavement' (extremely flat-lying outcrops) with nearby cobbles and boulders sometimes exhibiting fabric orientations that are consistent with pavement and therefore likely to be *in-situ*. The fresh surface is light pink and grey and shows a fine to medium grained granoblastic texture, which exhibits a conchoidal fracture in some outcrops near the gabbronorite body. Locally, macroscopic pre-impact gneissosity is preserved that strikes northwest and moderate folds have axial planes parallel to gneissosity and moderately plunge to the northwest. Rare m-scale bodies of meta-ironstone were observed within areas of ILG and presumably occur as xenoliths (Menuge 1982) as in other parts of the central uplift. The weathered surface is pink with minor darker domains due to gneissosity, and is defined by the small variations in mafic mineral content (Figure 3-3D), as well as leucocratic and often potassium feldspar-rich, cm-wide bands. The weathering texture reveals the positive relief of the pervasive equant to elongate polycrystalline domains of quartz glomerogranules, which has been noted by previous authors

(Gibson and Reimold 2005), and these domains range in the maximum dimension from 2 mm to 20 mm, sometimes defining a shape fabric (Figure 3-12B). Away from the ILG-gabbronorite contact, the axis of the glomerogranular quartz domains is commonly parallel to the Archean gneissosity, which sometimes exists locally axial planar to Archean minor folds; whereas close to the contact, the glomerogranular quartz domains can be large and equant.

Bulk major element analysis of representative ILG sample V238 at Site 2 shows a felsic composition of 75.63% SiO_2, 12.68% Al_2O_3, 6% K_2O and 2.82 % Na_2O. All other major oxides are below 1% (Table 3-1). There are notable spikes in trace elements Sr (395 ppm) and Ba (1553 ppm) and a strong depletion of REE, except Eu, relative to other pre-impact granitoids as demonstrated by earlier regional geochemical transects (Slawson 1976; Lana et al. 2003). A strong positive Eu anomaly distinguishes this unit from other granitoids. A plot of REE, (La to Yb) normalized to chondritic values (Anders and Grevesse 1989), shows that heavy REE abundance are generally strongly depleted leading to a very negative slope (Figure 3-6; Table 3-3; Appendix B-1-2).

3.4.1.4 Central Anatectic Granite (CAG)

This massive granitoid unit (V111) (Appendix C-1) is found only in the core of the central uplift, northwest of the map area shown in Site 2, and its contact with the surrounding ILG unit is not exposed. Drill core intersection indicates it is transitional to the ILG and has a lenticular form (Hart, pers. comm.). Its mineralogy and bulk chemistry are similar to the surrounding ILG, however it has some distinct trace element characteristics, being much richer in trace elements such as Zr, Th and U. The comparison of the CAG to the Vredefort granophyre dykes, which formed from a melt derived partly from the ILG, shows that the CAG is 10% higher in SiO_2, but less enriched in mafic components, having 30% and 11% less FeO and MgO, respectively (Figure 3-5). The REE concentration of the CAG is roughly one to two orders of magnitude higher than in the ILG but contains the same concentration of Eu. Compared to the REE pattern of the Vredefort granophyre dykes, the CAG displays a slightly steeper slope being enriched in light REE and depleted in Nd to Sm and Gd to Tm but contains the same concentration of Eu and Yb (Figure 3-6).

3.4.2 Mineralogy, Texture and Microstructure

3.4.2.1 Gabbronorite

Based on petrography, the main rock-forming minerals in the gabbronorite are plagioclase (60%), pyroxene (cpx 19%, opx 14%), fresh olivine (up to 5%) and Fe-Ti oxide phases (up to 4%). The ratio of orthopyroxene and clinopyroxene does vary between samples, for example V250 at Site 1 is orthopyroxene dominant, hence the original rock name of “norite” (Moser, 1997). The primary pyroxene grains are subhedral to anhedral, have a grain size of 0.10 to 1.00 mm and exsolution lamellae (Fig. 3-4), and are sometimes cross-cut by open (modern) fractures lined with fine-grained alteration minerals. No evidence was found of shock deformation microstructures or annealed planar features. The clinopyroxene is augite (49.6% SiO_2, 20.3% CaO, 16.8% FeO, 10.8% MgO, 1.3% Al_2O_3 and TiO_2 and MnO are under 1%) and end member values average; 42.0% Wo, 31.1% En and 27.1% Fs. The orthopyroxene is classified as ferrosilite [SiO_2 (48.6%), FeO (34.7%), MgO (13.7%), CaO (1.08) and under 1% Al_2O_3, TiO_2 and MnO], and end member values average: 57.4% Fs, 40.3% En and 2.3% Wo. Three analyzed grains fall within the range of pigeonite, having an average composition of 48.9 % SiO_2, 33.7% FeO, 12.7% MgO, 3.8% CaO and under 1% Al_2O_3, TiO_2 and MnO, and end member values average: 54.82% Fs, 36.91% En and 8.27% Wo. The plagioclase is subhedral to anhedral, has a grain size of 0.05 to 2.00 mm and features well-defined twins. The average plagioclase composition (n=40 to 59, between samples V250, V232, and V235) is andesine

[58.1% SiO_2, 26.4% Al_2O_3, 8.9% CaO 6.1% Na_2O, and 0.7% K_2O] (Appendix B-2). Some plagioclase grains contain inclusions of pyroxene.

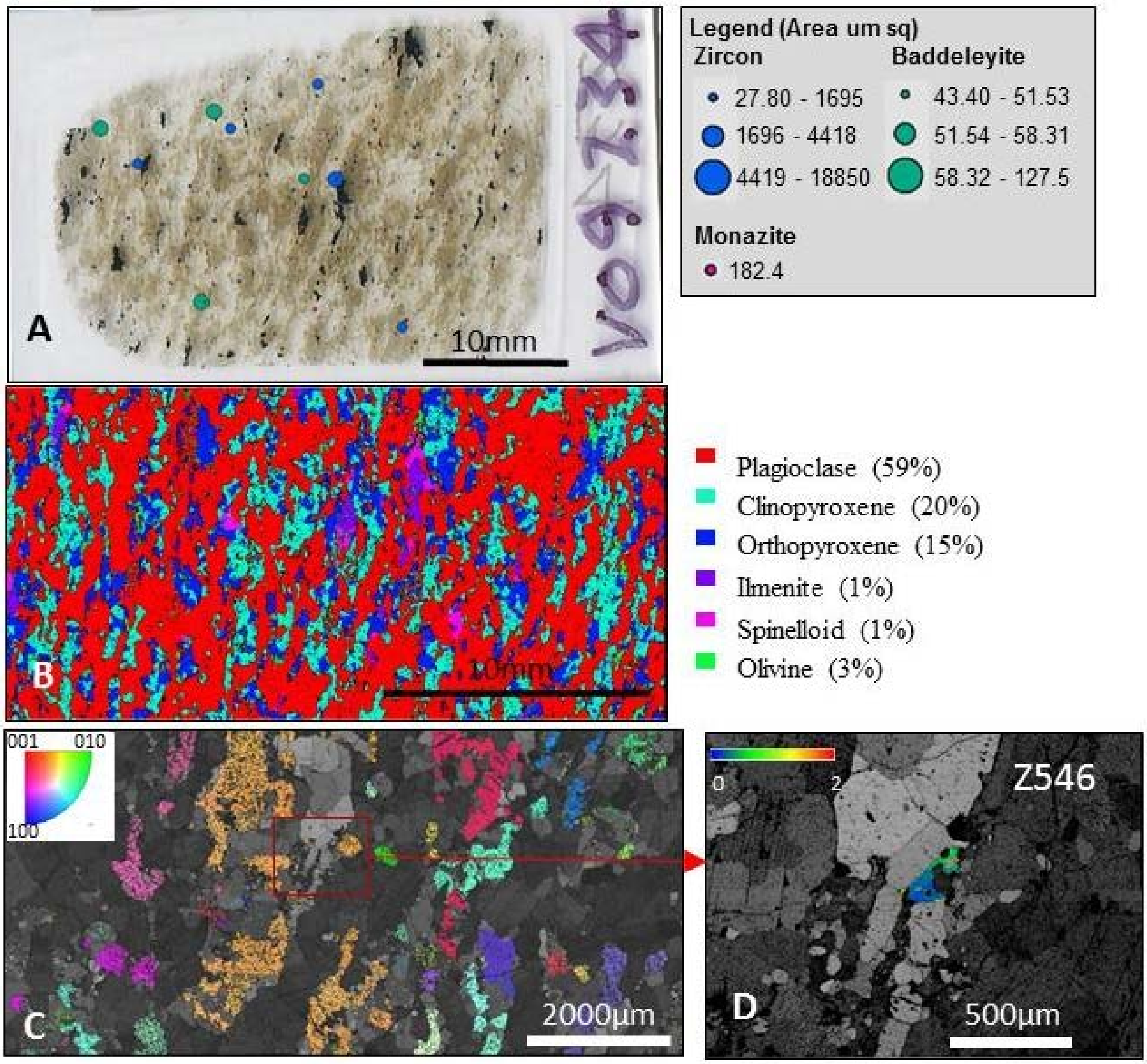

Figure 3-7: Mineralogy and texture of gabbronorite sample V234, western side of Site 2: A) Optical micrograph of thin section showing location and relative size of zircon and baddeleyite B) SEM-EDS major element chemistry map showing mineralogy and shape preferred orientation defined by pyroxenes C) EBSD inverse pole figure (IPF) orientation map showing that apparently disconnected orthopyroxene grains share the same crystal orientation, a possible relict primary igneous alignment. D) Higher magnification EBSD – band contrast (diffraction intensity) map centered on subhedral igneous zircon grain Z546 in ilmenite (brightest domains). The zircon has experienced very low degree (~1°) pervasive crystal-plastic deformation.

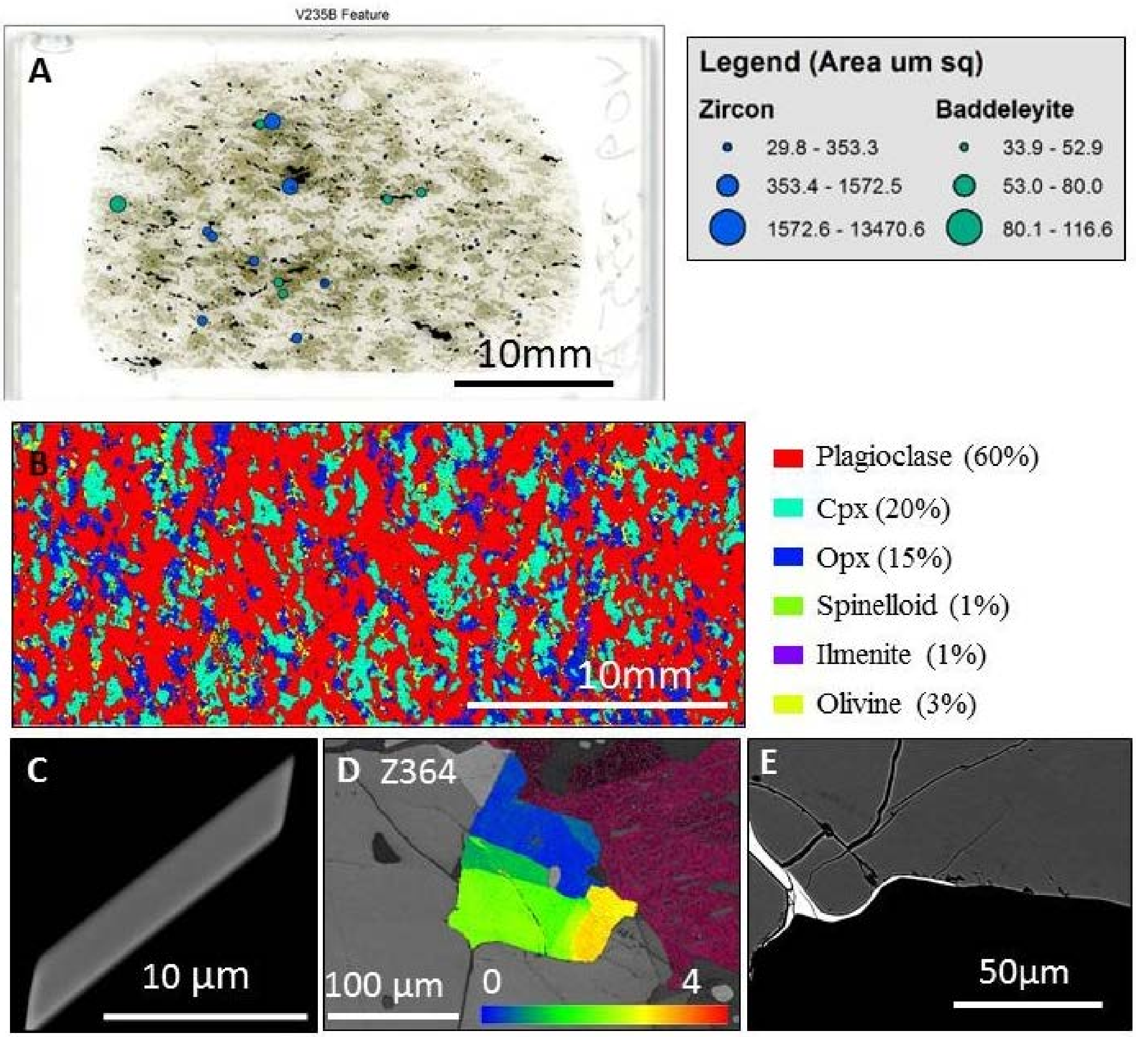

Figure 3-8: Mineralogy and texture of gabbronorite sample V235, centre of Site 2 body. A) Optical micrograph of thin section showing location and relative size of zircon and baddeleyite. B) SEM-EDS major element chemistry map showing mineralogy weaker shape preferred orientation defined by pyroxenes. C) BSE image of euhedral zircon grain Z37 in plagioclase. D) BSE image of early-formed subhedral zircon grain Z1780 which is intergrown with ilmenite (note inclusion) and shows several degrees of misorientation across low angle grain boundaries. E) Anhedral zircon growing along grain boundaries between pyroxene and plagioclase. None of the zircons carry shock microstructural deformation illustrating that zircon growth was post-shock and extended throughout the crystallization and texture development in the gabbronorite.

Optical investigation and EBSD mapping reveal that aggregates of orthopyroxene grains share a common orientation across distances of several mm (Figure 3-7C). Three thin sections were made of sample V235 (V235, V235A and V235B) from near the centre of the main dyke. Section V235B exhibits the most visible mineral fabric (Figure 3-8D and C) and this variation between the mineral fabric in V235B to a more massive texture in thin sections V235 and V235A, suggests a linear element to the shape fabric. Optical and EBSD analysis of plagioclase grains confirm that the major grains do not show evidence of strain. Minor lenticular domains of very fine grained granular intergrowths of pyroxene and plagioclase and oxide phases are randomly distributed in this sample, with their margins oriented parallel to the overall grain shape fabric.

3.4.2.2 Gabbronorite Accessory Phase Microstructure

Zircon crystals have grown at all stages of the crystallization sequence of the gabbronorite. This is based on their inclusions of magnetite, and zircon included within pyroxene and plagioclase (Figure 3-7D and 3-8D) and late stage anhedral zircon crystallization at grain boundaries. Euhedral baddeleyite occurs at grain boundaries and is in association with ilmenite which appears to have formed early in the crystallization sequence.

Accessory phase distributions were mapped in two gabbronorite samples from Site 2; foliated sample V234 and massive sample V235, and there does not appear to be any preferred distribution in relation to the major minerals (Figure 3-7B and 3-8B). The zircons (ranging in length from 7 to 299 μm) have morphologies that are predominantly anhedral, but there are subsets of subhedral and euhedral (Figure 3-8C) grains. Euhedral zircons exhibit internal igneous zoning and no shocked microstructures were observed. The zircons are also quite featureless but many are cracked and some have weak irregular zoning in BSE. One zircon of particular note is Z1780 (Figure 3-8E), from sample V235B, which appears to have grown along a grain boundary. EBSD analysis of zircon Z364 from V235 revealed low levels (4˚) of crystal-plastic strain (Figure 3-8D). Anhedral to subhedral baddeleyite grains (9 to 19 μm in length) and one anhedral monazite grain (29 μm in length) were also located, and did not exhibit any preferred distribution. The baddeleyite grains are featureless, unshocked and some are cracked.

3.4.2.3 Transition Zone

In the transition zone the grain size is significantly smaller down to 0.10 mm in samples V241, V246 and V249. These samples can vary between gabbronorite and noritegabbro compositions depending on the dominant pyroxene minerals and there textures are microgranular compared to that of the main gabbronorite (Figure 3-9). Closer inspection reveals large areas of the fine grained pyroxenes that share a common orientation and are in fact part of 0.5 to 1.0 mm scale sieve-textured grains intergrown at a fine scale with plagioclase (Figure 3-10). An area of the V249 thin section was mapped with EBSD and it was observed that none of the major mineral phases appear to have a shape preferred orientation.

3.4.2.4 Transition Zone Accessory Phase Microstructure

In thin section V241, the zircons are predominantly located within the ILG material, while the monazites ($(Ca, La, Nd,Th,Y)PO_4$) and baddeleyites are found within the gabbronorite near the contacts. In thin section V249 the zircons and baddeleyite occur predominantly in the gabbronorite whereas the monazites are located in the ILG inclusion (Figure 3-10). Accessory phase from sample V241 are largely anhedral with a small subset of subhedral and euhedral grains. The zircons are found along grain boundaries of quartz or feldspar in the ILG material and range in size from 8 to 53 µm in length. Typically accessory phases are internally featureless but some grains contain cracks and pits. Zircons from V249 are internally featureless and range in morphology from predominantly anhedral to subhedral. These zircons range from 4 to 89 µm in length and the baddeleyite range from 4 to 10 µm in length. The zircons are featureless in terms of internal zoning and four of the grains have weak igneous zonation (Appendix F-1 and F-3). BSE imaging of two anhedral zircons from the ILG inclusion reveals prominent irregular concentric zoning. Two zircons and one baddeleyite from gabbronorite sample V246, located in the transition zone were analyzed using EBSD. A high angle boundary (~10° of misorientation across the grain boundary) bisects the baddeleyite (Figure 3-9C) and the two zircons showed 3.5˚ of misorientation along the edge of the grains.

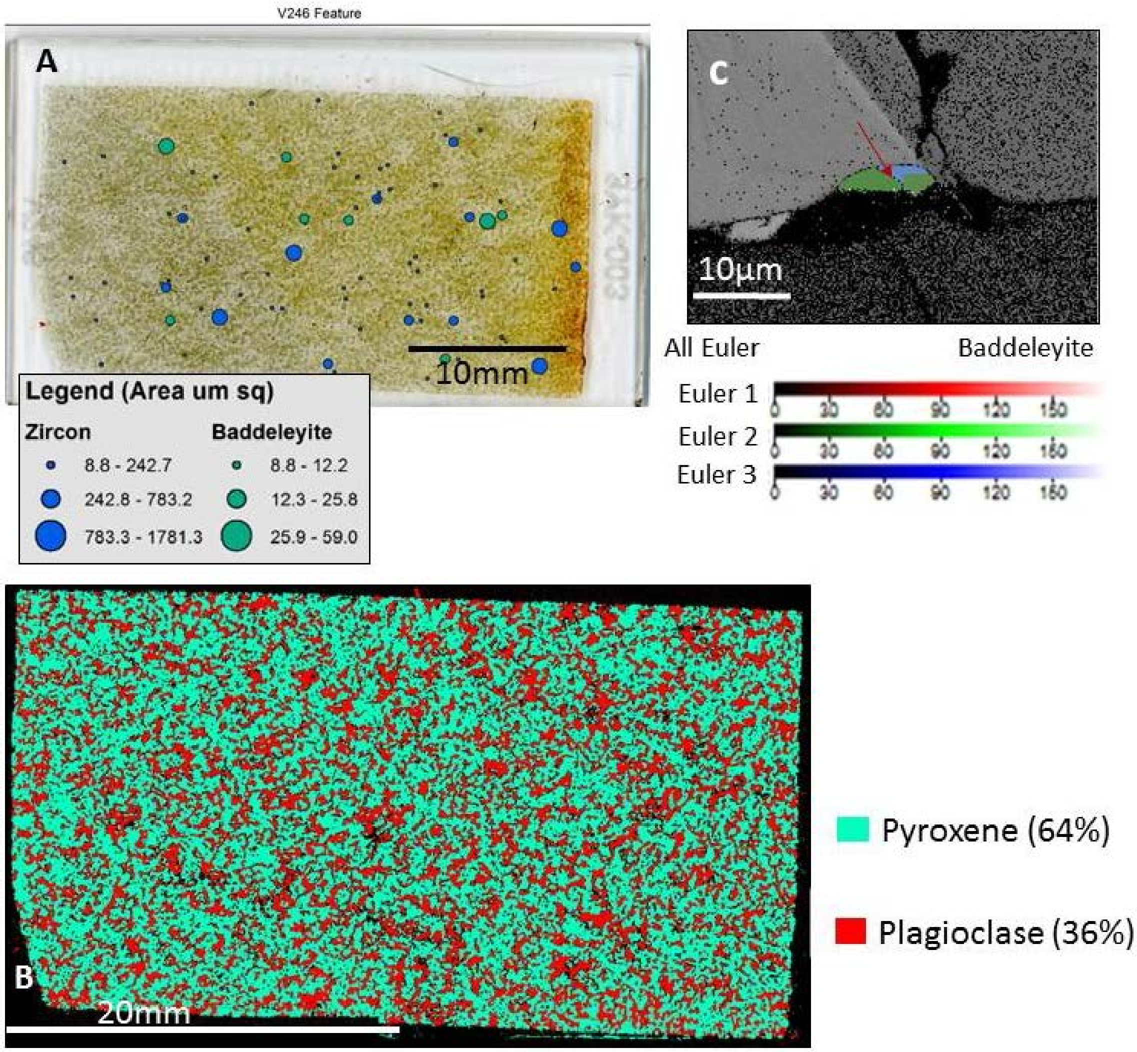

Figure 3-9: Mineralogy and texture of gabbronorite sample V246 from the fine-grained eastern margin of the gabbronorite at Site 2. A) Optical micrograph of thin section showing location and relative size of zircon and baddeleyite. B) SEM-EDS major element chemistry map showing homogeneous intergrown pyroxene and plagioclase texture. C) EBSD band contrast image of baddeleyite grain B4959 at pyroxene grain boundaries showing bisecting low angle grain boundary (accommodating 10° misorientation) and Euler angle map showing typical igneous cooling twin domains (blue and green).

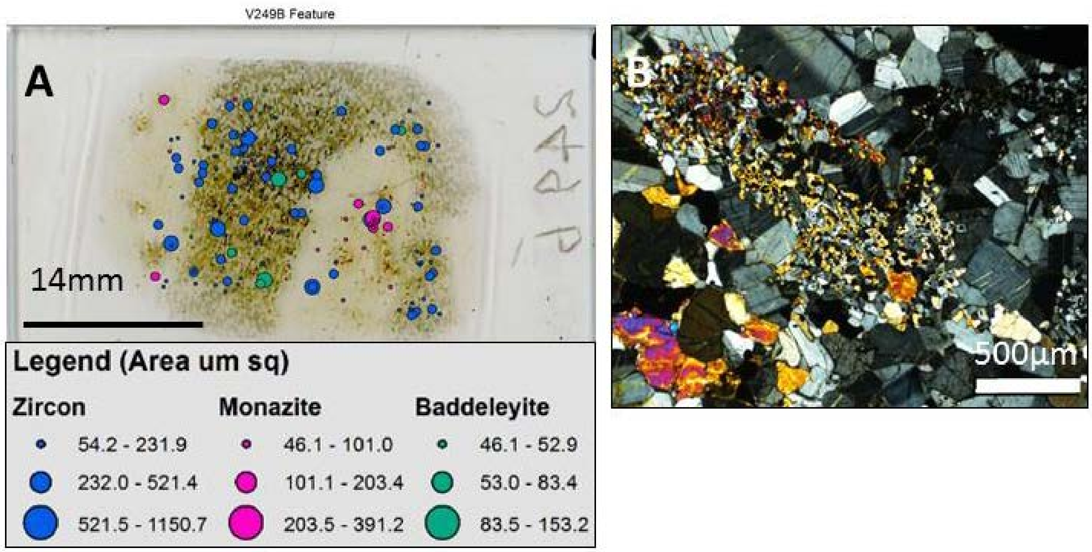

Figure 3-10: Microtextures of gabbronorite containing ILG xenoliths in transition zone, eastern margin of Site 2. A) Optical micrograph of thin section V249 showing distribution and relative size of zircon, baddeleyite and monazite. Note that monazite is restricted to ILG domains (light). B) Photomicrograph of sieve-textured pyroxene grains intergrown at a fine scale with plagioclase in transition zone sample V241. Note uniform orientation of pyroxene sieve-textured domains with oxide inclusions (opaque).

3.4.2.5 Inlandsee Leucogranofels (ILG)

The mineral assemblage of the ILG's main rock forming minerals is 42% quartz, 28% plagioclase and 30% potassium feldspar. The texture of the ILG, at Sites 1 and 2, have distinctive glomerogranular aggregates of fine-grained quartz and overall granofels texture (Stepto 1979; Stepto 1990; Hart et al. 1990; Gibson et al. 2002). The shape of the granular quartz domains range from spheroidal to ellipsoidal and in the latter case the long axes are parallel to the gneissic banding. Grain size is generally smaller at the margins of the agglomerates, where the grains often exhibit fan-like crystal aggregates, and myrmekitic intergrowths occur between quartz and feldspar. No evidence of shock deformation microstructures in the main phase minerals were observed, whereas relict shock features are present in accessory minerals. Distal sample V262 (95 m from the gabbronorite) was compared with the gabbronorite proximal sample V252 (<5 m from the gabbronorite), which both occur at Site 1, in order to assess the degree of variation in the ILG textures with distance from the gabbronorite contacts. The main textural difference appears to be constrained to the quartz glomerogranules, which are three times larger in diameter the closer the sample is towards to gabbronorite contact (Figure 3-11A and B and 3-12A and B). When a similar comparison is applied at Site 2 using the distal sample V238 (35 m from the gabbronorite) and proximal samples V245 and V234 (both of which are <5 m from the gabbronorite), the same size increase relationship of glomerogranule domains relative to the gabbronorite is observed but with exceptions, both distal sample V238 and proximal sample V245 have large glomerogranules (≤ 13 mm and ≤ 20 mm, respectively), however proximal sample V234-2 has much smaller glomerogranules (≤ 6 mm).

3.4.2.6 ILG Accessory Phase Microstructure

The distribution and microstructure of the accessory phase's zircon, monazite and baddeleyite were measured in five thin sections of ILG samples; two distal samples (V238 and V262) and three proximal samples (V234-2, V245 and V252) (Figure 3-1 and 3-2). No clear grain distribution difference was observed among the distal and proximal accessory phase populations, nor was any preferred orientation or association of the three accessory phases with respect to any of the major mineral phases. Zircon ranges in size between 4 to 432 µm in length and based on SEM investigation of ~10 grains per sample, 65% zircon grains showed microstructural evidence of shock metamorphism (including, planar features (PFs), curveaplaner (CPFs) and granular textures) (Appendix F-3 Figure F-3-6).

A growth and deformation sequence can be observed within the zircons having the earliest crystal growth stages typified by oscillatory growth that are sometimes surrounded by relatively unzoned rims of metamorphic appearance. Both growth stages are cross-cut by shock microstructures, such as PF and CPF which are present in up to 20% of grains, micro-twin lamellae and associated aluminosilicate glass inclusions. These growth zones are sometimes recrystallized forming unshocked zircon, which at its completion, results in a granoblastic coarsely granular zircon aggregate that pseudomorphs the original grain (Appendix F-3 Figure F-3-6E). Grain Z138 from sample V245 typifies this sequence (Figure 3-13). Two zircons from distal ILG sample V238 (Z972 and Z3779) exhibit slight (3˚ to 4˚) crystal-plastic strain deformation instead of strain at their edges. Zircon Z3402 from proximal sample V234-2 showed 16˚of strain caused by shock and a shock micro-twin.

Monazite grains are between 4 to 303 µm in length, are dominantly anhedral and 17% showed microstructural evidence of shock metamorphism. In the proximal sample V234-2 the morphologies range from irregular to prismatic. Rounded monazites exhibit a polycrystalline texture (Figure 3-13C and Appendix F-3 Figure F-3-5C), whereas the irregular and prismatic variety predominantly contain cracks that have not been annealed. In the proximal sample V245, monazite is only found in mottled or granular form.

Baddeleyite was discovered in both distal and proximal samples of the ILG in glomerogranular quartz domains. Both distal samples (V262 and V238) contained baddeleyite that is subhedral to anhedral and internally featureless in BSE (Figure 3-12C), they are also quite small, ranging from 4 to 21 µm in length; proximal samples V252 and V234-2 also contained baddeleyite ranging from 4 to 12 µm in length. One baddeleyite from V252 and five from V234-2 were imaged, and show rounded to subhedral morphologies and featureless internal textures. Two baddeleyites (B1699 and B1860) were analyzed using EBSD; grain B1860 had one consistent orientation with only 2˚ of misorientation, but B1699 had multiple orientations (Figure 3-13D), revealing that the grain has a twinned texture.

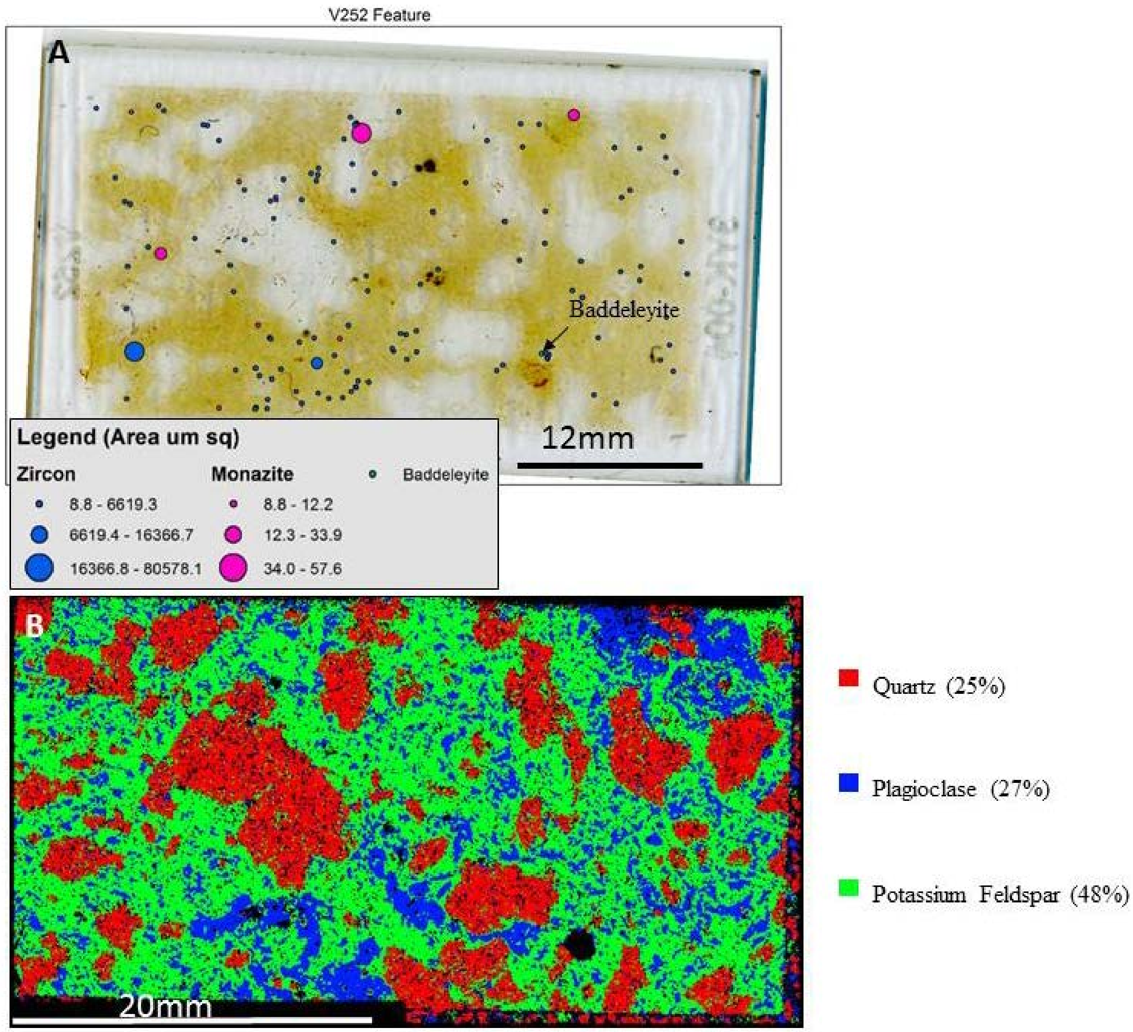

Figure 3-11: Mineralogy and texture of ILG sample V252 located adjacent to the type gabbronorite at Site 1. A) Optical micrograph of thin section showing location and relative size of zircon, monazite and microbaddeleyite. B) SEM-EDS major element chemistry map showing distribution and shape of glomerogranular aggregates of fine-grained quartz.

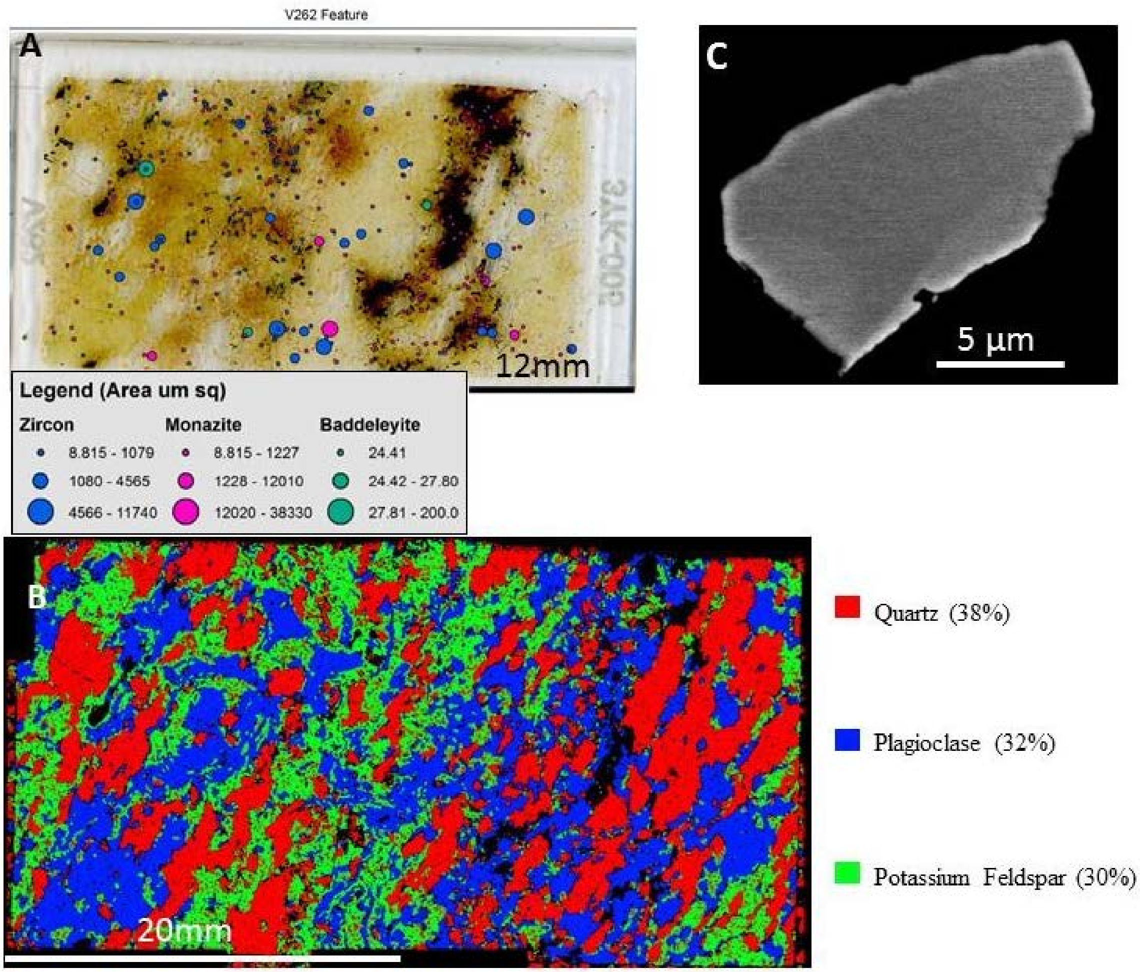

Figure 3-12: Mineralogy and texture of ILG sample V262 located northeast of the gabbronorite at Site 1. A) Optical micrograph of thin section showing location and relative size of zircon, monazite and baddeleyite. B) SEM-EDS major element chemistry map showing distribution and shape of glomerogranular aggregates of fine-grained quartz. C) BSE image of baddeleyite grain B6652 with featureless internal texture and subhedral morphology.

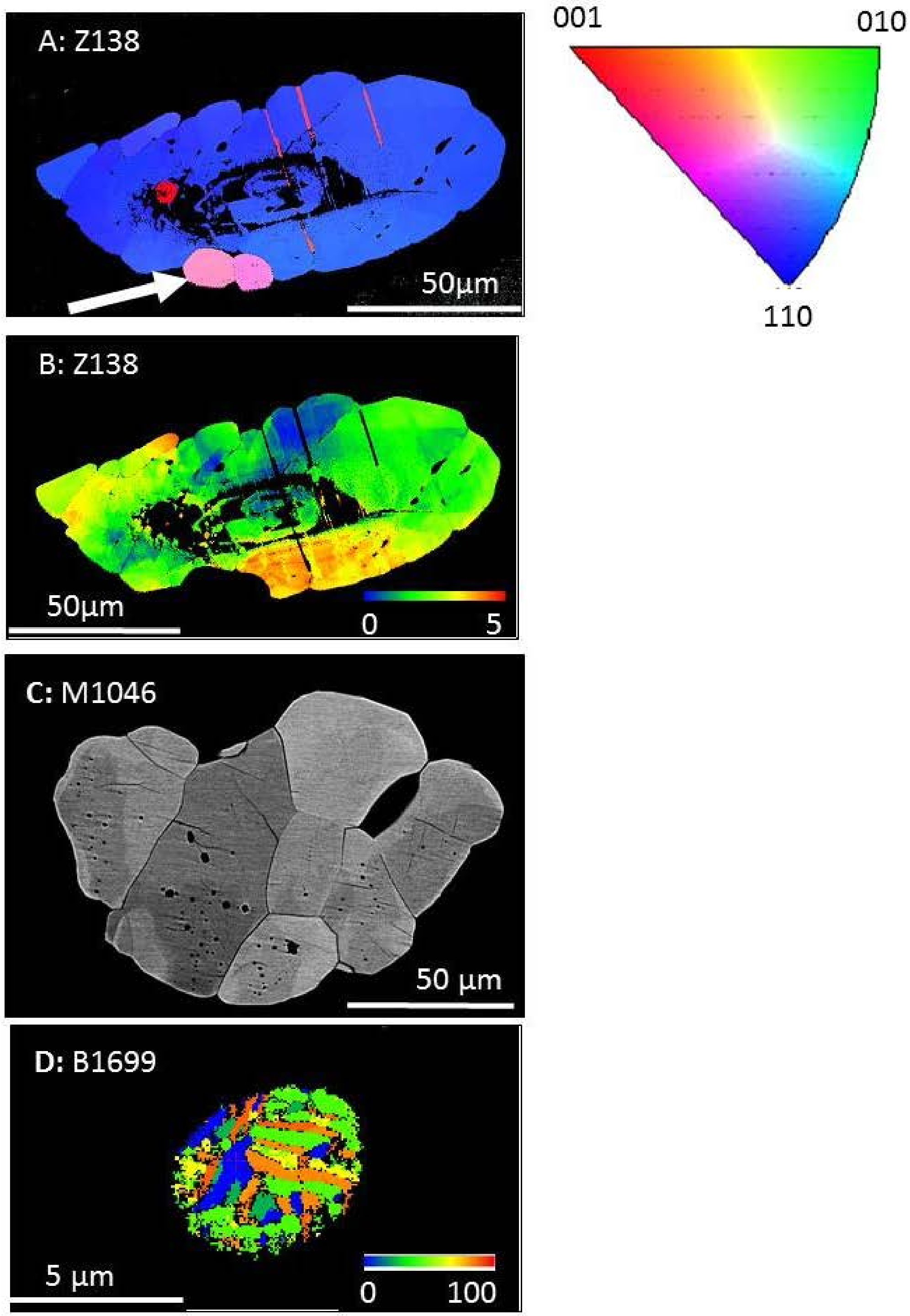

Figure 3-13: Accessory mineral microstructures from ILG sample at Site 2. A and B) Zircon grain V245 showing areas of regrowth (indicated with white arrow in A) and planar features, image A is a map showing grain orientation and image B is a map of strain. C) BSE image of a monazite (M1046) from ILG sample V234-2 showing polycrystalline texture and a subrounded morphology. D) Baddeleyite grain (B1699) from sample V234-2 displays baddeleyite twins.

3.5 Discussion

Comparison of these new field, mineralogical, microstructural and geochemical gabbronorite and transition zone observations to the CAG, ILG and units from the surrounding area, provide constraints on the source and crystallization history of these rock bodies during and following impact. This has the potential to address larger questions pertaining to the response of the continental crust to intense shock metamorphism deep beneath the centre of a giant impact, and to generally serve as a model for other large impact structures, particularly those early in Earth's history, by providing an interpretation of detrital Hadean zircon populations.

3.5.1 Textural Evolution of Vredefort Gabbronorite

The distinctive mineral textures of the gabbronorite contribute information which, like the geochemistry, is helpful to evaluate possible source regions and processes for the generation of the gabbronorite magmas following impact. Grain-scale relationships deduced from optical and SEM petrography indicate a crystallization sequence of rock forming minerals as follows; olivine, ilmenite, clinopyroxene, pigeonite, magnetite, plagioclase. Some crystallization was contemporaneous as some pyroxene grains contain inclusions of plagioclase and some pigeonite grains contain inclusions of clinopyroxene.

The EBSD analyses of the gabbronorite thin sections, reveal that the unit no longer have a primary igneous mineral texture that is typical of an impact melt sheet, for example, the North Range Sublayer Norite of the SIC (Figure 3-14). However, the microstructural data for main and accessory minerals provides some insight into the intrusive history of these bodies, in addition to the timing of modification of the original igneous texture. The gradient in grain size at Site 2 from coarse in the west to fine-grained in the east (e.g. Figure 3-8 and 3-9) is, for now, seen as an igneous crystallization-rate profile, due to the more rapid crystallization rate and/or different degrees of country rock assimilation and cooling, in the ILG xenolith-rich eastern margin (transition zone). EBSD and optical properties show that the primary grain size of the pyroxenes in the gabbronorite in this zone was much greater, with relict, elongate and aligned crystals up to 5 mm in length, defining a shape preferred orientation fabric (‘foliation’; Moser 1997). On the western sided of Site 2 where the fabric is more defined (V234), EBSD mapping of 5 mm aggregates of pyroxene domains indicate that separate grains share a common crystallographic orientation, and are not randomly oriented, as might be suggested by widespread 120° triple junctions surrounding the plagioclase and oxides (Figure 3-7C). The shape preferred orientation of the grains could indicate that they are connected deeper in the thin section or that these grains are the pieces of grains that have now been broken apart. This fabric could not have been created by ductile deformation after crystallization and cooling because exsolution lamellae in pyroxene and twinning in the surrounding plagioclase crystals are unstrained. The fabric is strongest near the contact with the surrounding country rock or within m-scale dyke apophyses (e.g. V250 the ‘type’ locality at Site 1) that parallel the contact margins. Therefore, the alignment of pyroxene and oxide minerals was produced by dyke-parallel flow during the injection of the gabbronorite bodies, or alternatively, during movement of the dyke walls at the early stages of crystallization.

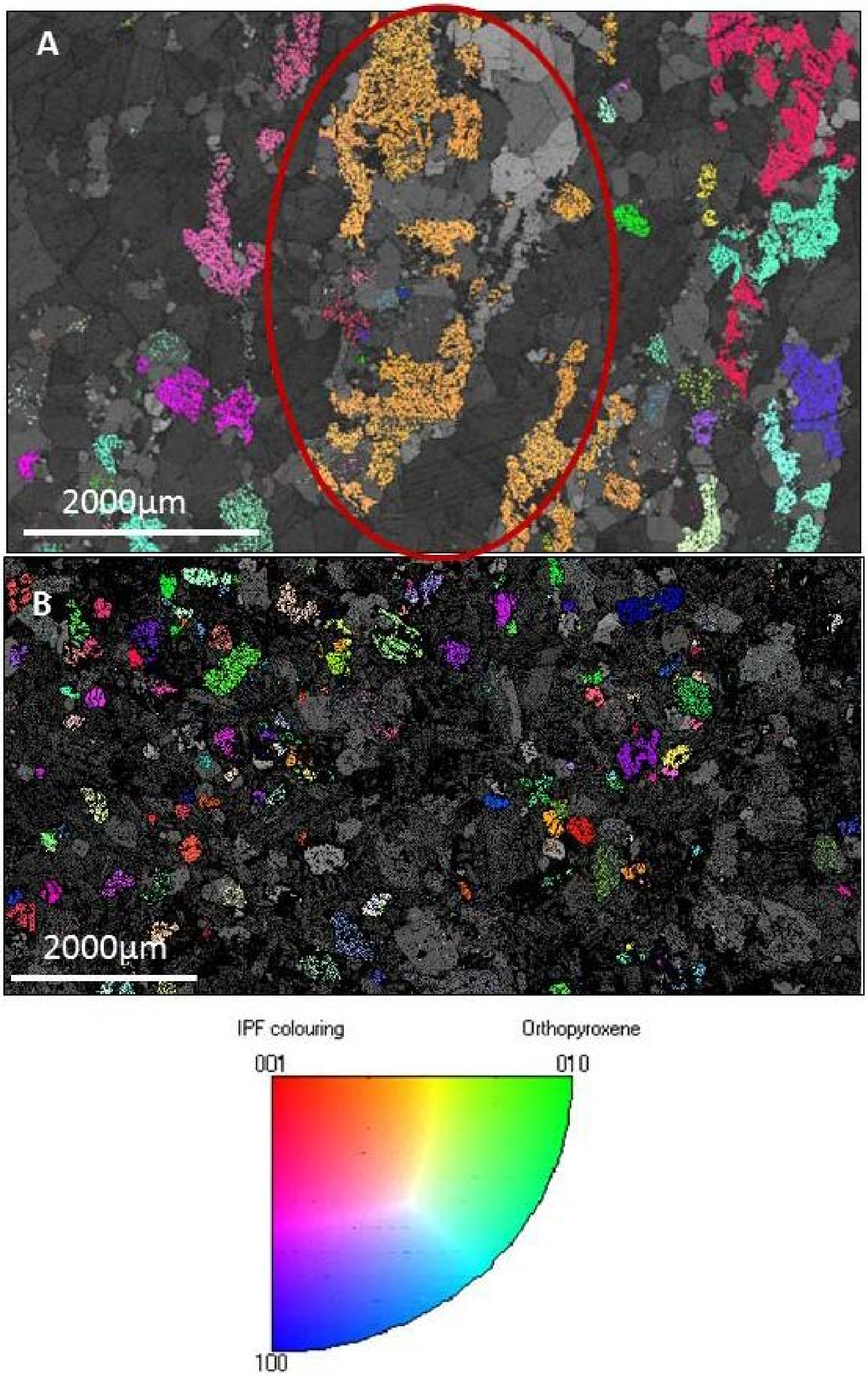

Figure 3-14: EBSD maps of the orthopyroxene orientation in A) Vredefort gabbronorite sample V234. In this sample the grains are aligned showing a complex mobile environment during formation. This alignment is noted by colour which indicates the axis the camera is looking down, the red arrows point to the best example. Image B is a Sublayer matrix sample (93PCL349A) from the Sudbury structure which displays a more common igneous type texture where there is no preferred orientation of the orthopyroxene grains.

Recrystallization of the igneous mineral assemblages due to the rate of crystallization in the transition zone has produced the present granoblastic interlobate texture, possibly as a response to minor plastic deformation while still at high temperature. Evidence for the early timing of recrystallization is suggested by the microstructural and textural properties of the accessory grains. Zircon grains that formed early in the gabbronorite crystallization sequence with ilmenite, one from sample V234 (Figure 3-7D) and one from V235 (Figure 3-8D), on the west side of Site 2 were found to exhibit several degrees of misorientation across low-angle boundaries, whereas anhedral zircon is observed growing along the present grain boundary triple-junctions. Hence the transition from igneous fabric to recrystallized fabric occurred within error of the age of zircon crystallization (2019 ± 2Ma (Moser 1997)). On the eastern side, in the xenolith-rich transition zone, low-angle grain boundaries are seen at the edges of fine-grained zircon or propagating across microbaddeleyite in sample V246 (Figure 3-9), however, this misorientation and minor ductile strain is not seen in surrounding minerals. The minor recrystallization of the pyroxenes and plagioclase is due to crystallographic recovery from the minor deformation that has been evidenced by the zircon microstructures. This ability of zircon to retain minor deformation microstructures, amid completely recovered main phase mineralogy, has been documented in lower-crustal mafic granulites elsewhere (Moser et al. 2011). The recrystallized gabbronorite texture is not the same as a typical mafic high-grade “granulite”, expected if the unit had a preimpact origin. In fact, the recrystallized texture in the gabbronorite is similar to the cumulate textures seen in some early formed components (granular cognate xenoliths) of the Skaergaard layered mafic intrusions (Wager 1960) and is strikingly similar to that of the main series of the Bushveld Igneous Complex (Wager 1960; Ashwal, pers. comm.) that pre-dates the gabbronorite by 30 million years (Olsson et al. 2010).

Textural evidence suggests a sequence of high temperature crystallization, formation of an igneous shape fabric in mafic minerals, a high temperature low-magnitude ductile deformation event that prompted recrystallization of pyroxene and plagioclase, which was followed by cooling and pyroxene exsolution at low pressures. This sequence is most easily connected with the crater modification phase of the Vredefort central uplift in the minutes to years after crater floor rebound and heating by the overlying ~13,000 km^3 melt sheet modeled by Ivanov (2005). Textures from the ILG country rock to the gabbronorite provide insight into this environment, whereby the distinctive glomerogranular quartz texture of the ILG (and its general “granofels” metamorphic texture) have been ascribed to ultra-high temperature metamorphism that is analogous to lunar environments (Gibson and Reimold 2002). The microbaddeleyite grains included within these quartz domains support this, as the quartz-zirconia phase relationship indicates temperatures of 1775˚C, which has been demonstrated to occur in tektites (El Goresy 1965). The gabbronorite provided a heat source, which caused thermal metamorphism of the ILG unit following impact. The central uplift assemblage of impact-heated lower crustal gneisses and newly introduced mafic impact melt bodies record minor strain and recrystallization early during post-impact cooling. This sequence is also seen in the ILG zircon with early shock microstructures such as microtwins having been overprinted by recrystallization domains and coarse granular zircon (Figure 3-13A). The 2017 ± 5 Ma (Gibson et al. 1997) age of the undeformed state of the Central Anatectic Granite may mark an end stage to ILG deformation in the central uplift. In summary the evidence points to a protracted period of impact melting, deformation and recrystallization of impact-generated melts and their host shocked gneiss early during isostatic and thermal re-equilibration of the deep crust uplifted 10 to 20 km to form the crater floor.

3.5.2 Magma Provenance

The source of the gabbronorite melt has not yet been established. The geochemical data from the Vredefort central uplift, Witwatersrand Basin and the Bushveld Intrusive Complex allow contemplation of both a crustal and cratonic mantle source for the gabbronorite bodies in the central uplift. The gabbronorite major and trace element composition has little in common with the granophyre and CAG, which are the other known impact related melt bodies at Vredefort. In order to rule out an origin from the impactor for the gabbronorite a comparison was made to the granophyre which contains traces of the impactor (Koeberl et al. 1996). The granophyre's Cr composition is five times higher than that of the gabbronorite (Appendix B-1); the CAG, also has low Cr values. The relatively low levels of Cr within the gabbronorite indicates that it does not contain a contribution from the impactor.

With regard to the bulk rock major element groupings, the gabbronorites are high Fe tholeiites (Figure 3-5, AFM plots after Best (1982)), and are distinct from the high Mg komatiitic bodies described by Stepto (1990) and the low Al, high Mg mafic granulites described by Lana et al. (2004) (Figure 3-15). The gabbronorite has similar Fe-rich major element chemistry to the Bushveld cumulates (melanorite), and this chemistry, combined with the mineral texture of large orthopyroxene crystals in V232, suggests a cumulate or melt dissemination process seen in the main mass of the Bushveld intrusive complex (Wager et al. 1960). The mantle beneath Lace kimberlite in the south west quadrant of the crater has been shown to be anomalous with respect to Kaapvaal mantle in that it is particularly Fe and Ni rich. This suggests that an orthopyroxenite rich upper mantle source may have been present to produce or contribute to the melt that formed the gabbronorite (Schulze 2001). The gabbronorite also has similar Fe-rich major element chemistry compared to the melanorite inclusions from the Whistle Mine embayment at the base of the Sudbury Igneous Complex.

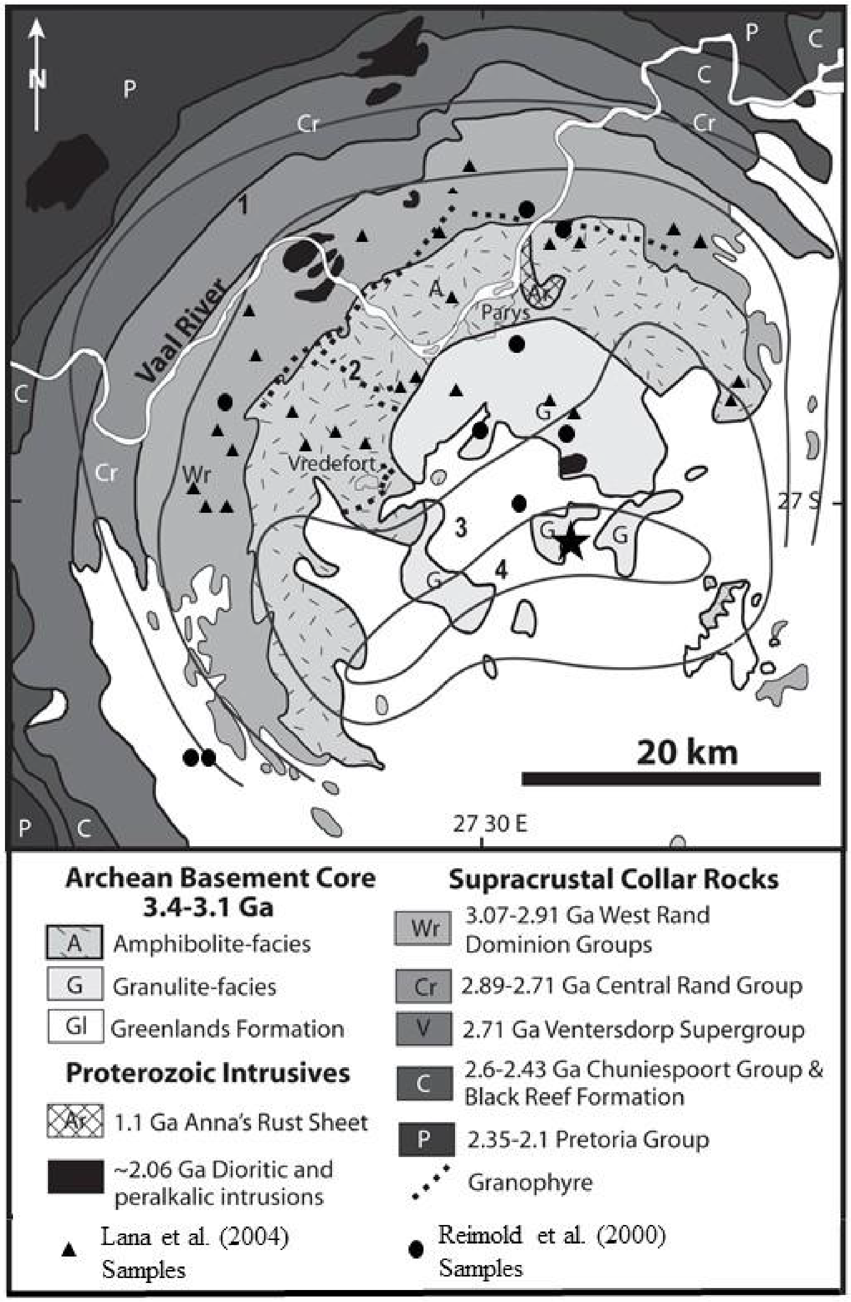

Figure 3-15: Generalized bedrock geology map of the Vredefort Dome (after Gibson and Reimold 2008). Grey contours represent degree of post-shock thermal annealing of planar deformation features in quartz (Grieve et al. 1990), with zone 4 representing complete annealing and 1 representing the least annealing. Samples from Hart et al. (1990) and the study area for this paper are indicated with a star, Lana et al. (2003) samples are indicated with triangles and Reimold et al. (2000) samples are indicated with circles.

REE compositions of the gabbronorite are distinctive relative to the other units of the Vredefort Structure, and are similar to only a few other rock types in the region, such as the Anna's Rust gabbro and Ventersdorp basalts. The average gabbronorite pattern is highly enriched, particularly in heavy REE, relative to the central uplift geology at Vredefort and the pattern of REE signature has a remarkably shallow slope (Figure 3-16). In comparison to the units in the Vredefort bedrock studied by Lana et al. (2004), none of those high grade gneisses exhibit a similar REE pattern or enrichment as the gabbronorite studied here. Accordingly, the bedrock values are much more depleted and Gd/Yb and La/Sm ratios are much higher (Appendix B-1-7). In terms of Vredefort mantle compositions, the best local example is the Archean Harzburgite at the Inlandsee Pan, originally described by Hart et al. (1981), which is highly depleted in light REE relative to the gabbronorite (Figure 3-16A). However, it is observed that the slope and enrichment of gabbronorite REE pattern is similar to both the Pneil unit, of the Ventersdorp flood basalt flows (Figure 3-16B) in the once superjacent Witwatersrand supergroup, and the Anna's Rust suite of 1.1 Ga gabbros and dykes that were emplaced after the impact event and provide a comparison to evolving mantle values (Figure 3-17A). The similarity of the gabbronorite to the Anna's Rust samples can also be seen in the comparison of Gd/Yb vs La/Sm (Appendix B-1-7). A similar REE slope and pattern can be observed in the Bushveld Wittekopjes Norite (Coetzee et al. 2006), however the gabbronorite REE are ten times more enriched. The REE pattern and concentrations were compared to the Sudbury and Morokweng impact melts, which show a pattern similar to the main mass granophyre of the Sudbury impact structure, however, the main mass granophyre is more enriched in light REE by ~50 times from Sm to La than the gabbronorite. Overall, when compared to the mafic impact-generated magmas from the Morokweng and Sudbury impact structures, the gabbronorite has a more mantle melt signature, being depleted in light REE and enriched in heavy REE (Figure 3-17B).

The principal question regarding the source of the gabbronorite melt is whether the melt was derived from the crust, or mantle, or was related to a source that was derived from a combination of both. When compared, the MgO versus Ni composition of the gabbronorites are higher compared to the units in the surrounding Vredefort bedrock (Appendix B-1-3) (Lana et al. 2004); with the exception of an ultramafic unit studied by Hart et al. (1990) that outcrops several kilometres from the gabbronorite exposures. Similarly, the MgO versus Ni gabbronorite compositions are comparable to the values observed in the Ventersdorp Platberg group and the Anna's Rust Sheet, but are distinct from the values of the Sudbury and Morokweng impact melts.

Figure 3-16A: Comparison with regional bedrock compositions.

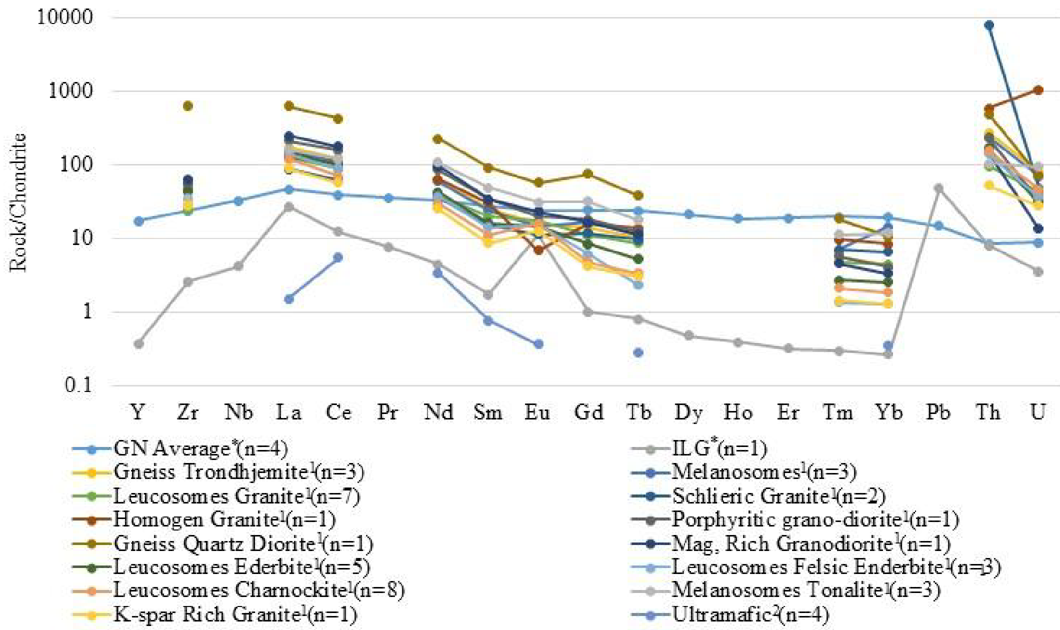

Figure 3-16B: Vredefort impact melt and bedrock compositions compared to Ventersdorp basalt

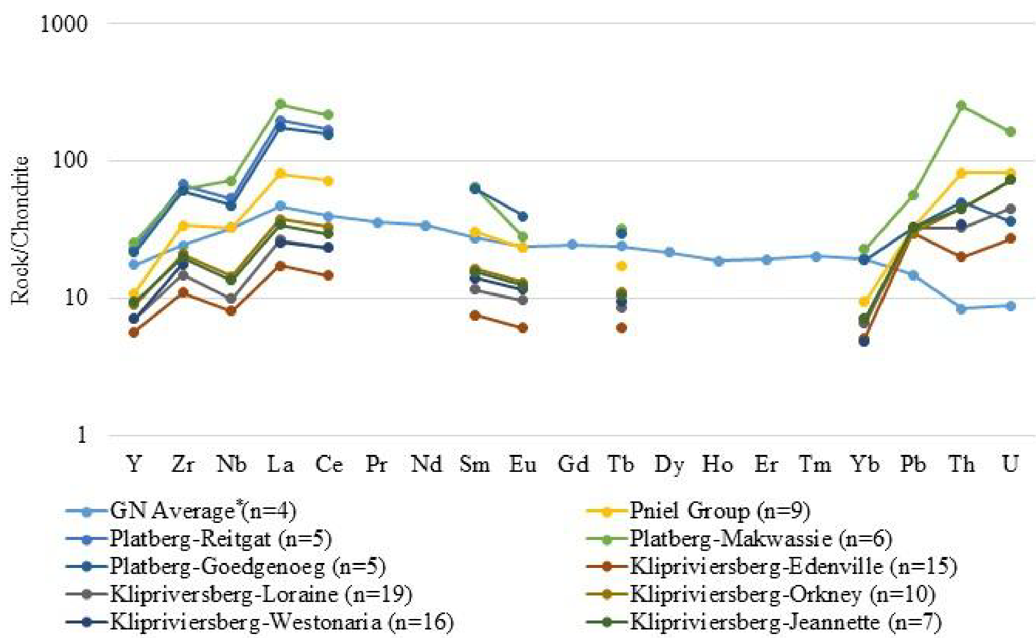

Figure 3-16: Spidergram comparing the samples from this study that are marked with an astrix (Inlandsee Leucogranofels (ILG), Gabbronorite) to those found in the literature for A) Units within the regional bedrock (Lana et al. 2004[1]; Hart et al. 1990[2]) and B) Units from the Ventersdorp Group (Crow and Condie 1988). Note that in both cases the gabbronorite is has a shallower slope and is more enriched in heavy REE.

Figure 3-17A: Vredefort impact melt and bedrock compositions compared to Anna's Rust Sheet and associated mafic units

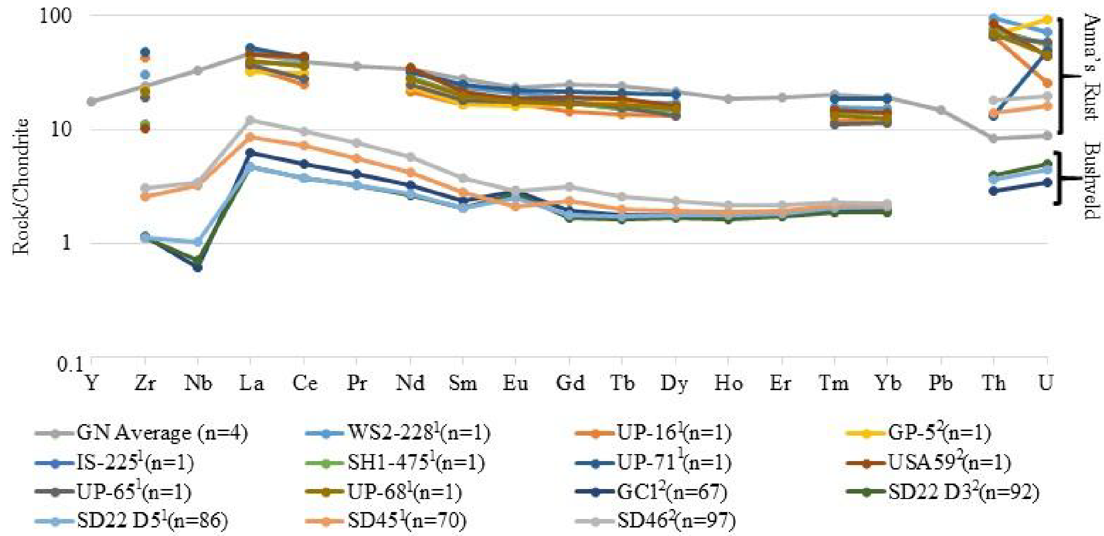

Figure 3-17B: Vredefort impact melt and impact melts from the Sudbury and Morokweng impact structures

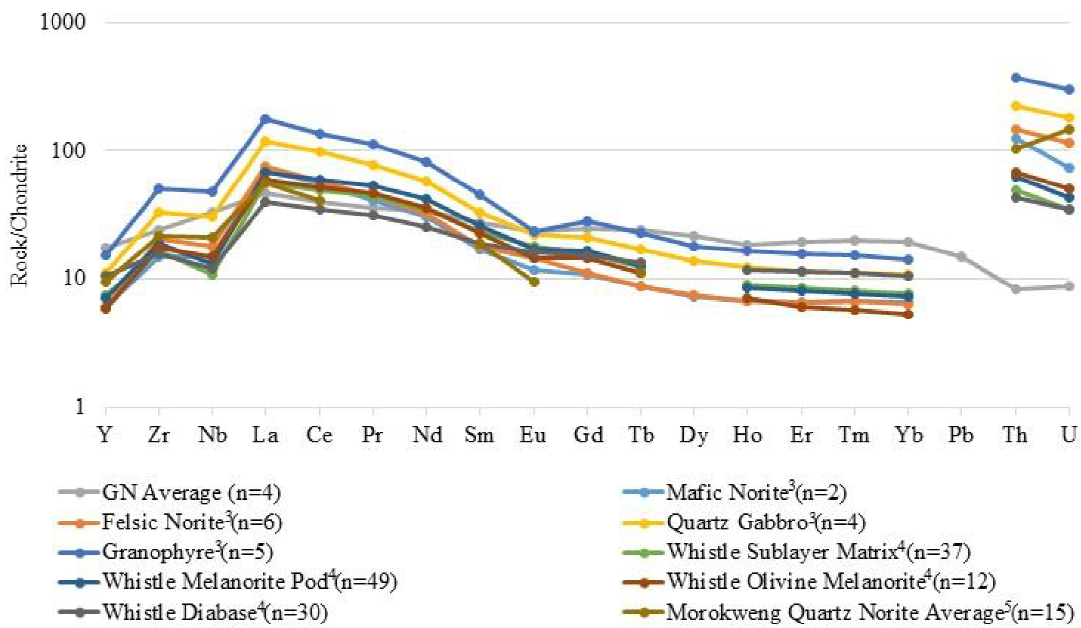

Figure 3-17: Spidergram comparing gabbronorite (GN Average) from this study to those found in the literature for A) The 1.1 Ga Anna's Rust sheet and its associated mafic units (note that the sample numbers used in the original study by Reimold et al. (2000)[1] are used here) located within the Vredefort dome and samples from the BIC (Wilson and Chunlett 2006[2]) located north-east of the Vredefort dome and B) Impact melt units from the Sudbury (Lightfoot et al. 2001[3]; Lightfoot et al. 1996[4]) and Morokweng (Andreoli et al. 1999[5]) impact structures.

The gabbronorite REE and MgO versus Ni signatures are very similar to those from pre and post impact endogenous Kaapvaal mafic magmatism (Ventersdorp and Anna's Rust), suggesting a possible mantle origin for the gabbronorite. Furthermore, the Fe-rich major element chemistry of cumulates from Bushveld melanorite and the Anna's Rust sheet gabbros are similar to the Fe content of the gabbronorite. Based on this chemistry data a lithospheric mantle origin appears to be the source of the Vredefort gabbronorites.

3.5.3 Scenarios for Gabbronorite Evolution

The geochemical and microstructural record of the gabbronorite and the local country rock allow for two possible paragenetic scenarios throughout impact processes, remobilization from deep levels of an already-formed mafic magma, or intrusion from a fractionated melt sheet that was once above the central uplift. Evidence for the first scenario, the remobilization of deeply formed mafic magmas, includes the geochemical similarity to other mantle-derived melts that have passed through the Kaapvaal lithosphere. Specifically, the comparison of REE profiles of the gabbronorite to that of the 2.7 Ga Ventersdorp lavas and the 1.1 Ga Anna's Rust suite intrusions. The evidence becomes contradictory however when the Hf isotopes are considered. The highly negative εHf values of gabbronorite zircon at T_{DM} =2.02 Ga (-1.4 to -7.9) reported in Chapter two suggest that the gabbronorite melt was derived from melting units of the Witwatersrand basin (Chapter 2: Cupelli et al. 2014), however, later published εHf zircon data from the 2.05 Ga Bushveld Intrusive Complex are in the range of -9 to -6.8 (Zirakparvar et al. 2014) and now allows for derivation from basaltic partial melts of the Kaapvaal subcontinental lithospheric mantle. The negative εHf isotopic compositions could be explained by the gabbronorite melt being released from a relict magma body from the Bushveld event during collapse of the central uplift. However, in this case, the relict magma chamber would have to reside at great depth (~100 km or more) in the lithosphere (Figure 3-18), since there is no evidence of a Bushveld age metamorphic overprint at the Moho beneath Vredefort (Moser et al. 2009). The second scenario, intrusion of a crustal fractionated melt sheet, differs from the first, mainly in regard to the additional time needed to segregate the mafic magma from the impact melt sheet. Cooling estimates for the Sudbury impact melt sheet are up to a 100 thousand years (Zieg and Marsh 2005), and so intrusion of the gabbronorite into the Archean gneisses of the central uplift would have had to occur after this time interval. This time lag, would require that the microstructural sequence of igneous shape fabrics, deformation of the high temperature quartz domains in the ILG, and recrystallization would all occur even later, implying a very long-lived ductile deformation regime in the central uplift. Either scenario points to a protracted history of igneous and metamorphic events in the crater modification stage that produces a range of impact melting textures and differentiation that have not been previously reported.

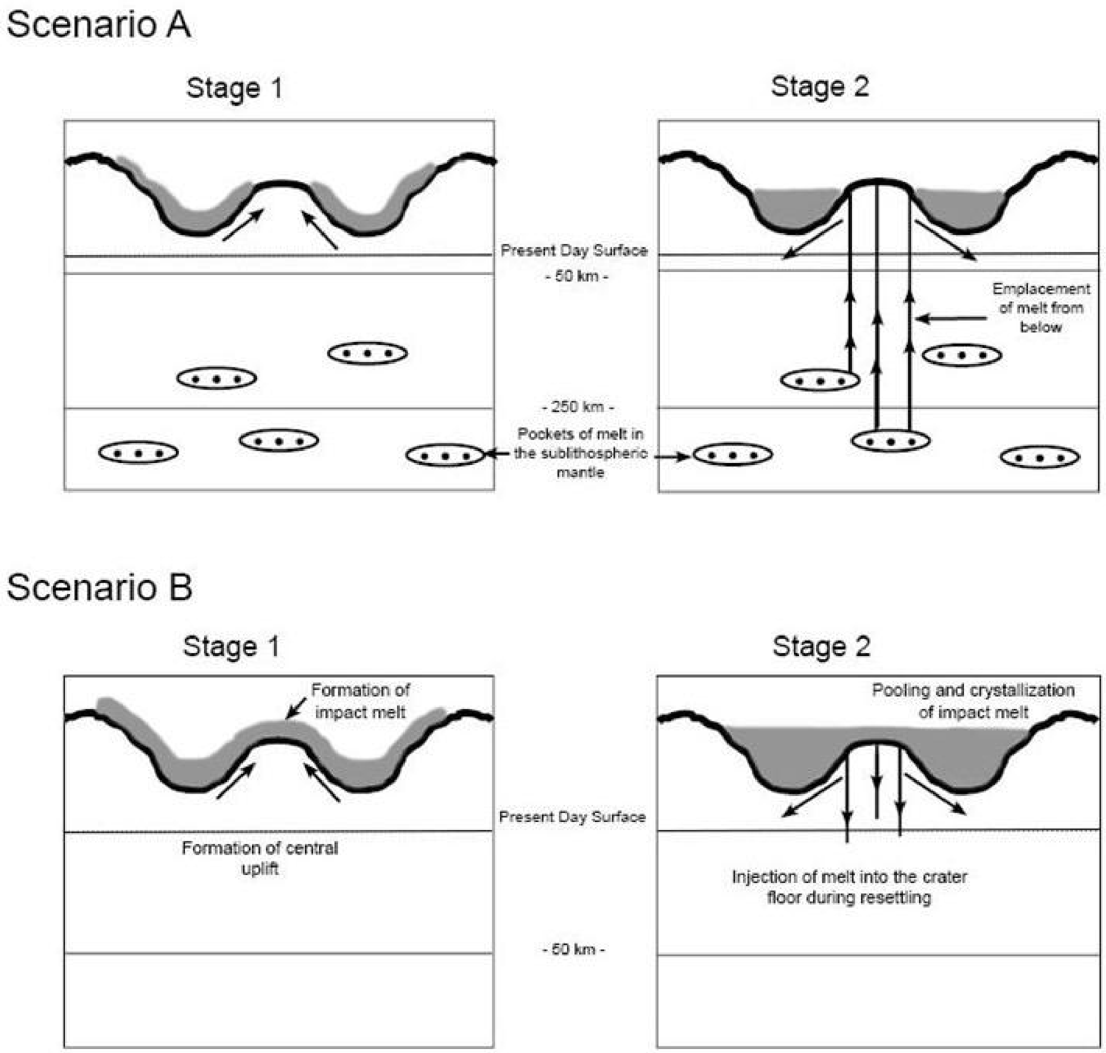

Figure 3-18: Possible emplacement scenarios for the gabbronorite. Scenario A considers emplacement from subsurface pods of melt from either deep below in the sublithospheric mantle or the lower crust, which would have been remobilized during readjustment of the central uplift. Scenario B considers emplacement of the gabbronorite from a conventional melt sheet with injection of melt into the crater floor during readjustment of the central uplift, this unit would have a crustal composition.

3.6 Conclusions

By studying the texture and chemistry of the gabbronorite found in the center of the Vredefort dome, we are able to build on our findings in Cupelli et al (2014) (Chapter 2) to better understand the impact-related processes that may have generated Vredefort gabbronorite intrusions. The gabbronorite no longer has a pristine igneous texture, minerals near intrusive margins are aligned, and igneous zircon formation extends throughout the crystallization sequence suggesting that the unit underwent textural modification during its crystallization. Whole rock chemistry of both major and minor elements indicates that the gabbronorite is a Fe-rich tholeiite that is similar to intracontinental basaltic magmas, and the REE chemistry is similar to the pre-impact 2.71 Ga Ventersdorp lavas (Armstrong et al. 1991) and to the post-impact 1.1 Ga Anna's Rust units (Reimold et al. 2000). When the gabbronorite is compared to pre-impact Bushveld Igneous Complex the $_{\varepsilon}$Hf zircon values and the mineral texture of the units are surprisingly similar, providing evidence for a deep mantle derived source. This has led to the present conclusion that the gabbronorite formed from a mantle source, however, the Hf isotope analysis conducted in Chapter two indicates a crustal contribution to its chemistry through contamination should not be completely ruled out at this time. The hypothesis presently favoured, and that should be tested in future work, is that the gabbronorite bodies were intruded from below into the sub-crater Archean target rocks, having been remobilized from pre-existing mantle magmas by the impact event. Future work on more samples and accessory phase analyses from other mafic units in the region would be needed to further the understanding of the gabbronorite formation and the complex history of the Vredefort Impact Basin.

It is known that zircon can be used to date an impact event, but their chemistry and textures may play a bigger role in the identification of an impact structures. The presence of baddeleyite in felsic units could function as a new indicator for the ultra-high temperature environments we expect to find associated with an impact event, and the foliation of impact-related intrusions may require researchers to re-evaluate units that have since been overlooked. There is still much to be learned about the effects of large impacts on the early crust but it is clear that we may have to expand our parameters in order to find old impacts on Earth.

3.7 References

Anders, E., and Grevesse, N.1989. Abundances of the Elements: Meteoritic and solar. Geochimica et Cosmochimica Acta, **53**(1): 197-214.

Andreoli, M.A.G., Ashwal, L.D., Hart, R.J. and Huizenga, J.M. 1999. A Ni- and PGE-enriched quartz norite impact melt complex in the Late Jurassic Morokweng impact structure, South Africa. Geological. *In* Large Meteorite Impacts and Planetary Evolution II: Boulder Colorado. *Edited by* Dressler, B.O., and Sharpton, V.L. Society Special Paper **339**: 91-108.

Armstrong, R.A., Compston, W., Retief, E.A., Williams, L.S. and Welke, H.J. 1991. Zircon ion microprobe studies bearing on the age and evolution of the Witwatersrand Basin. Precambrian Research, **53**:243–266. doi: 10.1016/0301-9268(91)90074-K.

Best, M.G. 1982. Igneous and Metamorphic Petrology. Blackwell Publishing, USA, 630p.

Coetzee, M.S., Beukes, G.J., de Bruiyn, H. and Bisschoff, A.A. 2006. Geochemistry and petrogenesis of tholeiitic intrusions of possible Bushveld-age in the Vredefort Dome, South Africa. Journal of African Earth Sciences, **45:** 213-235.

Crow, C. and Condie, K.C. 1988. Geochemistry and origin of late Archean volcanics from the ventersdorp supergroup, South Africa. Precambrian Research, **42**(1-2): 19-37.

Cupelli, C.L., Moser, D. E., Barker, I.R., Darling, J.R., Bowman, J.R. and Dhuime, B. 2014. Discovery of mafic impact melt in the centre of the Vredefort dome: Archetype for continental residua of early Earth cratering? Geology, **42**(5): 403-406.

Dietz, R.S. 1961a. Vredefort Ring Structure: Meteorite impact scar? Journal of Geology, **69**: 499-516.

El Goresy, A. 1965. Baddeleyite and its significance in impact glasses. Journal of Geophysical Research, **70**(14): 3453-3456.

French, B.M., Orth, C.J. and Quintana, C.R. 1989. Iridium in the Vredefort bronzite granophyres: Impact melting and limits on a possible extraterrestrial component. 19^{th} Proceedings of Lunar and Planetary Science Conference, 733-744.

French, B.M. and Nielsen, R.L. 1990. Vredefort bronzite granophyres: chemical evidence for an origin as meteorite impact melt. Tectonophysics, **171:** 119-138.

Gibson, R.L., Armstrong, R.A. and Reimold, W.U. 1997. The age and thermal evolution of the Vredefort impact structure: A single-grain U-Pb zircon study. Geochimica et Cosrnochimica Acta, **61**: 1531-1540.

Gibson, R.L. and Reimold, W.U. 2005. Shock pressure distribution in the Vredefort impact Structure, South Africa. GSA Special Papers, **384**: 329-349.

Gibson, R.L. and Reimold, W.U. 2008. Geology of the Vredefort impact structure, a guide to sites of interest. Council of Geoscience, Memoir **97**, Pretoria, 181 p.

Gibson, R.L., Reimold, W.U., Ashley, A.J. and Koeberl, C. 2002. Metamorphism on the Moon: A terrestrial analogue in the Vredefort dome, South Africa? Geology, **30**(5): 475-478.

Grieve, R.A.F. 1980. Impact bombardment and its role in proto-continental growth on the early earth. Precambrian Research, **10**(3-4): 217-247.

Grieve, R.A.F., Coderre, J.M., Robertson, P.B. and Alexopoulos, J. 1990. Microscopic planar deformation features in quartz of the Vredefort structure: Anomalous but still suggestive of an impact origin. Tectonophysics, **171**: 185-200.

Hart, R.J., Welke, H.J. and Nicolaysen, L.O. 1981. Geochronology of the deep profile through Archean basement at Vredefort, with implication for early crustal evolution. Journal of Geophysical Research, **86(**B11): 10663-10680.

Hart, R.J., Andreoli, M.A.G., Smith, C.B., Otter, M.L. and Durrheim, R. 1990. Ultramafic rocks in the centre of the Vredefort structure (South Africa): Possible exposure of the upper mantle? Chemical Geology, **83**: 233-248.

Ivanov, B.A. 2005. Modeling of the largest terrestrial meteoritecraters. Solar System Research, **39**: 381–409.

Koeberl, C., Reimold, W.U. and Shirey, S.B. 1996. Re-Os isotope and geochemical study of the Vredefort Granophyre: Clues to the origin of the Vredefort structure, South Africa. Geology, **24*:*** 913-916.

Kring D.A. and Cohen B.A. 2002. Cataclysmic bombardment throughout the inner solar system 3.9-4.0 Ga. Journal of Geophysical Research, **107**: 4-6.

Krogh, T.E., Davis, D.W. and Corfu, F. 1984. Precise U-Pb zircon and baddeleyite ages for the Sudbury area. *In* The Geology and Ore Deposits of the Sudbury Structure. *Edited by* Pye, E.G., Naldrett, A.J., and Giblin, P.E. Ontario Geological Survey, Special Volume **1**: 431-446.

Lana, C., Gibson, R.L. and Reimold, W.U. 2003. Impact tectonics in the core of the Vredefort dome, South Africa: Implication for central uplift formation in very large impact structures. Meteoritics and Planetary Science, **38(**7): 1093-1107.

Lana, C., Reimold, W.U., Gibson, R.L., Koeberl, C. and Siegesmund, S. 2004. Nature of the Archean midcrust in the core of the Vredefort Dome, Central Kaapvaal Craton, South Africa. Geochimica et Cosmochimica Acta, **68**(3): 623-642.

Lightfoot, P.C. and Doherty, W. 2001. Chemical Evolution and Origin of Nickel Sulfide Mineralization in the Sudbury Igneous Complex, Ontario, Canada. Economic Geology, **96**(8): 1855-1875.

Lightfoot, P.C., Keays, R.R., Morrison, G.G., Bite, A. and Farrell, K.P. 1996. Geologic and geochemical relationships between the contact sublayer, inclusions, and the main mass of the Sudbury Igneous Complex; a case study of the Whistle Mine Embayment, Economic Geology, **92**: 647-673.

Marchi, S., Bottke, W.F., Elkins-Tanton, L.T., Bierhaus, M., Wuennemann, K., Morbidelli, A. and Kring, D.A. 2014. Widespread mixing and burial of Earth's Hadean crust by asteroid impacts. Nature, **511**: 578-582.

Mazdab, F.M. and Wooden, J.L. 2006. Trace element analysis in zircon by ion microprobe (SHRIMP-RG); technique and applications. Geochimica et Cosmochimica Acta, **70**(Supp.1): A405, doi:10.1016/j.gca.2006.06.817.

Menuge, J.F. 1982. Nd isotope studies of crust-mantle evolution: the Proterozoic of south Norway and the Archaean of southern Africa. Ph.D. thesis, University of Cambridge, United Kingdom.

Moser, D.E. 1997. Dating the shock wave and thermal imprint of the giant Vredefort impact, South Africa. Geology, **25**: 7-10.

Moser, D.E., Cupelli, C.L., Barker, I.R., Flowers, R.M., Bowman, J.R., Wooden, J. and Hart, J.R. 2011. New Zircon Shock Phenomenon and their use for Dating and Reconstruction of Large Impact Structures Revealed by Electron

Nanobeam (EBSD, CL, EDS), and Isotopic U-Pb, and (U-Th)/He Analysis of the Vredefort dome. Canadian Journal of Earth Sciences, **4**: 117–139.

Moser, D.E., Davis, W.J., Reddy, S.M., Flemming, R.L. and Hart, R.J. 2009. Zircon U-Pb strain chronometry reveals deep impact-triggered flow. Earth and Planetary Science Letters, **277**:73–79. doi:10.1016/j.epsl.2008.09.036.

Murphy, A.J. and Spray, J.G. 2002. Geology, mineralization, and emplacement of the Whistle-Parkin offset dike, Sudbury. Economic Geology, **97**: 1399-1418.

O'Connell-Cooper, C.D. and Spray, J.G. 2011. Geochemistry of the Impact-Generated Melt Sheet at Manicouagan: Evidence for Fractional Crystallization. Journal of Geophysical Research, **116:** 1-22.

Olsson, J.R., Soderlund, U., Klausen, M.B. and Ernst, R.E. 2010. U–Pb baddeleyite ages linking major Archean dyke swarms to volcanic-rift forming events in the Kaapvaal craton (South Africa), and a precise age for the Bushveld Complex. Precambrian Research, **183**: 490–500.

Reimold, W.U. and Gibson, R.L. 1996. Geology and evolution of the Vredefort Impact Structure, South Africa. Journal of African Earth Sciences, **23:** 125-162.

Reimold, W.U., Pybus, G.Q.J., Kruger, F.J., Layer, P.W. and Koeberl, C. 2000. The Anna's Rust Sheet and related gabbroic intrusions in the Vredefort Dome-Kibaran magmatic event on the Kaapvaal Craton and beyond? Journal of African Earth Science, **31**(3-4): 499-521.

Schreyer, W. 1983. Metamorphism and Fluid Inclusions in the Basement of the Vredefort Dome, South Africa: Guidelines to the Origin of the Structure. Journal of Petrology, **24**: 26-47.

Schulze, D.J. 2001. Origins of chromian and aluminous spinel macrocrysts from kimberlites in Southern Africa. Canadian Mineralogist, **39**: 361-376.

Slawson, W.F. 1976. Vredefort Core: a cross-section of the upper crust. Geochimica Cosmochimica Acta, **40**: 117-121.

Spray, J.G., Butler, H.R. and Thompson, L.M. 2004. Tectonic influences on the morphometry of the Sudbury impact structure: Implications for terrestrial cratering and modeling. Meteoritics & Planetary Science, **39**(2): 287–301.

Stepto, D.1979. A geological and geophysical study of the central portion of the Vredefort Dome Structure. PhD Dissertation, University of Witwatersrand, Johannesburg, 378p.

Stepto, D. 1990. The geology and gravity field in the central core of the Vredefort structure. Tectonophysics, **171**: 75-103.

Streckeisen, A. 1975. To each plutonic rock its proper name. Earth Science Review, **12**: 1-33.

Stevens, G., Gibson, R.L. and Droop, G.T.R. 1997. Mid-crustal granulite facies metamorphism in the Central Kaapvaal craton: the Bushveld Complex connection. Precambrian Research, **82**:113-132.

Therriault, A.M., Ostermann, M., Grieve, R.A.F. and Deutsch, A. 1996. Are Vredefort Granophyre and Sudbury Offsets Birds of a Feather? Meteoritics & Planetary Science, **31**: A142.

Tuchscherer, M.G. and Spray, J.G. 2002. Geology, mineralization, and emplacement of the Foy Offset dike, Sudbury Impact Structure. Economic Geology, **97**: 1377-1397.

Wager, L.R., Brown, G.M. and Wadsworth, W.J. 1960. Types of Igneous Cumulates. Journal of Petrology, **1**(1): 73-85.

Walraven, F., Armstrong, R.A. and Kruger, F.J. 1990. A chronostratigraphic framework for the north-central Kaapvaal craton, the Bushveld Complex and the Vredefort structure. Tectonophysics, **171**: 23-48.

Zieg, M.J. and Marsh, B.D. 2005. The Sudbury Igneous Complex: Viscous emulsion differentiation of a superheated impact melt sheet. Geological Society of America Bulletin, **117**(11-12): 1427-1450. doi: 10.1130/B25579.1

Zirakparvar, N.A., Mathez, E.A., Scoates, J.S. and Wall, C.J. 2014. Zircon Hf isotope evidence for an enriched mantle source for the Bushveld Igneous Complex. Contribution in Mineral Petrology, **168**:1050-1068. DOI 10.1007/s00410-014-1050-2

Chapter 4: Microstructural Analysis of the Mafic-Ultramafic Inclusions in the Sublayer of the Sudbury Igneous Complex.

***Cupelli, C.L.[1], Moser, D.E.[1], Lightfoot, P.C.[2,3], Barker, I.R.[1]**

[1]*Department of Earth Sciences, University of Western Ontario, 1151 Richmond Street, London, Ontario, Canada, N6A 5B7.*

[2]*Department of Earth Sciences, Laurentian University, Sudbury, Ontario P3E 2C6, Canada*

4.1 Introduction

The Sudbury Igneous Complex (SIC) in Sudbury, Ontario, Canada (Figure 4-1) is now accepted as one of the largest surviving impact melt sheets (French 1998) and is an ideal place to study the crystallization processes of superheated magma bodies (Zieg and Marsh 2005) that are believed to have been more common on the early Earth (Grieve 1980). A number of cm- to m-scale ultramafic inclusions have been found within embayments and troughs (paleotopographic low points) at the base of the melt sheet (Pattison 1979) and are believed to be a product of the early crystallization of the SIC. A previous investigation of the Whistle embayment established the age of some of the inclusions (Corfu and Lightfoot 1996), however it still needs to be confirmed if the 1850 Ma igneous zircon and baddeleyite grains reported from the inclusions are cogenetic with the inclusion mineralogy and representative of the initial age of formation. Alternatively, the secondary zircon and baddeleyite grains could have grown while the inclusions resided in the melt sheet, which would be consistent with the incorporation of pre-impact country rock during melt sheet genesis and/or thermal erosion of the crater floor and would exhibit microstructures indicating shock (Wang et al. 2016). If the former model is correct, then it requires two early crystallization stages of the SIC melt during cooling.

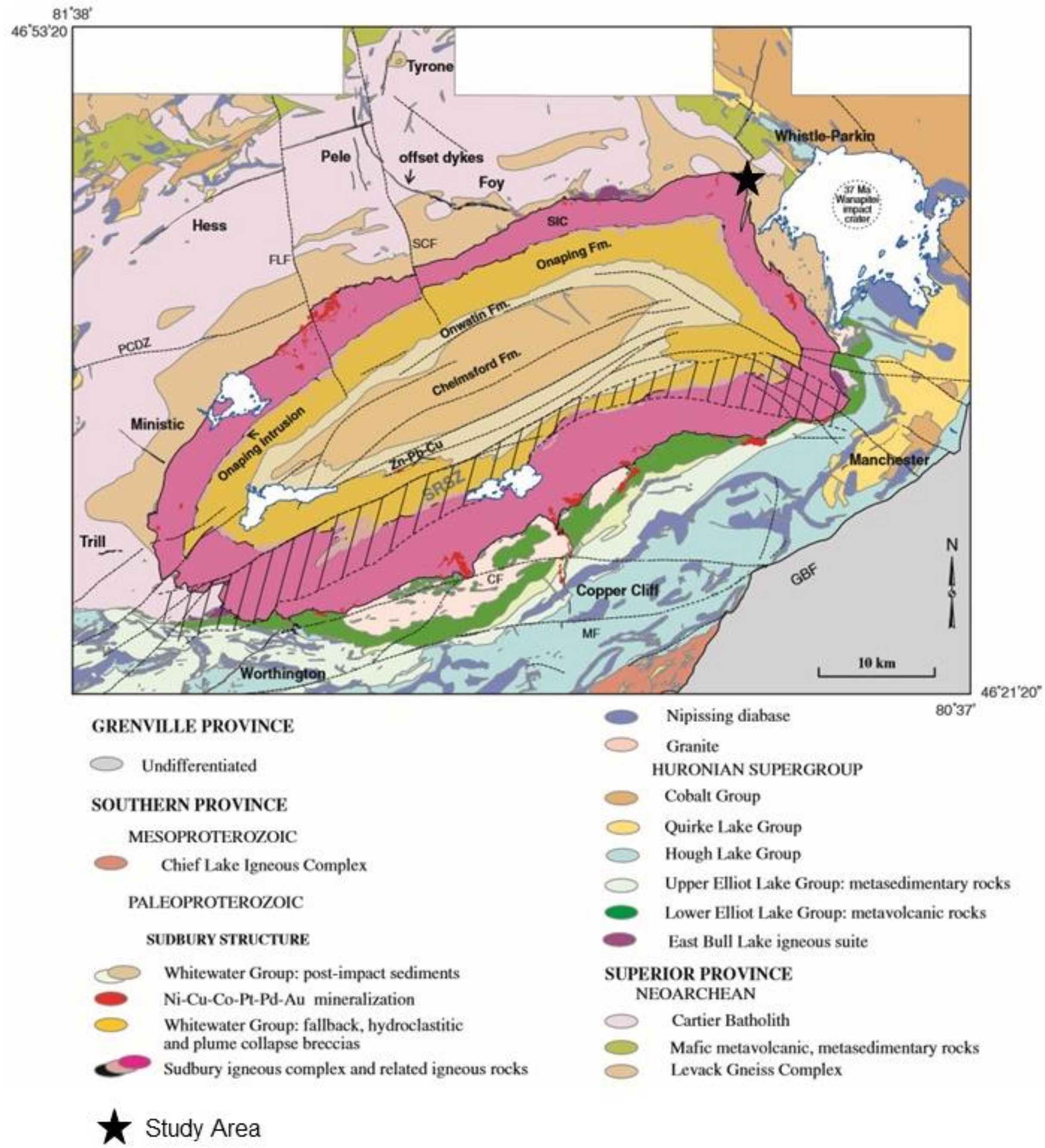

Figure 4-1: Geologic map from Ames et al. (2008) showing the surface relationship of the SIC to the surrounding country rock. Shows the location of the proximal impactites (units labelled), footwall rock types, and mineralization of the Sudbury impact structure. Abbreviations: Pumphouse Creek deformation zone (PCDZ), Sandcherry Creek fault (SCF), Fecunis Lake fault (FLF), Murray fault (MF), Creighton fault (CF), South Range shear zone (SRSZ) (hatched area), Grenville Front boundary fault (GBF). The sample area from this study is indicated with a black star.

Six Sublayer ultramafic inclusions and their norite matrix, and one mafic inclusion in the re-worked felsic Archean gneisses from beneath the SIC, were collected from the Whistle Mine in the North Range of the Sudbury impact structure (Figure 4-2), and analyzed. In-situ analysis of microstructural textures of accessory baddeleyite and zircon and the surrounding host minerals were conducted using optical and electron microscopy (backscatter electron (BSE), energy dispersive spectroscopy (EDS), electron backscatter diffraction (EBSD)). This was done in an effort to further test formation models of the mafic and ultramafic inclusions and the early stages of melt sheet crystallization at the interface between the melt sheet and the crater floor.

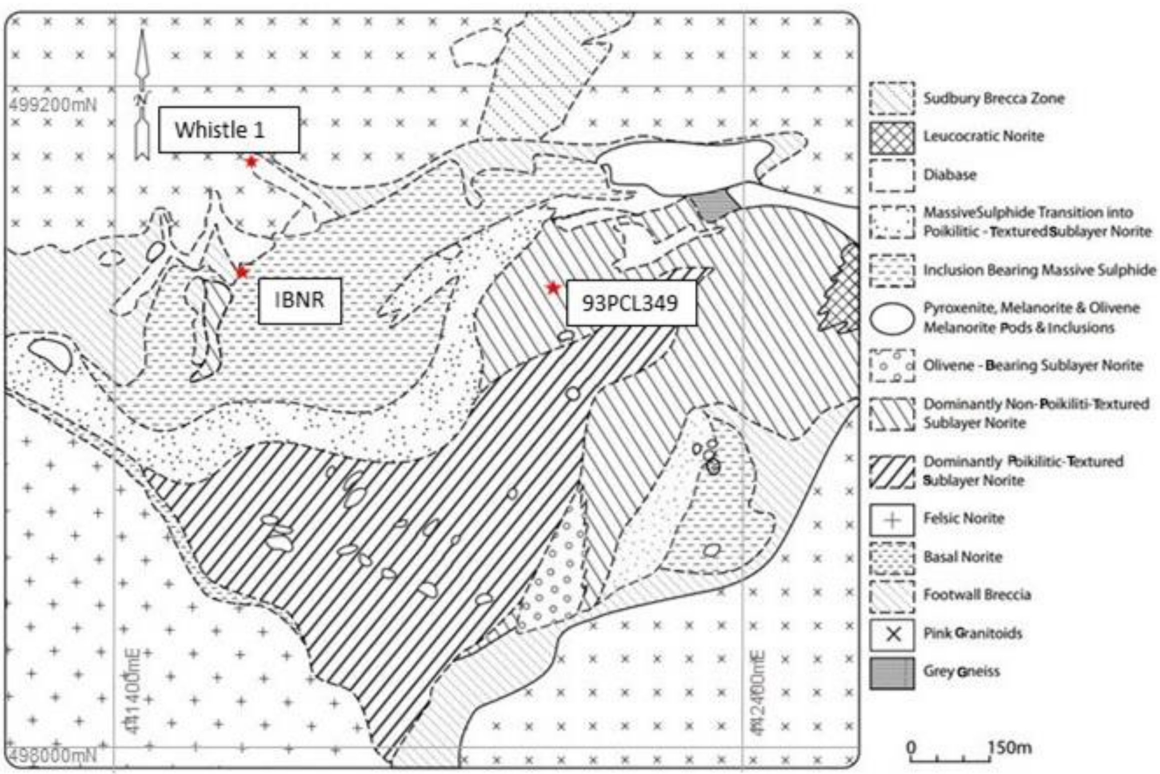

Figure 4-2: Whistle area map modified from Lightfoot et al. (1997a). Sample areas are marked with stars. 93PCL349 is a sulphide-bearing poikilitic mafic inclusion, IBNR is an inclusion basic norite and Whistle 1 is a felsic inclusion in sulphide-rich footwall environment. Sample RX187432 was taken from the footwall to the north east of this map.

4.2 Background

The effect of meteorite impacts on continental crust target material, as well as the detailed interaction of a large melt body with the interface of the crater floor, is not well understood (Grieve 1980; Ivanov 2005). A more complete understanding in these areas could help identify ancient craters on Earth and other planetary bodies, in addition to advancing aspects of economic geology within the Sudbury impact structure of Canada. The 1849 ± 0.2 Ma Sudbury impact structure (Davis 2008) contains the largest known differentiated melt sheet on Earth, and its preservation is partly due to the deformation of the impact basin during the Penokean and Mazatzal orogenies (Szabo and Hall 2006; Riller 2005; Raharimahefa et al. 2014). The excellent preservation of the structure, along with exceptional access to both surficial and deep samples (mine access and drill cores), has allowed researchers (eg. Rae 1975; Farrell et al. 1995; Corfu and Lightfoot 1996; Lightfoot et al. 1997c) to study the melt sheet at its contact with the basement rocks in order to develop a better understanding of the melt crystallization sequence and gain insight into the interaction between the melt sheet and the crater floor. This knowledge serves as a reference point for evaluating other poorly preserved and less extensive igneous bodies of impact origin such as the Vredefort Impact structure (Dietz 1961), the Manicouagan and Morokweng melt sheets, and possibly the Manitsoq structure in Greenland (Garde et al. 2012; Garde et al. 2014). The base of the Sudbury melt sheet is a discontinuous unit of variably mineralized inclusion-rich noritic and granitic breccia, which is known as the Sublayer (Pattison 1979). The norite and granite breccia matrix hosts many exotic mafic and ultramafic inclusions (Rae 1975; Scribbins 1984; Farrell 1997) that are more mafic than the Main Mass yet have a pronounced crustal geochemical signature (Lightfoot et al. 1997b; Farrell 1997; Prevec et al. 2000).

The origin of the inclusions is not presently understood, as they do not match the chemistry and age of any known adjacent country rocks (see below). It is assumed, that if the inclusions formed from mafic bodies in the country rock such as the mafic components of the Levack

Gneiss (Pattison 1979), Nippissing Gabbro (Card & Pattison 1973), East Bull Lake or Matachewan dykes (Prevec and Baadsgaard 2005) then the inclusion petrology should be similar to the parent rock as should the ages of the zircon and baddeleyite grains found in the inclusions. Instead, it was found that their ages corresponded to that of the Sudbury impact event (1.85 Ga) (Corfu and Lightfoot 1996). The composition of the inclusions, as well as the formation conditions that are required to produce them, is not conducive to their origin during early fractionation of the Main Mass (Lightfoot et al. 1997b). It is possible that the impact-age zircons have been reset, leading to a false age for the inclusions, however, the zircons structures (Corfu and Lightfoot 1996) have a primary magmatic origin.

4.2.1 Regional geology

The Sudbury impact structure is located abreast the Archean-aged Superior Province in the north and the Early Proterozoic Huronian supracrustal rocks of the Southern province to the south (Card et al. 1984). The 0.5 to 5.0 km wide Levack Gneiss Complex forms the northern borders of the Sudbury structure and is thought to have formed at 2711 ± 7 Ma and was subsequently metamorphosed at ~2640 Ma (Krogh et al. 1984). The granodioritic Cartier Batholith intruded the Levack Gneiss at 2642 ± 1 Ma (Szabo and Hall 2006). The Early Proterozoic supracrustal sequence of the Southern Province, which includes the basaltic and rhyolite comagmatic differentiated anorthosite-gabbro intrusions of the East Bull Lake Group (Lightfoot 2016), the Huronian Supergroup in the east, the Marquette Range Supergroup, the Animikie Group and associative rocks in the west make a discontinuous linear fold belt ~1,300 km long trending along the southern margin of the Superior Province (Card et al. 1972). The sequence was deposited between 2500 Ma and 1900 Ma ago and thickens southward from an erosional edge to reach a maximum of more than 10 km thick. The clastic sedimentary rocks were derived mainly from the Superior Province Archean craton to the north (Card et al. 1984). The Matachewan dyke swarm which consists of Fe-rich quartz tholeiite dykes that trend north-northwest, were intruded into the Archean rocks to the north at ~ 2473 +16/-9 Ma (Heaman 1997). The pyroxene and hornblende gabbro Nipissing dykes were emplaced at 2219 ± 4 Ma (Corfu and Andrews 1986; Noble and Lightfoot 1992; Sproule et al. 2007).

4.2.2 Geology of the Sudbury Structure

The Sudbury Impact Basin is a multi-ring impact structure, which based on U-Pb age dating of zircons, is determined to have formed synchronously with the Sudbury Igneous Complex (SIC) that has been dated at 1850.5 ± 3 Ma (Krogh et al. 1984). Using high precision Pb-Pb dating techniques of zircon, Davis (2008) established the age of the SIC to be 1849.53 ± 0.21 Ma for Felsic Norite from the lower contact of the intrusion and 1849.11± 0.19 Ma for the Black Norite found higher in the SIC.

The Sudbury region records evidence for multiple deformation events (Lightfoot 2016). The most important deformation events to occur to the Sudbury impact structure were the Penokean and Mazatzal orogenies. During the Penokean and Matatzal events, the South Range of the originally circular Sudbury Structure was displaced 8 km to the northwest which likely produced the elliptical form of the basin that is seen today (Szabo and Hall 2006; Riller 2005; Raharimahefa et al. 2014). In plan view, the SIC is now approximately 27 km by 60 km in size (Murphy and Spray 2002), and ~1.5 to 5 km thick (Ripley et al. 2015). The main units of the SIC are comprised of the radial and concentric offset dykes, the Sublayer; which is a discontinuous zone at the base of the SIC, the South Range Norite and Felsic Norite in the North Range, a transitional quartz gabbro, and the granophyre and plagioclase-rich granophyres (Figure 4-3) (Lightfoot et al. 1997b; Rousell and Gibson 1997).

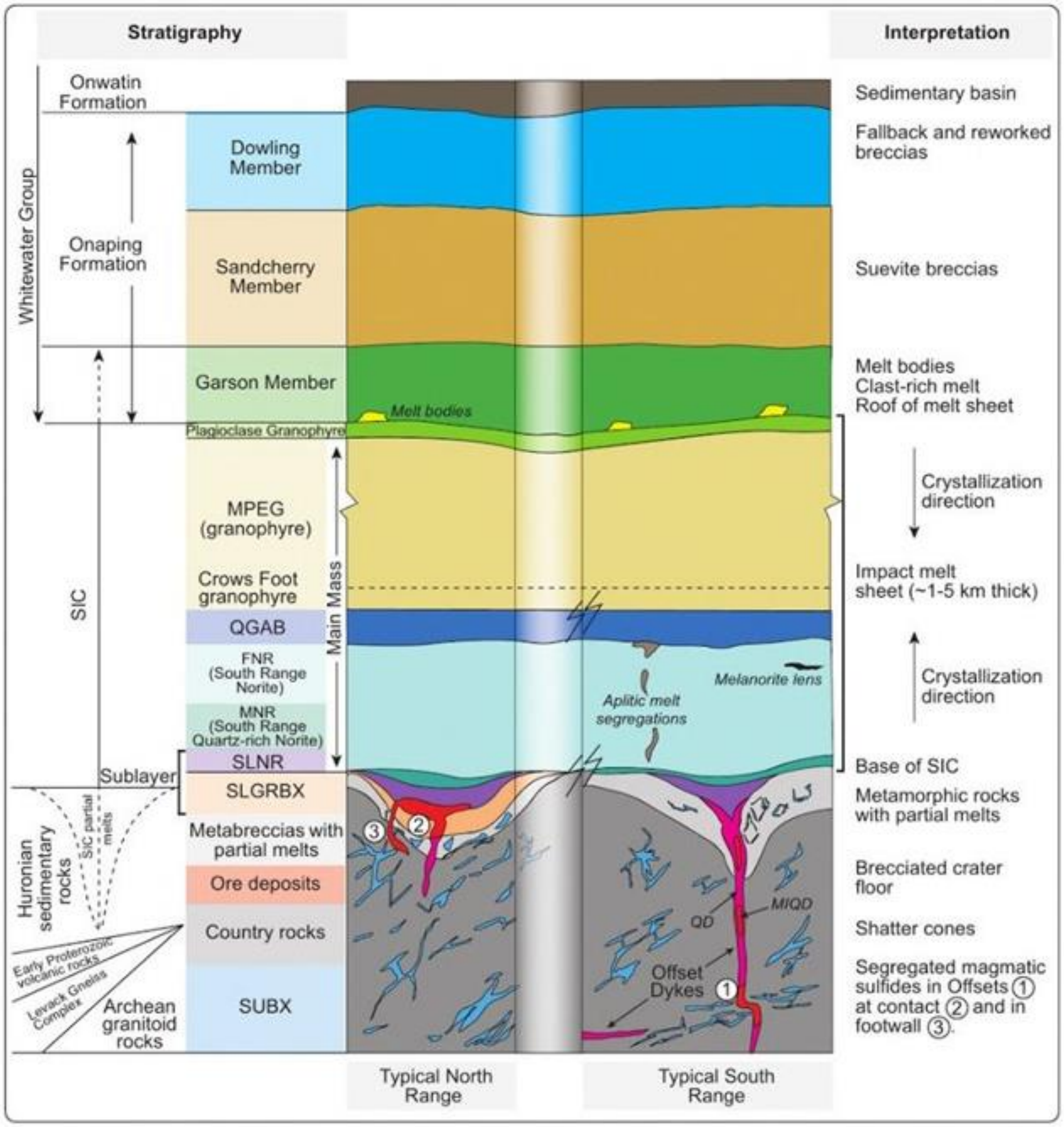

Figure 4-3: Cross section showing a simplified stratigraphic section through the Sudbury structure and its associated country rocks (Lightfoot 2016).

The Sudbury structure is best known for hosting the world's second largest nickel copper and platinum group element deposits. Its resource estimates exceed 1,549 million tons of ore (Keays and Lightfoot 2004). There is a strong relationship between the presence of mafic-ultramafic inclusions in the Sublayer and the development of Cu-Ni-Fe sulphide mineralization. This association includes both exotic and endogenic intrusive and extrusive mafic and ultramafic inclusions, but there are rarely any gneiss, granite, or meta-sedimentary inclusions. This has led to the suggestion that the sulphide is derived from the target protolith with chemical contributions of Ni, Cu, and PGE from pre-existing mineralization associated with mafic-ultrmafic rocks (Pattison 1979).

4.2.3 The Inclusions of the Sublayer

The Sublayer of the SIC contains many inclusions that can be broadly divided into two types. The first are those derived from the local footwall rocks and their impact-metamorphosed counterparts, an example of this can be observed at the Worthington offset (Lightfoot and Farrow 2002), and the second consists of mafic to ultramafic inclusions with unknown protoliths, belonging to the following rock types: diabase, less common anorthosite, troctolite and gabbro, melanorite, olivine-melanorite, and rare altered melanorite (Lightfoot et al. 1997b) similar to the exotic inclusions that occur with locally derived inclusions at the Whistle embayment (Lightfoot et al. 1997a). The diabase inclusions are composed of porphyritic plagioclase with matrices of augite, plagioclase, magnetite and secondary amphibole and the melanorites consist of inter cumulus plagioclase augite, biotite and cumulate spinel. The olivine in the olivine melanorite, is often altered to serpentine. The same inclusions contain unusually abundant biotite which alters to chlorite and apatite. Dunite, peridotites, orthopyroxenite and clinopyroxenites are developed in some of the embayments (Rae 1975; Scribbins 1984; Zhou et al. 1997). Accessory chromite, zircon, and apatite are also found in the inclusions (Lightfoot et al. 1997b; Zhou et al. 1997). The sulphide content of these compositional types ranges from rich (~45 wt %) to very low abundances (<1 %).

A number of different theories are given in the literature for the source of the mafic and ultramafic inclusions. Possible sources include, inheritance from pre-impact mafic bodies in the crater floor (footwall), early fractional crystallization products of the SIC, and relict fragments of mantle-derived picritic melts generated from mantle-derived magmas created by the impact that have been incompletely mixed with the crustal melt sheet and incorporated inclusions from the country rocks (Keays and Lightfoot 2004; Zhou et al. 1997). With regard to inheritance from the footwall, possible sources are the mafic components of the Archean Levack gneiss complex, the Nippissing diabase dykes and sills (Card & Pattison 1973), and Matachewan diabase dykes (Lightfoot et al. 1997c), and finally the Huronian mafic intrusive suite, consisting of the East Bull Lake and Shakespeare-Dunlop intrusions to the west, the River Valley intrusion in the east, and a number of smaller intrusions that occur in between these major bodies (Prevec and Baadsgaard 2005). Pattison (1979) and Farrell et al. (1995) have dismissed the Levack complex as a source, based on compositional and textural differences, and this was later supported by geochronological data. Lightfoot et al. (1997c) found that compositionally the Matachewan diabase dykes are a better fit for the diabase inclusions at Whistle than Nipissing, and showed that this diabase controlled the local composition of the Sublayer norite. The Matachewan dykes however, have an age of 2.45 Ga, and do not match the 1848.1 to 1849.8 Ma zircon and baddelyite ages found for the inclusions or the zircon ages for a raft of plagioclase porphyritic diabase at the Whistle Mine (Corfu and Lightfoot 1996). Lightfoot et al. (1997c) suggests that the diabase inclusions formed from country rock that was not directly underlying the Whistle Mine embayment, and due to the mafic country rocks having a higher melting point than the felsic rocks in the footwall, they were not completely melted; their greater density relative to the felsic melt sheet caused them to accumulate at the bottom of the melt sheet (Keays and Lightfoot 2004).

Morrison et al. (1994) have also hypothesized that the inclusions are products derived from the SIC, they suggested that the inclusions were a product of the early stages of crystallization which had accumulated at the base of the footwall embayment's prior to disturbance and inclusion in later norite. It was argued however that the mineral composition and cooling history of the SIC did not fit with this origin because of the enrichment in MgO and incompatible trace elements (Lightfoot et al. 1997c) relative to the Main Mass. Based on an unusual MgO enrichment, as well as an enrichment of Cr in aluminous spinel, and zircon inclusions within spinel, it was hypothesized by Lightfoot et al. (1997c), that the Sublayer mafic-ultramafic inclusions post-date the earliest melt sheet formation, and instead represent crystallization of a mantle-derived picritic melt that was injected from the base of the SIC (Zhou et al. 1997). Farrell (1997) conducted an in-depth study of the inclusions found at the Whistle embayment, and discovered that the contacts between the melanorite inclusions and the Sublayer matrix is hard to distinguish due to their gradational nature. Mafic-ultramafic inclusions analyzed from within massive sulphide rich zones were found to be extremely altered, resulting in the loss of primary mineralogy, however relict textures are preserved and show similarities with the olivine bearing ultramafic inclusions from the silicate rich Sublayer. Farrell (1997) also studied the chemistry of the inclusions from the Whistle embayment and found that the similarity in trace element chemistry and a continuous trend of SiO_2, Al_2O_3, Na_2O, TiO_2 and K_2O when plotted against MgO for both the igneous textured Sublayer matrix (ITSM) and the mafic to ultramafic inclusions supported a definitive genetic link (Figure 4-4). This evidence supports Morrison et al. (1994) earlier hypothesis and proposes that the inclusions are cumulates that formed early from the source magma and that the residual melt then crystallized to produce the ITSM.

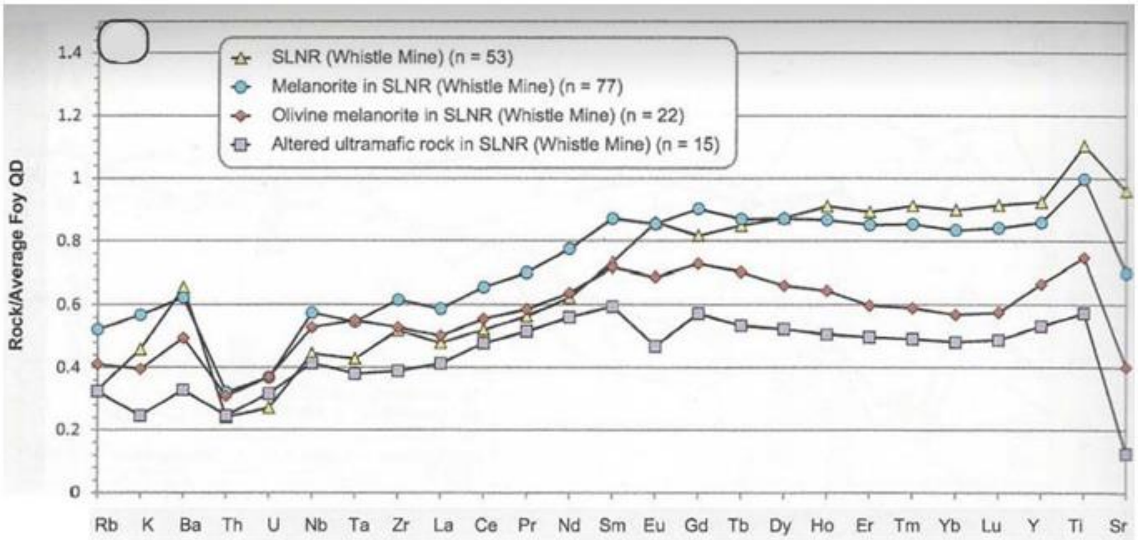

Figure 4-4: Geochemistry of Sublayer norite matrix, and inclusions of melanorite, olivine melanorite and altered melanorite from the Whistle embayment normalized to the average composition of the quartz diorite from the Foy Offset Dyke (from Lightfoot 2016).

A U-Pb geochronology study by Corfu and Lightfoot (1996) reported the analysis of five mafic and ultramafic inclusions from the Whistle embayment and found zircon ages ranged between 1848.1 to 1849.8 Ma suggesting syn-impact formation. A skeletal igneous crystal form for the zircon and a typical bladed form of igneous baddeleyite was inferred from the dominant fragments observed (Corfu and Lightfoot 1996), however because grains were recovered through mechanical crushing contextual relationships of the zircon and host could not be evaluated. A main unresolved issue is if zircon and baddeleyite crystals have re-set U-Pb age, are products of crystallizations of secondary melt pockets within older rocks, or are igneous crystallization products of the SIC.

4.3 Methods - Petrography and Electron Microscopy

Samples were obtained by Dr. Peter Lightfoot as part of Ontario Geological Survey research in 1993 at the former Whistle Mine open pit (Figure 4-2). Petrographic and SEM analyses of polished thin sections were conducted with a Hitachi SU6600 Field Emission Gun-Scanning Electron Microscope (FEG-SEM) at Western University's Zircon and Accessory Phase Laboratory (ZAPLab). Secondary electron (SE) and backscatter electron (BSE) imaging was performed using a beam accelerating voltage of 15 kV. The typical working distance between the pole piece and sample was ~ 10 mm. For cathodeoluminescence (CL) imaging beam conditions varied slightly with a higher probe current and an accelerating voltage of 10 kV. The working distance for CL was set to ~ 14 mm. Accessory minerals were located in thin section using an automated energy dispersive spectroscopy (EDS)-BSE analysis routine (Oxford INCA's Feature module) and mapped out using ArcGIS software to create MicroGIS maps; these maps allow the relationships of accessory and primary minerals to be examined. Once all accessory phases were located, grains of interest were imaged and the mineralogy of accessory phases and surrounding minerals were manually confirmed using qualitative EDS point analyses.

Samples were prepared for electron backscatter diffraction (EBSD) by using vibratory colloidal alumina polishing methods to ascertain that no subsurface damage existed that would hinder diffraction. Once polished, the samples were carbon coated and mounted at a 70˚ angle. The sample was then placed in the FEG-SEM for imaging using the approach described in Moser et al. (2011). An accelerating voltage of 20 kV was used to obtain a strong diffraction signal. EBSD mapping consisted of 'large area maps', which were stitched together using many smaller rastered frames and were used to assess any textures and identify phases. Higher magnification maps were produced of individual zircons to test for impact-related strain. Microstructural EBSD offline analyses were performed with Channel 5 Oxford/HKL software. SEM-CL and EBSD mapping of select zircon and baddeleyite targets were carried out where possible however high U content and metamictization common in SIC zircon (Davis 2008) often precluded CL and EBSD analyses.

4.4 Results

A range of inclusion types and matrix rock environments from different sites across seven hundred meters were selected for analysis and seven inclusions and some of their contacts with the Sublayer matrix were examined in detail. The results are grouped by inclusion mineralogy and matrix composition. Generally, the inclusion contacts are gradational, and inclusions are round with a diameter range of ~ 1 cm up to several metres (Lightfoot 1997a). In two cases, two or three thin sections were made of the same hand sample to test for local differences in the transition between inclusion and matrix. Automated EDS-BSE mapping was performed on 12 thin sections. Zircon was found in nine of those thin sections, baddeleyite in six, monazite in seven, and zirconolite in five. The accessory phases are randomly distributed in all of the sections.

4.4.1 Mafic Inclusion in Sulphide-Poor Norite Matrix Samples (93PCL349A,-B,-C)

Three thick (~4 mm) sections were prepared, representing a transect across the sulphide-poor norite matrix (93PCL349A), inclusion contact (93PCL349B) and a sulphide-bearing poikilitic mafic inclusion (93PCL349C) (Fig. 4-5A, B, C). Both the inclusion and matrix have a similar igneous texture, differing mainly in grain size. The matrix being medium grained (average pyroxene dimension 2 mm) and the inclusion being medium to coarse grained with some pyroxene grains as large as 5 to 6 mm. Phase mapping of the Sublayer matrix by EBSD (Figure 4-6 and 4-7) identified intercumulus plagioclase, orthopyroxene and clinopyroxene occurring in a ~4:1 ratio, allowing it to be classified as a gabbronorite. Whereas, the inclusion is closer to a pyroxenite composition because clinopyroxene is the dominant phase, occurring in a

~3:1 ratio with orthopyroxene. In both the inclusion and matrix material, the EBSD analysis did not show any preferred orientation of any minerals (Figure 4-6C and 4-7C).

Zircon, baddeleyite, monazite and zirconolite were present in thick sections 93PCL349A of the norite matrix and 93PCL349C of the inclusion. Simple euhedral grain outlines are rare and most commonly grains are subhedral in both thick sections. There is no preferred association with any of the main rock forming minerals (Figure 4-5), and no shock deformation features were observed in any of the minerals. In the norite matrix, the accessory phase sizes are larger than those found in the inclusion which vary from 8 to 33 μm for baddeleyite, 8 to 30 μm for monazite, 7 to 114 μm for zircon, and 8 to 57 μm for zirconolite.

In the inclusion, these minerals are smaller on average compared to the matrix (8 to 29 μm for baddeleyite, 8 to 22 μm for monazite, 8 to 51 μm for zircon and 10 to 34 μm for zirconolite). The internal regions of the baddeleyite grains are typically featureless, with the exception of small inclusions and cracks. The zircons often have weak planar or irregular zoning, which is expressed strongest near the edges, and many are cracked. The monazite and zirconolite grains have cracks and inclusions but are otherwise featureless with the exception of one monazite and two zirconolite from the inclusion that show weak concentric zonation.

The thick section that spans the contact between the matrix and the inclusion (93PCL349B) contains zircon, zirconolite and baddeleyite. The zircon and baddeleyite grains in the matrix are typically larger than in the inclusion (up to 133 μm for zircon from the matrix and up to 14 μm for those from the inclusion, and up to 20 μm for baddeleyite from the matrix and up to 14 μm for those from the inclusion), with no preferred association to any rock-forming minerals. No shock deformation features were observed (Fig. 4-5B). In the matrix half of thick section 93PCL349B, baddeleyite with a rim of zircon was present (Figure 4-7F). A similar relationship was also noted in an olivine melanorite inclusion (RX187409) that was not studied here in detail due to pervasive alteration, in that case the zirconolite grain had a zircon rim and baddeleyite inclusion (Figure 4-8).

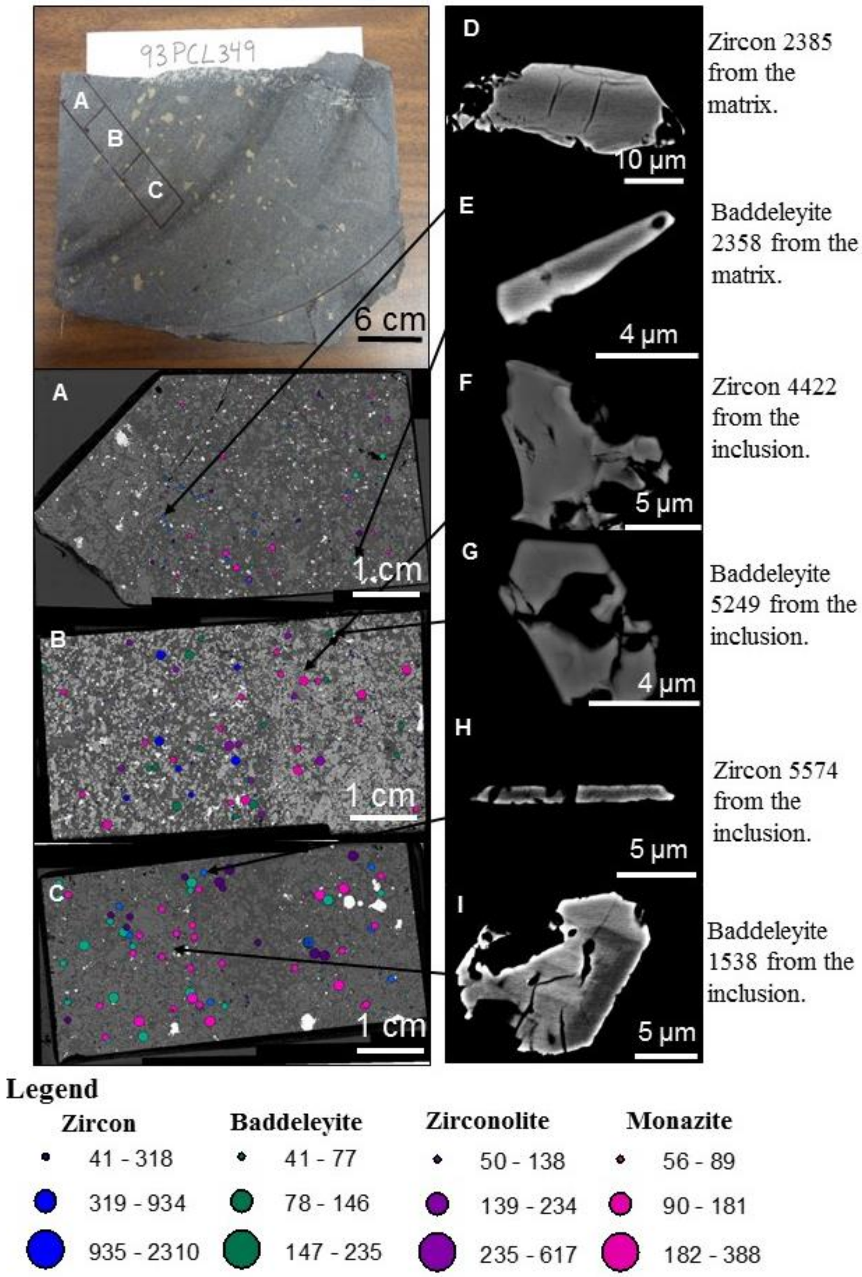

Figure 4-5: Plate of poikilitic norite pod in Sublayer Norite (93PCL349); The hand sample image showing the location of thin section transect from matrix to inclusion is in the upper left corner. A-C are BSE maps of thick sections A-C showing location and relative size of zircon and baddeleyite. D-I are BSE images of zircon and baddeleyite morphologies and textures. Note that the phases are generally subhedral and the accessory mineral poor region in the center of thin section C which may be a vein of Sublayer norite.

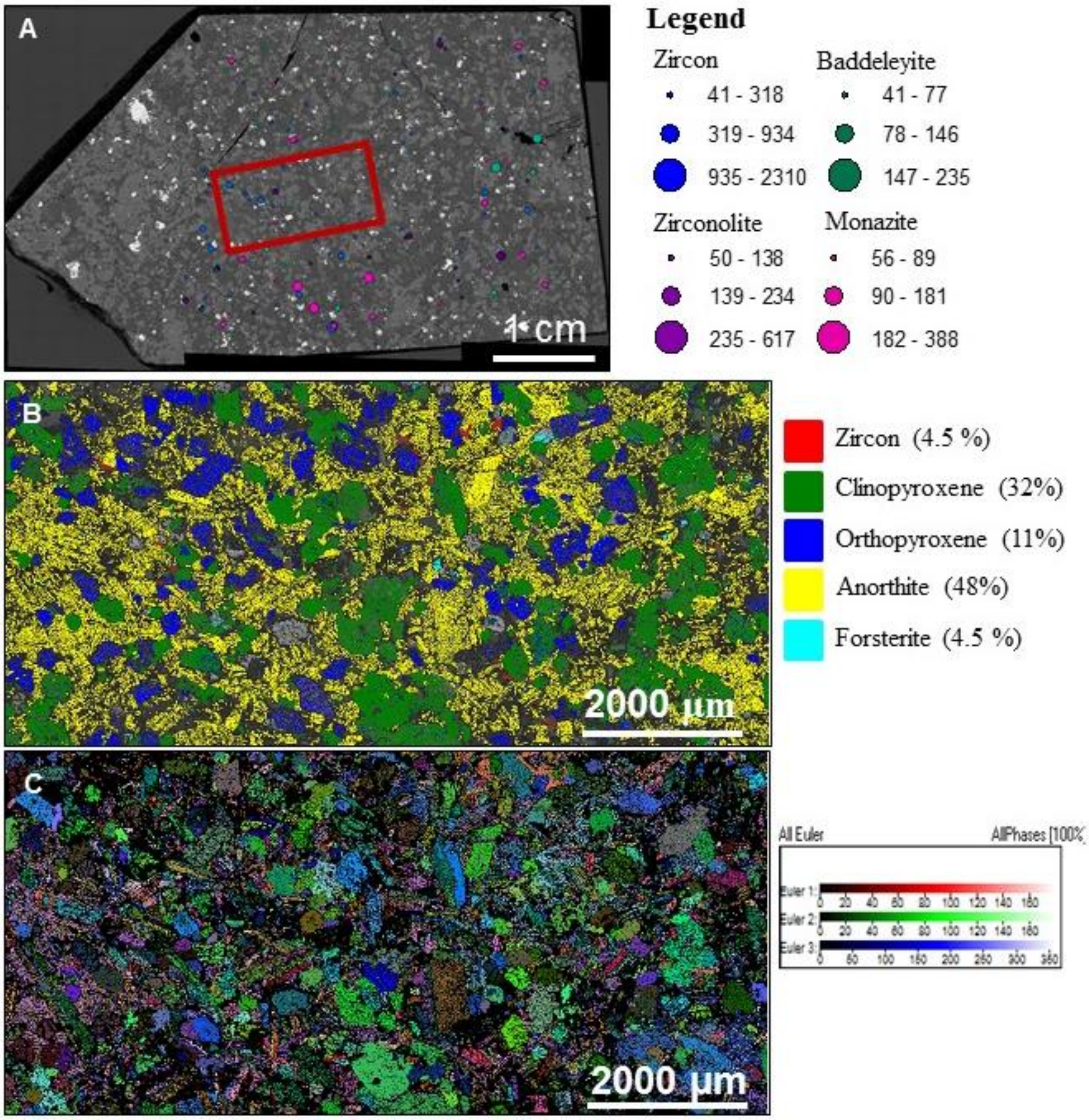

Figure 4-6: Plate of 93PCL349A which contains only Sublayer norite. A) BSE map of thick section showing location and relative size of zircon and baddeleyite, red box indicates area imaged with EBSD. B) EBSD phase map showing abundance and distribution of major mineral phases C) EBSD Euler angle map showing grain orientation, note that there does not appear to be a preferred orientation among the main minerals.

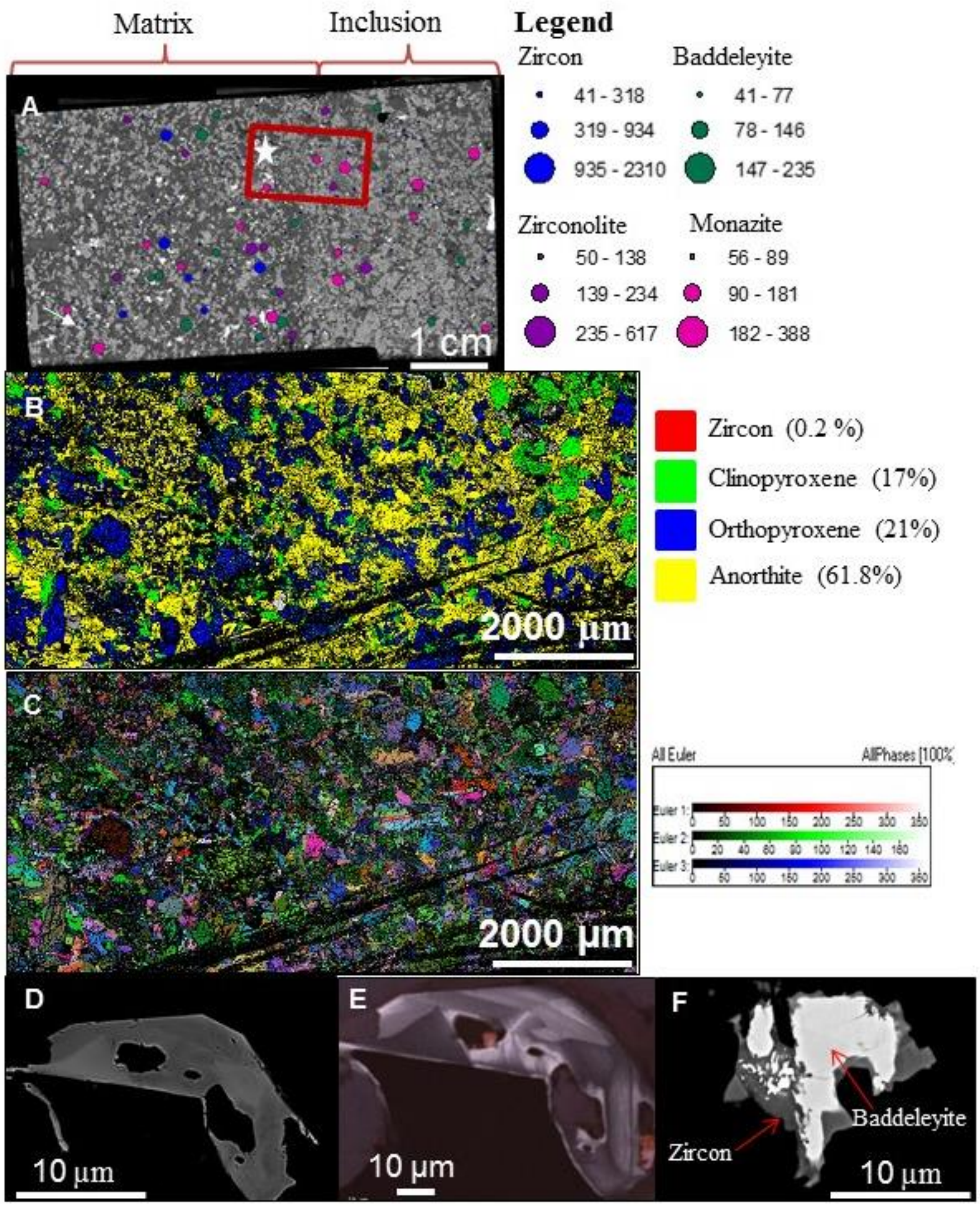

Figure 4-7: Plate of 93PCL349B which contains both matrix and inclusion material. A) BSE map of thick section showing location and relative size of zircon and baddeleyite, red box indicates area imaged with EBSD. B) EBSD phase map showing abundance and distribution of major mineral phases. C) EBSD Euler angle map showing random orientation in matrix and inclusion domains. D) BSE image of zircon 4538. E) CL image of zircon 4538, the location of Z4538 is noted on the feature map (A) with a white star. F) BSE image of feature 877 (location indicated with a white arrow), baddeleyite with a rim of zircon.

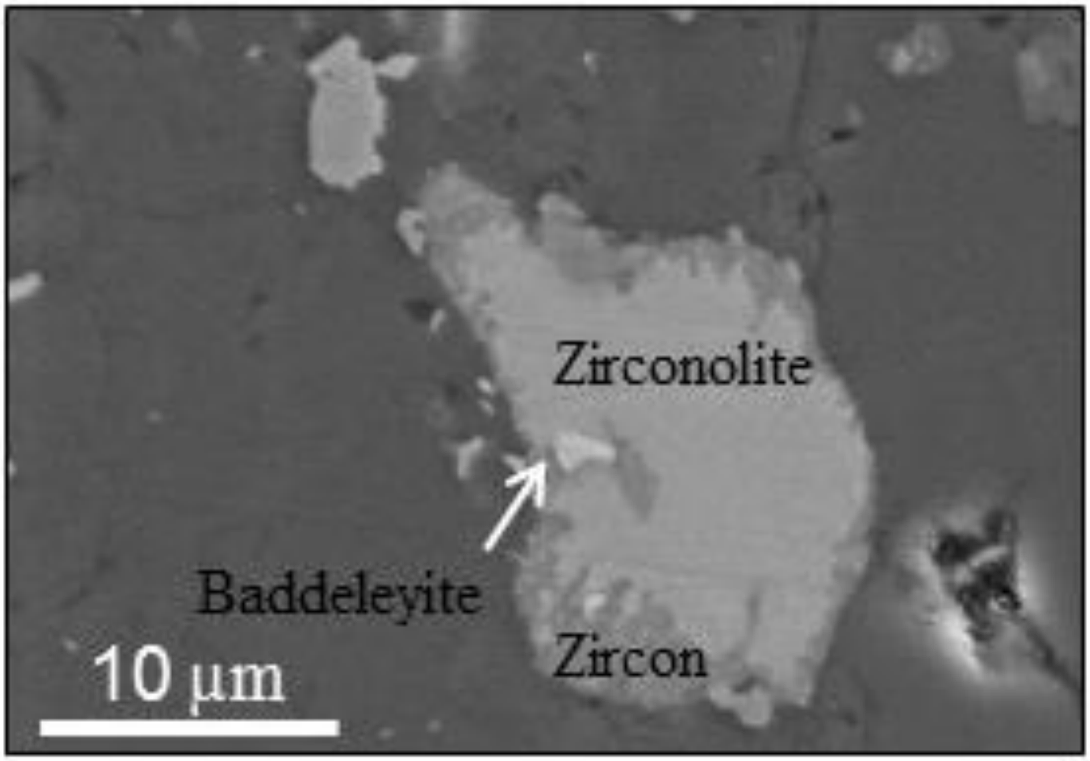

Figure 4-8: SE image of Zircon, Baddeleyite, and Zirconolite from an inclusion in olivine mela-norite sample RX187409.

4.4.2 Ultramafic Inclusions in the Sulphide-Rich Noritic Matrix Sample (IBNR_A,B)

The Sublayer contains a type of norite that Grant and Bite (1984) refer to as inclusion basic norite (IBNR); it commonly occurs near to the base of the embayment structure and has a more complex matrix of small heavily digested fragments. IBNR samples A and B (Figure 4-9 and 4-10) consist of an ultramafic inclusion within a sulphide-rich component of the Sublayer and were cut to straddle the inclusion-matrix contact at two different locations.

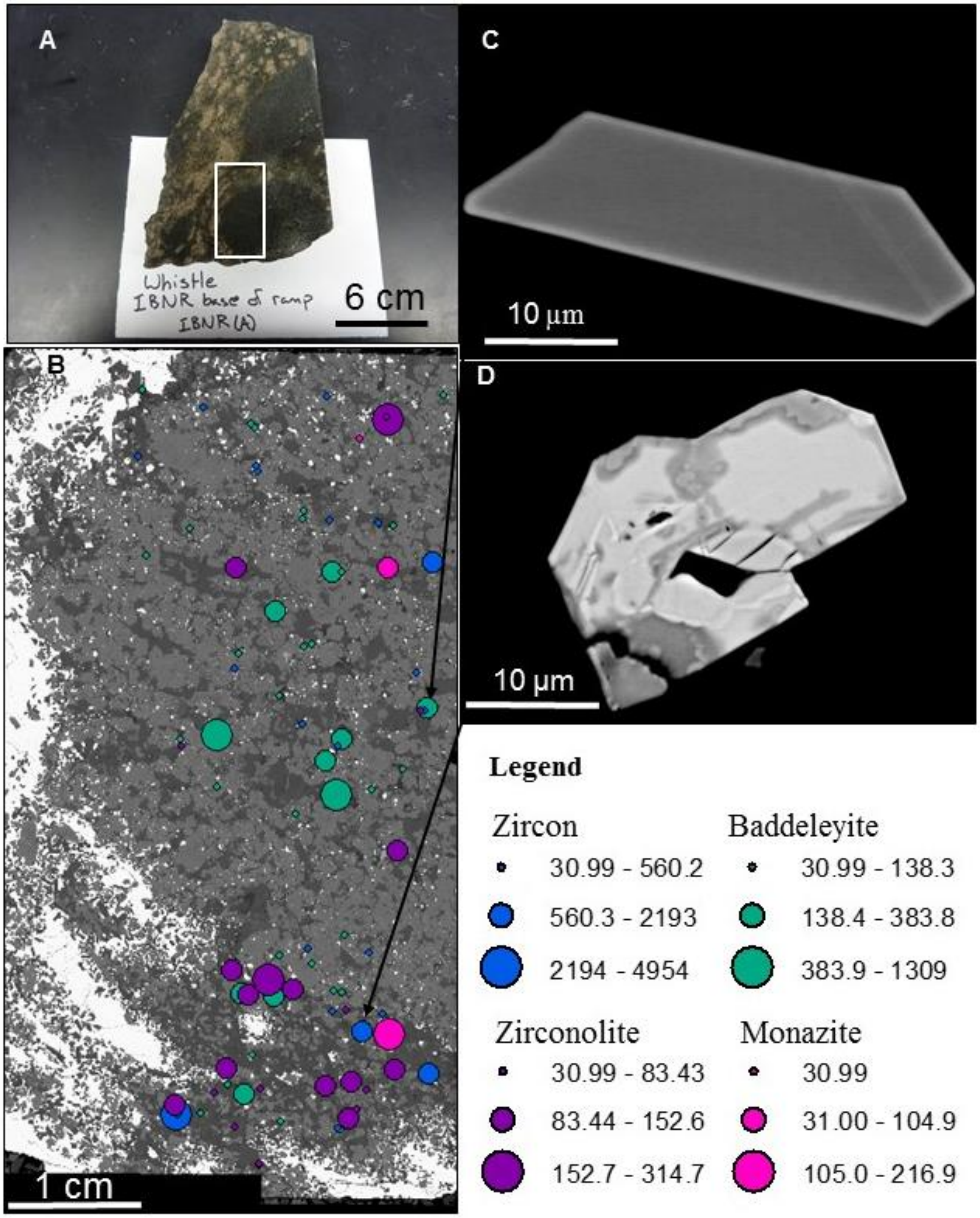

Figure 4-9: Plate of sulphide rich inclusion bearing norite (IBNR(A)). A) Hand sample image showing location of thin section. B) BSE maps of thin section showing location and relative size of zircon and baddeleyite. C) BSE image of baddeleyite 755 exhibiting prismatic texture. D) BSE image of zircon 2063.

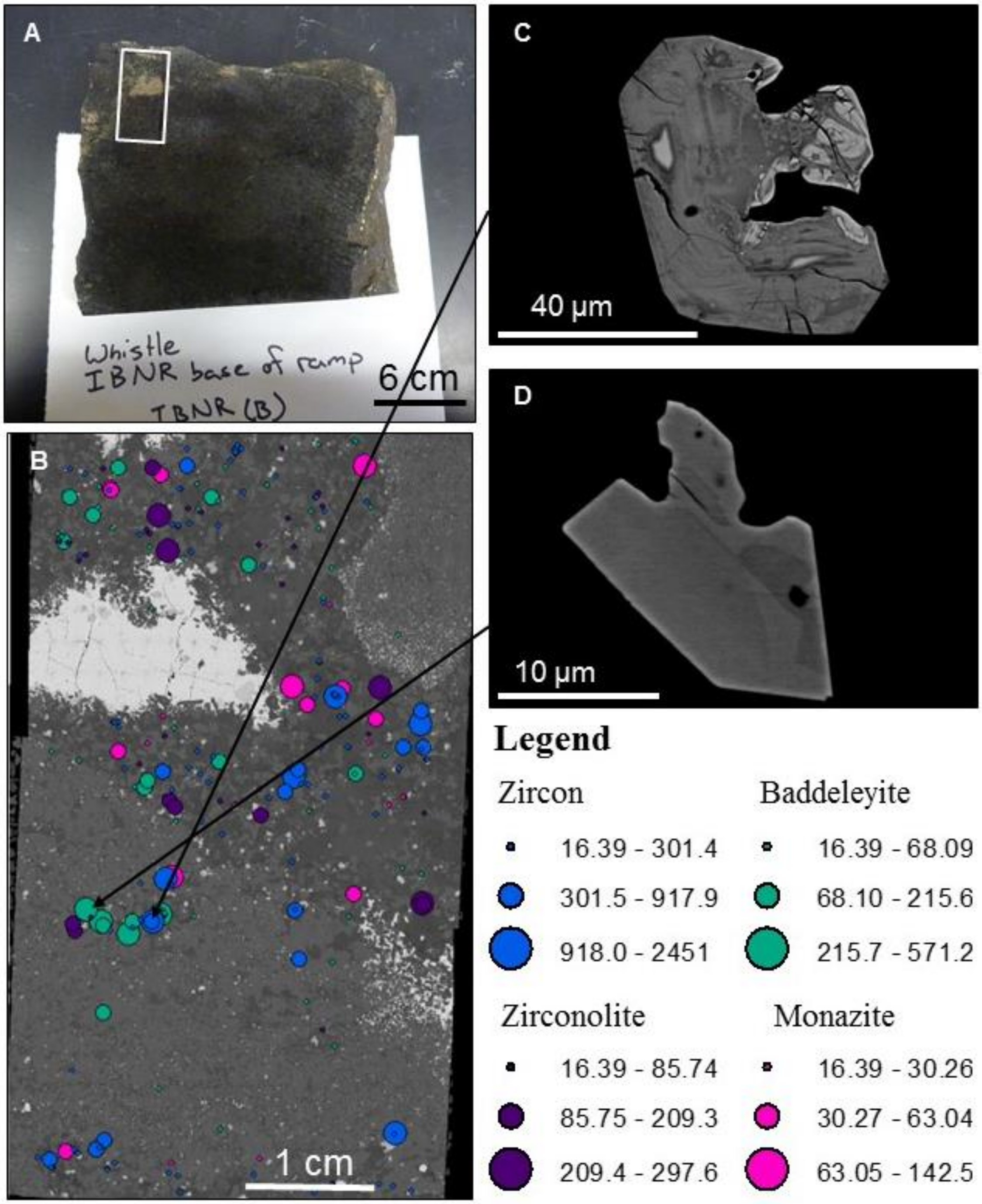

Figure 4-10: Plate of sulphide rich inclusion bearing norite (IBNR(B)). A) Hand sample image showing location of thin section. B) BSE maps of thin section showing location and relative size of zircon and baddeleyite. C) BSE image of zircon 8103. D) BSE image of baddeleyite 2356 exhibiting semi- prismatic texture.

The matrix in thin section IBNR(A) is dominantly massive sulphide with finer grained carbonate minerals, whereas the inclusion consists mainly of coarser-grained orthopyroxene and clinopyroxene and contains disseminated sulphides at the contact with the matrix. In thin section IBNR(B), the matrix material is coarser grained than in IBNR(A), whereas the inclusion material is a fine-grained assemblage of roughly equal amounts of clinopyroxene and orthopyroxene, with ~15% opaque (including oxides) that is arranged in a granoblastic ophitic to sub-ophitic texture. Plagioclase makes up ~25 to 40 % of the matrix in general, and the grains are up to 2 mm in size and are mostly needle-shaped and euhedral. Local graphic textures in quartz and feldspar occur alongside subhedral and seemingly primary biotite. Most of the plagioclase grains exhibit simple twins and occasionally contain inclusions of pyroxene or sulphide. The pyroxenes make up 35 to 45 % of the section and are up to 2 mm in size. The morphology of the pyroxene grains is typically anhedral to rounded, and exsolution lamellae are present within a subset of these. Many of the grains contain cracks and inclusions of opaques or plagioclase. The sulphides make up ~15 to 20 % in IBNR(A) and ~5 % in IBNR(B) and range from small cubic grains to massive stringers. The sulphides are generally made up of pyrrhotite with minor pentlandite; the pentlandite is finer grained than the pyrrhotite. IBNR(A) also contains up to 5 % biotite, which can be up to 1 mm in size that occurs mainly as anhedral grains, although there is a fraction of smaller euhedral grains. Quartz is present in the matrix material of IBNR(B), where it occurs in patches and contains many inclusions of plagioclase and pyroxene.

Secondary calcite alteration and triple junctions that are indicative of recrystallization are present within both samples, and carbonate alteration almost completely replaces some of the pyroxene grains. Late sericite alteration occurs along fractures and crosscuts the sulphides and fine-grained pyrite appearing to have grown outward from fractures, replacing the pyrrhotite

(Figure 4-11). In places, the biotite is observed to be truncated, or replaced, by alteration, and has inclusions of sulphide. In thin section IBNR(B), a secondary phase of crystallization, defined by small opaque and pyroxene grains is present.

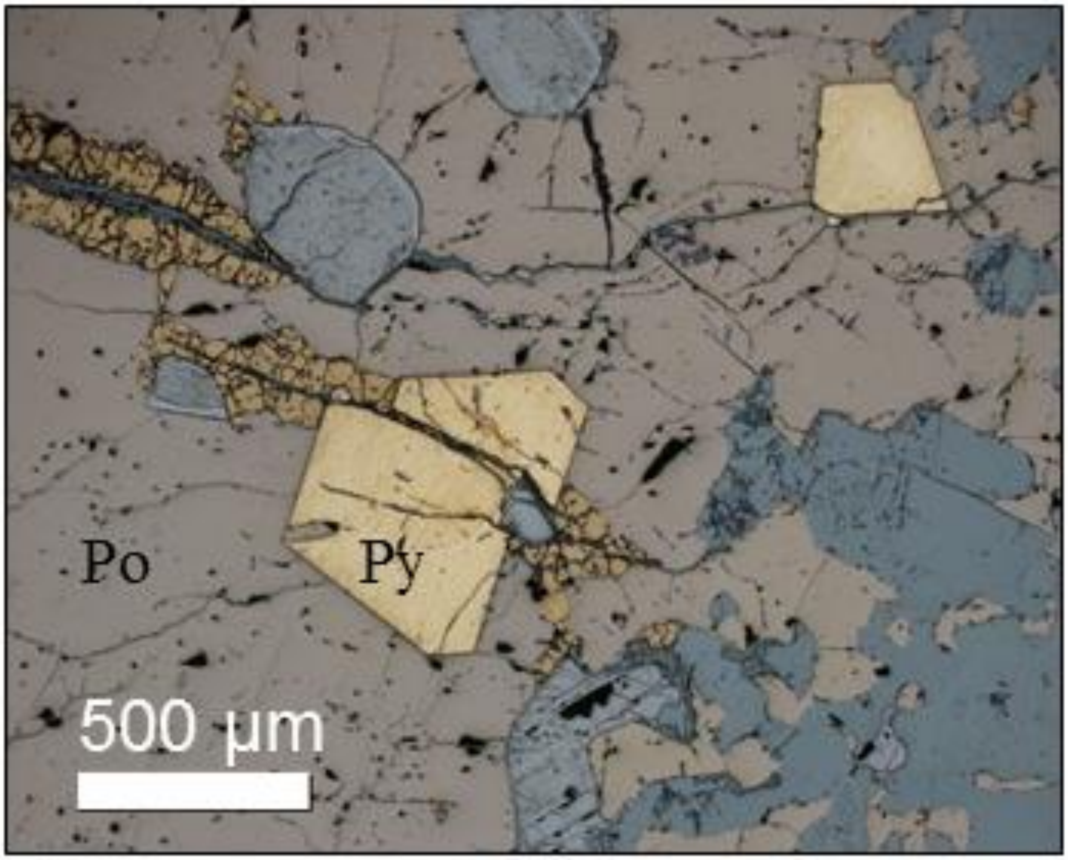

Figure 4-11: Photomicrograph of sample IBNR(B) taken in reflective light, showing pyrite (Py) growing outward from alteration along fractures and replacing primary pyrrhotite (Po) sulphide grains.

Zircon, baddeleyite, zirconolite and monazite were all found in sample IBNR. The distribution of accessory phases in IBNR(A) appears random whereas the baddeleyite grains in IBNR(B) are rare although a few grains appear concentrated in one domain. No accessory minerals were found as inclusions in the sulphide minerals. The zircons range in length from 6 to 151 μm, baddeleyites from 6 to 99 μm, monazites from 6 to 21 μm and zirconolite from 6 to 51 μm. It was observed that IBNR(A) contained a larger fraction of large zircon grains than

IBNR(B), whereas, regardless of sample, the grain morphologies all range from subhedral to euhedral. Most accessory phases contain cracks and pits, however the zircon contains additional internal features, such as mottled internal textures and zoning. Generally, none of the grains show any indication of shock microstructures or deformation.

4.4.3 Ultramafic Inclusions from the Footwall Environment (RX187432)

Thin section RX187432 (Appendix C-2) represents a mafic inclusion found in the felsic plutonic rocks of the Whistle footwall. The thin section is biotite rich, coarse-grained and highly altered. Carbonate alteration is present throughout the thin section completely replacing the parent mineralogy. Small quartz grains are distributed randomly, occurring as inclusions within other phases, as well as occurring as isolated grains. The opaque minerals (Fe-Ti oxides) occur throughout the thin section and are subrounded to anhedral, not appearing to be spatially associated with any mineral phase.

Zircons were the only accessory phase found in the thin section of sample RX187432 and appear randomly oriented (Appendix D-2). They range in size from 5 to 70 µm, with morphologies ranging from anhedral to prismatic and subrounded to rounded. The internal features include a mottled or pervasively fractured and altered texture in zircon, slight to irregular inclusions and cracks. In one anhedral zircon, linear trains of inclusions are observed within a metamict core, correlating with recrystallized linear features as revealed in EBSD mapping (Figure 4). It is possible that these were once curviplanar features due to shock metamorphism that recrystallized preferentially during post-shock fluid alteration although, none of the grains currently express any indication of planar shock microstructures (Figure 4-12A).

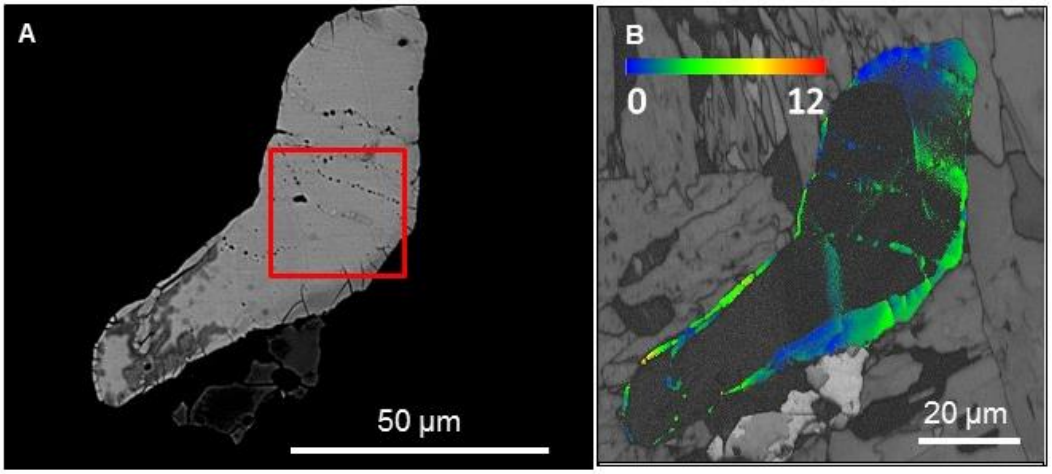

Figure 4-12: A) BSE image of zircon 26277 from sample RX187432 with possible decorated curviplanar features shown with a red box. B) Higher magnification EBSD –band contrast (diffraction intensity) map of zircon 26277 from sample RX187432 showing a rim with up to 7˚ of strain

4.4.4 Felsic Inclusion in Sulphide-Rich Footwall Environment (Leucocratic Norite Matrix) (Whistle 1 A,B,C)

Whistle 1 is a sulphide rich granitoid that contains fine grained recrystallized patches of quartz and plagioclase with visible triple junctions. There are patches of finer grained quartz and plagioclase that have been heavily altered and contain inclusions. Three thin sections of Whistle 1 (A,B,C) were made of the norite matrix (A), the contact with the inclusion (B), and the ultramafic inclusion itself (C). Feldspars make up 30 to 50 % of the sample, are up to 2 mm in length and have morphologies that range from euhedral to anhedral. Many of the larger grains of feldspar are altered, with ragged edges and contain inclusions and the small crystals are dominantly equant with some being lath-shaped; twinning is present within both the small and large grains. Quartz makes up 20 to 30 % of the sample, are anhedral and some grains contain inclusions. The grains can be up to 2 mm in size and many of the larger grains have a mosaic texture, though in some cases, the shape of the original grain is visible. The quartz appears to be less altered than the feldspar. Sulphides compose 15 to 20 % of the sections and are cubic to anhedral. The predominant sulphide is chalcopyrite with secondary pentlandite. The margins of the sulphide domains are irregular, but small cubic pyrite domains are present. Epidote grains are often present at the edges of the sulphide domains. Chlorite is found throughout the sample, and does not appear to have a preference to any other mineral.

No accessory phases were found in the sulphide, however the leucocratic material in both W1A and W1C both contain zircon and monazite, whereas W1B contains only two baddeleyite grains, no zriconalite was found in this sample (Appendix D-2). The zircons range in length from 6 to 162 μm, the monazites from 6 to 33 μm, and the baddeleyites are both 6 μm. Most of the accessory grains appear unshocked, and common features include, ragged edges, cracks and pits. The monazite grains are small and irregularly distributed, often found in ragged patches that appear in pockets suggesting a secondary growth generation (Figure 4-13B). The zircons range from irregular to prismatic to sub-rounded, many have irregular to concentric zoning and discernible cores and rims, grains are often cracked and contain pits and some have zones of mottling. Zircon 2524 from thin section Whistle 1A displays a more granular appearance not seen in the zircons from the ultramafic inclusions. The baddeleyite grains are both internally featureless and have subrounded to prismatic morphologies.

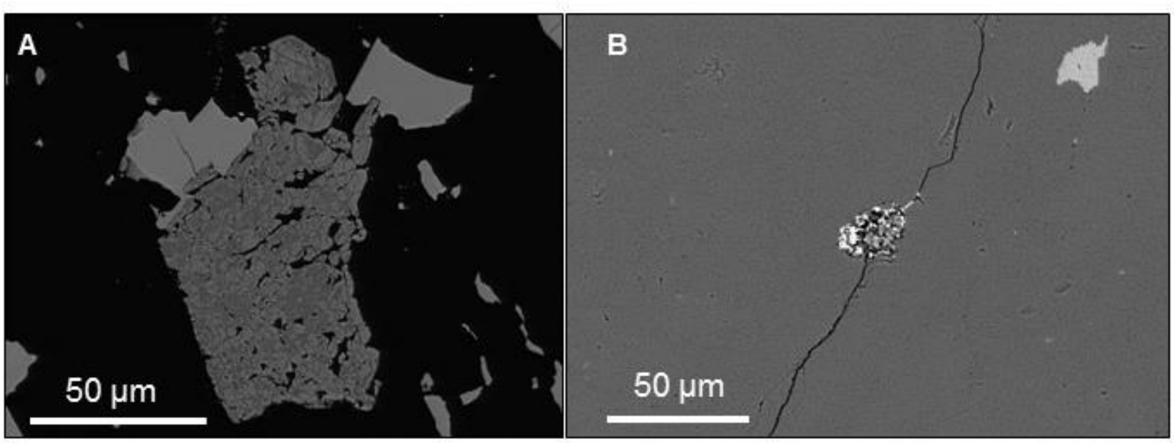

Figure 4-13: A) BSE image of Whistle 1A, zircon 2524 exhibiting anhedral form, metamicatization and alteration. B) BSE image of monazite 47 from Whistle 1C, the monazite appears to be a secondary phase growing as a granular aggregate within quartz.

4.5 Discussion

In order to determine if the inclusions from the Sublayer originate from the footwall or by crystallization of the melt sheet, it must first be established whether the grains used to date them are primary or reset. Inherited mafic material from the footwall should be distinguishable by the accessory mineral population, particularly from inherited zircon within mafic Sublayer xenoliths. Analysis of mafic xenolith RX187432, within the footwall felsic gneiss, did not show any of the euhedral baddeleyite or skeletal zircon, suggesting it is a xenolith. The distinctive anhedral zircon population, along with possible annealed shock features indicate that inherited inclusions derived from the footwall are unlikely sources for the zircons.

Alteration of the Sublayer environment is evident from accessory phase mineral habit and zonation. From the grains imaged in this study, one monazite (F11068) and one zircon (F2524 See Fig. 4-13A) have recrystallized rim textures. EBSD analyses of three grain rims showed evidence of slight misorientation of the crystal lattice of the accessory grains, but this minor deformation could be caused by radiation damage induced by expansion of high uranium zircon cores; Farrell (1997) also did not find any evidence of zircon or baddeleyite resetting. Only one grain, from sample RX187423, has possible healed impact-related fractures (Figure 4-12A), but this interpretation is equivocal given that similar features can be observed in tectonic settings (e.g. Kovaleva et al. 2015).

Our results confirm that the inclusions and matrix have igneous textures, and establish the similar source of the different accessory phases. Examination of zircon and baddeleyite in-situ supports the earlier geochronology interpretation that the inclusion crystallized at the same time as the melt sheet (Corfu and Lightfoot 1996). Corfu and Lightfoot (1996) dated euhedral baddeleyite and fragments of skeletal zircon. We find these forms inter-grown and randomly distributed with the main igneous minerals. Baddeleyite was concentrated in one small zone of an ultramafic inclusion allowing for a possible origin from introduced matrix melt, however in another section (93PCL349C) a veinlet of matrix norite in the middle of the inclusion is conspicuous by the absence of baddeleyite grains (Figure 4-14).

The unshocked, impact-age zircon and baddeleyite populations (Corfu and Lightfoot 1996) contained within the mafic to ultramafic inclusions co-crystallized with the surrounding inclusion matrix. Petrography and electron microscopy of zircon and baddeleyite, at Whistle Mine confirms that they are co-genetic igneous minerals formed in association with primary silicate minerals, and having unshocked and even prismatic or nearly prismatic igneous morphologies (Figure 4-9C and D and 4-10C and D). This observation together with similar observations of ultramafic inclusions from Farrell (1997) indicating a complex environment linked to the formation of mafic to ultramafic inclusions.

Evidence for the associated nature of the ultramafic xenoliths allows for new hypotheses about the emplacement of these bodies as rounded inclusions in the Sublayer. Based on the size of the initial melt sheet it is unlikely that complete mixing would have occurred (Keays and Lightfoot 2004), leading to pockets of more primitive composition, which are now observed as inclusions. The rounded shape and minor geochemical differences with the Sublayer norite, indicates advective mixing of norite with these primitive melt pockets into the embayment environment. A gravitational slumping may have caused this, supported by the fact that the crater floor beneath the crystallizing SIC may have been undergoing isostatic re-adjustment during the crater modification stage as the thermal pulse created by the impact diffused into the lithosphere (e.g. Ivanov 2005). Additionally, recent structural reconstructions of the SIC, and the crater floor, indicate that the Whistle embayment may have been on or near the base of a peak ring topographic high in the crater (Dreuse et al. 2010) (Figure 4-15) providing ideal conditions for gravitational slumping. Either crater modification or gravitational slumping could lead to mixing of dense primitive magmas with basal norite early in SIC crystallization, and account for the rock assemblage now observed at Whistle Mine.

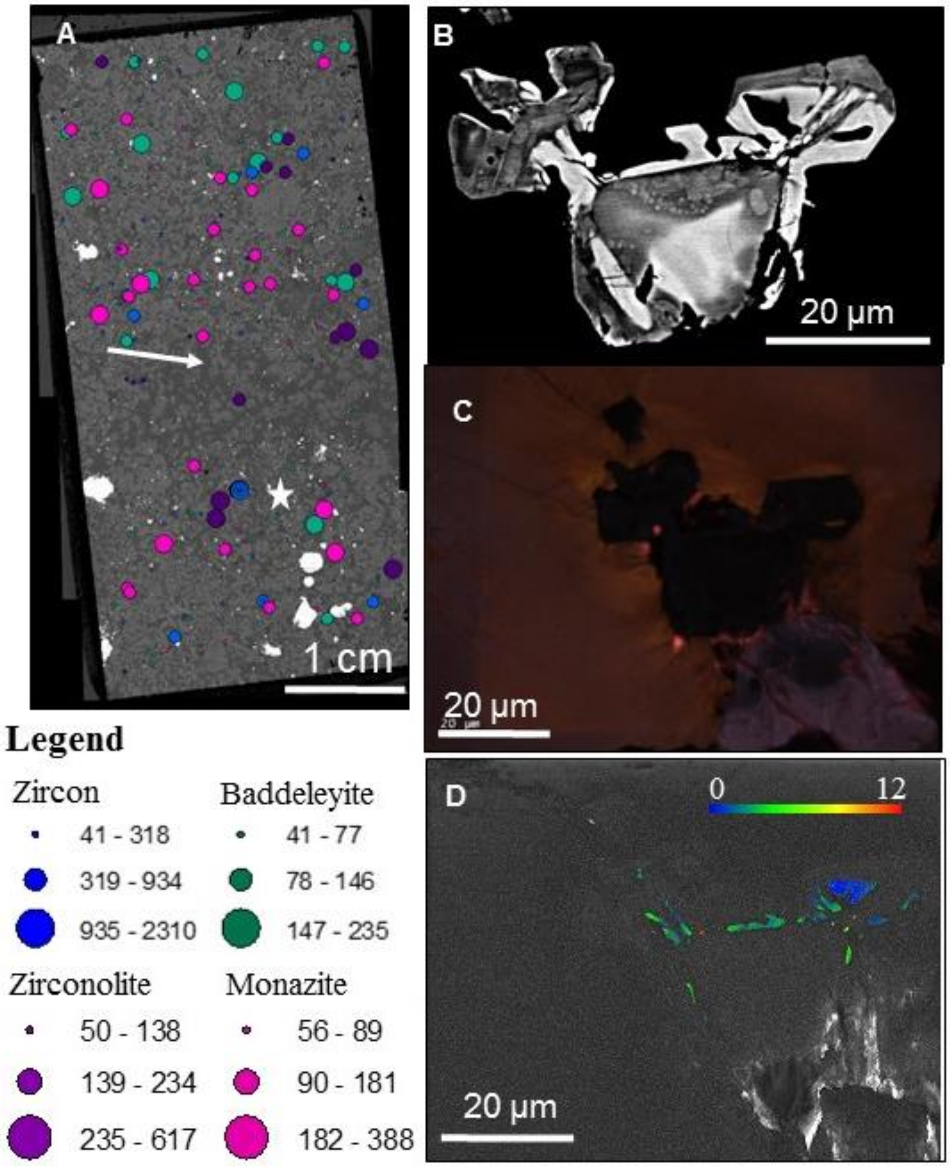

Figure 4-14: Plate of thin section 93PCL349C, which contains only the inclusion. A) BSE map of thick section showing location and relative size of zircon and baddeleyite, note domain of sulphide poor matrix indicated with white arrow, B-D are images of zircon 3686 (location on feature map indicated with white star) in BSE, CL and EBSD modes respectively. Note skeletal nature of grains and high U content that results in lack of CL emission and diffraction. Only the outermost low U zone diffracts, and it is distorted by zircon expansion due to radiation.

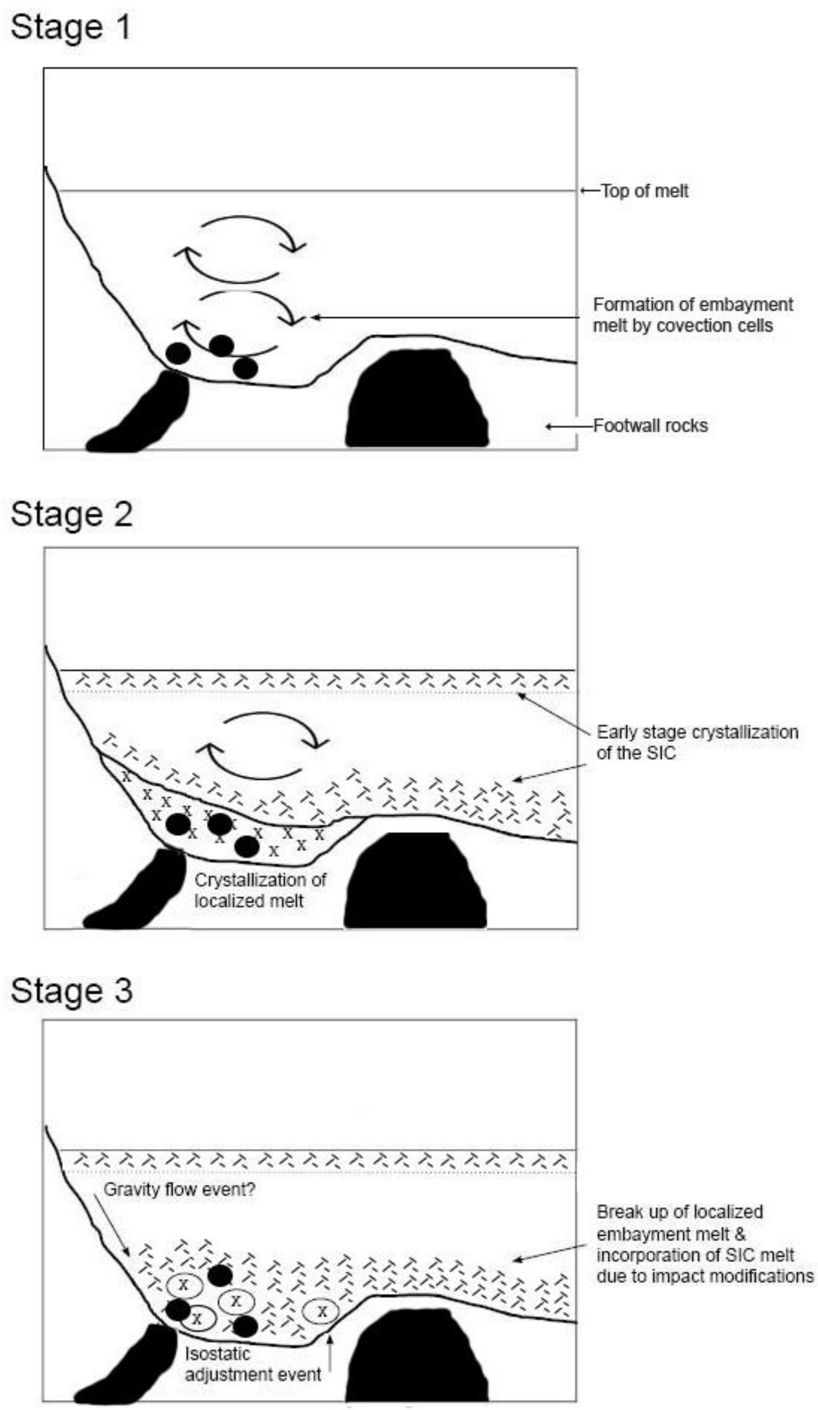

Figure 4-15: Possible emplacement scenario for the formation of the mafic to ultramafic inclusions from an early crystallization event with in the SIC. The black areas in the footwall represent pre-impact mafic bodies that are the source of the inherited inclusions in the Sublayer. Stage 1 shows the formation of the embayment by convection cell as suggested by Zieg and Marsh (2005). Stage 2 shows the early stage crystallization of the SIC from top and bottom, incomplete mixing would account for the slightly different embayment melt from that of the Main Mass. Stage 3 depicts the breakup of the primitive embayment rocks by either a gravity event that caused slumping and/or an adjustment period during impact modification. Note that this would have to occur early in the crystallization of the main SIC formation to incorporate the mafic to ultramafic inclusions.

4.6 Conclusions

Results from transects across the inclusions, including their respective contacts with the Sublayer norite and sulphide matrix, show that accessory phases are randomly distributed, with the paragenetic sequence of zircon and baddeleyite extending throughout the formation of the rock forming mineralogy. Although shock features have been observed by others (Wang et al. 2016) no shock microstructures were observed in any grains from the Sublayer environment in this study, conversely grains of possible pre-impact origin, including anhedral and recrystallized zircons, were noted within a felsic inclusion from a sulphide-rich vein in the footwall gneiss region, providing a comparison in accessory phase textures. Secondary zircon and zirconolite rims were replaced by igneous baddeleyite, which is attributed to late fluids causing in places alteration of the inclusions and local recrystallization of sulphides, signifying a dynamic environment during the formation of the mafic to ultramafic inclusions. The results indicate that the accessory phases dated by Corfu and Lightfoot (1996) were not reset and that the formation of the mafic-ultramafic inclusions at Whistle occurred at the same time as the SIC. This conclusion further supports the origin of the inclusions studied here as remnants of an early, basal SIC crystallization layer that may have co-mingled with the norite by gravitationally driven flow on the flank of a proposed topographic ring in the crater floor, near the eventual Whistle Mine location.

4.7 References

Ames, D.E., Davidson, A. and Wodicka, N. 2008. Geology of the Giant Sudbury Polymetallic Mining Camp, Ontario, Canada. Economic Geology, **103**: 1057-1077.

Card, K.D., Church, W.R., Franklin, J.M., Frarey, M.J., Robertson, J.A., West, G.F. and Young, G.M. 1972. The Southern Provinec *In* Variations in Tectonic Style in Canada. *Edited by* Price, R.A. and Douglas, R.J.W. Geological Association of Canada, Special Paper **11:** 335-380.

Card, K.D., Gupta, V.K., McGrath, P.H. and Grant, F.S. 1984.The Sudbury Structure: Its regional geological and geophysical setting *In* The Geology and Ore Deposits of the Sudbury Structure. *Edited by* Pye, E.G., Naldrett, A.J., and Giblin, P.E. *Ontario Geological Survey Special* **1**: 25-43.

Card, K.D. & Pattison, E.F. 1973. Nipissing diabase of the Southern province Ontario. *In* Huronian Stratigraphy and Sedimentation. *Edited by* Young, G.M. Geological Association of Canada, Special Paper **L2**: 7-30.

Corfu, F. and Andrews, A. 1986. A U-Pb age for mineralized Nipissing diabase, Gowganda, Ontario. Canadian Journal of Earth Science, **23**: 107-112.

Corfu, F., and Lightfoot, P.C. 1996. U-Pb geochronology of the sublayer environment, Sudbury Igneous Complex, Ontario. Economic Geology, **91**: 1263-1269.

Davis, D. 2008. Sub-million-year age resolution of Precambrian igneous events by thermal extraction-thermal ionization mass spectrometer Pb dating of zircon: application to crystallization of the Sudbury impact melt sheet. Geology **36**(5): 383-386.

Dietz, R.S. 1961. Vredefort Ring Structure: Meteorite impact scar? Journal of Geology, **69**: 499-516.

Dreuse, R., Doman, D., Santimano, T. and Riller, U. 2010. Crater floor topography and impact melt sheet geometry of the Sudbury impact structure, Canada. Terra Nova, **22**(6): 463–469. doi: 10.1111/j.1365-3121.2010.00965.x

Farrell, K.P.J. 1997. Mafic to ultramafic inclusions in the Sublayer of the Sudbury Igneous Complex at Whistle Mine, Sudbury, Ontario, Canada. Master Thesis, Laurentian University, Sudbury, Ontario, 251p.

Farrell, K.P.J., Lightfoot, P.C. and Keays, R.R. 1995. Mafic-ultramafic inclusions in the Sublayer of the Sudbury Igneous Complex, Whistle mine, Sudbury, Ontario. Ontario Geological Survey Miscellaneous Paper, **164**: 126-128.

French B.M. 1998. Traces of catastrophe: A handbook of shock-metamorphic effects in terrestrial meteorite impact structures. LPI Contribution No. **954**, Lunar and Planetary Institute, Huston.

Garde, A.A., McDonald, I., Dyck, B. and Keulen, N. 2012. Searching for giant, ancient impact structures on Earth: The Mesoarchean Maniitsoq structure, West Greenland. Earth and Planetary Science Letters, **337–338**: 197–210. doi:10.1016/j.epsl.2012.04.026.

Garde, A.A., Dyck, B., Esbensen, K.H., Johansson, L. and Moller, C. 2014. The Finnefjeld domain, Maniitsoq structure, West Greenland: Differential rheological features and mechanical homogenization in response to impacting? Precambrian Research, **255**: 791-808.

Grant, R.W. and Bite, A. 1984. Sudbury quartz diorite offset dikes. *In* The Geology and Ore Deposits of the Sudbury Structure, *Edited by* Pye, E.G., Naldrett, A.J., and Giblin, P.E. Ontario Geological Survey, Special Volume **1**: 275-301.

Grieve, R.A.F. 1980. Impact bombardment and its role in proto-continental growth on the early earth. Precambrian Research, **10**(3-4): 217-247.

Heaman, L.M. 1997. Global mafic magmatism at 2.45Ga: remnants of an ancient large igneous province? Geology, **25**(4): 299-302.

Ivanov, B.A. 2005. Modeling of the largest terrestrial meteorite craters. Solar System Research, **39(5)**: 381-409.

Keays, R.R. and Lightfoot, P.C. 2004. Formation of Ni-Cu-platinum group element sulphide mineralisation in the Sudbury Impact melt sheet. Mineralogy and Petrology, **82**(3-4): 217-258.

Kovaleva, E., Klotzli, U., Habler, G. and Wheeler, J. 2015. Planar microstructures in zircon from paleo-seismic zones. American Mineralogist, **100:** 1834–1847.

Krogh, T.E., Davis, D.W., Corfu. 1984. Precise U-Pb zircon and baddeleyite ages for the Sudbury area. *In* The Geology and Ore Deposits of the Sudbury Structure. *Edited by* Pye, E.G., Naldrett, A.J., and Giblin, P.E. Ontario Geological Survey, Special Volume **1**: 431-446.

Lightfoot, P.C. 2016. Nickel Sulfide Ores and Impact Melts Origin of the Sudbury Igneous Complex. Elsevier Cambridge, M.A.

Lightfoot, P.C., Doherty, W., Farrell, K., Keays, R.R., Moore, M. and Peleski, D. 1997a. Geochemistry of the main mass, sublayer, offsets, and inclusions from the Sudbury Igneous Complex, Ontario. Ontario Geological Survey, Open File Report **5959**: 231p.

Lightfoot, P.C. and Farrow, C.E.G. 2002. Geology, Geochemistry, and Mineralogy of the Worthington Offset Dike: A Genetic Model for Offset Dike Mineralization in the Sudbury Igneous Complex. Economic Geology, **97**(7): 1419-1446.

Lightfoot, P.C., Keays, R.R., Morrison, G.G., Bite, A. and Farrell, K.P. 1997b. Geochemical relationships in the Sudbury Igneous Complex: origin of the main mass and offset dike. Economic Geology, **92**: 289-207.

Lightfoot, P.C., Keays, R.R., Morrisson, G.G., Bite, A. and Farrell, K.P. 1997c. Geologic and geochemical relationships between the contact sublayer, inclusions and main mass of the Sudbury Igneous Complex: A case study of the Whistle mine embayment: Economic Geology, **92**: 647-672.

Morrison, G. G., Jago, B. C. and White, T.L. 1994. Footwall mineralization of the Sudbury igneous Complex: Ontario Geological Survey, Special Volume **5**: 57-64.

Moser, D.E., Cupelli, C.L., Barker, I.R., Flowers, R.M., Bowman, J.R., Wooden, J. and Hart, J.R. 2011. New zircon shock phenomenon and their use for dating and reconstruction of large impact structures revealed by electron nanobeam (EBSD, CL, EDS), and isotopic U-Pb, and (U-Th)/He analysis of the Vredefort dome. Canadian Journal of Earth Science, **4**: 117-139.

Murphy, A.J. and Spray, J.G. 2002. Geology, mineralization, and emplacement of the Whistle-Parkin offset dike, Sudbury. Economic Geology, **97**: 1399-1418.

Noble, S.R. and Lightfoot, P.C. 1992. U-Pb baddeleyite ages of the Kerns and Triangle Mountain intrusions, Nipissing Diabase, Ontario. Canadian Journal of Earth Science, **29**: 1424-1429.

Pattison, E.F. 1979. The Sudbury Sublayer: its characteristics and relationships with the Main Mass of the Sudbury Irruptive. Canadian Mineralogist, **17**: 257-274.

Prevec, S.A. and Baadsgaard, H. 2005. Evolution of Palaeoproterozoic mafic intrusions located within the thermal aureole of the Sudbury Igneous Complex, Canada: Isotopic, geochronological and geochemical evidence. Geochemica et Cosmochimica Acta, **69**(14): 3653-3669.

Prevec, S.A., Lightfoot, P.C. and Keays, R.R. 2000. Evolution of the sublayer of the Sudbury Igneous Complex: geochemical, Sm-Nd isotopic and petrologic evidence Lithos, **51**: 271-292.

Rae, D.R. 1975. Inclusions in the sublayer from Strathcona Mine, Sudbury, and their significance. Master Thesis, University of Toronto.

Raharimahefa, T., Lafrance, B. and Tinkham, D.K. 2014. New structural, metamorphic, and U–Pb geochronological constraints on the Blezardian Orogeny and Yavapai Orogeny in the Southern Province, Sudbury, Canada. Canadian Journal of Earth Science, **51**: 750-774.

Riller, U. 2005. Structural characteristics of the Sudbury Impact Structure, Canada: Impact-induced versus orogenic deformation-A Review. Meteoritics & Planetary Science, **40**(11): 1723-1740.

Ripley, E.M., Lightfoot, P.C., Stifter, E.C., Underwood, B., Taranovic, V., Dunlop, M. and Donoghue, K.A. 2015. Heterogeneity of S isotope compositions recorded in the Sudbury Igneous Complex, Canada: Significance to Formation of Ni-Cu sulfide ores and the host rocks. Economic Geology, **110**: 1125–1135.

Rousell, D.H. and Gibson, H.L. 1997. The tectonic, magmatic and mineralization history of the Sudbury Structure. Exploration and Mining Geology, **6**(1):1-22.

Scribbins, B., Rae, D.R. and Naldrett, A.J. 1984. Mafic and ultramafic inclusions in the Sublayer of the Sudbury Igneous Complex. Canadian Mineralogist, **22**: 67-75.

Sproule, R.A., Sutcliffe, R., Tracanelli, H. and Lesher, C.M. 2007. Palaeoproterozoic Ni–Cu–PGE mineralisation in the Shakespeare intrusion, Ontario, Canada: a new style of Nipissing gabbro-hosted mineralisation. Applied Earth Science (Trans. Inst. Min. Metall. B), **116**(4):188-200.

Szabo, E. and Hall, H.C. 2006. Deformation of the Sudbury Structure: paleomagnetic evidence from the Sudbury breccias. Precambrian Research, **150**: 27-48.

Wang, Y. Lesher, C.M., Lightfoot, P.C. Pattison, E.F. and Golightly, J.P. 2016. Shock metamorphic features of olivine, orthopyroxene, amphibole, and plagioclase in phlogopite-bearing ultramafic-mafic inclusions in Sublayer, Sudbury Igneous Complex, Sudbury, Canada. 35th International Geological Congress, Cape Town, South Africa.

Zieg, M.J. and Marsh, B.D. 2005. The Sudbury Igneous Complex: Viscous emulsion differentiation of a superheated impact melt sheet. Geological Society of America Bulletin, **117**(11-12): 1427-1450. doi: 10.1130/B25579.1

Zhou, M, Lightfoot, P.C., Keays, R.R., Moore, M.L. and Morrison, G.G.1997. Petrogenetic significance of chromian spinels from the Sudbury Igneous Complex, Ontario, Canada. Canadian Journal of Earth Science, **34:** 1405-1419.

Chapter 5: Conclusions

The Vredefort and Sudbury impact basins have been studied for over a hundred years and have raised many questions regarding impact processes, including their effect on the upper and lower crust, shock features, and melt formation. This thesis looked at both impact basins and addressed melt related questions unique to each site but which share overarching themes. At Vredefort the goal was to address a debated question regarding the origin and extent of a small mafic unit found in the central dome. At Sudbury the goal was to answer the question of resetting in accessory phase grains found in mafic-ultra-mafic inclusions from the Sublayer, dated by Corfu and Lightfoot (1996). Although these questions are unique to each site, the two underlying questions considered are what effects meteorite impacts have on the crust and which microscopic features can be utilized when investigating potential impact sites. This is of specific interest in structures that no longer display a physiographic expression at surface, as more conventional methods are not available. Here the broad conclusions of this thesis are summarised, along with suggestions for future work.

5.1 Major Conclusions

5.1.1 Vredefort

A number of hand samples and geochronology samples of gabbronorite were studied from the Vredefort impact structure to distinguish the nature of the zircon morphologies, U-Pb age, Lu-Hf ratios, temperature of zircon formation and bulk chemistry. These analyses were done to test for an impact age and see if the unit was formed from the melting of the target rocks or by injection of magma from the mantle. It was determined that the unit has an upper intercept age for igneous zircons from V250 of 2036 ± 45 Ma, and samples V232 and V235 have a combined upper intercept age of 2039 ± 33 Ma which is within error of the age of the structure (2019 ± 2 Ma) determined using TIMS analysis (Moser 1997).

It has been suggested here that the gabbronorite melt may have one of two possible origins. The first possibility is that the melt was derived from a pocket of Ventersdorp magma located in the lithosphere beneath the crater and intruded the crater rocks beneath the melt sheet due to the crustal disturbance caused by the impact. The second possibility is that the melt was derived due to segregation of the melt sheet which would have cooled over a long period of time allowing more mafic minerals to settle to the bottom as at the Sudbury structure. Based on the whole rock chemistry a mantle origin appears to be the most likely source. The Lu-Hf analysis from Chapter 2 suggests that the gabbronorite is consistent with derivation from a Ventersdorp unit (Stevenson and Patchett 1990) suggesting it was derived from melting of the country rock. Comparison to later published work on the Bushveld Igneous Complex (BIC) (Zirakparvar et al. 2014), however, supports formation by injection from a relict magma chamber residing at ≥100 km in the lithosphere. The overall similarity in bulk trace element chemistry to other Kaapvaal craton mafic intrusions (e.g. Ventersdop, Anna’s Rust) point to derivation of the gabbronorite from regions beneath the crater.

The gabbronorite was not accepted as an impact unit because it has a foliation defined by the alignment of mafic minerals (Gibson and Reimold 2008), which is similar to the main mass of the BIC (Wager et al. 1960). Based on microstructural measurements herein, it is clear that all minerals in the gabbronorite are un-shocked and igneous. It is possible that their shape-preferred orientation (foliation) developed during the intrusion of the gabbronorite from the mantle and/or from long term modification including isostatic adjustment that may have caused the still-crystallizing ductile impact melt to become foliated. If the original melt sheet was as large as that seen at the Sudbury structure, there would have been enough heat from the overlying unit to allow the crystallized base to remain ductile. Gibson and Reimold (2008), discussed the lack of large faults associated with the impact, and suggested that this could be attributed to ductility owing to the initial mid-crustal pre-impact levels and high shock induced temperatures. This is borne out by the flattened or elongate pockets of glomerogranular quartz (impact melt pockets) reported here in the Inlandsee Leucogranofels. If re-adjustment of the central uplift occurred during this ductile phase, the margins of the gabbronorite units could have become foliated at this time too. It is also possible that the melt could have a preferred mineral orientations due to melt flow. This theory is based on the interpretation that Vredefort's melt sheet was similar or larger than that of the Sudbury impact and that cooling could take anywhere up to 100 thousand years (Zieg and Marsh 2005).

5.1.2 Sudbury

The lack of shock seen in the inclusions in the Sublayer of the Sudbury Igneous Complex (SIC) shows that the datable mineral phases in the inclusions have not been reset and the ages found in baddeleyite by Corfu and Lightfoot (1996), were indeed accurate ages. This is shown by the lack of planar features seen in grains of zircon, baddeleyite, monazites or zirconalite. These are post-impact igneous grains and there is no reason to suspect that their U-Pb compositions were reset due to the impact. This does still leave the question of what the source of the Sublayer inclusions are. Based on the work conducted here and literature reviewed on both Sudbury and Vredefort, it is recommended that more work be conducted on the hypothesis that these inclusions are derived from the SIC itself. Chapter 4 proposes the development of the mafic-ultramafic inclusion from an early basal melt by incomplete mixing at the base of the early melt sheet that was broken up by the post impact modification or tectonic activity, or due to gravitational slumping along the walls of the embayment (Figure 4-15).

5.2 Similarities Between Vredefort and Sudbury

The Vredefort and Sudbury impact structures are similar in basin size and are relatively close in age. In addition, they also share a number of similarities on a micro-scale. Both sites contain the accessory phase baddeleyite in the felsic footwall rocks. At first, this was thought to be peculiar as baddeleyite grains only occur terrestrially within mafic material. A more detailed examination of the literature found that baddeleyite occurs in tektite glass that has reached temperatures of 1775˚C (El Goresy 1965).

Zircon morphologies and lack of shock in the Sublayer and the gabbronorite is also similar across both structures. SEM analysis of both sites found zircons to be anhedral to euhedral. Anhedral grains include zircons that are discontinuous to stringer-like and follow major mineral boundaries. The grains are often cracked or contain pits and inclusions and some of the subhedral to euhedral grains contain concentric zoning.

Apparent (Fu et al. 2008) Ti-in-zircon crystallization temperatures from the gabbronorite range from 928 ± 10˚C to 795 ± 8.7˚C, this falls within the range of mafic basal units of the SIC (Darling et al. 2009). There are also similar trends in the chemistry of the gabbronorite and the Sudbury units. Of particular note is the large variation in εHf values of V250 and V235, which have similar variations to what are seen in the Sudbury Sublayer Sm-Nd compositions (Prevec et al. 2000). This suggests that both sites have isotopic variation in local, upper crustal target lithology.

5.3 Differences Between Vredefort and Sudbury

The main difference observed between the Vredefort and Sudbury sites is the presence of mafic-ultramafic inclusions at Sudbury and the absence of such inclusions at Vredefort. Sudbury contains a diverse range of inclusion types depending on location in the structure, and are often related to the country rocks. There are inclusions of the country rocks in the Transition zone at Vredefort but there are no mafic-ultramafic inclusions present. There are two possible explanations for this. The first explanation is that the inclusions are present in the Sudbury Sublayer due to inheritance from the country rock, and are not present in the Vredefort melt as the dominant rock types in the study area are felsic. The second possibility is that the inclusions in the Sublayer were formed from the first phase of cooling in the impact melt sheet and then were broken up by either late stage modification of the impact structure or orogenic activity and a similar unit at Vredefort either did not exist or was eliminated by erosion.

5.4 Impact Crater Indicators

Along with furthering the understanding of both the Vredefort and Sudbury Impact basins, it was intended that this work would provide more methods for discovering and confirming ancient impact basins. The presence of baddeleyite could be used as an indicator of ancient impact craters when little is left of the target material. However, more work needs to be done on this area to determine the maximum distance from the centre in which baddeleyite can occur in felsic material, as well as, a more in-depth study of what could cause baddeleyite to form in sites unrelated to impact events. EBSD of accessory phases could also help in determining if a structure has an impact origin by mapping out the strain history of the grains. This is of particular use in cases where grains may have been annealed and/or reset.

5.5 Future Work

Although this work has looked at different methods to study crater-floor environments on Earth there is still a lot to be done to fully understand the dynamics of these environments. Some immediate work to follow up on this study would be to continue the Lu-Hf analysis at Vredefort to build a larger data set, including comparing grains from the ILG, Central Anatectic Granite and pseudotachylite. At Sudbury, future high precision Pb-Pb geochronology with uncertainty of ~200,000 years (e,g, Davis 2008; Bleeker et al. 2015) could be conducted on inclusion zircon and baddeleyite to test for an earliest SIC age of the grains. Zirconolite ages may yield cooling ages of the base of the SIC. Finally comparison of inclusion Lu-Hf values with those of the Sublayer would also help test this hypothesis and if compared to other mafic units such as the Huronian gabbros, Nippissing diabase or Matachawan dykes could simultaneously test other proposed sources of the ultramafic inclusions.

Lastly a larger data set of zircon morphologies and EBSD mapping, from other impact sites would help build a template of what to expect in impact zircons from different locations within the structures. This is particularly useful in areas where impact features in quartz grains may have been annealed due to high temperatures or post impact processes such as tectonic deformation.

5.6 References

Corfu, F. and Lightfoot, P.C. 1996. U-Pb geochronology of the sublayer environment, Sudbury Igneous Complex, Ontario. Economic Geology, **91**: 1263-1269.

Darling, J., Storey, C. and Hawkesworth, C. 2009. Impact melt sheet zircons and their implications for the Hadean crust. Geology, **37**: 927–930. doi:10.1130/G30251A.1.

El Goresy, A. 1965. Baddeleyite and its significance in impact glasses. Journal of Geophysical Research, **70**(14): 3453-3456.

Fu, B., Page, F.Z., Cavosie, A.J., Fournelle, J., Kita, N.T. Lackey, J.S., Wilde, S.A. and Valley, J.W. 2008. Ti-in-zircon thermometry: applications and limitations. Contributions to Mineralogy and Petrology, **156**:197-215.

Gibson, R.L. and Reimold, W.U. 2008. Geology of the Vredefort impact structure, a guide to sites of interest. Council of Geoscience, Memoir **97**, Pretoria, 181 p.

Ivanov, B.A. 2005. Modeling of the largest terrestrial meteoritecraters. Solar System Research, **39**: 381–409.

Moser, D.E. 1997. Dating the shock wave and thermal imprint of the giant Vredefort impact, South Africa: Geology, **25**: 7–10. doi:10.1130/0091-7613(1997)025<0007:DTSWAT>2.3.CO;2.

Prevec, S.A., Lightfoot, P.C. and Keays, R.R. 2000. Evolution of the Sublayer of the Sudbury Igneous Complex: Geochemical, Sm-Nd isotopic and petrologic evidence. Lithos, **51**: 271–292. doi:10.1016/S0024-4937(00)00005-0.

Stevenson, R.K. and Patchett, P.J. 1990. Implications for the evolution of continental crust from Hf isotope systematic of Archean detrital zircons. Geochimica et Cosmochimica Acta, **54**: 1683–1697. doi:10.1016/0016-7037(90)90400-F.

Wager, L.R., Brown, G.M. and Wadsworth, W.J. 1960. Types of Igneous Cumulates. Journal of Petrology, **1**(1): 73-85.

Zieg, M.J. and Marsh, B.D. 2005. The Sudbury Igneous Complex: Viscous emulsion differentiation of a superheated impact melt sheet. Geological Society of America Bulletin, **117**(11-12): 1427-1450. doi: 10.1130/B25579.1

Zirakparvar, N.A., Mathez, E.A., Scoates, J.S. and Wall, C.J. 2014. Zircon Hf isotope evidence for an enriched mantle source for the Bushveld Igneous Complex. Contribution in Mineral Petrology, **168**:1050-1068. DOI 10.1007/s00410-014-1050-2

Appendix A: Methods

A-1 Mapping and Sampling

A-1-1 Vredefort

In February of 2009 two weeks were spent conducting detailed field mapping of the area surrounding the 'type' gabbro-norite dyke (Moser, 1997), in hopes of increasing the known exposure of the unit. Mapping started with a 10 m grid spacing of the 200 x 200 m area around the type body at (548414E, 7007454N), referred to in this study as Site 1. On further examination of an adjacent property 1.23 km to the southeast (Site 2) another body of the gabbro-norite dyke was discovered which led to the identification and sampling of dm-scale bedrock exposures of the same rock type. A 273 by 229 m area was mapped out at site 2.

A-1-2 Sudbury

Hand samples were provided by Dr. Peter Lightfoot at Vale, and were collected from the Whistle pit. Vale no longer owns the Whistle open pit but still had a few samples on hand. The Whistle pit is located in the north-east corner of the Sudbury impact basin at the base of the Whistle-Parkin offset.

A-2 Zircon Separation

Mineral separation for geochronology was conducted at the Jack Satterly Geochronology lab at the University of Toronto using standard procedures. Many of the gabbronorite samples did not undergo all the stages of Franz separation due to the limited amount of zircon available in some of the samples.

A-3 Sample Polishing

Samples were either prepared as polished thin sections produced at external labs, or thick sections of billets glued to a microscope slide prior to polishing by hand in seven stages of grit.

Both approaches were completed with vibratory colloidal alumina 0.05 micron polishing stage for ~1.5 hours for any samples that underwent analysed by EBSD.

A-4 Zircon Imaging

Zircon imaging was conducted with a Hitachi SU6600 Variable Pressure Field Emission Gun-Scanning Electron Microscope (FEG-SEM) at Western University, Zircon and Accessory Phase Laboratory (ZAPLab). Samples were analysed in high vacuum mode and carbon coated using a carbon rod evaporative coater. Coatings thicknesses were not measured routinely but are estimated to be between 20 and 50 nm thick based on qualitative colour change of polished brass (Kerrick et al. 1973) observed using standard settings.

A-4-1 SE & BSE

Thin sections were mounted in an aluminum stage for SE and BSE imaging at an acceleration voltage between 10 kV and 15 kV. Condenser lens setting of medium 6 to 10, depending on the sample, and an aperture setting of 3/1. The typical working distance between pole piece and sample images was ~ 10 mm.

A-4-2 CL

The mounting procedure for CL imaging is the same as SE and BSE imaging however the beam conditions vary slightly. When CL images are taken the condenser lens is set to Large 1, this increases the probe current which causes less spatial resolution. To offset the loss of spatial resolution, a low acceleration voltage of 10 kV and a small aperture size of 2/3 is used. The working distance for CL is ~ 14 mm.

A-4-3 EBSD

Samples analysed for EBSD were required to undergo special polishing methods in order to be certain no subsurface damage is left that could cause Braggs Law not to be satisfied and hindering diffraction. Once polished the sample was carbon coated and mounted at a 70˚ angle. The sample is then placed in the FEG-SEM for imaging. The beam conditions used for EBSD are unique to this type of imaging. The acceleration voltage is 20 kV; for a stronger diffraction signal, condenser lens is set to medium 6 and the aperture is set to 3/2; to improve special resolution.

A-5 SHRIMP Analysis

A-5-1 Ti-in-zircon thermometry

Ti-thermometry was conducted at the Stanford/ U.S.G.S. SHRIMP-RG facility according to previously published procedures (Mazdab and Wooden, 2006), and referenced to internal zircon geochronology standard VP-10. Due to the presence of ilmenite in all the samples, an $aTiO_2$ = 0.7 is assumed (Ferry and Watson, 2006).

A-5-2 Zircon Chemistry

Zircon trace element chemistry was conducted at the Stanford/ U.S.G.S. SHRIMP-RG facility according to previously published procedures (Mazdab and Wooden, 2006) and referenced to internal zircon geochronology standard VP-10.

A-6 Bulk and Mineral Elemental Chemistry

A representative portions of the geochronology samples were analysed for major, minor and trace element composition using fusion-inductively coupled plasma (ICP), at Actlabs in Ancaster, Ontario, using their 4Litho research package.

Mineralogical types were determined by optical microscopy and EDS analyses of petrographic thin sections. Targets were selected in the thin sections where multiple minerals could be seen together and compared for differences. Using the FEG-SEM with the same beam conditions as SE and BSE imaging, four analyses were run for each spectrum to ensure accuracy.

For comparison the compound percents of the multiple runs of each spectrum were averaged, this can be seen in Appendix B-2.

A-7 Lu-Hf Analysis

Hf Laser Ablation ICPMS analyses was conducted at the University of Bristol, UK. according to previously published procedures (Hawkesworth, and. Kemp, 2006; Fisher et al. 2011). The standards used were Plesovice which had an average of 0.282487 ± 0.000023, mud tank with an average of 0.282523 ± 0.000021 and Temora-2 which had an average of 0.282700 ± 0.000044.

A-8 References

Ferry, J.M. and Watson, E.B. 2007. New thermodynamic models and revised calibrations for the Ti-in-zircon and Zr-in-rutile thermometers. Contribution in Mineral Petrology, **154**: 429-437.

Fisher, C.M., Hanchar, J.M., Samson, S.D., Dhuime, B., Blichert-Toft, J., Vervoort, J.D. and Lam, R. 2011. Synthetic zircon doped with hafnium and rare earth elements: A reference material for in situ hafnium isotope analysis. Chemical Geology, **286**: 32-47.

Hawkesworth, C.J. and Kemp, A. I. S. 2006. Using hafnium and oxygen isotopes in zircons to unravel the record of crustal evolution. Chemical Geology, **226**: 144-162. doi:10.1016/j.chemgeo.2005.09.018 13

Kerrick, D.M., Eminhizer, L.B. and Villaume, J.F. 1973. The role of carbon film thickness in electron microprobe analysis. American Mineralogist, **58**: 920-925.

Mazdab, F.M. and Wooden, J.L. 2006. Trace element analysis in zircon by ion microprobe (SHRIMP-RG); technique and applications. Geochimica et Cosmochmica Acta, **70**: Supp. 1, p. A40.

Moser, D.E. 1997. Dating the shock wave and thermal imprint of the giant Vredefort impact. South Africa. Geology, **25**: 7-10.

Appendix B-1: Whole Rock Chemistry

Appendix: B-1-1 Major Element Chemistry Table

Vredefort

Analyte Symbol	**Source**	Samples from this study							Koeberl, Reimold, and Shirey 1996				
	Analysis Method	Major elements determined using FUS-ICP and trace elements determined using FUS-ICP and FUS-MS							Major elements (and Y& Nd) determined using XRF and trace elements determined using XRF and Neutron Activation Analysis				
	Rock Type	CAG	ILG	Gabbro Norite					Witwaters rand Shale	Ventersdorp Andesitic			OGG
	Unit Symbol	VO9-111	VO9-238	VO9-232	VO9-234	VO9-235	VO9-250	Average	VG-SNE	UP-61	UP-63	Average	OT-1
SiO_2	%	71.27	75.63	40.38	49.45	49.66	45.97	46.37	30.26	57.34	56.88	57.11	65.70
Al_2O_3	%	15.85	12.68	8.67	13.89	14.44	12.30	12.33	2.49	14.18	13.70	13.94	14.80
Fe_2O_3(T)	%	2.06	0.75	30.54	16.62	16.63	21.79	21.40	57.49	10.11	10.01	10.06	4.90
$FeO^{\dagger}$	Calculated	1.85	0.68	27.49	14.96	14.97	19.61	19.26	51.74	9.10	9.01	9.05	4.41
MnO	%	0.02	0.01	0.31	0.21	0.21	0.24	0.24	4.45	0.13	0.13	0.13	0.10
MgO	%	0.38	0.13	5.14	5.57	5.62	4.47	5.20	0.72	4.53	6.19	5.36	1.90
CaO	%	2.13	0.66	7.79	9.75	9.92	8.98	9.11	0.27	6.22	7.66	6.94	3.40
Na_2O	%	4.28	2.82	1.74	2.76	2.77	2.53	2.45	0.01	4.86	2.27	3.57	4.81
K_2O	%	3.83	6.00	0.28	0.34	0.32	0.42	0.34	0.05	0.42	1.02	0.72	2.25
TiO_2	%	0.25	0.06	5.23	1.66	1.72	3.13	2.93	0.11	1.05	0.53	0.79	0.80
P_2O_5	%	0.04	0.02	0.19	0.22	0.20	0.32	0.23	0.10	0.15	0.06	0.11	0.20

†Note: When FeO content is shown in red it denotes that it has been calculated by multiplying the Fe_2O_3 content by 0.9.

[1]It was discovered on July 28th 2016 that Lieger, D., Riller, U., and Gibson, R.L. 2010 was withdrawn at the request of the author(s).

Analyte Symbol	**Source**	Koeberl, Reimold, and Shirey 1996							Reimold & Gibson 2006		Lieger, Riller, and Gibson 2010[1]		
	Analysis Method	Major elements (and Y& Nd) determined using XRF and trace elements determined using XRF and Neutron Activation Analysis							XRF?		XRF		
	Rock Type	Wits Siltstone clase in Granophyre	Vredefort Granophyre						Vredefort Granophyre		Granitoid		
	Unit Symbol	BG-S1	BG-4	BG-7	BG-9	BG-10	BG-168	Average	Granophyre with outliers	Granophyre without outliers	WR 669A3	PT 669A2	WR 200C2
SiO_2	%	79.70	67.50	66.40	67.40	67.60	66.20	67.02	66.77	66.97	72.10	72.05	73.25
Al_2O_3	%	11.50	12.70	12.80	12.60	12.60	12.80	12.70	12.63	12.63	13.89	14.08	15.55
Fe_2O_3(T)	%	1.39	7.21	7.06	6.81	6.83	7.29	7.04	7.03	7.09	2.33	1.72	0.30
FeO†	Calculated	1.25	6.49	6.35	6.13	6.15	6.56	6.34	6.33	6.38	2.10	1.55	0.27
MnO	%	0.04	0.14	0.13	0.13	0.13	0.15	0.14	0.14	0.14	0.02	0.03	0.01
MgO	%	0.50	3.50	3.50	3.40	3.40	3.70	3.50	3.58	3.54	0.34	0.29	0.01
CaO	%	0.70	3.80	3.70	3.60	3.60	4.20	3.78	3.95	3.87	1.16	1.32	1.13
Na_2O	%	2.42	2.54	3.09	2.89	2.89	2.57	2.80	2.70	2.70	2.52	3.90	5.02
K_2O	%	2.61	2.14	2.36	2.43	2.41	2.43	2.35	2.23	2.26	5.69	4.34	5.15
TiO_2	%	0.30	0.50	0.55	0.52	0.49	0.50	0.51	0.49	0.48	0.32	0.21	0.02
P_2O_5	%	0.10	0.10	0.11	0.10	0.10	0.10	0.10	0.12	0.12	0.09	0.08	0.01

†Note: When FeO content is shown in red it denotes that it has been calculated by multiplying the Fe_2O_3 content by 0.9.

[1]It was discovered on July 28th 2016 that Lieger, D., Riller, U., and Gibson, R.L. 2010 was withdrawn at the request of the author(s).

Analyte Symbol	Source	Lieger, Riller, and Gibson 2010[1]													
	Analysis Method	XRF													
	Rock Type	Granitoid												Quartzite/ Conglomerate	
	Unit Symbol	PT 200C1	WR 453A2	PT 453A1	PT 652A1	PT 652A2	WR KuduA3	PT KuduA2	PT KuduA1	WR 518A2	PT 518A1	WR Average	PT Average	WR 6A4	PT 6A1
SiO_2	%	71.56	73.12	65.73	73.62	73.74	72.99	51.41	52.07	67.13	55.64	71.72	64.48	96.92	94.94
Al_2O_3	%	14.98	14.47	15.26	13.06	14.33	13.97	9.90	11.52	14.46	14.46	14.47	13.45	1.06	2.58
Fe_2O_3(T)	%	2.18	1.40	5.05	1.82	1.81	1.49	13.98	12.94	5.77	11.25	2.26	6.34	0.38	1.46
FeO[†]	Calculated	1.96	1.26	4.55	1.64	1.63	1.34	12.58	11.65	5.19	10.13	2.03	5.71	0.34	1.31
MnO	%	0.02	0.03	0.08	0.02	0.02	0.02	0.19	0.20	0.07	0.14	0.03	0.09	0.00	0.01
MgO	%	0.35	0.24	2.09	0.07	0.08	0.28	6.24	6.44	1.18	2.98	0.41	2.32	0.05	0.01
CaO	%	1.51	1.07	2.55	0.45	0.71	1.35	7.74	8.06	2.21	4.55	1.38	3.36	0.04	0.00
Na_2O	%	5.03	5.25	4.10	3.03	4.15	8.23	4.64	4.41	5.03	5.94	5.21	4.40	0.02	0.00
K_2O	%	3.96	3.28	3.17	5.01	4.62	0.80	0.46	2.02	1.95	1.74	3.37	3.17	0.28	0.24
TiO_2	%	0.25	0.24	0.52	0.25	0.23	0.16	2.20	1.92	0.51	1.89	0.25	0.93	0.03	0.21
P_2O_5	%	0.07	0.08	0.29	0.11	0.06	0.02	0.44	0.42	0.24	0.47	0.09	0.24	0.01	0.01

[†]Note: When FeO content is shown in red it denotes that it has been calculated by multiplying the Fe_2O_3 content by 0.9.

[1]It was discovered on July 28th 2016 that Lieger, D., Riller, U., and Gibson, R.L. 2010 was withdrawn at the request of the author(s).

Analyte Symbol	Source	Lieger, Riller, and Gibson 2010[1]														
	Analysis Method	XRF														
	Rock Type	Quartzite														
	Unit Symbol	WR 621A3	PT 621A2	PT 621A1	PT 2A2	PT 2B2	WR 64A3	PT 64A2	PT 64A1	WR 102A2	PT 102A1	PT 1A1	PT 1A2	PT 1A3	Average WR	Average PT
SiO_2	%	91.55	80.46	81.45	81.19	79.78	94.81	91.59	89.96	95.85	93.73	73.56	73.47	72.64	94.07	81.78
Al_2O_3	%	4.96	11.12	11.24	10.39	12.06	2.40	3.78	4.21	1.98	4.40	12.86	13.12	14.24	3.11	9.74
Fe_2O_3(T)	%	1.34	1.53	1.33	2.57	1.23	0.55	1.56	1.80	2.78	0.79	3.72	3.74	3.57	1.56	2.18
FeO[†]	Calculated	1.21	1.38	1.20	2.31	1.11	0.50	1.40	1.62	2.50	0.71	3.35	3.37	3.21	1.40	1.97
MnO	%	0.00	0.01	0.01	0.01	0.01	0.01	0.01	0.05	0.01	0.01	0.04	0.04	0.03	0.01	0.02
MgO	%	0.01	0.24	0.25	0.27	0.17	0.00	0.05	0.79	0.01	0.12	1.41	1.38	1.29	0.01	0.60
CaO	%	0.00	0.00	0.03	0.00	0.00	0.08	0.00	0.35	0.00	0.00	0.75	0.65	0.08	0.03	0.19
Na_2O	%	0.03	0.10	0.12	0.08	0.73	0.02	0.06	0.00	0.02	0.02	1.86	1.85	0.00	0.02	0.48
K_2O	%	1.12	3.16	3.01	2.48	2.80	0.64	0.88	0.98	0.50	1.04	2.32	2.43	2.47	0.75	2.16
TiO_2	%	0.08	0.38	0.38	0.32	0.45	0.12	0.16	0.18	0.19	0.21	0.53	0.56	0.57	0.13	0.37
P_2O_5	%	0.02	0.02	0.03	0.01	0.02	0.01	0.03	0.06	0.01	0.02	0.01	0.01	0.01	0.01	0.02

[1]It was discovered on July 28th 2016 that this paper was withdrawn at the request of the author(s).

[†]Note: When FeO content is shown in red it denotes that it has been calculated by multiplying the Fe_2O_3 content by 0.9.

[1]It was discovered on July 28th 2016 that Lieger, D., Riller, U., and Gibson, R.L. 2010 was withdrawn at the request of the author(s).

Analyte Symbol	**Source**	Lieger, Riller, and Gibson 2010[1]				Schwarzman et al. 1983								Bischoff 1972	Bischoff 1973
	Analysis Method	XRF													
	Rock Type	Alkali Granite		Epidiorite		Granitoid	Gabbro		Diorite	Alkali Granite		Epidiorite		Diorite	Alkali Granite
	Unit Symbol	WR 4A2	PT 4A1	WR 564A2	PT 564A1	PT	PT	PT	PT	PT	PT	PT	PT	WR	WR
SiO_2	%	70.01	67.32	51.18	54.12	65.00	57.60	59.30	58.70	65.60	66.10	52.50	52.40	54.80	73.57
Al_2O_3	%	14.89	15.35	14.65	13.78	17.50	11.30	12.10	13.80	15.60	15.80	15.50	15.40	15.70	13.58
Fe_2O_3(T)	%	2.65	6.30	7.55	7.28	8.60	8.12	8.13	8.16	8.14	8.15	8.80	8.90	8.50	8.40
FeO†	Calculated	2.39	5.67	6.80	6.55	7.74	7.31	7.32	7.34	7.33	7.34	7.92	8.01	7.65	7.56
MnO	%	0.07	0.08	0.12	0.13	0.05	0.16	0.14	0.11	0.10	0.10	0.15	0.15	0.16	0.05
MgO	%	0.20	0.72	9.28	8.59	1.20	11.60	9.40	4.20	0.59	0.62	8.10	8.10	2.70	0.13
CaO	%	0.69	0.60	13.41	12.00	4.00	7.80	6.60	4.10	1.00	0.87	12.50	12.50	5.80	0.49
Na_2O	%	7.82	7.86	1.37	2.08	5.20	1.60	1.70	6.70	8.90	8.20	2.20	2.20	5.70	5.85
K_2O	%	2.94	2.51	0.08	0.55	1.30	0.53	0.56	1.40	1.70	2.60	0.19	0.18	1.50	3.98
TiO_2	%	0.25	0.29	0.30	0.35	0.73	0.36	0.33	0.98	0.36	0.33	0.44	0.45	1.60	0.15
P_2O_5	%	0.06	0.08	0.02	0.04										

†Note: When FeO content is shown in red it denotes that it has been calculated by multiplying the Fe_2O_3 content by 0.9.

[1]It was discovered on July 28th 2016 that Lieger, D., Riller, U., and Gibson, R.L. 2010 was withdrawn at the request of the author(s).

Analyte Symbol	**Source**	Reimold 1991				Wilshire 1971	McIver et al 1981		Tankard et al. 1982					
	Analysis Method													
	Rock Type	Gabbro		Norite		Epidiorite	Mafic Rock		Mafic Rock	Alkali Granite WR	Alkali Granite PT	Epidote PT	Gabbro PT	Mafic Rock WR
	Unit Symbol	WR	PT	WR	PT	PT	WR	WR	WR	Average	Average	Average	Average	Average
SiO_2	%	50.70	54.50	51.80	56.70	52.80	43.56	49.02	54.92	71.79	66.34	52.96	57.13	49.17
Al_2O_3	%	13.50	13.30	15.70	15.10	14.50	8.56	8.44	14.72	14.24	15.58	14.80	12.23	10.57
Fe_2O_3(T)	%	14.30	12.00	8.60	7.90	8.30	1.27	1.06	12.70	5.53	7.53	8.32	9.42	5.01
FeO[†]	Calculated	12.87	10.80	7.74	7.11	7.47	1.14	0.95	11.43	4.97	6.78	7.49	8.48	4.51
MnO	%	0.20	0.20	0.10	0.10	0.15	0.21	0.18	0.19	0.06	0.09	0.15	0.17	0.19
MgO	%	6.00	6.10	9.30	7.30	8.50	17.58	14.42	4.93	0.17	0.64	8.32	9.03	12.31
CaO	%	9.30	7.70	12.70	10.10	12.10	8.50	7.91	6.88	0.59	0.82	12.28	7.37	7.76
Na_2O	%	2.20	2.60	1.40		1.70	0.04	0.83	3.51	6.84	8.32	2.05	1.97	1.46
K_2O	%	1.00	1.50	0.10	0.60	0.14	0.21	0.18	0.68	3.46	2.27	0.27	0.86	0.36
TiO_2	%	1.80	1.40	0.40	0.40	0.43	1.00	1.04	1.22	0.20	0.33	0.42	0.70	1.09
P_2O_5	%	0.30	0.30	0.10	0.10					0.06	0.08	0.04	0.30	

[†]Note: When FeO content is shown in red it denotes that it has been calculated by multiplying the Fe_2O_3 content by 0.9.

[1]It was discovered on July 28^{th} 2016 that Lieger, D., Riller, U., and Gibson, R.L. 2010 was withdrawn at the request of the author(s).

Analyte Symbol	Source	Crow and Condie 1988								
	Analysis Method	Major and some trace elements (Rb, Sr, Ba,Nb, Y, Zr, Ni, V, Pb) determined with XRF other trace elements (Cs, Th, U, Sc, Cr, Co, Hf, Ta, 7 REE) determined by Istrumental Neutrin Activation								
	Rock Type	Porphyritic lava	Basaltic Andesite	Felsic Porphyritic Lava	Porphyritic Basaltic Andesite	Basalt	Basalt			
	Unit Symbol	Pniel Group Allanridge	Platberg Group Reitgat	Platberg Group Makwassie	Platberg Group Goedgenoeg	Platberg Group Average	Klipriviersberg Group Edenville	Klipriviersberg Group Loraine	Klipriviersberg Group Jeannette	Klipriviersberg Group Orkney
SiO_2	%	55.5	52.8	70.1	52.5	52.65	52.3	54.3	55.1	53.8
Al_2O_3	%	14.1	14.3	12.6	14.9	14.6	12.1	13.6	14.9	14.7
Fe_2O_3(T)	%	9.8	10.5	4.8	10.5	10.5	10.1	10.1	11.1	11.2
FeO[†]	Calculated	8.82	9.45	4.32	9.45	9.03	9.09	9.09	9.99	10.08
MnO	%	0.12	0.13	0.07	0.13	0.13	0.18	0.15	0.15	0.15
MgO	%	3.83	4.37	2.51	5.6	4.985	10.52	7.47	4.9	5.3
CaO	%	5.49	5.78	2.26	6.57	6.175	8.71	7.4	7.34	7.34
Na_2O	%	3.73	3.72	2.71	3.39	3.555	2.37	2.92	3.34	3.58
K_2O	%	1.5	1.08	3.65	1.23	1.155	0.74	1.25	1.35	0.92
TiO_2	%	1.17	1.37	0.66	1.36	1.365	0.54	0.82	0.94	1
P_2O_5	%	0.32	0.49	0.22	0.57	0.53	0.06	0.21	0.12	0.13

[†]Note: When FeO content is shown in red it denotes that it has been calculated by multiplying the Fe_2O_3 content by 0.9.

[1]It was discovered on July 28th 2016 that Lieger, D., Riller, U., and Gibson, R.L. 2010 was withdrawn at the request of the author(s).

Analyte Symbol	Source	Crow and Condie 1988 Continued		Wronkiewicz and Condie 1990							
	Analysis Method	Major and some trace elements (Rb, Sr, Ba,Nb, Y, Zr, Ni, V, Pb) determined with XRF other trace elements (Cs, Th, U, Sc, Cr, Co, Hf, Ta, 7 REE) determined by Istrumental Neutrin Activation		Major and some trace elements (Zr, Y, Sr, Nb, V,Pb and Rb) determined with XRF other trace elements (Hf, Ta, Sc, Cr, Co, Ni, Ba, Cs, Th, U and 7 REE) determined by Istrumental Neutrin Activation							
	Rock Type	Basalt		Pelites & Shales							Quartzite
	Unit Symbol	Klipriviersberg Group Westonaria	Klipriviersberg Average	Average Bothaville Formation P&S	Average Selati Formation P&S	Average Black Reef Formation P&S	Average Timeball Hill Formation P&S	Average Strubenkop Formation P&S	Average Silverton Formation P&S	NASC P&S	Bothaville Formation Quartzite C6
SiO_2	%	54.7	54.04	63.64	59.86	53.84	59.36	57.09	61.18	64.8	90.44
Al_2O_3	%	9.1	12.88	15.54	14.93	18.44	20.75	21.17	10.51	16.9	3.18
Fe_2O_3(T)	%	12.9	11.08	6.29	10.88	7.45	8.52	12.18	7.48	6.33	3.06
FeO†	Calculated	11.61	9.972	5.66	9.79	6.71	7.67	10.96	6.73	5.70	2.75
MnO	%	0.19	0.164	0.01	0.02	0.19	0.05	0.06	0.06	0.06	3.06
MgO	%	13.97	8.432	4.98	3.71	4.44	1.78	1.35	2.74	2.85	0.59
CaO	%	7.62	7.682	1.25	0.6	2.02	0.7	0.2	0.66	3.56	0.03
Na_2O	%	1.36	2.714	0.23	0.28	0.09	0.84	0.6	1.35	1.15	0.29
K_2O	%	0.19	0.89	3.27	4.89	4.54	3.52	1.43	2.91	3.99	0.24
TiO_2	%	1.06	0.872	0.44	0.89	0.89	0.7	0.85	0.75	0.78	0.07
P_2O_5	%	0.16	0.136	0.12	0.19	0.14	0.19	0.14	0.08	0.11	0.08

†Note: When FeO content is shown in red it denotes that it has been calculated by multiplying the Fe_2O_3 content by 0.9.

[1]It was discovered on July 28th 2016 that Lieger, D., Riller, U., and Gibson, R.L. 2010 was withdrawn at the request of the author(s).

Analyte Symbol	Source	Wronkiewicz and Condie 1990 Continued										
	Analysis Method	Major and some trace elements (Zr, Y, Sr, Nb, V,Pb and Rb) determined with XRF other trace elements (Hf, Ta, Sc, Cr, Co, Ni, Ba, Cs, Th, U and 7 REE) determined by Istrumental Neutrin Activation										
	Rock Type	Quartzite	Quartzite	Quartzite	Quartzite	Quartzite	Quartzite	Quartzite		Quartzite	Quartzite	Quartzite
	Unit Symbol	Sekororo Formation Quartzite D53	Sekororo Formation Quartzite D36	Sekororo Formation Quartzite D47	Average Sekororo Formation Quartzite D47	Selati Formation Quartzite D35	Black Reef Quartzite D34	Black Reef Quartzite C201	Average Black Reef Quartzite C201	Rooihoogte Formation Quartzite C76	Daspoort Formation Quartzite C81	Daspoort Formation Quartzite M8F-2-10
SiO_2	%	95.06	79.61	82.83	85.83	77.9	96.07	94.19	95.13	94.93	95.61	90.38
Al_2O_3	%	2.28	8.27	8.19	6.25	12.15	2.05	4.11	3.08	2.31	2.05	3.38
Fe_2O_3(T)	%	0.6	2.19	1.92	1.57	1.69	0.62	0.6	0.61	0.82	0.66	4.24
FeO†	Calculated	0.54	1.97	1.73	1.41	1.52	0.56	0.54	0.549	0.74	0.59	3.82
MnO	%		0.02	0.01	0.02							0.01
MgO	%	0.41	1.51	1.36	1.09	2.04	0.27	0.22	0.245	0.23	0.32	0.73
CaO	%	0.02	2.46	0.52	1.00	0.09	0.03	0.03	0.03	0.01	0.03	0.05
Na_2O	%	0.08		0.1	0.09		0.52		0.52		0.34	0.56
K_2O	%	0.29	2.82	2.32	1.81	6.26	0.12	0.04	0.08		0.14	0.01
TiO_2	%	0.01	0.03	0.06	0.03	0.15	0.02	0.01	0.015	0.01	0.06	0.05
P_2O_5	%	0.01	0.02	0.02	0.02	0.03	0.01		0.01			0.02

†Note: When FeO content is shown in red it denotes that it has been calculated by multiplying the Fe_2O_3 content by 0.9.

[1]It was discovered on July 28th 2016 that Lieger, D., Riller, U., and Gibson, R.L. 2010 was withdrawn at the request of the author(s).

Analyte Symbol	Source	Wronkiewicz and Condie 1990 Continued					Lana et al. 2004				
	Analysis Method	Major and some trace elements (Zr, Y, Sr, Nb, V,Pb and Rb) determined with XRF other trace elements (Hf, Ta, Sc, Cr, Co, Ni, Ba, Cs, Th, U and 7 REE) determined by Istrumental Neutrin Activation					XRF Analysis				
	Rock Type		Quartzite	Quartzite		Quartzite	Gneiss (amphibolite facies) Trondhjemite NE-Part				
	Unit Symbol	Average Daspoort Formation Quartzite M8F-2-10	Magaliesberg Formation Quartzite C207	Magaliesberg Formation Quartzite D77	Average Magaliesberg Formation Quartzite D77	Rayton Formatio n Quartzite C56	ABBG-1	ABBG-2	ABBG-3	ABG-1	ABG-2
SiO_2	%	92.995	94.23	66.46	80.345	96.02	70.16	69.75	69.17	70.76	70.7
Al_2O_3	%	2.715	2.58	13.19	7.885	1.82	15.56	15.45	15.39	15.77	15.73
Fe_2O_3(T)	%	2.45	0.7	3.24	1.97	0.59	3.28	3.38	3.42	2.45	2.49
FeO[†]	Calculated	2.205	0.63	2.92	1.773	0.53	2.95	3.04	3.08	2.21	2.24
MnO	%	0.01		0.06	0.06		0.03	0.05	0.06	0.04	0.06
MgO	%	0.525	0.44	4.3	2.37	0.17	0.67	0.72	0.77	0.25	0.29
CaO	%	0.04	0.02	4.22	2.12	0.01	2.59	2.62	2.59	2.13	2.14
Na_2O	%	0.45	0.33	1.79	1.06	0.16	5.23	5.41	5.64	4.91	4.96
K_2O	%	0.075	0.52	5.92	3.22	0.11	1.84	1.88	1.89	3.34	3.28
TiO_2	%	0.055	0.03	0.47	0.25	0.02	0.57	0.56	0.57	0.45	0.45
P_2O_5	%	0.02	0.01	0.04	0.025		0.16	0.18	0.19	0.12	0.11

[†]Note: When FeO content is shown in red it denotes that it has been calculated by multiplying the Fe_2O_3 content by 0.9.

[1]It was discovered on July 28th 2016 that Lieger, D., Riller, U., and Gibson, R.L. 2010 was withdrawn at the request of the author(s).

Analyte Symbol	Source	Lana et al. 2004 Continued											
	Analysis Method	XRF Analysis											
	Rock Type	Gneiss (amphibolite facies) Trondhjemite NE-Part				Porphyritic granodiorite W-Part				Gneiss (Granulite Facies) Quartz Diorite Central Part			
	Unit Symbol	ABP-1	ABP-2	ABP-3	Average	POR-1	POR-2	POR-3	Average	SCH-1	SCH-2	SCH-3	Average
SiO_2	%	70.83	71.59	70.98	70.49	69.93	69.56	69.36	69.62	66.14	67.74	67.14	67.01
Al_2O_3	%	15.33	15.15	15.29	15.46	15.19	15.37	15.23	15.26	16.25	16.05	16.17	16.16
Fe_2O_3(T)	%	2.31	2.28	2.35	2.75	3.65	3.75	3.71	3.70	3.5	2.8	2.87	3.06
FeO†	Calculated	2.08	2.05	2.12	2.47	3.29	3.38	3.34	3.33	3.15	2.52	2.58	2.75
MnO	%	0.05	0.04	0.06	0.05	0.05	0.06	0.07	0.06	0.08	0.08	0.08	0.08
MgO	%	0.28	0.31	0.32	0.45	0.54	0.6	0.55	0.56	0.52	0.46	0.5	0.49
CaO	%	1.49	1.5	1.61	2.08	2.2	2.25	2.14	2.20	1.91	1.89	1.98	1.93
Na_2O	%	5.38	5.22	5.38	5.27	5.86	5.67	5.74	5.76	7.17	6.85	6.9	6.97
K_2O	%	3.56	3.41	3.09	2.79	1.99	1.99	2.31	2.10	3.95	3.94	4	3.96
TiO_2	%	0.41	0.41	0.41	0.48	0.56	0.59	0.57	0.57	0.44	0.43	0.44	0.44
P_2O_5	%	0.15	0.15	0.16	0.15	0.19	0.21	0.2	0.20	0.19	0.19	0.21	0.20

†Note: When FeO content is shown in red it denotes that it has been calculated by multiplying the Fe_2O_3 content by 0.9.

[1]It was discovered on July 28th 2016 that Lieger, D., Riller, U., and Gibson, R.L. 2010 was withdrawn at the request of the author(s).

Analyte Symbol	Source	Lana et al. 2004 Continued												
	Analysis Method	XRF Analysis												
	Rock Type	Melanosomes Trondhjemite Outer Parts												
	Unit Symbol	RG1	RG14	RG15	SAG-1	SAG-2	EG1	EG3A	EG3B	EG6	BEG-1	BEG-2	VAL-1	Average
SiO_2	%	70.08	71.75	69.29	70.45	70.7	69.12	70.26	69.21	70.12	70.08	69.97	72.58	70.30
Al_2O_3	%	15.27	14.53	14.19	15.64	15.78	15.72	15.4	15.45	15.83	15.29	15.56	14.99	15.30
Fe_2O_3(T)	%	3.51	3.27	4.59	2.87	2.82	4.2	4.08	4.28	2.6	3.32	3.16	2.18	3.41
$FeO^{\dagger}$	Calculated	3.16	2.94	4.13	2.58	2.54	3.78	3.67	3.85	2.34	2.99	2.84	1.96	3.07
MnO	%	0.06	0.04	0.04	0.06	0.07	0.08	0.06	0.07	0.04	0.07	0.06	0.04	0.06
MgO	%	0.65	0.5	1.11	0.6	0.63	0.84	0.75	0.87	0.12	0.61	0.52	0.18	0.62
CaO	%	2.24	2.19	3.05	2.43	2.43	2.7	2.71	2.72	1.71	2.5	2.43	1.9	2.42
Na_2O	%	5.67	5.35	6.2	6.09	5.78	5.22	5.19	5.5	5.85	5.66	5.57	5.12	5.60
K_2O	%	2.57	3.38	1.47	1.38	1.4	2.01	1.59	1.91	3.92	1.81	2.01	2.51	2.16
TiO_2	%	0.41	0.38	0.59	0.43	0.44	0.54	0.5	0.53	0.27	0.51	0.48	0.38	0.46
P_2O_5	%	0.19	0.19	0.22	0.12	0.13	0.22	0.17	0.2	0.07	0.16	0.17	0.09	0.16

[†]Note: When FeO content is shown in red it denotes that it has been calculated by multiplying the Fe_2O_3 content by 0.9.

[1]It was discovered on July 28th 2016 that Lieger, D., Riller, U., and Gibson, R.L. 2010 was withdrawn at the request of the author(s).

Analyte Symbol	Source	Lana et al. 2004 Continued													
	Analysis Method	XRF Analysis													
	Rock Type	Melanosomes Tonalite Central Parts				Mafic Granulites Central Parts				Leucosomes Granite Outer Parts					
	Unit Symbol	vdf-4	vdf-1	vdf-8	Average	vdf2-12	vdf2-21	vdf2-2	Average	EG-4	EG-7	EG-8	EG-9	EG-10	Pr12
SiO_2	%	52.06	54.24	51.84	52.71	50.55	40.93	47.22	46.23	70.62	71.64	73.88	73.74	73.24	73.92
Al_2O_3	%	15.76	15.77	14.02	15.18	9.92	12.16	9.66	10.58	14.23	14.88	14.05	14.48	14.22	14.21
Fe_2O_3(T)	%	10.67	9.22	12.24	10.71	8.38	13.27	25	15.55	2.49	1.9	1.69	1.22	1.81	1.52
FeO[†]	Calculated	9.60	8.30	11.02	9.64	7.54	11.94	22.50	14.00	2.24	1.71	1.52	1.10	1.63	1.37
MnO	%	0.12	0.12	0.2	0.15	0.17	0.19	0.38	0.25	0.03	0.04	0.04	0.02	0.02	0.02
MgO	%	5.95	5.17	5.99	5.70	12.56	9.77	8.96	10.43	0.28	0.07	0.12	0	0.17	0.16
CaO	%	6.93	6.81	9.26	7.67	8.94	13.52	4.38	8.95	0.83	1.01	1.36	1.19	1.48	1.51
Na_2O	%	3.62	3.76	2.32	3.23	2.12	1.79	1.98	1.96	2.91	4.56	5.14	4.65	5.18	5.26
K_2O	%	1.2	1.37	0.77	1.11	1.38	1.33	0.3	1.00	8.08	6.16	3.77	4.82	3.88	3.39
TiO_2	%	1.3	1.07	1.68	1.35	0.45	1.93	0.53	0.97	0.2	0.15	0.2	0.07	0.25	0.19
P_2O_5	%	0.47	0.46	0.17	0.37	0.15	2.6	0.09	0.95	0.17	0.07	0.04	0.02	0.08	0.04

[†]Note: When FeO content is shown in red it denotes that it has been calculated by multiplying the Fe_2O_3 content by 0.9.

[1]It was discovered on July 28th 2016 that Lieger, D., Riller, U., and Gibson, R.L. 2010 was withdrawn at the request of the author(s).

Analyte Symbol	Source	Lana et al. 2004 Continued														
	Analysis Method	XRF Analysis														
	Rock Type	Leucosomes Granite Outer Parts									K-feldspar-rich Granite Transition Zone			Schlieric Granite Northern Parts		
	Unit Symbol	Pr2	RG11	RG12	RG13	RG2	RG3	RG7	RG9	SAL-1	LEP-1	LEP-2	LEP-3	SPW-1	SPW-2	ScSPW-3
SiO_2	%	74.44	73.16	74.01	75.2	74.97	75.33	73.16	72.95	73.49	74.3	74.64	74.97	74.07	74.13	73.65
Al_2O_3	%	14.08	14.67	14.34	13.53	13.59	13.42	14.5	14.24	14.45	14.43	14.36	14.17	14.47	14.46	14.26
Fe_2O_3(T)	%	1.31	1.57	1.35	0.14	1.19	1.33	1.45	2.32	1.78	1.84	1.62	1.72	1.48	1.36	1.62
FeO†	Calculated	1.18	1.41	1.22	0.13	1.07	1.20	1.31	2.09	1.60	1.66	1.46	1.55	1.33	1.22	1.46
MnO	%	0.01	0.03	0.02	0.01	0.02	0.04	0.03	0.04	0.03	0.01	0	0.01	0.02	0	0.01
MgO	%	0.01	0.38	0.25	0	0.1	0.07	0.38	0.47	0	0.21	0.16	0.17	0.04	0.02	0.06
CaO	%	1.17	1.73	1.51	0.99	1.06	1.32	1.61	1.31	1.3	1.77	1.73	1.6	1.52	1.48	1.47
Na_2O	%	4.56	5.37	4.89	4	4.15	4.93	5.59	4.31	5.28	3.83	4.07	3.76	4.79	4.4	5.14
K_2O	%	4.46	3.07	3.54	5.16	4.94	3.66	3.5	4.66	3.33	3.12	3.14	3.29	3.48	3.6	3.45
TiO_2	%	0.15	0.24	0.28	0.1	0.14	0.16	0.1	0.2	0.26	0.3	0.29	0.29	0.25	0.25	0.24
P_2O_5	%	0.03	0.04	0.04	0.03	0.04	0.03	0.04	0.1	0.05	0.05	0.04	0.04	0.05	0.06	0.05

†Note: When FeO content is shown in red it denotes that it has been calculated by multiplying the Fe_2O_3 content by 0.9.

[1]It was discovered on July 28th 2016 that Lieger, D., Riller, U., and Gibson, R.L. 2010 was withdrawn at the request of the author(s).

Analyte Symbol	**Source**	Lana et al. 2004 Continued			Hart et al. 1990	Remiold et al. 2000								
	Analysis Method	XRF Analysis			Major-XRF Trace-INAA	XRF								
	Rock Type	Homogen Granite Southwestern			Ultramafics	Anne Rust Sheet								
	Unit Symbol	ESP-1	ESP-2	Average	Avg. Beta -1	Mean IV	Mean III	Anna's Rust Sheet	Vredefort mafic complex	OCEAAN	Core	CoreBH	Collar	SWBH
SiO_2	%	74.58	74.67	74.625	42.59	50.57	50	50.92	51.26	50.28	49.5	49.93	50.88	50.43
Al_2O_3	%	13.83	13.93	13.88	1.52	14.75	14.87	14.87	15.2	15.29	13.94	14.11	15.04	14.33
Fe_2O_3(T)	%	1.42	1.34	1.38	11.67	13.72	13.77	13.35	12.68	13.09	16.19	14.24	13.63	13.89
FeO[†]	Calculated	1.28	1.21	1.242		0	0.01	12.015	11.412	11.781	14.571	12.816	12.267	12.501
MnO	%	0.05	0.02	0.035	0.13	0.19	0.2	0.2	0.19	0.18	0.2	0.19	0.18	0.18
MgO	%	0	0	0	36.63	6.31	6.59	6.52	6.88	6.75	5.57	6.12	6.12	6.02
CaO	%	0.97	0.93	0.95	3.45	9.74	9.86	9.79	10.2	10.05	9.28	9.62	9.83	9.6
Na_2O	%	4.89	4.58	4.735	0.28	2.25	2.17	2.08	1.78	2	2.57	2.6	2.19	2.76
K_2O	%	4.08	4.31	4.195	0.13	0.69	0.69	0.72	0.6	0.53	0.73	0.74	0.73	0.66
TiO_2	%	0.24	0.24	0.24	0.22	1.58	1.57	1.48	1.32	1.36	1.9	1.8	1.6	1.73
P_2O_5	%	0.03	0.02	0.025	0.04	0.17	0.2	0.16	0.14	0.14	0.25	0.17	0.18	0.18

[†]Note: When FeO content is shown in red it denotes that it has been calculated by multiplying the Fe_2O_3 content by 0.9.

[1]It was discovered on July 28th 2016 that Lieger, D., Riller, U., and Gibson, R.L. 2010 was withdrawn at the request of the author(s).

Analyte Symbol	**Source**	Coetzee et al. 2006						de Waal, Graham, and Armstrong 2006			
	Analysis Method	Mafic and Trace by XRF and REE by ICP-MS						Major and trace elements by XRF, REE by ICP-MS			
	Rock Type	Tholeiitic Intrusions			Mafic Dykes and sills			Lindeques drift and Heidelberg Intrusions			
	Unit Symbol	Wittekopjes norite	Parsons Rust Dol-Norite	Reebokkop dolerite	Bushveld micopyroxenitic sills	Bushveld Ultramafic Sills	Noritic sills and dykes E Wittswatersrand	Lindeques Drift Contamspess	Lindeques Drift Even-grained spessartite mean	Lindeques Drift Porphyritic spessartite mean	Heidelberg Porphyritic spess mean
SiO_2	%	54.17	52.21	54.19	55.7	44.4	52	39.78	36.96	39.16	38.61
Al_2O_3	%	6.73	8.05	13.14	11.3	4.5	11.1	3.89	3.61	5.91	5.2
Fe_2O_3(T)	%	10.09	10.74	10.13				21.33	29.36	26.63	25.44
FeO†	Calculated	9.081	9.666	9.117	0	0	0	19.197	26.424	23.967	22.896
MnO	%	0.19	0.18	0.15				0.29	0.3	0.3	0.31
MgO	%	20.2	14.61	8.27	13	32.1	11	12.08	9.96	8.33	9.31
CaO	%	6.02	10.59	8.75	6.4	2.8	8	17.92	13.77	12	9.58
Na_2O	%	0.82	1.31	2.52				1.45	1.19	2.31	2.25
K_2O	%	0.19	0.3	0.69	0.9	0.3	0.2	0.3	0.31	0.6	0.57
TiO_2	%	0.22	0.37	0.51	0.3	0.1	0.7	1.76	3.57	3.18	6.11
P_2O_5	%	0.03	0.05	0.08	0.07	0.03	0.08	0.33	0.12	0.23	1.42

†Note: When FeO content is shown in red it denotes that it has been calculated by multiplying the Fe_2O_3 content by 0.9.

[1]It was discovered on July 28th 2016 that Lieger, D., Riller, U., and Gibson, R.L. 2010 was withdrawn at the request of the author(s).

Analyte Symbol	Source	de Waal, Graham, and Armstrong 2006 Continued								
	Analysis Method	Major and trace elements by XRF, REE by ICP-MS								
	Rock Type	Lindeques drift and Heidelberg Intrusions								
	Unit Symbol	Lindeques Drift Low-silica diorite mean	Lindeques Drift diorite mean	Lindeques Drift syeno-diorite mean	Lindeques Drift feeder	Roodekraal Complex Lava	Roodekraal Complex Cumulate	Roodekraal Complex Diorite	Roodekraal Complex Lava Clark 1972	Roodekraal Complex Diorite Clark 1972
SiO_2	%	47.54	53.51	58.43	47.18	53.98	43.17	52.18	51.31	51.72
Al_2O_3	%	10.84	12.36	16.99	15.38	12.41	5.94	15.13	11.72	12.06
Fe_2O_3(T)	%	16.94	13.96	8.42	14.21	13.01	23.32	12.24	15.23	15.79
FeO†	Calculated	15.246	12.564	7.578	12.789	11.709	20.988	11.016	13.707	14.211
MnO	%	0.26	0.19	0.12	0.21	0.19	0.37	0.17	0.18	0.19
MgO	%	4.72	3.85	1.87	4.66	3.37	7.57	2.85	2.89	4.16
CaO	%	8.21	6.22	3.93	9.06	5.5	10.35	5.93	5.1	5.72
Na_2O	%	6.12	4.67	6.33	2.74	5.51	2.8	5.53	4.73	5.2
K_2O	%	1.16	1.16	1.29	1.02	1.78	0.91	1.32	1.81	1.6
TiO_2	%	1.92	1.82	1.03	2.28	1.77	3.2	1.84	1.77	1.9
P_2O_5	%	0.44	0.48	0.39	0.28	0.52	0.23	0.71	0.5	0.51

†Note: When FeO content is shown in red it denotes that it has been calculated by multiplying the Fe_2O_3 content by 0.9.

[1]It was discovered on July 28th 2016 that Lieger, D., Riller, U., and Gibson, R.L. 2010 was withdrawn at the request of the author(s).

Analyte Symbol	**Source**	Maier, Barnes, and Marsh 2003						Wilson and Chunnett 2006			
	Analysis Method	XRF						ICP-MS			
	Rock Type	Bushveld Complex						Bushveld Complex			
	Unit Symbol	Dominion Low Ti/V	Dominion High Ti/V	Loraine/ Edenville	Hekpoort	Machadodorp	Bushveld Mg basalt	GC1 Average	SD22 D5 Average	SD45 Average	SD46 Average
SiO_2	%	52.44	57.19	53.69	54.01	50.15	55.87	50.82	51.75	50.71	53.16
Al_2O_3	%							13.22	11.26	6.95	7.27
Fe_2O_3(T)	%							1.01	1.04	1.31	1.13
FeO†	Calculated							8.16	8.41	10.61	9.16
MnO	%							0.17	0.19	0.21	0.21
MgO	%	9.07	5.26	10.97	8.38	8.55	12.65	16.09	18.32	23.55	21.99
CaO	%							7.92	7.19	4.50	5.10
Na_2O	%							1.06	0.90	0.54	0.77
K_2O	%							0.09	0.08	0.16	0.23
TiO_2	%							0.19	0.18	0.23	0.24
P_2O_5	%							0.02	0.02	0.02	0.03

†Note: When FeO content is shown in red it denotes that it has been calculated by multiplying the Fe_2O_3 content by 0.9.

[1]It was discovered on July 28th 2016 that Lieger, D., Riller, U., and Gibson, R.L. 2010 was withdrawn at the request of the author(s).

Sudbury

Analyte Symbol	**Source**	Lightfoot et al. 1996												
	Analysis Method													
	Rock Type	Main Mass Mafic Norite Average	Main Mass Felsic Norite Average	Main Mass Grano-phyre Average	Igneous textured sublayer matrix Whistle Mine Average	Mela-norite Pod or Inclusion Whistle Mine Average	Olivine Melanorite Whistle Mine Average	Diabase Whistle Mine Average	Little Stobie Mine Igneous Textured Sublayer Matrix		Crean Hill Mine Igneous Textured Sublayer Matrix			
	Unit Symbol								93PCL-001	93PCL-001	93PCL-20	93PCL-22	93PCL-23	93PCL-25
SiO_2	%	55.78	56.47	67.57	50.01	49.6	46.64	49.05	49.36	49.61	51.09	49.9	51.42	51.96
Al_2O_3	%	11.71	16.3	12.79	13.37	10.39	6.91	13.62	16.16	16.45	18.84	16.63	16.48	15.37
Fe_2O_3(T)	%	9.93	7.91	6.47	13.49	14.57	15.11	15.03	12.86	12.86	10.28	11.94	10.81	11.62
FeO[†]	Calculated	8.937	7.119	5.823	8.18	8.81	9.18	9.04	9.48	9.79	7.7	8.77	8.3	8.57
MnO	%	0.16	0.13	0.09	0.18	0.18	0.19	0.22	0.18	0.18	0.15	0.17	0.16	0.16
MgO	%	10.61	4.95	1.23	7.73	10.51	18.09	6	8.57	6.79	5.76	6.67	6.08	6.71
CaO	%	4.54	6.38	1.8	8.49	7.25	6.41	9.55	8.52	9.02	7.46	7.7	8.37	7.66
Na_2O	%	2.03	2.85	3.62	2.41	1.73	0.57	2.19	1.75	1.93	2.12	1.98	2.2	2.17
K_2O	%	1.41	1.81	3.46	1	1.2	0.83	0.78	0.4	0.47	1.08	1.02	0.76	0.9
TiO_2	%	0.56	0.62	0.89	0.83	0.68	0.61	1.15	0.88	0.99	0.85	0.93	1.02	0.84
P_2O_5	%	0.11	0.16	0.22	0.19	0.2	0.17	0.15	0.2	0.2	0.18	0.2	0.22	0.17

[†]Note: When FeO content is shown in red it denotes that it has been calculated by multiplying the Fe_2O_3 content by 0.9.

[1]It was discovered on July 28th 2016 that Lieger, D., Riller, U., and Gibson, R.L. 2010 was withdrawn at the request of the author(s).

Analyte Symbol	Source	Lightfoot et al. 1996 Continued												
	Analysis Method													
	Rock Type	Levack West Mine Igneous Textured Sublayer Matrix		Levack West Mine Melanorite Pod or Inclusion			McCreedy West Mine Igneous Textured Sublayer Matrix					Fraser Mine Igneous Textured Sublayer Matrix		
	Unit Symbol	93PCL-45	93PCL-46	93PCL-66	93PCL-67	93PCL-68	93PCL-50	93PCL-51	93PCL-53	93PCL-55	93PCL-59	93PCL-342	93PCL-343	93PCL-344
SiO_2	%	57.04	54.97	53.77	44.36	44.3	54.62	56.08	57.69	53.21	54.12	57.15	54.45	56.61
Al_2O_3	%	11.95	8.4	7.49	3.33	3.23	9.79	11.71	11.13	11.95	13.73	11.99	11.6	10.93
Fe_2O_3(T)	%	9.54	11.5	12.04	13.17	13.31	15.07	10.66	10.07	12.51	9.83	9.08	9.97	10.49
FeO[†]	Calculated	7.18	7.57	8.12	7.44	7.22	8.1	8.12	7.04	7.49	6.31	7.08	7.18	7.55
MnO	%	0.15	0.18	0.18	0.17	0.16	0.16	0.17	0.16	0.17	0.15	0.14	0.15	0.15
MgO	%	9.52	13.29	16.03	26	25.1	9.93	10.92	9.83	10	9.11	8.47	9.89	10.13
CaO	%	4.95	5.61	5.3	8.86	8.77	4.15	4.89	4.48	5.62	7.37	4.99	4.57	4.65
Na_2O	%	2.53	1.54	1.24	0.14	0.15	1.82	2.08	2.18	2.34	2.39	2.42	1.91	2.05
K_2O	%	1.33	0.78	0.54	0.35	0.39	1.1	1.02	1.4	0.87	0.79	1.16	1.15	1.2
TiO_2	%	0.57	0.32	0.36	0.36	0.36	0.55	0.55	0.71	0.51	0.34	0.65	0.54	0.57
P_2O_5	%	0.15	0.08	0.09	0.06	0.06	0.15	0.13	0.17	0.13	0.09	0.11	0.11	0.09

[†]Note: When FeO content is shown in red it denotes that it has been calculated by multiplying the Fe_2O_3 content by 0.9.

[1]It was discovered on July 28th 2016 that Lieger, D., Riller, U., and Gibson, R.L. 2010 was withdrawn at the request of the author(s).

Analyte Symbol	Source	Lightfoot et al. 1996 Continued					Lightfoot et al. 2001							
	Analysis Method						Major Elements determined by WD-XRF; FeO deteremined by Potentiometric titration; Minor and REE determined by ICP-MS; Co, Cu, Ni, Sc, V, Y, Zn, Sr determined by ICP-OES							
	Rock Type	Fraser Mine Igneous Textured Sublayer Matrix		Creighton Mine Igneous Textured Sublayer Matrix			Mafic Norite		Felsic Norite					
	Unit Symbol	92PCL-345	93PCL-346	94PCL-128	94PCL-131	94PCL-132	94PCL 2011	94PCL 2016	94PCL 2066	94PCL 2072	94PCL 2076	94PCL 2033	94PCL 2028	94PCL 2013
SiO_2	%	57.11	54.96	47.67	49.43	49.53	55.19	53.79	57.45	56.6	56.49	55.67	55.11	55.22
Al_2O_3	%	10.18	10.55	12.93	14.77	12.57	12.31	10.67	16.12	16.84	17.26	17.94	17.53	15.63
Fe_2O_3(T)	%	10.49	10.21	12.34	12.24	14.8	9.84	11.01	7.56	7.27	6.66	6.82	7.08	8.08
FeO[†]	Calculated	8.02	7.3	10.33	10.33	8.59	7.48	7.56	5.96	4.84	4.29	4.24	4.56	5.89
MnO	%	0.17	0.15	0.19	0.18	0.18	0.158	0.165	0.116	0.123	0.106	0.097	0.111	0.125
MgO	%	11.52	10.58	11.03	6.44	8.38	11.35	12.15	4.37	4.75	4.75	5.2	5.57	8.25
CaO	%	4.2	4.26	8.14	8.26	6.8	5.19	4.54	7.31	6.12	7.29	7.04	7.06	6.57
Na_2O	%	1.79	1.86	1.51	2.4	1.68	2.11	2.04	3.15	3.14	2.91	2.81	2.66	2.49
K_2O	%	1.24	1.25	1.4	1.15	1.5	1.14	1.07	1.47	1.56	1.49	1.6	1.45	1.2
TiO_2	%	0.55	0.55	0.7	1.02	0.67	0.48	0.65	0.52	0.5	0.47	0.46	0.47	0.48
P_2O_5	%	0.12	0.12	0.13	0.24	0.13	0.089	0.122	0.108	0.096	0.092	0.082	0.079	0.097

[†]Note: When FeO content is shown in red it denotes that it has been calculated by multiplying the Fe_2O_3 content by 0.9.

[1]It was discovered on July 28th 2016 that Lieger, D., Riller, U., and Gibson, R.L. 2010 was withdrawn at the request of the author(s).

Analyte Symbol	Source	Lightfoot et al. 2001 Continued													
	Analysis Method	Major Elements determined by WD-XRF; FeO deteremined by Potentiometric titration; Minor and REE determined by ICP-MS; Co, Cu, Ni, Sc, V, Y, Zn, Sr determined by ICP-OES													
	Rock Type	Quartz Gabbro				Granophyre					Mafic Norite Average	Felsic Norite Average	Quartz Gabbro Average	Grano-phyre Average	Main Mass Average
	Unit Symbol	94PCL 2080	93PCL 290	94PCL 2052	94PCL 2079	93PCL 336	93PCL 293	93PCL 297	93PCL 312	93PCL 334					
SiO_2	%	54.88	63.82	56.38	55.13	64.16	69.84	69.22	66.34	63.1	56.2	57.9	59.3	69.1	62.5
Al_2O_3	%	16	13.59	15.01	16.82	12.98	12.47	12.57	13.03	13.33	10.1	17.4	14.3	13	14.8
Fe_2O_3(T)	%	9.41	8.24	9.03	8.72	8.15	5.41	5.65	7.35	9.31	11.6	7.2	10.3	6.4	7.6
FeO†	Calculated	5.77	3.39	5.46	5.11	4.49	3.19	3.16	4.17	5.41					
MnO	%	0.137	0.11	0.103	0.112	0.103	0.07	0.066	0.1	0.088	0.18	0.12	0.13	0.09	0.11
MgO	%	3.89	0.85	3.77	3.8	1.47	1.04	1.08	1.42	1.6	13.7	5.2	2.9	1.2	3.7
CaO	%	5.96	3.26	5.74	5.78	2.48	1.42	1.37	1.88	1.9	4.3	6.9	5.3	1.8	4.5
Na_2O	%	3.68	3.68	4.87	4.34	3.37	3.32	3.5	3.85	2.94	1.9	3.2	4.1	3.7	3.4
K_2O	%	1.9	2.99	0.93	1.44	3.3	4.06	4.03	2.78	3.64	1.2	1.5	1.9	3.6	2.4
TiO_2	%	0.9	1.14	0.93	0.79	1.07	0.71	0.76	1	1.09	0.59	0.51	1.46	0.89	0.81
P_2O_5	%	0.124	0.28	0.142	0.121	0.269	0.16	0.173	0.277	0.29	0.11	0.1	0.38	0.22	0.19

†Note: When FeO content is shown in red it denotes that it has been calculated by multiplying the Fe_2O_3 content by 0.9.

[1]It was discovered on July 28th 2016 that Lieger, D., Riller, U., and Gibson, R.L. 2010 was withdrawn at the request of the author(s).

Namaqualand

Analyte Symbol	**Source**	Duchesne et al. 2007												
	Analysis Method	Major Elements determined by XRF, Minor and REE determined by ICP-MS												
	Rock Type	Anorthosites			Tonalite	Leuconorite			Norite Sample 85b				Melanorite	
	Unit Symbol	Sample 70[b]	Sample 66	Sample 108	Sample 30[a]	Sample 119	Sample 120	Sample 121	Sample 85[b]	Sample 86[b]	Sample 116	Sample 122	Sample 88[b]	Sample 87[b]
SiO_2	%	55.17	55.7	54.66	65.63	50.79	51.72	52.09	50.3	48.99	48.01	52.52	47.51	44.25
Al_2O_3	%	26.7	25.76	24.08	21.12	21.65	23.19	22.22	16.34	14.8	18.61	16.94	5.54	7.69
Fe_2O_3(T)	%	1.42	1.25	3.77	0.46	11.01	9.02	6.92	14.08	15.49	12.3	10.25	22.13	21.93
FeO[†]	Calculated	1.278	1.125	3.393	0.414	9.909	8.118	6.228	12.672	13.941	11.07	9.225	19.917	19.737
MnO	%	0.02	0.02	0.04	0.07	0.08	0.07	0.05	0.2	0.29	0.14	0.15	0.3	0.29
MgO	%	0.41	0.66	0.98	0.15	3.7	2.58	1.91	8.04	9.13	5.26	7.69	16.7	14.82
CaO	%	9.84	8.37	8.62	6.08	6.92	7.98	9.25	5.92	5.11	7.74	6.32	1.66	3.86
Na_2O	%	4.14	5.71	4.65	5.36	3.75	4.29	4.54	3.16	2.57	3.33	2.52	0.96	1.16
K_2O	%	0.92	0.85	0.81	1.11	0.94	0.71	1.04	0.55	0.63	0.43	0.95	0.57	0.2
TiO_2	%	0.05	0.09	0.13	0.03	0.35	0.54	0.53	0.36	0.31	1.38	0.34	0.6	1.55
P_2O_5	%	0.23	0.23	0.01	0.12	0.08	0.01	0.14	0.08	0.07	1.05	0.13	0.07	0.68

[†]Note: When FeO content is shown in red it denotes that it has been calculated by multiplying the Fe_2O_3 content by 0.9.

[1]It was discovered on July 28[th] 2016 that Lieger, D., Riller, U., and Gibson, R.L. 2010 was withdrawn at the request of the author(s).

Analyte Symbol	**Source**	Duchesne et al. 2007 Continued											
	Analysis Method	Major Elements determined by XRF, Minor and REE determined by ICP-MS											
	Rock Type	Melanorite	Hypersthenite		Glimmerite	Magnetite		Biotite Diorite					
	Unit Symbol	Sample 110	Sample 90[b]	Sample 117	Sample 123	Sample 82[b]	Sample 125[b]	Sample 78[b]	Sample 112	Sample 109	Sample 114	Sample 118	Sample 126
SiO_2	%	41.25	48.3	41.5	40.5	25.87	29.38	50.97	49.38	54	60.01	43.74	52.28
Al_2O_3	%	8.31	4.1	2.9	11	2.45	2.69	22.63	22.37	22.11	16.82	19.43	21.78
Fe_2O_3(T)	%	30.52	24.33	25.9	10.8	47.91	39.66	10.03	8.8	5.8	8.14	8.94	7.35
FeO[†]	Calculated	27.468	21.897	23.31	9.72	43.119	35.694	9.027	7.92	5.22	7.326	8.046	6.615
MnO	%	0.39	0.49	0.25	0.03	0.37	0.43	0.08	0.06	0.08	0.11	0.16	0.13
MgO	%	12.09	20.41	19	17.5	11.48	11.39	2.67	3.11	1.55	2.32	7.11	4.83
CaO	%	2.45	1.21	3.8	3.5	2.91	6.62	6.68	7.09	5.47	6.55	6.51	7.95
Na_2O	%	0.75	0	0.35	0.5	0.06	0.03	4.06	4.18	5.1	3.42	3.95	3.82
K_2O	%	0.3	0	2	6.7	0.09	0.07	1.8	1.85	2.72	0.72	4.3	0.71
TiO_2	%	0.79	0.55	0.95	5	7.11	1.89	0.93	1	0.74	0.96	2.41	0.26
P_2O_5	%	0.11	0.09	1.5	1.9	2.05	4.8	0.05	0.43	0.33	0.31	1.33	0.23

[†]Note: When FeO content is shown in red it denotes that it has been calculated by multiplying the Fe_2O_3 content by 0.9.

[1]It was discovered on July 28th 2016 that Lieger, D., Riller, U., and Gibson, R.L. 2010 was withdrawn at the request of the author(s).

Morokweng

Analyte Symbol	Source	Andreoli et al. 1999								
	Analysis Method	Major and Trace elements V to Nb determined by XRF, U to Au determined by INAA								
	Rock Type	Medium Grained Quartz Norite						Vein	Medium Grained Quartz Norite	Heterogeneous Quartz Norite
	Unit Symbol	N-5	LA-137	N-4	LA-141	LA-161	N-3	V-170.3	LA-172	LA-174
SiO_2	%	64.65	64.27	65.42	64.14	65.78	64.38	12	64.63	67.33
Al_2O_3	%	13.24	13.18	13.38	13.17	12.77	13.03	1	13.03	13.37
Fe_2O_3(T)	%	1.23	3.01	1.17	2.61	3.16	1.17	18.4	3.15	3.12
FeO†	Calculated	4.42	2.78	4.22	3.07	2.36	4.21		2.14	1.51
MnO	%	0.09	0.08	0.09	0.1	0.07	0.09		0.08	0.03
MgO	%	4.05	3.71	3.93	3.92	3.15	4.04		3.58	2.36
CaO	%	3.49	3.38	3.38	3.31	3.25	3.36		3.16	2.9
Na_2O	%	3.88	4.39	3.86	4.65	3.97	3.58		4.04	4.28
K_2O	%	2.05	2.04	2.14	2.2	2.28	2.21		2.31	2.42
TiO_2	%	0.43	0.38	0.43	0.37	0.47	0.43		0.41	0.52
P_2O_5	%	0.12	0.09	0.1	0.05	0.08	0.12		0.11	0.09

†Note: When FeO content is shown in red it denotes that it has been calculated by multiplying the Fe_2O_3 content by 0.9.

[1]It was discovered on July 28th 2016 that Lieger, D., Riller, U., and Gibson, R.L. 2010 was withdrawn at the request of the author(s).

Analyte Symbol	Source	Andreoli et al. 1999 Continued							
	Analysis Method	Major and Trace elements V to Nb determined by XRF, U to Au determined by INAA							
	Rock Type	Heterogeneous Quartz Norite		Fine Grained Quartz Norite				Chilled Quartz Norite	Quartz Norite Mean
	Unit Symbol	N-2	LA-186	N-1	LA-197	LA-213	LA-216	LA-224	
SiO_2	%	62.84	64.24	59.32	59.93	60.68	64.27	61.99	63.59
Al_2O_3	%	14.1	13.74	13.43	13.18	13.28	12.86	13.3	13.27
Fe_2O_3(T)	%	1.32	3.21	1.8	4.55	4.12	3.58	4.36	2.77
FeO†	Calculated	4.75	2.55	6.46	3.59	3.25	2.17	2.46	3.35
MnO	%	0.09	0.07	0.14	0.11	0.1	0.07	0.08	0.09
MgO	%	3.81	3.15	4.88	4.7	4.5	3.86	3.68	3.82
CaO	%	4.23	3.95	5.26	5.12	4.24	3.16	3.87	3.74
Na_2O	%	4.02	4.55	3.5	3.91	4.4	4.44	3.91	4.09
K_2O	%	1.52	1.85	1.67	1.95	1.97	2.54	1.71	2.05
TiO_2	%	0.54	0.5	0.79	0.77	0.61	0.42	0.64	0.51
P_2O_5	%	0.11	0.09	0.16	0.14	0.09	0.1	0.12	0.1

†Note: When FeO content is shown in red it denotes that it has been calculated by multiplying the Fe_2O_3 content by 0.9.

[1]It was discovered on July 28th 2016 that Lieger, D., Riller, U., and Gibson, R.L. 2010 was withdrawn at the request of the author(s).

Appendix B-1-2: REE Comparison Tables and Plots

Vredefort

	My Samples							Koeberl, Reimold and Shirey 1996
	Anatectic Melt	ILG	Gabbro Norite					Witwatersrand Shale
Analyte Symbol	VO9-111	VO9-238	VO9-232	VO9-234	VO9-235	VO9-250	Average	VG-SNE
Y	4.72	0.38	18.07	15.52	15.00	21.18	17.44	4.53
Zr	44.96	2.61	27.24	17.35	13.43	38.43	24.11	4.48
Nb	35.27	4.18	40.05	24.51	25.11	41.25	32.73	6.28
La	118.18	27.34	59.56	41.07	36.68	51.41	47.18	46.71
Ce	77.68	12.44	47.07	35.37	31.22	44.63	39.57	27.93
Pr	52.48	7.69	40.33	32.56	28.26	42.23	35.85	0.00
Nd	33.82	4.50	36.59	31.06	27.15	40.33	33.78	22.44
Sm	15.15	1.75	28.85	25.35	22.75	34.10	27.76	16.95
Eu	11.91	11.30	22.76	22.11	21.32	28.29	23.62	11.32
Gd	8.99	1.01	24.83	22.36	20.90	30.04	24.53	10.15
Tb	6.90	0.81	24.14	21.50	20.69	29.01	23.83	9.53
Dy	5.88	0.48	22.06	19.15	18.36	26.27	21.46	8.79
Ho	5.03	0.40	19.21	16.56	16.03	22.65	18.61	0.00
Er	5.28	0.32	20.28	17.27	16.34	23.15	19.26	0.00
Tm	5.62	0.30	21.85	17.84	17.05	23.77	20.13	5.78
Yb	5.75	0.27	22.17	17.42	16.02	22.35	19.49	6.52
Pb	41.68	47.63	14.88	14.88	14.88	14.88	14.88	0.00
Th	322.63	8.00	10.00	10.25	6.00	7.25	8.38	25.26
U	85.33	3.63	9.08	7.26	4.54	14.52	8.85	56.28

Note: Data normalized to chondrite values from Anders & Grevesse (1989)[1] multiplied by 1.36 as per Korotev[26]
*Vredefort Granophyre data was provided by Peter Lightfoot.

Koeberl, Reimold and Shirey 1996									
	Ventersdorp Andesitic			OGG	Wits Siltstone clase in Granophyre	Vredefort Granophyre			
Analyte Symbol	UP-61	UP-63	Average	OT-1	BG-S1	BG-4	BG-7	BG-9	BG-10
Y	7.74	7.08	7.41	0.00	0.00	0.00	0.00	0.00	0.00
Zr	18.66	13.62	16.14	47.01	37.31	29.29	30.78	30.41	27.99
Nb	20.33	12.55	16.44	0.00	0.00	0.00	0.00	0.00	0.00
La	50.47	25.83	38.15	136.36	145.77	98.43	106.90	101.57	99.69
Ce	36.95	22.07	29.51	85.49	104.27	72.44	75.98	70.49	71.71
Pr	0.00	0.00	0.00	0.00	0.00	0.00	0.00	0.00	0.00
Nd	26.83	15.30	21.07	43.74	57.07	39.19	39.84	38.05	39.67
Sm	21.10	9.45	15.28	18.10	26.25	19.80	19.65	19.05	18.80
Eu	15.92	8.29	12.11	12.89	13.82	12.76	13.03	11.71	12.24
Gd	14.23	7.45	10.84	9.36	9.48	14.79	13.26	9.70	13.86
Tb	14.40	6.90	10.65	6.90	7.91	10.14	9.33	8.92	9.13
Dy	12.73	6.67	9.70	5.76	6.36	9.39	8.18	8.18	8.48
Ho	0.00	0.00	0.00	0.00	0.00	0.00	0.00	0.00	0.00
Er	0.00	0.00	0.00	0.00	0.00	0.00	0.00	0.00	0.00
Tm	8.81	6.38	7.60	3.95	4.26	6.69	6.69	6.38	6.99
Yb	7.15	6.02	6.58	3.30	3.71	6.15	5.79	5.61	5.66
Pb	0.00	0.00	0.00	0.00	0.00	0.00	0.00	0.00	0.00
Th	59.77	36.51	48.14	222.09	230.34	147.81	167.82	168.32	169.57
U	59.01	21.79	40.40	50.84	275.05	95.32	131.63	155.23	128.90

Note: Data normalized to chondrite values from Anders & Grevesse (1989)[1] multiplied by 1.36 as per Korotev[26]
*Vredefort Granophyre data was provided by Peter Lightfoot.

			Peter Lightfoot's Granophyre Samples						Reimold & Gibson 2006
			Vredefort Granophyre						Vredefort Granophyre
Analyte Symbol	BG-168	Average	372905A	372906A	372906B	372907A	372907B	Average	Granophyre with outliers
Y	0.00	0.00	6.18	7.83	7.64	7.64	7.50	7.36	7.97
Zr	26.12	28.92	28.84	29.66	29.29	30.65	29.55	29.60	27.37
Nb	0.00	0.00	23.61	25.71	24.81	25.41	24.51	24.81	21.40
La	90.60	99.44	95.61	125.71	121.32	126.02	120.69	117.87	102.38
Ce	62.56	70.63	70.73	87.80	85.37	89.02	87.80	84.15	63.24
Pr	0.00	0.00	52.07	54.55	53.72	56.20	51.24	53.55	
Nd	33.66	38.08	34.63	40.16	38.21	38.21	38.86	38.02	37.72
Sm	17.95	19.05	19.50	21.50	20.00	22.00	18.50	20.30	20.85
Eu	10.92	12.13	10.53	14.47	11.84	10.53	11.84	11.84	11.58
Gd	11.99	12.72	11.24	11.99	11.61	11.61	12.36	11.76	
Tb	8.72	9.25	8.11	8.11	10.14	10.14	10.14	9.33	10.34
Dy	7.88	8.42	8.79	8.18	9.09	7.88	7.58	8.30	8.42
Ho	0.00	0.00	6.62	6.62	6.62	6.62	6.62	6.62	
Er	0.00	0.00	6.94	6.02	6.48	6.94	6.48	6.57	
Tm	6.08	6.57	6.08	6.08	6.08	6.08	6.08	6.08	6.69
Yb	6.11	5.86	6.33	5.88	6.33	6.79	5.88	6.24	5.34
Pb	0.00	0.00	86.33	80.38	77.40	83.35	71.45	79.78	
Th	159.06	162.52	165.07	167.57	160.06	157.56	160.06	162.06	159.81
U	147.97	131.81	118.01	108.93	108.93	108.93	108.93	110.75	128.90

Note: Data normalized to chondrite values from Anders & Grevesse (1989)[1] multiplied by 1.36 as per Korotev[26]
*Vredefort Granophyre data was provided by Peter Lightfoot.

	Crow and Condie 1988						
	Porphyritic lava	Basaltic Andesite	Felsic Porphyritic Lava	Porphyritic Basaltic Andesite	Basalt	Basalt	
Analyte Symbol	Pniel Group Allanridge	Platberg Group Reitgat	Platberg Group Makwassie	Platberg Group Goedgenoeg	Platberg Group Average	Klipriviersberg Group Edenville	Klipriviersberg Group Loraine
Y	10.85	23.11	25.47	21.70	23.43	5.66	7.08
Zr	34.14	67.35	61.38	60.82	63.18	11.01	14.74
Nb	32.88	53.80	71.74	47.82	57.79	8.07	9.86
La	81.50	197.49	260.19	175.55	211.08	17.24	26.65
Ce	71.95	169.51	217.07	157.32	181.30	14.63	23.17
Pr							
Nd							
Sm	30.50	65.00	65.00	63.00	64.33	7.50	11.50
Eu	23.42	40.79	28.03	39.87	36.23	6.05	9.61
Gd							
Tb	17.04	32.86	32.25	30.02	31.71	6.09	8.52
Dy							
Ho							
Er							
Tm							
Yb	9.41	19.14	22.85	19.00	20.33	5.11	6.52
Pb	32.75	41.68	56.56	32.75	43.66	29.77	32.75
Th	82.53	60.02	252.60	50.02	120.88	20.01	32.51
U	81.70	45.39	163.40	36.31	81.70	27.23	45.39

Note: Data normalized to chondrite values from Anders & Grevesse (1989)[1] multiplied by 1.36 as per Korotev[26]
*Vredefort Granophyre data was provided by Peter Lightfoot.

	Crow and Condie 1988				Wronkiewicz and Condie 1990		
	Basalt				Pelites & Shales		
Analyte Symbol	Klipriviersberg Group Jeannette	Klipriviersberg Group Orkney	Klipriviersberg Group Westonaria	Klipriviersberg Average	Average Bothaville Formation P&S	Average Selati Formation P&S	Average Black Reef Formation P&S
Y	9.43	8.96	7.08	7.64	12.74	15.09	14.15
Zr	19.96	20.90	17.72	16.87	23.13	33.21	29.29
Nb	13.45	14.35	0.00	9.15	17.93	29.89	23.31
La	34.48	37.62	25.39	28.28	119.12	59.56	90.91
Ce	29.27	32.93	23.17	24.63	92.68	48.78	69.51
Pr							
Nd							
Sm	15.50	16.50	14.00	13.00	23.00	19.00	26.00
Eu	12.37	13.03	11.58	10.53	10.66	12.76	15.79
Gd							
Tb	10.55	11.16	9.53	9.17	10.34	11.56	13.59
Dy							
Ho							
Er							
Tm							
Yb	7.10	7.06	4.84	6.13	9.05	11.31	10.86
Pb	32.75	29.77		31.26	80.38	26.79	44.65
Th	45.02	45.02	35.01	35.51	155.06	142.56	140.06
U	72.62	72.62		54.47	154.32	190.63	190.63

Note: Data normalized to chondrite values from Anders & Grevesse (1989)[1] multiplied by 1.36 as per Korotev[26]
*Vredefort Granophyre data was provided by Peter Lightfoot.

	Wronkiewicz and Condie 1990							
	Pelites & Shales				Quartzite	Quartzite	Quartzite	Quartzite
Analyte Symbol	Average Timeball Hill Formation P&S	Average Strubenkop Formation P&S	Average Silverton Formation P&S	NASC P&S	Bothaville Formation Quartzite C6	Sekororo Formation Quartzite D53	Sekororo Formation Quartzite D36	Sekororo Formation Quartzite D47
Y	15.09	16.98	13.68	16.51	2.41	0.94	3.25	3.11
Zr	31.72	43.66	27.99	37.31	11.01	7.65	9.33	13.25
Nb	44.84	53.80	38.86	38.86	15.24	9.56	11.96	12.25
La	175.55	153.61	112.85	97.18	34.48	15.99	37.62	23.51
Ce	123.17	129.27	68.29	81.71	18.29	11.59	29.27	18.29
Pr								
Nd								
Sm	37.50	38.00	27.00	28.00	7.00	5.00	12.00	7.50
Eu	19.74	21.05	14.47	15.79	4.74	2.37	5.79	4.08
Gd								
Tb	22.31	20.28	16.02	17.24	3.25	1.62	4.26	3.85
Dy								
Ho								
Er								
Tm								
Yb	14.03	15.84	11.31	14.03	2.53	1.04	4.03	2.44
Pb	101.21	59.54	62.51	0.00	53.58	29.47	35.72	25.30
Th	550.22	500.20	400.16	300.12	70.03	21.01	30.01	40.02
U	653.59	544.66	354.03	245.10	208.79	39.03	13.62	39.94

Note: Data normalized to chondrite values from Anders & Grevesse (1989)[1] multiplied by 1.36 as per Korotev[26]
*Vredefort Granophyre data was provided by Peter Lightfoot.

	Wronkiewicz and Condie 1990							
	Quartzite	Quartzite	Quartzite	Quartzite		Quartzite	Quartzite	Quartzite
Analyte Symbol	Average Sekororo Formation Quartzite D47	Selati Formation Quartzite D35	Black Reef Quartzite D34	Black Reef Quartzite C201	Average Black Reef Quartzite C201	Rooihoogte Formation Quartzite C76	Daspoort Formation Quartzite C81	Daspoort Formation Quartzite M8F-2-10
Y	3.18	7.55	2.12	0.52	1.32	1.13	1.65	2.03
Zr	11.29	21.64	8.77	7.28	8.02	6.34	11.38	10.07
Nb	12.11	13.75	10.16	11.06	10.61	14.35	11.06	10.76
La	30.56	27.59	14.42	23.51	18.97	8.46	23.82	28.84
Ce	23.78	24.39	11.59	17.07	14.33	6.46	14.63	21.95
Pr								
Nd								
Sm	9.75	9.00	4.60	4.80	4.70	2.00	3.30	5.00
Eu	4.93	8.16	2.37	2.76	2.57	1.32	1.84	3.16
Gd								
Tb	4.06	7.30	1.01	1.22	1.12	0.61	1.42	2.84
Dy								
Ho								
Er								
Tm								
Yb	3.24	7.24	1.63	1.18	1.40	1.54	2.04	2.53
Pb	30.51	65.49	523.93	32.75	278.34	41.68	23.82	101.21
Th	35.01	97.54	25.01	32.51	28.76	85.03	50.02	232.59
U	26.78	127.09	57.19	37.22	47.20	136.17	83.51	354.03

Note: Data normalized to chondrite values from Anders & Grevesse (1989)[1] multiplied by 1.36 as per Korotev[26]
*Vredefort Granophyre data was provided by Peter Lightfoot.

	Wronkiewicz and Condie 1990 Continued					Lana et al. 2004		
		Quartzite	Quartzite		Quartzite	Gneiss (amphibolite facies) Trondhjemite NE-Part		
Analyte Symbol	Average Daspoort Formation Quartzite	Magaliesberg Formation Quartzite C207	Magaliesberg Formation Quartzite D77	Average Magaliesberg Formation Quartzite D77	Rayton Formation Quartzite C56	ABBG-3	ABG-2	ABP-1
Y	1.84	1.70	14.62	8.16	0.61			
Zr	10.73	10.45	56.34	33.40	9.33	56.90	70.90	36.38
Nb	10.91	9.56	32.88	21.22	9.86			
La	26.33	27.90	94.04	60.97	9.09	155.49	224.14	146.71
Ce	18.29	20.73	54.88	37.80	6.46	114.88	156.10	100.61
Pr								
Nd						63.25	79.35	49.92
Sm	4.15	6.00	27.00	16.50	2.15	29.10	28.05	17.40
Eu	2.50	3.42	15.79	9.61	1.18	17.76	17.37	12.89
Gd						17.00	17.87	8.24
Tb	2.13	2.64	16.84	9.74	1.22	14.20	11.76	4.67
Dy								
Ho								
Er								
Tm						8.21	6.99	1.98
Yb	2.29	1.49	10.86	6.18	0.95	5.61	5.93	1.63
Pb	62.51	23.82	101.21	62.51	32.75			
Th	141.31	67.53	375.15	221.34	50.02	230.59	442.68	139.81
U	218.77	99.85	290.49	195.17	69.90	131.63	49.93	62.64

Note: Data normalized to chondrite values from Anders & Grevesse (1989)[1] multiplied by 1.36 as per Korotev[26]
*Vredefort Granophyre data was provided by Peter Lightfoot.

	Lana et al. 2004 Continued								
	Gneiss (amphibolite facies) Trondhjemite NE-Part	Melanosomes Trondhjemite Outer Parts				Leucosomes Granite			
Analyte Symbol	Average	BEG-2	SAG-2	VAL-1	Average	EG-8	RG11	RG7	Pr12
Y									
Zr	54.73	47.57	43.84	43.84	45.09	20.71	25.93	20.15	19.22
Nb									
La	175.44	186.52	131.97	140.75	153.08	87.77	68.97	115.99	210.03
Ce	123.86	141.46	89.39	99.51	110.12	67.07	53.66	91.46	97.56
Pr									
Nd	64.17	77.72	51.38	50.08	59.73	29.27	26.02	39.02	32.52
Sm	24.85	34.40	20.55	19.15	24.70	14.00	16.50	13.00	14.00
Eu	16.01	20.39	12.11	12.50	15.00	17.89	21.97	19.21	14.34
Gd	14.37	21.99	17.60	10.86	16.82	7.45	6.03	7.08	4.98
Tb	10.21	16.84	11.16	5.48	11.16	5.27	3.65	4.06	6.29
Dy									
Ho									
Er									
Tm	5.72	8.81	8.51	3.65	6.99	2.74	1.82	1.52	1.82
Yb	4.39	6.56	7.33	29.95	14.62	2.67	1.72	1.72	1.99
Pb									
Th	271.03	234.84	248.85	235.34	239.68	73.28	43.52	61.52	53.02
U	81.40	95.32	77.16	38.13	70.20	27.23	31.77	36.31	36.31

Note: Data normalized to chondrite values from Anders & Grevesse (1989)[1] multiplied by 1.36 as per Korotev[26]
*Vredefort Granophyre data was provided by Peter Lightfoot.

	Lana et al. 2004 Continued								
	Leucosomes Granite				Schlieric Granite Northern Parts			Homogen Granite	Porphyritic grano-diorite
Analyte Symbol	SALP-1	EG-4	EG-7	Average	SPW-2	SPW-3	Average	ESP-1	POR-1
Y									
Zr	24.25	39.18	20.15	24.23	73.69	35.45	54.57	45.71	55.97
Nb									
La	105.33	87.77	203.76	125.66	105.96	71.79	88.87	130.09	215.05
Ce	77.80	76.83	150.00	87.77	72.32	52.32	62.32	105.98	158.54
Pr									
Nd	45.37	42.28	55.28	38.54	40.49	32.68	36.59	64.55	86.34
Sm	21.05	30.00	30.00	19.79	12.70	17.75	15.23	30.40	34.05
Eu	10.92	22.37	16.58	17.61	12.89	9.61	11.25	6.97	20.26
Gd	18.84	18.73	14.98	11.16	7.94	15.92	11.93	16.22	18.16
Tb	16.63	15.01	9.74	8.66	4.26	15.21	9.74	13.79	12.37
Dy									
Ho									
Er									
Tm	11.25	9.12	5.17	4.78	3.34	10.94	7.14	9.73	5.78
Yb	10.00	7.92	5.25	4.47	2.76	10.45	6.61	8.51	4.12
Pb									
Th	307.62	50.02	87.54	96.65	15456.18	213.84	7835.01	587.74	233.34
U	113.47	29.96	26.33	43.05	61.73	37.22	49.47	1062.09	32.68

Note: Data normalized to chondrite values from Anders & Grevesse (1989)[1] multiplied by 1.36 as per Korotev[26]
*Vredefort Granophyre data was provided by Peter Lightfoot.

	Lana et al. 2004 Continued								
	Gneiss Quartz Diorite	Mag. Rich Granod.	Leucosomes ederbite					Leucosomes Felsic enderbite	
Analyte Symbol	SCH-2	GRAD3	LEG-3	Strip1	Strip2	Strip3	Strip4	Average	LEW-1	vdf2-6
Y										
Zr	644.59	64.37	39.93	57.46	38.99	48.51	38.25	44.63	37.31	30.78
Nb										
La	630.09	250.78	196.24	113.48	106.27	172.10	166.14	150.85	126.96	206.58
Ce	430.49	176.83	136.59	66.10	69.51	115.37	107.80	99.07	72.44	134.15
Pr										
Nd	227.64	96.26	59.84	26.83	31.06	46.99	47.80	42.50	30.73	56.91
Sm	93.00	34.40	17.40	11.00	13.60	20.40	19.00	16.28	6.55	22.05
Eu	58.03	23.55	17.89	13.82	12.24	13.42	17.76	15.03	14.21	17.37
Gd	75.28	16.78	8.35	2.43	4.79	14.42	12.36	8.47	3.37	12.25
Tb	38.34	11.36	5.48	2.43	4.46	7.10	6.90	5.27	1.40	4.06
Dy										
Ho										
Er										
Tm	18.54	4.56	2.95	1.82	2.13	3.04	3.65	2.72	1.03	1.82
Yb	10.68	3.39	1.99	1.76	2.62	2.76	3.53	2.53	0.95	1.00
Pb										
Th	492.70	149.31	110.54	270.11	67.53	206.33	198.83	170.67	75.53	177.07
U	72.62	13.62	34.50	42.67	15.43	33.59	27.23	30.68	14.52	45.39

Note: Data normalized to chondrite values from Anders & Grevesse (1989)[1] multiplied by 1.36 as per Korotev[26]
*Vredefort Granophyre data was provided by Peter Lightfoot.

	Lana et al. 2004 Continued									
	Leucosomes Felsic enderbite		Leucosomes Charnockite							
Analyte Symbol	vdf12	Average	vdf2-4	vdf11	vdf13	vdf19	vdf2-24	vdf24	vdf5	vdf7
Y										
Zr	39.37	35.82	21.08	36.94	10.97	27.61	36.01	31.16	27.99	31.16
Nb										
La	95.61	143.05	109.72	187.15	116.30	126.02	200.63	71.16	62.38	96.24
Ce	66.95	91.18	66.95	121.83	65.98	62.20	116.46	39.27	35.85	55.12
Pr										
Nd	24.72	37.45	24.72	52.85	27.97	24.55	57.72	16.91	14.31	21.95
Sm	14.50	14.37	14.50	16.55	10.65	12.65	17.50	5.65	4.00	8.00
Eu	15.13	15.57	15.13	14.87	17.76	11.58	26.71	11.84	14.47	14.87
Gd	2.81	6.14	2.81	5.99	4.49	5.06	10.86	3.00	1.69	4.87
Tb	1.62	2.36	1.62	3.65	2.64	5.07	8.92	1.22	1.01	2.84
Dy										
Ho										
Er										
Tm	1.22	1.36	1.22	2.43	1.52	2.74	4.56	1.52	0.91	2.28
Yb	1.99	1.31	1.99	1.40	0.50	2.85	3.98	1.18	0.86	2.04
Pb										
Th	176.82	143.14	137.05	365.15	123.55	164.32	1.75	177.07	56.27	230.34
U	49.93	36.61	33.59	44.48	27.23	26.33	36.31	45.39	88.05	72.62

Note: Data normalized to chondrite values from Anders & Grevesse (1989)[1] multiplied by 1.36 as per Korotev[26]
*Vredefort Granophyre data was provided by Peter Lightfoot.

	Lana et al. 2004 Continued						Hart et al 1990	Remiold et al. 2000		
	Leucosomes Charnockite	Melanosomes tonalite				K-feldspar-rich Granite	Ultra-mafics	Anne Rust Sheet		
Analyte Symbol	Average	Vdf8	Vdf4	Vdf1	Average	LEP-1	Avg. Beta -1	WS2-228	UP-16	GP-5
Y										
Zr	27.86	35.63	41.42	25.19	34.08	28.36		30.78	42.91	22.39
Nb										
La	121.20	156.74	167.40	157.68	160.61	91.22	4.83	48.59	34.80	32.29
Ce	70.46	115.24	145.00	104.15	121.46	57.07	6.77	41.10	24.88	30.98
Pr										
Nd	30.12	156.42	92.20	78.86	109.16	25.53	5.56	32.20	21.79	23.74
Sm	11.19	48.00	53.00	46.50	49.17	8.70	3.90	23.55	16.75	16.75
Eu	15.90	28.95	32.89	32.89	31.58	12.76	4.87	21.18	17.24	16.18
Gd	4.85	35.58	40.07	19.85	31.84	4.19		19.10	14.61	16.48
Tb	3.37	23.12	24.34	5.48	17.65	3.04	5.88	17.85	13.79	17.65
Dy								17.27	13.33	16.06
Ho										
Er										
Tm	2.15	12.16	10.33	11.25	11.25	1.46		15.81	11.85	13.98
Yb	1.85	9.95	12.22	13.67	11.95	1.31	1.58	15.43	11.81	11.81
Pb										
Th	156.94	98.54	131.55	84.53	104.88	53.02	0.00	94.54	66.03	68.03
U	46.75	63.54	163.40	53.56	93.50	28.14	0.00	71.71	25.42	93.50

Note: Data normalized to chondrite values from Anders & Grevesse (1989)[1] multiplied by 1.36 as per Korotev[26]
*Vredefort Granophyre data was provided by Peter Lightfoot.

	Remiold et al. 2000						Coetzee et al. 2006		
	Anne Rust Sheet						Tholeiitic Intrusions		
Analyte Symbol	IS-225	SH1-475	UP-71	USA59	UP-65	UP-68	Wittekopjes norite	Parsons Rust Dol-Norite	Reebokkop dolerite
Y							3.11	5.19	6.60
Zr	11.19	32.65	47.57	10.26	19.22	21.46	5.97	8.40	12.50
Nb							9.86	14.95	17.93
La	39.81	41.38	51.72	45.45	36.99	40.44	8.40	10.85	24.86
Ce	36.71	38.54	43.05	44.02	27.93	36.22	7.00	9.21	20.37
Pr							5.70	7.85	16.61
Nd	28.78	29.11	32.03	35.12	24.55	27.80	4.76	6.83	13.51
Sm	20.15	21.35	24.65	21.75	17.90	19.70	3.60	5.45	9.45
Eu	18.55	19.08	22.50	18.68	17.76	17.76	3.16	5.00	8.42
Gd	17.23	19.10	21.72	19.48	17.60	16.48	3.07	4.76	7.53
Tb	15.42	16.43	21.10	18.86	15.82	16.63	2.84	4.46	6.69
Dy	14.85	15.45	20.61	16.06	13.33	15.45	3.03	4.42	6.36
Ho							2.91	4.11	5.83
Er							3.15	4.35	6.06
Tm	13.68	13.98	18.84	14.89	11.25	13.37	3.04	3.95	5.78
Yb	14.16	14.21	18.42	13.98	11.63	12.40	3.12	4.07	5.66
Pb									
Th	77.03	86.03	13.26	85.53	66.03	70.28			
U	55.37	62.64	49.02	44.48	58.10	45.39			

Note: Data normalized to chondrite values from Anders & Grevesse (1989)[1] multiplied by 1.36 as per Korotev[26]
*Vredefort Granophyre data was provided by Peter Lightfoot.

	de Waal, Graham and Armstrong 2006						
	Lindeques drift and Heidelberg Intrusions						
Analyte Symbol	Lindeques Drift Even-grained spessartite mean	Lindeques Drift Porphyritic spessartite mean	Heidelberg Porphy-ritic spess mean	Lindeques Drift Low-silica diorite mean	Lindeques Drift diorite mean	Lindeques Drift syeno-diorite mean	Roodekraal Complex Lava
Y	7.08	8.30	11.46	9.15	9.06	8.58	7.08
Zr	11.42	13.90	14.51	17.35	27.24	24.78	26.12
Nb	26.30	20.62	70.84	42.14	23.61	18.83	56.79
La	11.91	34.80	104.08	40.13	53.92	57.68	84.64
Ce	11.34	30.00	81.83	32.80	43.78	47.93	62.23
Pr	11.57	27.27	64.46	28.93	36.36	37.19	47.36
Nd	11.22	24.07	51.38	24.23	29.59	29.43	34.93
Sm	9.00	16.50	29.50	16.00	19.00	17.50	18.75
Eu	7.89	13.16	25.00	14.47	15.79	18.42	13.95
Gd	7.49	12.73	20.97	12.73	13.11	11.24	12.73
Tb	6.09	10.14	14.20	10.14	12.17	10.14	9.74
Dy	5.76	9.09	12.12	9.39	10.00	8.48	8.79
Ho	5.30	7.95	10.60	7.95	9.27	7.95	7.55
Er	4.63	7.41	8.80	8.33	9.26	7.41	7.41
Tm	3.04	6.08	6.08	9.12	9.12	6.08	6.69
Yb	4.07	6.33	6.33	7.24	8.14	6.79	6.38
Pb	13.69	17.56	30.66	14.88	2.98	2.98	23.82
Th	55.02	55.02	125.05	130.05	125.05	125.05	225.09
U	136.17	163.40		290.49	272.33	272.33	272.33

Note: Data normalized to chondrite values from Anders & Grevesse (1989)[1] multiplied by 1.36 as per Korotev[26]
*Vredefort Granophyre data was provided by Peter Lightfoot.

	de Waal, Graham and Armstrong 2006		Wilson and Chunnett 2006				
	Lindeques drift and Heidelberg Intrusions		Bushveld Complex				
Analyte Symbol	Roodekraal Complex Cumulate	Roodekraal Complex Diorite	GC1	SD22 D3	SD22 D5	SD45	SD46
Y	1.89	9.91					
Zr	6.53	17.91	1.15	1.14	1.11	2.59	3.06
Nb	50.81	50.81	0.61	0.70	1.03	3.21	3.49
La	52.98	69.28	6.20	4.74	4.66	8.65	12.12
Ce	41.22	55.85	5.02	3.78	3.74	7.34	9.61
Pr	32.23	46.28	4.12	3.28	3.28	5.68	7.73
Nd	24.72	37.07	3.26	2.66	2.71	4.16	5.70
Sm	14.50	21.50	2.34	2.02	2.06	2.79	3.76
Eu	10.53	18.42	2.89	2.71	2.48	2.08	2.93
Gd	10.11	14.23	1.96	1.67	1.76	2.35	3.14
Tb	8.11	10.14	1.80	1.65	1.75	2.00	2.57
Dy	6.97	9.70	1.76	1.66	1.77	1.93	2.36
Ho	6.62	7.95	1.72	1.64	1.77	1.87	2.19
Er	5.56	8.33	1.77	1.71	1.84	1.95	2.20
Tm	6.08	6.08	1.94	1.90	2.08	2.15	2.31
Yb	4.98	6.79	1.94	1.90	2.08	2.16	2.23
Pb	53.58	17.86					
Th	75.03	75.03	2.87	3.98	3.63	13.92	18.13
U	272.33	272.33	3.47	4.95	4.48	16.35	19.62

Note: Data normalized to chondrite values from Anders & Grevesse (1989)[1] multiplied by 1.36 as per Korotev[26]
*Vredefort Granophyre data was provided by Peter Lightfoot.

Sudbury

	Lightfoot et al. 1996								
								Little Stobie Mine Igneous Textured Sublayer Matrix	
Analyte Symbol	Main Mass Mafic Norite Average	Main Mass Felsic Norite Average	Main Mass Granophyre Average	Igneous textured sublayer matrix Whistle Mine Average	Melanorite Pod or Inclusion Whistle Mine Average	Olivine Melanorite Whistle Mine Average	Diabase Whistle Mine Average	93PCL-001	93PCL-001
Y	7.17	7.78	15.33	7.59	7.17	5.90	10.52	7.83	12.12
Zr	21.08	25.00	50.56	16.42	19.03	17.35	15.86	16.60	20.15
Nb	19.25	22.42	46.78	10.91	13.06	15.12	12.14	18.14	21.85
La	85.02	95.92	176.43	56.83	67.87	59.62	40.13	63.04	64.95
Ce	67.17	73.90	136.01	49.21	59.94	52.66	34.77	49.80	53.59
Pr	50.74	60.25	112.15	44.38	52.81	46.20	30.99	40.66	46.12
Nd	37.22	42.28	80.50	35.32	41.77	35.84	25.53	30.89	37.20
Sm	20.65	24.50	45.15	23.20	26.35	22.75	18.95	19.05	24.70
Eu	14.21	18.42	23.95	17.76	16.97	14.47	16.32	17.24	20.39
Gd	6.93	16.82	28.46	15.66	16.82	14.57	15.24	14.01	19.03
Tb	42.80	12.78	22.92	12.37	12.58	11.16	13.59	11.16	16.02
Dy									
Ho	7.81	9.27	16.42	9.01	8.61	7.02	11.92	8.74	13.38
Er	7.50	8.70	15.65	8.47	8.15	6.06	11.53	8.38	12.87
Tm	7.60	8.81	15.20	8.21	7.60	5.78	11.25	8.51	13.37
Yb	7.29	8.24	14.25	7.69	7.24	5.25	10.59	8.42	12.81
Pb									
Th	154.81	172.57	372.65	48.77	62.02	68.03	43.52	36.01	44.27
U	112.56	136.17	295.93	34.50	42.67	50.84	34.50	27.23	40.85

Note: Data normalized to chondrite values from Anders & Grevesse (1989)[1] multiplied by 1.36 as per Korotev[26]
*Vredefort Granophyre data was provided by Peter Lightfoot.

	Lightfoot et al. 1996 Continued								
	Crean Hill Mine Igneous Textured Sublayer Matrix				Levack West Mine Igneous Textured Sublayer Matrix		Levack West Mine Melanorite Pod or Inclusion		
Analyte Symbol	93PCL-20	93PCL-22	93PCL-23	93PCL-25	93PCL-45	93PCL-46	93PCL-66	93PCL-67	93PCL-68
Y	10.05	11.56	10.75	9.72	7.26	2.88	3.54	4.86	4.86
Zr	22.95	25.00	25.56	23.69	22.20	13.06	13.43	10.26	13.43
Nb	26.21	28.49	31.32	24.39	18.05	5.95	5.50	5.65	7.14
La	76.46	74.45	77.37	74.55	80.44	33.51	35.96	32.23	32.07
Ce	61.84	64.72	62.54	60.29	63.23	26.34	29.99	30.24	31.13
Pr	50.66	56.78	52.07	50.00	50.00	21.16	25.54	27.85	28.68
Nd	37.35	44.24	38.52	36.70	35.97	15.37	19.33	22.91	23.12
Sm	24.45	28.50	25.20	23.20	20.70	9.50	11.80	16.00	16.75
Eu	17.50	19.61	21.05	17.76	14.47	7.50	9.21	10.79	10.53
Gd	16.52	20.00	17.87	16.89	13.71	6.10	7.38	10.82	10.90
Tb	14.20	16.63	15.21	13.79	10.75	4.46	5.88	7.71	8.52
Dy									
Ho	11.39	13.38	12.19	11.26	7.95	3.05	3.97	5.30	5.43
Er	10.97	12.41	11.25	10.69	7.50	2.59	3.52	4.54	4.49
Tm	11.25	12.77	12.16	10.64	7.29	2.43	3.65	3.95	3.95
Yb	10.41	11.72	11.45	10.27	7.10	2.44	3.53	3.89	3.89
Pb									
Th	138.31	71.78	95.29	92.79	142.56	30.01	22.26	76.53	112.29
U	133.44	76.25	91.68	78.07	108.02	21.79	15.43	23.60	29.96

Note: Data normalized to chondrite values from Anders & Grevesse (1989)[1] multiplied by 1.36 as per Korotev[26]
*Vredefort Granophyre data was provided by Peter Lightfoot.

	Lightfoot et al. 1996 Continued									
	McCreedy West Mine Igneous Textured Sublayer Matrix					Fraser Mine Igneous Textured Sublayer Matrix				
Analyte Symbol	93PCL-50	93PCL-51	93PCL-53	93PCL-55	93PCL-59	93PCL-342	93PCL-343	93PCL-344	92PCL-345	93PCL-346
Y	5.66	6.79	7.41	4.81	4.15	7.41	6.98	7.12	6.65	6.98
Zr	22.20	16.60	25.37	11.75	12.69	23.32	20.34	21.46	19.03	19.96
Nb	14.35	16.44	21.85	6.25	8.37	22.15	18.14	17.64	16.92	18.23
La	74.73	71.50	87.40	45.99	46.08	69.66	70.31	69.40	70.41	78.90
Ce	61.12	55.29	69.90	37.17	36.49	58.10	56.62	56.33	57.44	62.67
Pr	49.42	44.05	57.36	31.24	29.83	45.70	44.79	44.79	44.38	49.50
Nd	36.70	31.76	41.53	23.93	21.82	34.55	31.87	31.85	32.44	35.15
Sm	20.05	17.60	23.30	14.60	13.00	20.75	18.65	18.40	18.85	20.40
Eu	13.03	13.29	15.26	12.63	11.84	14.21	13.55	14.08	12.37	12.89
Gd	12.85	12.25	14.72	9.48	8.28	13.22	11.84	12.10	11.50	12.92
Tb	9.74	9.94	11.36	7.10	6.49	10.75	9.94	9.94	9.13	10.14
Dy										
Ho	6.09	7.42	7.81	5.17	4.50	8.08	7.55	7.81	6.89	7.81
Er	5.42	7.04	7.13	4.58	4.31	7.87	7.22	7.45	6.67	7.50
Tm	5.47	6.69	6.99	4.86	4.26	7.29	7.29	7.29	6.69	7.29
Yb	5.29	6.88	6.79	4.66	4.07	7.10	6.83	7.10	6.83	6.92
Pb										
Th	74.78	105.29	141.81	20.76	34.76	139.31	135.80	127.05	115.80	134.80
U	39.94	78.98	96.22	13.62	27.23	95.32	113.47	98.95	88.96	104.39

Note: Data normalized to chondrite values from Anders & Grevesse (1989)[1] multiplied by 1.36 as per Korotev[26]
*Vredefort Granophyre data was provided by Peter Lightfoot.

	Lightfoot et al. 1996 Continued			Lightfoot et al. 2001				
	Creighton Mine Igneous Textured Sublayer Matrix			Mafic Norite		Felsic Norite		
Analyte Symbol	94PCL-128	94PCL-131	94PCL-132	94PCL2011	94PCL2016	94PCL2066	94PCL2072	94PCL2076
Y	10.14	5.90	10.42	6.23	6.70	6.65	6.04	5.47
Zr	30.60	22.20	19.03					
Nb	31.32	19.85	29.95	15.00	15.45	18.77	18.86	16.29
La	68.97	65.24	73.73	62.48	74.26	81.32	74.42	69.12
Ce	56.22	52.90	61.18	49.95	61.48	64.88	58.87	54.55
Pr	49.01	45.12	54.38	37.60	45.21	47.85	44.30	39.75
Nd	37.71	34.55	42.83	29.25	34.03	36.18	33.04	29.89
Sm	23.75	21.00	26.65	17.00	18.65	20.00	18.75	16.45
Eu	15.26	14.21	17.76	11.97	12.76	16.32	15.00	15.26
Gd	16.67	14.98	18.76	1.42	1.72	1.80	1.65	1.46
Tb	13.39	12.78	15.21	57.00	63.49	65.92	62.07	55.78
Dy				7.09	7.67	8.27	7.64	7.09
Ho	10.86	10.46	11.66	6.62	7.42	7.28	7.02	6.36
Er	11.30	10.88	11.76	6.90	6.90	7.45	6.90	6.48
Tm	10.94	10.64	11.25	6.38	7.29	6.69	6.69	5.78
Yb	10.63	10.36	10.68	6.06	7.15	6.79	6.65	6.06
Pb								
Th	99.04	116.30	77.28	127.30	129.05	179.32	147.06	133.30
U	77.16	97.13	60.82	97.13	62.64	92.59	120.73	113.47

Note: Data normalized to chondrite values from Anders & Grevesse (1989)[1] multiplied by 1.36 as per Korotev[26]
*Vredefort Granophyre data was provided by Peter Lightfoot.

	Lightfoot et al. 2001 Continued							
	Felsic Norite			Quartz Gabbro				Granophyre
Analyte Symbol	94PCL2033	94PCL2028	94PCL2013	94PCL2080	93PCL290	94PCL2052	94PCL2079	93PCL336
Y	5.85	5.90	6.23	7.31	14.86	8.49	7.55	14.29
Zr								
Nb	17.52	16.65	16.23	19.37	51.74	22.87	18.59	42.74
La	70.41	68.81	69.56	80.03	165.52	95.77	79.56	166.36
Ce	55.06	54.99	55.23	64.72	127.72	76.96	62.61	131.65
Pr	40.58	40.33	41.24	48.18	111.24	58.68	47.44	104.38
Nd	30.68	30.00	30.78	37.15	81.12	45.30	36.08	77.02
Sm	17.05	16.85	17.40	20.95	46.90	24.80	20.55	42.90
Eu	15.53	13.55	13.68	15.92	30.53	18.68	16.71	24.21
Gd	1.50	1.54	1.65	2.06	4.34	2.28	2.06	3.97
Tb	56.19	56.80	56.39	74.04	158.01	89.45	75.25	148.88
Dy	7.30	7.27	7.18	9.70	18.39	10.64	9.15	17.58
Ho	6.62	6.75	6.49	8.08	16.56	9.01	8.34	15.89
Er	6.71	6.34	6.34	7.96	15.56	9.03	8.01	14.58
Tm	6.99	6.38	6.38	7.90	15.20	8.81	7.90	13.98
Yb	5.93	5.88	6.43	7.38	13.89	8.73	7.65	13.17
Pb								
Th	136.05	133.05	124.30	161.06	306.12	165.32	146.06	336.38
U	106.21	109.84	93.50	133.44	230.57	141.61	111.66	280.50

Note: Data normalized to chondrite values from Anders & Grevesse (1989)[1] multiplied by 1.36 as per Korotev[26]
*Vredefort Granophyre data was provided by Peter Lightfoot.

	Lightfoot et al. 2001 Continued								
	Granophyre								
Analyte Symbol	93PCL 293	93PCL 297	93PCL 312	93PCL 334	Mafic Norite Average	Felsic Norite Average	Quartz Gabbro Average	Granophyre Average	Main Mass Average
Y	16.13	15.47	15.42	14.67	6.13	6.08	11.04	15.38	10.57
Zr					14.93	20.52	33.21	50.93	34.33
Nb	49.32	49.77	47.70	42.06	14.95	17.93	30.49	47.53	31.38
La	191.07	182.41	178.87	174.36	68.97	75.24	119.12	175.55	122.26
Ce	143.37	137.54	140.21	135.12	56.10	58.54	97.56	135.37	95.12
Pr	121.40	113.64	115.87	109.42	41.32	43.80	76.86	112.40	76.03
Nd	85.79	81.28	82.99	79.38	30.89	32.52	58.54	81.30	55.28
Sm	47.70	46.25	47.20	43.40	17.00	18.00	33.50	45.00	31.00
Eu	25.66	23.55	24.87	24.87	11.84	14.47	22.37	23.68	19.74
Gd	4.57	4.38	4.42	4.23	10.86	11.24	21.35	28.46	19.85
Tb	158.42	157.20	161.46	151.93	8.72	8.72	17.04	22.92	15.62
Dy	19.55	18.79	18.27	18.48	7.27	7.58	13.94	18.18	12.73
Ho	17.62	16.95	16.69	16.03	6.75	6.75	12.32	16.56	11.52
Er	16.48	16.30	16.30	15.51	6.48	6.48	11.57	15.74	11.11
Tm	16.72	16.11	15.50	15.50	6.69	6.69	11.25	15.50	10.94
Yb	15.25	15.07	14.75	14.39	6.56	6.33	10.72	14.30	10.18
Pb									
Th	384.90	395.91	360.39	337.64	126.05	145.56	220.84	375.15	247.60
U	290.49	311.37	292.30	279.59	72.62	115.29	178.83	297.75	195.17

Note: Data normalized to chondrite values from Anders & Grevesse (1989)[1] multiplied by 1.36 as per Korotev[26]
*Vredefort Granophyre data was provided by Peter Lightfoot.

Namaqualand

	Duchesne et al. 2007								
	Anorthosites				Tonalite	Leuconorite			
Analyte Symbol	Sample 70[b]	Sample 66	Sample 108	Average	Sample 30[a]	Sample 119	Sample 120	Sample 121	Average
Y	6.13	9.43	3.87	6.48	2.64	4.15	4.91	9.91	6.32
Zr	25.19	9.70	13.25	16.04	14.37	4.66	3.54	34.51	14.24
Nb	5.68	10.46	8.67	8.27	1.49	12.25	24.51	21.52	19.43
La		197.49		197.49	134.80	84.64	134.80	184.95	134.80
Ce	150.00	119.51	119.51	129.67	89.02	52.44	63.41	115.85	77.24
Pr		94.21		94.21	57.85	42.98			42.98
Nd	74.80	66.67	52.03	64.50	35.77	23.74	28.13	56.91	36.26
Sm	36.50	33.00	20.00	29.83	17.00	12.00	9.00	28.00	16.33
Eu	27.63	27.63	31.58	28.95	25.00	14.47	18.42	19.74	17.54
Gd	16.48	15.36	7.87	13.23	8.61	3.37	3.00	15.36	7.24
Tb		13.39		13.39	5.68				
Dy	8.48	10.61		9.55	3.94	3.33	3.64	9.70	5.56
Ho					3.18				
Er	6.48	7.87	4.54	6.30	2.69	2.73	6.02	12.04	6.93
Tm		6.69		6.69	3.04				
Yb	4.39	5.43	4.07	4.63	2.49	3.17	7.69	12.67	7.84
Pb	83.35	68.47	83.35	78.39	77.40	44.65	74.42	53.58	57.55
Th	402.66	105.04	312.63	273.44	182.57	57.52		105.04	81.28
U	81.70	54.47	63.54	66.57	99.85	36.31	27.23	90.78	51.44

Note: Data normalized to chondrite values from Anders & Grevesse (1989)[1] multiplied by 1.36 as per Korotev[26]
*Vredefort Granophyre data was provided by Peter Lightfoot.

	Duchesne et al. 2007 Continued								
	Norite Sample 85b					Melanorite			
Analyte Symbol	Sample 85[b]	Sample 86[b]	Sample 116	Sample 122	Average	Sample 88[b]	Sample 87[b]	Sample 110	Average
Y	5.09	11.32	25.94	12.74	13.77	11.32	19.81	17.45	16.19
Zr	2.99	19.22	148.32	27.80	49.58	6.34	13.25	42.16	20.58
Nb	4.48	8.97	44.84	10.16	17.11	5.38	32.88	15.24	17.83
La	75.24	87.77	291.54	178.68	158.31	42.32	100.31	137.93	93.52
Ce	39.02	59.76	260.98	93.90	113.41	26.83	91.46	90.24	69.51
Pr	18.18	43.80	247.93	78.51	97.11	27.27	90.08	71.90	63.09
Nd	16.75	30.57	193.50	56.91	74.43	22.93	69.92	48.78	47.21
Sm	8.00	17.50	102.50	27.50	38.88	10.00	42.50	26.00	26.17
Eu	14.47	17.11	38.16	17.11	21.71	6.71	15.79	9.74	10.75
Gd	5.24	11.61	67.42	15.73	25.00	6.74	26.59	17.23	16.85
Tb	4.26	9.53	56.80	16.23	21.70	0.00	24.34	15.42	13.25
Dy	4.55	8.48	33.33	12.73	14.77	9.09	20.30	14.24	14.55
Ho			29.14	11.52	20.33				
Er	4.40	11.57	25.93	12.96	13.72	12.50	18.98	22.69	18.06
Tm	4.86	13.37	20.97	12.46	12.92	14.29	18.24	30.09	20.87
Yb	7.69	17.19	20.81	12.67	14.59	14.93	18.55	40.27	24.59
Pb	35.72	41.68	41.68	44.65	40.93	20.84	17.86	35.72	24.81
Th	10.00	40.02	532.71	100.04	170.69	45.02	75.03	730.29	283.45
U	9.08	81.70	208.79	81.70	95.32	27.23	45.39	245.10	105.91

Note: Data normalized to chondrite values from Anders & Grevesse (1989)[1] multiplied by 1.36 as per Korotev[26]
*Vredefort Granophyre data was provided by Peter Lightfoot.

	Duchesne et al. 2007 Continued						
	Hypersthenite			Glimmerite	Magnetite		
Analyte Symbol	Sample 90[b]	Sample 117	Average	Sample 123	Sample 82[b]	Sample 125[b]	Average
Y	10.38	15.57	12.97	52.36	33.02	91.98	62.50
Zr	19.59	10.26	14.93	7.28	235.07	6.72	120.90
Nb	11.66	16.44	14.05	95.65	176.35	12.55	94.45
La	46.08	169.28	107.68	316.61	322.88	567.40	445.14
Ce	32.93	143.90	88.41	348.78	324.39	586.59	455.49
Pr	28.93		28.93			575.21	575.21
Nd	22.11	105.69	63.90	279.67	237.40	478.05	357.72
Sm	13.50	53.50	33.50	150.00	128.50	300.00	214.25
Eu	8.95	22.37	15.66	53.95	39.47	39.47	39.47
Gd	8.99	27.72	18.35	82.40	71.54	228.46	150.00
Tb						158.22	158.22
Dy	9.39	15.76	12.58	46.06	36.06	111.82	73.94
Ho						96.69	96.69
Er	10.65	15.28	12.96	51.85	32.41	80.56	56.48
Tm	12.77		12.77			63.83	63.83
Yb	14.03	12.22	13.12	42.53	27.60	58.37	42.99
Pb	17.86	5.95	11.91	20.84		17.86	17.86
Th	17.51	60.02	38.77	100.04	200.08	402.66	301.37
U	18.16	27.23	22.69	108.93	190.63	272.33	231.48

Note: Data normalized to chondrite values from Anders & Grevesse (1989)[1] multiplied by 1.36 as per Korotev[26]
*Vredefort Granophyre data was provided by Peter Lightfoot.

	Duchesne et al. 2007 Continued					
	Biotite Diorite					
Analyte Symbol	Sample 112	Sample 109	Sample 114	Sample 118	Sample 126	Average
Y	30.66	54.72	26.42	10.85	7.55	23.35
Zr	218.84	36.01	124.25	12.13	41.79	80.22
Nb	50.81	161.41	44.84	44.84	8.97	54.30
La	1896.55	288.40	219.44	300.94	122.26	498.43
Ce	1330.49	180.49	181.71	257.32	87.80	357.52
Pr	942.15		163.64		66.94	315.29
Nd	616.26	105.69	121.95	162.60	48.78	185.37
Sm	265.00	70.00	69.00	74.50	26.00	88.83
Eu	50.00	32.89	32.89	39.47	14.47	31.36
Gd	108.61	56.18	45.32	36.33	15.73	45.51
Tb			41.18		11.36	21.77
Dy	42.73	55.15	32.42	16.36	8.48	27.68
Ho	33.11		29.14		8.74	19.97
Er	23.61	58.33	28.70	10.65	7.41	23.30
Tm	20.97		27.36		7.29	16.79
Yb	17.65	53.85	24.89	5.88	7.24	20.29
Pb	98.24	160.75	50.61	53.58	38.70	75.91
Th	10454.18	1328.03	220.09	80.03	37.52	2044.15
U	717.14	535.58	245.10	18.16	36.31	273.84

Note: Data normalized to chondrite values from Anders & Grevesse (1989)[1] multiplied by 1.36 as per Korotev[26]
*Vredefort Granophyre data was provided by Peter Lightfoot.

Morokweng

	Andreoli et al. 1999						
	Medium Grained Quartz Norite					Fine Grained Quartz Norite	Quartz Norite Mean
Analyte Symbol	N-5	N-4	N-3	Average	N-2	N-1	Quartz Norite Mean
Y	8.02	8.49	8.49	8.33	8.49	11.32	9.43
Zr	20.90	22.39	22.95	22.08	20.90	22.20	21.64
Nb	19.43	17.93	18.83	18.73	14.65	15.84	20.92
La	59.59	59.44	58.21	59.08	50.91	51.82	55.99
Ce	42.59	41.60	43.48	42.55	38.32	40.59	41.32
Pr							
Nd							
Sm	18.55	18.15	19.45	18.72	18.25	20.30	18.95
Eu	8.29	9.34	8.95	8.86	9.61	11.05	9.47
Gd							
Tb	11.56	11.16	12.37	11.70	12.37	14.60	11.16
Dy							
Ho							
Er							
Tm							
Yb							
Pb							
Th	112.55	112.55	117.55	114.21	85.03	80.03	102.54
U	154.32	163.40	172.48	163.40	136.17	118.01	145.24

Note: Data normalized to chondrite values from Anders & Grevesse (1989)[1] multiplied by 1.36 as per Korotev[26]
*Vredefort Granophyre data was provided by Peter Lightfoot.

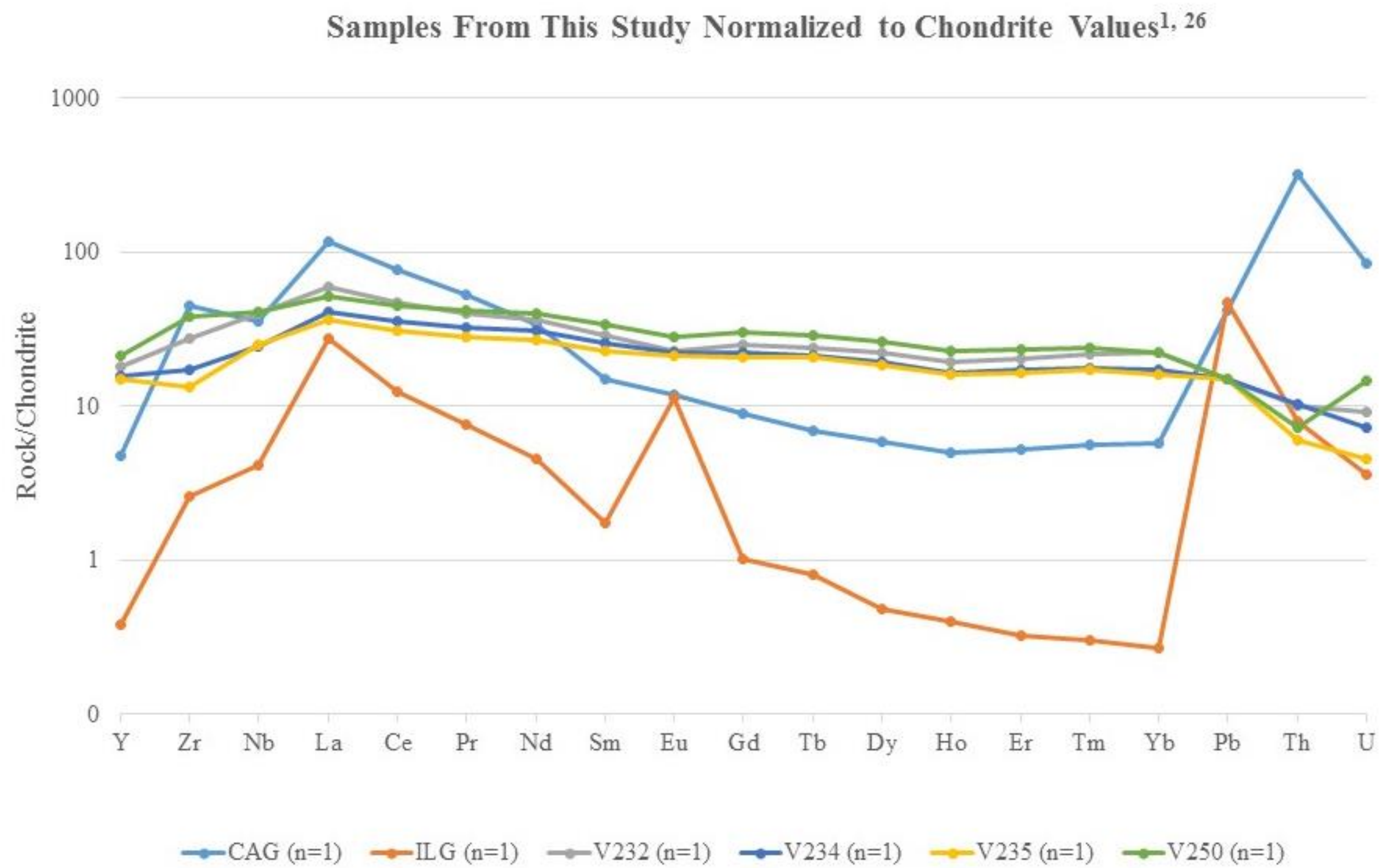

Note: Data normalized to chondrite values from Anders & Grevesse (1989)[1] multiplied by 1.36 as per Korotev[26]
*Vredefort Granophyre data was provided by Peter Lightfoot.

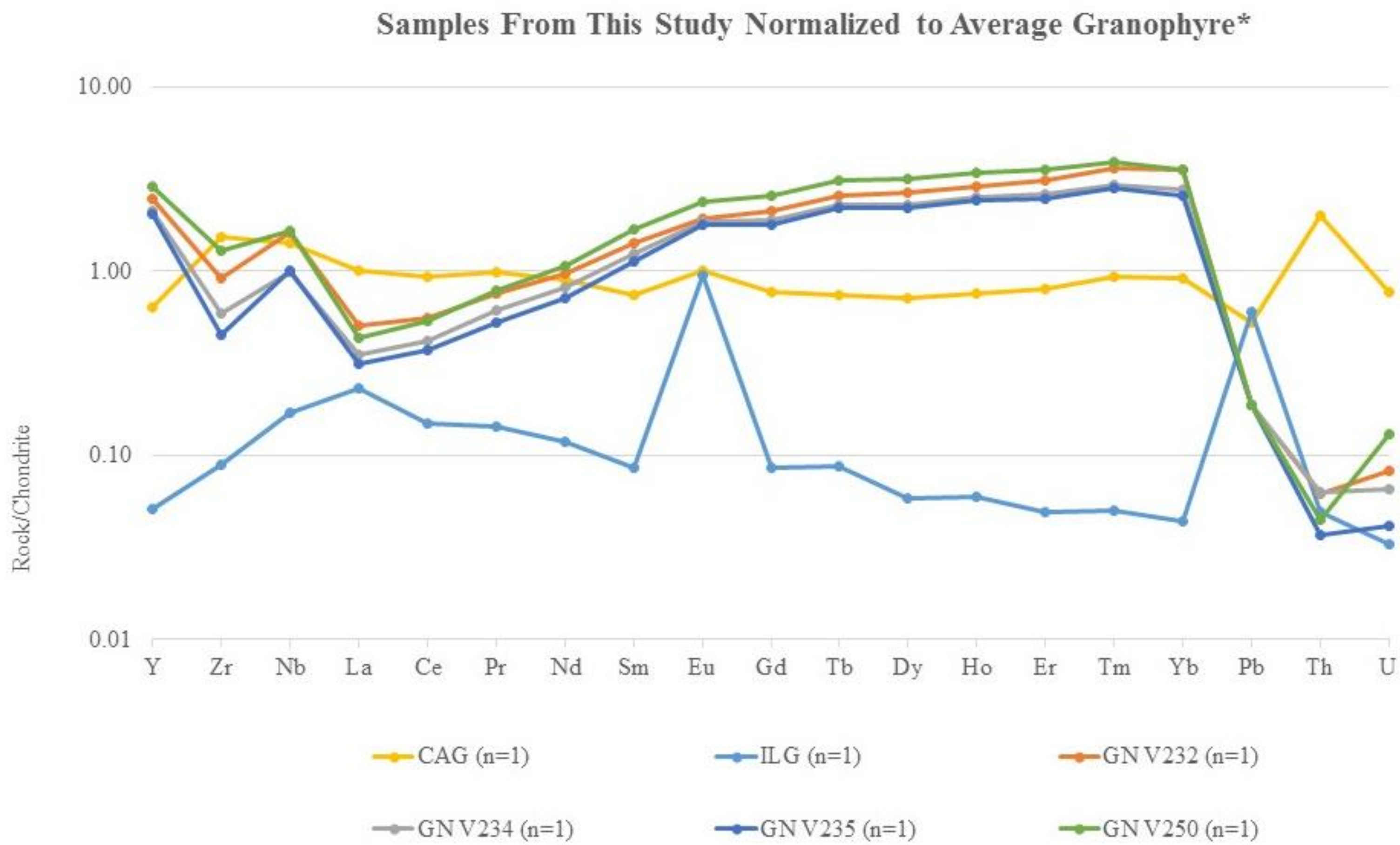

Note: Data normalized to chondrite values from Anders & Grevesse (1989)[1] multiplied by 1.36 as per Korotev[26]
*Vredefort Granophyre data was provided by Peter Lightfoot.

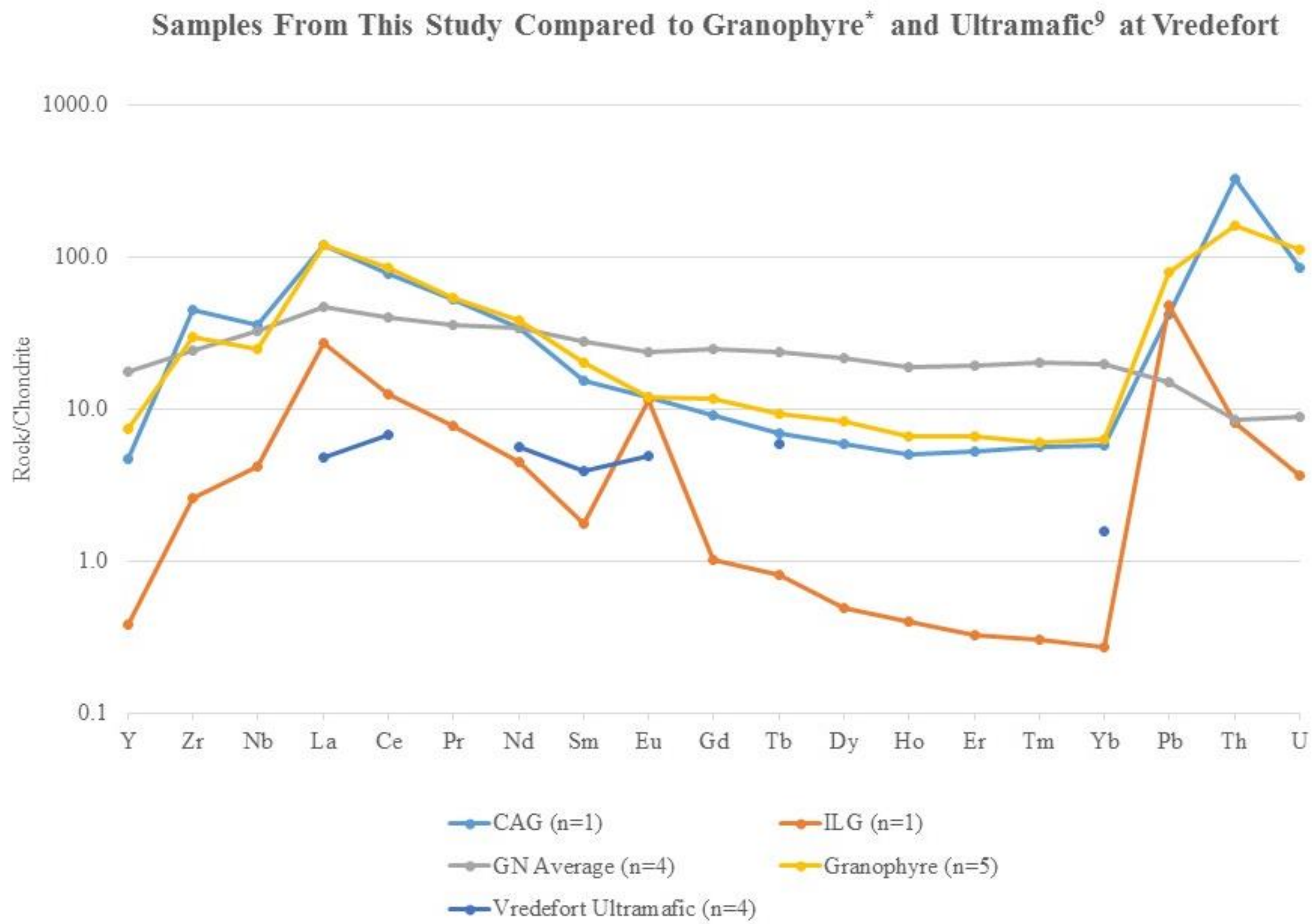

Note: Data normalized to chondrite values from Anders & Grevesse (1989)[1] multiplied by 1.36 as per Korotev[26]
*Vredefort Granophyre data was provided by Peter Lightfoot.

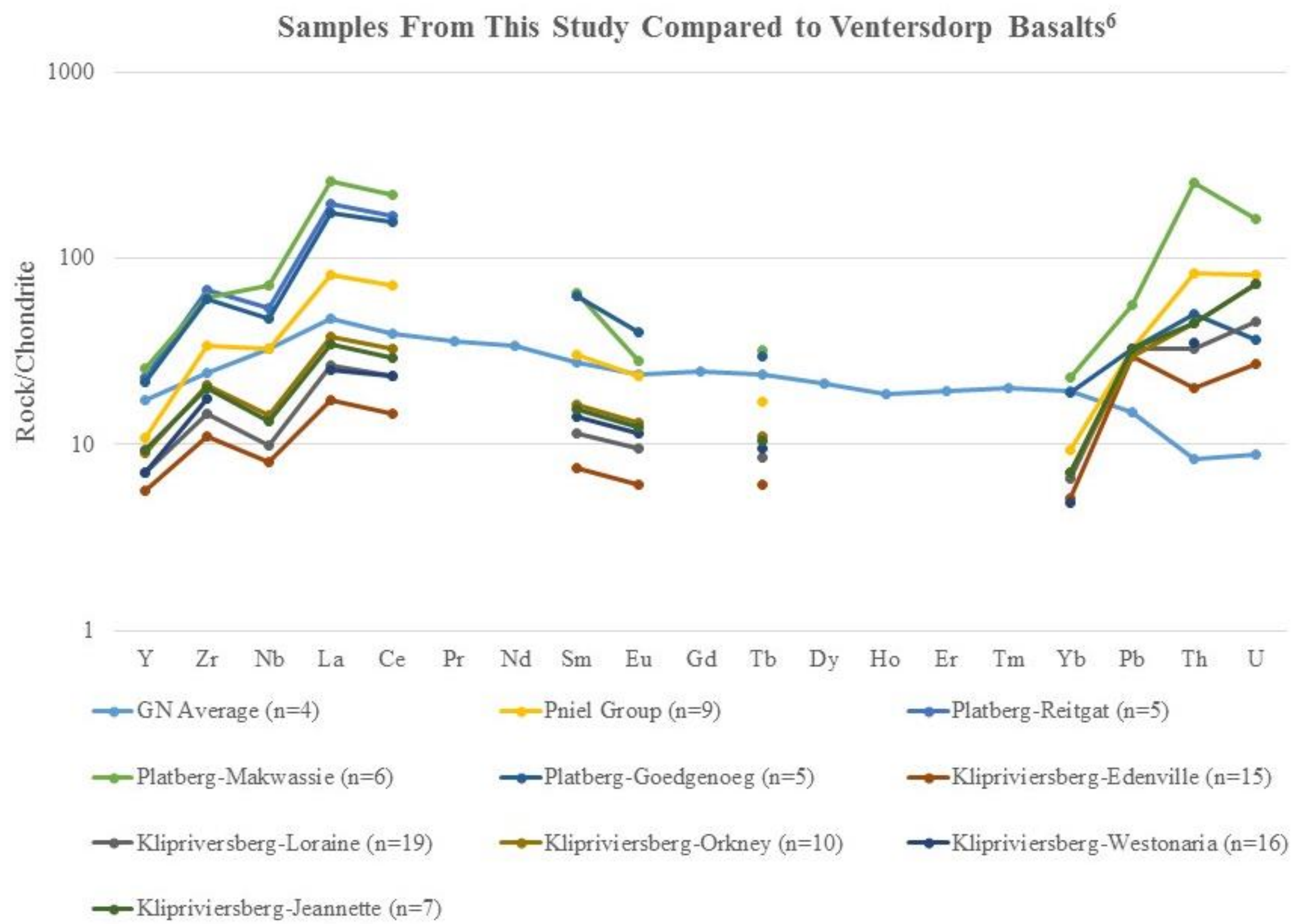

Note: Data normalized to chondrite values from Anders & Grevesse (1989)[1] multiplied by 1.36 as per Korotev[26]
*Vredefort Granophyre data was provided by Peter Lightfoot.

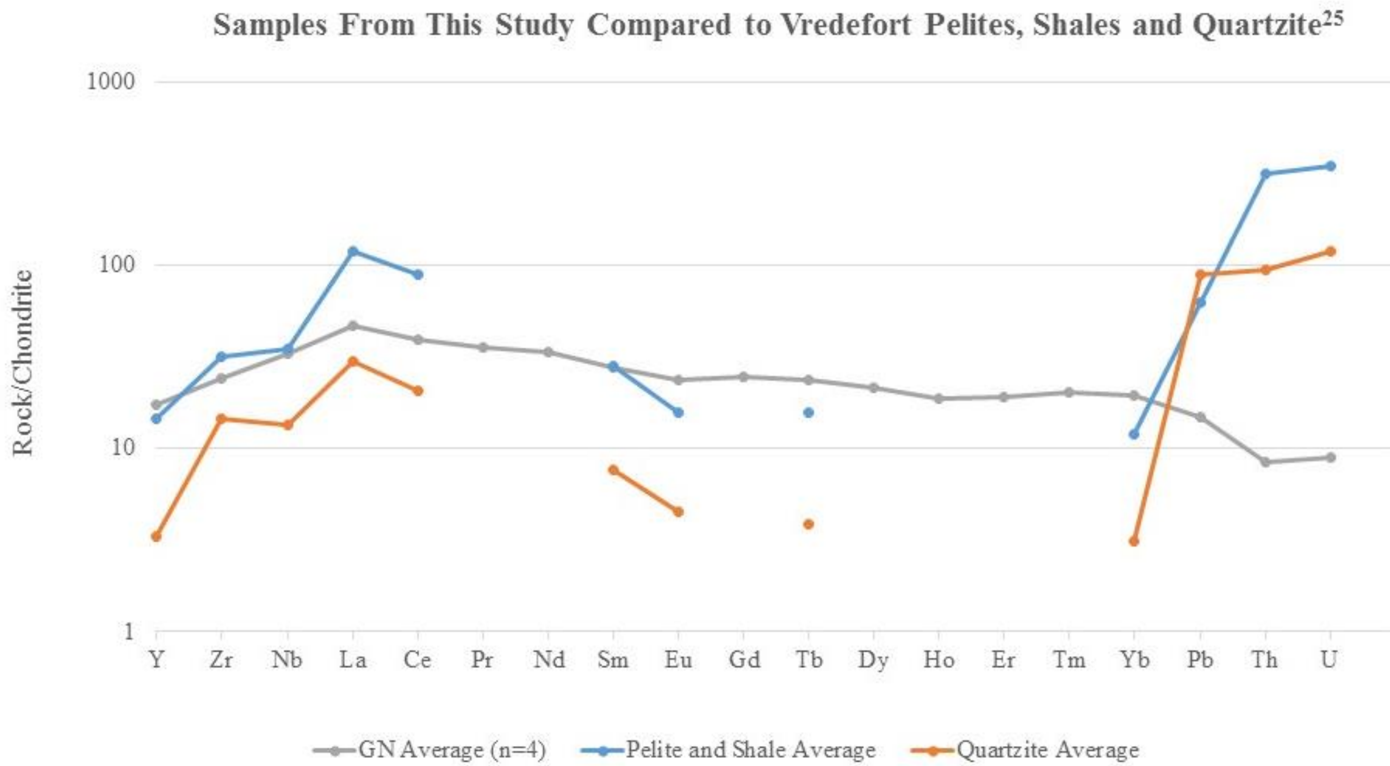

Note: Data normalized to chondrite values from Anders & Grevesse (1989)[1] multiplied by 1.36 as per Korotev[26]
*Vredefort Granophyre data was provided by Peter Lightfoot.

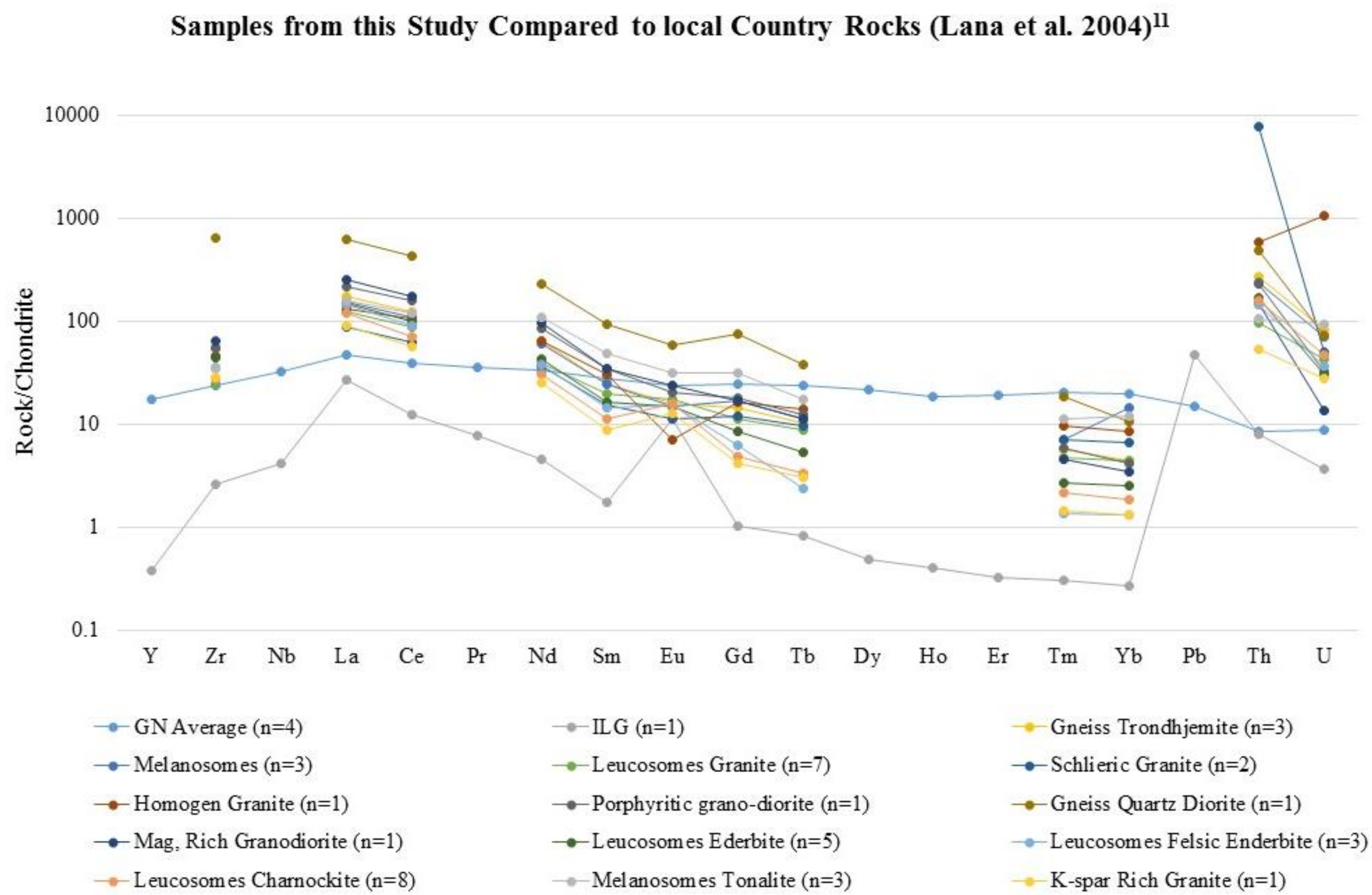

Note: Data normalized to chondrite values from Anders & Grevesse (1989)[1] multiplied by 1.36 as per Korotev[26]
*Vredefort Granophyre data was provided by Peter Lightfoot.

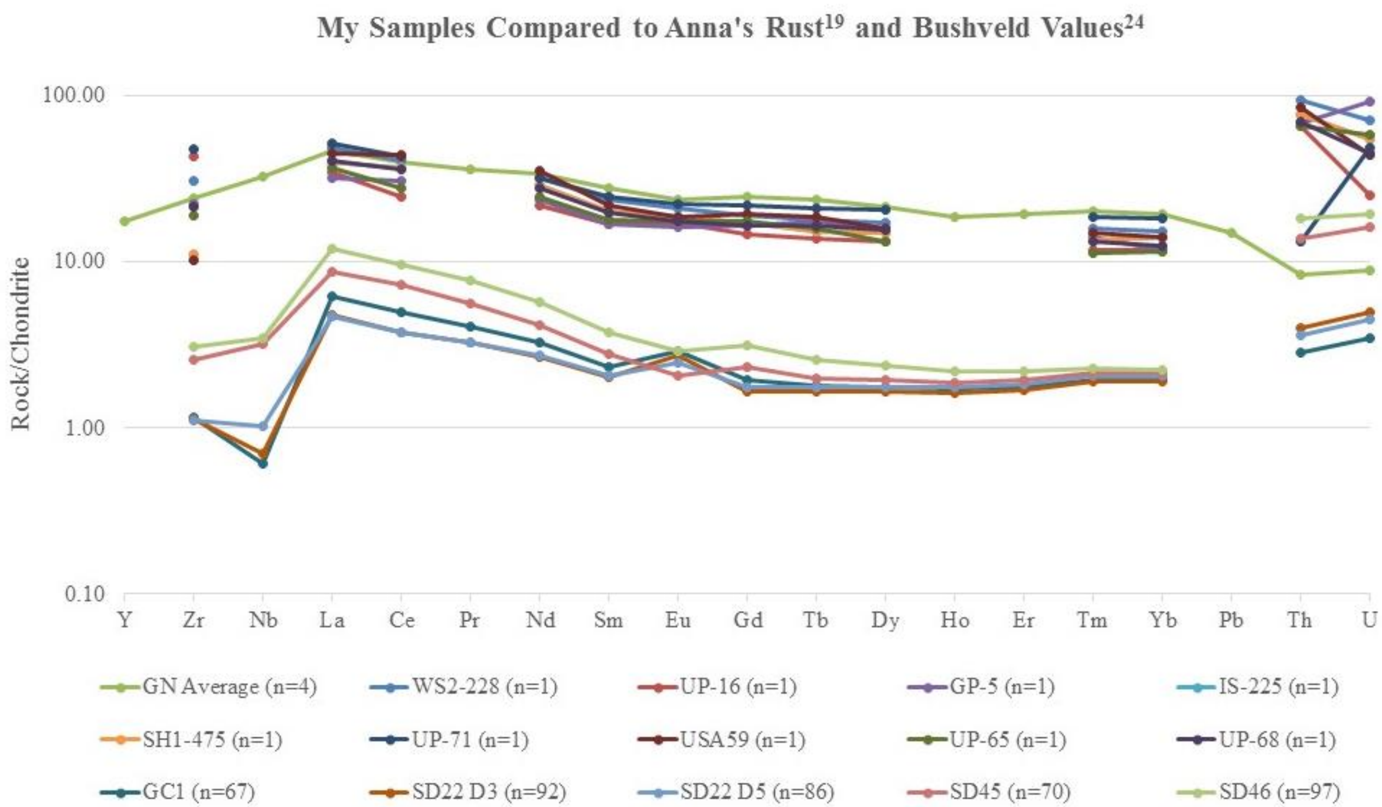

Note: Data normalized to chondrite values from Anders & Grevesse (1989)[1] multiplied by 1.36 as per Korotev[26]
*Vredefort Granophyre data was provided by Peter Lightfoot.

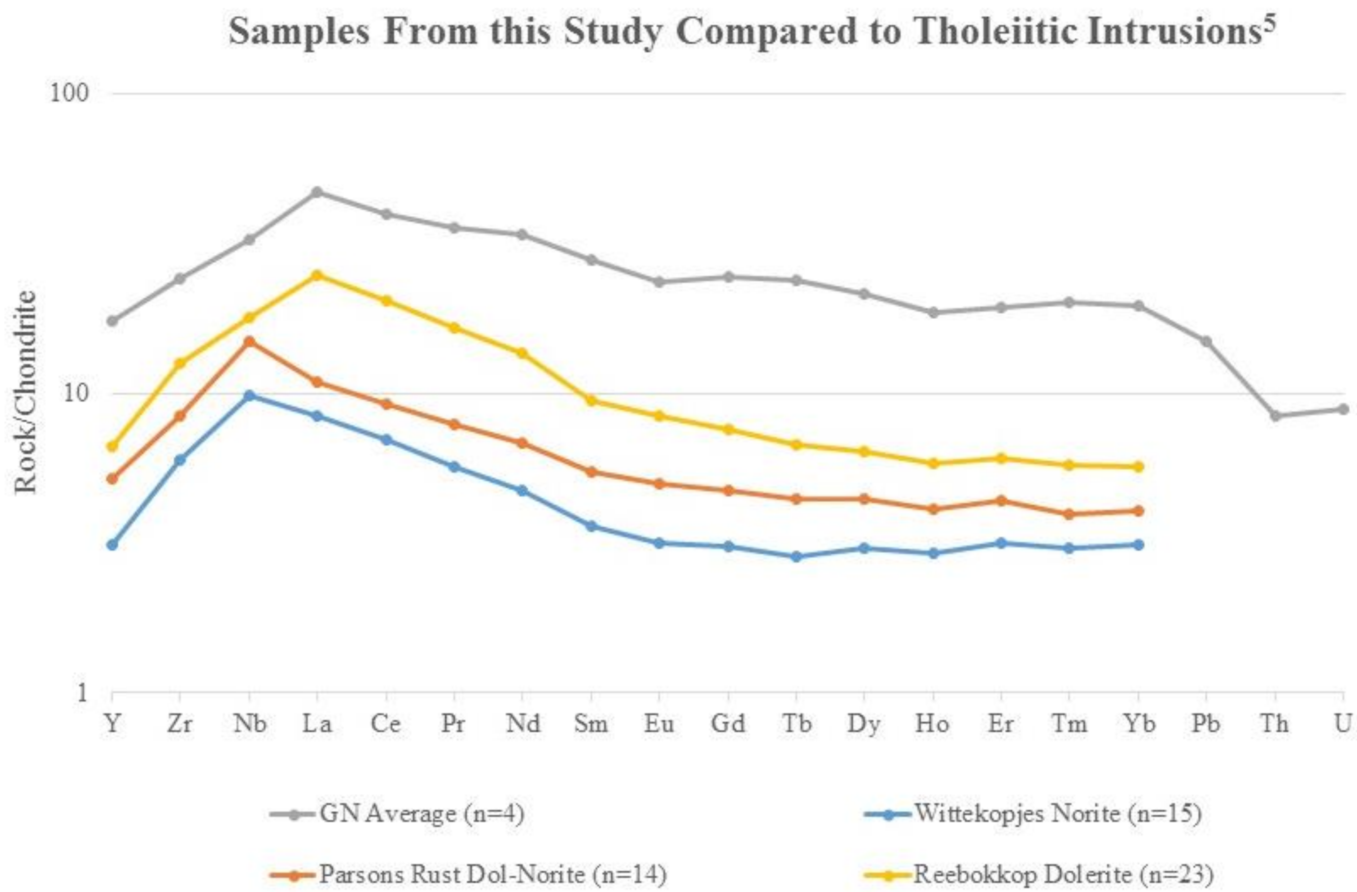

Note: Data normalized to chondrite values from Anders & Grevesse (1989)[1] multiplied by 1.36 as per Korotev[26]
*Vredefort Granophyre data was provided by Peter Lightfoot.

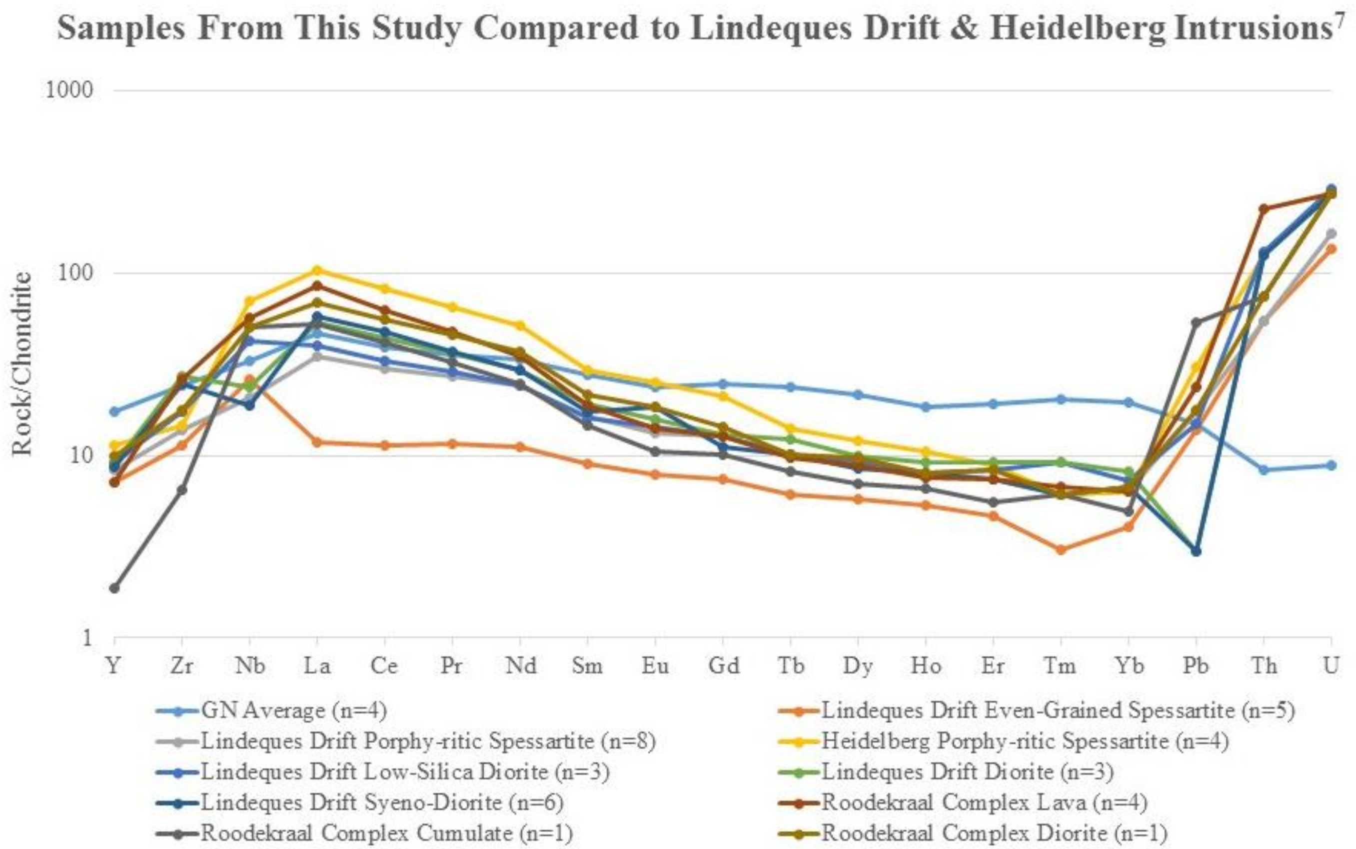

Note: Data normalized to chondrite values from Anders & Grevesse (1989)[1] multiplied by 1.36 as per Korotev[26]
*Vredefort Granophyre data was provided by Peter Lightfoot.

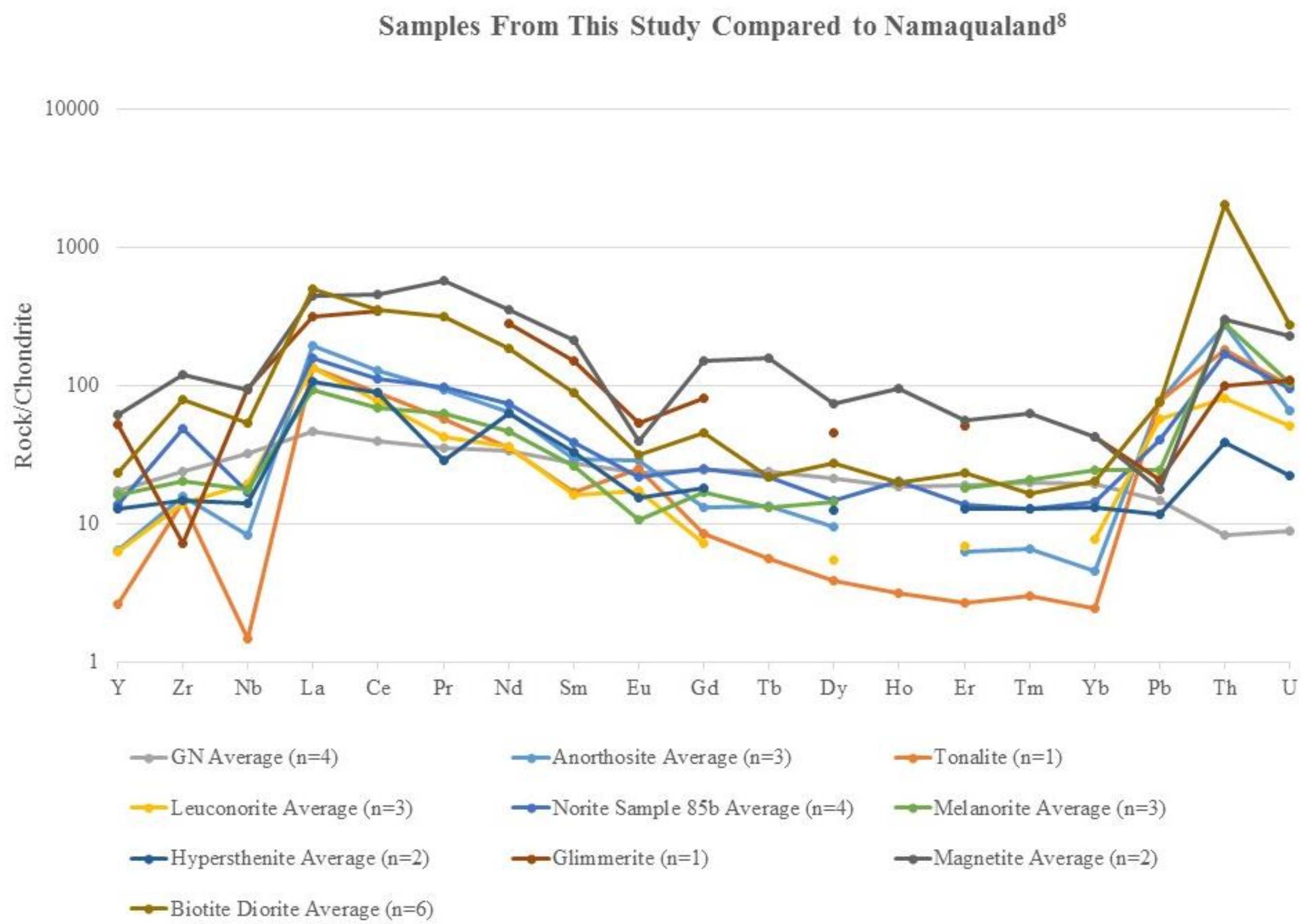

Note: Data normalized to chondrite values from Anders & Grevesse (1989)[1] multiplied by 1.36 as per Korotev[26]
*Vredefort Granophyre data was provided by Peter Lightfoot.

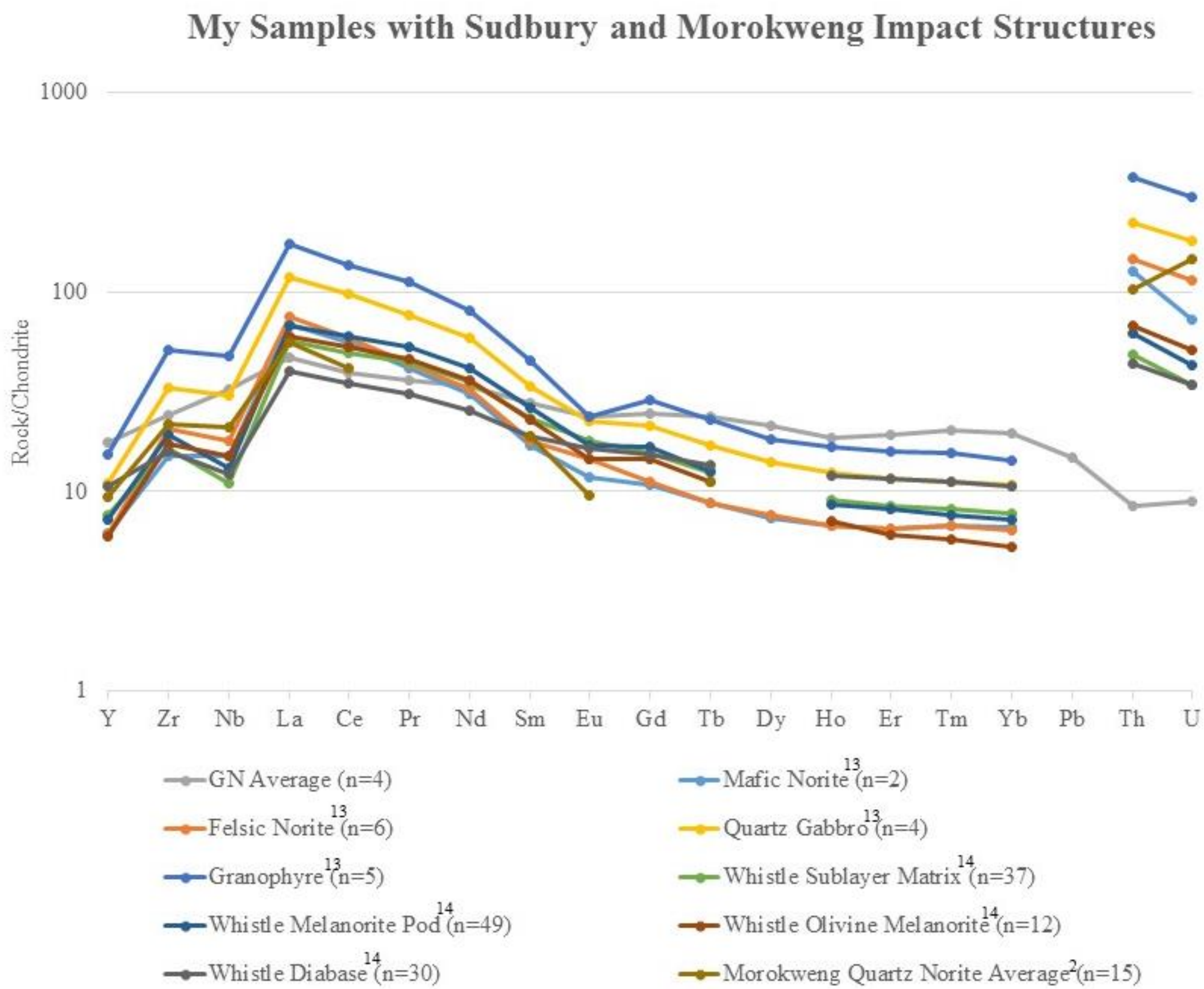

Note: Data normalized to chondrite values from Anders & Grevesse (1989)[1] multiplied by 1.36 as per Korotev[26]
*Vredefort Granophyre data was provided by Peter Lightfoot.

Appendix B-1-3: MgO vs Ni Comparison Tables and Plots

Vredefort

	Samples from this study							Koeberl, Reimold and Shirey 1996					
	Anatectic Melt	ILG	Gabbro Norite					Witwatersrand Shale	Ventersdorp Andesitic			OGG	Wits Siltstone clase in Granophyre
	VO9-111	VO9-238	VO9-232	VO9-234	VO9-235	VO9-250	Average	VG-SNE	UP-61	UP-63	Average	OT-1	BG-S1
MgO	0.38	0.13	5.14	5.57	5.62	4.47	5.20	0.72	4.53	6.19	5.36	1.90	0.50
Ni	20.00	20.00	130.00	100.00	110.00	70.00	102.50	55.00	132.00	130.00	131.00	18.00	77.00

	Koeberl, Reimold and Shirey 1996 Continued						Reimold & Gibson Chemie der Erde 66 2006	Lieger, Riller and Gibson 2010[1]								
	Vredefort Granophyre						Vredefort Granophyre	Granitoid								
	BG-4	BG-7	BG-9	BG-10	BG-168	average	Granophyre with outliers	WR 669A3	WR 200C2	PT 200C1	WR 453A2	PT 453A1	WR KuduA3	PT KuduA2	PT KuduA1
MgO	3.50	3.50	3.40	3.40	3.70	3.50	3.58	0.34	0.01	0.35	0.24	2.09	0.28	6.24	6.44
Ni	129.00	121.00	111.00	125.00	126.00	122.40	104.40	11.00	10.00	12.00	9.00	26.00	11.00	87.00	88

	Lieger, Riller and Gibson 2010[1] Continued														
	Granitoid				Quartzite/ Conglomerate	Quartzite									
	WR 518A2	PT 518A1	WR Average	PT Average	WR 6A4	WR 621A3	PT 621A2	PT 621A1	PT 2A2	PT 64A1	WR 102A2	PT102A1	PT 1A1	PT 1A2	Average WR
MgO	1.18	2.98	0.41	4.44	0.05	0.01	0.24	0.25	0.27	0.79	0.01	0.12	1.41	1.38	0.01
Ni	42.00	37.00	16.60	59.50	13.00	18.00	20.00	18.00	23.00	104.00	36.00	25.00	115.00	118.00	27

[1]It was discovered on July 28th 2016 that Lieger, D., Riller, U., and Gibson, R.L. 2010 was withdrawn at the request of the author(s).

	Lieger, Riller and Gibson 2010[1] Continued					Reimold 1991				McIver et al 1981			Crow and Condie 1988		
		Alkali Granite		Epidiorite		Gabbro		Norite		Mafic Rock		Mafic Rock WR	Porphyritic lava	Basaltic Andesite	Felsic Porphyritic Lava
	Average PT	WR 4A2	PT 4A1	WR 564A2	PT 564A1	WR	PT	WR	PT	WR	WR	Average	Pniel Group Allanridge	Platberg Group Reitgat	Platberg Group Makwassie
MgO	0.64	0.20	0.72	9.28	8.59	6.00	6.10	9.30	7.30	17.58	14.42	16.00	3.83	4.37	2.51
Ni	60.43	7.00	33.00	217.00	175.00	124.00	119.00	247.00	189.00	1241.00	804.00	1022.50	99	94	12

	Crow and Condie 1988 Continued								Wronkiewicz and Condie 1990	
	Porphyritic Basaltic Andesite	Basalt	Basalt						Pelites & Shales	
	Platberg Group Goedgenoeg	Platberg Group Average	Klipriviersberg Group Edenville	Klipriviersberg Group Loraine	Klipriviersberg Group Jeannette	Klipriviersberg Group Orkney	Klipriviersberg Group Westonaria	Klipriviersberg Average	Average Bothaville Formation P&S	Average Selati Formation P&S
MgO	5.6	4.985	10.52	7.47	4.9	5.3	13.97	8.432	4.98	3.71
Ni	105	99.5	331	197	122	146	705	300.2	266	142

	Wronkiewicz and Condie 1990												
	Pelites & Shales					Quartzite	Quartzite	Quartzite	Quartzite	Quartzite	Quartzite	Quartzite	Quartzite
	Average Black Reef Formation P&S	Average Timeball Hill Formation P&S	Average Strubenkop Formation P&S	Average Silverton Formation P&S	NASC P&S	Bothaville Formation Quartzite C6	Sekororo Formation Quartzite D53	Sekororo Formation Quartzite D36	Sekororo Formation Quartzite D47	Average Sekororo Formation Quartzite D47	Selati Formation Quartzite D35	Black Reef Quartzite D34	Black Reef Quartzite C201
MgO	4.44	1.78	1.35	2.74	2.85	0.59	0.41	1.51	1.36	1.09333	2.04	0.27	0.22
Ni	327	57	90	66	58	35	8.1	11	14	11.0333	13	5.8	5.6

[1]It was discovered on July 28th 2016 that Lieger, D., Riller, U., and Gibson, R.L. 2010 was withdrawn at the request of the author(s).

Wronkiewicz and Condie 1990									Lana et al. 2004		
		Quartzite	Quartzite	Quartzite		Quartzite	Quartzite		Quartzite	Gneiss (amphibolite facies) Trondhjemite NE-Part		
	Average Black Reef Quartzite C201	Rooihoogte Formation Quartzite C76	Daspoort Formation Quartzite C81	Daspoort Formation Quartzite M8F-2-10	Average Daspoort Formation Quartzite M8F-2-10	Magaliesberg Formation Quartzite C207	Magaliesberg Formation Quartzite D77	Average Magaliesberg Formation Quartzite D77	Rayton Formation Quartzite C56	ABBG-1	ABBG-2	ABBG-3
MgO	0.245	0.23	0.32	0.73	0.525	0.44	4.3	2.37	0.17	0.67	0.72	0.77
Ni	5.7	12	7.4	9.6	8.5	7.9	35	21.45	5.4	10	12	11

Lana et al. 2004 Continued														
Gneiss (amphibolite facies) Trondhjemite NE-Part							Porphyritic granodiorite W-Part				Gneiss (Granulite Facies) Quartz Diorite Central Part			
	ABG-1	ABG-2	ABP-1	ABP-2	ABP-3	Average	POR-1	POR-2	POR-3	Average	SCH-1	SCH-2	SCH-3	Average
MgO	0.25	0.29	0.28	0.31	0.32	0.45	0.54	0.6	0.55	0.56	0.52	0.46	0.5	0.49
Ni	9	9	9	9	9	9.75	9	9	9	9	22.5	20.6	154	65.7

Lana et al. 2004 Continued																
Melanosomes Trondhjemite Outer Parts						Melanosomes Tonalite Central Parts				Mafic Granulites Central Parts				Leucosomes Granite Outer Parts		
	SAG-1	SAG-2	EG6	VAL-1	Average	vdf-4	vdf-1	vdf-8	Average	vdf2-12	vdf2-21	vdf2-2	Average	EG-4	EG-7	Pr12
MgO	0.6	0.63	0.12	0.18	0.38	5.95	5.17	5.99	5.70	12.56	9.77	8.96	10.43	0.28	0.07	0.16
Ni	12	12	8	9	10.25	13	8	9	10	9	9	12	10	9	9	8

[1]It was discovered on July 28th 2016 that Lieger, D., Riller, U., and Gibson, R.L. 2010 was withdrawn at the request of the author(s).

	Lana et al. 2004 Continued											Hart et al. 1990	Remiold et al. 2000		
	Leucosomes Granite Outer Parts			K-feldspar-rich Granite Transition Zone				Schlieric Granite Northern Parts				Ultramafics	Anne Rust Sheet		
	RG9	SAL-1	Average	LEP-1	LEP-2	LEP-3	Average	SPW-1	SPW-2	ScSPW-3	Average	Avg. Beta -1	Mean IV	Mean III	Anna's Rust Sheet
MgO	0.47	0	0.196	0.21	0.16	0.17	0.18	0.04	0.02	0.06	0.04	36.63	6.31	6.59	6.52
Ni	8	9	8.6	54	8	27	29.67	9	9	9	9	3212	93	103	93

	Remiold et al. 2000 Continued						Coetzee et al. 2006					
	Anne Rust Sheet						Tholeiitic Intrusions			Mafic Dykes and sills		
	Vredefort mafic complex	OCEAAN	Core	Core BH	Collar	SWBH	Wittekopjes norite	Parsons Rust Dol-Norite	Reebokkop dolerite	Bushveld micopyroxenitic sills	Bushveld Ultramafic Sills	Noritic sills and dykes E Witts
MgO	6.88	6.75	5.57	6.12	6.12	6.02	20.2	14.61	8.27	13	32.1	11
Ni	95	1123	95	84	91	84	823	829	577	328	1838	266

	de Waal, Graham and Armstrong 2006											
	Lindeques drift and Heidelberg Intrusions											
	Lindeques Drift Contamspess	Lindeques Drift Even-grained spessartite mean	Lindeques Drift Porphyritic spessartite mean	Lindeques Drift Spessartite Average	Heidelberg Porphy-ritic spess mean	Lindeques Drift Low-silica diorite mean	Lindeques Drift diorite mean	Lindeques Drift syeno-diorite mean	Lindeques Drift Diorite Average	Lindeques Drift feeder	Roodekraal Complex Lava	Roodekraal Complex Cumulate
MgO	12.08	9.96	8.33	10.1233	9.31	4.72	3.85	1.87	3.48	4.66	3.37	7.57
Ni	82	101.4	66.1	83.1667	159.5	31.1	15.8	3	16.6333	39	31	61

[1]It was discovered on July 28th 2016 that Lieger, D., Riller, U., and Gibson, R.L. 2010 was withdrawn at the request of the author(s).

de Waal, Graham and Armstrong 2006 Continued			Maier, Barnes and Marsh 2003							
Lindeques drift and Heidelberg Intrusions			Bushveld Complex							
	Roodekraal Complex Diorite	Roodekraal Complex Average	Dominion Low Ti/V	Dominion High Ti/V	Loraine/Edenville	Hekpoort	Machadodorp	Bushveld Mg basalt	Average Bushveld
MgO	2.85	4.59667	9.07	5.26	10.97	8.38	8.55	12.65	9.14667
Ni	22	38	317	128	322	187	110	257	220.167

Sudbury

Lightfoot et al 1996													
	Main Mass Mafic Norite Average	Main Mass Felsic Norite Average	Main Mass Granophyre Average	Igneous textured sublayer matrix Whistle Mine Average	Melanorite Pod or Inclusion Whistle Mine Average	Olivine Melanorite Whistle Mine Average	Diabase Whistle Mine Average	Little Stobie Mine Igneous Textured Sublayer Matrix		Crean Hill Mine Igneous Textured Sublayer Matrix			
								93PCL-001	93PCL-001	93PCL-20	93PCL-22	93PCL-23	93PCL-25
MgO	10.61	4.95	1.23	7.73	10.51	18.09	6	8.57	6.79	5.76	6.67	6.08	6.71
Ni	341	126	5	803	1104	1202	165	605	227	322	430	113	561

Lightfoot et al 1996 Continued															
Levack West Mine Igneous Textured Sublayer Matrix			Levack West Mine Melanorite Pod or Inclusion			McCreedy West Mine Igneous Textured Sublayer Matrix					Fraser Mine Igneous Textured Sublayer Matrix				
	93PCL-45	93PCL-46	93PCL-66	93PCL-67	93PCL-68	93PCL-50	93PCL-51	93PCL-53	93PCL-55	93PCL-59	93PCL-342	93PCL-343	93PCL-344	92PCL-345	93PCL-346
MgO	9.52	13.29	16.03	26	25.1	9.93	10.92	9.83	10	9.11	8.47	9.89	10.13	11.52	10.58
Ni	206	1494	1174	549	724	2526	269	334	1529	571	256	313	374	344	417

[1]It was discovered on July 28th 2016 that Lieger, D., Riller, U., and Gibson, R.L. 2010 was withdrawn at the request of the author(s).

Lightfoot et al 1996 Continued				Lightfoot et al. 2001							
Creig hton Mine Igneous Textured Sublayer Matrix				Mafic Norite		Felsic Norite					
	94PCL-128	94PCL-131	94PCL-132	94PCL2011	94PCL2016	94PCL2066	94PCL2072	94PCL2076	94PCL2033	94PCL2028	94PCL2013
MgO	11.03	6.44	8.38	11.35	12.15	4.37	4.75	4.75	5.2	5.57	8.25
Ni	834	5431	1436	313	485	17	18	24	34	64	222

Lightfoot et al. 2001 Continued											
Quartz Gabbro					Granophyre					Mafic Norite Average	Felsic Norite Average
	94PCL2080	93PCL290	94PCL2052	94PCL2079	93PCL336	93PCL293	93PCL297	93PCL312	93PCL334		
MgO	3.89	0.85	3.77	3.8	1.47	1.04	1.08	1.42	1.6	13.7	5.2
Ni	17	5	14	16	6	5	5	5	5	542	34

Lightfoot et al. 2001 Continued			
	Quartz Gabbro Average	Granophyre Average	Main Mass Average
MgO	2.9	1.2	3.7
Ni	9	5	44

[1]It was discovered on July 28th 2016 that Lieger, D., Riller, U., and Gibson, R.L. 2010 was withdrawn at the request of the author(s).

Namaqualand

Duchesne et al. 2007														
	Anorthosites				Tonalite	Leuconorite				Norite Sample 85b				
	Sample 70[b]	Sample 66	Sample 108	Average	Sample 30[a]	Sample 119	Sample 120	Sample 121	Average	Sample 85[b]	Sample 86[b]	Sample 116	Sample 122	Average
MgO	0.41	0.66	0.98	0.68	0.15	3.7	2.58	1.91	2.73	8.04	9.13	5.26	7.69	7.53
Ni	351	19	8	126	0	78	46	64	62.67	262	236	147	180	206.25

Duchesne et al. 2007 Continued											
	Melanorite				Hypersthenite			Glimmerite	Magnetite		
	Sample 88[b]	Sample 87[b]	Sample 110	Average	Sample 90[b]	Sample 117	Average	Sample 123	Sample 82[b]	Sample 125[b]	Average
MgO	16.7	14.82	12.09	14.5367	20.41	19	19.705	17.5	11.48	11.39	11.435
Ni	883	757	160	600	549	846	697.5	945	568	480	524

Duchesne et al. 2007 Continued							
	Biotite Diorite						
	Sample 78[b]	Sample 112	Sample 109	Sample 114	Sample 118	Sample 126	Average
MgO	2.67	3.11	1.55	2.32	7.11	4.83	3.59833
Ni	115	94	10	10	155	78	77

[1]It was discovered on July 28[th] 2016 that Lieger, D., Riller, U., and Gibson, R.L. 2010 was withdrawn at the request of the author(s).

Morokweng

Andreoli et al. 1999																
Medium Grained Quartz Norite							Medium Grained Quartz Norite	Heterogeneous Quartz Norite			Fine Grained Quartz Norite				Chilled Quartz Norite	Quartz Norite Mean
	N-5	LA-137	N-4	LA-141	LA-161	N-3	LA-172	LA-174	N-2	LA-186	N-1	LA-197	LA-213	LA-216	LA-224	
MgO	4.05	3.71	3.93	3.92	3.15	4.04	3.58	2.36	3.81	3.15	4.88	4.7	4.5	3.86	3.68	3.82
Ni	535	900	519	577	500	634	513	205	363	312	361	364	479	541	480	485

[1]It was discovered on July 28th 2016 that Lieger, D., Riller, U., and Gibson, R.L. 2010 was withdrawn at the request of the author(s).

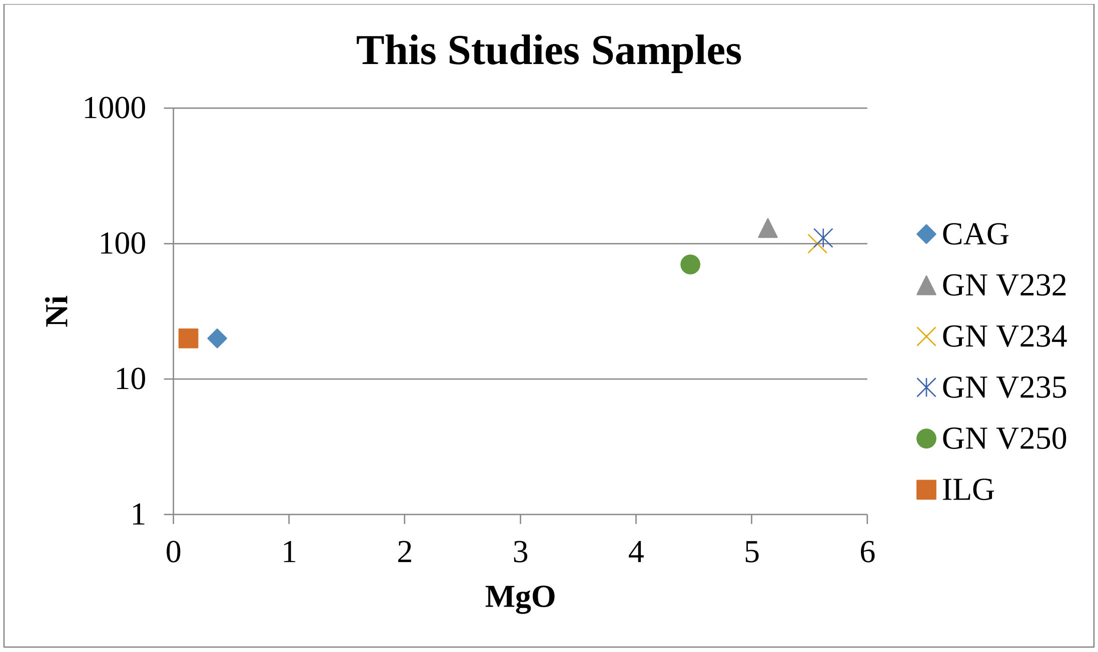

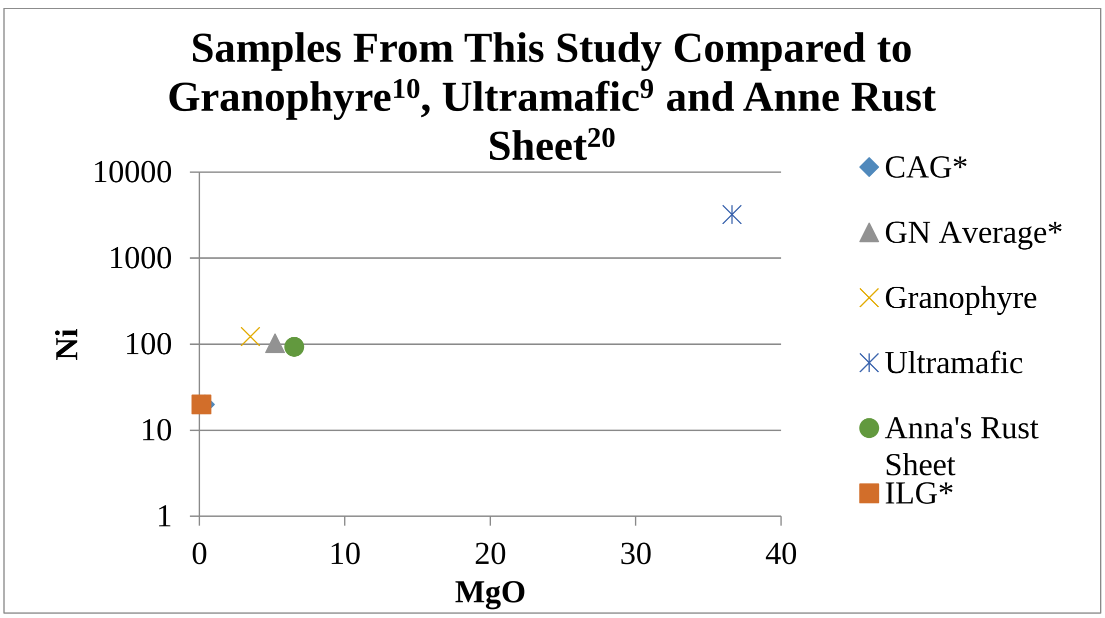

[1]It was discovered on July 28th 2016 that Lieger, D., Riller, U., and Gibson, R.L. 2010 was withdrawn at the request of the author(s).
*The Central Anatectic Granite (CAG), Gabbronorite (GN Average) and Inlandsee Leucogranofels (ILG) are samples from this study.

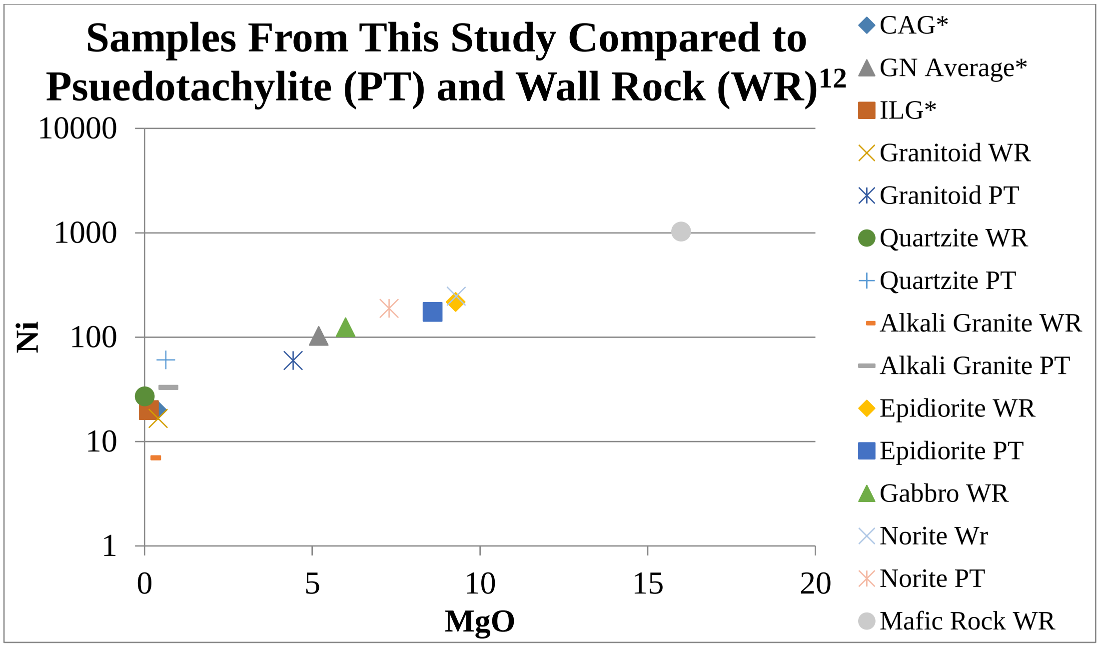

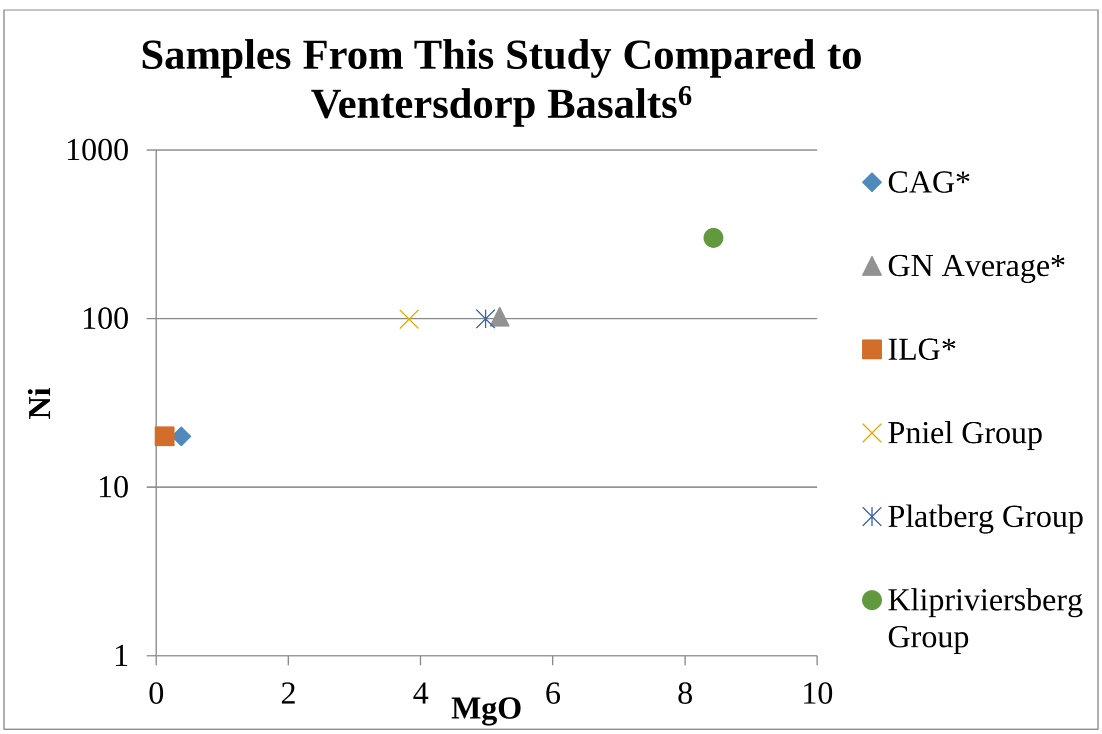

[1]It was discovered on July 28th 2016 that Lieger, D., Riller, U., and Gibson, R.L. 2010 was withdrawn at the request of the author(s).
*The Central Anatectic Granite (CAG), Gabbronorite (GN Average) and Inlandsee Leucogranofels (ILG) are samples from this study.

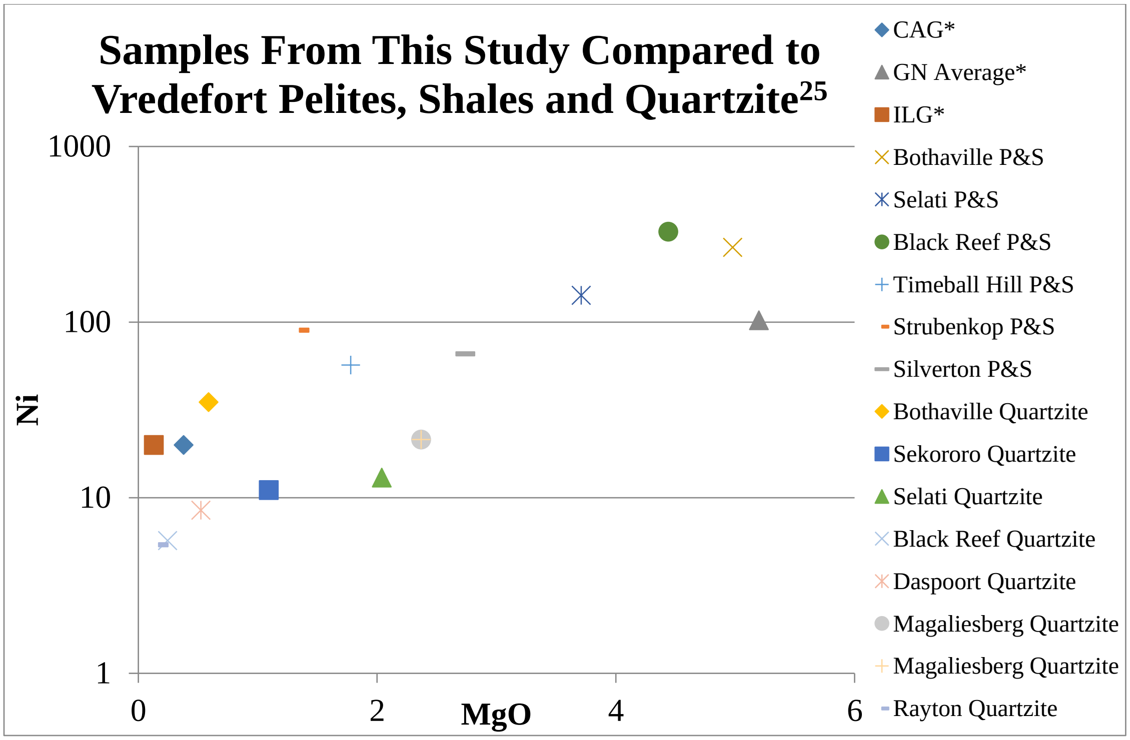

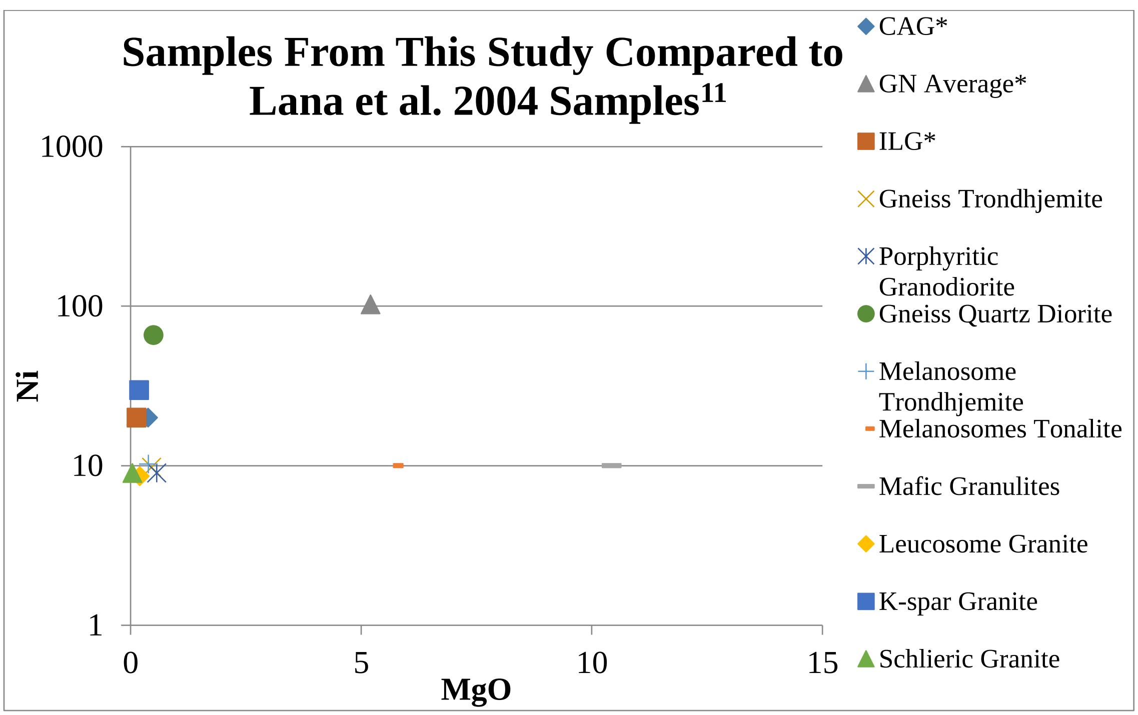

[1]It was discovered on July 28th 2016 that Lieger, D., Riller, U., and Gibson, R.L. 2010 was withdrawn at the request of the author(s).
*The Central Anatectic Granite (CAG), Gabbronorite (GN Average) and Inlandsee Leucogranofels (ILG) are samples from this study.

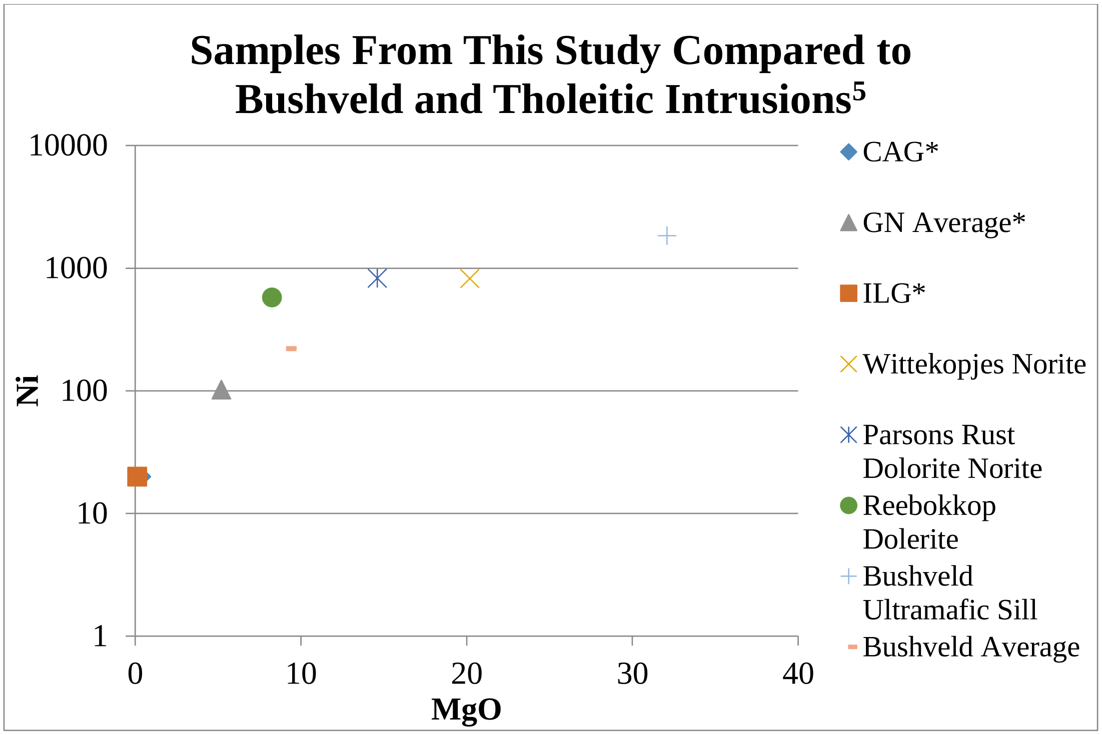

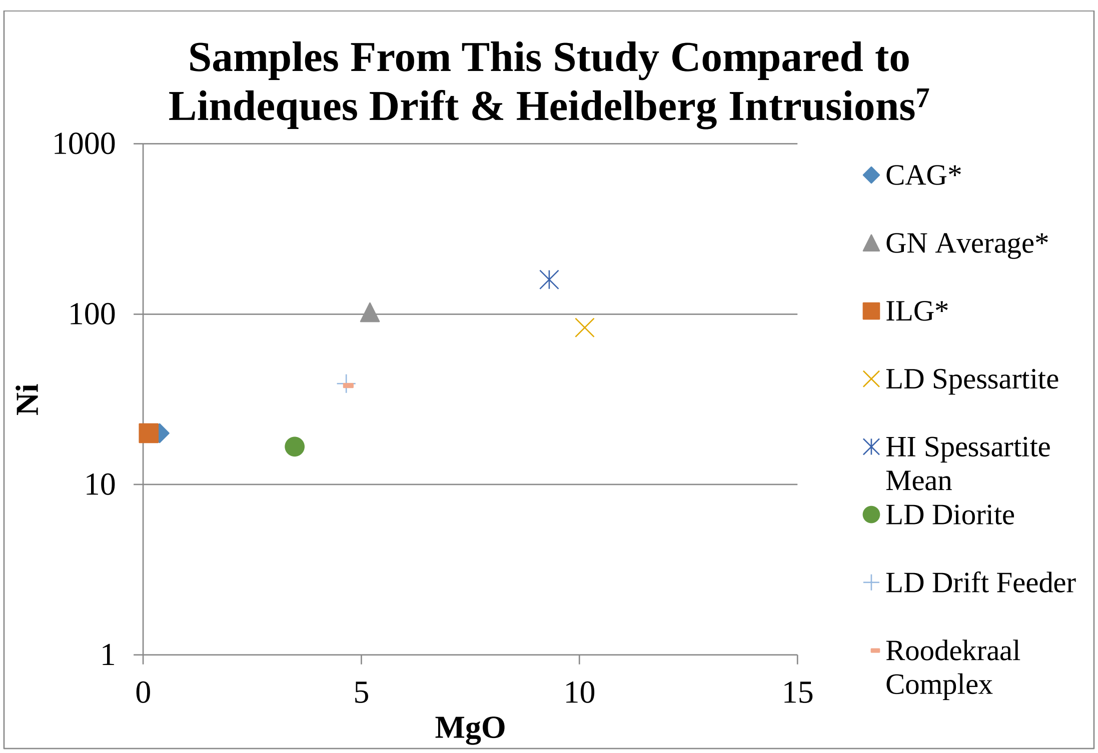

[1]It was discovered on July 28th 2016 that Lieger, D., Riller, U., and Gibson, R.L. 2010 was withdrawn at the request of the author(s).
*The Central Anatectic Granite (CAG), Gabbronorite (GN Average) and Inlandsee Leucogranofels (ILG) are samples from this study.

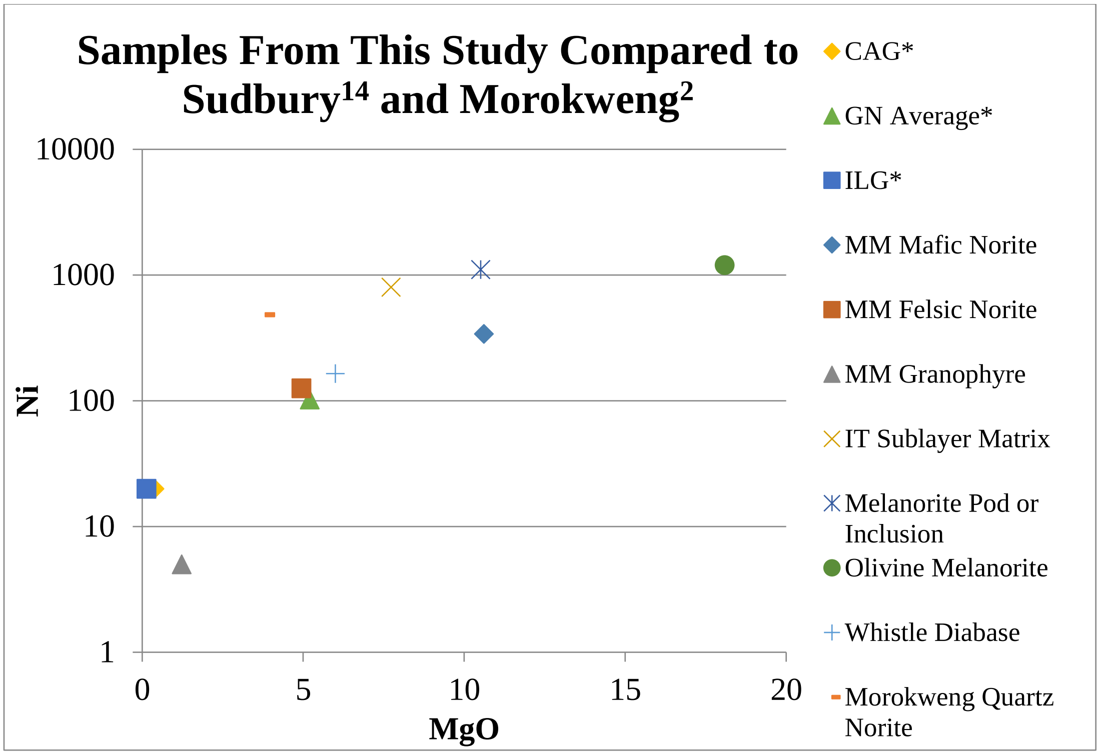

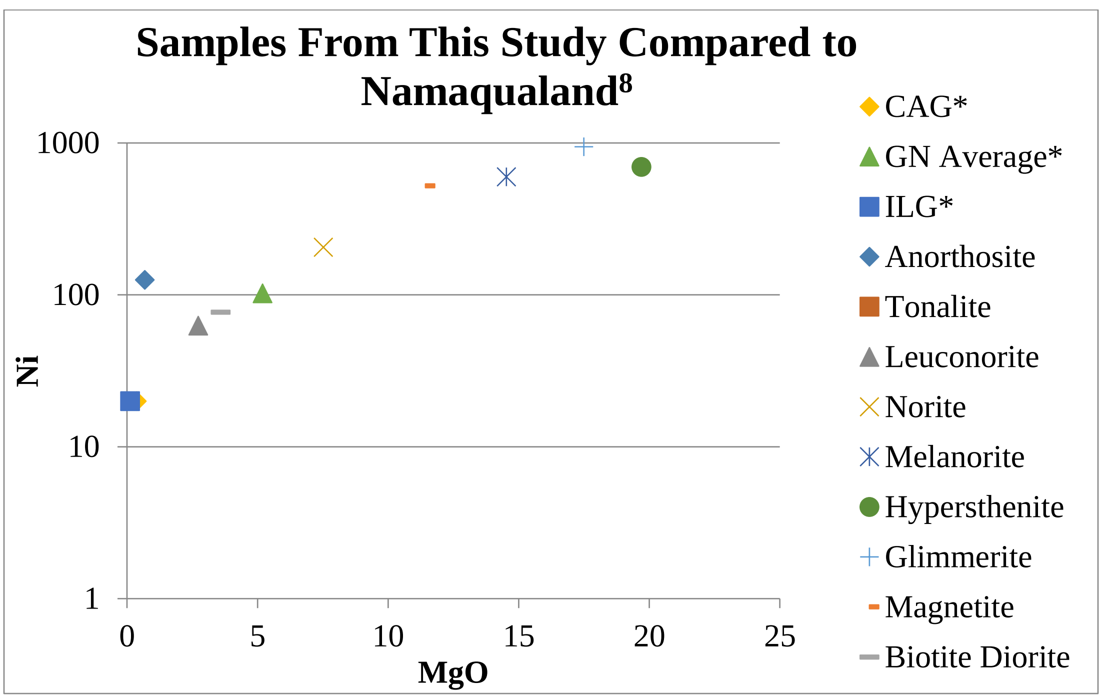

[1]It was discovered on July 28th 2016 that Lieger, D., Riller, U., and Gibson, R.L. 2010 was withdrawn at the request of the author(s).
*The Central Anatectic Granite (CAG), Gabbronorite (GN Average) and Inlandsee Leucogranofels (ILG) are samples from this study.

Appendix B-1-4: MgO vs Cu/Zr Comparison Table and Plots

Vredefort

	Samples from this study							Reimold & Gibson 2006	Lieger, Riller and Gibson 2010[1]					
	CAG	ILG	Gabbro Norite					Vredefort Granophyre	Granitoid					
	VO9-111	VO9-238	VO9-232	VO9-234	VO9-235	VO9-250	Average	Granophyre with outliers	WR 669A3	WR 200C2	PT 200C1	WR 453A2	PT 453A1	WR KuduA3
MgO	0.380	0.130	5.140	5.570	5.620	4.470	5.200	3.580	0.340	0.010	0.350	0.240	2.090	0.280
Cu/Zr	0.041	0.714	1.849	2.258	3.750	1.019	1.857	0.287	0.041	0.060	0.034	0.033	0.412	0.130

Lieger, Riller and Gibson 2010[1] Continued															
	Granitoid					Quartzite/ Conglomerate	Quartzite								
	PT KuduA1	WR 518A2	PT 518A1	WR Average	PT Average	WR 6A4	WR 621A3	PT 621A2	PT 621A1	PT 2A2	WR 64A3	PT 64A1	WR 102A2	PT 102A1	PT 1A1
MgO	6.440	1.180	2.980	0.410	3.620	0.050	0.010	0.240	0.250	0.270	0.000	0.790	0.010	0.120	1.410
Cu/Zr	2.352	0.154	0.563	0.088	0.954	0.257	0.277	0.100	0.111	0.217	0.157	0.127	0.051	0.112	0.235

	Lieger, Riller and Gibson 2010[1] Continued							McIver et al 1981			Lana et al. 2004				
	Quartzite			Alkali Granite		Epidiorite		Mafic Rock		Mafic Rock WR	Gneiss (amphibolite facies) Trondhjemite NE-Part				
	PT 1A2	Average WR	Average PT	WR 4A2	PT 4A1	WR 564A2	PT 564A1	WR	WR	Average	ABBG-1	ABBG-2	ABBG-3	ABG-1	ABG-2
MgO	1.380	0.007	0.637	0.200	0.720	9.280	8.590	17.580	14.420	16.000	0.670	0.720	0.770	0.250	0.290
Cu/Zr	0.238	0.077	0.158	0.020	0.031	1.658	1.415	1.167	1.000	0.806	0.008	0.038	0.045	0.008	0.008

[1]It was discovered on July 28th 2016 that Lieger, D., Riller, U., and Gibson, R.L. 2010 was withdrawn at the request of the author(s).

Lana et al. 2004 Continued																
	Gneiss (amphibolite facies) Trondhjemite NE-Part				Porphyritic granodiorite W-Part				Gneiss (Granulite Facies) Quartz Diorite Central Part				Melanosomes Trondhjemite Outer Parts			
	ABP -1	ABP-2	ABP-3	Average	POR-1	POR-2	POR-3	Average	SCH-1	SCH-2	SCH-3	Average	SAG-1	SAG-2	EG6	VAL-1	Aver-age
MgO	0.280	0.310	0.320	0.451	0.540	0.600	0.550	0.563	0.520	0.460	0.500	0.493	0.600	0.630	0.120	0.180	0.383
Cu/Zr	0.011	0.011	0.011	0.018	0.009	0.009	0.008	0.009	0.036	0.014	0.011	0.021	0.010	0.010	0.162	0.010	0.053

Lana et al. 2004 Continued																
	Melanosomes Tonalite Central Parts				Mafic Granulites Central Parts				Leucosomes Granite Outer Parts						K-feldspar-rich Granite Transition Zone	
	vdf-4	vdf-1	vdf-8	Average	vdf2-12	vdf2-21	vdf2-2	Average	EG-4	EG-7	Pr12	RG9	SAL-1	Average	LEP-1	LEP-2
MgO	5.950	5.170	5.990	5.703	12.560	9.770	8.960	10.430	0.280	0.070	0.160	0.470	0.000	0.196	0.210	0.160
Cu/Zr	0.009	0.010	0.009	0.009	0.006	0.006	0.018	0.008	0.011	0.012	0.039	0.051	0.019	0.029	0.138	0.014

Lana et al. 2004 Continued											Remiold et al. 2000				
K-feldspar-rich Granite Transition Zone			Schlieric Granite Northern Parts				Homogen Granite Southwestern				Anne Rust Sheet				
	LEP-3	Average	SPW-1	SPW-2	ScSP W-3	Average	ESP-1	ESP-2	Average	Melanos ome Average	Mean IV	Mean III	Anna's Rust Sheet	Vredefort mafic complex	OCEAAN
MgO	0.170	0.180	0.040	0.020	0.060	0.040	0.000	0.000	0.000	2.663	6.310	6.590	6.520	6.880	6.750
Cu/Zr	0.013	0.061	0.015	0.015	0.015	0.015	0.015	0.016	0.016	0.032	0.878	0.705	0.886	0.092	0.895

[1]It was discovered on July 28th 2016 that Lieger, D., Riller, U., and Gibson, R.L. 2010 was withdrawn at the request of the author(s).

	Remiold et al. 2000 Continued				Coetzee et al. 2006			de Waal, Graham and Armstrong 2006				
	Anne Rust Sheet				Tholeiitic Intrusions			Lindeques drift and Heidelberg Intrusions				
	Core	CoreBH	Collar	SWBH	Wittekopjes norite	Parsons Rust Dol-Norite	Reebokkop dolerite	Lindeques Drift Contamspess	Lindeques Drift Even-grained spessartite mean	Lindeques Drift Porphyritic spessartite mean	LD spessartite Avg	Heidelberg Porphy-ritic spessartite mean
MgO	5.570	6.120	6.120	6.020	20.200	14.610	8.270	12.080	9.960	8.330	10.123	9.310
Cu/Zr	0.929	0.954	0.763	0.813	1.063	1.133	1.015	16.451	37.441	9.393	21.095	14.537

	de Waal, Graham and Armstrong 2006 Continued									Maier, Barnes and Marsh 2003		
	Lindeques drift and Heidelberg Intrusions									Bushveld Complex		
	Lindeques Drift Low-silica diorite mean	Lindeques Drift diorite mean	Lindeques Drift syeno-diorite mean	LD Diorite	Lindeques Drift feeder	Roodekraal Complex Lava	Roodekraal Complex Cumulate	Roodekraal Complex Diorite	Roodekraal Complex Avg.	Dominion Low Ti/V	Dominion High Ti/V	Loraine/ Edenville
MgO	4.720	3.850	1.870	3.480	4.660	3.370	7.570	2.850	4.597	9.070	5.260	10.970
Cu/Zr	1.739	1.832	0.256	1.275	0.239	2.507	4.886	2.760	3.384	0.790	0.450	0.950

	Maier, Barnes and Marsh 2003 Continued			
	Bushveld Complex			
	Hekpoort	Machadodorp	Bushveld Mg basalt	Average Bushveld Values
MgO	8.380	8.550	12.650	9.147
Cu/Zr	0.765	0.987	0.824	0.794

[1]It was discovered on July 28th 2016 that Lieger, D., Riller, U., and Gibson, R.L. 2010 was withdrawn at the request of the author(s).

Sudbury

Lightfoot et al. 1996													
	Main Mass Mafic Norite Average	Main Mass Felsic Norite Average	Main Mass Granophyre Average	Igneous textured sublayer matrix Whistle Mine Average	Melanorite Pod or Inclusion Whistle Mine Average	Olivine Melanorite Whistle Mine Average	Diabase Whistle Mine Average	Little Stobie Mine Igneous Textured Sublayer Matrix		Crean Hill Mine Igneous Textured Sublayer Matrix			
								93PCL-001	93PCL-001	93PCL-20	93PCL-22	93PCL-23	93PCL-25
MgO	10.610	4.950	1.230	7.730	10.510	18.090	6.000	8.570	6.790	5.760	6.670	6.080	6.710
Cu/Zr	3.168	1.157	0.114	7.080	7.167	4.903	3.412	7.326	3.778	3.008	2.030	0.861	5.378

Lightfoot et al. 1996 Continued															
	Levack West Mine Igneous Textured Sublayer Matrix		Levack West Mine Melanorite Pod or Inclusion			McCreedy West Mine Igneous Textured Sublayer Matrix					Fraser Mine Igneous Textured Sublayer Matrix				
	93PCL-45	93PCL-46	93PCL-66	93PCL-67	93PCL-68	93PCL-50	93PCL-51	93PCL-53	93PCL-55	93PCL-59	93PCL-342	93PCL-343	93PCL-344	92PCL-345	93PCL-346
MgO	9.520	13.290	16.030	26.000	25.100	9.930	10.920	9.830	10.000	9.110	8.470	9.890	10.130	11.520	10.580
Cu/Zr	1.513	14.729	4.264	14.291	22.625	6.958	2.674	2.375	11.032	4.647	1.384	2.688	2.461	2.853	3.654

Lightfoot et al. 1996 Continued				Lightfoot et al. 2001				
Creighton Mine Igneous Textured Sublayer Matrix				Mafic Norite Average	Felsic Norite Average	Quartz Gabbro Average	Granophyre Average	Main Mass Average
	94PCL-128	94PCL-131	94PCL-132					
MgO	11.030	6.440	8.380	13.700	5.200	2.900	1.200	3.700
Cu/Zr	4.091	25.437	20.725	6.625	0.227	0.107	0.051	0.245

[1]It was discovered on July 28th 2016 that Lieger, D., Riller, U., and Gibson, R.L. 2010 was withdrawn at the request of the author(s).

Namaqualand

Duchesne et al. 2007														
	Anorthosites				Tonalite	Leuconorite				Norite Sample 85b				
	Sample 70[b]	Sample 66	Sample 108	Average	Sample 30[a]	Sample 119	Sample 120	Sample 121	Average	Sample 85[b]	Sample 86[b]	Sample 116	Sample 122	Average
MgO	0.410	0.660	0.980	0.683	0.150	3.700	2.580	1.910	2.730	8.040	9.130	5.260	7.690	7.530
Cu/Zr	3.407	38.346	3.831	15.195	1.143	32.600	226.105	3.605	87.437	744.063	13.621	11.952	10.087	194.931

Duchesne et al. 2007 Continued											
	Melanorite				Hypersthenite			Glimmerite	Magnetite		
	Sample 88[b]	Sample 87[b]	Sample 110	Average	Sample 90[b]	Sample 117	Average	Sample 123	Sample 82[b]	Sample 125[b]	Average
MgO	16.700	14.820	12.090	14.537	20.410	19.000	19.705	17.500	11.480	11.390	11.435
Cu/Zr	999.294	330.268	102.456	477.339	168.714	1046.291	607.503	603.667	2.395	405.806	204.100

Duchesne et al. 2007 Continued							
Biotite Diorite							
	Sample 78[b]	Sample 112	Sample 109	Sample 114	Sample 118	Sample 126	Average
MgO	2.670	3.110	1.550	2.320	7.110	4.830	3.598
Cu/Zr	12.683	0.344	2.036	0.060	29.600	5.946	8.445

[1]It was discovered on July 28th 2016 that Lieger, D., Riller, U., and Gibson, R.L. 2010 was withdrawn at the request of the author(s).

Morokweng

Andreoli et al. 1999												
	Medium Grained Quartz Norite							Medium Grained Quartz Norite	Heterogeneous Quartz Norite			
	N-5	LA-137	N-4	LA-141	LA-161	N-3	Average	LA-172	LA-174	N-2	LA-186	Average
MgO	4.050	3.710	3.930	3.920	3.150	4.040	3.800	3.580	2.360	3.810	3.150	3.107
Cu/Zr	0.196	0.418	0.167	0.339	0.280	0.244	0.274	0.263	0.305	0.214	0.400	0.306

Andreoli et al. 1999 Continued							
	Fine Grained Quartz Norite					Chilled Quartz Norite	Quartz Norite Mean
	N-1	LA-197	LA-213	LA-216	Average	LA-224	
MgO	4.880	4.700	4.500	3.860	4.485	3.680	3.820
Cu/Zr	0.395	0.595	0.463	0.339	0.448	0.333	0.328

[1]It was discovered on July 28th 2016 that Lieger, D., Riller, U., and Gibson, R.L. 2010 was withdrawn at the request of the author(s).

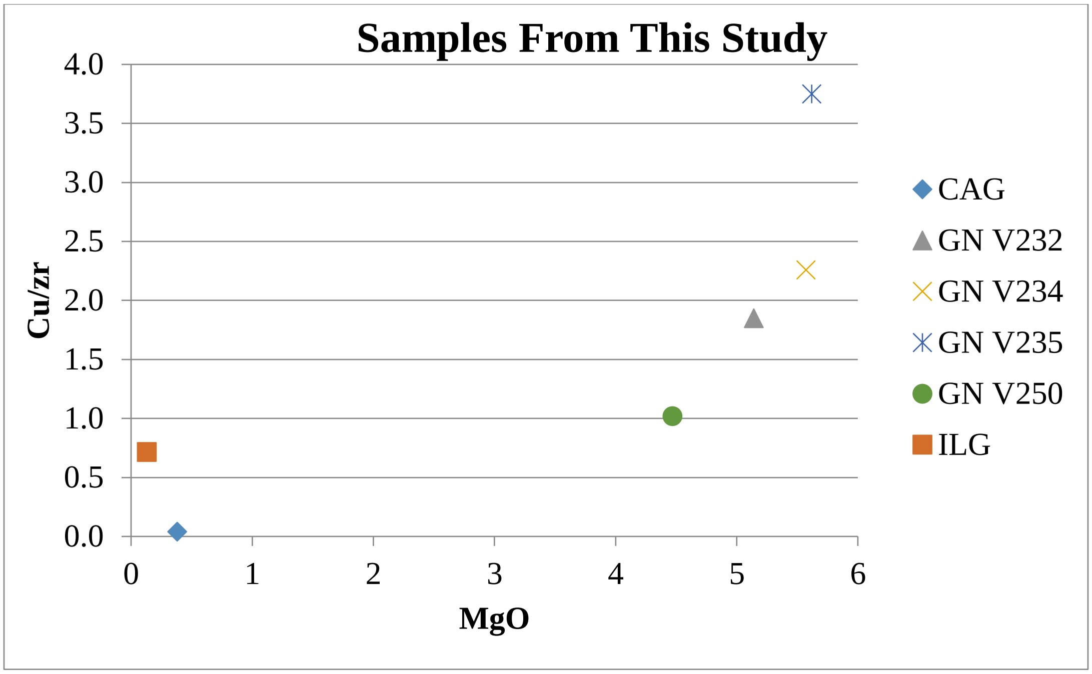

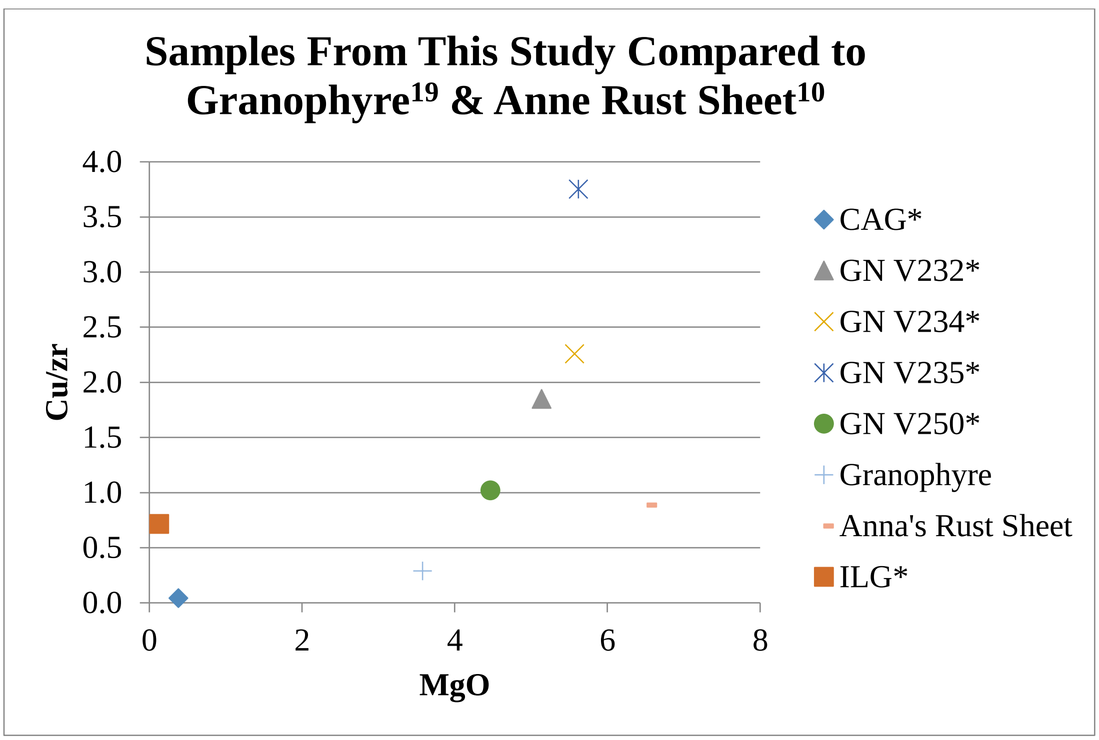

[1]It was discovered on July 28th 2016 that Lieger, D., Riller, U., and Gibson, R.L. 2010 was withdrawn at the request of the author(s).
*The Central Anatectic Granite (CAG), Gabbronorite (GN Average) and Inlandsee Leucogranofels (ILG) are samples from this study.

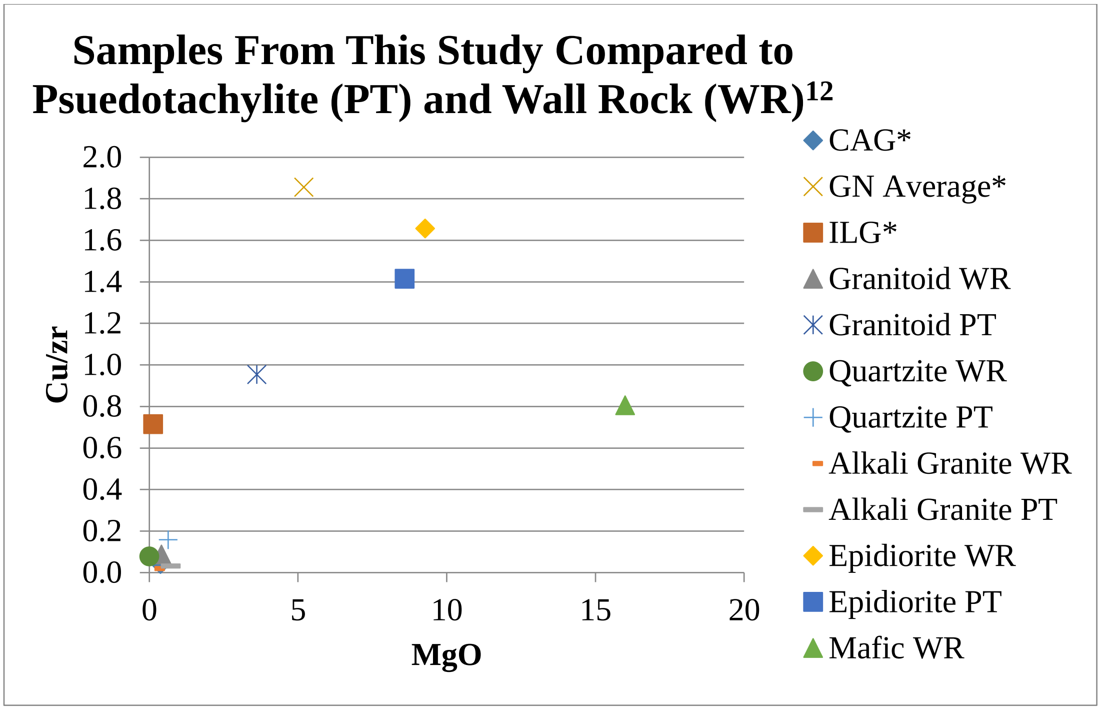

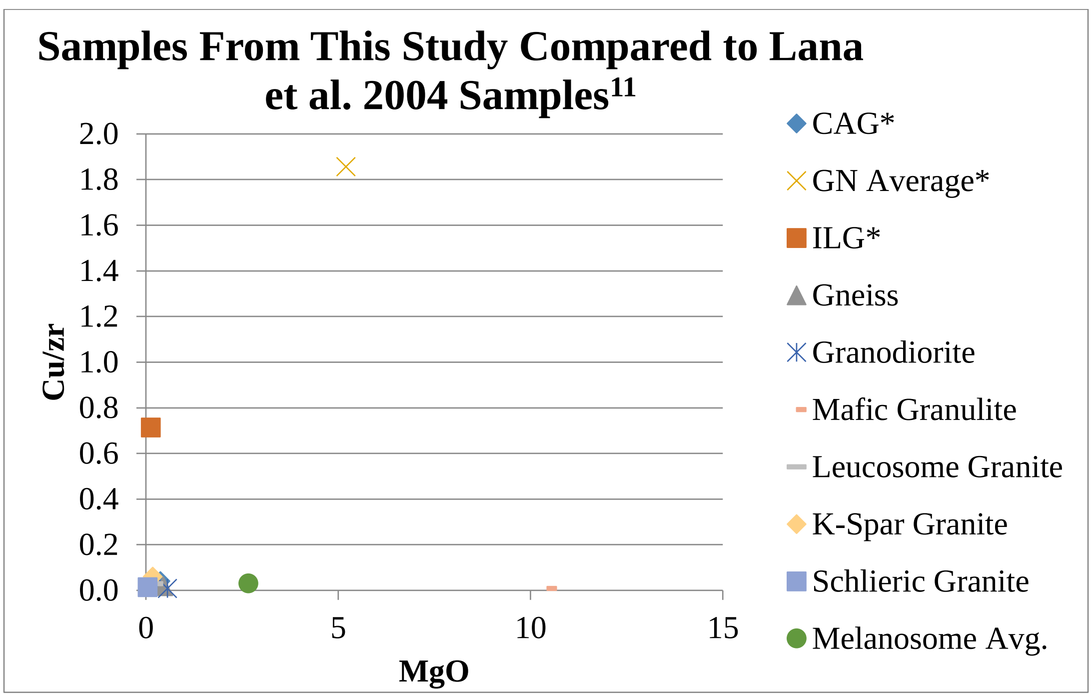

[1]It was discovered on July 28th 2016 that Lieger, D., Riller, U., and Gibson, R.L. 2010 was withdrawn at the request of the author(s).

*The Central Anatectic Granite (CAG), Gabbronorite (GN Average) and Inlandsee Leucogranofels (ILG) are samples from this study.

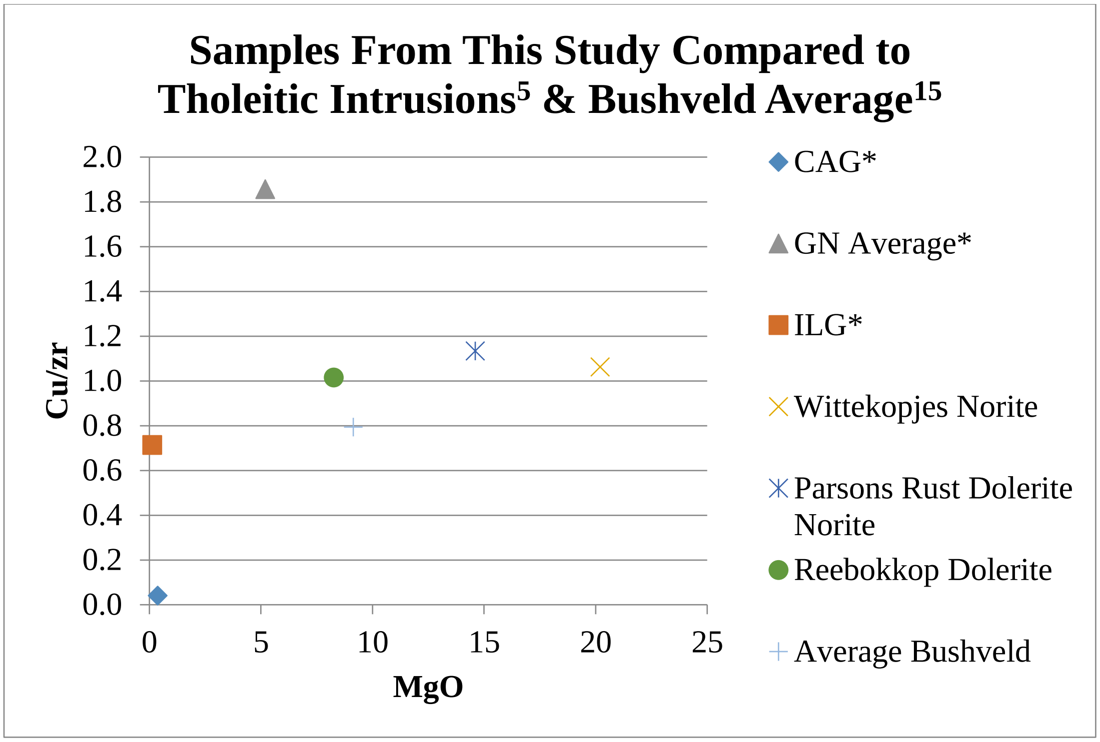

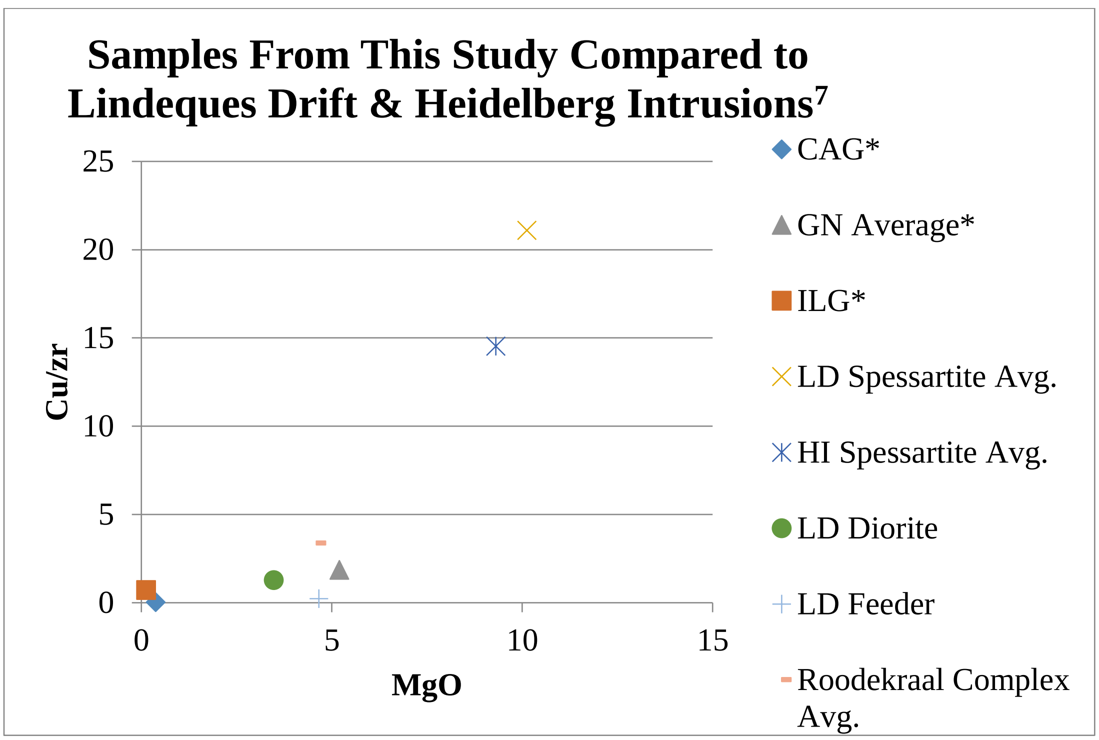

[1]It was discovered on July 28th 2016 that Lieger, D., Riller, U., and Gibson, R.L. 2010 was withdrawn at the request of the author(s).
*The Central Anatectic Granite (CAG), Gabbronorite (GN Average) and Inlandsee Leucogranofels (ILG) are samples from this study.

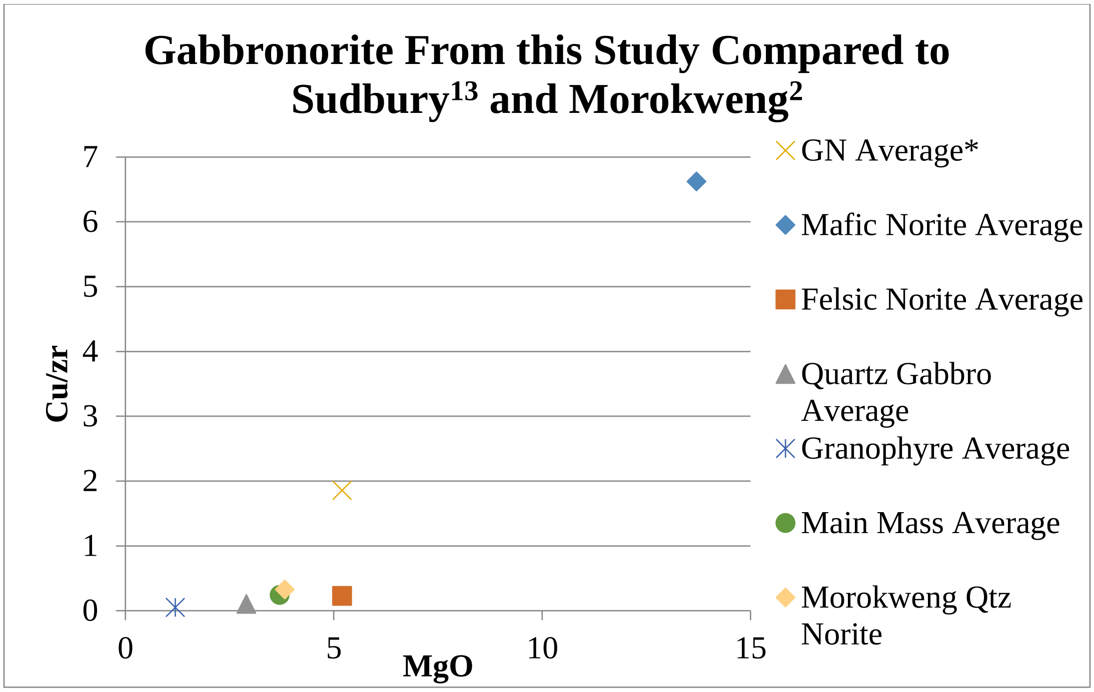

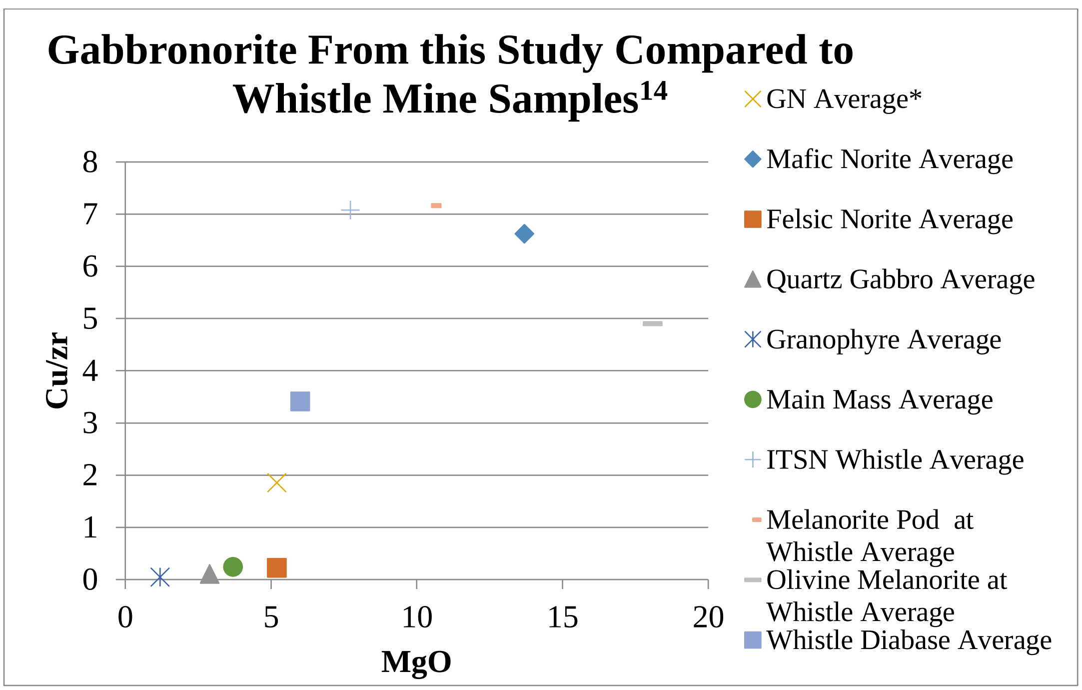

[1]It was discovered on July 28th 2016 that Lieger, D., Riller, U., and Gibson, R.L. 2010 was withdrawn at the request of the author(s).
*The Central Anatectic Granite (CAG), Gabbronorite (GN Average) and Inlandsee Leucogranofels (ILG) are samples from this study.

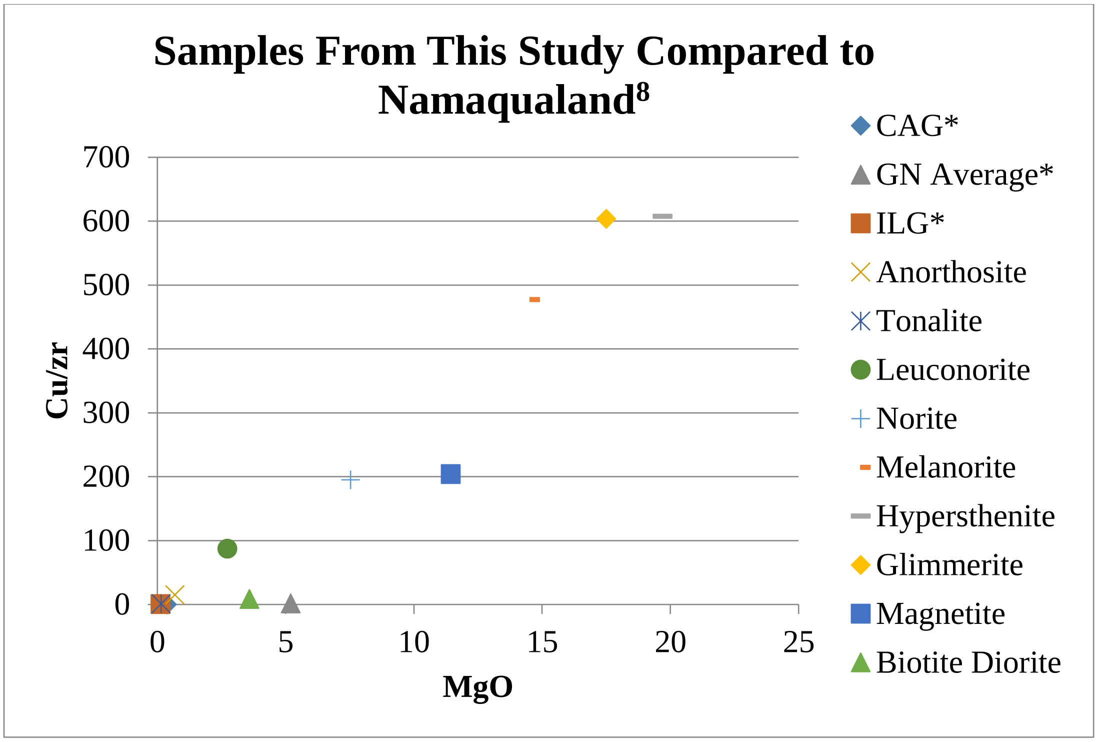

[1]It was discovered on July 28th 2016 that Lieger, D., Riller, U., and Gibson, R.L. 2010 was withdrawn at the request of the author(s).
*The Central Anatectic Granite (CAG), Gabbronorite (GN Average) and Inlandsee Leucogranofels (ILG) are samples from this study.

Appendix B-1-5: MgO vs Cr Comparison Table and Plots

Vredefort

	Samples from this Study							Koeberl, Reimold and Shirey 1996					
	CAG	ILG	Gabbro Norite					Witwatersrand Shale	Ventersdorp Andesitic			OGG	Wits Siltstone clase in Granophyre
	VO9-111	VO9-238	VO9-232	VO9-234	VO9-235	VO9-250	Average	VG-SNE	UP-61	UP-63	Average	OT-1	BG-S1
MgO	0.38	0.13	5.14	5.57	5.62	4.47	5.20	0.72	4.53	6.19	5.36	1.90	0.50
Cr	20.00	20.00	50.00	110.00	120.00	20.00	93.33	142.00	121.00	223.00	172.00	205.00	138.00

	Koeberl, Reimold and Shirey 1996 Continued						Reimold & Gibson Chemie der Erde 66 2006	Lieger, Riller and Gibson 2010[1]							
	Vredefort Granophyre						Vredefort Granophyre	Granitoid							
	BG-4	BG-7	BG-9	BG-10	BG-168	average	Granophyre with outliers	WR 669A3	WR 200C2	PT 200C1	WR 453A2	PT 453A1	WR KuduA3	PT KuduA2	
MgO	3.50	3.50	3.40	3.40	3.70	3.50	3.58	0.34	0.01	0.35	0.24	2.09	0.28	6.24	
Cr	429.00	424.00	419.00	425.00	428.00	425.00	350.20	144.00	138.00	149.00	104.00	165.00	186.00	182.00	

	Lieger, Riller and Gibson 2010[1] Continued													
	Granitoid					Quartzite/ Conglomerate	Quartzite							
	PT KuduA1	WR 518A2	PT 518A1	WR Average	PT Average	WR 6A4	WR 621A3	PT 621A2	PT 621A1	PT 2A2	WR 64A3	PT 64A1	WR 102A2	PT102A1
MgO	6.44	1.18	2.98	0.41	2.32	0.05	0.01	0.24	0.25	0.27	0.00	0.79	0.01	0.12
Cr	192.00	1626.00	107.00	439.60	159.00	309.00	342.00	468.00	478.00	382.00	559.00	1069.00	2282.00	422.00

[1]It was discovered on July 28th 2016 that Lieger, D., Riller, U. and Gibson, R.L. 2010 was withdrawn at the request of the author(s).

	Lieger, Riller and Gibson 2010[1] Continued								Reimold 1991				McIver et al 1981	
	Quartzite				Alkali Granite		Epidiorite		Gabbro		Norite		Mafic Rock	
	PT 1A1	PT 1A2	Average WR	Average PT	WR 4A2	PT 4A1	WR 564A2	PT 564A1	WR	PT	WR	PT	WR	WR
MgO	1.41	1.38	0.01	0.60	0.20	0.72	9.28	8.59	6.00	6.10	9.30	7.30	17.58	14.42
Cr	656.00	546.00	1061.00	574.43	137.00	171.00	985.00	854.00	338.00	331.00	138.00	85.00	1982.00	1867.00

						Crow and Condie 1988						
	Alkali Granite WR	Alkali Granite PT	Epidote PT	Gabbro PT	Mafic Rock WR	Porphyritic lava	Basaltic Andesite	Felsic Porphyritic Lava	Porphyritic Basaltic Andesite	Basalt	Basalt	
	Average	Average	Average	Average	Average	Pniel Group Allanridge	Platberg Group Reitgat	Platberg Group Makwassie	Platberg Group Goedgenoeg	Platberg Group Average	Klipriviersberg Group Edenville	Klipriviersberg Group Loraine
MgO	0.17	0.64	8.32	9.03	12.31	3.83	4.37	2.51	5.6	4.985	10.52	7.47
Cr	137.00	171.00	854.00	331.00	1924.50	15	199	19	175	187	1017	323

	Crow and Condie 1988 Continued				Wronkiewicz and Condie 1990						
	Basalt				Pelites & Shales						
	Klipriviersberg Group Jeannette	Klipriviersberg Group Orkney	Klipriviersberg Group Westonaria	Klipriviersberg Average	Average Bothaville Formation P&S	Average Selati Formation P&S	Average Black Reef Formation P&S	Average Timeball Hill Formation P&S	Average Strubenkop Formation P&S	Average Silverton Formation P&S	NASC P&S
MgO	4.9	5.3	13.97	8.432	4.98	3.71	4.44	1.78	1.35	2.74	2.85
Cr	20	54	1616	606	579	447	421	140	174	141	125

[1]It was discovered on July 28th 2016 that Lieger, D., Riller, U. and Gibson, R.L. 2010 was withdrawn at the request of the author(s).

Wronkiewicz and Condie 1990 Continued													
	Quartzite	Quartzite	Quartzite	Quartzite	Quartzite	Quartzite	Quartzite	Quartzite		Quartzite	Quartzite	Quartzite	
	Bothaville Formation Quartzite C6	Sekororo Formation Quartzite D53	Sekororo Formation Quartzite D36	Sekororo Formation Quartzite D47	Average Sekororo Formation Quartzite D47	Selati Formation Quartzite D35	Black Reef Quartzite D34	Black Reef Quartzite C201	Average Black Reef Quartzite C201	Rooihoogte Formation Quartzite C76	Daspoort Formation Quartzite C81	Daspoort Formation Quartzite M8F-2-10	Average Daspoort Formation Quartzite M8F-2-10
MgO	0.59	0.41	1.51	1.36	1.093	2.04	0.27	0.22	0.245	0.23	0.32	0.73	0.52
Cr	25	10	11	16	12.33	59	22	14	18	25	9.9	30	19.95

Wronkiewicz and Condie 1990 Continued					Lana et al. 2004								
	Quartzite	Quartzite		Quartzite	Gneiss (amphibolite facies) Trondhjemite NE-Part								
	Magaliesberg Formation Quartzite C207	Magaliesberg Formation Quartzite D77	Average Magaliesberg Formation Quartzite D77	Rayton Formation Quartzite C56	ABBG-1	ABBG-2	ABBG-3	ABG-1	ABG-2	ABP-1	ABP-2	ABP-3	Average
MgO	0.44	4.3	2.37	0.17	0.67	0.72	0.77	0.25	0.29	0.28	0.31	0.32	0.45
Cr	7.6	97	52.3	4	20	25	26	10	14	14	14	12	16.87

Lana et al. 2004 Continued															
Porphyritic granodiorite W-Part					Gneiss (Granulite Facies) Quartz Diorite Central Part				Melanosomes Trondhjemite Outer Parts					Melanosomes Tonalite Central Parts	
	POR-1	POR-2	POR-3	Average	SCH-1	SCH-2	SCH-3	Average	SAG-1	SAG-2	EG6	VAL-1	Average	vdf-4	vdf-1
MgO	0.54	0.6	0.55	0.56	0.52	0.46	0.5	0.49333	0.6	0.63	0.12	0.18	0.615	5.95	5.17
Cr	14	11	12	12.33	13.3	11.6	3.93	9.61	28	30	11	14	20.75	19.4	24

[1]It was discovered on July 28th 2016 that Lieger, D., Riller, U. and Gibson, R.L. 2010 was withdrawn at the request of the author(s).

Lana et al. 2004 Continued																
Melanosomes Tonalite Central Parts			Mafic Granulites Central Parts				Leucosomes Granite Outer Parts						K-feldspar-rich Granite Transition Zone			
	vdf-8	Average	vdf2-12	vdf2-21	vdf2-2	Average	EG-4	EG-7	Pr12	RG9	SAL-1	Average	LEP-1	LEP-2	LEP-3	Average
MgO	5.99	5.70	12.56	9.77	8.96	10.43	0.28	0.07	0.16	0.47	0	0.164	0.21	0.16	0.17	0.18
Cr	9	17.47	9	9	5.65	7.88	9	9	8	15	10	10.2	110	23	8.38	47.13

Lana et al. 2004 Continued					Hart et al 1990	Remiold et al. 2000								
Schlieric Granite Northern Parts					Ultramafics	Anne Rust Sheet								
	SPW-1	SPW-2	ScSPW-3	Average	Avg. Beta -1	Mean IV	Mean III	Anna's Rust Sheet	Vredefort mafic complex	OCEAAN	Core	CoreBH	Collar	SWBH
MgO	0.04	0.02	0.06	0.04	36.63	6.31	6.59	6.52	6.88	6.75	5.57	6.12	6.12	6.02
Cr	9	9	15	11	1028	151	203	135	165	180	249	116	144	111

Coetzee et al. 2006							de Waal, Graham and Armstrong 2006				
Tholeiitic Intrusions				Mafic Dykes and sills			Lindeques drift and Heidelberg Intrusions				
	Wittekopjes norite	Parsons Rust Dol-Norite	Reebokkop dolerite	Bushveld micopyroxenitic sills	Bushveld Ultramafic Sills	Noritic sills and dykes E Witts	Lindeques Drift Contamspess	Lindeques Drift Even-grained spessartite mean	Lindeques Drift Porphyritic spessartite mean	Lindeques Drift Spessarite Average	Heidelberg Porphy-ritic spess mean
MgO	20.2	14.61	8.27	13	32.1	11	12.08	9.96	8.33	10.12	9.31
Cr	3669	2045	685	1104	5843	1034	50	74.4	47.1	57.17	167

[1]It was discovered on July 28th 2016 that Lieger, D., Riller, U. and Gibson, R.L. 2010 was withdrawn at the request of the author(s).

	de Waal, Graham and Armstrong 2006 Continued								Maier, Barnes and Marsh 2003			
	Lindeques drift and Heidelberg Intrusions								Bushveld Complex			
	Lindeques Drift Low-silica diorite mean	Lindeques Drift syeno-diorite mean	Lindeques Diorite Average	Lindeques Drift feeder	Roodekraal Complex Lava	Roodekraal Complex Cumulate	Roodekraal Complex Diorite	Roodekraal Complex Average	Dominion Low Ti/V	Dominion High Ti/V	Loraine/ Edenville	Hekpoort
MgO	4.72	1.87	3.29	4.66	3.37	7.57	2.85	4.60	9.07	5.26	10.97	8.38
Cr	46.5	4	25.25	110	70	74	15	53	997	43	1242	791

	Maier, Barnes and Marsh 2003 Continnued		
	Bushveld Complex		
	Machadodorp	Bushveld Mg basalt	Average Bushveld Values
MgO	8.55	12.65	9.15
Cr	302	950	720.83

[1]It was discovered on July 28th 2016 that Lieger, D., Riller, U. and Gibson, R.L. 2010 was withdrawn at the request of the author(s).

Sudbury

Lightfoot et al 1996													
	Main Mass Mafic Norite Average	Main Mass Felsic Norite Average	Main Mass Granophyre Average	Igneous textured sublayer matrix Whistle Mine Average	Melanorite Pod or Inclusion Whistle Mine Average	Olivine Melanorite Whistle Mine Average	Diabase Whistle Mine Average	Little Stobie Mine Igneous Textured Sublayer Matrix		Crean Hill Mine Igneous Textured Sublayer Matrix			
								93PCL-001	93PCL-001	93PCL-20	93PCL-22	93PCL-23	93PCL-25
MgO	10.61	4.95	1.23	7.73	10.51	18.09	6	8.57	6.79	5.76	6.67	6.08	6.71
Cr	1690	213	6	407	767	1409	125	567	363	308	374	314	642

Lightfoot et al 1996 Continued															
	Levack West Mine Igneous Textured Sublayer Matrix		Levack West Mine Melanorite Pod or Inclusion			McCreedy West Mine Igneous Textured Sublayer Matrix					Fraser Mine Igneous Textured Sublayer Matrix				
	93PCL-45	93PCL-46	93PCL-66	93PCL-67	93PCL-68	93PCL-50	93PCL-51	93PCL-53	93PCL-55	93PCL-59	93PCL-342	93PCL-343	93PCL-344	92PCL-345	93PCL-346
MgO	9.52	13.29	16.03	26	25.1	9.93	10.92	9.83	10	9.11	8.47	9.89	10.13	11.52	10.58
Cr	1406	1295	1849	3223	3109	1036	1033	959	1563	843	1413	1431	1582	1677	1636

Lightfoot et al 1996 Continued			
	Creighton Mine Igneous Textured Sublayer Matrix		
	94PCL-128	94PCL-131	94PCL-132
MgO	11.03	6.44	8.38
Cr	458	591	365

[1]It was discovered on July 28th 2016 that Lieger, D., Riller, U. and Gibson, R.L. 2010 was withdrawn at the request of the author(s).

Namaqualand

Duchesne et al. 2007														
	Anorthosites				Tonalite	Leuconorite				Norite Sample 85b				
	Sample 70[b]	Sample 66	Sample 108	Average	Sample 30[a]	Sample 119	Sample 120	Sample 121	Average	Sample 85[b]	Sample 86[b]	Sample 116	Sample 122	Average
MgO	0.41	0.66	0.98	0.68	0.15	3.7	2.58	1.91	2.73	8.04	9.13	5.26	7.69	7.53
Cr	110	27	12	49.67	4.6	22	26	50	32.67	555	438	413	508	478.5

Duchesne et al. 2007 Continued														
	Melanorite				Hypersthenite			Glimmerite	Magnetite			Biotite Diorite		
	Sample 88[b]	Sample 87[b]	Sample 110	Average	Sample 90[b]	Sample 117	Average	Sample 123	Sample 82[b]	Sample 125[b]	Average	Sample 78[b]	Sample 112	Sample 109
MgO	16.7	14.82	12.09	14.5367	20.41	19	19.705	17.5	11.48	11.39	11.44	2.67	3.11	1.55
Cr	2769	2265	93	1709	2213	3508	2860.5	2383	239	1023	631	123	5	33

Duchesne et al. 2007 Continued				
	Biotite Diorite			
	Sample 114	Sample 118	Sample 126	Average
MgO	2.32	7.11	4.83	3.60
Cr	13	161	189	87.33

[1]It was discovered on July 28th 2016 that Lieger, D., Riller, U. and Gibson, R.L. 2010 was withdrawn at the request of the author(s).

Morokweng

Andreoli et al. 1999																
Medium Grained Quartz Norite							Medium Grained Quartz Norite	Heterogeneous Quartz Norite			Fine Grained Quartz Norite				Chilled Quartz Norite	Quartz Norite Mean
	N-5	LA-137	N-4	LA-141	LA-161	N-3	LA-172	LA-174	N-2	LA-186	N-1	LA-197	LA-213	LA-216	LA-224	
MgO	4.05	3.71	3.93	3.92	3.15	4.04	3.58	2.36	3.81	3.15	4.88	4.7	4.5	3.86	3.68	3.82
Cr	427	415	415	415	333	414	398	208	292	234	306	315	384	430	385	358

[1]It was discovered on July 28th 2016 that Lieger, D., Riller, U. and Gibson, R.L. 2010 was withdrawn at the request of the author(s).

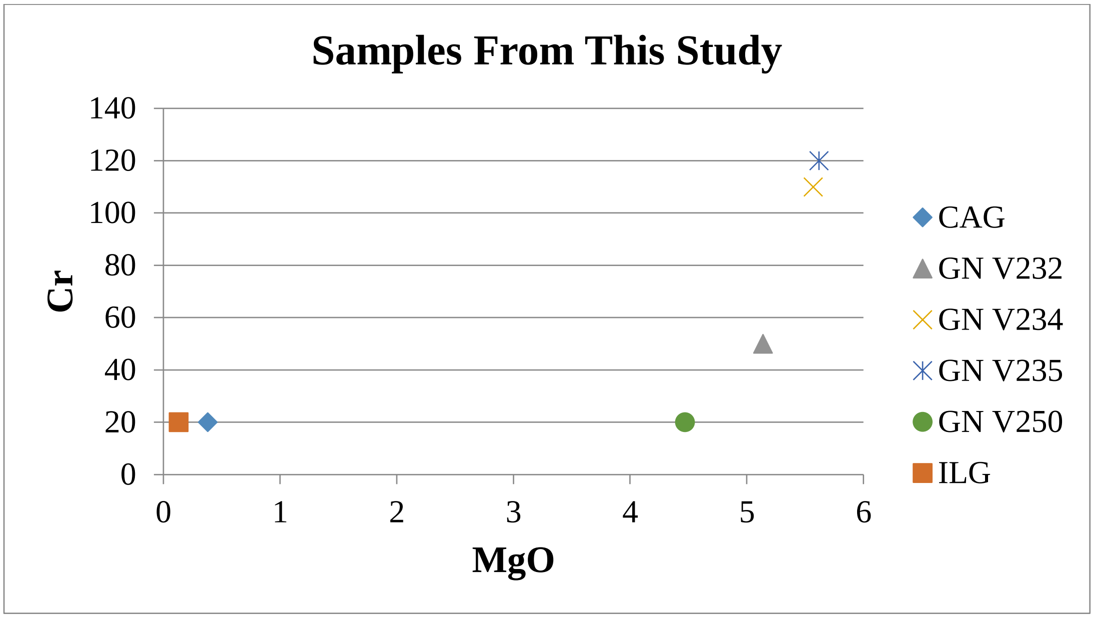

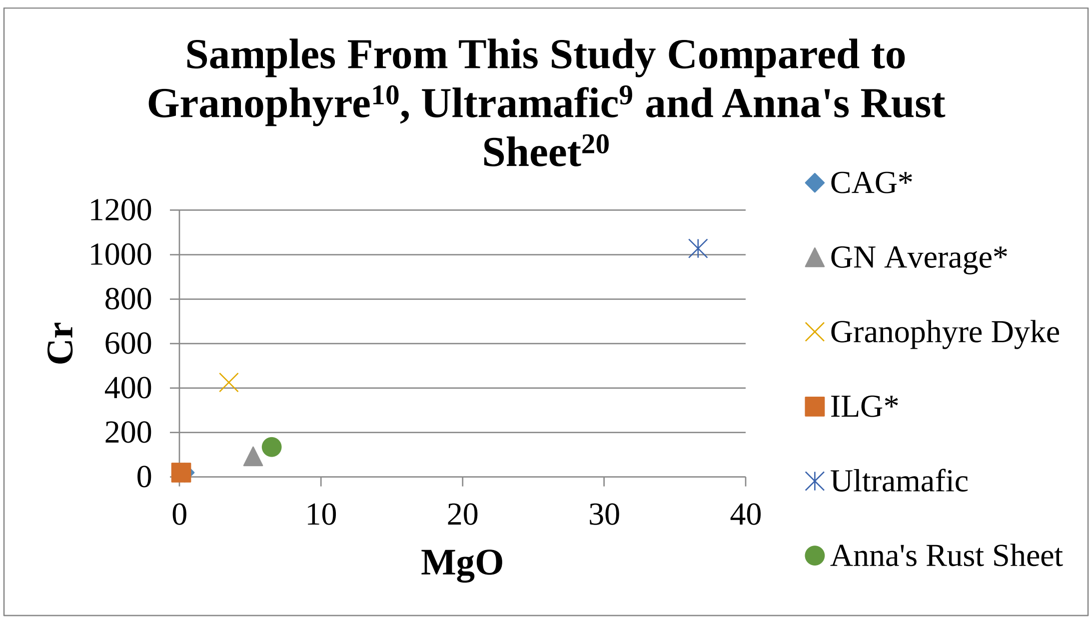

[1]It was discovered on July 28th 2016 that Lieger, D., Riller, U. and Gibson, R.L. 2010 was withdrawn at the request of the author(s).
*The Central Anatectic Granite (CAG), Gabbronorite (GN Average) and Inlandsee Leucogranofels (ILG) are samples from this study.

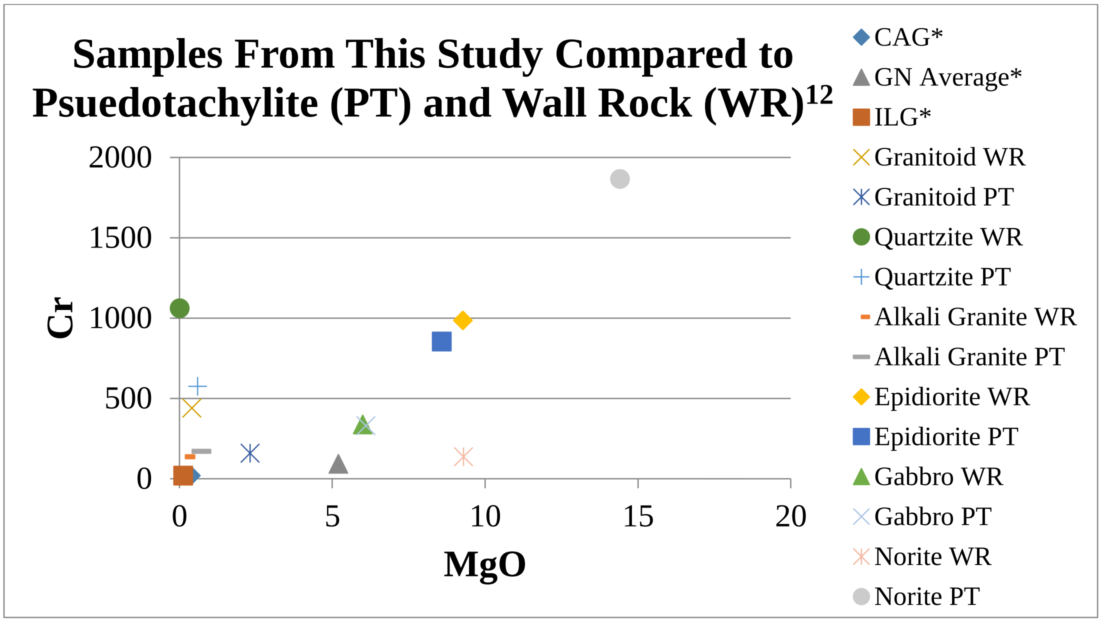

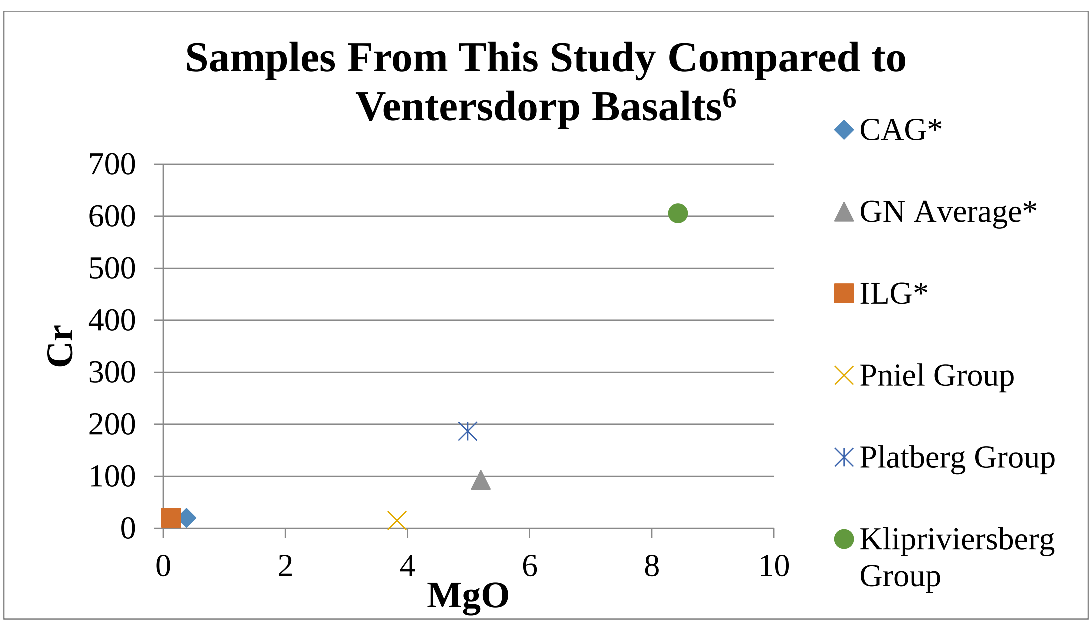

[1]It was discovered on July 28th 2016 that Lieger, D., Riller, U. and Gibson, R.L. 2010 was withdrawn at the request of the author(s).
*The Central Anatectic Granite (CAG), Gabbronorite (GN Average) and Inlandsee Leucogranofels (ILG) are samples from this study.

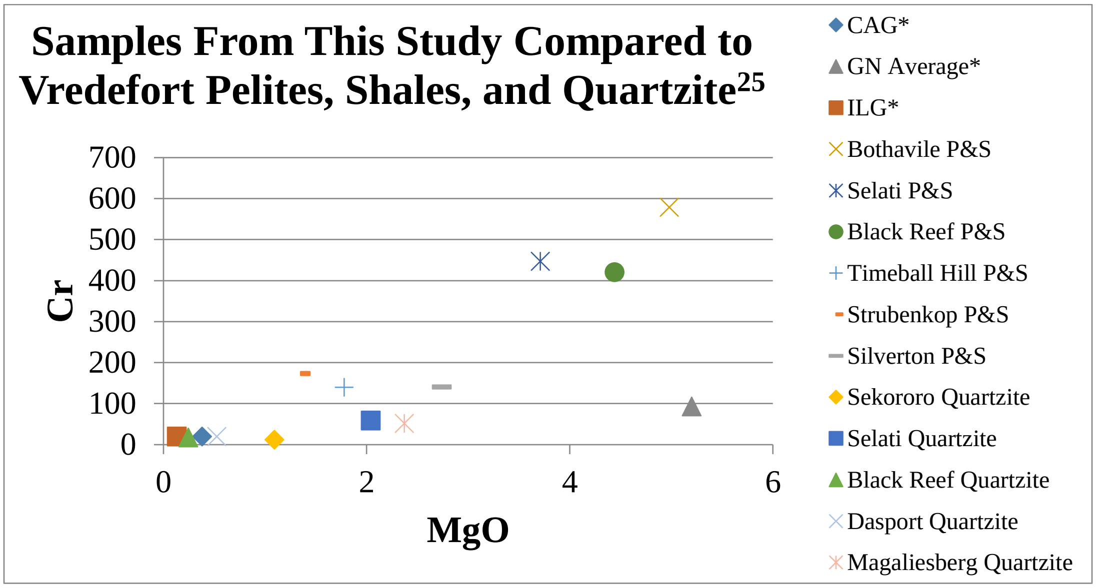

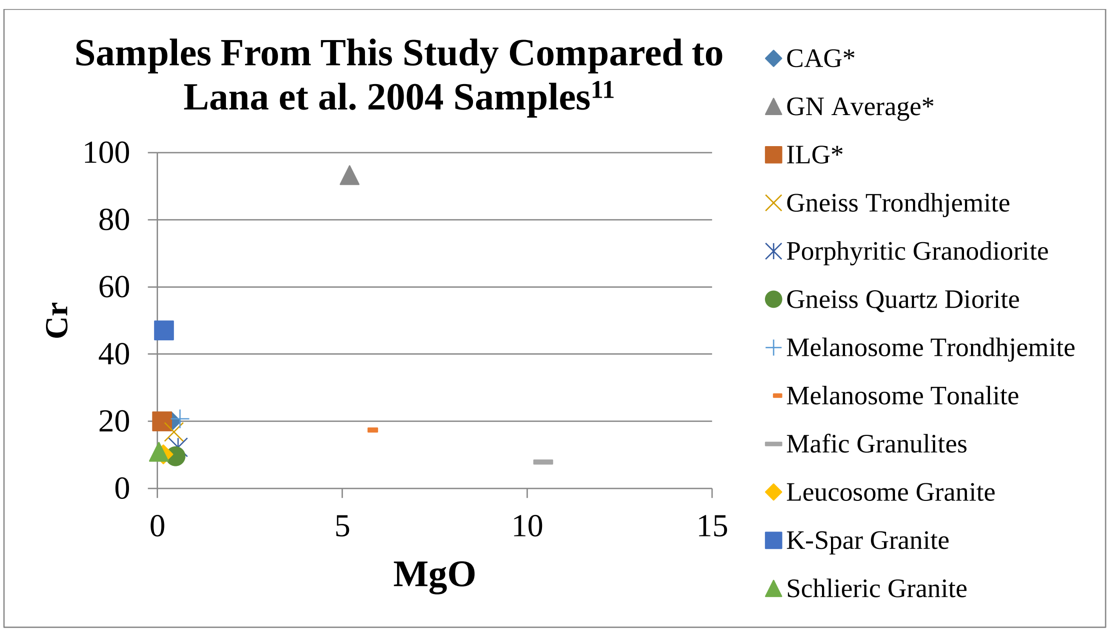

[1]It was discovered on July 28th 2016 that Lieger, D., Riller, U. and Gibson, R.L. 2010 was withdrawn at the request of the author(s).
*The Central Anatectic Granite (CAG), Gabbronorite (GN Average) and Inlandsee Leucogranofels (ILG) are samples from this study.

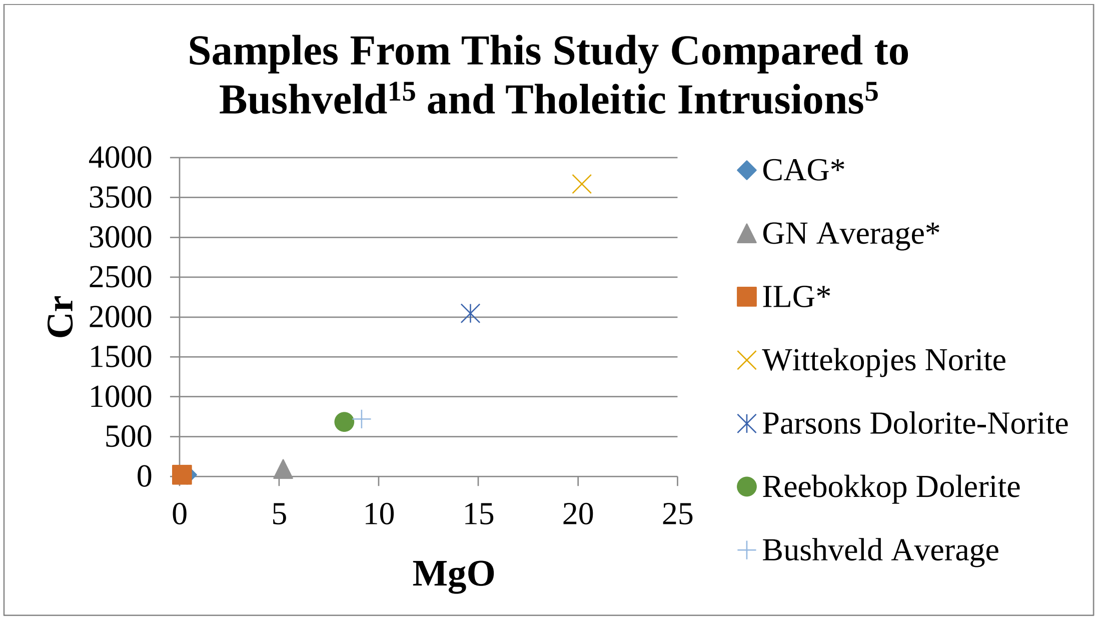

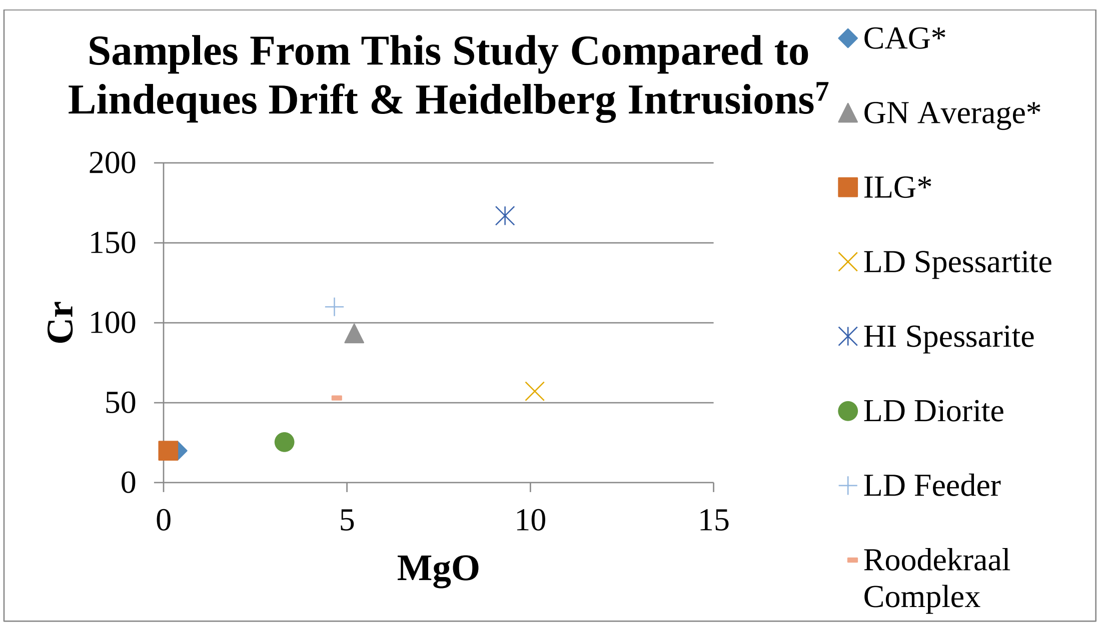

[1]It was discovered on July 28th 2016 that Lieger, D., Riller, U. and Gibson, R.L. 2010 was withdrawn at the request of the author(s).
*The Central Anatectic Granite (CAG), Gabbronorite (GN Average) and Inlandsee Leucogranofels (ILG) are samples from this study.

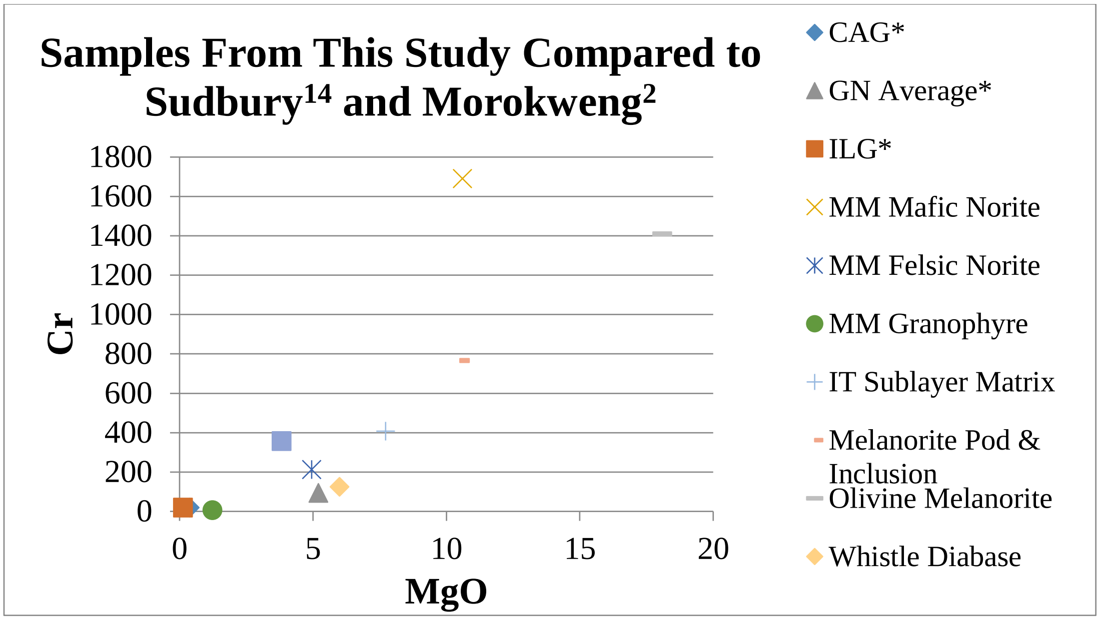

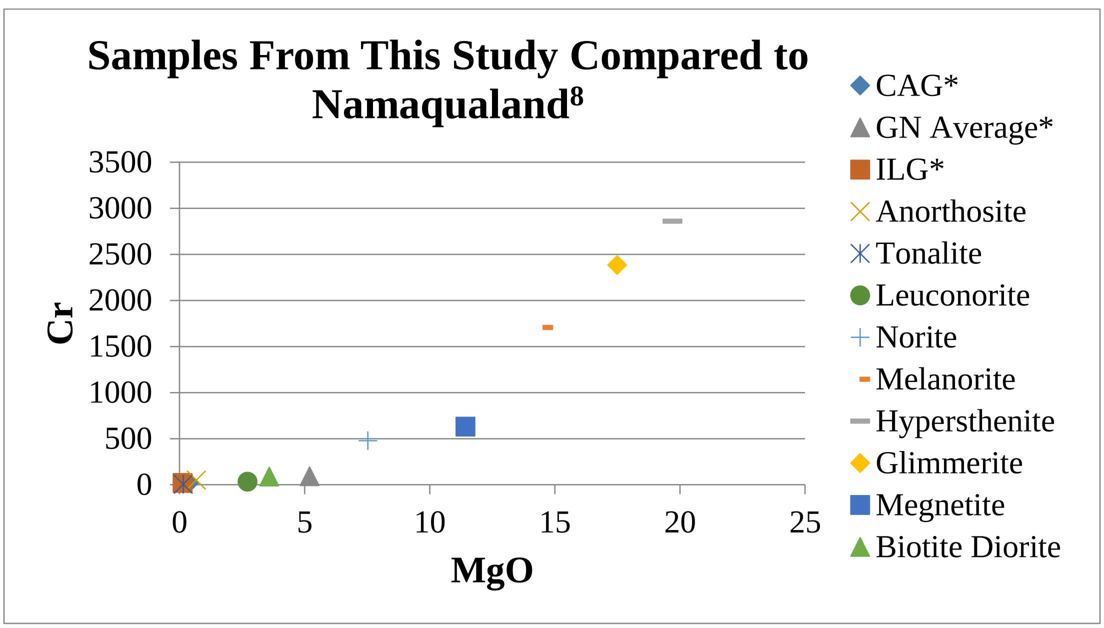

[1]It was discovered on July 28th 2016 that Lieger, D., Riller, U. and Gibson, R.L. 2010 was withdrawn at the request of the author(s).
*The Central Anatectic Granite (CAG), Gabbronorite (GN Average) and Inlandsee Leucogranofels (ILG) are samples from this study.

Appendix B-1-6: Ce/Yb vs Th/Nb Comparison Table and Plots

Vredefort

	Samples from this study							Koeberl, Reimold and Shirey 1996				Reimold & Gibson 2006
	CAG	ILG	Gabbro Norite					Witwatersrand Shale	Ventersdorp Andesitic			Vredefort Granophyre
	VO9-111	VO9-238	VO9-232	VO9-234	VO9-235	VO9-250	Average	VG-SNE	UP-61	UP-63	Average	Granophyre with outliers
Ce/Yb	50.16	170	7.88	7.53	7.23	7.41	7.53	15.90	19.18	13.61	16.63	43.95
Th/Nb	1.09	0.23	0.03	0.05	0.03	0.02	0.03	0.48	0.35	0.35	0.35	0.89

	Crow and Condie 1988									
	Porphyritic lava	Basaltic Andesite	Felsic Porphyritic Lava	Porphyritic Basaltic Andesite	Basalt	Basalt				
	Pniel Group Allanridge	Platberg Group Reitgat	Platberg Group Makwassie	Platberg Group Goedgenoeg	Platberg Group Average	Klipriviersberg Group Edenville	Klipriviersberg Group Loraine	Klipriviersberg Group Jeannette	Klipriviersberg Group Orkney	Klipriviersberg Average
Ce/Yb	28.37	32.86	35.25	30.71	31.79	10.62	13.19	15.29	17.31	14.92
Th/Nb	0.30	0.13	0.42	0.13	0.13	0.30	0.39	0.40	0.38	0.37

	Wronkiewicz and Condie 1990											
	Pelites & Shales							Quartzite	Quartzite	Quartzite	Quartzite	Quartzite
	Average Bothaville Formation P&S	Average Selati Formation P&S	Average Black Reef Formation P&S	Average Timeball Hill Formation P&S	Average Strubenkop Formation P&S	Average Silverton Formation P&S	NASC P&S	Bothaville Formation Quartzite C6	Sekororo Formation Quartzite D53	Sekororo Formation Quartzite D36	Sekororo Formation Quartzite D47	Average Sekororo Formation Quartzite D47
Ce/Yb	38.00	16.00	23.75	32.58	30.29	22.40	21.61	26.79	41.30	26.97	27.78	29.22
Th/Nb	1.03	0.57	0.72	1.47	1.11	1.23	0.92	0.55	0.26	0.30	0.39	0.32

Wronkiewicz and Condie 1990												
	Quartzite	Quartzite	Quartzite		Quartzite	Quartzite	Quartzite		Quartzite	Quartzite		Quartzite
	Selati Formation Quartzite D35	Black Reef Quartzite D34	Black Reef Quartzite C201	Average Black Reef Quartzite C201	Rooihoogte Formation Quartzite C76	Daspoort Formation Quartzite C81	Daspoort Formation Quartzite M8F-2-10	Average Daspoort Formation Quartzite M8F-2-10	Magaliesberg Formation Quartzite C207	Magaliesberg Formation Quartzite D77	Average Magaliesberg Formation Quartzite D77	Rayton Formation Quartzite C56
Ce/Yb	12.50	26.39	53.85	37.90	15.59	26.67	32.14	29.70	51.52	18.75	22.71	25.24
Th/Nb	0.85	0.29	0.35	0.32	0.71	0.54	2.58	1.55	0.84	1.36	1.25	0.61

de Waal, Graham and Armstrong 2006												
Lindeques drift and Heidelberg Intrusions												
	Lindeques Drift Even-grained spessartite mean	Lindeques Drift Porphyritic spessartite mean	Lindeques Spessartite Average	Heidelberg Porphy-ritic spess mean	Lindeques Drift Low-silica diorite mean	Lindeques Drift diorite mean	Lindeques Drift syeno-diorite mean	Lindeques Diorite Average	Roodekraal Complex Lava	Roodekraal Complex Cumulate	Roodekraal Complex Diorite	Roodekraal Complex Average
Ce/Yb	10.33	17.57	13.95	47.93	16.81	19.94	26.20	20.99	36.19	30.73	30.53	32.48
Th/Nb	0.25	0.32	0.28	0.21	0.37	0.63	0.79	0.60	0.47	0.18	0.18	0.28

Sudbury

Lightfoot et al. 1996												
	Main Mass Mafic Norite Average	Main Mass Felsic Norite Average	Main Mass Granophyre Average	Igneous textured sublayer matrix Whistle Mine Average	Melanorite Pod or Inclusion Whistle Mine Average	Olivine Melanorite Whistle Mine Average	Diabase Whistle Mine Average	Little Stobie Mine Igneous Textured Sublayer Matrix		Crean Hill Mine Igneous Textured Sublayer Matrix			
								93PCL-001	93PCL-001	93PCL-20	93PCL-22	93PCL-23	93PCL-25
Ce/Yb	34.21	33.30	35.41	23.74	30.72	37.22	12.18	21.96	15.53	22.05	20.49	20.27	21.78
Th/Nb	0.96	0.92	0.95	0.53	0.57	0.54	0.43	0.24	0.24	0.63	0.30	0.36	0.45

Lightfoot et al. 1996 Continued															
Levack West Mine Igneous Textured Sublayer Matrix			Levack West Mine Melanorite Pod or Inclusion		McCreedy West Mine Igneous Textured Sublayer Matrix					Fraser Mine Igneous Textured Sublayer Matrix					
	93PCL-45	93PCL-46	93PCL-66	93PCL-67	93PCL-68	93PCL-50	93PCL-51	93PCL-53	93PCL-55	93PCL-59	93PCL-342	93PCL-343	93PCL-344	92PCL-345	93PCL-346
Ce/Yb	33.03	40.00	31.53	28.84	29.69	42.84	29.83	38.21	29.59	33.24	30.34	30.75	29.42	31.19	33.59
Th/Nb	0.94	0.60	0.48	1.62	1.88	0.62	0.77	0.78	0.40	0.50	0.75	0.89	0.86	0.82	0.88

Lightfoot et al. 1996 Continued				Lightfoot et al. 2001							
Creighton Mine Igneous Textured Sublayer Matrix				Mafic Norite		Felsic Norite					
	94PCL-128	94PCL-131	94PCL-132	94PCL2011	94PCL2016	94PCL2066	94PCL2072	94PCL2076	94PCL2033	94PCL2028	94PCL2013
Ce/Yb	19.62	18.94	21.26	30.57	31.91	35.47	32.84	33.38	34.47	34.68	31.89
Th/Nb	0.38	0.70	0.31	1.01	1.00	1.14	0.93	0.98	0.93	0.96	0.92

Lightfoot et al. 2001 Continued														
	Quartz Gabbro				Granophyre					Mafic Norite Average	Felsic Norite Average	Quartz Gabbro Average	Granophyre Average	Main Mass Average
	94PCL2 080	93PCL2 90	94PCL2 052	94PCL2 079	93PCL3 36	93PCL2 93	93PCL2 97	93PCL3 12	93PCL3 34					
Ce/Yb	32.56	34.11	32.70	30.38	37.10	34.88	33.87	35.27	34.84	31.72	34.29	33.76	35.13	34.67
Th/Nb	0.99	0.71	0.86	0.94	0.94	0.93	0.95	0.90	0.96	1.01	0.97	0.87	0.94	0.94

Namaqualand

Duchesne et al. 2007													
Anorthosites					Tonalite	Leuconorite			Norite Sample 85b				
	Sample 70[b]	Sample 66	Sample 108	Average	Sample 30[a]	Sample 119	Sample 121	Average	Sample 85[b]	Sample 86[b]	Sample 116	Sample 122	Average
Ce/Yb	126.80	81.67	108.89	105.79	132.73	61.43	33.93	47.68	18.82	12.89	46.52	27.50	26.44
Th/Nb	8.47	1.20	4.31	4.66	14.60	0.56	0.58	0.57	0.27	0.53	1.42	1.18	0.85

Duchesne et al. 2007 Continued											
Melanorite					Hypersthenite			Glimmerite	Magnetite		
	Sample 88[b]	Sample 87[b]	Sample 110	Average	Sample 90[b]	Sample 117	Average	Sample 123	Sample 82[b]	Sample 125[b]	Average
Ce/Yb	6.67	18.29	8.31	11.09	8.71	43.70	26.21	30.43	43.61	37.29	40.45
Th/Nb	1.00	0.27	5.73	2.33	0.18	0.44	0.31	0.13	0.14	3.83	1.98

Duchesne et al. 2007 Continued							
Biotite Diorite							
	Sample 78[b]	Sample 112	Sample 109	Sample 114	Sample 118	Sample 126	Average
Ce/Yb	32.59	279.74	12.44	27.09	162.31	45.00	93.20
Th/Nb	1.16	24.59	0.98	0.59	0.21	0.50	4.67

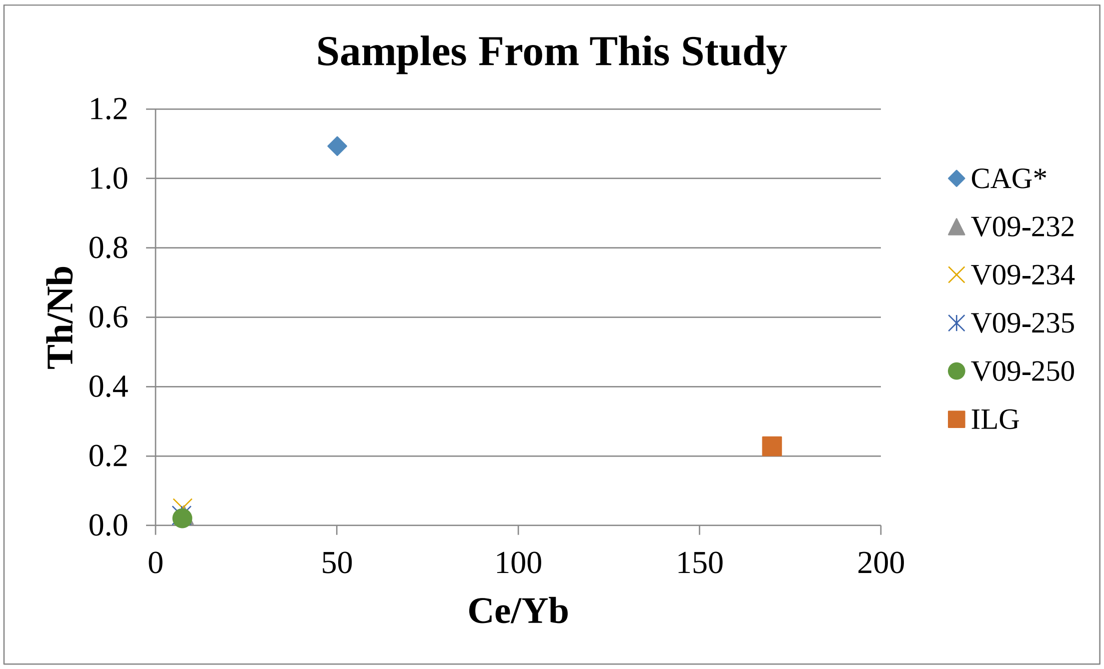

*The Central Anatectic Granite (CAG), Gabbronorite (GN Average) and Inlandsee Leucogranofels (ILG) are samples from this study.

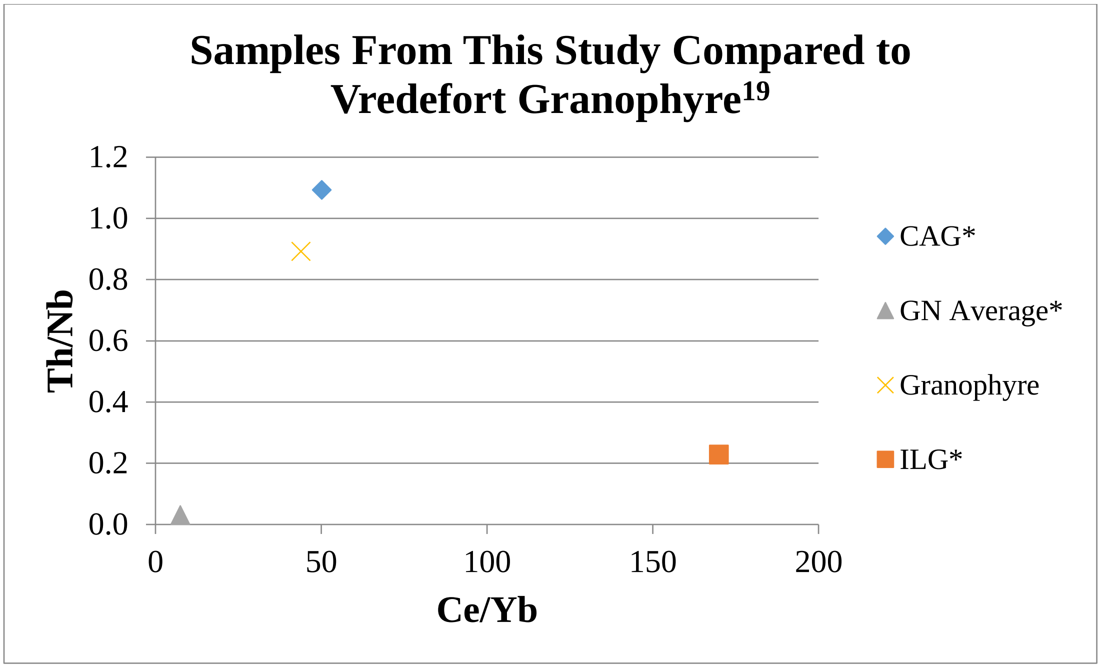

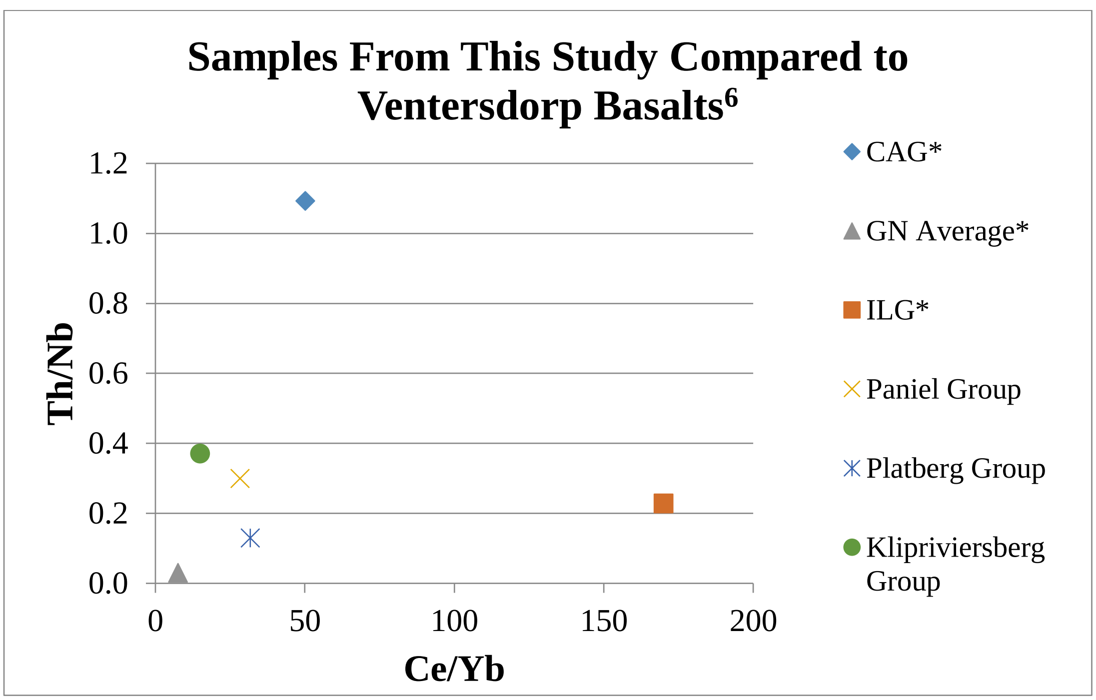

*The Central Anatectic Granite (CAG), Gabbronorite (GN Average) and Inlandsee Leucogranofels (ILG) are samples from this study.

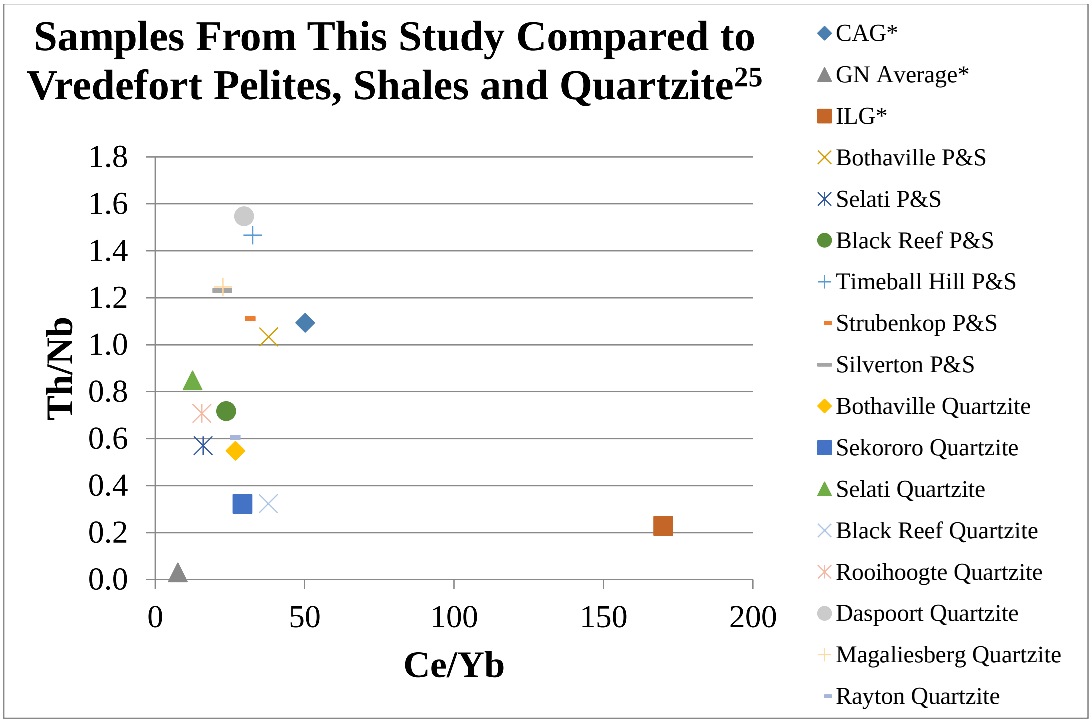

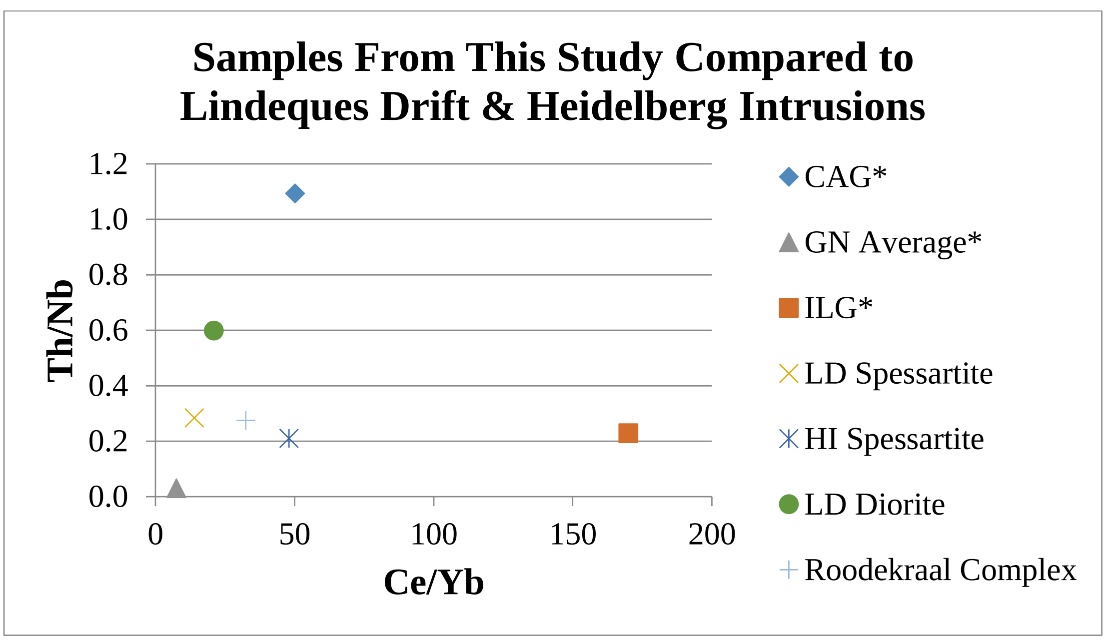

*The Central Anatectic Granite (CAG), Gabbronorite (GN Average) and Inlandsee Leucogranofels (ILG) are samples from this study.

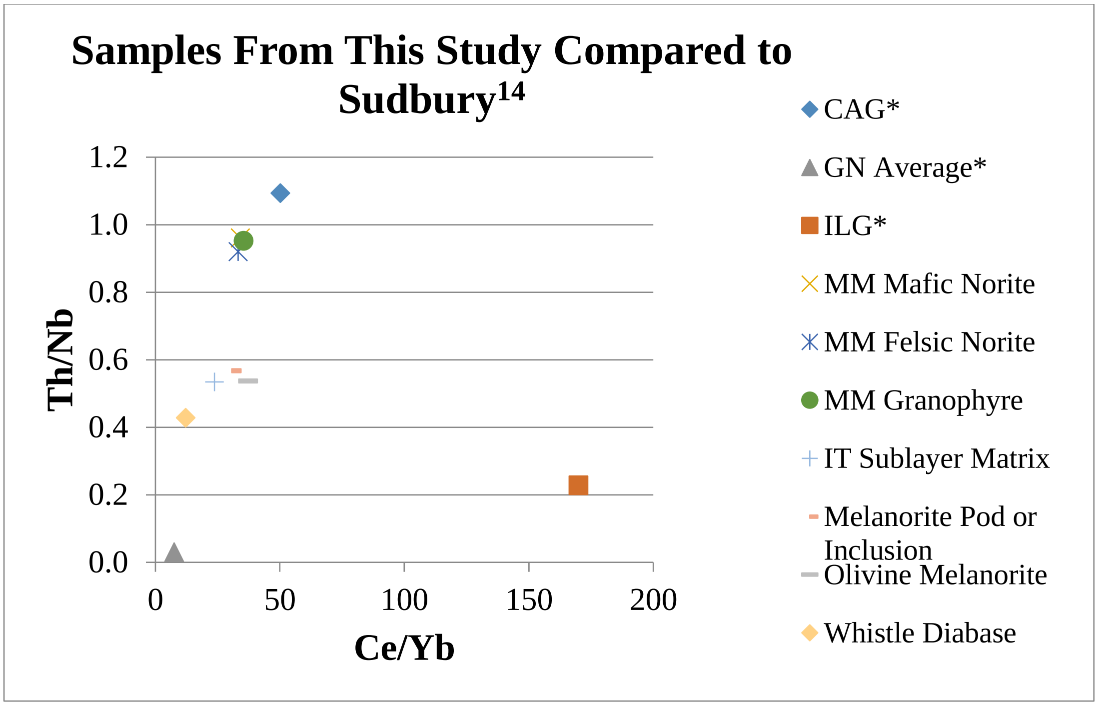

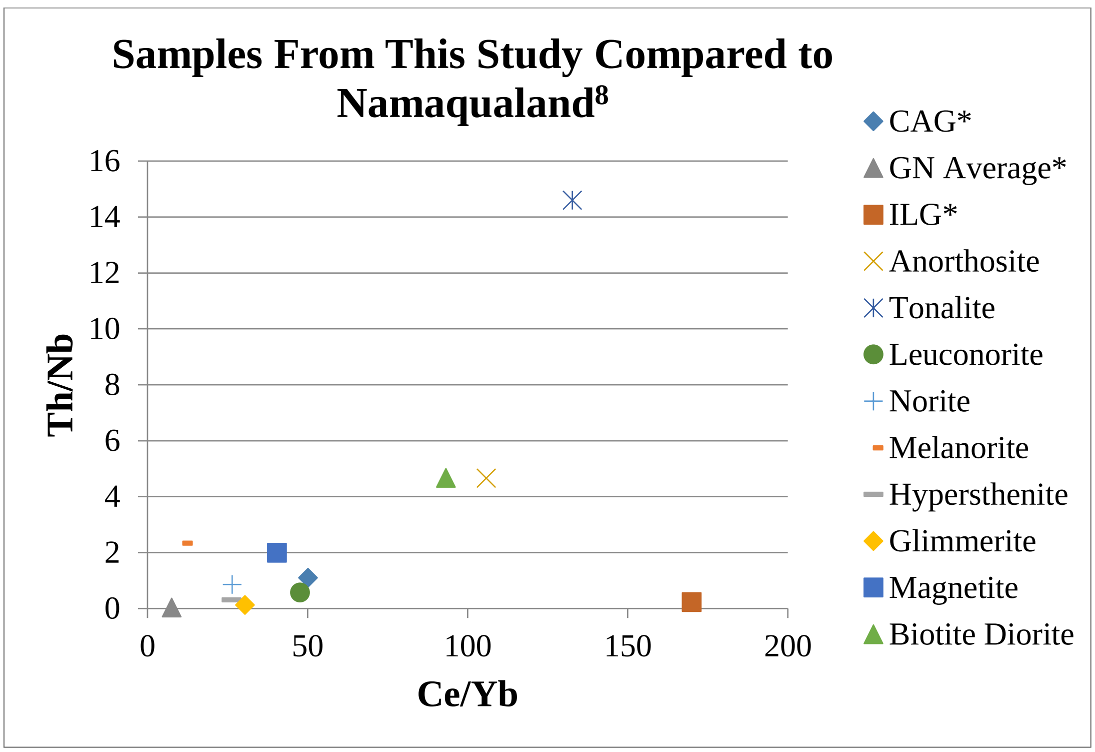

*The Central Anatectic Granite (CAG), Gabbronorite (GN Average) and Inlandsee Leucogranofels (ILG) are samples from this study.

Appendix B-1-7: La/Sm vs Gd/Yb Comparison Table and Plots

Vredefort

	Samples from this study							Koeberl, Reimold and Shirey 1996					
	CAG	ILG	Gabbro Norite					Witwatersrand Shale	Ventersdorp Andesitic			OGG	Wits Siltstone clase in Granophyre
	VO9-111	VO9-238	VO9-232	VO9-234	VO9-235	VO9-250	Average	VG-SNE	UP-61	UP-63	Average	OT-1	BG-S1
La/Sm	12.44	24.91	3.29	2.58	2.57	2.40	2.71	4.40	3.82	4.36	3.98	12.02	8.86
Gd/Yb	1.89	4.50	1.35	1.55	1.58	1.62	1.52	1.88	2.41	1.50	1.99	3.42	3.09

	Koeberl, Reimold and Shirey 1996 Continued						Lana et al. 2004							
	Vredefort Granophyre						Gneiss (amphibolite facies) Trondhjemite NE-Part				Melanosomes Trondhjemite Outer Parts			
	BG-4	BG-7	BG-9	BG-10	BG-168	Average	ABBG-3	ABG-2	ABP-1	Average	BEG-2	SAG-2	VAL-1	Average
La/Sm	7.93	8.68	8.50	8.46	8.05	8.33	8.52	12.75	13.45	11.26	8.65	10.24	11.72	9.89
Gd/Yb	2.90	2.77	2.09	2.96	2.37	2.62	3.66	3.64	6.11	3.96	4.05	2.90	0.44	1.39

	Lana et al. 2004 Continued													
	Leucosomes Granite								Schlieric Granite Northern Parts			Homogen Granite	Porphyritic grano-diorite	Gneiss Quartz Diorite
	EG-8	RG11	RG7	Pr12	SALP-1	EG-4	EG-7	Average	SPW-2	SPW-3	Average	ESP-1	POR-1	SCH-2
La/Sm	10.00	6.67	14.23	23.93	7.98	4.67	10.83	10.13	13.31	6.45	9.31	6.83	10.07	10.81
Gd/Yb	3.37	4.24	4.97	3.02	2.28	2.86	3.45	3.02	3.48	1.84	2.18	2.30	5.33	8.52

Lana et al. 2004 Continued													
	Mag. Rich Granod.	Leucosomes ederbite						Leucosomes Felsic enderbite				Leucosomes Charnockite	
	GRAD3	LEG-3	Strip1	Strip2	Strip3	Strip4	Average	LEW-1	vdf2-6	vdf12	Average	vdf2-4	vdf11
La/Sm	11.63	17.99	16.45	12.46	13.46	13.95	14.78	30.92	14.94	10.52	15.88	12.07	18.04
Gd/Yb	5.97	5.07	1.67	2.21	6.31	4.23	4.04	4.29	14.86	1.70	5.66	1.70	5.16

Lana et al. 2004 Continued											
								Melanosomes tonalite			K-feldspar-rich Granite
	vdf13	vdf19	vdf2-24	vdf24	vdf5	vdf7	Average	Vdf8	Vdf4	Vdf1	Average	LEP-1
La/Sm	17.42	15.89	18.29	20.09	24.88	19.19	17.28	5.21	5.04	5.41	5.21	16.72
Gd/Yb	10.91	2.14	3.30	3.08	2.37	2.89	3.17	4.32	3.96	1.75	3.22	3.86

Remiold et al. 2000										Coetzee et al. 2006		
Anne Rust Sheet										Tholeiitic Intrusions		
	WS2-228	UP-16	GP-5	IS-225	SH1-475	UP-71	USA59	UP-65	UP-68	Wittekopjes norite	Parsons Rust Dol-Norite	Reebokkop dolerite
La/Sm	3.29	3.31	3.07	3.15	3.09	3.35	3.33	3.30	3.27	3.72	3.17	4.20
Gd/Yb	1.50	1.49	1.69	1.47	1.62	1.43	1.68	1.83	1.61	1.19	1.41	1.61

de Waal, Graham and Armstrong 2006												
Lindeques drift and Heidelberg Intrusions												
	Lindeques Drift Even-grained spessartite mean	Lindeques Drift Porphyritic spessartite mean	Lindeques Drift Spessartite Average	Heidelberg Porphy-ritic spess mean	Lindeques Drift Low-silica diorite mean	Lindeques Drift diorite mean	Lindeques Drift syeno-diorite mean	Lindeques Drift Diorite Average	Roodekraal Complex Lava	Roodekraal Complex Cumulate	Roodekraal Complex Diorite	Roodekraal Complex Average
La/Sm	2.11	3.36	2.74	5.63	4.00	4.53	5.26	4.59	7.20	5.83	5.14	6.06
Gd/Yb	2.22	2.43	2.33	4.00	2.13	1.94	2.00	2.02	2.41	2.45	2.53	2.47

Sudbury

Lightfoot et al. 1996											
	Main Mass Mafic Norite Average	Main Mass Felsic Norite Average	Main Mass Granophyre Average	Igneous textured sublayer matrix Whistle Mine Average	Melanorite Pod or Inclusion Whistle Mine Average	Olivine Melanorite Whistle Mine Average	Diabase Whistle Mine Average	Little Stobie Mine Igneous Textured Sublayer Matrix		Crean Hill Mine Igneous Textured Sublayer Matrix	
								93PCL-001	93PCL-001	93PCL-20	93PCL-22
La/Sm	6.57	6.24	6.23	3.91	4.11	4.18	3.38	5.28	4.19	4.99	4.17
Gd/Yb	1.15	2.47	2.41	2.46	2.81	3.35	1.74	2.01	1.80	1.92	2.06

Lightfoot et al. 1996 Continued												
Crean Hill Mine Igneous Textured Sublayer Matrix			Levack West Mine Igneous Textured Sublayer Matrix		Levack West Mine Melanorite Pod or Inclusion			McCreedy West Mine Igneous Textured Sublayer Matrix				
	93PCL-23	93PCL-25	93PCL-45	93PCL-46	93PCL-66	93PCL-67	93PCL-68	93PCL-50	93PCL-51	93PCL-53	93PCL-55	93PCL-59
La/Sm	4.90	5.13	6.20	5.63	4.86	3.21	3.05	5.95	6.48	5.98	5.02	5.65
Gd/Yb	1.89	1.99	2.33	3.02	2.53	3.36	3.38	2.93	2.15	2.62	2.46	2.46

Lightfoot et al. 1996 Continued									Lightfoot et al. 2001	
Fraser Mine Igneous Textured Sublayer Matrix						Creighton Mine Igneous Textured Sublayer Matrix			Mafic Norite	
	93PCL-342	93PCL-343	93PCL-344	92PCL-345	93PCL-346	94PCL-128	94PCL-131	94PCL-132	94PCL2011	94PCL2016
La/Sm	5.35	6.01	6.02	5.96	6.17	4.63	4.95	4.41	5.86	6.35
Gd/Yb	2.25	2.09	2.06	2.03	2.25	1.89	1.75	2.12	0.28	0.29

Lightfoot et al. 2001 Continued										
Felsic Norite							Quartz Gabbro			
	94PCL2066	94PCL2072	94PCL2076	94PCL2033	94PCL2028	94PCL2013	94PCL2080	93PCL290	94PCL2052	94PCL2079
La/Sm	6.49	6.33	6.70	6.59	6.51	6.38	6.09	5.63	6.16	6.18
Gd/Yb	0.32	0.30	0.29	0.31	0.32	0.31	0.34	0.38	0.32	0.33

Lightfoot et al. 2001 Continued										
Granophyre						Mafic Norite Average	Felsic Norite Average	Quartz Gabbro Average	Granophyre Average	Main Mass Average
	93PCL336	93PCL293	93PCL297	93PCL312	93PCL334					
La/Sm	6.19	6.39	6.29	6.04	6.41	6.47	6.67	5.67	6.22	6.29
Gd/Yb	0.36	0.36	0.35	0.36	0.36	2.00	2.14	2.41	2.41	2.36

Namaqualand

Duchesne et al. 2007										
	Anorthosite	Tonalite	Leuconorite				Norite Sample 85b				
	Sample 66	Sample 30[a]	Sample 119	Sample 120	Sample 121	Average	Sample 85[b]	Sample 86[b]	Sample 116	Sample 122	Average
La/Sm	9.55	12.65	11.25	23.89	10.54	15.22	15.00	8.00	4.54	10.36	9.48
Gd/Yb	3.42	4.18	1.29	0.47	1.46	1.07	0.82	0.82	3.91	1.50	1.76

Duchesne et al. 2007 Continued											
Melanorite					Hypersthenite			Glimmerite	Magnetite		
	Sample 88[b]	Sample 87[b]	Sample 110	Average	Sample 90[b]	Sample 117	Average	Sample 123	Sample 82[b]	Sample 125[b]	Average
La/Sm	6.75	3.76	8.46	6.33	5.44	5.05	5.25	3.37	4.01	3.02	3.51
Gd/Yb	0.55	1.73	0.52	0.93	0.77	2.74	1.76	2.34	3.13	4.73	3.93

Duchesne et al. 2007 Continued							
Biotite Diorite							
	Sample 78[b]	Sample 112	Sample 109	Sample 114	Sample 118	Sample 126	Average
La/Sm	9.12	11.42	6.57	5.07	6.44	7.50	7.69
Gd/Yb	1.07	7.44	1.26	2.20	7.46	2.63	3.68

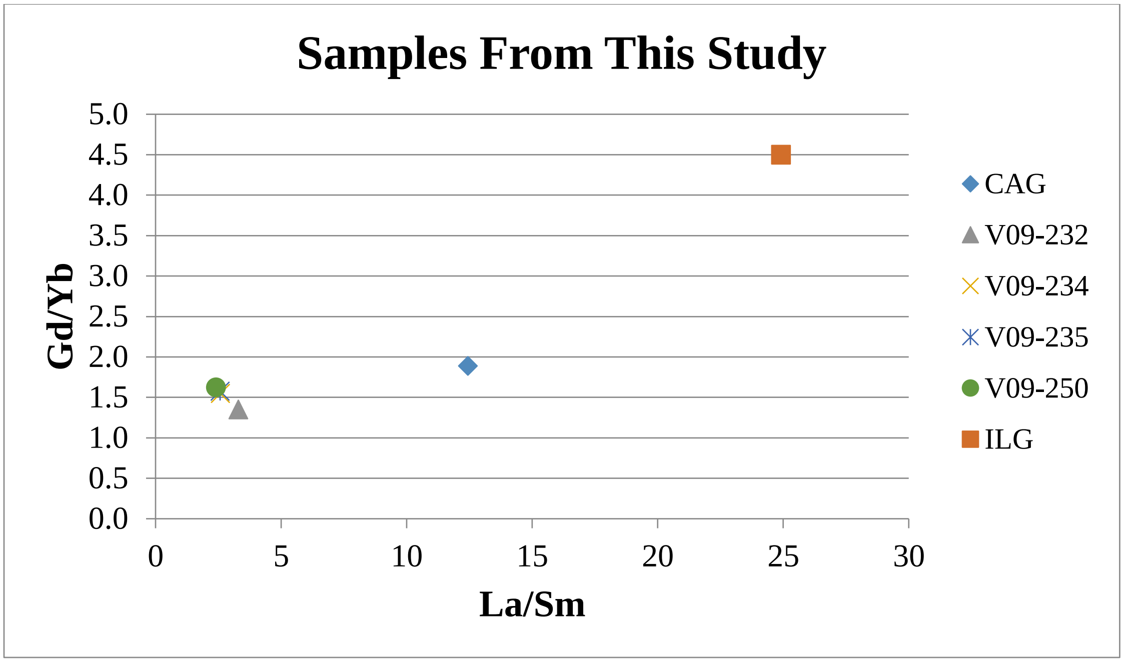

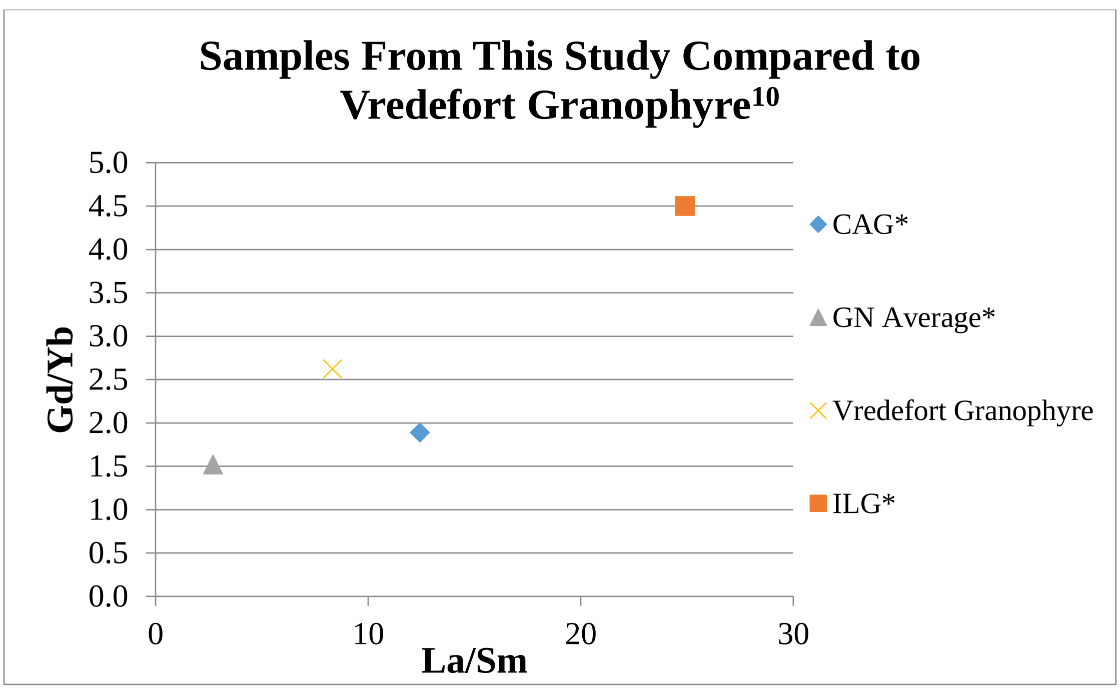

*The Central Anatectic Granite (CAG), Gabbronorite (GN Average) and Inlandsee Leucogranofels (ILG) are samples from this study.

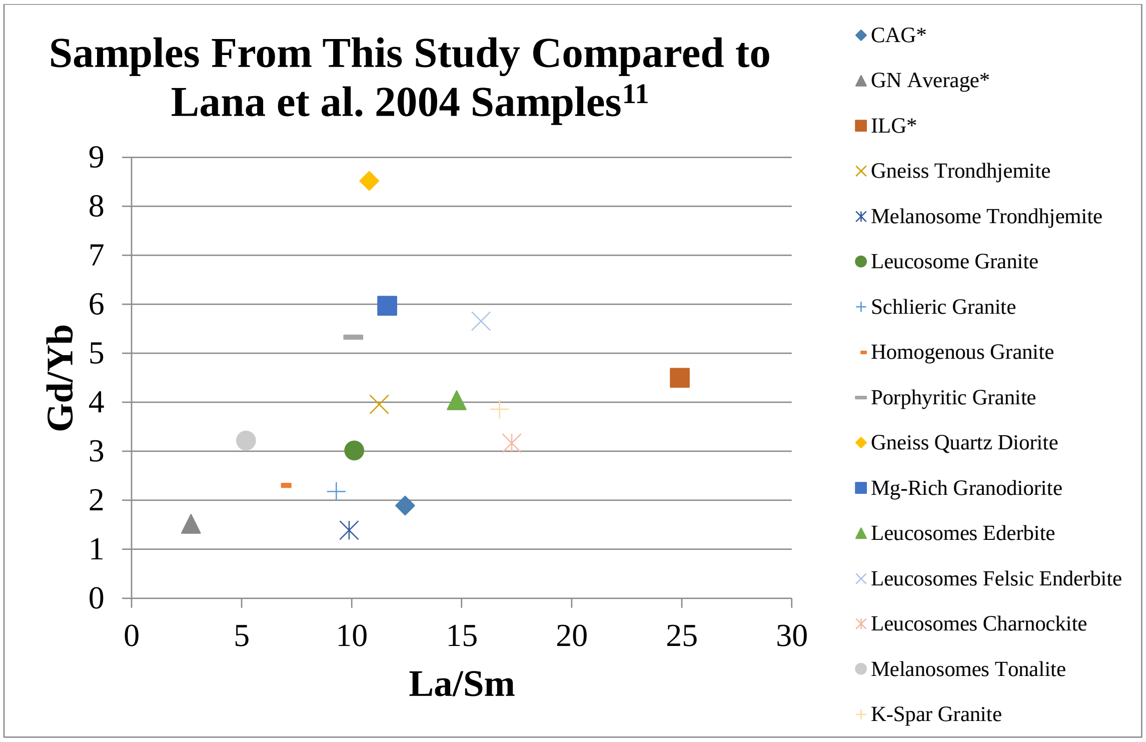

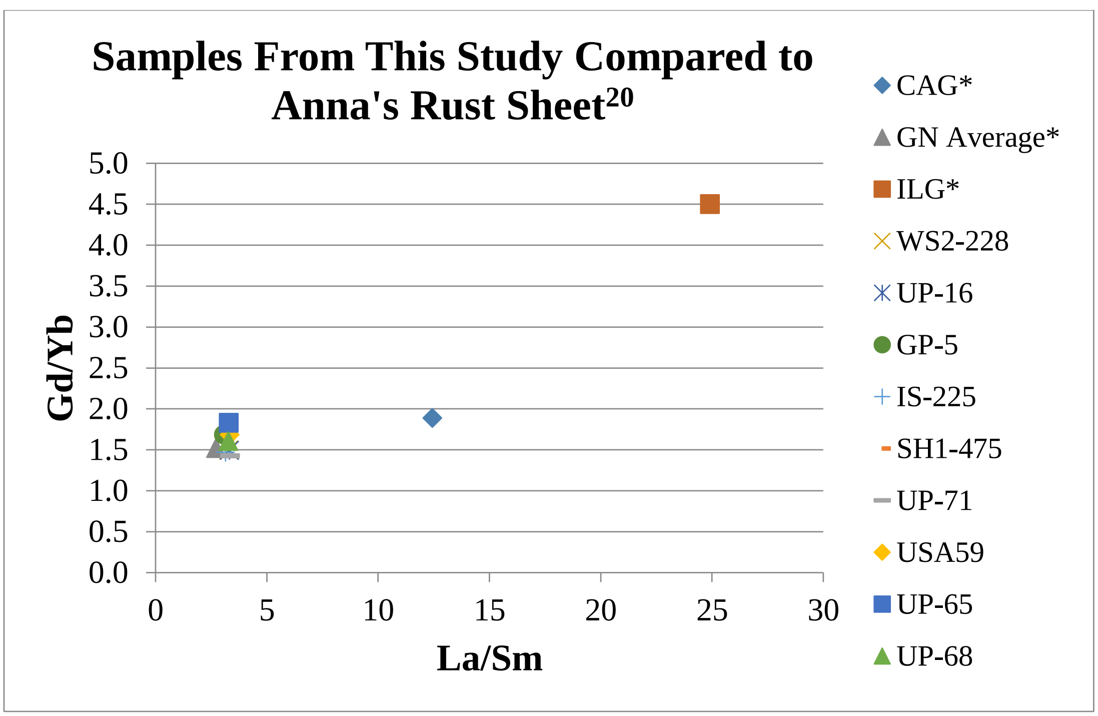

*The Central Anatectic Granite (CAG), Gabbronorite (GN Average) and Inlandsee Leucogranofels (ILG) are samples from this study.

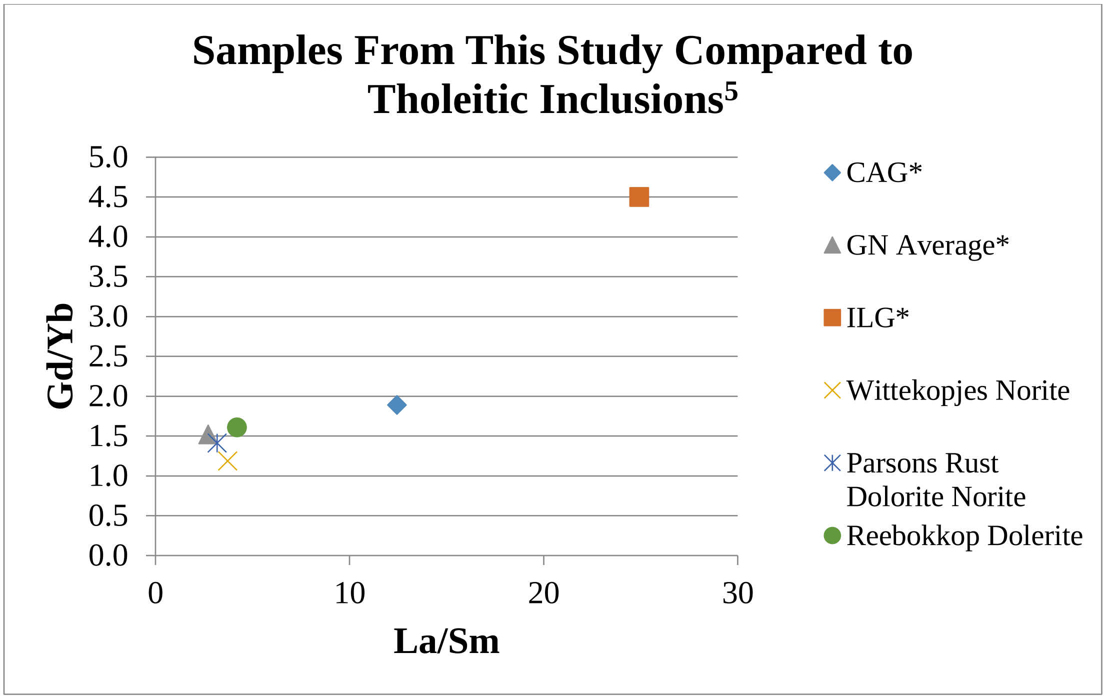

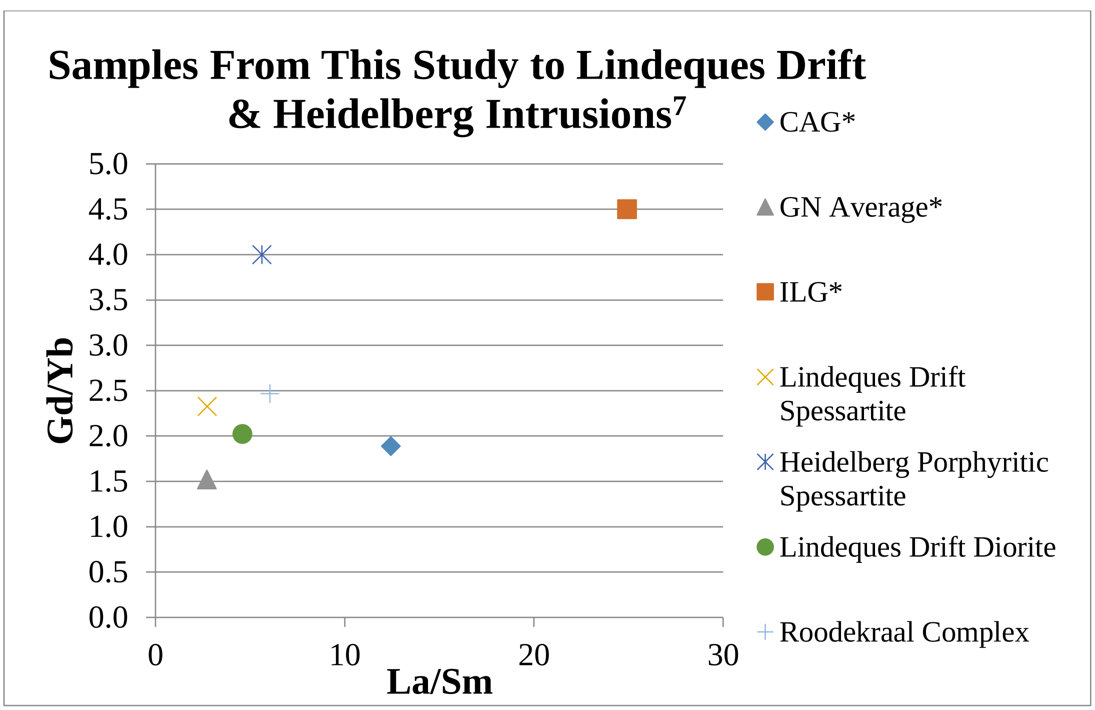

*The Central Anatectic Granite (CAG), Gabbronorite (GN Average) and Inlandsee Leucogranofels (ILG) are samples from this study.

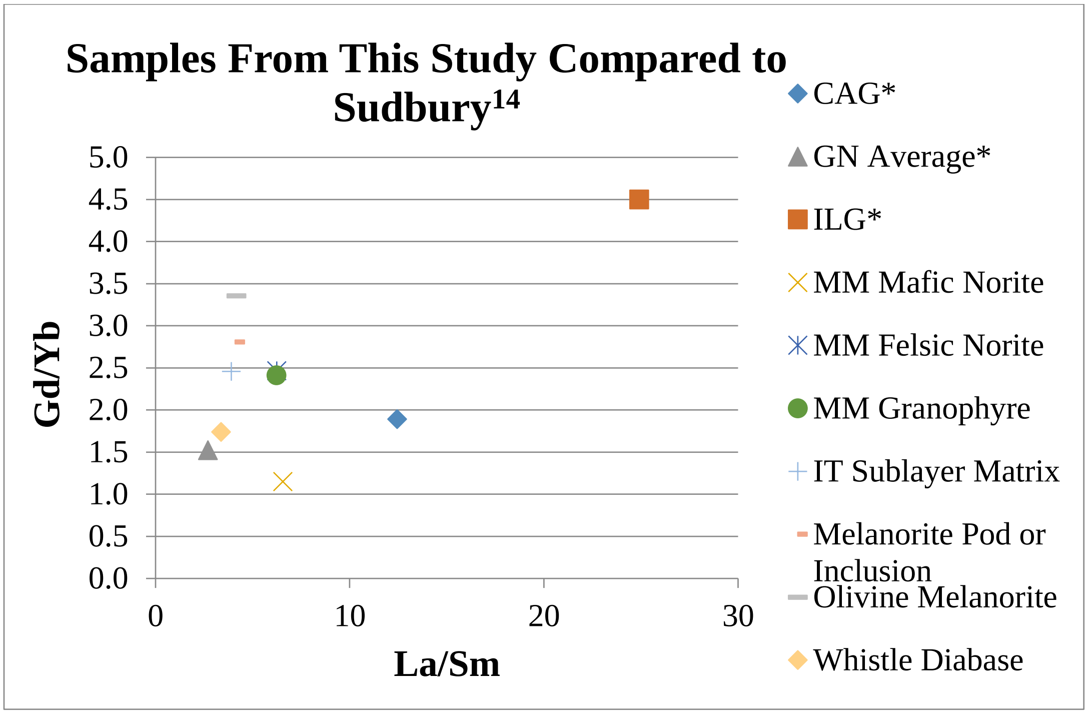

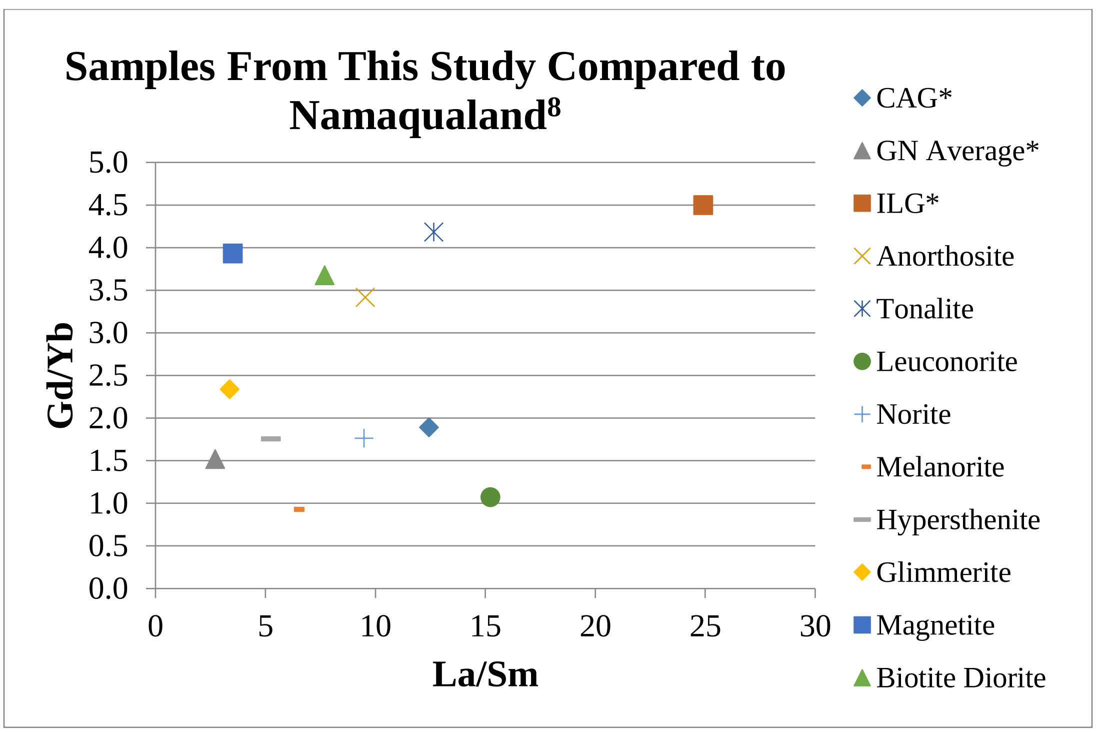

*The Central Anatectic Granite (CAG), Gabbronorite (GN Average) and Inlandsee Leucogranofels (ILG) are samples from this study.

Appendix B-1-8: Th/Nb vs Th/U Comparison Table and Plots

Vredefort

	Samples from this study							Koeberl, Reimold and Shirey 1996				Reimold & Gibson 2006
	CAG	ILG	Gabbro Norite					Witwatersrand Shale	Ventersdorp Andesitic			Vredefort Granophyre
	VO9-111	VO9-238	VO9-232	VO9-234	VO9-235	VO9-250	Average	VG-SNE	UP-61	UP-63	Average	Granophyre with outliers
Th/Nb	1.09	0.23	0.03	0.05	0.03	0.02	0.03	0.48	0.35	0.35	0.35	0.89
Th/U	13.72	8.00	4.00	5.13	4.80	1.81	3.44	1.63	3.68	6.08	4.33	4.50

	Crow and Condie 1988									
	Porphyritic lava	Basaltic Andesite	Felsic Porphyritic Lava	Porphyritic Basaltic Andesite	Basalt	Basalt				
	Pniel Group Allanridge	Platberg Group Reitgat	Platberg Group Makwassie	Platberg Group Goedgenoeg	Platberg Group Average	Klipriviersberg Group Edenville	Klipriviersberg Group Loraine	Klipriviersberg Group Jeannette	Klipriviersberg Group Orkney	Klipriviersberg Average
Th/Nb	0.30	0.13	0.42	0.13	0.13	0.30	0.39	0.40	0.38	0.37
Th/U	3.67	4.80	5.61	5.00	4.89	2.67	2.60	2.25	2.25	2.37

	Wronkiewicz and Condie 1990											
	Pelites & Shales							Quartzite	Quartzite	Quartzite	Quartzite	Quartzite
	Average Bothaville Formation P&S	Average Selati Formation P&S	Average Black Reef Formation P&S	Average Timeball Hill Formation P&S	Average Strubenkop Formation P&S	Average Silverton Formation P&S	NASC P&S	Bothaville Formation Quartzite C6	Sekororo Formation Quartzite D53	Sekororo Formation Quartzite D36	Sekororo Formation Quartzite D47	Average Sekororo Formation Quartzite D47
Th/Nb	1.03	0.57	0.72	1.47	1.11	1.23	0.92	0.55	0.26	0.30	0.39	0.32
Th/U	3.65	2.71	2.67	3.06	3.33	4.10	4.44	1.22	1.95	8.00	3.64	3.57

Wronkiewicz and Condie 1990 Continued											
	Quartzite	Quartzite		Quartzite	Quartzite	Quartzite		Quartzite	Quartzite		Quartzite
	Black Reef Quartzite D34	Black Reef Quartzite C201	Average Black Reef Quartzite C201	Rooihoogte Formation Quartzite C76	Daspoort Formation Quartzite C81	Daspoort Formation Quartzite M8F-2-10	Average Daspoort Formation Quartzite M8F-2-10	Magaliesberg Formation Quartzite C207	Magaliesberg Formation Quartzite D77	Average Magaliesberg Formation Quartzite D77	Rayton Formation Quartzite C56
Th/Nb	0.29	0.35	0.32	0.71	0.54	2.58	1.55	0.84	1.36	1.25	0.61
Th/U	1.59	3.17	2.21	2.27	2.17	2.38	2.34	2.45	4.69	4.12	2.60

de Waal, Graham and Armstrong 2006												
Lindeques drift and Heidelberg Intrusions												
	Lindeques Drift Even-grained spessartite mean	Lindeques Drift Porph-yritic spessartite mean	Lindeques Drift spessartite Average	Lindeques Drift Low-silica diorite mean	Lindeques Drift diorite mean	Lindeques Drift syeno-diorite mean	Lindeques Drift diorite Average	Lindeques Drift feeder	Roodekraal Complex Lava	Roodekraal Complex Cumulate	Roodekraal Complex Diorite	Roodekraal Complex Average
Th/Nb	0.25	0.32	0.28	0.37	0.63	0.79	0.60	0.18	0.47	0.18	0.18	0.28
Th/U	1.47	1.22	1.34	1.63	1.67	1.67	1.65	0.30	3.00	1.00	1.00	1.67

Sudbury

	Lightfoot et al. 1996												
	Main Mass Mafic Norite Average	Main Mass Felsic Norite Average	Main Mass Granophyre Average	Igneous textured sublayer matrix Whistle Mine Average	Melanorite Pod or Inclusion Whistle Mine Average	Olivine Melanorite Whistle Mine Average	Diabase Whistle Mine Average	Little Stobie Mine Igneous Textured Sublayer Matrix		Crean Hill Mine Igneous Textured Sublayer Matrix			
								93PCL-001	93PCL-001	93PCL-20	93PCL-22	93PCL-23	93PCL-25
Th/Nb	0.96	0.92	0.95	0.53	0.57	0.54	0.43	0.24	0.24	0.63	0.30	0.36	0.45
Th/U	4.99	4.60	4.57	5.13	5.28	4.86	4.58	4.80	3.93	3.76	3.42	3.77	4.31

	Lightfoot et al. 1996 Continued										
	Levack West Mine Igneous Textured Sublayer Matrix		Levack West Mine Melanorite Pod or Inclusion			McCreedy West Mine Igneous Textured Sublayer Matrix					Fraser Mine Igneous Textured Sublayer Matrix	
	93PCL-45	93PCL-46	93PCL-66	93PCL-67	93PCL-68	93PCL-50	93PCL-51	93PCL-53	93PCL-55	93PCL-59	93PCL-342	93PCL-343
Th/Nb	0.94	0.60	0.48	1.62	1.88	0.62	0.77	0.78	0.40	0.50	0.75	0.89
Th/U	4.79	5.00	5.24	11.77	13.61	6.80	4.84	5.35	5.53	4.63	5.30	4.34

	Lightfoot et al. 1996 Continued						Lightfoot et al. 2001			
	Fraser Mine Igneous Textured Sublayer Matrix			Creighton Mine Igneous Textured Sublayer Matrix			Mafic Norite		Felsic Norite	
	93PCL-344	92PCL-345	93PCL-346	94PCL-128	94PCL-131	94PCL-132	94PCL2011	94PCL2016	94PCL2066	94PCL2072
Th/Nb	0.86	0.82	0.88	0.38	0.70	0.31	1.01	1.00	1.14	0.93
Th/U	4.66	4.72	4.69	4.66	4.35	4.61	4.76	7.48	7.03	4.42

Lightfoot et al. 2001 Continued											
	Felsic Norite				Quartz Gabbro				Granophyre		
	94PCL2076	94PCL2033	94PCL2028	94PCL2013	94PCL2080	93PCL290	94PCL2052	94PCL2079	93PCL336	93PCL293	93PCL297
Th/Nb	0.98	0.93	0.96	0.92	0.99	0.71	0.86	0.94	0.94	0.93	0.95
Th/U	4.26	4.65	4.40	4.83	4.38	4.82	4.24	4.75	4.35	4.81	4.62

Lightfoot et al. 2001 Continued							
	Granophyre		Mafic Norite Average	Felsic Norite Average	Quartz Gabbro Average	Granophyre Average	Main Mass Average
	93PCL312	93PCL334					
Th/Nb	0.90	0.96	1.01	0.97	0.87	0.94	0.94
Th/U	4.48	4.38	6.30	4.58	4.48	4.57	4.60

Namaqualand

Duchesne et al. 2007											
	Anorthosites				Tonalite	Leuconorite				Norite Sample 85b	
	Sample 70[b]	Sample 66	Sample 108	Average	Sample 30[a]	Sample 119	Sample 120	Sample 121	Average	Sample 85[b]	Sample 86[b]
Th/Nb	8.47	1.20	4.31	4.66	14.60	0.56	0.00	0.58	0.38	0.27	0.53
Th/U	17.89	7.00	17.86	14.25	6.64	5.75	0.00	4.20	3.32	4.00	1.78

Duchesne et al. 2007 Continued											
	Norite Sample 85b			Melanorite				Hypersthenite			Glimmerite
	Sample 116	Sample 122	Average	Sample 88[b]	Sample 87[b]	Sample 110	Average	Sample 90[b]	Sample 117	Average	Sample 123
Th/Nb	1.42	1.18	0.85	1.00	0.27	5.73	2.33	0.18	0.44	0.31	0.13
Th/U	9.26	4.44	4.87	6.00	6.00	10.81	7.60	3.50	8.00	5.75	3.33

Duchesne et al. 2007 Continued										
	Magnetite			Biotite Diorite						
	Sample 82[b]	Sample 125[b]	Average	Sample 78[b]	Sample 112	Sample 109	Sample 114	Sample 118	Sample 126	Average
Th/Nb	0.14	3.83	1.98	1.16	24.59	0.98	0.59	0.21	0.50	4.67
Th/U	3.81	5.37	4.59	5.80	52.91	9.00	3.26	16.00	3.75	15.12

Morokweng

Andreoli et al. 1999						
Medium Grained Quartz Norite				Heterogeneous Quartz Norite	Fine Grained Quartz Norite	Quartz Norite Mean
	N-5	N-4	N-3	N-2	N-1	
Th/Nb	0.69	0.75	0.75	0.69	0.60	0.59
Th/U	2.65	2.50	2.47	2.27	2.46	2.56

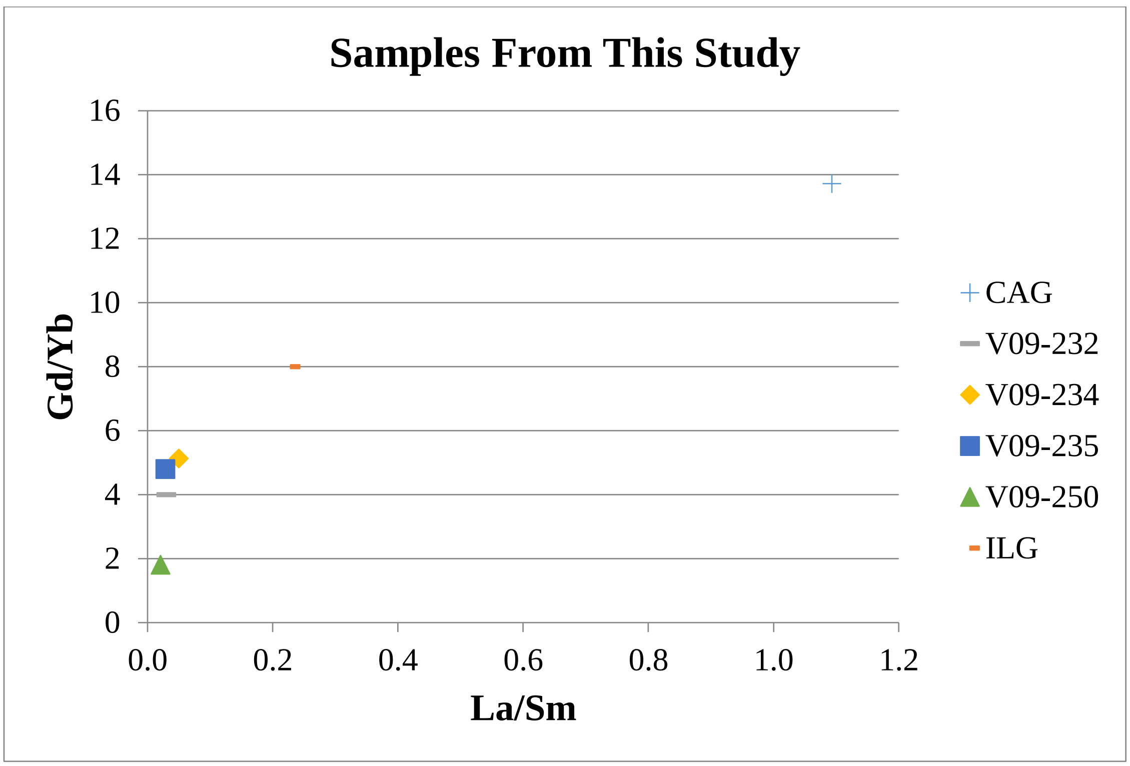

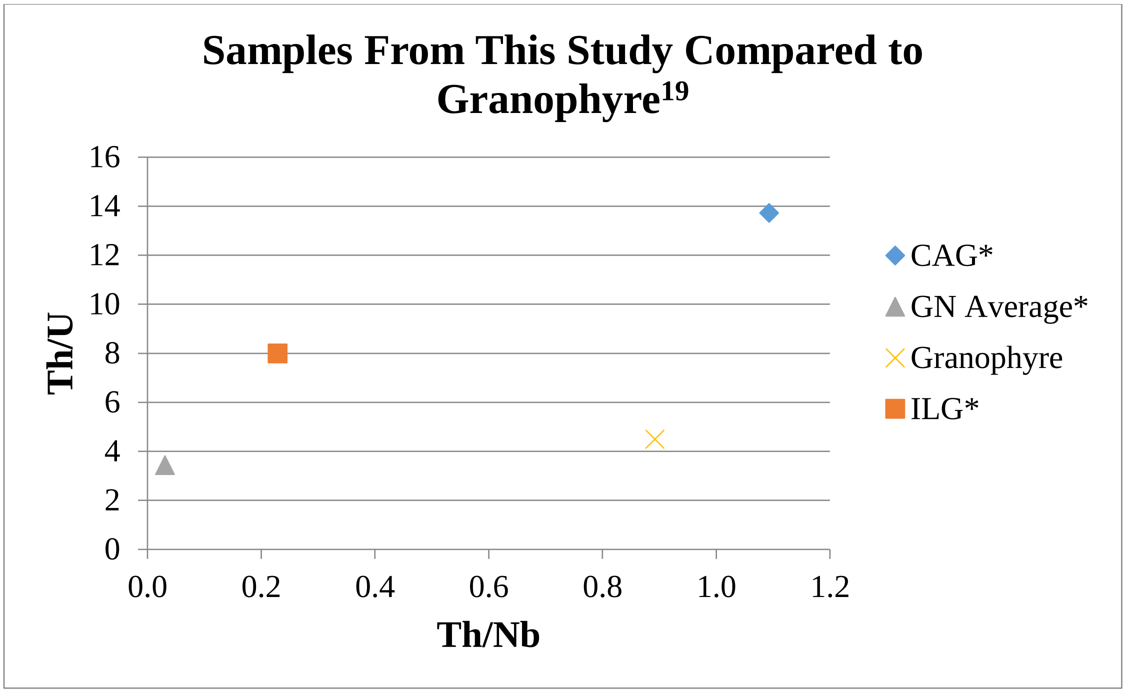

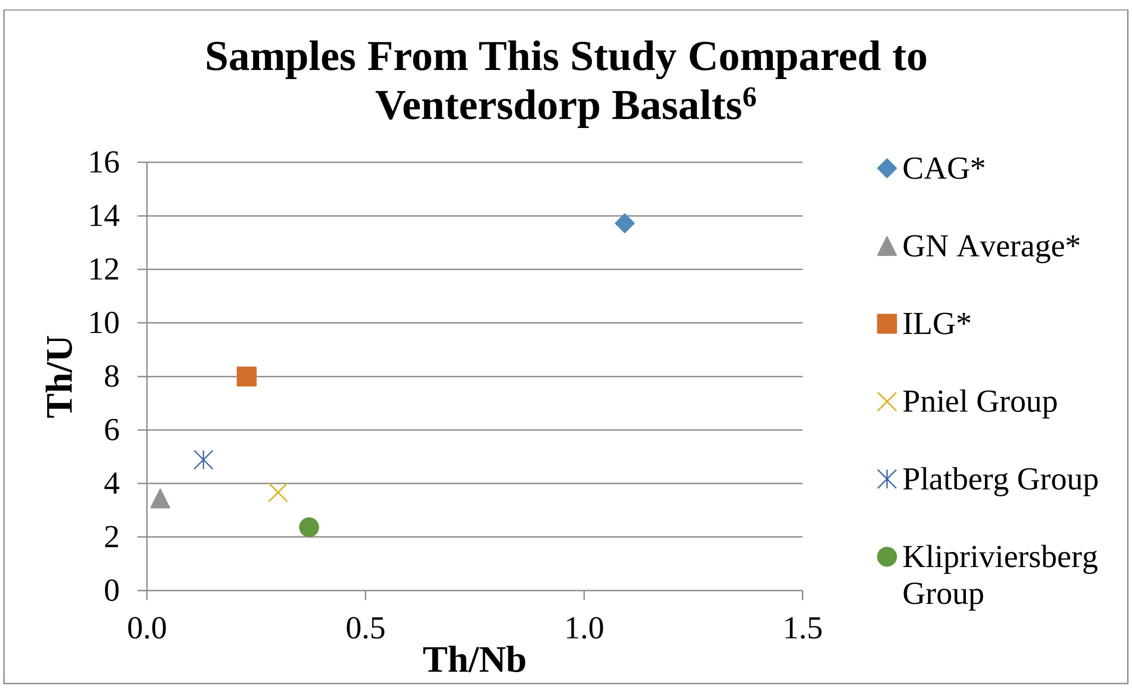

*The Central Anatectic Granite (CAG), Gabbronorite (GN Average) and Inlandsee Leucogranofels (ILG) are samples from this study.

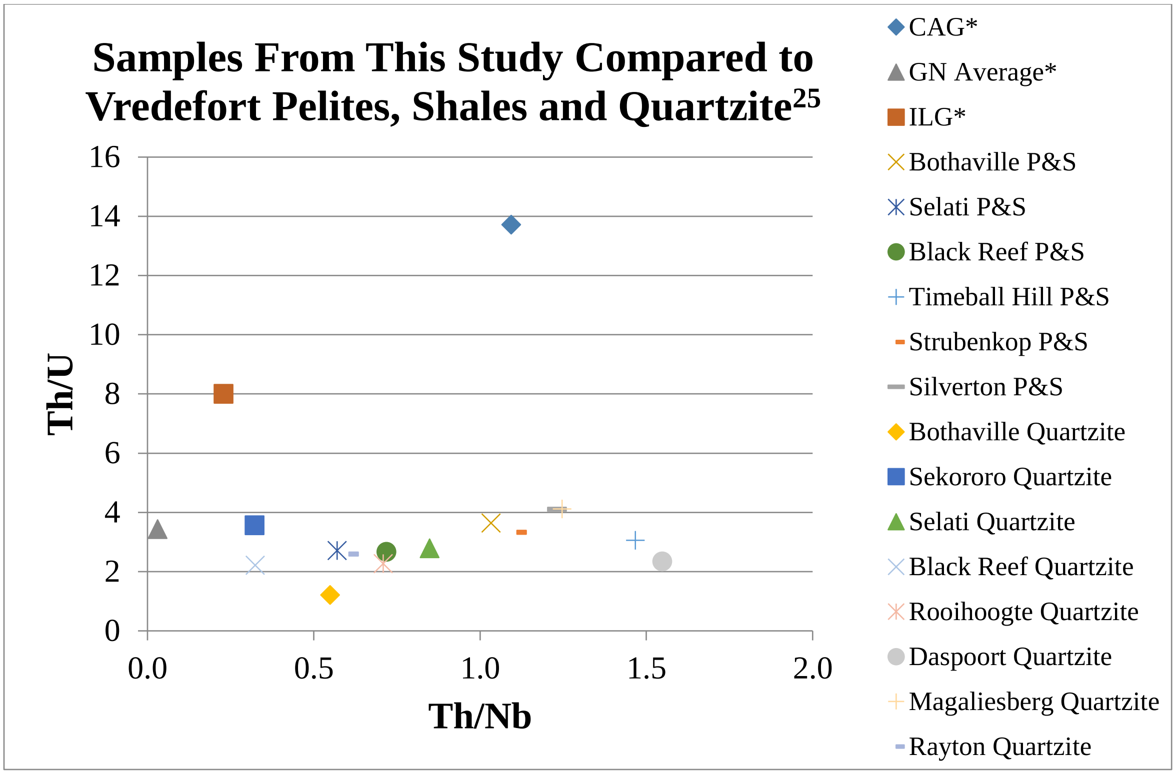

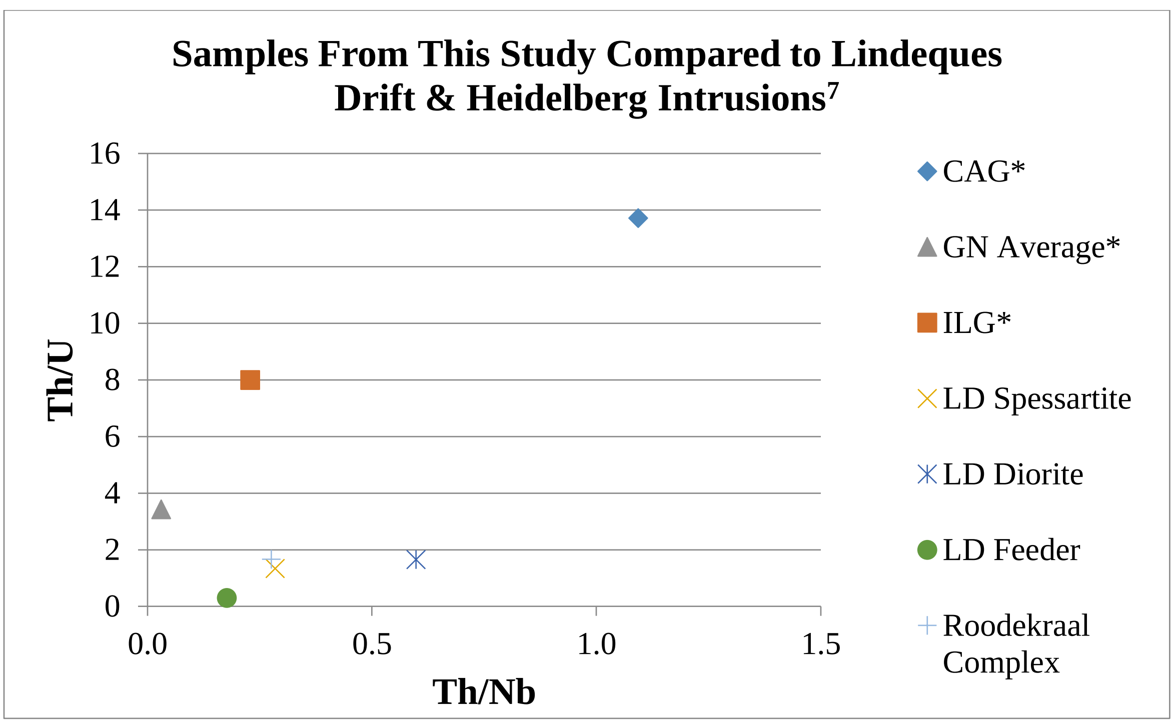

*The Central Anatectic Granite (CAG), Gabbronorite (GN Average) and Inlandsee Leucogranofels (ILG) are samples from this study.

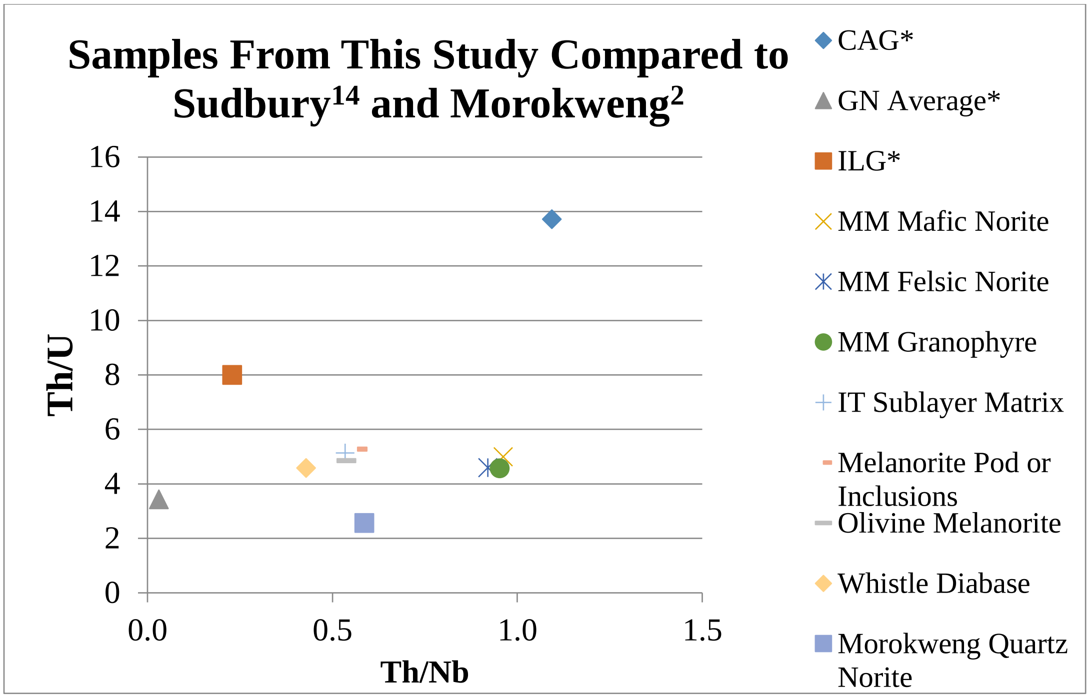

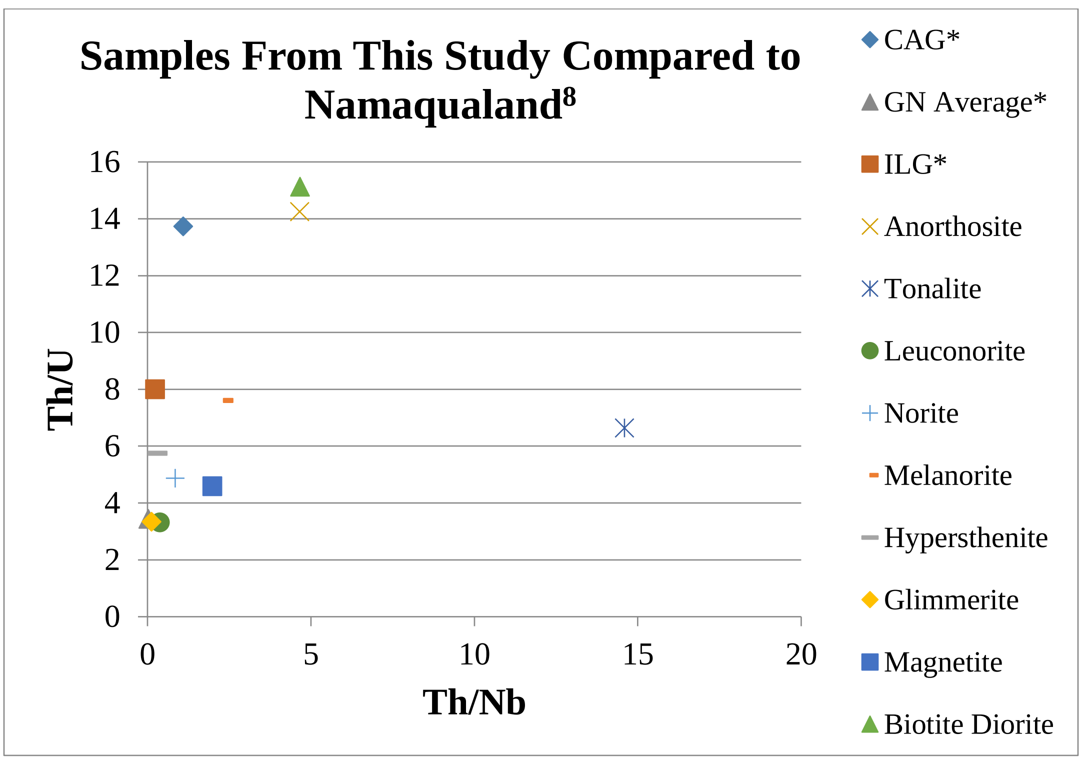

*The Central Anatectic Granite (CAG), Gabbronorite (GN Average) and Inlandsee Leucogranofels (ILG) are samples from this study.

Appendix B-1-9: AMF Comparison Table

Vredefort														
			Na2O	K2O	A	Fe2O3(T)	FeO	F	MgO	Total		Normalized		
Source	**Rock Type**	**Unit Symbol**	%	%		%			%			A	M	F
My Samples*	CAG	VO9-111	4.28	3.83	8.11	2.06		2.06	0.38	10.55		77	4	20
	ILG	VO9-238	2.82	6.00	8.82	0.75		0.75	0.13	9.70		91	1	8
	Gabbro Norite	VO9-232	1.74	0.28	2.02	30.54		30.54	5.14	37.70		5	14	81
		VO9-234	2.76	0.34	3.10	16.62		16.62	5.57	25.29		12	22	66
		VO9-235	2.77	0.32	3.09	16.63		16.63	5.62	25.34		12	22	66
		VO9-250	2.53	0.42	2.95	21.79		21.79	4.47	29.21		10	15	75
		Average	2.45	0.34	2.79	21.40		21.40	5.20	29.39		9	18	73
Koeberl, Reimold and Shirey 1996	Witwatersrand Shale	VG-SNE	0.01	0.05	0.06	57.49		57.49	0.72	58.27		0	1	99
	Ventersdorp Andesitic	UP-61	4.86	0.42	5.28	10.11		10.11	4.53	19.92		27	23	51
		UP-63	2.27	1.02	3.29	10.01		10.01	6.19	19.49		17	32	51
		Average	3.57	0.72	4.29	10.06		10.06	5.36	19.71		22	27	51
	OGG	OT-1	4.81	2.25	7.06	4.90		4.90	1.90	13.86		51	14	35
	Wits Siltstone clase in Granophyre	BG-S1	2.42	2.61	5.03	1.39		1.39	0.50	6.92		73	7	20
	Vredefort Granophyre	BG-4	2.54	2.14	4.68	7.21		7.21	3.50	15.39		30	23	47
		BG-7	3.09	2.36	5.45	7.06		7.06	3.50	16.01		34	22	44
		BG-9	2.89	2.43	5.32	6.81		6.81	3.40	15.53		34	22	44
		BG-10	2.89	2.41	5.30	6.83		6.83	3.40	15.53		34	22	44
		BG-168	2.57	2.43	5.00	7.29		7.29	3.70	15.99		31	23	46
		Average*	2.80	2.35	5.15	7.04		7.04	3.50	15.69		33	22	45
Reimold & Gibson 2006	Vredefort Granophyre	Granophyre with outliers	2.70	2.23	4.93	7.03		7.03	3.58	15.54		32	23	45

[1]It was discovered on July 28th 2016 that Lieger, D., Riller, U. and Gibson, R.L. 2010 was withdrawn at the request of the author(s).

*These samples were used to create the Figure 3-4 (AMF plot) in Chapter 3.

Lieger, Riller and Gibson 2010	Granitoid	WR 669A3	2.52	5.69	8.21	2.33		2.33	0.34	10.88		75	3	21
		PT 669A2	3.90	4.34	8.24	1.72		1.72	0.29	10.25		80	3	17
		WR 200C2	5.02	5.15	10.17	0.30		0.30	0.01	10.48		97	0	3
		PT 200C1	5.03	3.96	8.99	2.18		2.18	0.35	11.52		78	3	19
		WR 453A2	5.25	3.28	8.53	1.40		1.40	0.24	10.17		84	2	14
		PT 453A1	4.10	3.17	7.27	5.05		5.05	2.09	14.41		50	15	35
		PT 652A1	3.03	5.01	8.04	1.82		1.82	0.07	9.93		81	1	18
		PT 652A2	4.15	4.62	8.77	1.81		1.81	0.08	10.66		82	1	17
		WR KuduA3	8.23	0.80	9.03	1.49		1.49	0.28	10.80		84	3	14
		PT KuduA2	4.64	0.46	5.10	13.98		13.98	6.24	25.32		20	25	55
		PT KuduA1	4.41	2.02	6.43	12.94		12.94	6.44	25.81		25	25	50
		WR 518A2	5.03	1.95	6.98	5.77		5.77	1.18	13.93		50	8	41
		PT 518A1	5.94	1.74	7.68	11.25		11.25	2.98	21.91		35	14	51
		WR Average	5.21	3.37	8.58	2.26		2.26	0.41	11.25		76	4	20
		PT Average	4.40	3.17	7.57	6.34		6.34	2.32	16.23		47	14	39
	Quartzite/ Conglomerate	WR 6A4	0.02	0.28	0.30	0.38		0.38	0.05	0.73		41	7	52
		PT 6A1	0.00	0.24	0.24	1.46		1.46	0.01	1.71		14	1	85
	Quartzite	WR 621A3	0.03	1.12	1.15	1.34		1.34	0.01	2.50		46	0	54
		PT 621A2	0.10	3.16	3.26	1.53		1.53	0.24	5.03		65	5	30
		PT 621A1	0.12	3.01	3.13	1.33		1.33	0.25	4.71		66	5	28
		PT 2A2	0.08	2.48	2.56	2.57		2.57	0.27	5.40		47	5	48
		PT 2B2	0.73	2.80	3.53	1.23		1.23	0.17	4.93		72	3	25
		WR 64A3	0.02	0.64	0.66	0.55		0.55	0.00	1.21		55	0	45
		PT 64A2	0.06	0.88	0.94	1.56		1.56	0.05	2.55		37	2	61
		PT 64A1	0.00	0.98	0.98	1.80		1.80	0.79	3.57		27	22	50
		WR 102A2	0.02	0.50	0.52	2.78		2.78	0.01	3.31		16	0	84
		PT102A1	0.02	1.04	1.06	0.79		0.79	0.12	1.97		54	6	40
		PT 1A1	1.86	2.32	4.18	3.72		3.72	1.41	9.31		45	15	40
		PT 1A2	1.85	2.43	4.28	3.74		3.74	1.38	9.40		46	15	40

[1]It was discovered on July 28th 2016 that Lieger, D., Riller, U. and Gibson, R.L. 2010 was withdrawn at the request of the author(s).
*These samples were used to create the Figure 3-4 (AMF plot) in Chapter 3.

		PT 1A3	0.00	2.47	2.47	3.57		3.57	1.29	7.33		34	18	49
		Average WR	0.02	0.75	0.78	1.56		1.56	0.01	2.34		33	0	67
		Average PT	0.48	2.16	2.64	2.18		2.18	0.60	5.42		49	11	40
	Alkali Granite	WR 4A2	7.82	2.94	10.76	2.65		2.65	0.20	13.61		79	1	19
		PT 4A1	7.86	2.51	10.37	6.30		6.30	0.72	17.39		60	4	36
	Epidiorite	WR 564A2	1.37	0.08	1.45	7.55		7.55	9.28	18.28		8	51	41
		PT 564A1	2.08	0.55	2.63	7.28		7.28	8.59	18.50		14	46	39
Schwarzman et al. 1983	Granitoid	PT	5.20	1.30	6.50	8.60		8.60	1.20	16.30		40	7	53
	Gabbro	PT	1.60	0.53	2.13	8.12		8.12	11.60	21.85		10	53	37
		PT	1.70	0.56	2.26	8.13		8.13	9.40	19.79		11	47	41
	Diorite	PT	6.70	1.40	8.10	8.16		8.16	4.20	20.46		40	21	40
	Alkali Granite	PT	8.90	1.70	10.60	8.14		8.14	0.59	19.33		55	3	42
		PT	8.20	2.60	10.80	8.15		8.15	0.62	19.57		55	3	42
	Epidiorite	PT	2.20	0.19	2.39	8.80		8.80	8.10	19.29		12	42	46
		PT	2.20	0.18	2.38	8.90		8.90	8.10	19.38		12	42	46
Bischoff 1972	Diorite	WR	5.70	1.50	7.20	8.50		8.50	2.70	18.40		39	15	46
Bischoff 1973	Alkali Granite	WR	5.85	3.98	9.83	8.40		8.40	0.13	18.36		54	1	46
Reimold 1991	Gabbro	WR	2.20	1.00	3.20	14.30		14.30	6.00	23.50		14	26	61
		PT	2.60	1.50	4.10	12.00		12.00	6.10	22.20		18	27	54
	Norite	WR	1.40	0.10	1.50	8.60		8.60	9.30	19.40		8	48	44
		PT		0.60	0.60	7.90		7.90	7.30	15.80		4	46	50
Wilshire 1971	Epidiorite	PT	1.70	0.14	1.84	8.30		8.30	8.50	18.64		10	46	45
McIver et al. 1981	Mafic Rock	WR	0.04	0.21	0.25	1.27		1.27	17.58	19.10		1	92	7
		WR	0.83	0.18	1.01	1.06		1.06	14.42	16.49		6	87	6
Tankard et al. 1982	Mafic Rock	WR	3.51	0.68	4.19	12.70		12.70	4.93	21.82		19	23	58
	Alkali Granite WR	Average	6.84	3.46	10.30	5.53		5.53	0.17	15.99		64	1	35
	Alkali Granite PT	Average	8.32	2.27	10.59	7.53		7.53	0.64	18.76		56	3	40
	Epidote PT	Average	2.05	0.27	2.31	8.32		8.32	8.32	18.95		12	44	44
	Gabbro PT	Average	1.97	0.86	2.83	9.42		9.42	9.03	21.28		13	42	44
	Mafic Rock WR	Average	1.46	0.36	1.82	5.01		5.01	12.31	19.14		9	64	26

[1]It was discovered on July 28th 2016 that Lieger, D., Riller, U. and Gibson, R.L. 2010 was withdrawn at the request of the author(s).

*These samples were used to create the Figure 3-4 (AMF plot) in Chapter 3.

Crow and Condie 1988	Porphyritic lava	Pniel Group Allanridge	3.73	1.50	5.23	9.80		9.80	3.83	18.86		28	20	52
	Basaltic Andesite	Platberg Group Reitgat	3.72	1.08	4.80	10.50		10.50	4.37	19.67		24	22	53
	Felsic Porphyritic Lava	Platberg Group Makwassie	2.71	3.65	6.36	4.80		4.80	2.51	13.67		47	18	35
	Porphyritic Basaltic Andesite	Platberg Group Goedgenoeg	3.39	1.23	4.62	10.50		10.50	5.60	20.72		22	27	51
	Basalt	Platberg Group Average	3.56	1.16	4.71	10.50		10.50	4.99	20.20		23	25	52
	Basalt	Klipriviersberg Group Edenville	2.37	0.74	3.11	10.10		10.10	10.52	23.73		13	44	43
		Klipriviersberg Group Loraine	2.92	1.25	4.17	10.10		10.10	7.47	21.74		19	34	46
		Klipriviersberg Group Jeannette	3.34	1.35	4.69	11.10		11.10	4.90	20.69		23	24	54
		Klipriviersberg Group Orkney	3.58	0.92	4.50	11.20		11.20	5.30	21.00		21	25	53
		Klipriviersberg Group Westonaria	1.36	0.19	1.55	12.90		12.90	13.97	28.42		5	49	45
		Klipriviersberg Average	2.71	0.89	3.60	11.08		11.08	8.43	23.12		16	36	48
Wronkiewicz and Condie 1990	Pelites & Shales	Average Bothaville Formation P&S	0.23	3.27	3.50	6.29		6.29	4.98	14.77		24	34	43
		Average Selati Formation P&S	0.28	4.89	5.17	10.88		10.88	3.71	19.76		26	19	55
		Average Black Reef Formation P&S	0.09	4.54	4.63	7.45		7.45	4.44	16.52		28	27	45
		Average Timeball Hill Formation P&S	0.84	3.52	4.36	8.52		8.52	1.78	14.66		30	12	58
		Average Strubenkop Formation P&S	0.60	1.43	2.03	12.18		12.18	1.35	15.56		13	9	78

[1]It was discovered on July 28th 2016 that Lieger, D., Riller, U. and Gibson, R.L. 2010 was withdrawn at the request of the author(s).

*These samples were used to create the Figure 3-4 (AMF plot) in Chapter 3.

		Average Silverton Formation P&S	1.35	2.91	4.26	7.48		7.48	2.74	14.48		29	19	52
		NASC P&S	1.15	3.99	5.14	6.33		6.33	2.85	14.32		36	20	44
	Quartzite	Bothaville Formation Quartzite C6	0.29	0.24	0.53	3.06		3.06	0.59	4.18		13	14	73
	Quartzite	Sekororo Formation Quartzite D53	0.08	0.29	0.37	0.60		0.60	0.41	1.38		27	30	43
	Quartzite	Sekororo Formation Quartzite D36		2.82	2.82	2.19		2.19	1.51	6.52		43	23	34
	Quartzite	Sekororo Formation Quartzite D47	0.10	2.32	2.42	1.92		1.92	1.36	5.70		42	24	34
	Quartzite	Average Sekororo Formation Quartzite D47	0.09	1.81	1.90	1.57		1.57	1.09	4.56		42	24	34
	Quartzite	Selati Formation Quartzite D35		6.26	6.26	1.69		1.69	2.04	9.99		63	20	17
	Quartzite	Black Reef Quartzite D34	0.52	0.12	0.64	0.62		0.62	0.27	1.53		42	18	41
	Quartzite	Black Reef Quartzite C201		0.04	0.04	0.60		0.60	0.22	0.86		5	26	70
		Average Black Reef Quartzite C201	0.52	0.08	0.60	0.61		0.61	0.25	1.46		41	17	42
	Quartzite	Rooihoogte Formation Quartzite C76			0.00	0.82		0.82	0.23	1.05		0	22	78
	Quartzite	Daspoort Formation Quartzite C81	0.34	0.14	0.48	0.66		0.66	0.32	1.46		33	22	45
	Quartzite	Daspoort Formation Quartzite M8F-2-10	0.56	0.01	0.57	4.24		4.24	0.73	5.54		10	13	77
		Average Daspoort Formation Quartzite M8F-2-10	0.45	0.08	0.53	2.45		2.45	0.53	3.50		15	15	70
	Quartzite	Magaliesberg Formation Quartzite C207	0.33	0.52	0.85	0.70		0.70	0.44	1.99		43	22	35
	Quartzite	Magaliesberg Formation Quartzite D77	1.79	5.92	7.71	3.24		3.24	4.30	15.25		51	28	21
		Average Magaliesberg Formation Quartzite D77	1.06	3.22	4.28	1.97		1.97	2.37	8.62		50	27	23
	Quartzite	Rayton Formation Quartzite C56	0.16	0.11	0.27	0.59		0.59	0.17	1.03		26	17	57

[1]It was discovered on July 28th 2016 that Lieger, D., Riller, U. and Gibson, R.L. 2010 was withdrawn at the request of the author(s).

*These samples were used to create the Figure 3-4 (AMF plot) in Chapter 3.

Lana et al. 2004	Gneiss (amphibolite facies) Trondhjemite NE-Part	ABBG-1	5.23	1.84	7.07	3.28		3.28	0.67	11.02		64	6	30
		ABBG-2	5.41	1.88	7.29	3.38		3.38	0.72	11.39		64	6	30
		ABBG-3	5.64	1.89	7.53	3.42		3.42	0.77	11.72		64	7	29
		ABG-1	4.91	3.34	8.25	2.45		2.45	0.25	10.95		75	2	22
		ABG-2	4.96	3.28	8.24	2.49		2.49	0.29	11.02		75	3	23
		ABP-1	5.38	3.56	8.94	2.31		2.31	0.28	11.53		78	2	20
		ABP-2	5.22	3.41	8.63	2.28		2.28	0.31	11.22		77	3	20
		ABP-3	5.38	3.09	8.47	2.35		2.35	0.32	11.14		76	3	21
		Average	5.27	2.79	8.05	2.75		2.75	0.45	11.25		72	4	24
	Porphyritic granodiorite W-Part	POR-1	5.86	1.99	7.85	3.65		3.65	0.54	12.04		65	4	30
		POR-2	5.67	1.99	7.66	3.75		3.75	0.60	12.01		64	5	31
		POR-3	5.74	2.31	8.05	3.71		3.71	0.55	12.31		65	4	30
		Average	5.76	2.10	7.85	3.70		3.70	0.56	12.12		65	5	31
	Gneiss (Granulite Facies) Quartz Diorite Central Part	SCH-1	7.17	3.95	11.12	3.50		3.50	0.52	15.14		73	3	23
		SCH-2	6.85	3.94	10.79	2.80		2.80	0.46	14.05		77	3	20
		SCH-3	6.90	4.00	10.90	2.87		2.87	0.50	14.27		76	4	20
		Average	6.97	3.96	10.94	3.06		3.06	0.49	14.49		75	3	21
	Melanosomes Trondhjemite Outer Parts	RG1	5.67	2.57	8.24	3.51		3.51	0.65	12.40		66	5	28
		RG14	5.35	3.38	8.73	3.27		3.27	0.50	12.50		70	4	26
		RG15	6.20	1.47	7.67	4.59		4.59	1.11	13.37		57	8	34
		SAG-1	6.09	1.38	7.47	2.87		2.87	0.60	10.94		68	5	26
		SAG-2	5.78	1.40	7.18	2.82		2.82	0.63	10.63		68	6	27
		EG1	5.22	2.01	7.23	4.20		4.20	0.84	12.27		59	7	34
		EG3A	5.19	1.59	6.78	4.08		4.08	0.75	11.61		58	6	35
		EG3B	5.50	1.91	7.41	4.28		4.28	0.87	12.56		59	7	34
		EG6	5.85	3.92	9.77	2.60		2.60	0.12	12.49		78	1	21
		BEG-1	5.66	1.81	7.47	3.32		3.32	0.61	11.40		66	5	29
		BEG-2	5.57	2.01	7.58	3.16		3.16	0.52	11.26		67	5	28
		VAL-1	5.12	2.51	7.63	2.18		2.18	0.18	9.99		76	2	22
		Average	5.60	2.16	7.76	3.41		3.41	0.62	11.79		66	5	29

[1]It was discovered on July 28th 2016 that Lieger, D., Riller, U. and Gibson, R.L. 2010 was withdrawn at the request of the author(s).
*These samples were used to create the Figure 3-4 (AMF plot) in Chapter 3.

	Melanosomes Tonalite Central Parts	vdf-4	3.62	1.20	4.82	10.67		10.67	5.95	21.44		22	28	50
		vdf-1	3.76	1.37	5.13	9.22		9.22	5.17	19.52		26	26	47
		vdf-8	2.32	0.77	3.09	12.24		12.24	5.99	21.32		14	28	57
		Average	3.23	1.11	4.35	10.71		10.71	5.70	20.76		21	27	52
	Mafic Granulites Central Parts	vdf2-12	2.12	1.38	3.50	8.38		8.38	12.56	24.44		14	51	34
		vdf2-21	1.79	1.33	3.12	13.27		13.27	9.77	26.16		12	37	51
		vdf2-2	1.98	0.30	2.28	25.00		25.00	8.96	36.24		6	25	69
		Average	1.96	1.00	2.97	15.55		15.55	10.43	28.95		10	36	54
	Leucosomes Granite Outer Parts	EG-4	2.91	8.08	10.99	2.49		2.49	0.28	13.76		80	2	18
		EG-7	4.56	6.16	10.72	1.90		1.90	0.07	12.69		84	1	15
		EG-8	5.14	3.77	8.91	1.69		1.69	0.12	10.72		83	1	16
		EG-9	4.65	4.82	9.47	1.22		1.22	0.00	10.69		89	0	11
		EG-10	5.18	3.88	9.06	1.81		1.81	0.17	11.04		82	2	16
		Pr12	5.26	3.39	8.65	1.52		1.52	0.16	10.33		84	2	15
		Pr2	4.56	4.46	9.02	1.31		1.31	0.01	10.34		87	0	13
		RG11	5.37	3.07	8.44	1.57		1.57	0.38	10.39		81	4	15
		RG12	4.89	3.54	8.43	1.35		1.35	0.25	10.03		84	2	13
		RG13	4.00	5.16	9.16	0.14		0.14	0.00	9.30		98	0	2
		RG2	4.15	4.94	9.09	1.19		1.19	0.10	10.38		88	1	11
		RG3	4.93	3.66	8.59	1.33		1.33	0.07	9.99		86	1	13
		RG7	5.59	3.50	9.09	1.45		1.45	0.38	10.92		83	3	13
		RG9	4.31	4.66	8.97	2.32		2.32	0.47	11.76		76	4	20
		SAL-1	5.28	3.33	8.61	1.78		1.78	0.00	10.39		83	0	17
		Average	4.72	4.43	9.15	1.54		1.54	0.16	10.85		84	2	14
	K-feldspar-rich Granite Transition Zone	LEP-1	3.83	3.12	6.95	1.84		1.84	0.21	9.00		77	2	20
		LEP-2	4.07	3.14	7.21	1.62		1.62	0.16	8.99		80	2	18
		LEP-3	3.76	3.29	7.05	1.72		1.72	0.17	8.94		79	2	19
		Average	3.89	3.18	7.07	1.73		1.73	0.18	8.98		79	2	19
	Schlieric Granite Northern Parts	SPW-1	4.79	3.48	8.27	1.48		1.48	0.04	9.79		84	0	15
		SPW-2	4.40	3.60	8.00	1.36		1.36	0.02	9.38		85	0	14

[1]It was discovered on July 28th 2016 that Lieger, D., Riller, U. and Gibson, R.L. 2010 was withdrawn at the request of the author(s).
*These samples were used to create the Figure 3-4 (AMF plot) in Chapter 3.

		ScSPW-3	5.14	3.45	8.59	1.62		1.62	0.06	10.27		84	1	16
		Average	4.78	3.51	8.29	1.49		1.49	0.04	9.81		84	0	15
	Homogen Granite Southwestern	ESP-1	4.89	4.08	8.97	1.42		1.42	0.00	10.39		86	0	14
		ESP-2	4.58	4.31	8.89	1.34		1.34	0.00	10.23		87	0	13
		Average	4.74	4.20	8.93	1.38		1.38	0.00	10.31		87	0	13
Hart et al. 1990	Ultramafics	Avg. Beta -1	0.28	0.13	0.41	11.67		11.67	36.63	48.71		1	75	24
Remiold 2000	Anne Rust Sheet	Mean IV	2.25	0.69	2.94	13.72	0.00	13.72	6.31	22.97		13	27	60
		Mean III	2.17	0.69	2.86	13.77	0.01	13.78	6.59	23.23		12	28	59
		Anna's Rust Sheet*	2.08	0.72	2.80	13.35		13.35	6.52	22.67		12	29	59
		Vred mafic complex	1.78	0.60	2.38	12.68		12.68	6.88	21.94		11	31	58
		OCEAAN	2.00	0.53	2.53	13.09		13.09	6.75	22.37		11	30	59
		Core	2.57	0.73	3.30	16.19		16.19	5.57	25.06		13	22	65
		CoreBH	2.60	0.74	3.34	14.24		14.24	6.12	23.70		14	26	60
		Collar	2.19	0.73	2.92	13.63		13.63	6.12	22.67		13	27	60
		SWBH	2.76	0.66	3.42	13.89		13.89	6.02	23.33		15	26	60
Coetzee 2006	Tholeiitic Intrusions	Wittekopjes norite	0.82	0.19	1.01	10.09		10.09	20.20	31.30		3	65	32
		Parsons Rust Dol-Norite	1.31	0.30	1.61	10.74		10.74	14.61	26.96		6	54	40
		Reebokkop dolerite	2.52	0.69	3.21	10.13		10.13	8.27	21.61		15	38	47
	Mafic Dykes and sills	Bushveld micopyroxenitic sills		0.90	0.90			0.00	13.00	13.90		6	94	0
		Bushveld Ultramafic Sills		0.30	0.30			0.00	32.10	32.40		1	99	0
		Noritic sills and dykes E Witts		0.20	0.20			0.00	11.00	11.20		2	98	0
de Waal, Graham and Armstrong 2006	Lindeques drift and Heidelberg Intrusions	Lindeques Drift Contamspess	1.45	0.30	1.75	21.33		21.33	12.08	35.16		5	34	61
		Lindeques Drift Even-grained spessartite mean	1.19	0.31	1.50	29.36		29.36	9.96	40.82		4	24	72

[1]It was discovered on July 28th 2016 that Lieger, D., Riller, U. and Gibson, R.L. 2010 was withdrawn at the request of the author(s).

*These samples were used to create the Figure 3-4 (AMF plot) in Chapter 3.

		Lindeques Drift Porphyritic spessartite mean	2.31	0.60	2.91	26.63		26.63	8.33	37.87		8	22	70
		Heidelberg Porphy-ritic spess mean	2.25	0.57	2.82	25.44		25.44	9.31	37.57		8	25	68
		Lindeques Drift Low-silica diorite mean	6.12	1.16	7.28	16.94		16.94	4.72	28.94		25	16	59
		Lindeques Drift diorite mean	4.67	1.16	5.83	13.96		13.96	3.85	23.64		25	16	59
		Lindeques Drift syeno-diorite mean	6.33	1.29	7.62	8.42		8.42	1.87	17.91		43	10	47
		Lindeques Drift feeder	2.74	1.02	3.76	14.21		14.21	4.66	22.63		17	21	63
		Roodekraal Complex Lava	5.51	1.78	7.29	13.01		13.01	3.37	23.67		31	14	55
		Roodekraal Complex Cumulate	2.80	0.91	3.71	23.32		23.32	7.57	34.60		11	22	67
		Roodekraal Complex Diorite	5.53	1.32	6.85	12.24		12.24	2.85	21.94		31	13	56
		Roodekraal Complex Lava Clark 1972	4.73	1.81	6.54	15.23		15.23	2.89	24.66		27	12	62
		Roodekraal Complex Diorite Clark 1972	5.20	1.60	6.80	15.79		15.79	4.16	26.75		25	16	59
Sudbury														
Lightfoot et al. 1996	Main Mass Mafic Norite Average		2.03	1.41	3.44	9.93		9.93	10.61	23.98		14	44	41
	Main Mass Felsic Norite Average		2.85	1.81	4.66	7.91		7.91	4.95	17.52		27	28	45
	Main Mass Granophyre Average		3.62	3.46	7.08	6.47		6.47	1.23	14.78		48	8	44
	Igneous textured sublayer matrix Whistle Mine Average		2.41	1.00	3.41	13.49	8.18	21.67	7.73	32.81		10	24	66
	Melanorite Pod or Inclusion Whistle Mine Average		1.73	1.20	2.93	14.57	8.81	23.38	10.51	36.82		8	29	63
	Olivine Melanorite Whistle Mine Average		0.57	0.83	1.40	15.11	9.18	24.29	18.09	43.78		3	41	55
	Diabase Whistle Mine Average		2.19	0.78	2.97	15.03	9.04	24.07	6.00	33.04		9	18	73
	Little Stobie Mine Igneous Textured Sublayer Matrix	93PCL-001	1.75	0.40	2.15	12.86	9.48	22.34	8.57	33.06		7	26	68
		93PCL-001	1.93	0.47	2.40	12.86	9.79	22.65	6.79	31.84		8	21	71
	Crean Hill Mine Igneous Textured Sublayer Matrix	93PCL-20	2.12	1.08	3.20	10.28	7.70	17.98	5.76	26.94		12	21	67
		93PCL-22	1.98	1.02	3.00	11.94	8.77	20.71	6.67	30.38		10	22	68
		93PCL-23	2.20	0.76	2.96	10.81	8.30	19.11	6.08	28.15		11	22	68

[1]It was discovered on July 28th 2016 that Lieger, D., Riller, U. and Gibson, R.L. 2010 was withdrawn at the request of the author(s).

*These samples were used to create the Figure 3-4 (AMF plot) in Chapter 3.

		93PCL-25	2.17	0.90	3.07	11.62	8.57	20.19	6.71	29.97		10	22	67
	Levack West Mine Igneous Textured Sublayer Matrix	93PCL-45	2.53	1.33	3.86	9.54	7.18	16.72	9.52	30.10		13	32	56
		93PCL-46	1.54	0.78	2.32	11.50	7.57	19.07	13.29	34.68		7	38	55
	Levack West Mine Melanorite Pod or Inclusion	93PCL-66	1.24	0.54	1.78	12.04	8.12	20.16	16.03	37.97		5	42	53
		93PCL-67	0.14	0.35	0.49	13.17	7.44	20.61	26.00	47.10		1	55	44
		93PCL-68	0.15	0.39	0.54	13.31	7.22	20.53	25.10	46.17		1	54	44
	McCreedy West Mine Igneous Textured Sublayer Matrix	93PCL-50	1.82	1.10	2.92	15.07	8.10	23.17	9.93	36.02		8	28	64
		93PCL-51	2.08	1.02	3.10	10.66	8.12	18.78	10.92	32.80		9	33	57
		93PCL-53	2.18	1.40	3.58	10.07	7.04	17.11	9.83	30.52		12	32	56
		93PCL-55	2.34	0.87	3.21	12.51	7.49	20.00	10.00	33.21		10	30	60
		93PCL-59	2.39	0.79	3.18	9.83	6.31	16.14	9.11	28.43		11	32	57
	Fraser Mine Igneous Textured Sublayer Matrix	93PCL-342	2.42	1.16	3.58	9.08	7.08	16.16	8.47	28.21		13	30	57
		93PCL-343	1.91	1.15	3.06	9.97	7.18	17.15	9.89	30.10		10	33	57
		93PCL-344	2.05	1.20	3.25	10.49	7.55	18.04	10.13	31.42		10	32	57
		92PCL-345	1.79	1.24	3.03	10.49	8.02	18.51	11.52	33.06		9	35	56
		93PCL-346	1.86	1.25	3.11	10.21	7.30	17.51	10.58	31.20		10	34	56
	Creighton Mine Igneous Textured Sublayer Matrix	94PCL-128	1.51	1.40	2.91	12.34	10.33	22.67	11.03	36.61		8	30	62
		94PCL-131	2.40	1.15	3.55	12.24	10.33	22.57	6.44	32.56		11	20	69
		94PCL-132	1.68	1.50	3.18	14.80	8.59	23.39	8.38	34.95		9	24	67
Lightfoot et al. 2001	Mafic Norite	94PCL2011	2.11	1.14	3.25	9.84	7.48	17.32	11.35	31.92		10	36	54
		94PCL2016	2.04	1.07	3.11	11.01	7.56	18.57	12.15	33.83		9	36	55
	Felsic Norite	94PCL2066	3.15	1.47	4.62	7.56	5.96	13.52	4.37	22.51		21	19	60
		94PCL2072	3.14	1.56	4.70	7.27	4.84	12.11	4.75	21.56		22	22	56
		94PCL2076	2.91	1.49	4.40	6.66	4.29	10.95	4.75	20.10		22	24	54
		94PCL2033	2.81	1.60	4.41	6.82	4.24	11.06	5.20	20.67		21	25	54
		94PCL2028	2.66	1.45	4.11	7.08	4.56	11.64	5.57	21.32		19	26	55
		94PCL2013	2.49	1.20	3.69	8.08	5.89	13.97	8.25	25.91		14	32	54
	Quartz Gabbro	94PCL2080	3.68	1.90	5.58	9.41	5.77	15.18	3.89	24.65		23	16	62
		93PCL290	3.68	2.99	6.67	8.24	3.39	11.63	0.85	19.15		35	4	61

[1]It was discovered on July 28th 2016 that Lieger, D., Riller, U. and Gibson, R.L. 2010 was withdrawn at the request of the author(s).
*These samples were used to create the Figure 3-4 (AMF plot) in Chapter 3.

		94PCL2052	4.87	0.93	5.80	9.03	5.46	14.49	3.77	24.06		24	16	60
		94PCL2079	4.34	1.44	5.78	8.72	5.11	13.83	3.80	23.41		25	16	59
	Granophyre	93PCL336	3.37	3.30	6.67	8.15	4.49	12.64	1.47	20.78		32	7	61
		93PCL293	3.32	4.06	7.38	5.41	3.19	8.60	1.04	17.02		43	6	51
		93PCL297	3.50	4.03	7.53	5.65	3.16	8.81	1.08	17.42		43	6	51
		93PCL312	3.85	2.78	6.63	7.35	4.17	11.52	1.42	19.57		34	7	59
		93PCL334	2.94	3.64	6.58	9.31	5.41	14.72	1.60	22.90		29	7	64
	Mafic Norite Average*		1.90	1.20	3.10	11.60		11.60	13.70	28.40		11	48	41
	Felsic Norite Average*		3.20	1.50	4.70	7.20		7.20	5.20	17.10		27	30	42
	Quartz Gabbro Average*		4.10	1.90	6.00	10.30		10.30	2.90	19.20		31	15	54
	Granophyre Average*		3.70	3.60	7.30	6.40		6.40	1.20	14.90		49	8	43
	Main Mass Average		3.40	2.40	5.80	7.60		7.60	3.70	17.10		34	22	44
Namaqualand														
Duchesne et al. 2007	Anorthosites	Sample 70[b]	4.14	0.92	5.06	1.42		1.42	0.41	6.89		73	6	21
		Sample 66	5.71	0.85	6.56	1.25		1.25	0.66	8.47		77	8	15
		Sample 108	4.65	0.81	5.46	3.77		3.77	0.98	10.21		53	10	37
	Tonalite	Sample 30[a]	5.36	1.11	6.47	0.46		0.46	0.15	7.08		91	2	6
	Leuconorite	Sample 119	3.75	0.94	4.69	11.01		11.01	3.70	19.40		24	19	57
		Sample 120	4.29	0.71	5.00	9.02		9.02	2.58	16.60		30	16	54
		Sample 121	4.54	1.04	5.58	6.92		6.92	1.91	14.41		39	13	48
	Norite Sample 85b	Sample 85[b]	3.16	0.55	3.71	14.08		14.08	8.04	25.83		14	31	55
		Sample 86[b]	2.57	0.63	3.20	15.49		15.49	9.13	27.82		12	33	56
		Sample 116	3.33	0.43	3.76	12.30		12.30	5.26	21.32		18	25	58
		Sample 122	2.52	0.95	3.47	10.25		10.25	7.69	21.41		16	36	48
	Melanorite	Sample 88[b]	0.96	0.57	1.53	22.13		22.13	16.70	40.36		4	41	55
		Sample 87[b]	1.16	0.20	1.36	21.93		21.93	14.82	38.11		4	39	58
		Sample 110	0.75	0.30	1.05	30.52		30.52	12.09	43.66		2	28	70
	Hypersthenite	Sample 90[b]	0.00	0.00	0.00	24.33		24.33	20.41	44.74		0	46	54

[1]It was discovered on July 28th 2016 that Lieger, D., Riller, U. and Gibson, R.L. 2010 was withdrawn at the request of the author(s).

*These samples were used to create the Figure 3-4 (AMF plot) in Chapter 3.

		Sample 117	0.35	2.00	2.35	25.90		25.90	19.00	47.25		5	40	55
	Glimmerite	Sample 123	0.50	6.70	7.20	10.80		10.80	17.50	35.50		20	49	30
	Magnetite	Sample 82[b]	0.06	0.09	0.15	47.91		47.91	11.48	59.54		0	19	80
		Sample 125[b]	0.03	0.07	0.10	39.66		39.66	11.39	51.15		0	22	78
	Biotite Diorite	Sample 78[b]	4.06	1.80	5.86	10.03		10.03	2.67	18.56		32	14	54
		Sample 112	4.18	1.85	6.03	8.80		8.80	3.11	17.94		34	17	49
		Sample 109	5.10	2.72	7.82	5.80		5.80	1.55	15.17		52	10	38
		Sample 114	3.42	0.72	4.14	8.14		8.14	2.32	14.60		28	16	56
		Sample 118	3.95	4.30	8.25	8.94		8.94	7.11	24.30		34	29	37
		Sample 126	3.82	0.71	4.53	7.35		7.35	4.83	16.71		27	29	44
Morokweng														
Andreoli et al. 1999	Medium Grained Quartz Norite	N-5	3.88	2.05	5.93	1.23	4.42	5.65	4.05	15.63		38	26	36
		LA-137	4.39	2.04	6.43	3.01	2.78	5.79	3.71	15.93		40	23	36
		N-4	3.86	2.14	6.00	1.17	4.22	5.39	3.93	15.32		39	26	35
		LA-141	4.65	2.20	6.85	2.61	3.07	5.68	3.92	16.45		42	24	35
		LA-161	3.97	2.28	6.25	3.16	2.36	5.52	3.15	14.92		42	21	37
		N-3	3.58	2.21	5.79	1.17	4.21	5.38	4.04	15.21		38	27	35
	Medium Grained Quartz Norite	LA-172	4.04	2.31	6.35	3.15	2.14	5.29	3.58	15.22		42	24	35
	Heterogeneous Quartz Norite	LA-174	4.28	2.42	6.70	3.12	1.51	4.63	2.36	13.69		49	17	34
		N-2	4.02	1.52	5.54	1.32	4.75	6.07	3.81	15.42		36	25	39
		LA-186	4.55	1.85	6.40	3.21	2.55	5.76	3.15	15.31		42	21	38
	Fine Grained Quartz Norite	N-1	3.50	1.67	5.17	1.80	6.46	8.26	4.88	18.31		28	27	45
		LA-197	3.91	1.95	5.86	4.55	3.59	8.14	4.70	18.70		31	25	44
		LA-213	4.40	1.97	6.37	4.12	3.25	7.37	4.50	18.24		35	25	40
		LA-216	4.44	2.54	6.98	3.58	2.17	5.75	3.86	16.59		42	23	35

[1]It was discovered on July 28th 2016 that Lieger, D., Riller, U. and Gibson, R.L. 2010 was withdrawn at the request of the author(s).
*These samples were used to create the Figure 3-4 (AMF plot) in Chapter 3.

	Chilled Quartz Norite	LA-224	3.91	1.71	5.62	4.36	2.46	6.82	3.68	16.12		35	23	42
	Quartz Norite Mean*		4.09	2.05	6.14	2.77	3.35	6.12	3.82	16.08		38	24	38
Manicouagan														
O-Connell-Cooper and Spray 2011	Undifferentiated Melt*		3.84	3.00	6.84	3.88	2.56	6.44	3.64	16.92		40	21	38
	Differentiated Melt*		3.90	3.19	7.09	1.93	4.00	5.93	3.40	16.42		43	21	36

[1]It was discovered on July 28th 2016 that Lieger, D., Riller, U. and Gibson, R.L. 2010 was withdrawn at the request of the author(s).
*These samples were used to create the Figure 3-4 (AMF plot) in Chapter 3.

Appendix B-1-10: Chemistry References

[1]Anders E. and Grevesse N. 1989. Abundances of the elements: Meteoritic and solar. Geochimica et Cosmochimica Acta, **53**:197-214.

[2]Andreoli, M.A.G., Ashwal, L.D., Hart, R.J. and Huizenga, J.M. 1999. A Ni- and PGE-enriched quartz norite impact melt complex in the Late Jurassic Morokweng impact structure, South Africa. Geological Society of America, Special Paper **339**: 91-108.

[3]Bisschoff A.A. 1972. The dioritic rocks of the Vredefort Dome. Geological Society of South Africa Transaction, **75**: 31-46.

[4]Bisschoff A.A. 1973. The petrology of some mafic and peralkaline intrusions in the Vredefort Dome. Geological Society of South Africa Transaction, **76**: 27-52.

[5]Coetzee, M.S., Beukes, G.J., de Bruiyn, H., Bisschoff, A.A. 2006. Geochemistry and petrogenesis of tholeiitic intrusions of possible Bushveld-age in the Vredefort Dome, South Africa. Journal of African Earth Science. **45**(2): 213-235.

[6]Crow, C. and Condie, K.C. 1988. Geochemistry and origin of late Archean volcanics from the ventersdorp supergroup, South Africa. Precambrian Research, **42**(1-2): 19-37.

[7]de Waal, S.A., Graham, I.T. and Armstrong, R.A. 2006. The Lindeques Drift and Heidelberg Intrusions and the Roodekraal Complex,Vredefort, South Africa: comagmatic plutonic and volcanic products of a 2055 Ma ferrobasaltic magma. South Africa Journal of Geology, **109**: 279-300.

[8]Duchesne, J.C., Auwera, J.V., Liegeois, J.P., Barton, E.S. and Clifford, T.N. 2007. Geochemical constraints of the petrogenesis of the O'okiep Koperberg Suite and granitic plutons in Namaqualand, South Africa: A crustal source in Namaquan (Grenville) times. Precambrian Research, **153**(1-2): 116-142.

[9]Hart, R.J., Andreoli, M.A.G., Smith, C.B., Otter, M.L. and Durrheim, R. 1990. Ultramafic rocks in the centre of the Vredefort structure (South Africa): Possible exposure of the upper mantle? Chemical Geology, **83**: 233-248.

[10]Koeberl, C., Reimold W.U. and Shirey, S.B. 1996. Re-Os isotope and geochemical study of the Vredefort Granophyre: Clues to the origin of the Vredefort structure, South Africa. Geology, **24**(10): 913-916.

[11]Lana, C., Reimold, W.U., Gibson, R.L., Koeberl, C. and Siegesmund, S. 2004. Nature of the Archean midcrust in the core of the Vredefort Dome, Central Kaapvaal Craton, South Africa. Geochimica et Cosmochimica Acta, 68(3): 623-642.

[12]Lieger, D., Riller, U. and Gibson, R.L. 2010. Whole rock geochemical, SEM and electron microprobe analysis of pseudotachylite from the Vredefort Impact Structure, South Africa: Evidence for injection of impact melt into target rocks. Geochimica et Cosmochimica Acta doi:10.1016/j.gca.2010.06.031

[13]Lightfoot, P.C. and Doherty, W. 2001. Chemical Evolution and Origin of Nickel Sulfide Mineralization in the Sudbury Igneous Complex, Ontario, Canada. Economic Geology, **96**(8): 1855-1875.

[14]Lightfoot, P.C., Keays, R.R., Morrison, G.G., Bite, A. and Farrell, K.P. 1996. Geologic and geochemical relationships between the contact sublayer, inclusions, and the main mass of the Sudbury Igneous Complex; a case study of the Whistle Mine Embayment, Economic Geology, **92**: 647-673.

[15]Maier, W.D., Barnes, S.J. and Marsh, J.S. 2003. The concentrations of the noble metals in Southern African flood-type basalts and MORB: implications for petrogenesis and magmatic sulphide exploration. Contributions to Mineralogy and Petrology, **146**(1): 44-61.

[16]McIver J.R., Cawthorn R.G. and Wyatt B.A. 1981. The Ventersdorp Supergroup – the youngest komatiitic sequence in South Africa. *In* Komatiites *Edited by* Nisbet, E.G. and Arndt, N.T. Allen and Unwin, London.

[17]O'Connell-Cooper, C.D. and Spray, J.G. 2011. Geochemistry of the Impact-Generated Melt Sheet at Manicouagan: Evidence for Fractional Crystallization. Journal of Geophysical Research, **116:** 1-22.

[18]Reimold, W.U. 1991. Geochemistry of pseudotachylites from the Vredefort Structure South Africa. Neues Jahrbuch Mineralogie Abh, **161**: 151-184.

[19]Reimold, W.U. and Gibson, R.L. 2006. The melt rocks of the Vredefort impact structure – Vredefort Granophyre and pseudotachylitic breccias: Implications for impact cratering and the evolution of the Witwatersrand Basin. Chemie der Erde – Geochemistry, **66**(1): 1-35.

[20]Remiold, W.U., Pybus, G.Q.J., Kruger, F.J., Layer, P.W. and Koeberl, C. 2000. The Anna's Rust Sheet and related gabbroic intrusions in the Vredefort Dome-Kibaran magmatic event on the Kaapvaal Craton and beyond? Journal of African Earth Science, **31**(3-4): 499-521.

[21]Schwarzman, E.C., Meyer, C and Wilshire, H.G. 1983. Pseudotachylite from the Vredefort Ring, South Africa, and the origins of some lunar breccias. Geological Society of America Bulletin, **94**(7): 926-935.

[22]Tankard, A.J. and Barwis, J.H. 1982. Wave-Dominated Deltaic Sedimentation in the Devonian Bokkeveld Basin of South Africa. Journal of Sedimentary Petrology, **52**(3): 959-974.

[23]Wilshire, H.G. 1971. Pseudotachylite from the Vredefort Ring, South Africa. The Journal of Geology, **79**(2): 195-206.

[24]Wilson, A. and Chunnett, G. 2006. Trace Element and Platinum Group Element Distributions and the Genesis of the Merensky Reef, Western Bushveld Complex, South Africa. Journal of Petrology, **47**(12):2369–2403.

[25]Wronkiewicz, D.J. and Condie, K.C. 1990.Geochemistry and mineralogy of sediments from the Ventersdorp and Transvaal Supergroups, South Africa: Cratonic evolution during the early Proterozoic. Geochimica et Cosmochimica Acta, **54**(2): 343-354. doi:10.1016/0016-7037(90)90323-D

[26]http://meteorites.wustl.edu/goodstuff/ree-chon.htm

Appendix B-2: Vredefort EDS Mineral Chemistry

Table of Vredefort mineral chemistry collected using EDS analysis on the FEG-SEM at Westerns ZAPLab.

Sample	Na_2O	Al_2O_3	SiO_2	K_2O	CaO	MgO	TiO_2	MnO	FeO
V232									
Plagioclase									
S1 Spec1	6.56	25.69	58.84	0.98	7.90				
S1 Spec2	6.43	27.10	58.97	0.67	8.99				
S1 Spec3	5.74	24.2	52.79	0.71	8.04				
S1 Spec4	6.15	26.21	57.07	0.72	8.69				
S5 Spec1	6.02	25.89	56.20	0.86	8.54				
S5 Spec2	5.77	24.94	53.92	0.78	8.22				
S5 Spec3	5.8	24.82	53.93	0.73	8.19				
S5 Spec4	6.09	26.08	56.62	0.81	8.50				
Pyroxene									
S2 Spec1		0.39	49.17		2.66	12.23	0.16	0.72	36.28
S2 Spec2		1.31	49.51		20.49	10.16	0.4	0.34	17.54
S2 Spec3		1.20	49.62		20.14	10.24	0.39	0.37	17.75
S2 Spec4		0.29	48.60		0.92	12.39	0.19	0.77	37.22
S2 Spec5		1.25	49.52		19.58	10.32	0.42	0.36	18.21
S4 Spec1		0.35	47.31		1.41	12.17	0.14	0.74	36.09
S4 Spec2		1.22	47.50		19.85	9.89	0.37	0.38	17.04
S4 Spec3		1.35	47.43		20.32	9.84	0.41	0.33	16.66
S4 Spec4		0.29	46.78		0.95	12.16	0.11	0.74	35.83
S4 Spec5		1.03	48.09		19.80	10.26	0.24	0.38	16.21
S4 Spec6		0.26	46.35		0.92	11.9	0.11	0.82	35.48
S6 Spec1		0.38	47.04		1.56	12.7	0.18	0.72	34.88
S6 Spec2		1	48.10		20.66	10.04	0.32	0.33	16.55
S6 Spec3		1.09	44.93		18.54	9.35	0.35	0.34	16.41
S6 Spec4		2.05	48.54		11.48	10.52	0.35	0.46	24.09
S6 Spec5		1.55	50.17		20.24	10.41	0.43	0.35	18.11
S6 Spec6		1.18	49.76		20.46	10.29	0.41	0.42	18.285

Sample	Na_2O	Al_2O_3	SiO_2	K_2O	CaO	MgO	TiO_2	MnO	FeO
V235									
Plagioclase									
S3 Spot1	5.61	30.51	55.93	0.54	9.93				
S3 Spot2	5.67	30.77	56.25	0.5	9.95				
S3 Spec3	5.68	30.90	56.36	0.52	9.93				
S8 Spec1	5.63	27.64	55.39	0.51	9.82				
S8 Spec2	5.62	27.64	55.51	0.52	9.89				
Pyroxene									
S2 Spec1		0.67	49.24		1.27	15.41	0.23	0.58	32.92
S2 Spec2		1.39	49.54		20.61	11.22	0.41	0.33	15.87
S2 Spec3		0.60	49.18		3.97	13.60	0.2	0.60	32.98
S2 Spec4		0.61	48.61		1.03	14.84	0.18	0.58	33.15
S2 Spec5		0.10	31.33		0.04	12.78	0.00	0.69	55.64
S2 Spec6		1.39	48.90		20.84	11.58	0.39	0.27	14.78
S4 Spec4		1.43	49.61		20.91	11.48	0.35	0.28	15.69
S4 Spec5		0.52	48.63		0.83	14.27	0.13	0.63	34.75
S6 Spec4		1.37	49.71		20.10	11.34	0.40	0.32	16.27
S6 Spec5		0.38	49.36		1.18	14.18	0.13	0.62	34.68
S7 Spec1		1.46	49.26		20.27	11.05	0.44	0.31	16.23
S7 Spec2		0.44	49.38		0.97	14.02	0.16	0.68	34.84
S7 Spec3		1.21	49.37		20.12	11.24	0.28	0.32	16.08
S7 Spec4		1.41	49.21		20.87	11	0.40	0.29	15.38
S7 Spec5		0.66	48.74		1.07	14.75	0.16	0.60	33.44
MN2									
Plagioclase									
S1 Spec1	5.96	24.58	56.37	0.72	8.17				
S1 Spec2	6.14	26.23	59.62	0.86	8.82				
S1 Spec3	5.99	25.44	57.94	0.80	8.52				
S4 Spec1	6.03	26.04	59.13	0.83	8.82				
S4 Spec2	6.11	25.92	58.82	0.60	8.8				
S4 Spec3	6.31	25.42	59.47	0.90	8.21				

Pyroxene	Na_2O	Al_2O_3	SiO_2	K_2O	CaO	MgO	TiO_2	MnO	FeO
S6 Spec1	6.09	26.17	59.16	0.78	8.96				0.28
S6 Spec2	6.22	25.69	59.46	0.92	8.51				0.30
S6 Spec3	6.01	25.81	58.38	0.81	8.8				0.26
S3 Spec1		0.37	46.90		1.08	12.6	0.17	0.72	34.38
S3 Spec2		0.85	47.89		20.31	9.97	0.3	0.33	16.43
S3 Spec3		1.00	48.24		19.48	10.02	0.3	0.4	17.63
S3 Spec4		0.62	48.17		5.14	12.11	0.22	0.66	31.18
S3 Spec5		0.93	45.46		18.9	9.31	0.30	0.36	16.09
S3 Spec6		0.47	48.16		1.07	12.78	0.16	0.7	34.99
S5 Spec1		1.37	46.68		1.39	12.36	0.13	0.68	34.35
S5 Spec2		1.47	47.17		5.37	11.87	0.15	0.63	30.43
S5 Spec3		1.91	47.79		19.8	9.81	0.33	0.37	17.02
S5 Spec4		2.26	47.50		19.47	9.73	0.36	0.35	16.90
S5 Spec5		1.61	47.53		1.04	12.31	0.17	0.69	35.44
S5 Spec6		2.08	47.36		18.45	9.75	0.34	0.41	18.09
S5 Spec7		2.31	47.41		19.37	9.77	0.34	0.37	17.17

Appendix B-3: Vredefort Zircon Trace Element Chemistry

	La Ch	Ce Ch	Pr Ch Calc	Nd Ch	Sm Ch	Eu Ch	Gd Ch	Tb Ch	Dy Ch	Ho Ch	Er Ch	Tm Ch	Yb Ch	Lu Ch	Sm/ Nd	Ce/ Ce*	Hf ppm	Eu/ Eu*
	0.319	0.82	0.121	0.615	0.2	0.076	0.267	0.0493	0.33	0.0755	0.216	0.0329	0.221	0.033	Chon			
V09-232-1.2	4.58	15	3.99	3.72	8.46	6.5	45	79	139	237	373	505	628	702	2.3	4	7535	0.33
V09-232-1.3	0.04	6	0.32	0.92	6.26	5.1	48	88	155	287	462	644	800	975	6.8	57	9272	0.29
V09-232-2.2	0.02	4	0.13	0.32	2.34	2.1	17	37	65	120	196	281	352	434	7.3	65	9882	0.32
V09-232-2.3	0.04	4	0.20	0.47	2.82	2.4	21	46	79	152	256	375	453	549	6.1	49	9897	0.31
V09-232-3.2	0.07	5	0.45	1.14	7.40	5.1	43	76	137	253	384	535	659	780	6.5	30	9161	0.28
V09-232-3.3	0.02	6	0.24	0.80	6.18	4.7	42	89	160	298	478	671	812	970	7.8	82	9913	0.29
V09-232-4.2	0.06	4	0.27	0.57	2.82	3.0	25	48	85	155	239	333	408	486	5.0	31	8507	0.36
V09-232-5.2	0.05	4	0.26	0.57	2.39	2.1	19	40	74	135	229	323	414	509	4.2	31	8749	0.31
V09-232-5.3	0.02	4	0.12	0.25	1.69	1.5	17	36	67	130	229	353	458	537	6.7	73	9646	0.27
V09-232-6.2	0.03	4	0.28	0.85	3.34	2.5	20	40	71	138	213	302	387	503	3.9	47	10162	0.31
V09-232-6.3	0.04	3	0.16	0.32	2.53	1.9	17	34	58	110	188	266	324	442	8.0	38	9516	0.28
V09-232-7.2	0.08	5	0.27	0.50	3.69	2.3	26	49	80	161	248	349	406	501	7.4	36	8855	0.23
V09-232-7.3	0.06	5	0.22	0.45	3.16	2.4	31	54	102	200	322	422	554	678	7.0	49	9608	0.24
V09-232-8.2	0.02	5	0.08	0.18	1.40	1.1	13	30	52	114	183	272	354	455	8.0	129	9686	0.26
V09-235-1.2	0.03	4	0.15	0.38	4.95	2.7	33	67	114	213	334	451	571	728	13.1	64	9783	0.21
V09-235-2.2	0.04	3	0.13	0.23	1.87	1.0	16	31	53	121	192	259	356	442	8.0	34	9856	0.18
V09-235-3.2	0.02	2	0.12	0.28	2.24	1.4	20	39	67	128	196	287	341	413	8.0	45	9465	0.20
V09-235-4.2	0.02	2	0.15	0.44	4.06	2.6	33	62	101	204	298	405	505	639	9.2	39	8449	0.23
V09-235-5.2	0.02	3	0.14	0.39	3.03	1.8	27	46	88	168	280	386	467	599	7.7	55	9221	0.20
V09-235-6.2	0.08	4	0.81	2.51	14.96	7.5	91	136	220	412	557	738	886	1030	6.0	15	8100	0.20
V09-235-7.2	0.04	4	0.52	1.79	14.98	8.5	106	176	273	497	706	945	1124	1301	8.4	27	9859	0.21
V09-235-8.2	0.02	3	0.10	0.23	2.24	1.5	19	40	77	153	250	332	449	561	9.8	71	10874	0.22
V09-235-9.2	0.01	3	0.35	1.96	12.08	7.6	85	150	251	442	643	860	1026	1194	6.2	52	9451	0.24

V09-235-9.3	0.01	2	0.07	0.18	1.79	0.7	13	26	45	94	142	200	265	310	10.2	70	8770	0.16
V09-235-10.2	0.02	4	0.15	0.43	4.86	3.2	42	71	127	252	378	530	637	806	11.2	65	9620	0.23
V09-111-1.2	0.03	30	0.48	1.83	11.85	3.0	75	126	194	332	490	628	716	849	6.5	239	9966	0.10
V09-111-1.3	0.05	23	0.39	1.05	7.90	3.4	46	80	129	229	346	453	521	669	7.5	158	9862	0.18
V09-111-2.2	0.43	28	2.22	5.01	26.18	10.4	134	200	292	479	665	852	929	1108	5.2	28	9503	0.18
V09-111-3.2	0.03	19	0.33	1.13	6.65	2.9	46	77	123	223	323	440	544	632	5.9	199	10131	0.16
V09-111-3.3	0.02	33	0.22	0.74	7.85	1.3	50	79	128	252	359	455	568	713	10.6	517	10758	0.07
V09-111-4.2	0.00	17	0.00	1.38	7.99	4.1	50	74	120	234	312	429	503	634	5.8	---	8635	0.21
V09-111-4.3	0.06	42	0.69	2.28	12.21	1.6	74	126	204	365	534	740	886	1053	5.4	200	12805	0.05
V09-237-1.2	0.61	28	1.76	2.98	21.08	7.2	137	189	278	466	601	779	854	1058	7.1	27	10763	0.13
V09-237-2.2	2.63	35	3.26	3.62	26.86	7.9	161	234	335	538	687	844	963	1129	7.4	12	10438	0.12
V09-237-3.2	0.19	22	0.73	1.41	10.52	3.3	65	104	157	266	373	487	577	695	7.5	60	9542	0.13
V09-237-4.5	22.62	36	8.63	5.33	8.85	5.1	39	62	105	179	272	357	431	561	1.7	3	10501	0.27
V09-237-4.6	9.64	26	5.58	4.24	13.54	4.5	79	119	186	325	461	593	716	886	3.2	3	10197	0.14
V09-237-5.2	2.90	15	1.49	1.07	4.77	1.2	29	48	74	140	187	259	314	401	4.5	7	10406	0.10
V09-250-1.2	0.91	5	0.79	0.73	3.91	2.6	43	70	127	247	370	513	621	770	5.3	5	10219	0.20
V09-250-2.2	0.02	5	0.30	1.16	8.17	6.5	73	118	199	384	542	748	896	1122	7.1	68	11174	0.27
V09-250-4.2	0.02	5	0.24	0.89	6.04	3.8	54	103	178	344	515	758	889	1086	6.8	81	10977	0.21
V09-250-5.2	0.03	5	0.17	0.44	2.50	1.8	26	49	85	180	287	402	516	648	5.7	66	10001	0.22
V09-250-6.2	0.05	5	0.26	0.58	5.44	3.0	37	66	125	241	354	506	592	725	9.4	40	9066	0.21
V09-250-6.3	0.02	7	0.17	0.47	4.44	3.0	36	68	118	237	351	500	606	773	9.4	126	10850	0.23

Appendix B-4: Vredefort SHRIMP Data.

Spots were omitted that contained cracks or inclusions that would have compromised the data.

Sample #	207 206 age	2sd error	Conc (%)	204 cts/ sec	204 /206	Pb/U: UO/U²	% err	Pb^{204} Corr 207r/ 206r	% err	Pb^{204} Corr 207r/ 235r	% err	Pb^{204} Corr 207r/ 238	% err	Err corr	U (ppm)	Th (ppm)	Th/U
V09_232																	
V09_232 _1.1	1993	46	2	0.06	8.5E-5	.02779	1.1	.1225	1.3	5.99	1.7	.3547	1.1	.653	37	17	0.49
V09_232 _2.1	1984	56	0	0.07	1.3E-4	.02828	1.3	.1219	1.6	6.06	2.1	.3606	1.3	.637	27	10	0.38
V09_232 _3.1	2000	40	0	0.05	5.0E-5	.02845	1.0	.1230	1.1	6.16	1.5	.3632	1.0	.670	53	27	0.53
V09_232 _4.1	2013	40	0	-0.07	-7.1E-5	.02874	1.0	.1239	1.1	6.28	1.5	.3676	1.0	.649	51	26	0.52
V09_232 _5.1	1995	60	1	0.05	1.0E-4	.02822	1.3	.1227	1.7	6.09	2.1	.3600	1.3	.621	33	11	0.35
V09_232 _6.1	2010	38	-1	0.08	5.4E-5	.02883	0.8	.1237	1.0	6.28	1.3	.3680	0.8	.607	75	37	0.51
V09_232 _ 7.1	2035	44	2	0.06	8.1E-5	.02830	1.1	.1255	1.3	6.25	1.7	.3611	1.1	.661	48	38	0.82
V09_232 _8.1	2003	36	1	-0.13	-9.3E-5	.02807	0.8	.1232	1.0	6.10	1.3	.3591	0.8	.633	81	41	0.51
V09_232 _9.1	2010	25	0	0.00	-2.1E-7	.02854	0.7	.1237	0.7	6.22	1.0	.3647	0.7	.685	133	64	0.50
V09_232 _9.2	2012	29	2	0.03	1.9E-5	.02789	0.8	.1238	0.8	6.08	1.1	.3563	0.8	.684	106	20	0.20
V09_232 _9.3	2023	20	3	0.03	9.6E-6	.02793	0.6	.1246	0.6	6.13	0.8	.3569	0.5	.671	202	81	0.41
V09_235																	
V09_235 _2.1	2015	28	1	0.07	3.8E-5	.02839	0.7	.1240	0.8	6.20	1.1	.3625	0.7	.666	106	48	0.46
V09_235 _4.1	2025	34	4	0.03	2.5E-5	.02747	0.9	.1248	1.0	6.04	1.3	.3509	0.9	.655	90	54	0.62
V09_235 _6.1	2003	32	2	0.06	4.1E-5	.02787	0.8	.1232	0.9	6.04	1.2	.3558	0.8	.655	106	62	0.61
V09_235 _7.1	2015	26	3	0.00	---	.02783	0.7	.1240	0.7	6.08	1.0	.3556	0.7	.681	140	81	0.60

V09_235 _8.1	2015	30	3	0.09	5.6E-5	.02773	0.7	.1240	0.8	6.05	1.1	.3541	0.7	.653	117	46	0.40
V09_237																	
V09_237 _1.1	2647	26	10	0.33	1.7E-4	.03925	0.8	.2062	0.8	14.22	1.1	.5003	0.8	.717	80	85	1.10
V09_237 _2.1	2926	18	8	0.00	---	.04107	0.8	.2127	0.6	15.39	1.0	.5248	0.8	.799	93	105	1.17
V09_237 _3.1	2866	20	7	0.04	2.0E-5	.04035	0.7	.2050	0.6	14.57	0.9	.5154	0.7	.784	99	82	0.85
V09_237 _4.1	2278	92	7	0.54	4.8E-4	.03329	1.3	.1509	1.3	8.79	1.6	.4224	1.0	.585	57	53	0.98
V09_237 _4.2	2232	67	23	0.03	2.9E-5	.03129	0.9	.1564	0.9	8.62	1.3	.3996	1.0	.723	67	62	0.96
V09_237 _4.3	2415	27	31	0.22	1.1E-4	.03523	0.7	.1923	0.7	11.92	1.0	.4495	0.7	.746	103	116	1.16
V09_237 _4.4	2482	22	28	0.19	6.6E-5	.03657	0.5	.1994	0.5	12.84	0.8	.4669	0.6	.770	164	222	1.40
V09_237 _5.1	2621	50	25	0.05	6.3E-5	.03018	1.1	.1766	1.5	9.38	1.9	.3852	1.1	.591	73	57	0.80
V09_250																	
V09_250 _1.1	2009	48	2	0.06	7.1E-5	.02802	1.0	.1236	1.4	6.10	1.7	.3576	1.0	.613	50	17	0.36
V09_250 _4.1	2030	50	1	0.00	---	.02864	1.3	.1251	1.4	6.31	1.9	3659	1.3	.691	29	7	0.24
V09_250 _5.1	2016	38	1	0.00	---	0.2843	1.0	.1241	1.1	6.22	1.5	.3633	1.0	.685	59	17	0.30
V09_111																	
V09_111 _1.1	2020	40	0	0.07	7.4E-5	.02891	1.0	.1244	1.1	6.33	1.5	.3689	1.0	.655	54	117	2.23
V09_111 _2.2	2017	40	3	0.00	---	.02786	1.1	.1242	1.1	6.10	1.5	.3560	1.1	.686	48	104	2.24
V09_111 _3.1	1998	52	3	0.00	---	.02762	1.3	.1229	1.4	5.98	2.0	.3529	1.3	.673	39	63	1.66
V09_111 _4.1	2037	42	2	0.00	---	.02828	1.1	.1256	1.2	6.26	1.6	.3613	1.1	.686	43	81	1.94

Appendix B-5: Vredefort Lu-Hf Data

Sample	Ratios (NB/59)	Spot size	Age Ma	$^{176}Hf/^{177}Hf$	^{176}Hf/^{177}Hf (JMC 475 corr)	±2σ	±1σ	^{176}Lu/^{177}Hf	±1σ
z1	**39**	40µ	**2020**	*0.281345*	**0.281368**	**0.000034**	*0.000017*	0.000595	0.000029
z2	**57**	40µ	**2020**	*0.281445*	**0.281468**	**0.000037**	*0.000019*	0.000858	0.000040
z6	**53**	40µ	**2020**	*0.281406*	**0.281429**	**0.000028**	*0.000014*	0.000549	0.000004
z9	**56**	40µ	**2020**	*0.281420*	**0.281443**	**0.000022**	*0.000011*	0.000439	0.000020
z10	**54**	40µ	**2020**	*0.281452*	**0.281475**	**0.000032**	*0.000016*	0.000556	0.000008
z11	**58**	40µ	**2020**	*0.281435*	**0.281458**	**0.000024**	*0.000012*	0.000389	0.000004
z12	**55**	40µ	**2020**	*0.281117*	**0.281140**	**0.000029**	*0.000014*	0.001548	0.000074
z13	**56**	40µ	**2020**	*0.281086*	**0.281109**	**0.000027**	*0.000013*	0.001188	0.000021
z15	**55**	40µ	**2020**	*0.281299*	**0.281322**	**0.000022**	*0.000011*	0.000689	0.000006
z16	**51**	40µ	**2020**	*0.281289*	**0.281312**	**0.000029**	*0.000015*	0.000560	0.000008
z20	**25**	40µ	**2020**	*0.281334*	**0.281357**	**0.000040**	*0.000020*	0.000398	0.000009
z21	**38**	40µ	**2020**	*0.281311*	**0.281334**	**0.000033**	*0.000016*	0.000445	0.000012
z25	**49**	40µ	**2020**	*0.281280*	**0.281303**	**0.000030**	*0.000015*	0.000281	0.000005
z26	**55**	40µ	**2020**	*0.281332*	**0.281354**	**0.000025**	*0.000013*	0.000652	0.000026
z27	**58**	40µ	**2020**	*0.281283*	**0.281306**	**0.000029**	*0.000015*	0.000529	0.000017
z30	**27**	40µ	**2020**	*0.281265*	**0.281288**	**0.000039**	*0.000020*	0.000418	0.000010
Decay consant: **1**=>**1.867E-11**(Sodelund et al., 2004); **2**=>**1.93E-11**(Blichert-Toft et al., 1997)									

Sample	^{176}Yb/^{177}Hf	^{176}Hf/^{177}Hf$_T$	±σ	εHf$_T$	±2σ	T(DM)^c $_{felsic}$Ma	T(DM)^c $_{mafic}$Ma	$^{176}Hf/^{177}Hf_T$ CHUR	$^{176}Hf/^{177}Hf_T$ DM
v						**0.015**	**0.022**		
z1	0.025532	0.281345	0.000017	**-5.3**	1.2	**2993**	**3404**	*0.281494*	*0.281774*
z2	0.032652	0.281435	0.000019	**-2.1**	1.3	**2791**	**3117**	*0.281494*	*0.281774*
z6	0.023084	0.281407	0.000014	**-3.1**	1.0	**2853**	**3204**	*0.281494*	*0.281774*
z9	0.017480	0.281426	0.000011	**-2.4**	0.8	**2811**	**3145**	*0.281494*	*0.281774*
z10	0.023501	0.281454	0.000016	**-1.4**	1.1	**2748**	**3056**	*0.281494*	*0.281774*
z11	0.015887	0.281443	0.000012	**-1.8**	0.9	**2772**	**3089**	*0.281494*	*0.281774*
z12	0.064351	0.281081	0.000015	**-14.7**	1.0	**3585**	**4239**	*0.281494*	*0.281774*
z13	0.048438	0.281064	0.000013	**-15.3**	1.0	**3622**	**4292**	*0.281494*	*0.281774*
z15	0.027850	0.281296	0.000011	**-7.0**	0.8	**3104**	**3561**	*0.281494*	*0.281774*
z16	0.022015	0.281290	0.000015	**-7.2**	1.0	**3116**	**3578**	*0.281494*	*0.281774*
z20	0.015387	0.281342	0.000020	**-5.4**	1.4	**3000**	**3413**	*0.281494*	*0.281774*
z21	0.016924	0.281317	0.000016	**-6.3**	1.2	**3057**	**3493**	*0.281494*	*0.281774*
z25	0.010548	0.281292	0.000015	**-7.2**	1.1	**3112**	**3572**	*0.281494*	*0.281774*
z26	0.024328	0.281329	0.000013	**-5.8**	0.9	**3028**	**3453**	*0.281494*	*0.281774*
z27	0.020668	0.281286	0.000015	**-7.4**	1.0	**3126**	**3591**	*0.281494*	*0.281774*
z30	0.016673	0.281272	0.000020	**-7.9**	1.4	**3158**	**3636**	*0.281494*	*0.281774*

References

Blichert-Toft, J. and Albarede, F. 1997. The Lu-Hf isotope geochemistry of chondrites and the evolution of the mantle-crust system. Earth and Planetary Science Letters, **148**(1-2): 243-258.

Sodelund, U., Patchett, J., Vervoort, J.D. and Isachsen, C.E. 2004. The ^{176}Lu decay constant determined by Lu^Hf and U^Pb isotope systematics of Precambrian ma¢c intrusions. Earth and Planetary Science Letters, **219**(3-4): 311-324.

Appendix C: Thin Section Scans

C-1: Vredefort

AM: Central Anatectic Granite

MN2: Type Gabbronorite

MN4: Type Gabbronorite

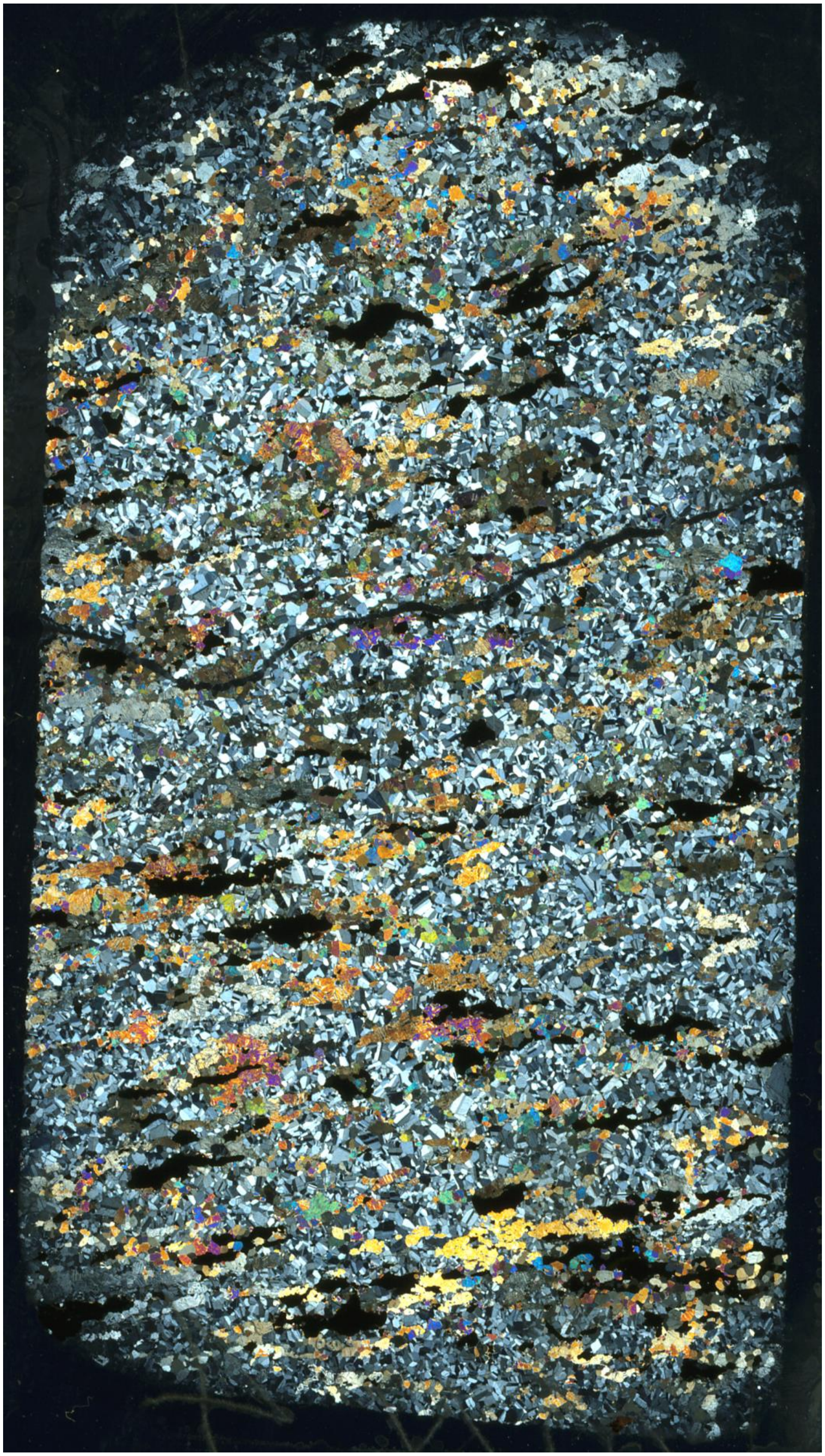

V09-111: Central Anatectic Granite

V09-232: Gabbronorite

V09-232A: Gabbronorite

V09-232B: Gabbronorite

V09-234: Gabbronorite

V09-235: Gabbronorite

V09-235A: Gabbronorite

V09-235B: Gabbronorite

V09-241A: Transition Zone Gabbronorite with ILG

V09-241B: Transition Zone Gabbronorite with ILG

V09-241C: Transition Zone Gabbronorite with ILG

V09-247: Transition Zone Gabbronorite

V09-248: Transition Zone Gabbronorite

V09-249A: Transition Zone Gabbronorite with ILG

V09-249B: Transition Zone Gabbronorite with ILG

V234-2: Proximal ILG from Site 2

V238: Distal ILG from Site 2

V245: Proximal ILG from Site 2

V246: Fine Grained Gabbronorite

V251-2: Proximal ILG from Site 1

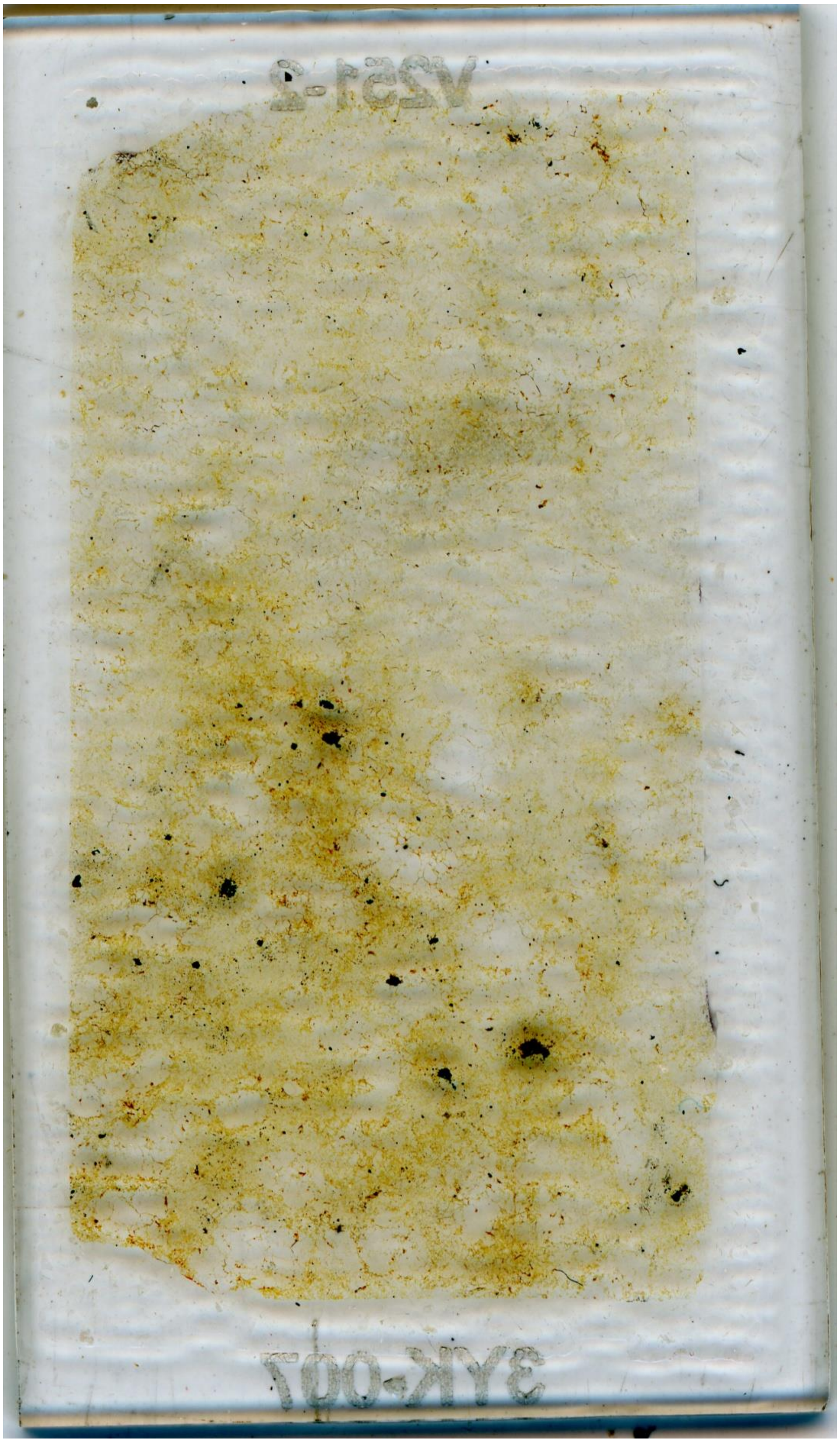

V252: Proximal ILG from Site 1

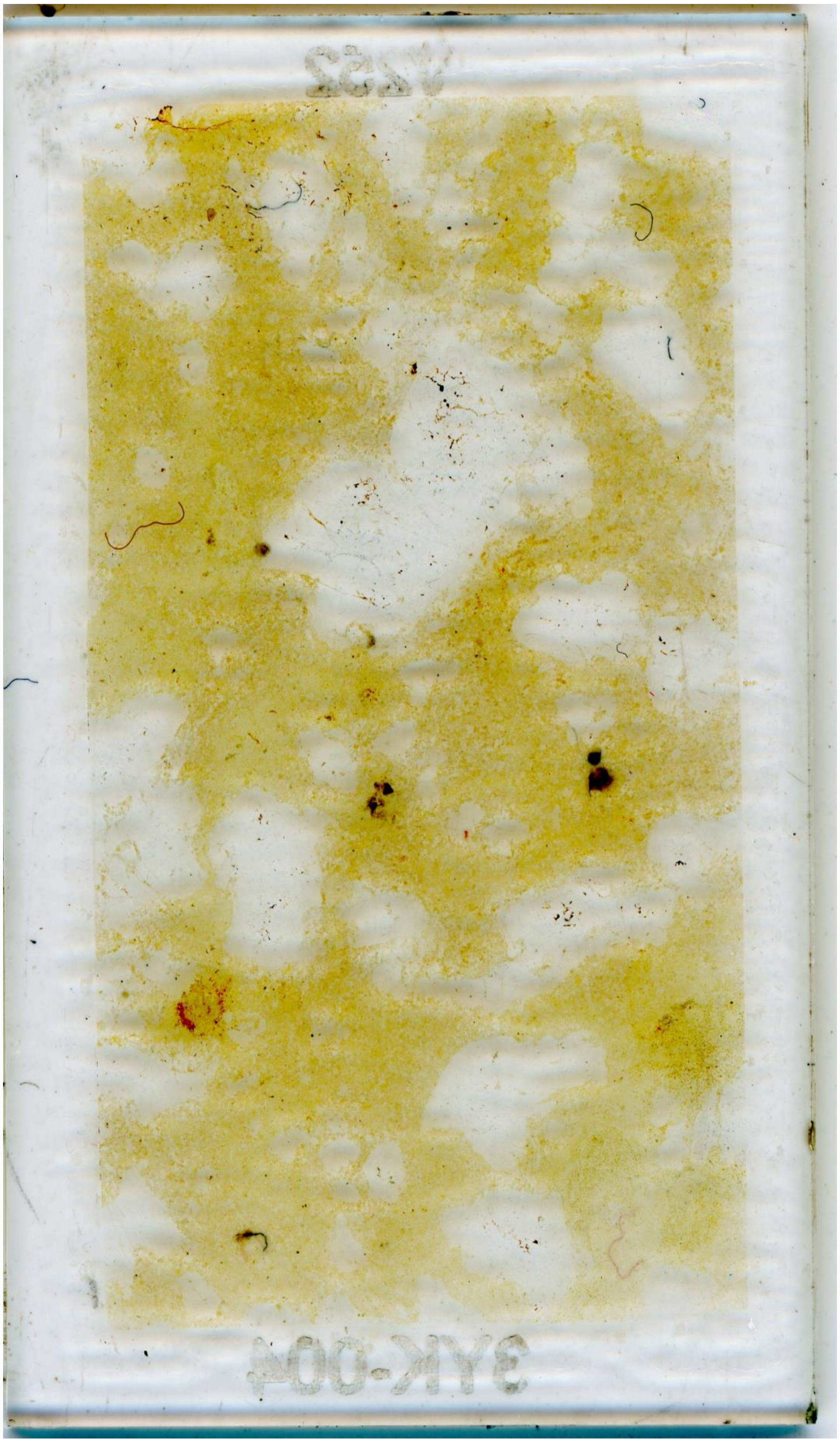

V262: Distal ILG from Site 1

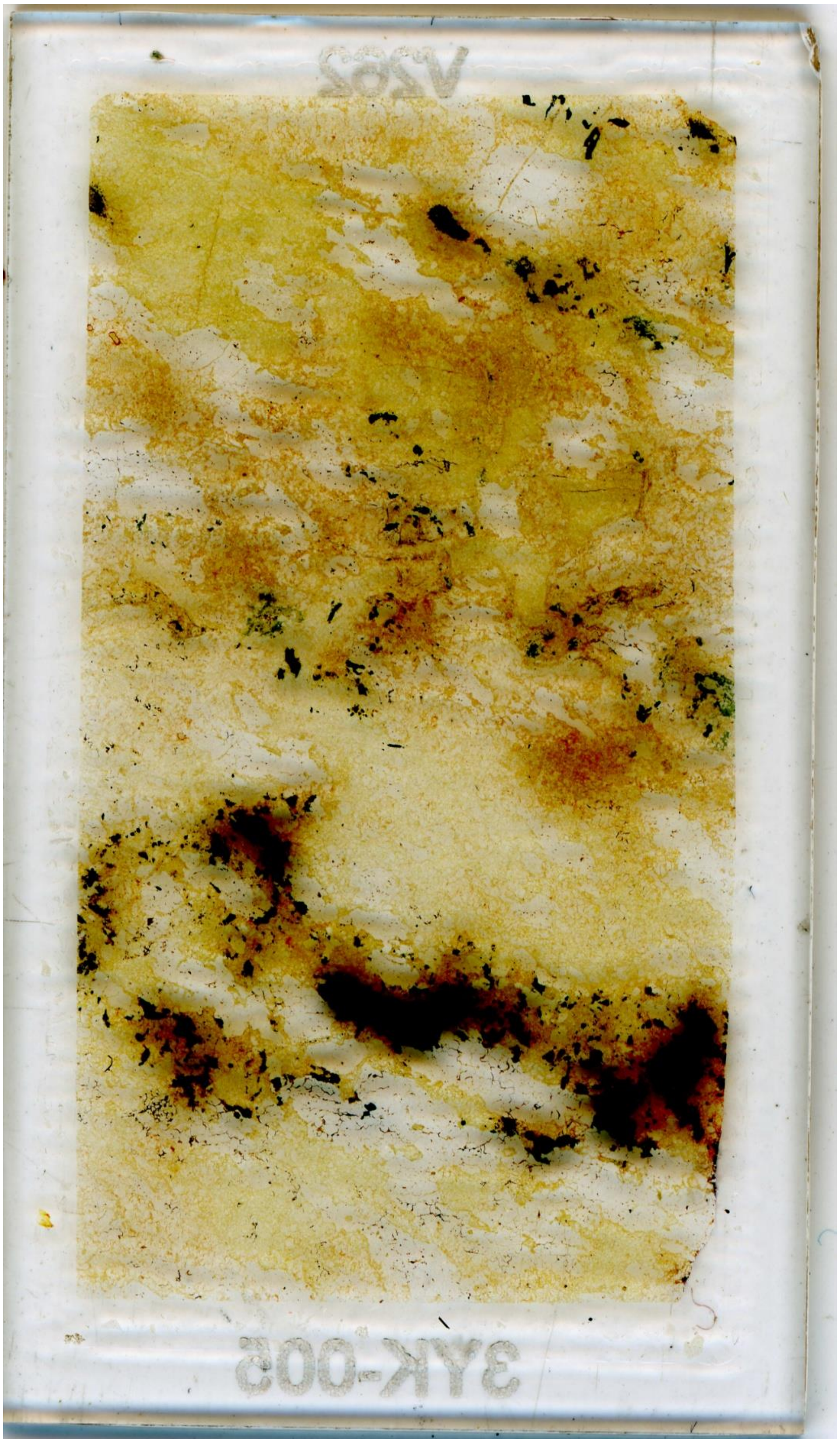

C-2: Sudbury

93PCL349A: Poikilitic Norite Pod in Sublayer Norite (Matrix)[†]

†Note that some of the Sudbury samples are thick sections and not thin sections.

93PCL349B: Poikilitic Norite Pod in Sublayer Norite (Matrix and Inclusion)

93PCL349C: Poikilitic Norite Pod in Sublayer Norite (Inclusion)

IBNR(A): Inclusion Bearing Norite

IBNR(B): Inclusion Bearing Norite

Whistle 1A: Leucocratic Sulphide-Rich Footwall

Whistle 1B: Leucocratic Sulphide-Rich Footwall

Whistle 1C: Leucocratic Sulphide-Rich Footwall

RX187432: Mafic Inclusion Found in Footwall

RX187408: Olivine Mela-Norite Inclusion

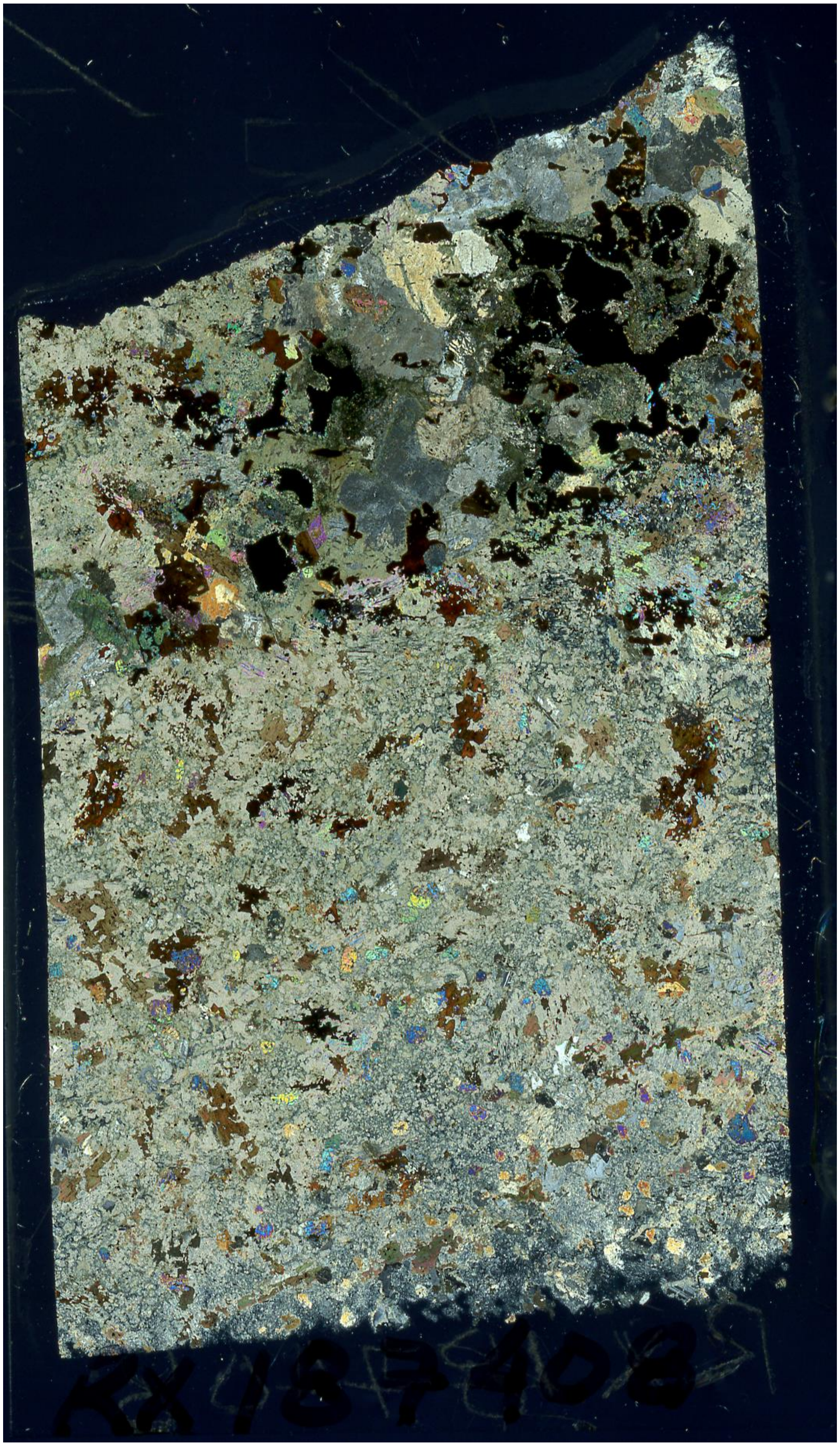

HSP: Highly Altered Olivine Melanorite

Appendix D: MicroGIS Feature Maps

D-1: Vredefort

V09-234: Gabbronorite

V09-235A: Gabbronorite

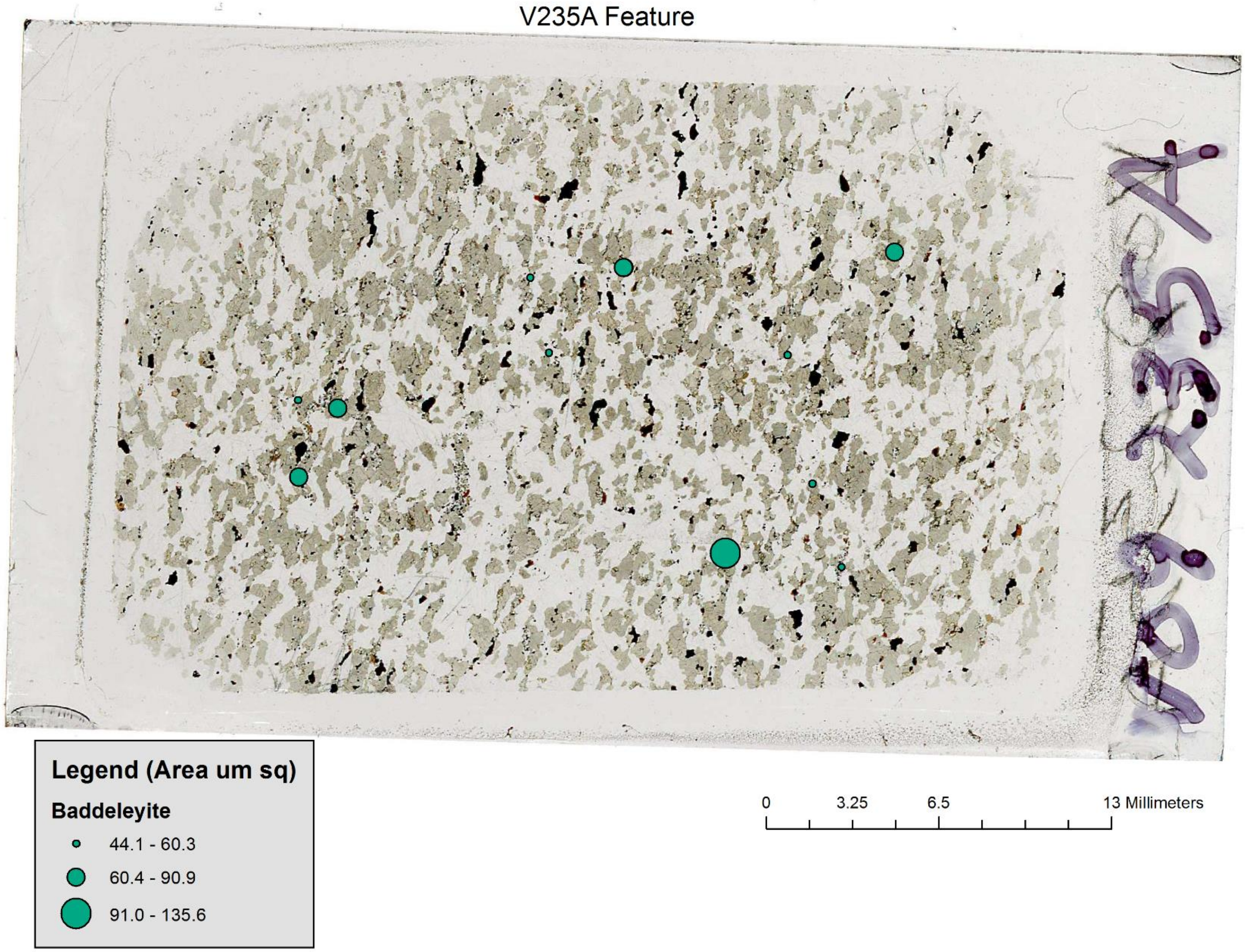

V09-235B: Gabbronorite

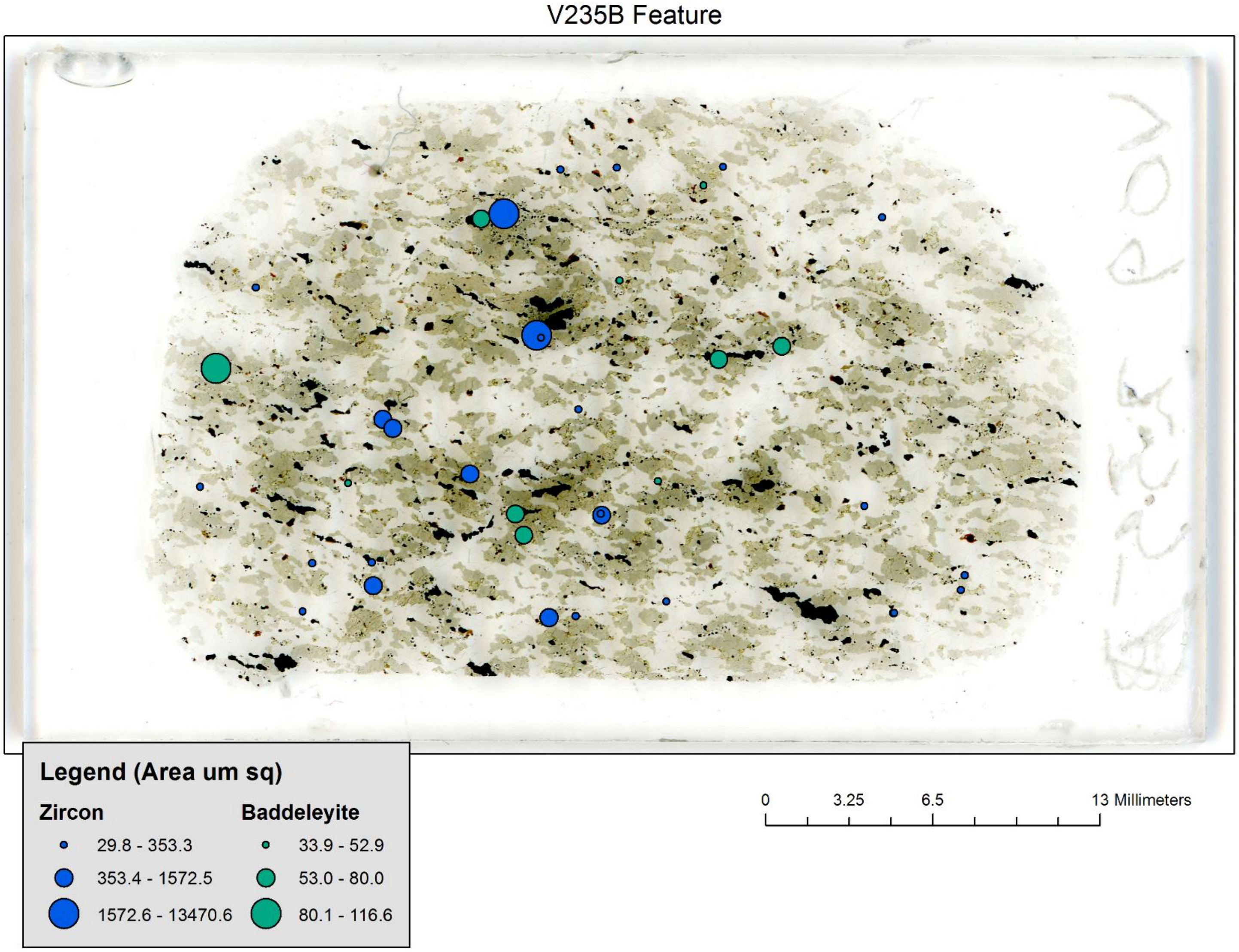

V238: Distal ILG from Site 2

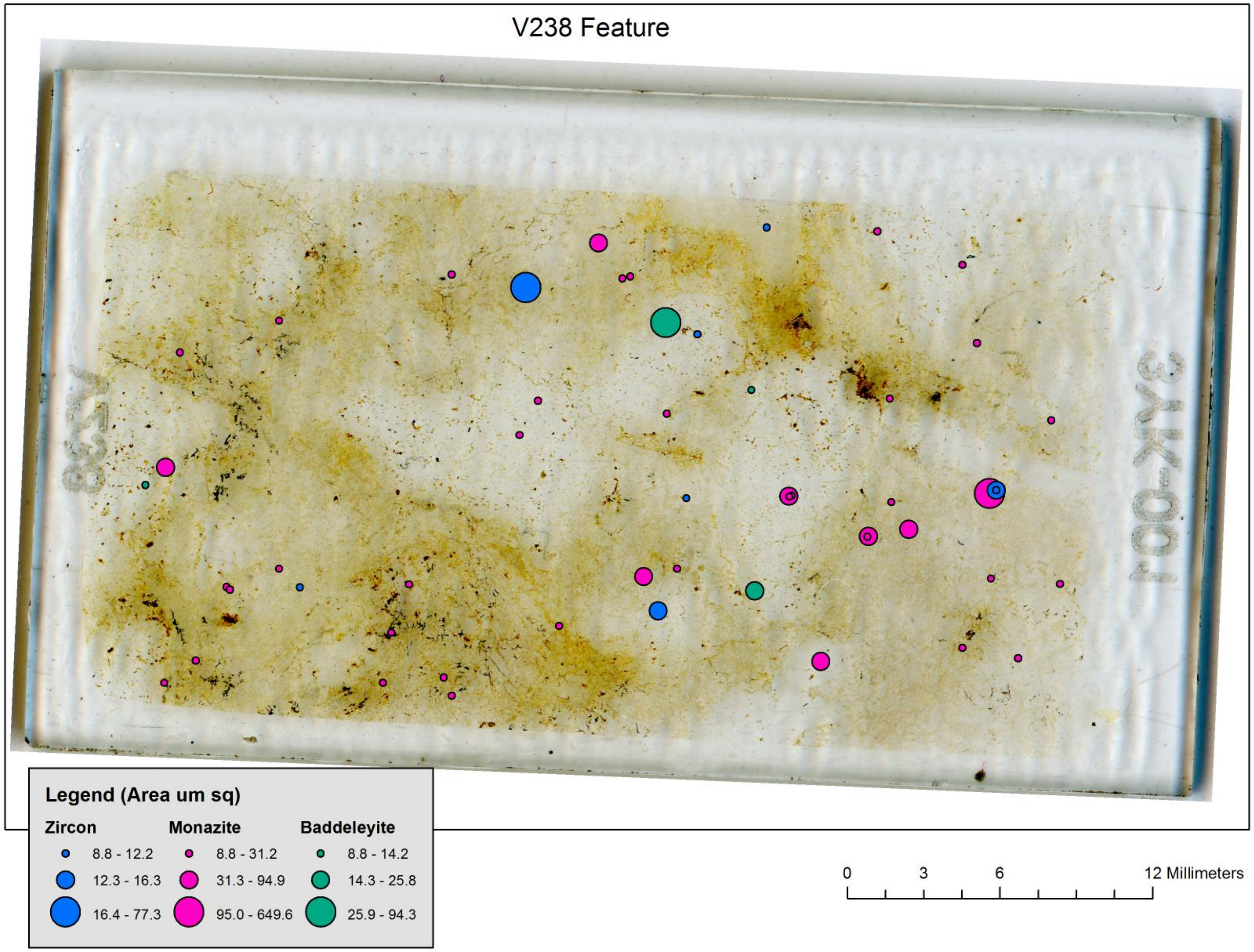

V09-241B: Transition Zone Sample, Gabbronorite with Inclusions of ILG.

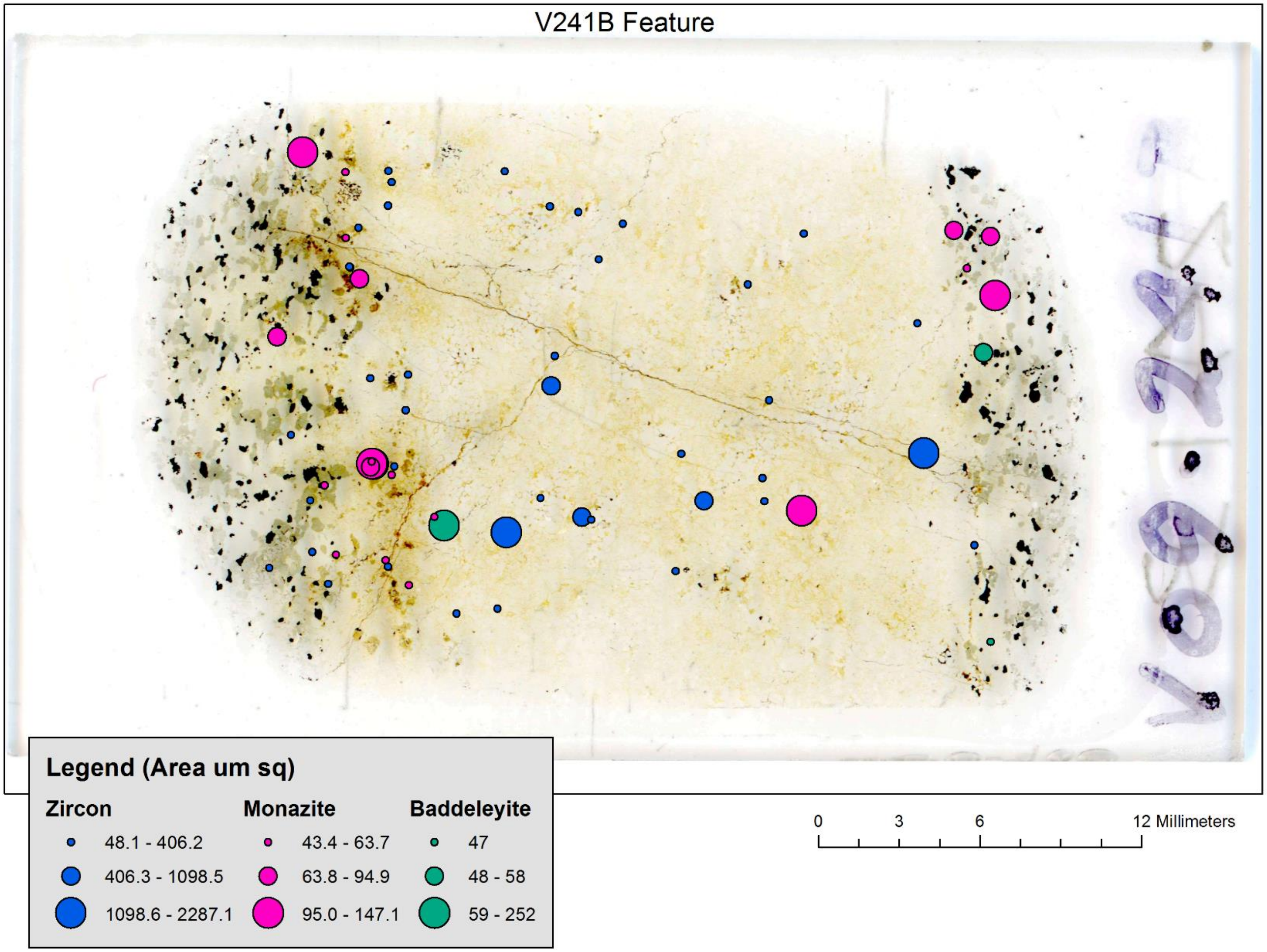

V09-249B: Transition Zone Sample, Gabbronorite with Inclusions of ILG.

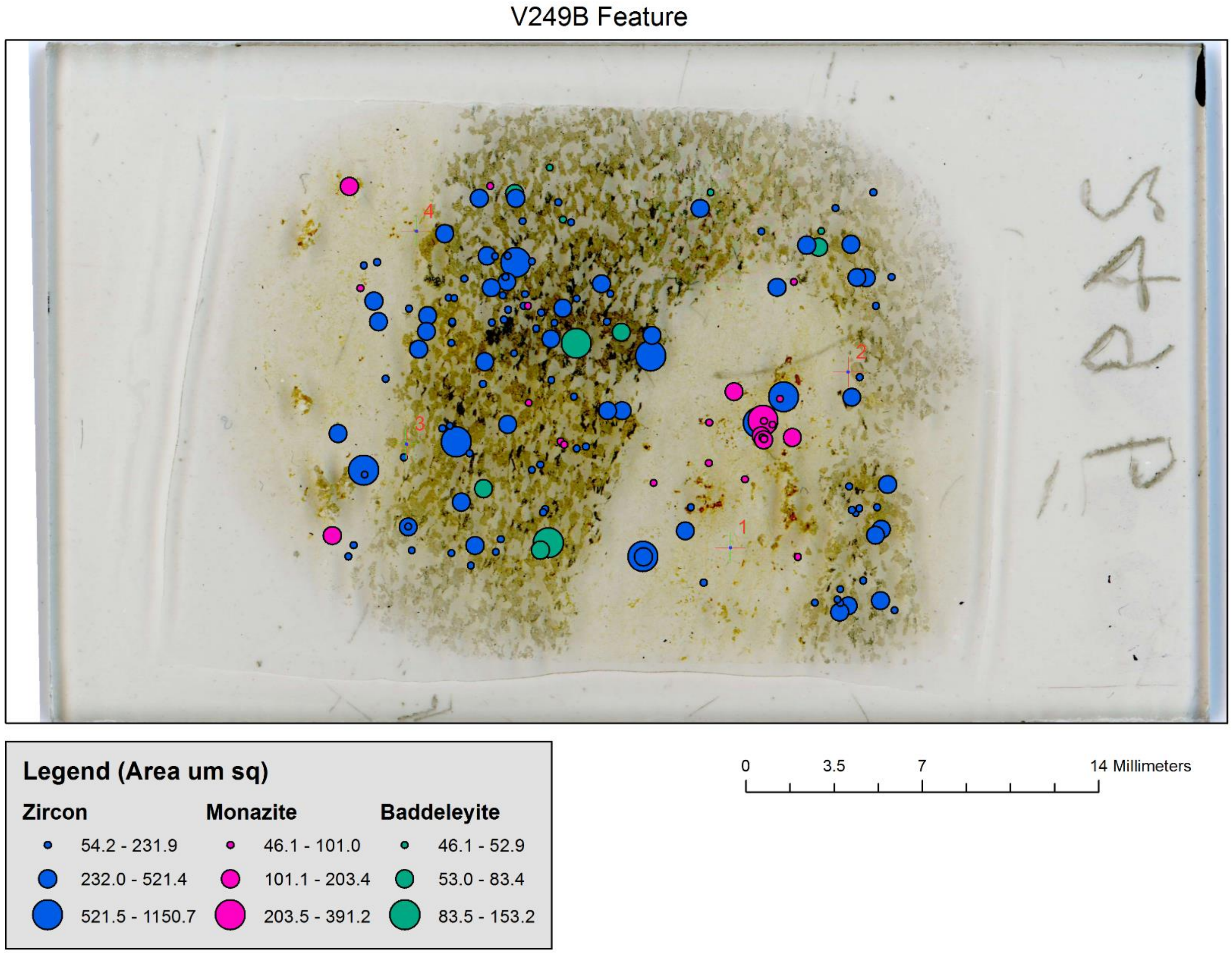

V234-2: Proximal ILG from Site 2

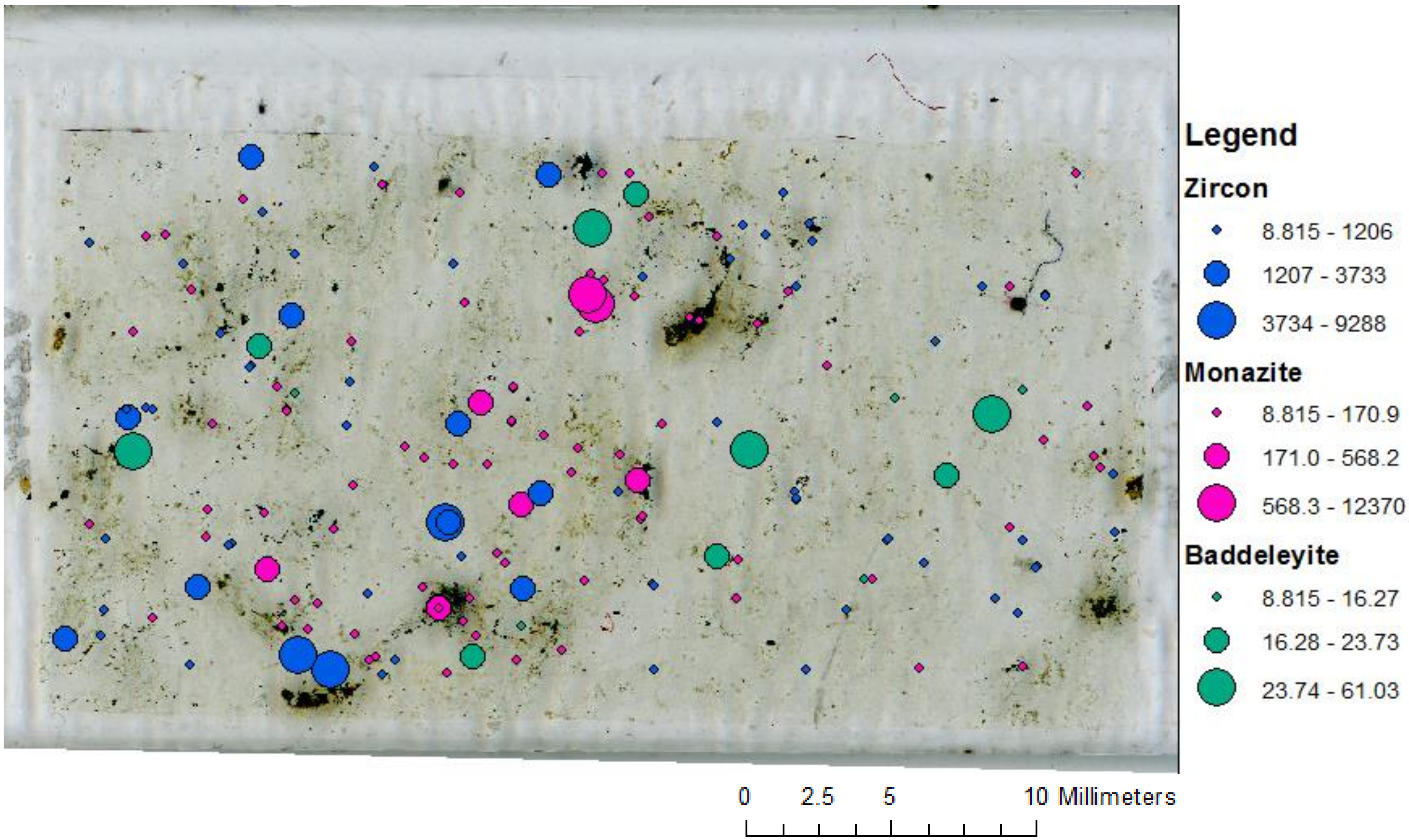

V245: Proximal ILG from Site 2

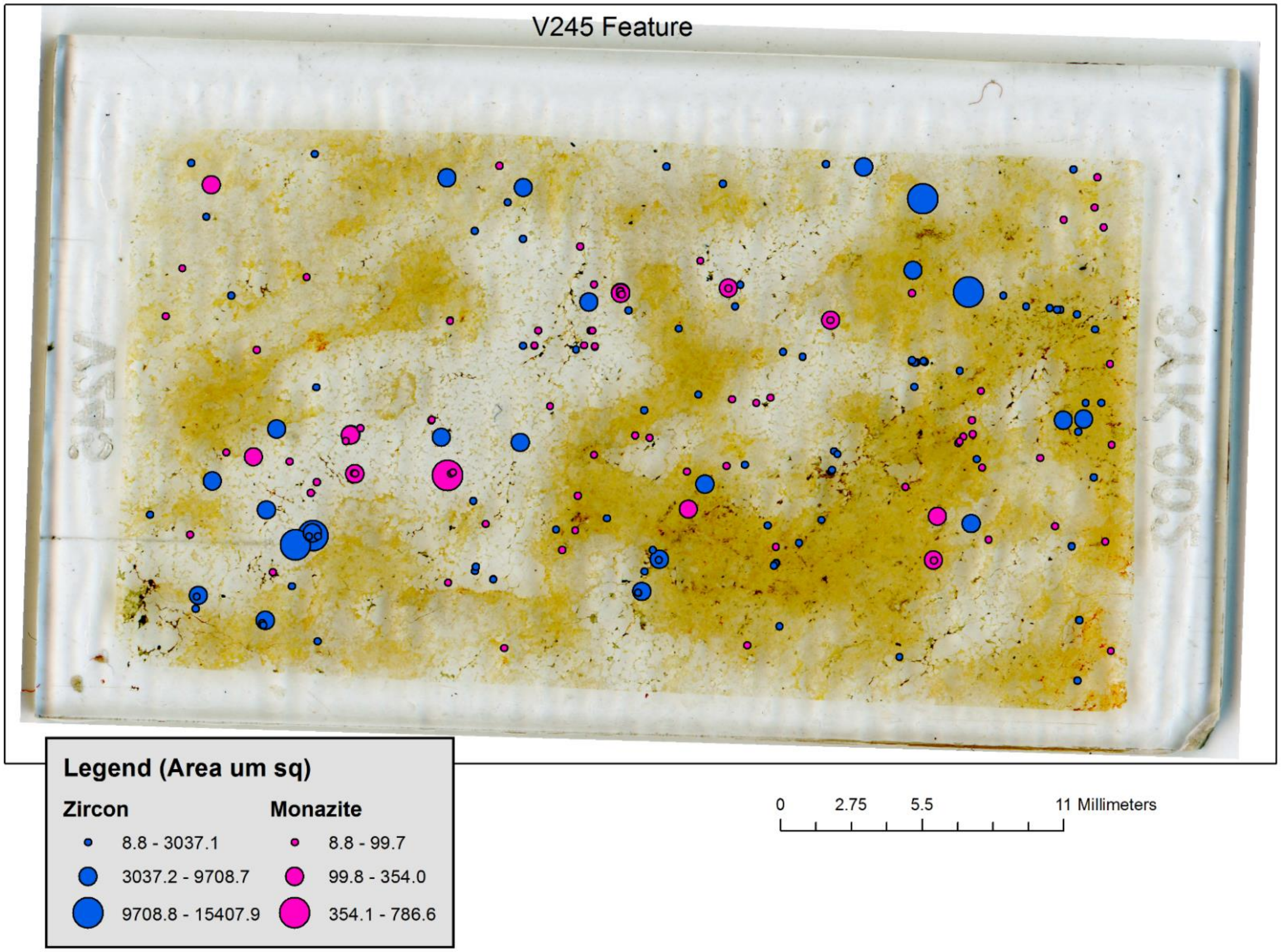

V246: Fine Grained Gabbronorite

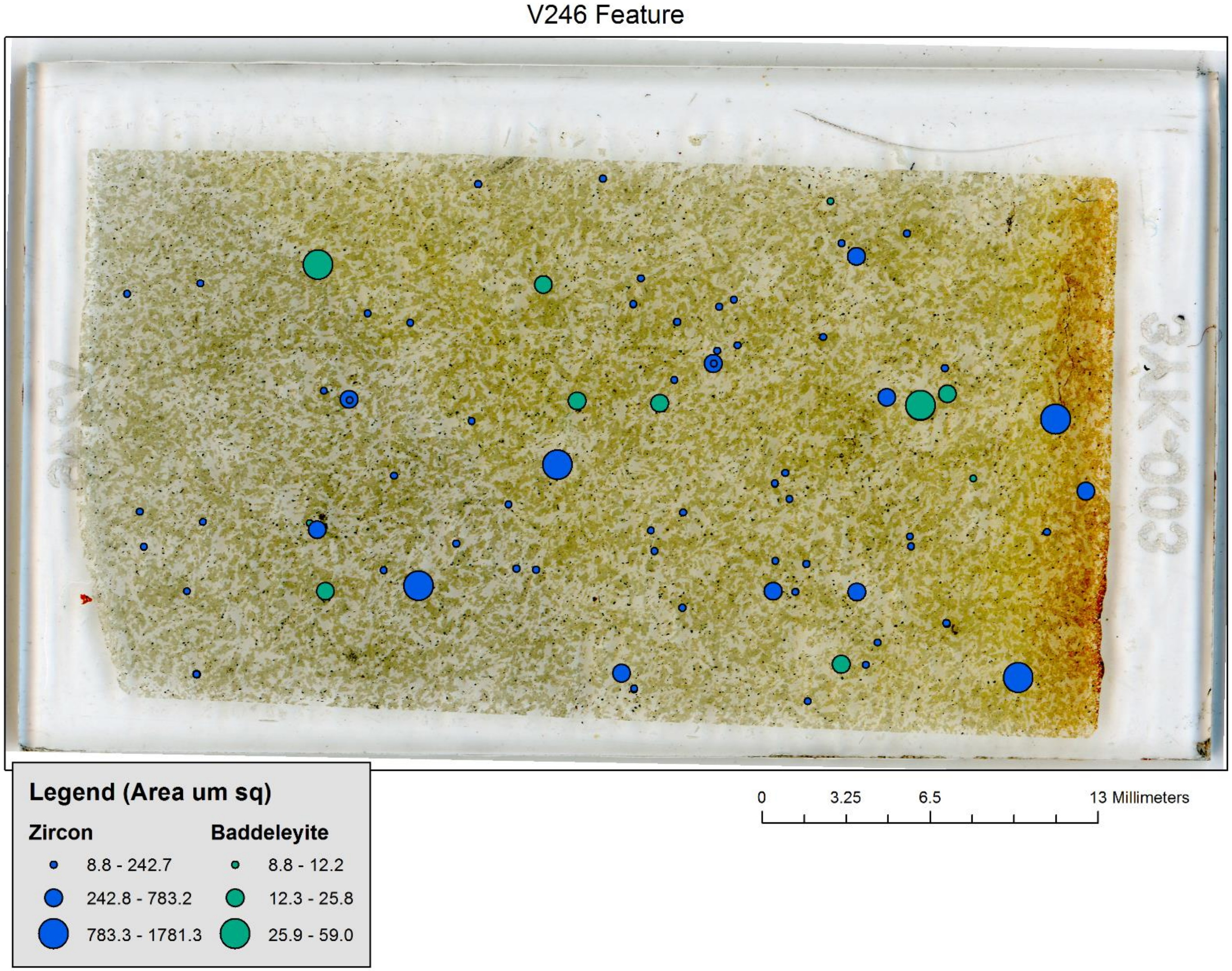

V252: Proximal ILG from Site 1

V252 Feature

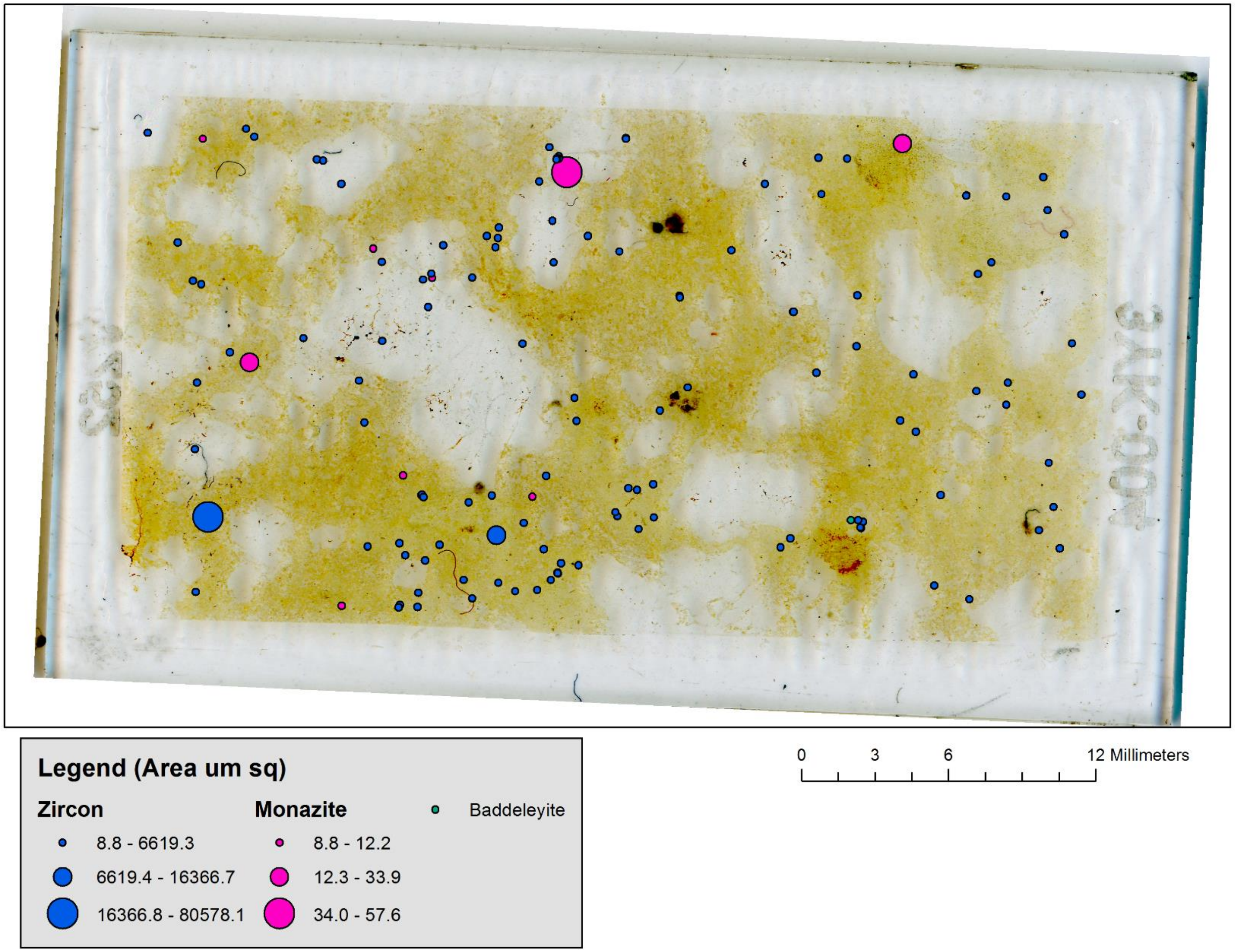

V262: Distal ILG from Site 1

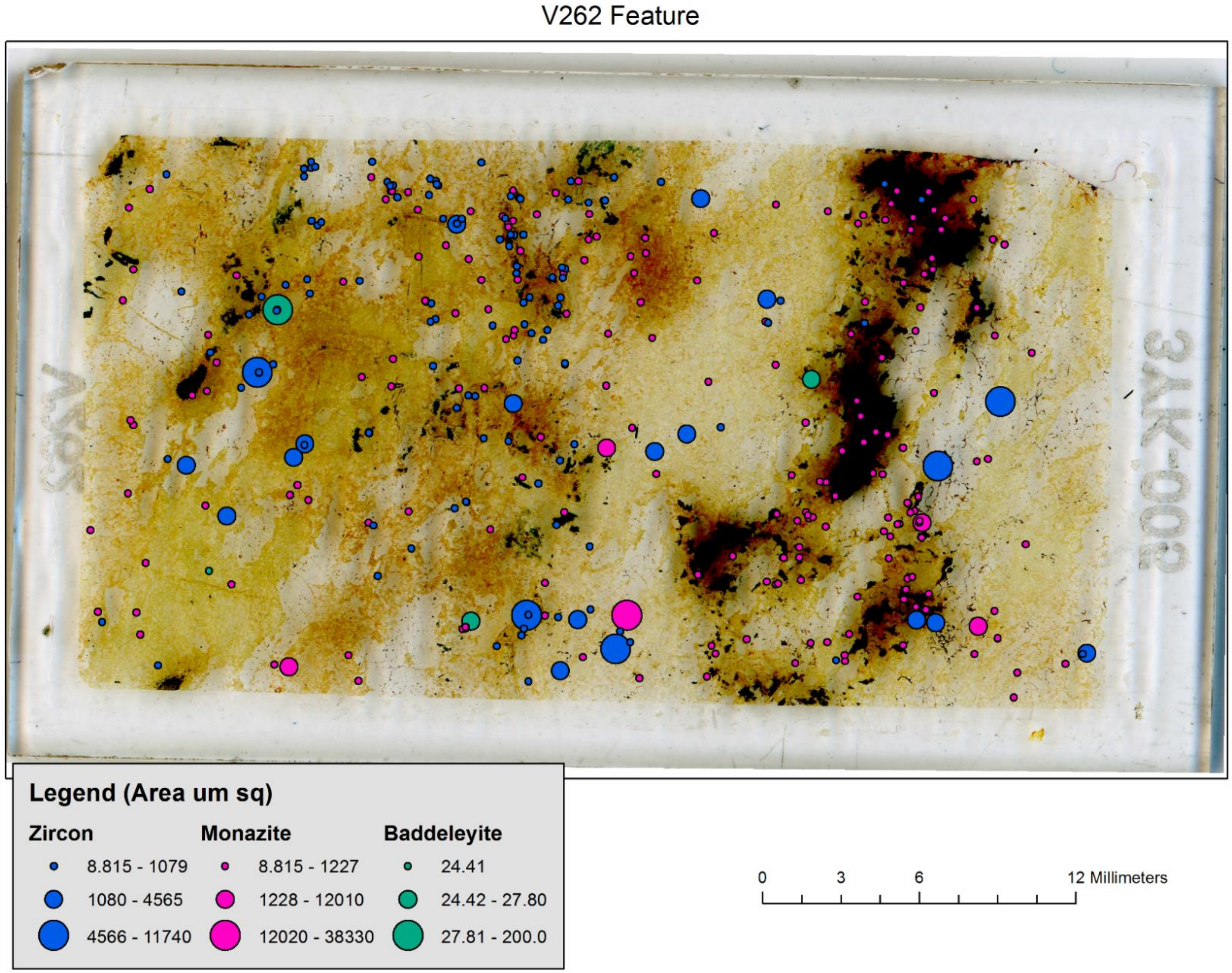

D-2: Sudbury

93PCL349A: Poikilitic Norite Pod in Sublayer Norite (Matrix)

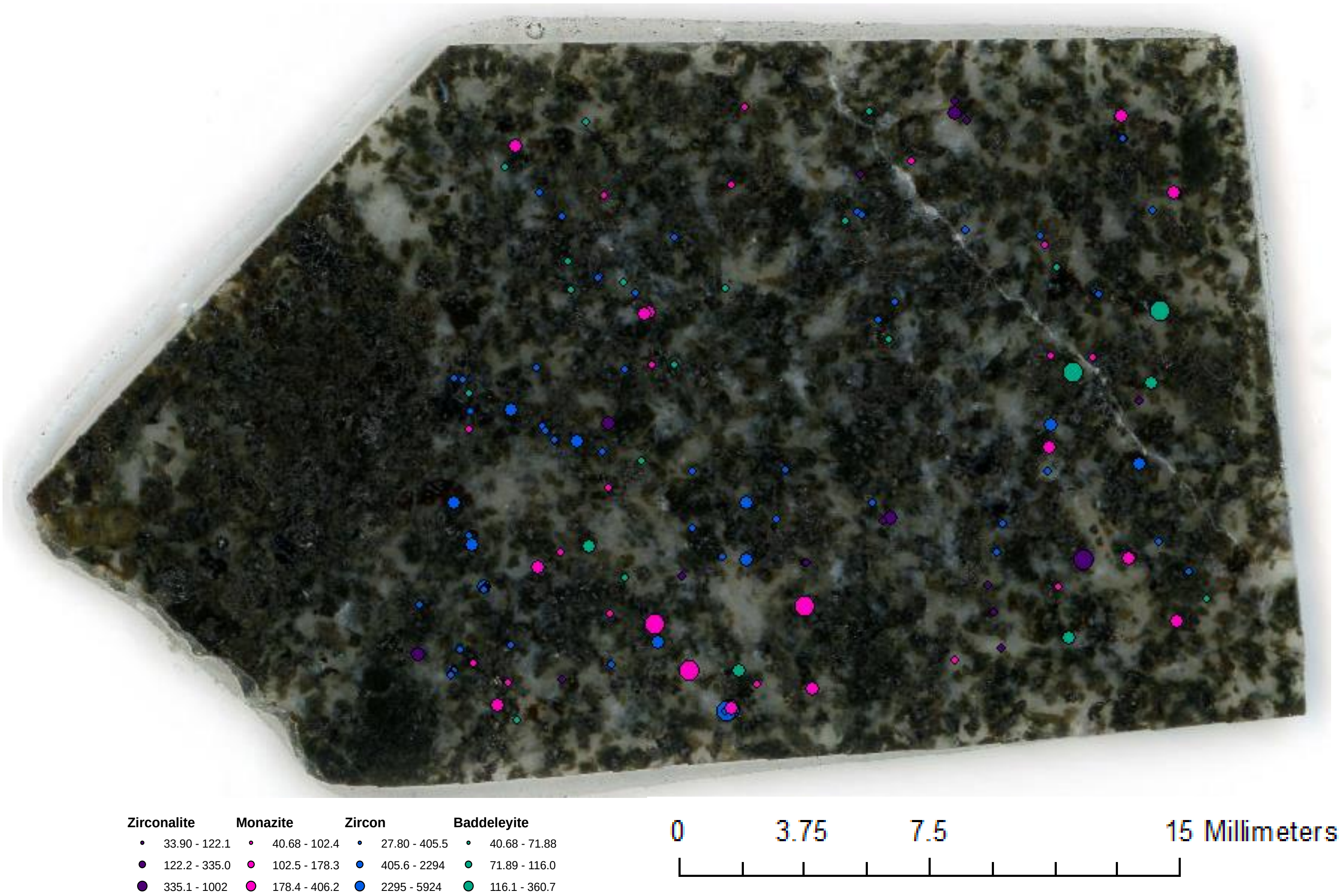

93PCL349B: Poikilitic Norite Pod in Sublayer Norite (Matrix and Inclusion)

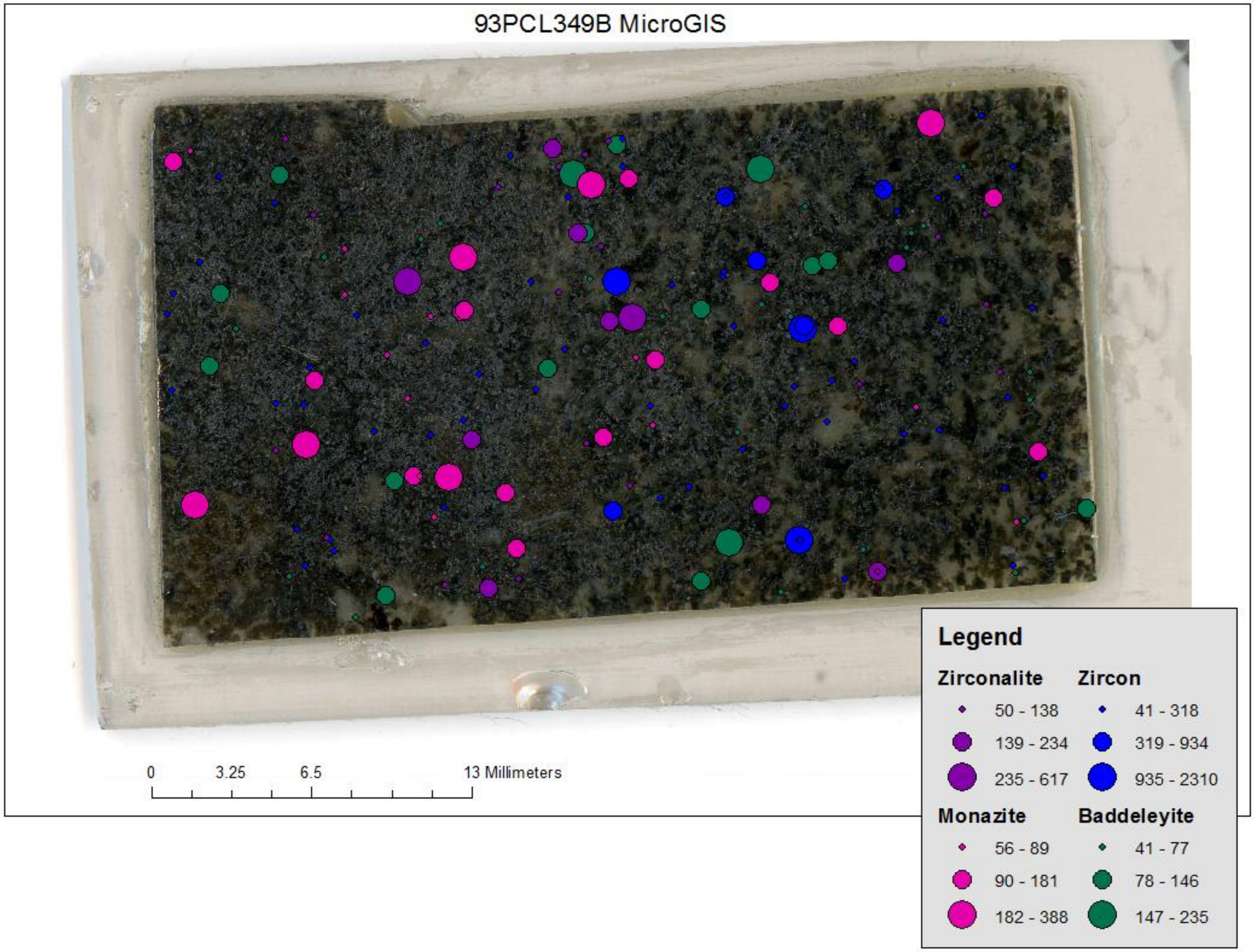

93PCL349C: Poikilitic Norite Pod in Sublayer Norite (Inclusion)

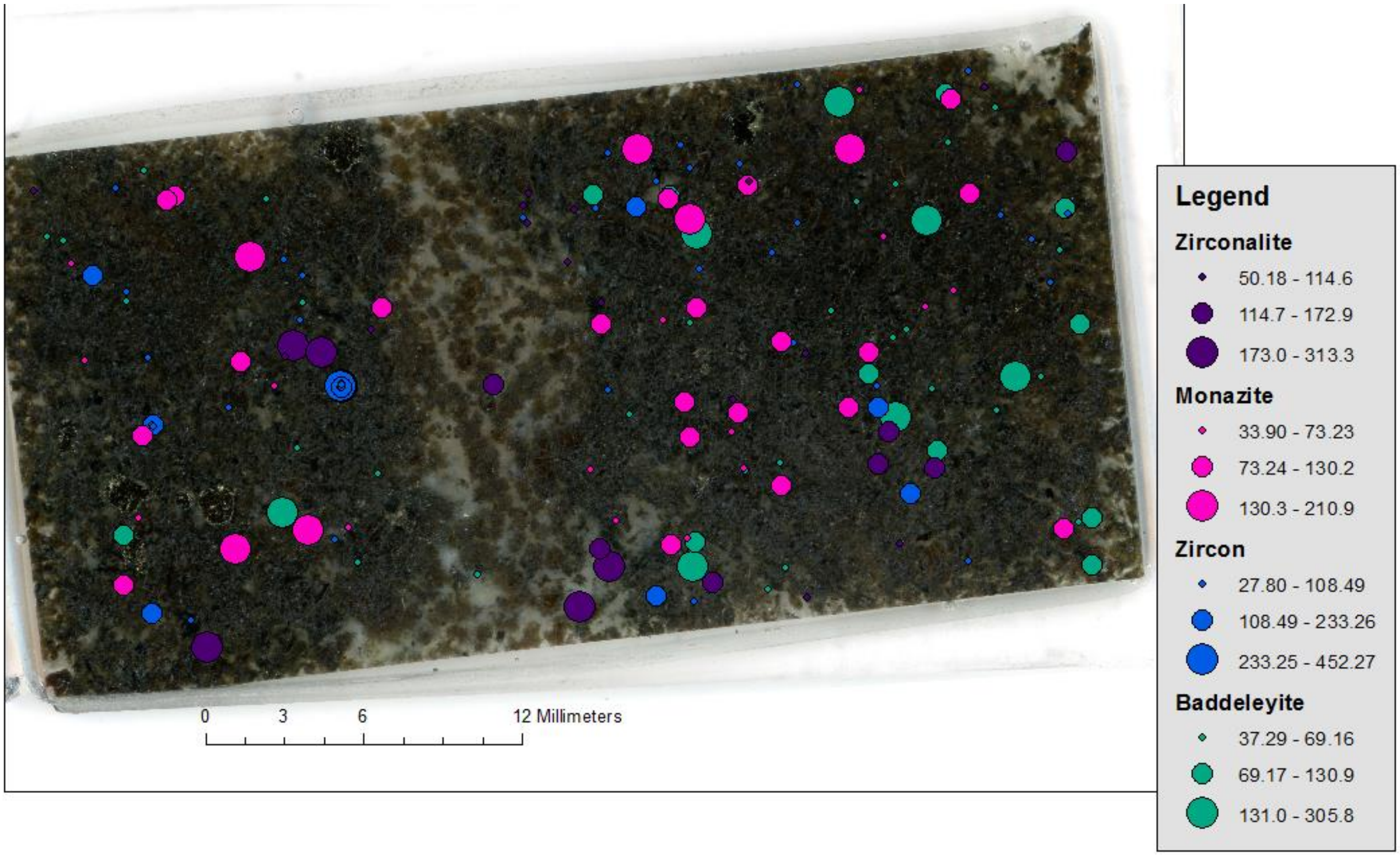

IBNR(A): Inclusion Bearing Norite

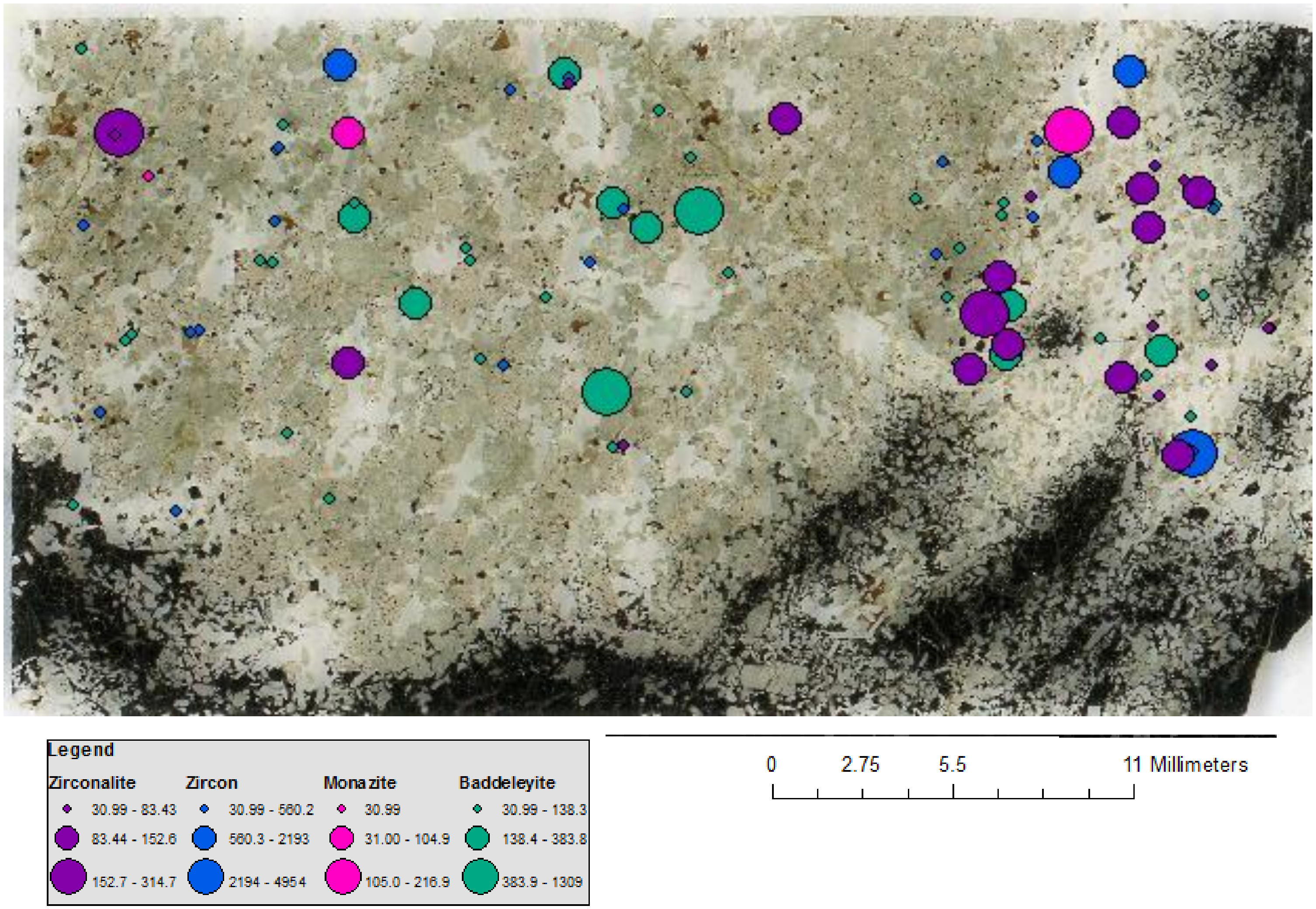

IBNR(B): Inclusion Bearing Norite

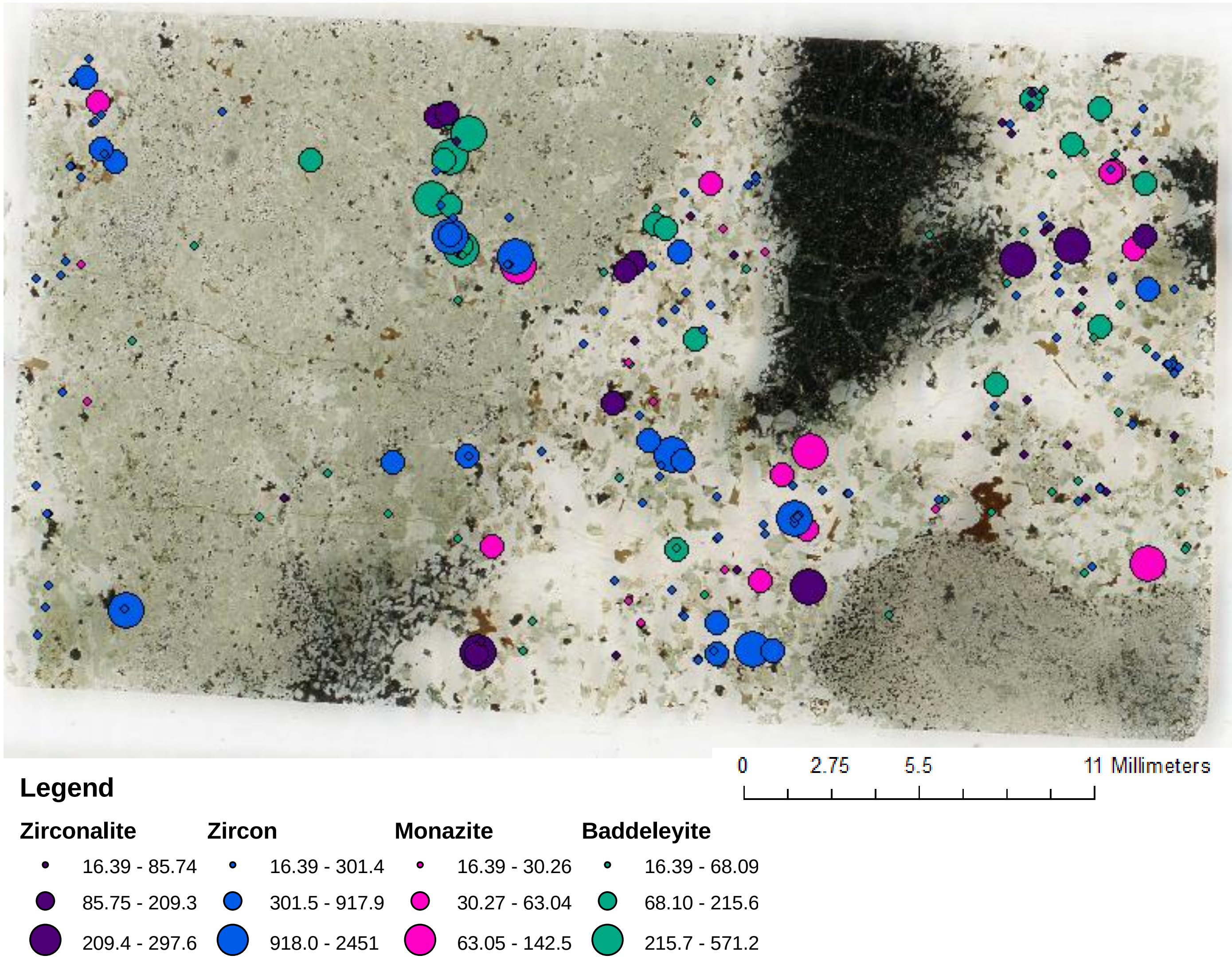

Whistle 1A: Leucocratic Sulphide-Rich Footwall

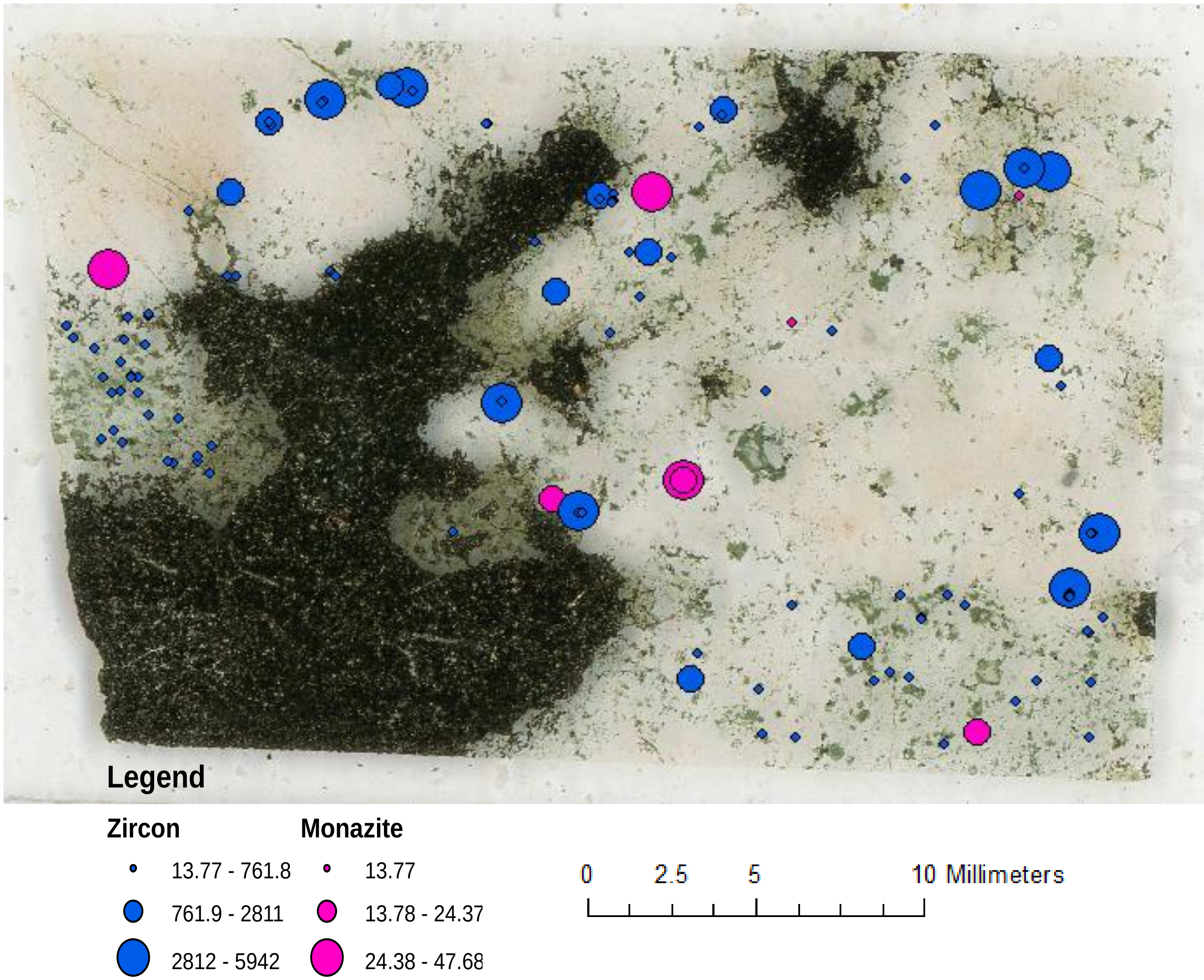

Whistle 1B: Leucocratic Sulphide-Rich Footwall

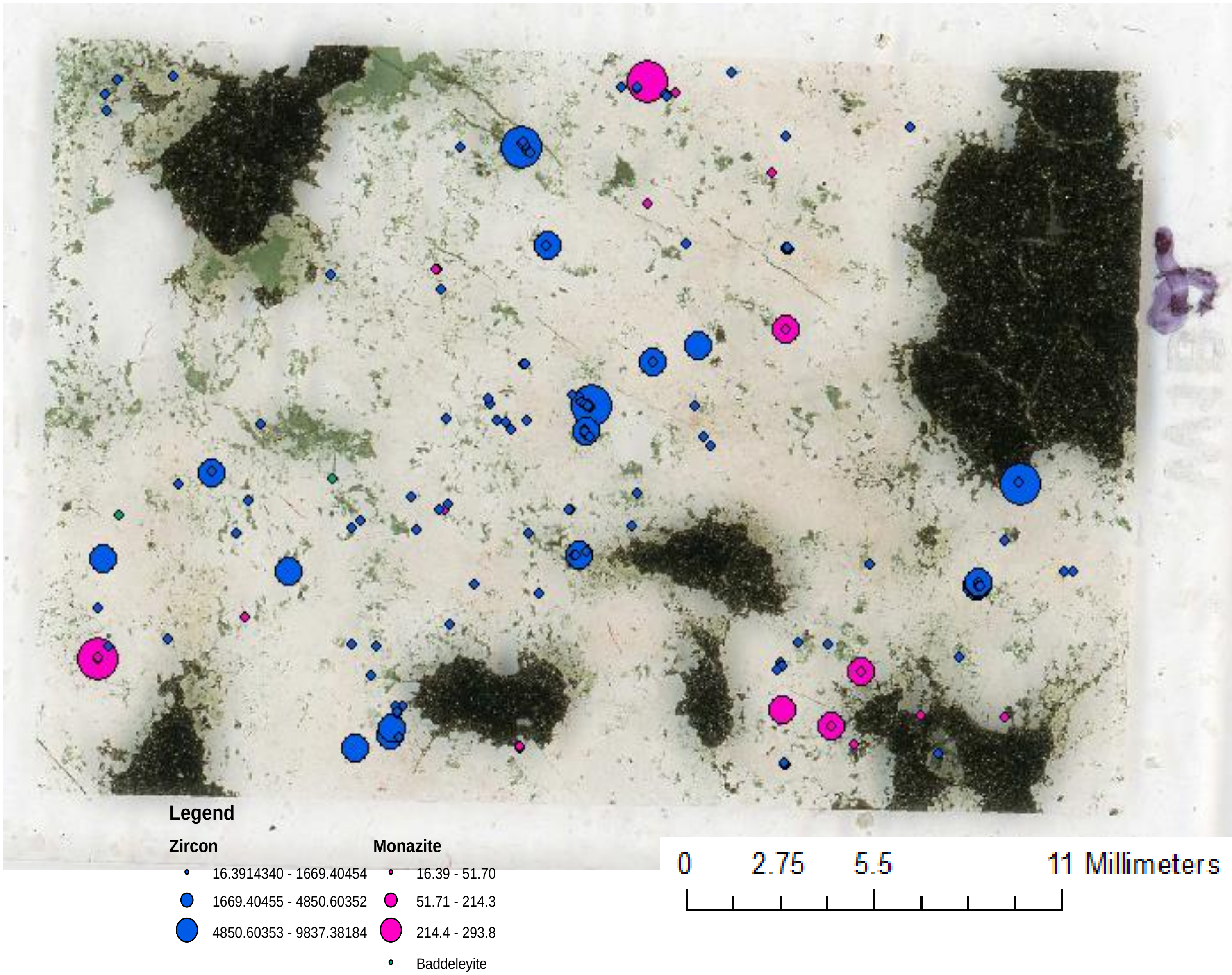

Whistle 1C: Leucocratic Sulphide-Rich Footwall

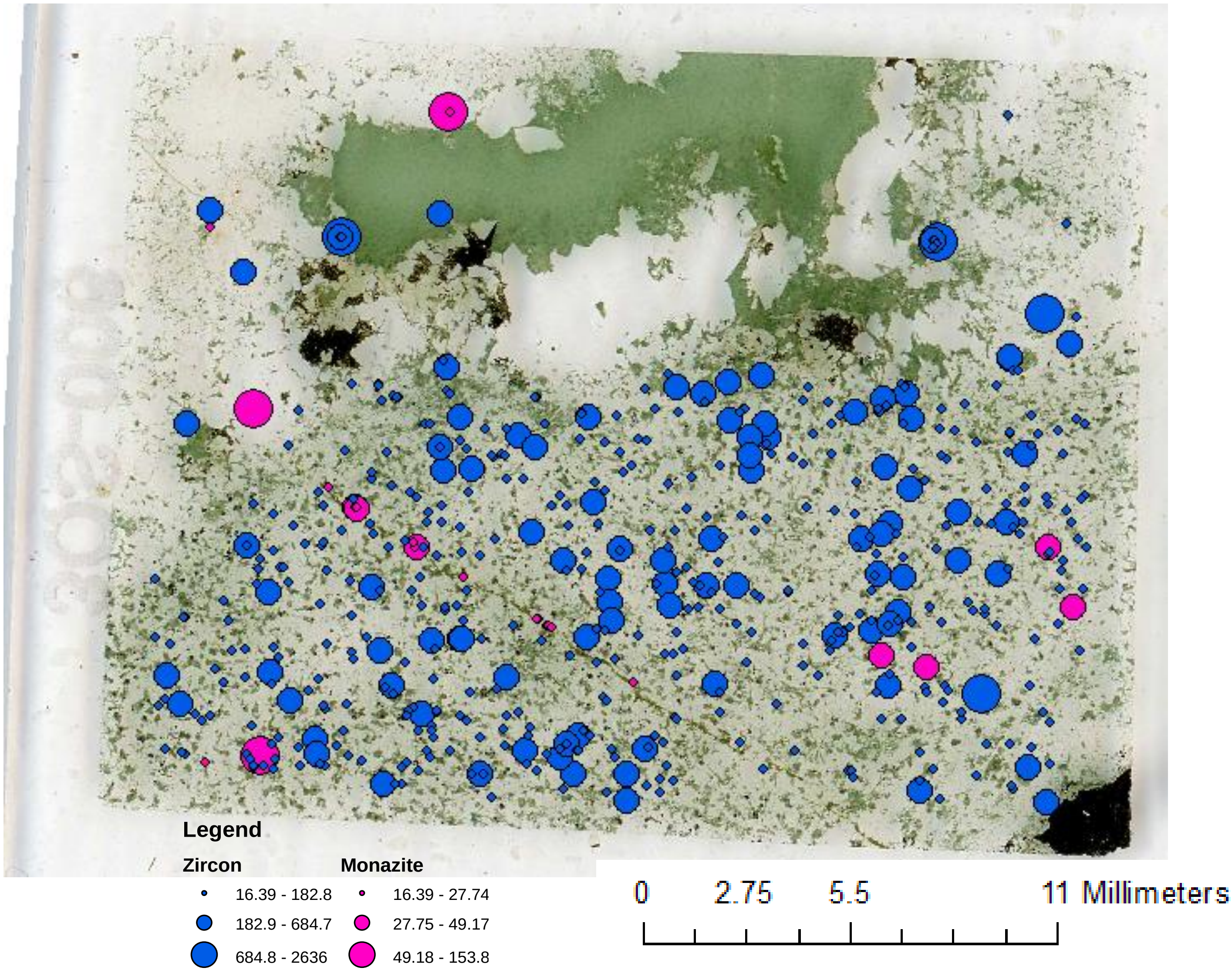

RX187432: Mafic Inclusion Found in Footwall

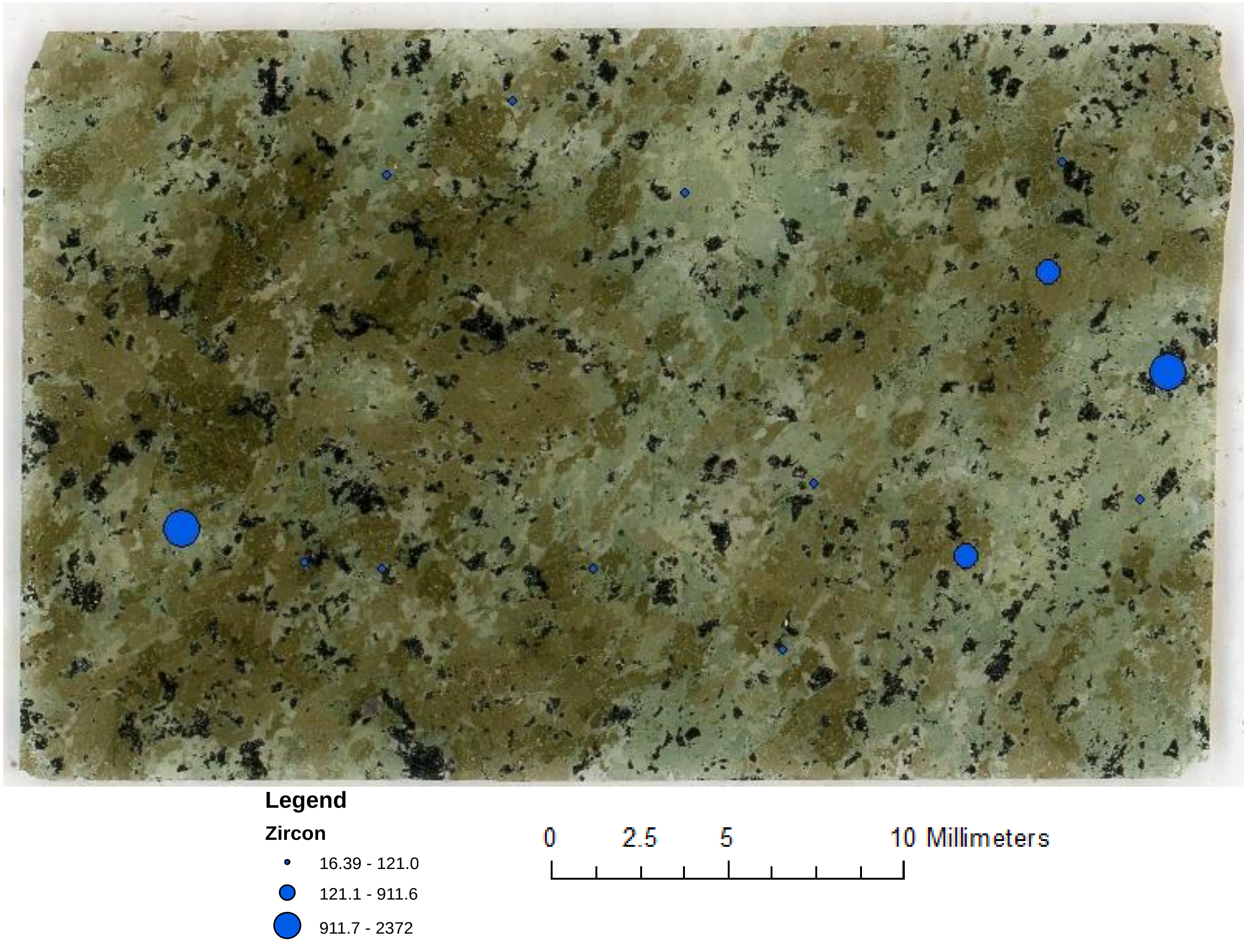

RX187408: Olivine Mela-Norite Inclusion

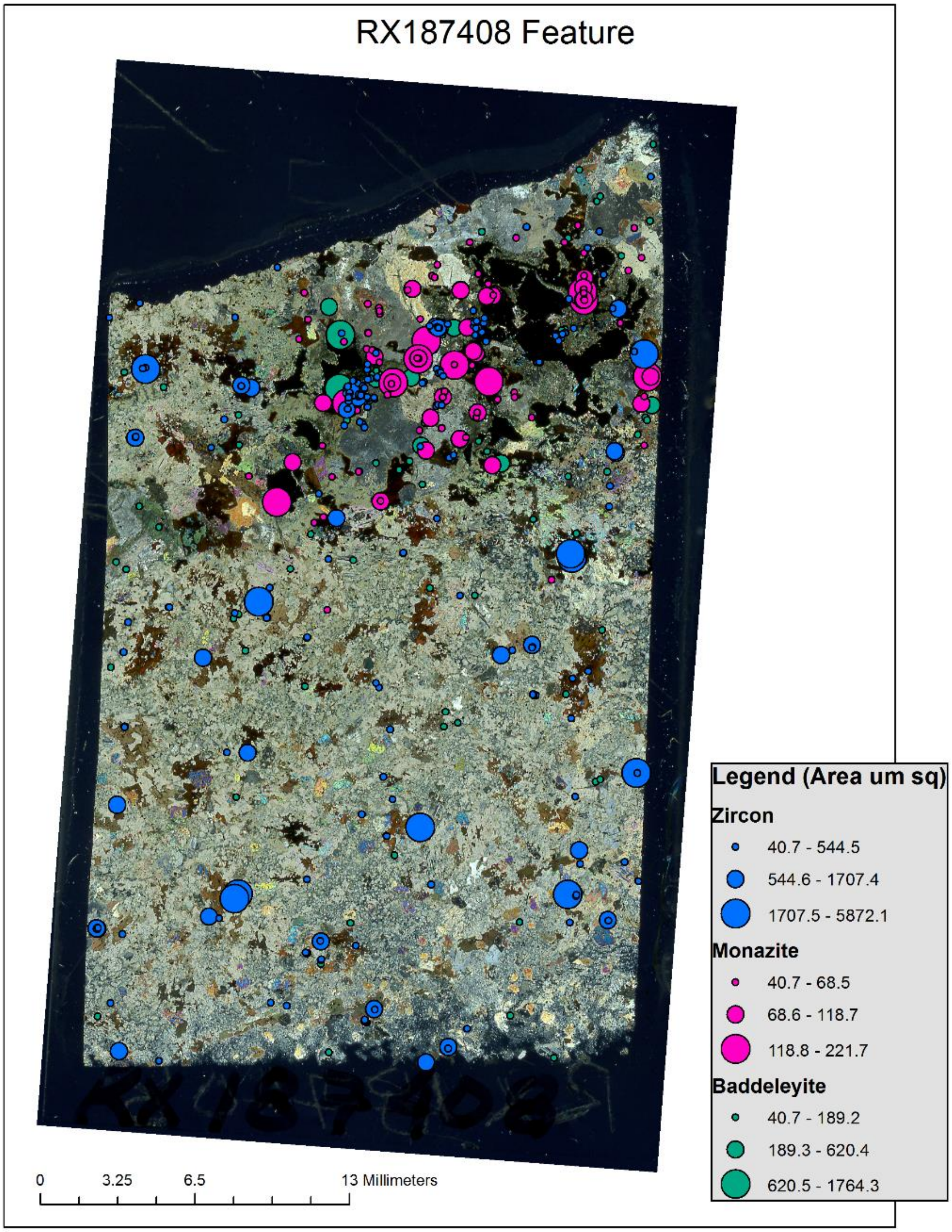

HSP: Highly Altered Olivine Melanorite

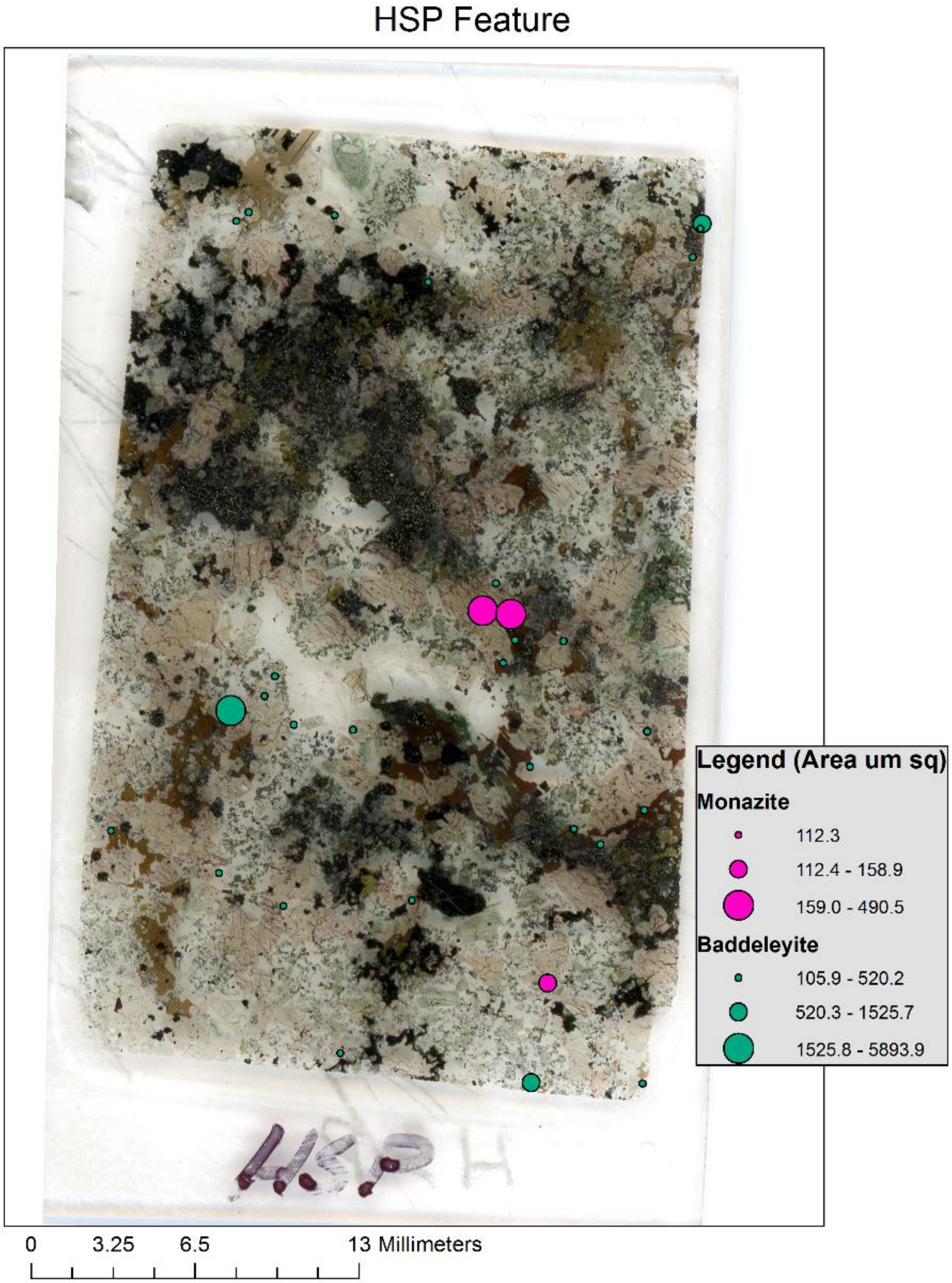

Appendix E.3: Phase Maps

E-1 Vredefort

V09-234: Gabbronorite

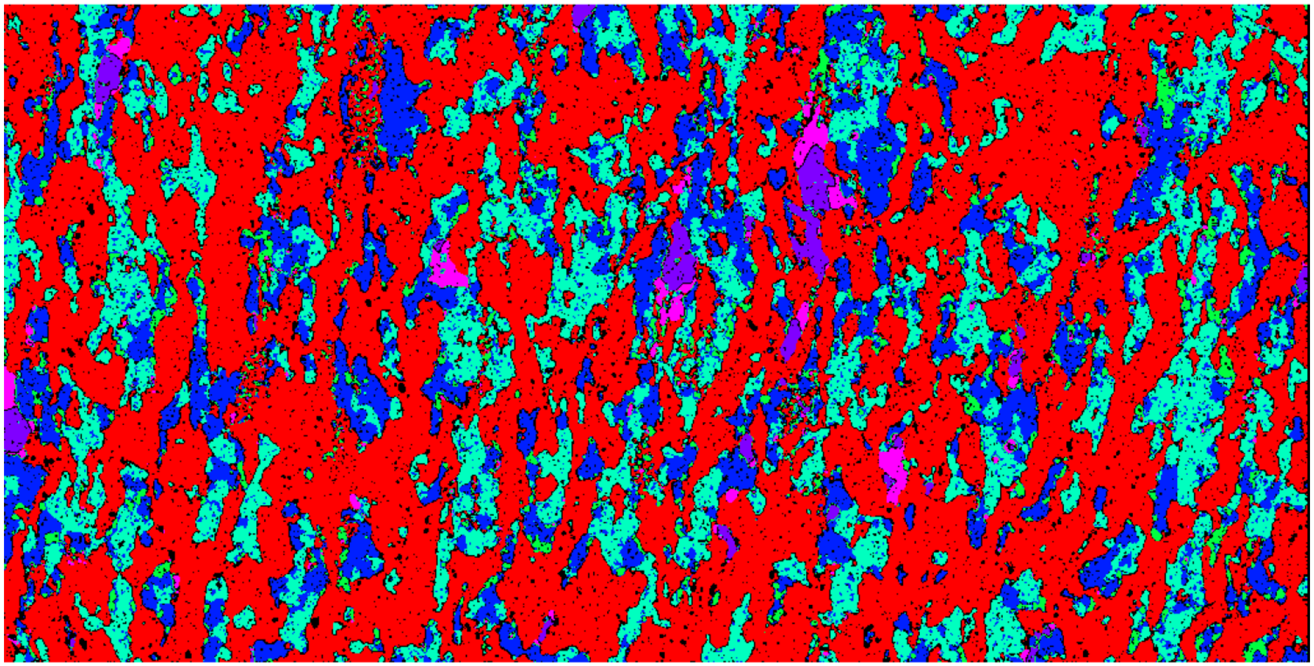

10mm

- Plagioclase (59%)
- Clinopyroxene (20%)
- Orthopyroxene (15%)
- Ilmenite (1%)
- Spinelloid (1%)
- Olivine (3%)

V09-235: Gabbronorite

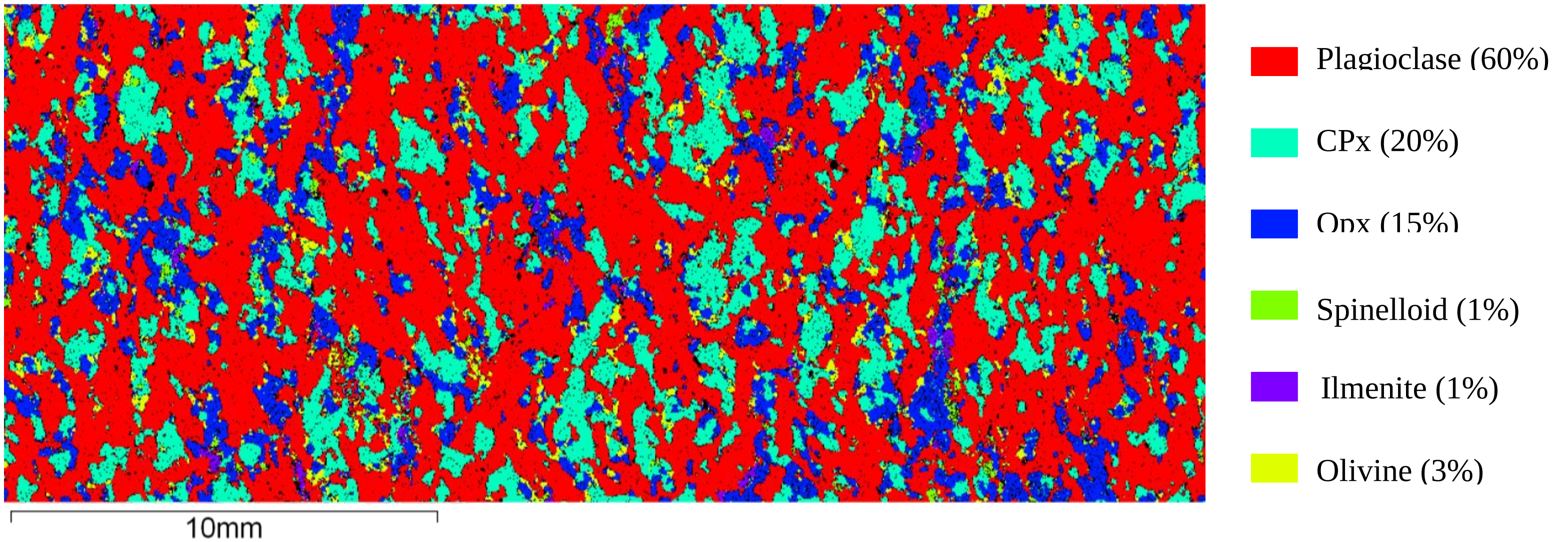

V09-235B: Gabbronorite

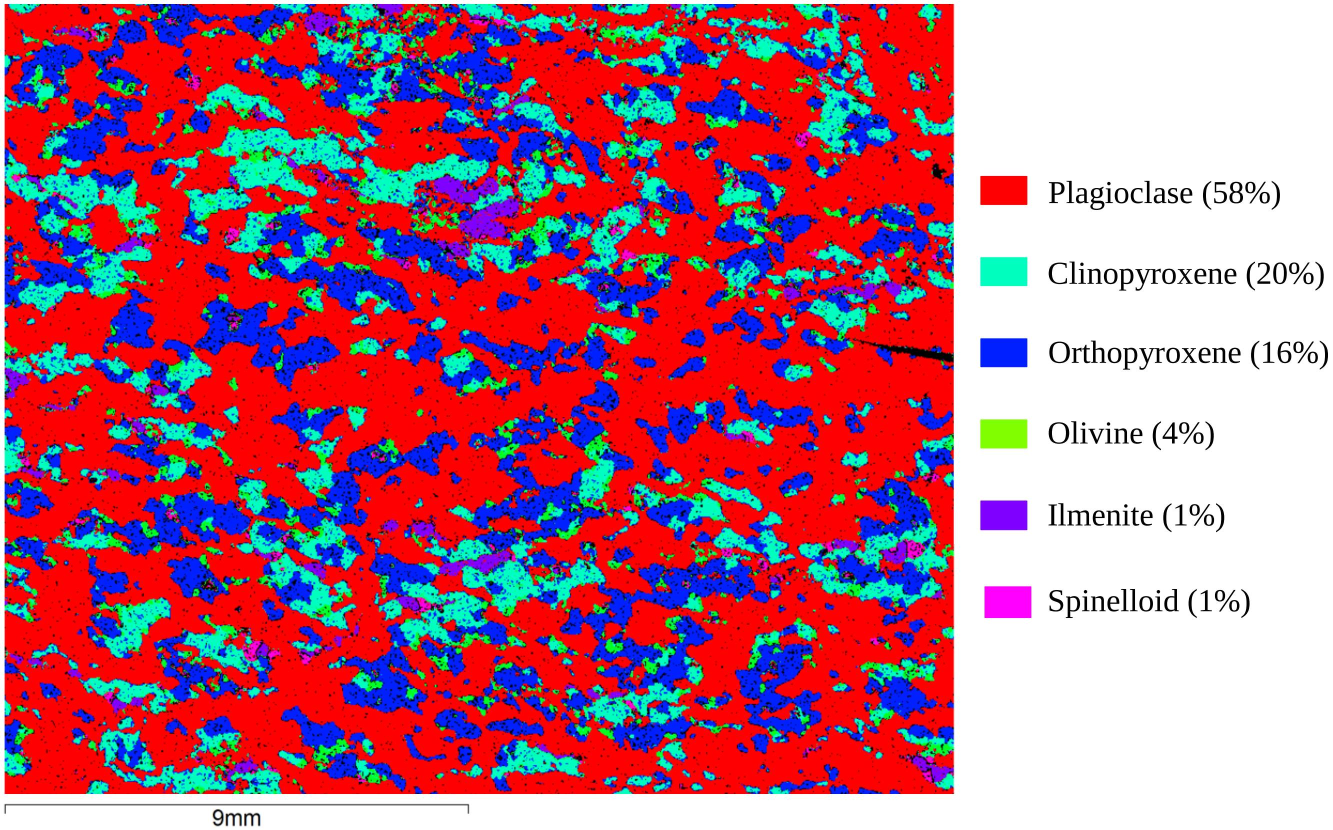

V238: Distal ILG from Site 2

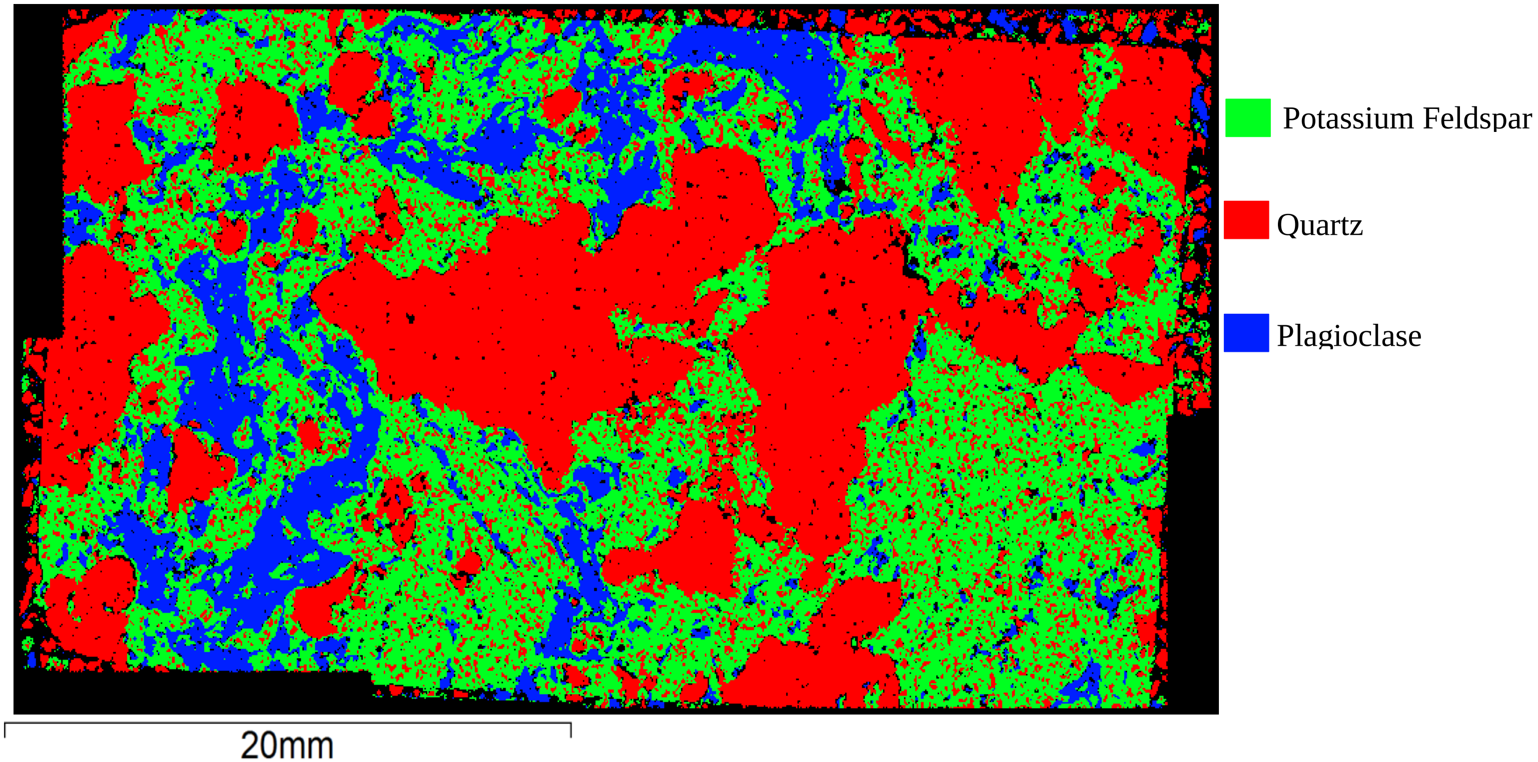

V09-249B: Transition Zone Sample, Gabbronorite with Inclusions of ILG.

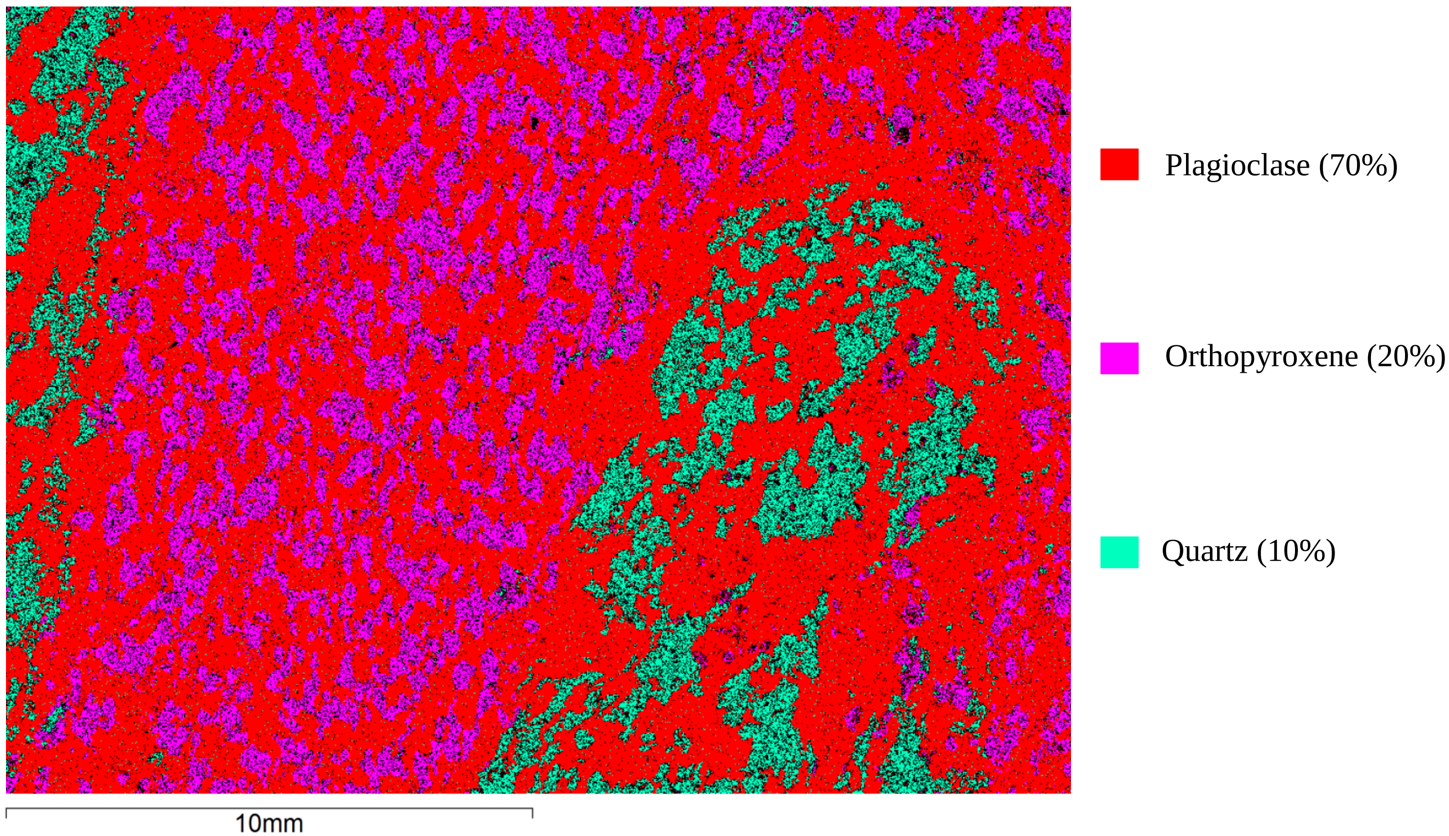

V234-2: Proximal ILG from Site 2

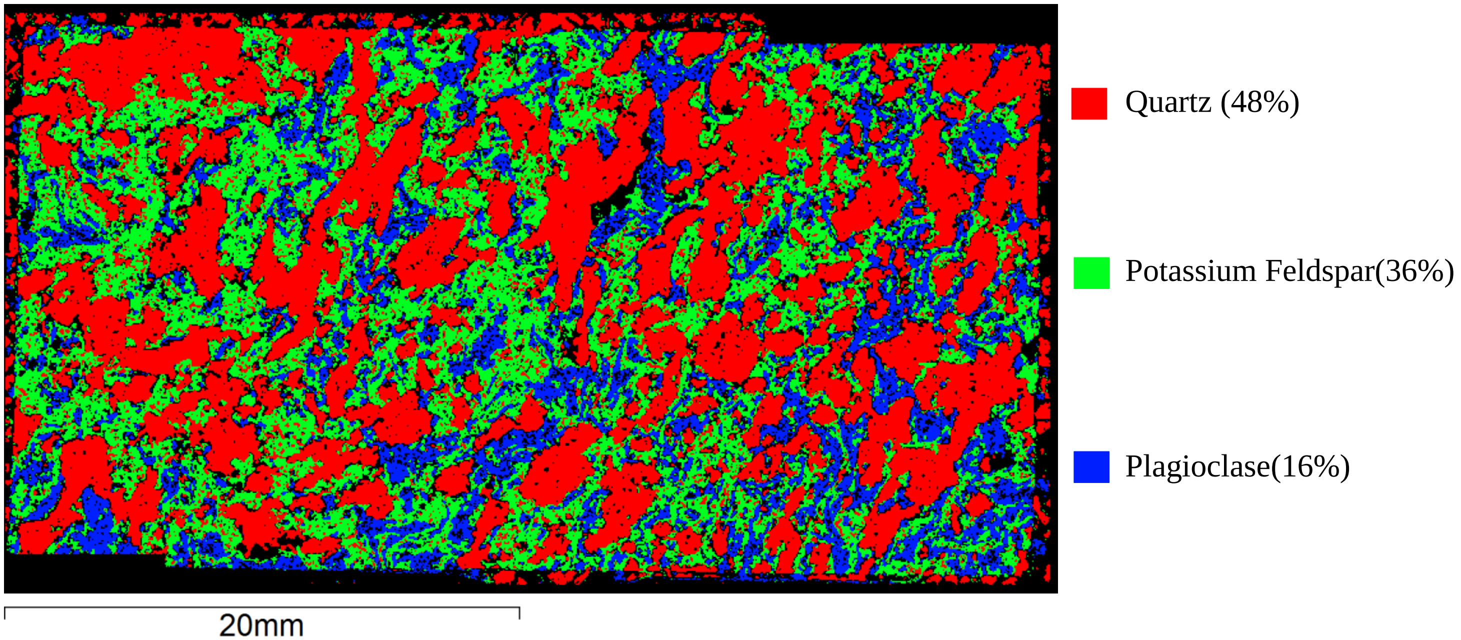

V245: Proximal ILG from Site 2

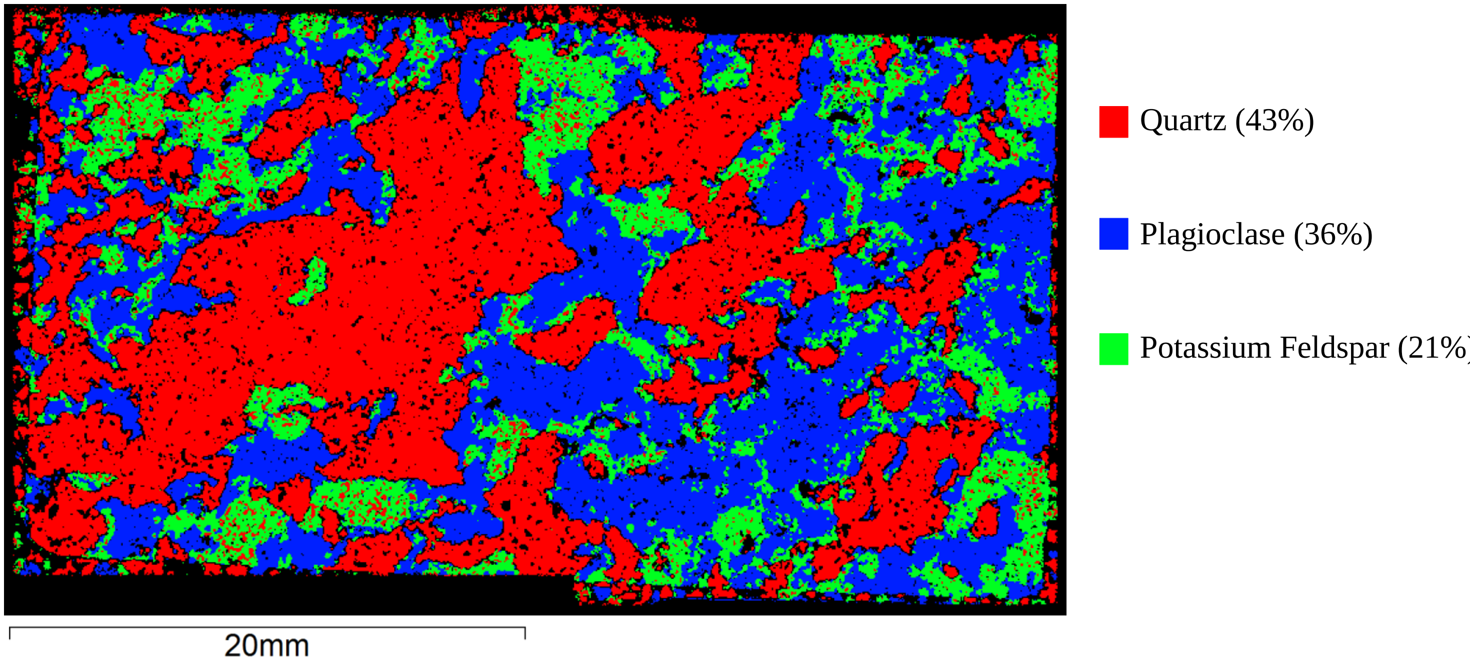

V246: Fine Grained Gabbronorite.

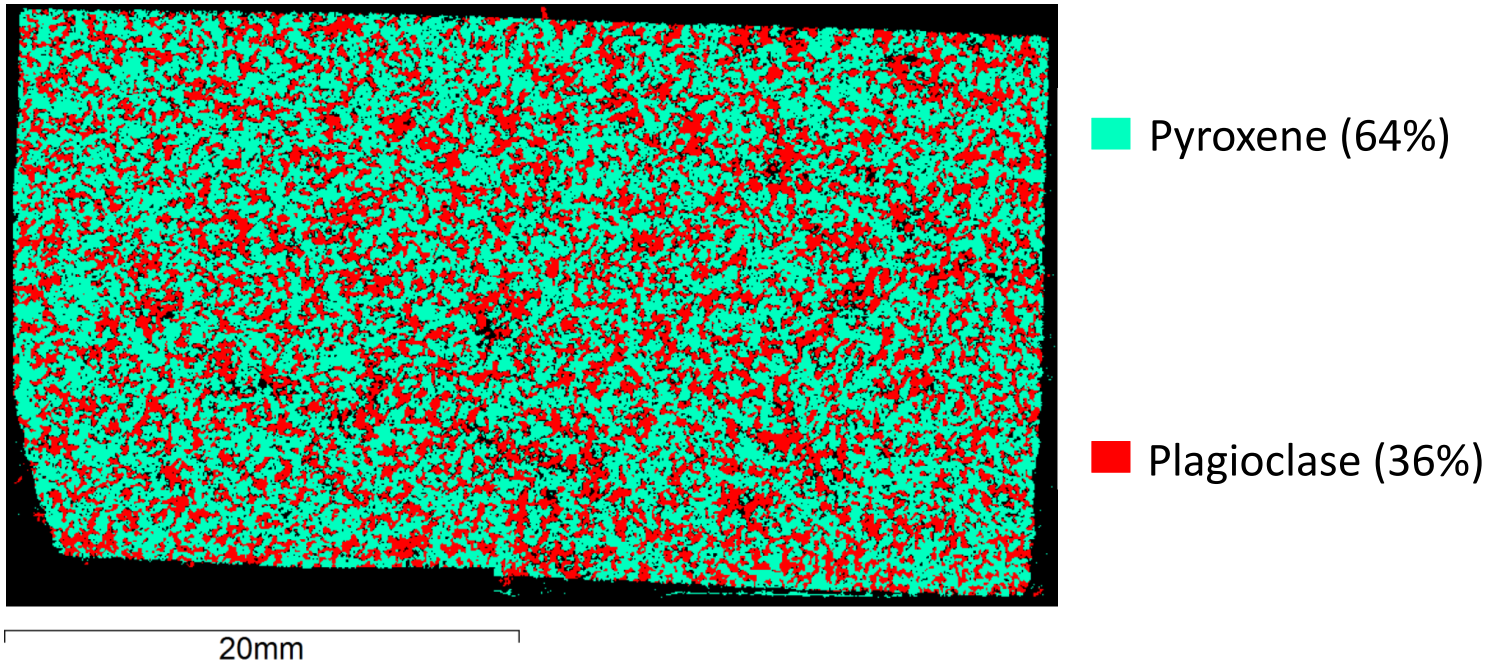

MN2: Gabbronorite from the Type Locality at Site 1

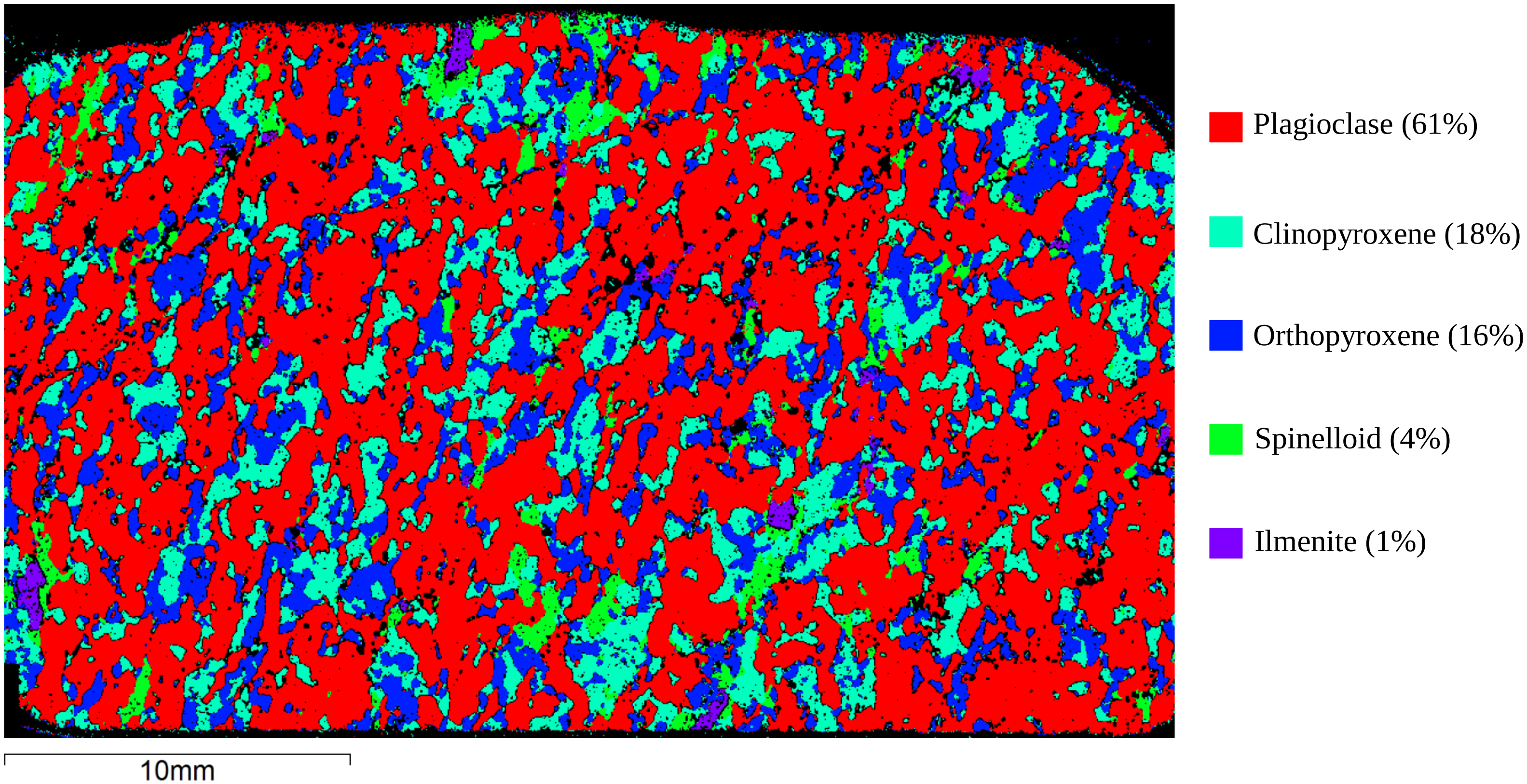

V252: Proximal ILG from Site 1

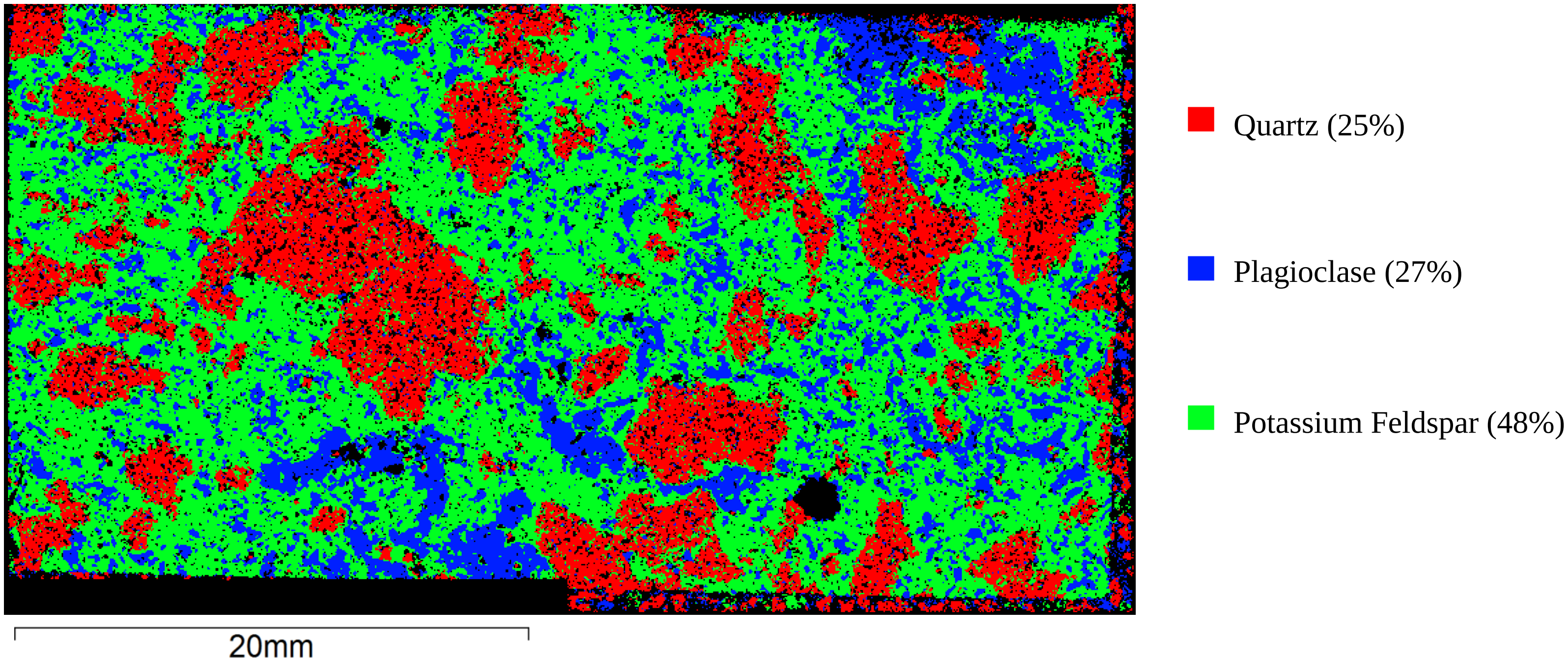

V262: Distal ILG from Site 1

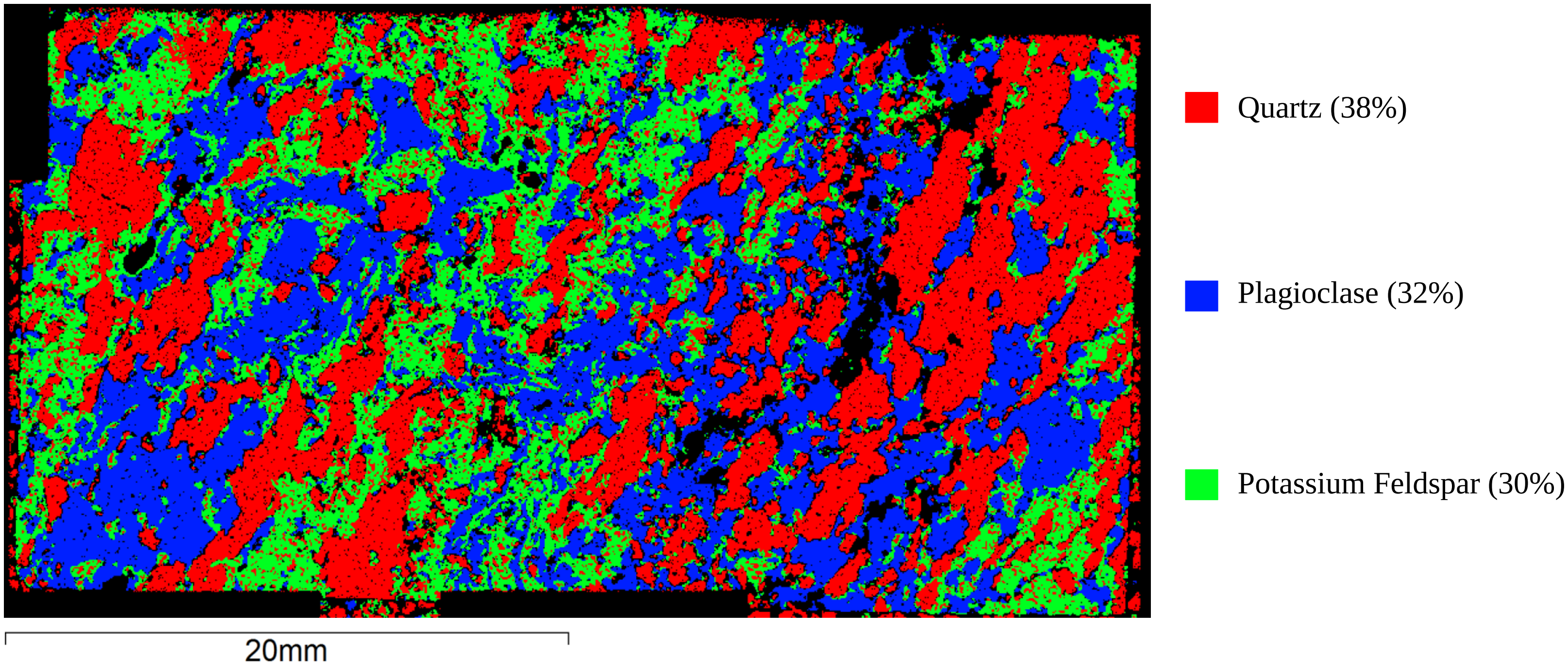

E-2 Sudbury

93PCL349A: Poikilitic Norite Pod in Sublayer Norite Matrix

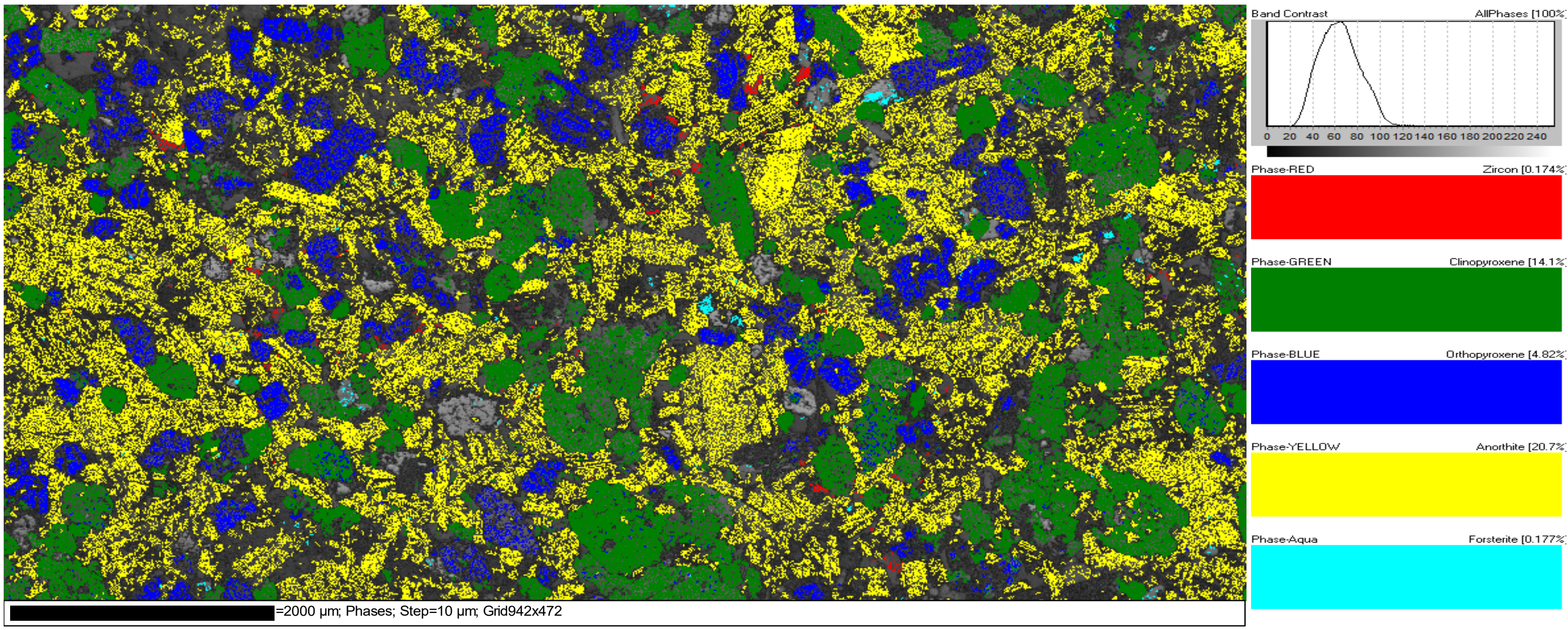

93PCL349B: Poikilitic Norite Pod in Sublayer Norite

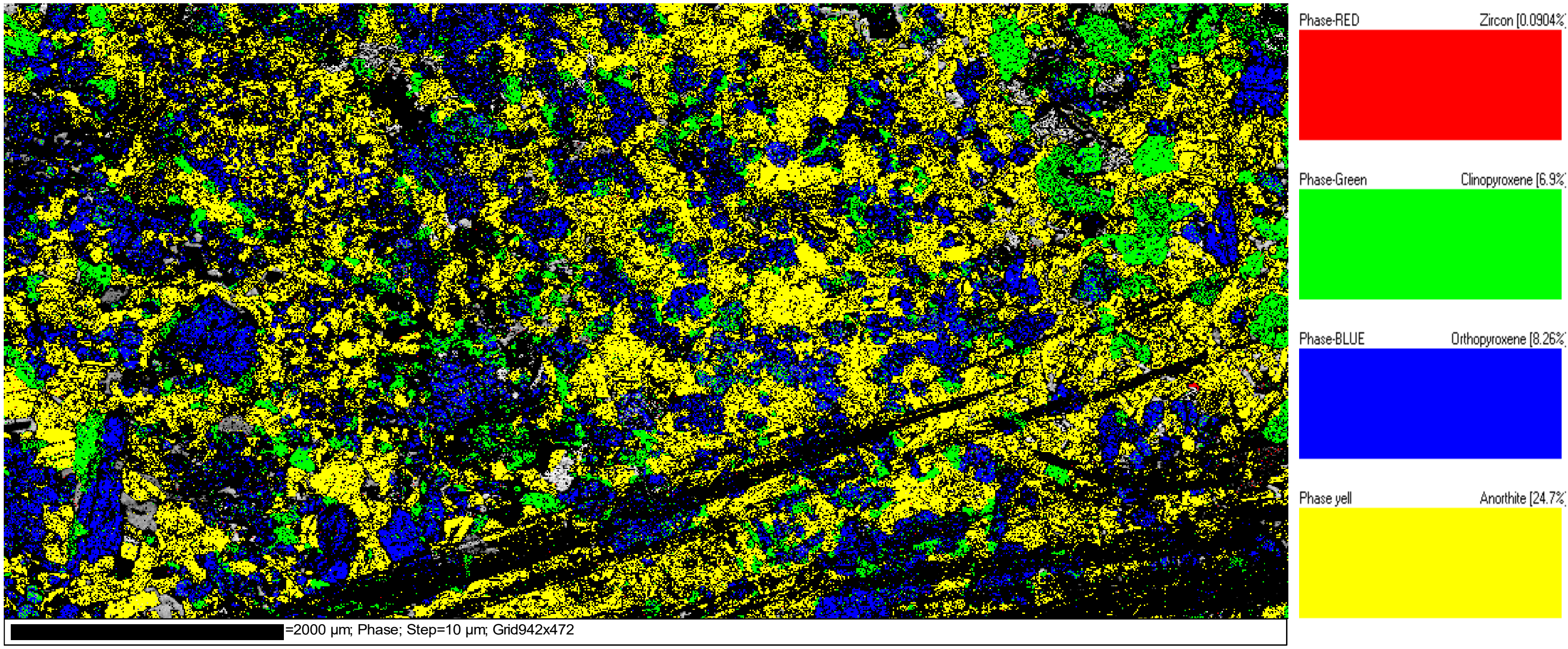

Appendix F-1: Imaged Vredefort Accessory Grains.

Feature #	Type	Area (μm^2)	Morphology	Surrounding Phases	Level of Shock	Comments	Size (~l by w μm)
				V09-234			
247	Baddeleyite	99	Anhedral	Boundary between high and low atomic #	None	Irregular shape	8x2
304	Baddeleyite	127	Anhedral	High atomic #	None	Irregular shape with a hole in the middle	6x2
565	Baddeleyite	58	Subhedral	High atomic #	None	Very small, featureless, has some sharp edges	3x1
1119	Baddeleyite	51	Anhedral	Med atomic #	None	2 small featureless baddeleyites	3x2 and 2x2
1121	Baddeleyite	117	Anhedral	Med atomic #	None	Featureless, slightly rounded	6x6
Average Baddeleyite Properties		*90.4*	*Dominantly Anhedral*		*0% shocked*	*Most often featureless*	*5x 2.5*
1143	Monazite	182	Anhedral	In crack in low atomic # (plagioclase)	None	Has a ragged appearance	15x2.5
87	Zircon	457	Anhedral	In pyroxene	None	Multiple cracks	15x10
140	Zircon	4418	Anhedral	High atomic #	None	3 small cracks and 3 holes	100x40
185	Zircon	1564	Subhedral	Med atomic #	None	Featureless,1 crack through the middle	30x30
208	Zircon	1695	Andedral	Low atomic # (plagioclase)	None	1 crack and one pit	60x?
211	Zircon	715	Euhedral	Grain boundary of pyroxenes	None	Featureless with 3 cracks	45x10
295	Zircon	4146	Anhedral	Low atomic # (plagioclase)	None	Featureless with a hole in the middle	75x50
467	Zircon	4206	Anhedral	Grain boundary of pyroxenes	None	Long and thin, stringer like, cracked	150x25
469	Zircon	315	Anhedral	Med atomic #	None	Featureless, with small crack on side	40x20
472	Zircon	872	Anhedral	Surrounded by Med and low atomic #	None	Slight irregular zoning, few cracks slightly rounded	25x25
530	Zircon	309	Subhedral	Surrounded by high and low atomic #	None	Small apophysis, 2 cracks	20x10
546	Zircon	18852	Anhedral	High and low atomic #	None	Slight zoning, few cracks, a few holes	200x50

Feature #	Type	Area (μm^2)	Morphology	Surrounding Phases	Level of Shock	Comments	Size (~l by w µm)
820	Zircon	442	Euhedral	Low atomic # (plagioclase)	None	Featureless	20x10
869	Zircon	572	Anhedral	Grain boundary high and low atomic #	None	Stringy discontinuous cracked	100x?
894	Zircon	691	Anhedral	Low atomic # (plagioclase)	None	2 cracks	60x30
1209	Zircon	3615	Anhedral	Med to high atomic #	None	Zoned, contains cracks slight irregular zoning	150x50
Average Zircon Properties		*2858*	*Anhedral*		*0% shocked*	*Most often featureless or cracked*	*73x28*
				V09-235A			
160	Baddeleyite	76	Euhedral		None	1 crack at the edge	50x30
195	Baddeleyite	68	Anhedral		None	3 separate small grains in a crack	10x?
224	Baddeleyite	60	Anhedral		None	Featureless	3x1.5
511	Baddeleyite	49	Subhedral		None	Featureless	1x1
533	Baddeleyite	47	Anhedral		None	Crack through the middle	3x1
673	Baddeleyite	91	Anhedral		None	Crack through the middle	4x4
676	Baddeleyite	44	Anhedral		None	Round and featureless	2x1
808	Baddeleyite	60	Anhedral		None	Two small featureless grains	2x1
829	Baddeleyite	90	Euhedral		None	Featureless, small crack	4x2
909	Baddeleyite	136	Subhedral		None	Featureless	10x3
930	Baddeleyite	55	Anhedral		None	Featureless, crack at the top	4x1
Average Baddeleyite Properties		*71*	*Anhedral*		*0% Shock*	*Most often featureless or cracked*	*8x5*
				V09-235B			
79	Baddeleyite	34	Anhedral	High atomic #	None	Featureless with 1 small crack on edge	1.5x0.5
510	Baddeleyite	77	Anhedral	Med atomic #	None	Contains a crack or pit	5x2
1023	Baddeleyite	53	Anhedral	Med atomic #	None	Featureless	3x1
1640	Baddeleyite	65	Anhedral	Med atomic #	None	Featureless	5x1

Feature #	Type	Area (μm²)	Morphology	Surrounding Phases	Level of Shock	Comments	Size (~l by w μm)
1760	Baddeleyite	71	Anhedral	Very high atomic #	None	Cracked, potential zoning	3x2
1826	Baddeleyite	117	Euhedral	Med atomic #	None	Cracked, appears to have a light offset to one of the cracks	6x3
2595	Baddeleyite	51	Anhedral	Grain boundary Med to high	None	Featureless	3x1
2666	Baddeleyite	47	Anhedral	Grain boundary Med to high	None	Featureless	2x1
2912	Baddeleyite	77	Anhedral	Med atomic #	None	Featureless	5x less than 1
3070	Baddeleyite	80	Subhedral	High atomic #	None	Featureless with 1 large and 1 small crack	3x2
Average Baddeleyite Properties		*672*	*Anhedral*		*0% Shock*	*Most often featureless or cracked*	*4x1*
37	Zircon	76	Prismatic	Low atomic # (Plagioclase)	None	Perfect featureless prismatic grain	15x3
39	Zircon	60	Subhedral	Med atomic # (Pyroxene)	None	Featureless	20x3
41	Zircon	164	Euhedral	Med atomic # (Pyroxene)	None	Featureless with 1 crack	25x5
293	Zircon	51	Euhedral	Low atomic # (Plagioclase)	None	Perfect rectangle	6x3
364	Zircon	13471	Anhedral	Med atomic #	None	Cracked, has 4 holes, and irregular zoning	100x100
1253	Zircon	45	Anhedral	In grain boundary between pyroxenes	None	Cracked	5x5
1778	Zircon	11210	Anhedral	High atomic #	None	Possible zoning, cracked top part looks to include an inclusion	200x100
1780	Zircon	39	Anhedral	High atomic #	None	Occurs as a line along a grain boundary tail of grain 1778	75x ?
2317	Zircon	199	Euhedral	Low atomic # (Plagioclase)	None	Prismatic grain with tapered tip	50x ?
2468	Zircon	1572	Subhedral	Med atomic #	None	Featureless	80x20
2472	Zircon	1160	Anhedral	Med atomic #	None	Crack at the bottom	50x20
2820	Zircon	742	Subhedral	Crosses grain boundaries	None	Has small apophysis off its sides crosses from edge of Med to Low to Med atomic #	100x?

Feature #	Type	Area (μm^2)	Morphology	Surrounding Phases	Level of Shock	Comments	Size (~l by w µm)
3062	Zircon	79	Euhedral	Low atomic # (Plagioclase)	None	Perfect prismatic grain	10x4
3108	Zircon	37	Euhedral	Low atomic # (Plagioclase)	None	Featureless	4x4
3311	Zircon	117	Subhedral	Med atomic # (Pyroxene)	None	Found dominantly in a pyroxene with lamella with the top crossing into plagioclase appears to have no features	10x6
3312	Zircon	659	Prismatic	Grain boundary Low (plagioclase) to Med (pyroxene)	None	Prismatic grain with small apophysis	50x10
3798	Zircon	247	Euhedral	High atomic #	None	Concentric zoning with a crack at the bottom	20x10
3815	Zircon	249	Anhedral	Med atomic #	None	Crack down the middle, found at the boundary between inclusion and grain the inclusion is in	20x5
3822	Zircon	66	Subhedral	Med atomic # (pyroxene)	None	Featureless	10x5
3934	Zircon	309	Anhedral	Grain boundary Med to high	None	Irregular and featureless	25x10
4001	Zircon	760	Anhedral	Grain boundary of pyroxene	None	Appears to follow around grain boundary	65x?
4023	Zircon	353	Anhedral	Grain boundary Low to Med	None	Has a small hole in the top of the grain	25x10
4024	Zircon	30	Euhedral	Med atomic #	None	Featureless	6x2
4035	Zircon	85	Prismatic	Low atomic # (Plagioclase)	None	Perfect featureless prismatic grain	10x4
4075	Zircon	243	Subhedral	From plag to med atomic #	None	Has a small apophysis	25x10
4110	Zircon	55	Euhedral	Low atomic # (Plagioclase)	None	Featurless grain	6x4
4114	Zircon	762	Euhedral	Crosses grain boundaries pyroxene to plagioclase	None	Thin long grain with small apophysis and 2 cracks one perpendicular and one sub parallel to the grain	20x?
Average Zircon Properties		*1216*	*44% Euhedral 30% Anhedral 22%Subhedral*		*0% Shock*	*Most often featureless or cracked*	38x16

Feature #	Type	Area (μm^2)	Morphology	Surrounding Phases	Level of Shock	Comments	Size (~l by w μm)
				V09-241B			
4	Baddeleyite		Anhedral	Quartz	None	Contains cracks	16x0.3
8	Monazite		Anhedral	Remodeled patch in quartz	None	Featureless	7x5
1	Zircon		Anhedral	Quartz	None	Featureless	8x8
2	Zircon		Subhedral	Feldspar	None	Featureless	14x5
3	Zircon		Anhedral	Feldspar	None	Contains cracks and pits	25x21
5	Zircon		Anhedral	Feldspar	None	Contains cracks, pits and one inclusion. The middle has slight mottling	53x40
6	Zircon		Euhedral	Quartz	None	Contains cracks and pits	33x22
7	Zircon		Anhedral	Quartz	None	Featureless	23x14
Average Zircon Properties			*67% Anhedral* *17% Subhedral* *17% Euhedral*	*50% Quartz* *50% Feldspar*	*None*	*50% Are featureless* *50% Contain cracks* *50% Contain pits* *16% Contain mottling and an inclusion*	*26x18*
				V09-249B			
46	Zircon	472	Subhedral		None	Featureless with 1inclusion and 1 small hole in it	30x10
183	Zircon	471	Anhedral		None	Featureless with a small hole in it	30x9
211	Zircon	563	Anhedral		None	3 separate irregular shaped grains that are featureless	
373	Zircon	617	Anhedral		None	Featureless with a few small cracks	20x10
465	Zircon	491	Anhedral		None	Slight irregular zoning, contains a few cracks	30x10

Feature #	Type	Area (µm²)	Morphology	Surrounding Phases	Level of Shock	Comments	Size (~l by w µm)
469	Zircon	1151	Anhedral		None	Slightly rounded, as a pit, contains some cracks, has visible irregular zones	30x30
499	Zircon	728	Anhedral		None	Contains many cracks	30x10
592	Zircon	651	Anhedral		None	Featureless	40x10
Average Zircon Properties		*643*	*Dominantly Anhedral*		*0% Shock*	*Most often featureless*	*30x14*
				V246			
2286	Baddeleyite	59	Subhedral	In a pit	None	Mottled edge, 2 cracks	5x3
4959	Baddeleyite	38	Subhedral	Pyroxene grain boundary	None	Featureless	10x3
Average Baddeleyite Properties		*48*	*Subhedral*		*0% Shock*		*7x3*
1805	Zircon	467	Anhedral	At the grain boundary of pyroxenes	None	Featureless, with the exception of one crack and one pit	23x13
3185	Zircon	243	Anhedral	Pyroxene	None	Slight irregular zoning and 3 cracks	23x8
4071	Zircon	319	Subhedral	Pyroxene grain boundary	None	Featureless, one crack	30x8
4624	Zircon	685	Anhedral	Pyroxene	None	Featureless, one pit	40x?
4825	Zircon	378	Anhderal	Pyroxene	None	Cracks and a pit	23x10
5226	Zircon	1288	Anhedral	At grain boundary	None	Crack 1 large inclusion, slight irregular zoning	33x31
6335	Zircon	1357	Subhedral	Grain boundary of pyroxene and feldspar	None	Slight irregular zoning, small inclusions and cracks	38x36
6449	Zircon	783	Anhedral	Found in pyroxene grain	None	Cracks and a pit	29x29
7519	Zircon	671	Subhedral	At grain boundary	None	Has 1 crack but otherwise is featureless	44x15
8536	Zircon	403	Anhedral	At pyroxene grain boundary	None	Featureless	63x3
8579	Zircon	655	Subhedral	Pyroxene	None	Featureless, one crack	21x16
8673	Zircon	1781	Subhedral	At grain boundary	None	Slight irregular zoning, small pits and cracks	53x20
9946	Zircon	1479	Anhedral	Grain boundary of pyroxene and feldspar	None	Featureless except for cracks	33x7
10053	Zircon	393	Anhedral	Pyroxene grain boundary	None	Featureless	30x8

Feature #	**Type**	**Area (μm^2)**	**Morphology**	**Surrounding Phases**	**Level of Shock**	**Comments**	**Size (~l by w µm)**
10366	Zircon	215	Anhedral	Pyroxene grain boundary	None	1 crack and 1 large inclusion	
Average Zircon Properties		*741*	*67% Anhedral 33% Subhedral*	*Often with pyroxene*	*0% Shock*	*Most often featureless or cracked*	*35x16*
V238 (thin section)							
1607	Baddeleyite	94	Subhedral	Quartz	None	Featureless	3.5x1
3777	Baddeleyite	14	Anhedral	Quartz	None	Featureless	3x2
4837	Baddeleyite	26	Anhedral	Quartz	None	Featureless with 2 cracks	3x3
Average Baddeleyite Properties		*45*	*Anhedral*	*Quartz*	*0% Shock*	*Most often featureless*	*3x2*
334	Monazite	38	Anhedral	Matrix	None	Cracked	5.5x2
3681	Monazite	42	Anhedral	Matrix	None	Featureless	4x4
3780	Monazite	645	Sub-rounded	Matrix	None	Featureless with 2 cracks	30x20
4181	Monazite	41	Anhedral	Matrix	None	Featureless	6x3
4331	Monazite	56	Rounded	Matrix	None	Featureless	4.5x6
4615	Monazite	22	Anhedral	Matrix	None	Featureless	2x4
4640	Monazite	34	Anhedral	Matrix	None	Ragged	5x0.5
5944	Monazite	31	Anhedral	Matrix	None	Polycrystaline and featureless	3x3
5950	Monazite	95	Subhedral	Quartz	None	Featureless and racked	5x5
Average Monazite Properties		*112*	*Anhedral*	*Matrix*	*0% Shock*	*Most often featureless*	*7x5*
972	Zircon	77	Subhedral	Quartz	None	Cracks and pits	5x6
3779	Zircon	16	Rounded	Matrix	None	Irregular zoning	2x3
Average Zircon Properties		*46*		*Matrix*	*0% Shock*		3x4
V238 (Thick Section)							
1607	Baddeleyite	94	Subhedral	Mottled patch	None	Featureless	4x1
3777	Baddeleyite	14	Anhedral	Quartz	None	Featureless	3x1.5
4837	Baddeleyite	26	Anhedral	Quartz boundary	None	Featureless	3x3
Average Baddeleyite Properties		*45*	*Anhedral*	*Most often in quartz*	*0% Shocked*	*Featureless*	*3x2*

Feature #	Type	Area (μm^2)	Morphology	Surrounding Phases	Level of Shock	Comments	Size (~l by w μm)
334	Monazite	38	Anhedral	Feldspar	None	Ragged edges, cracks	6x2
3681	Monazite	42	Anhedral	Feldspar	None	Ragged edges, cracks	5x4
3780	Monazite	650	Anhedral	Feldspar	None	Featureless with 2 cracks	30x7
4181	Monazite	41	Anhedral	Feldspar	None	Featureless	8x4
4331	Monazite	56	Rounded	Feldspar	None	Featureless	7x7
4615	Monazite	22	Anhedral	Quartz and feldspar	None	Featureless	4x2
4640	Monazite	34	Anhedral	Quartz and feldspar	None	Ragged edges, has inclusions	7x2
5944	Monazite	31	Anhedral	Quartz and feldspar	None	Polycrystalline	3x3
5950	Monazite	95	Subhedral	Quartz	None	Cracked	9x7
Average Monazite Properties		*112*	*Anhedral*	*Often found with feldspar*	*0% Shocked*	*Most often featureless or cracked*	*9x4*
972	Zircon	77	Subhedral	Quartz	None	Cracks and pits	8x7
3779	Zircon	16	Rounded	Quartz and feldspar	None	Has an inclusion	4x3
Average Zircon Properties		*47*		*Founded with quartz*	*0% Shocked*		*6x5*
V234-2							
539	Baddeleyite	41	Subhedral	Glomerogranular boundary	None	Featureless	5x3
1699	Baddeleyite	36	Rounded	Matrix	None	Featureless	5x3
1860	Baddeleyite	36	Subhedral	Grain boundary	None	Featureless	5x3
1947	Baddeleyite	61	Subhedral	Quartz	None	Featureless	7x5
3313	Baddeleyite	24	Subhedral	Near grain boundary	None	Featureless	4x2
Average Baddeleyite Properties		*40*	*Subhedral*		*0% Shock*	*Featureless*	5x3
1046	Monazite	11172	Anhedral	Matrix	Shocked	Polycrystalline, cracked, has pits through half of it	111x78
1051	Monazite	12369	Rounded	Matrix	Shocked	Polycrystalline, has pits	180x 150
1680	Monazite	410	Anhedral	Quartz	None	Cracked, slight zoning	106x11

Feature #	Type	Area (μm^2)	Morphology	Surrounding Phases	Level of Shock	Comments	Size (~l by w μm)
2073	Monazite	568	Anhedral	Quartz	None	Small inclusions (or pits) and small cracks	25x17
2379	Monazite	385	Prismatic	Quartz	None	Cracked	47x5
Average Monazite Properties		*4981*	*Anhedral*		*40% Shocked*	*Most often cracked*	*94x52*
58	Zircon	3220	Anhedral	Quartz	Shocked	Has a zoned/cracked central core and a cracked unzoned rim	80x40
191	Zircon	3733	Rounded	Quartz and feldspar	Shocked	Central core with zoning, and a cracked less zoned rim	72x53
2138	Zircon	2942	Rounded	Quartz	Shocked	Central core with zoning, and a cracked less zoned rim, has a large pit, possible healed PF's	58x58
2139	Zircon	5762	Anhedral	Quartz and feldspar	Shocked	Central core with zoning, and a cracked less zoned rim some small inclusions and pits	100x68
2719	Zircon	2335	Anhedral	Matrix	Shocked	Visible core with cracked rim, lots of inclusions	57x40
3267	Zircon	2218	Anhedral	Quartz and feldspar	Shocked	Core with cracked rim and some small inclusions	62x38
3323	Zircon	8767	Subhedral	Matrix	Shocked	Zoned core with cracked rim some inclusions, zone of modeling	128x67
3402	Zircon	9288	Anhedral	Quartz and feldspar	Shocked	Slightly visible core with cracked rim, line of inclusions	130x85
Average Zircon Properties		*4783*	*Anhedral*	*Most often in quartz*	*100% shocked*	*Most often has a concentrically zoned core and cracked rim*	*86x56*
V245							
864	Monazite	290	Anhedral	Matrix	None	Seems to be replacing something or being replaced	15x20
1848	Monazite	178	Anhedral	Quartz (crack)	None	Seems to be replacing something or being replaced	5x7.5
1990	Monazite	787	Anhedral	Quartz	None	Seems to be replacing something or being replaced	20x25
2185	Monazite	354	Anhedral	Matrix	None	Seems to be replacing something or being replaced	10x30
2254	Monazite	187	Anhedral	Quartz	None	Seems to be replacing something or being replaced	10x15

Feature #	Type	Area (µm^2)	Morphology	Surrounding Phases	Level of Shock	Comments	Size (~l by w µm)
Average Monazite Properties		*359*	*Anhedral*	*Often found with feldspar*	*0% Shocked*	*Only appears as a secondary phase*	*12x20*
33	Zircon	7052	Anhedral	Quartz	None	Polycrystalline with cracks and an older zone with concentric zoning	75x100
138	Zircon	6273	Anhedral	Matrix	Shocked	Has a visible core, areas of regrowth and planer features	50x100
181	Zircon	14543	Anhedral	Matrix	Shocked	cracked, appears to have concentric zoning, possible planner features	75x160
825	Zircon	15163	Anhedral	Quartz	Shocked	Cracked, appears to have weak concentric zoning, possible planner features, areas of regrowth	100x150
949	Zircon	6285	Subhedral	Quartz	Shocked	Cracked, has concentric zoning and regrown rim, possible planner features	50x75
2011	Zircon	6838	Subhedral	Quartz	None	Cracked, has inclusions	75x125
2232	Zircon	6840	Anhedral	Quartz	None	Cracked, has core with concentric zoning, polycrystalline regrowth	75x125
2250	Zircon	9709	Anhedral	Matrix	Shocked	Cracked, polycrystalline regrowth, concentric zoning, possible planner features	75x150
2441	Zircon	8826	Rounded	Quartz	None	Cracked, zoned, regrowth edges	100x100
2442	Zircon	15408	Anhedral	Quartz	None	Cracked, core with zoning, regrowth areas	100x125
2520	Zircon	14622	Anhedral	Quartz	Shocked	Polycrystalline with cracks and a possible visible core	100x100
2828	Zircon	7720	Anhedral	Quartz	Shocked	Polycrystalline with cracks and inclusions	100x100
Average Zircon Properties		*9940*	*Anhedral*	*Most often in quartz*	*58% Shocked*	*Often has PF's and areas of regrowth*	*81x118*
V252							
4418	Baddeleyite	9	Rounded	Feldspar	None	Featureless	2x1
84	Monazite	34	Anhedral	Quartz	None	Slight zoning, 3 inclusions	5x4
632	Monazite	58	Anhedral		None	Has pits and small cracks	5x2
2905	Monazite	22	Anhedral	Quartz and feldspar	None	Featureless	5x1

Feature #	**Type**	**Area (μm^2)**	**Morphology**	**Surrounding Phases**	**Level of Shock**	**Comments**	**Size (~l by w μm)**
Average Monazite Properties		*38*	*Anhedral*		0% Shocked		*5x2*
32	Zircon	389	Anhedral	Feldspar	Shocked	Mottled grain, irregular zoning, cracks	31x11
119	Zircon	1146	Anhedral	Quartz	None	Ragged core, cracked rim with small inclusions	43x23
349	Zircon	6619	Anhedral	Quartz and feldspar	Shocked	Has ragged patched and has a polycrystalline texture	130x50
350	Zircon	2105	Anhedral	Quartz and feldspar	None	Concentrically zoned core, some modeling, cracked rim with some inclusions and little zoning	48x30
364	Zircon	1264	Anhedral	Quartz	Shocked	Possible planner features, large cracks, and slight zoning	44x22
845	Zircon	3966	Anhedral	Quartz and feldspar	Shocked	Polycrystalline texture, small inclusions, dark modelled area	100x50
1025	Zircon	1831	Rounded	Quartz and feldspar	None	Concentrically zoned core with some modeling, cracked unzoned rim	44x42
1305	Zircon	3480	Anhedral	Quartz	None	Polycrystalline texture, small inclusions, dark modelled area	64x48
1426	Zircon	1449	Anhedral	Quartz	None	Slight polycrystalline texture some small cracks	62x25
2628	Zircon	1046	Anhedral	Feldspar	None	Mottled grain, zoning, cracks	33x30
3471	Zircon	1102	Anhedral	Quartz and feldspar	Shocked	Has a Mottled core, cracked unzoned rim and possible healed planer features	44x28
4720	Zircon	80578	Anhedral	Feldspar	Shocked	Has lines of small inclusions (possibly decorated PDF's) possible pf's	250x263
4745	Zircon	2674	Anhedral	Quartz	Shocked	Has a polycrystalline texture, and some small inclusions	93x29
4802	Zircon	16367	Anhedral	Quartz and feldspar	Shocked	slight zoning, strings of small inclusions , one crack through sample	218x109
5310	Zircon	1816	Anhedral	Quartz and feldspar	Shocked	Mottled core with concentric zoning edge, cracked unzoned rim with small inclusions	65x32
5370	Zircon	2844	Anhedral	Quartz and feldspar	Shocked	Slight zoning, small inclusions and some cracks possible healed and decorated PF’s	64x40

Feature #	Type	Area (μm^2)	Morphology	Surrounding Phases	Level of Shock	Comments	Size (~l by w µm)
Average Zircon Properties		*8042*	*Anhedral*	*Most often with quartz*	*63% Shocked*	*Often has PFs, polycrystalline texture or cores*	*83x52*
V262							
6652	Baddeleyite	200	Anhedral	Quartz and feldspar	None	Featureless	16x9
9306	Baddeleyite	27	Anhedral	Quartz and feldspar	None	Featureless	6x3
19393	Baddeleyite	28	Anhedral	Quartz and feldspar	None	Featureless	4x3
Average Baddeleyite Properties		*85*	*Anhedral*	*Quartz and feldspar*	0% Shocked	*Featureless*	*9x5*
7853	Monazite	669	Anhedral	Quartz and feldspar	Shocked	Polycrystalline, has an inclusion in the middle	37x17
12317	Monazite	4607	Anhedral	Quartz	None	Possible two different accessory phases, ragged edges	
12668	Monazite	1227	Anhedral	Quartz and feldspar	None	Few cracks, ragged edges	40x27
14831	Monazite	12013	Anhedral	Quartz and feldspar	None	Cracked, has some small inclusions	157x57
15443	Monazite	194	Anhedral	Ragged Mottled pocket	None	Small inclusions, ragged edges	12x5
18984	Monazite	38334	Rounded	Quartz and feldspar	Shocked	Polycrystalline, has an inclusion in it, small cracks	236x182
19126	Monazite	7195	Anhedral	Feldspar	None	Has cracks and small inclusions	96x54
20318	Monazite	5279	Anhedral	Quartz and feldspar	Shocked	Polycrystalline, has inclusions and small cracks, has a ragged halo around it.	400x129
Average Monazite Properties		*8690*	*Anhedral*	*Often with quartz*	*38% Shocked*	*Often polycrystalline and cracked*	*157x76*
1082	Zircon	2544	Subhedral	Quartz	None	Core with concentric zoning, has an unzoned cracked rim and small to medium inclusions	53x46
2652	Zircon	2412	Anhedral	Quartz	None	Multiple pieces, cracks and some inclusions.	61x29
8747	Zircon	11739	Subhedral	Feldspar	Shocked	Has an irregularly zoned central core, has a cracked unzoned rim, has an inclusion.	208x54

Feature #	Type	Area (μm^2)	Morphology	Surrounding Phases	Level of Shock	Comments	Size (~l by w µm)
9774	Zircon	10702	Subhedral	Quartz and feldspar	None	Has a core with concentric zoning, cracks and slightly reworked. Has a slightly zoned rim and cracks and inclusions	138x88
10134	Zircon	4565	Anhedral	Feldspar	Shocked	Polycrystalline, Mottled, reworked texture	100x46
12821	Zircon	6591	Rounded	Quartz and feldspar	Shocked	Has distinct concentric zones, has cracks and inclusions. The core is visible, its very dark but looks Mottled	96x81
15297	Zircon	4304	Subhedral	Quartz and feldspar	None	The core has very clean concentric zoning and is cracked. The rim has cracks and inclusions.	72x56
19022	Zircon	5364	Anhedral	Quartz and feldspar	Shocked	Polycrystalline, has Mottled areas and some inclusions.	127x46
19512	Zircon	2610	Subhedral	Quartz and feldspar	Shocked	Has a zoned and Mottled core with cracks, the rim is unzoned and has cracks.	81x38
19837	Zircon	5438	Subhedral	Quartz	Shocked	Has a zoned core with possible PDFs that are truncated by the less zoned cracked rim.	86x64
Average Zircon Properties		*5627*	*Subhedral*	*Often with quartz*	*60% Shocked*	*Most often has visible cores*	*102x55*

Appendix F-2: Imaged Sudbury Accessory Grains

Feature #	**Type**	**Area**	**Morphology**	**Surrounding Phases**	**Level of Shock**	**Comments**	**Size (~l*w µm)†**
				93PCL3489A			
1230	Baddeleyite	291	Anhedral	High Atomic #	None	Is somewhat 'Y' shaped with a thin bottom and wide top	18x3
2014	Baddeleyite	110	Anhedral	High Atomic #	None	Featureless but has 3 cracks on the bottom of the grain	5x2.5
2358	Baddeleyite	92	Euhedral	Low Atomic #	None	Has one inclusion at the end of the grain	8x2
2487	Baddeleyite	116	Anhedral	High Atomic #	None	Featureless with 3 inclusions on the bottom	8x2
1013	Baddeleyite & Zircon	361	Anhedral	Low Atomic #	None	Has baddeleyite in the center surrounded by zircon	20x10
Average Baddeleyite		*194*	*Anhedral*	*High Atomic #*	*None*	*Dominantly featureless*	*9x2*
2248	Monazite	402	Anhedral	High Atomic #	None	Has many cracks and a few small inclusions	20x10
2313	Monazite	406	Subhedral	High Atomic #	None	Is extremely cracked, it has cracks running from top to bottom	20x10
2488	Monazite	280	Subhedral	High Atomic #	None	Has some cracks and pits, weak concentric zoning	10x15
2664	Monazite	178	Anhedral	High Atomic #	None	Featureless	10x5
Average Monazite		*317*	*50% Anhedral 50% Subhedral*	*High Atomic #*	*None*	*75% Cracked*	*15x10*
1441	Zircon	842	Subhedral	Boundary of High Atomic # to Low Atomic #	None	Two grains, slight irregular and concentric zoning, has cracks	20x20
1460	Zircon	1232	Anhedral	Low Atomic #	None	There are 2 separate grains, with slightly irregular zoning	
1606	Zircon	732	Subhedral	Boundary of High Atomic # to Low Atomic #	None	Has slight concentric and irregular zoning, and small inclusions	25x20
1620	Zircon	1490	Anhedral	Boundary of High Atomic # to Low Atomic #	None	Has a pit in the center and some cracks	50x40

Feature #	**Type**	**Area (μm^2)**	**Morphology**	**Surrounding Phases**	**Level of Shock**	**Comments**	**Size (~l by w µm)**
1840	Zircon	1089	Semi-prismatic	Low Atomic #		Has cracks and slight zoning around the edges	40x26
1852	Zircon	797	Anhedral	Low Atomic #	None	Has a few cracks	50x25
2031	Zircon	780	Semi-prismatic	Low Atomic #	None	Has slight zoning on the edges and inclusion	30x20
2180	Zircon	630	Anhedral	High Atomic #	None	Has a few cracks	100x25
2385	Zircon	629	Subhedral	Boundary of High Atomic # to Low Atomic #	None	Has some cracks	30x10
2662	Zircon	5924	Semi-prismatic	Boundary of High Atomic # to Low Atomic #	None	Has ragged edges and holes	100x100
Average Zircon		*1415*	*40 % Anhedral 30% Subhedral 30% Semi-Prismatic*	*50% Boundary 50% Low Atomic #*	*None*	*Most often cracked, 50% have zoning*	*49x32*
42	Zirconolite	335	Semi-prismatic	High Atomic #	None	Has cracks on the ends	30x5
1513	Zirconolite	169	Anhedral	Boundary of High Atomic # to Low Atomic #	None	The grain is long and thin with a few tiny cracks	40x0.2
1884	Zirconolite	179	Anhedral	Boundary of High Atomic # to Low Atomic #	None	Cracked	10x5
2051	Zirconolite	1002	Irregular	Boundary of High Atomic # to Low Atomic #	None	Has a ragged edge and irregular zoning	40x20
2530	Zirconolite	250	Anhedral	High Atomic #	None	Has a large inclusion and a few small ones, has a few cracks	15x8
Average Zirconolite		*387*	*Anhedral*	*Along grain boundary*	*None*	*Most often cracked*	*27x8*
93PCL3489B							
715	Baddeleyite	235	Semi-prismatic	Matrix	None	Cracks and pits and small apophyses at the edge of the grain	20x3
799	Baddeleyite	210	Anhedral		None	Some cracks and inclusions	20x5
2536	Baddeleyite	146	Anhedral	Matrix	None	Multiple small cracks	11x4
3124	Baddeleyite	132	Anhedral	Matrix	None	Contains cracks and pits, has inversion twins	15x6

Feature #	Type	Area (μm²)	Morphology	Surrounding Phases	Level of Shock	Comments	Size (~l by w μm)
4800	Baddeleyite	183	Anhedral	Matrix	None	Has a crack and some small pits, has inversion twins	10x5
4900	Baddeleyite	311	Subhedral	Matrix	None	Slightly ragged edges	22x2.5
5249	Baddeleyite	115	Euhedral	Inclusion	None	Large pit in the middle, some small cracks	8x4
2104	Baddeleyite	104	Anhedral	Matrix	None	Ragged and pitted	6x3
Average Baddeleyite		*180*	*Anhedral*	*Matrix*	*None*	*Most often cracked*	*14x4*
890	Zircon	306	Andedral	Matrix	None	Has some small cracks	26x6
673	Zircon	171	Subhedral	Matrix	None	Contains small cracks and 2 small pits	12x10
892	Zircon	934	Anhedral	Matrix	None	Gets thinner towards one end, has some holes and cracks	70x20
1169	Zircon	828	Anhedral	Matrix	None	Cracked with some holes and cracks. Irregular zoning in CL	40x10
1983	Zircon	637	Anhedral		None	Featureless with the exception of small cracks on the edges	50x10
2276	Zircon	214	Anhedral	Matrix	None	Has ragged edges and small cracks and pits	13x7
2282	Zircon	1437	Subhedral	Matrix	None	Cracked with some pits on the edge. Weak concentric zoning	40x30
2692	Zircon	1796	Anhedral	Matrix	None	Has a thin top and wider bottom with some small cracks	133x21
3215	Zircon	252	Anhedral	Matrix	None	Cracked	13x11
4422	Zircon	169	Anhedral	Inclusion	None	Small cracks and pits	14x6
4538	Zircon	648	Anhedral	Matrix	None	Has irregular zoning and large pits	70x15
4652	Zirccon	2310	Euhedral	Matrix	None	Has concentric zoning visible in CL, and a pit	59x35
4819	Zircon	181	Anhedral	Matrix	None	Contains 2 large pits and several cracks	10x8
Average Zircon		*760*	*Anhedral*	*Matrix*	*None*	*86% of the grains are cracked* *69% contain pits* *31% of the grains have some form of zoning*	*42x14*
596	Zirconalite	167	Subhedral	Matrix	None	Contains a few small cracks	19x2
1876	Zirconalite	176	Subhedral	Matrix	None	Contains a few small cracks at the edges	36x3
1964	Zirconalite	216	Subhedral	Matrix	None	Contains small pits near the edges	17x5
2302	Zirconalite	617	Anhedral	Inclusion	None	Ragged grain with multiple pits	60x7

Feature #	Type	Area (μm²)	Morphology	Surrounding Phases	Level of Shock	Comments	Size (~l by w μm)
2564	Zirconalite	399	Subhedral	Matrix	None	Has ragged edges and small pits and cracks	20x6
2725	Zirconalite	227	Subhedral	Matrix	None	Ragged with multiple pits	15x4
3922	Zirconalite	187	Anhedral	Inclusion	None	Ragged with multiple pits	16x4
5089	Zirconalite	234	Euhedral	Matrix	None	Contains small cracks	26x4
5243	Zirconalite	218	Subhedral	Inclusion	None	Contains small pits and slight irregular zoning	12x5
Average Zirconalite		*271*	*Subhedral*	*Matrix*	*None*	*56% of the grains are cracked* *67% of the grains contain pits*	*25x4*
5116	Baddeleyite &Zircon	132	Subhedral	Matrix	None	Has some small cracks and inclusions	10x5
877	Zircon & Baddeleyite	302	Anhedral	Matrix	None	Baddeleyite on the inside has some cracks and the zircon on the rim is featureless	15x10
4242	Zirconolite &Baddeleyite	318	Anhedral	Matrix	None	Contains small cracks	10x15
93PCL3489C							
119	Baddeleyite	150	Anhedral	High Atomic #	None	Contains to small pits	10x3
1364	Baddeleyite	103	Anhedral	High Atomic #	None	Has a large pit in the center and a few cracks	6x3
1538	Baddeleyite	306	Anhedral	High Atomic #	None	Cracked and contains pits	12x6
2805	Baddeleyite	197	Subhedral	High Atomic #	None	Cracked and pitted	23x3
10969	Baddeleyite	153	Anhedral	Low Atomic #	None	Contains pits	10x2.5
Average Baddeleyite		*182*	*Anhedral*	*High Atomic #*	*None*	*All grains contain pits* *60% are cracked*	*12x3.5*
596	Monazite	179	Euhedral	Low Atomic #	None	Featureless	7x7
647	Monazite	179	Subhedral	Low Atomic #	None	Contains small pits	10x5
1888	Monazite	171	Subhedral	Low Atomic #	None	Slight concentric zoning, pit in the middle, and small cracks at the edges	7x6
10021	Monazite	211	Anhedral	High Atomic #	None	cracked and contains a pit	7x7
10755	Monazite	201	Anhedral	Low Atomic #	None	Has an 3 pits one in the middle and two on the edges	12x7
Average Monazite		*188*	*40% Anhedral and Subhedral* *20% Euhedral*	*Low Atomic #*	*None*	*80% contain pits* *40% contain cracks* *20% have zoning*	*9x6*

Feature #	Type	Area (μm^2)	Morphology	Surrounding Phases	Level of Shock	Comments	Size (~l by w µm)
3030	Zircon	452	Anhedral	Low Atomic #	None	Has more than one grain in the photo, few cracks and ragged edges	
3158	Zircon	125	Subhedral	Low Atomic #	None	Two grains in the image, top grain is cracked, the bottom has a pit	
5574	Zircon	128	Euhedral	Low Atomic #	None	Fairly featureless	12x1
3686-3688	Zircon	180, 78,52	Anhedral	Low Atomic #	None	Irregular zoning, inclusions and some cracks	20x30
Average Zircon			*Anhedral*	*Low Atomic #*	*None*	*50% are cracked* *33% contain pits* *17% have zoning*	
2762	Zirconolite	233	Euhedral	High Atomic #	None	Concentric zoning, crack across the top	18x7
11418	Zirconolite	313	Anhedral	High Atomic #	None	Small pits around the edges, the edges are ragged	16x7
12156	Zirconolite	257	Euhedral	Low Atomic #	None	Featureless	23x1
Average Zirconolite		*268*	*Euhedral*	*High Atomic #*	*None*		*19x5*
2636	Zirconolite &Baddeleyite	266	Subhedral	Low Atomic #	None	Slight concentric zoning, contains cracks and pits	12x3
IBNR(A)							
755	Baddeleyite	164	Prismatic	Inclusion	None	Featureless	18x5
3153	Baddeleyite	167	Anhedral	Inclusion	None	Cracked and has a few pits near the edge	15x6
3944	Baddeleyite	1309	Anhedral	Inclusion	None	Has some cracks and pits	95x10
3971	Baddeleyite	231	Euhedral	Inclusion	None	Cracked and contains has a few pits	15x13
4117	Baddeleyite	279	Subhedral	Inclusion	None	Has 3 lines of small inclusions and 5 pits	24x12
5529	Baddeleyite	157	Subhedral	Sublayer	None	1 small crack and 1 pit	18x5
5818	Baddeleyite	384	Anhedral	Inclusion	None	1 line of small pits and 1 larger pit	5x5
6299	Baddeleyite	169	Anhedral	Sublayer	None	Contains 2 pits	12x9
7418	Baddeleyite	191	Euhedral	Sublayer	None	1 small crack	20x6
8769	Baddeleyite	980	Anhedral	Inclusion	None	Has another phase around some of the edges. Contains some small cracks	65x20

Feature #	Type	Area (μm^2)	Morphology	Surrounding Phases	Level of Shock	Comments	Size (~l by w µm)
Average Baddeleyite		*403*	*50% Anhedral 30% Euhedral 20% Subhedral*	*70% Inclusion 30% Sublayer*	*None*	*60% Contain cracks 60% Contain pits*	*29x9*
1351	Monazite	217	Anhedral	Sublayer	None	Contains some cracks	17x10
1666	Monazite	105	Anhedral	Inclusion	None	Ragged edges and cracks	10x5
3445	Monazite	31	Subhedral	Inclusion	None	Featureless	4x3
Average Monazite		*118*	*Anhedral*	*Inclusion*	*None*	*Most often cracked*	*10x6*
450	Zircon	2193	Anhedral	Sublayer	None	Cracked and contains a large pit in the middle. Has slight concentric zoning	100 x 25
875	Zircon	810	Anhedral	Inclusion	None	Has a Mottled texture	55 x 10
2059	Zircon	846	Euhedral	Sublayer	None	Has irregular zoning and contains small cracks	25 X 40
2063	Zircon	467	Euhedral	Inclusion	None	Has irregular zoning and a large pit in the middle	30 x 15
4178	Zircon	405	Euhedral	Inclusion	None	Contains a pit with cracks radiating out of it and irregular zoning along the edges	20 x 20
4341	Zircon	560	Anhedral	Inclusion	None	Featureless	25 x 15
4574	Zircon	491	Anhedral	Inclusion	None	The left side is more Mottled and the right is cracked but otherwise featureless	25 x 15
7797	Zircon	341	Anhedral	Inclusion	None	Has irregular zoning	25 x 15
7800	Zircon	358	Subhedral	Inclusion	None	Has zoning and cracks around the edge but the middle is featureless	20 x15
9272	Zircon	4954	Anhedral	Sulfides?	None	Has an Fe + O rich inclusion in the middle of the grain and contains cracks	150 x 50
Average Zircon		*1143*	*60% Anhedral 30% Euhedral 10% Subhedral*	*88% Inclusion 22% Sublayer*	*None*	*70% Are zoned 10% Featureless 50% cracked 10% Inclusions 30% Contain pits 20% Mottled texture*	*47x22*
1306	Zirconolite	153	Euhedral	Sublayer	None	Contains 2 cracks	16x9
1789	Zirconolite	315	Anhedral	Inclusion	None	Cracked, has ragged edges	25x7
2819	Zirconolite	129	Anhedral	Sublayer	None	Contains many small pits	13x7
2858	Zirconolite	131	Subhedral	Sublayer	None	Contains cracks and some pits	12x6
4527	Zirconolite	112	Subhedral	Sublayer (contact)	None	Cracked	15x4

Feature #	Type	Area (μm^2)	Morphology	Surrounding Phases	Level of Shock	Comments	Size (~l by w µm)
5576	Zirconolite	234	Subhedral	Sublayer (contact)	None	One large crack across the grain and a few small pits	17x10
7479	Zirconolite	143	Subhedral	Sublayer (close to sulfide)	None	Featureless	15x5
7879	Zirconolite	131	Subhedral	Inclusion	None	Altered end but otherwise featureless	28x4
9304	Zirconolite	133	Subhedral	Sublayer	None	Slight irregular zoning, some pits	10x10
1527	Zirconolite and Baddeleyite	110	Subhedral	Inclusion	None	Featureless	13x5
Average Zirconolite		*159*	*70% Subhedral* *20% Anhedral* *10% Euhedral*	*70% Sublayer* *30% Inclusion*	*None*	*50% Are cracked* *40% Contain pits* *20% Are featureless* *10% Have zoning*	*16x7*
				IBNR(B)			
2356	Baddeleyite	260	Subhedral	Inclusion	None	Has a few small pits	20x10
5441	Baddeleyite	571	Euhedral	Inclusion	None	Contains pits and cracks, has ragged ends	32x10
12814	Baddeleyite	216	Euhedral	Sublayer	None	Featureless	31x5
Average Baddeleyite		*349*	*Euhedral*	*Inclusion*	*None*		*28x8*
3782	Monazite	58	Euhedral	Sublayer	None	Has concentric zoning and pits	5x5
9187	Monazite	84	Anhedral	Inclusion	None	Contains large pits	10x5
16285	Monazite	142	Anhedral	Sublayer	None	The top is striated and the bottom has multiple pits	16x5
18577	Monazite	63	Anhedral	Sublayer	None	Featureless	7x5
19057	Monazite	87	Subhedral	Sublayer	None	Featureless	10x5
Average Monazite		*87*	*60% Anhedral* *20% Euhedral* *20% Subhedral*	*Sublayer*	*None*	*60% contain pits* *40% are featureless* *20% have concentric zoning*	*9x5*
8103	Zircon	2451	Subhedral	Inclusion	None	Irregular zoning, cracks, some pits	64x48
8122	Zircon	1191	Anhedral	Inclusion	None	Mottled texture, small pits	60x23
18574	Zircon	1224	Euhedral	Sublayer	None	Mottled texture, contains pits	43x26
24968	Zircon	1437	Anhedral	Inclusion	None	Mottled texture, small pits and cracks around the edges	
29524	Zircon	1253	Euhedral	Sublayer	None	Irregular zoning, contains pits	37x30

Feature #	Type	Area (μm^2)	Morphology	Surrounding Phases	Level of Shock	Comments	Size (~l by w μm)
Average Zircon		*1511*	*40% Euhedral* *40% Anhedral* *20% Subhedral*	*60% Inclusion* *40% Sublayer*	*None*	*100% contain pits* *60% are Mottled* *40% are cracked* *40% are have irregular zoning*	*51x32*
2364	Zirconalite	209	Anhedral	Inclusion	None	Has two directions of cracks and small pits	20x8
7571	Zirconalite	282	Subhedral	Sublayer	None	Small cracks and pits	43x5
7648	Zirconalite	287	Euhedral	Sublayer	None	4 small cracks	52x3
21406	Zirconalite	255	Subhedral	Sublayer	None	Small cracks	77x5
29591	Zirconalite	298	Subhedral	Sublayer	None	Small cracks and 1 pit	81x5
Average Zirconalite		*266*	*60% Subhedral* *20% Anhedral* *20% Euhedral*	*80% Sublayer* *20% Inclusion*	*None*	*100% Are cracked* *60% Contain pits*	*55x5*
3352	Baddeleyite & Zircon	396	Anhedral	Inclusion	None	Baddeleyite with a rim of zircon has some small pits and cracks	40x14
8127	Baddeleyite & Zircon	306	Anhedral	Inclusion	None	Baddeleyite with a rim of zircon. contains a few cracks	22x10
				RX187432			
2770	Zircon	26	Anhedral		None	Mottled appearance some small pits.	6.5x4
4725	Zircon	111	Anhedral		None	Has a string of small pits	12x6
6741	Zircon	26	Anhedral		None	Mottled appearance some small pits	5x4
11223	Zircon	912	Anhedral		None	String of small pits some cracks across the right side, 4 larger pits	40x22
16147	Zircon	2286	Subhedral		None	One large pit at the top of the grain with cracks radiating outward. Sting of smaller inclusions across the sample	63x34
22712	Zircon	30	Subhedral		None	Slight zoning	6x4
26277	Zircon	2372	Anhedral		None	Multiple strings of small pits, cracks along the edges	70x30
26639	Zircon	769	Anhedral		None	Irregular zoning, cracks along the edges	33x17
27452	Zircon	45	Anhedral		None	Slight zoning	6x5
27648	Zircon	76	Anhedral		None	Found along edge of other grain, irregular zoning	36x2

Feature #	Type	Area (μm^2)	Morphology	Surrounding Phases	Level of Shock	Comments	Size (~l by w μm)
30989	Zircon	121	Euhedral		None	Zoned, cracks along edge	11x8
Average Zircon		*616*	*73% Anhedral* *18% Subhedral* *9% Euhedral*		*None*	*55% contain pits* *18% are Mottled* *45% are cracked* *45% are have irregular zoning* *9% contain inclusions*	*26x12*
				W1A			
2856	Monazite	43	Anhedral	Felsic Minerals	None	Mottled texture, ragged edges, riddled with pits	5x4
4940	Monazite	44	Anhedral	Felsic Minerals	None	Mottled texture, ragged edges, with pits	8x2
11068	Monazite	48	Anhedral	Felsic Minerals	None	Small disconnected grains possibly altered granular texture	40x25
15469	Monazite	22	Anhedral	Felsic Minerals	None	Has pits	4x2
Average Monazite		*39*	*Anhedral*	*Felsic Minerals*	*None*	*50% contain pits* *50% are Mottled*	*14x8*
359	Zircon	4576	Subhedral	Felsic Minerals	None	Cracked, has irregularly zoned edges and contains pits	90x60
364	Zircon	4012	Anhedral	Felsic Minerals	None	Cracked edges, pits, irregular zoning, possible remnants of concentric zoning	100x30
1581	Zircon	3320	Subhedral	Felsic Minerals	None	Irregular zoning and cracks around edges, zone of modeling and contains some pits	76x48
1595	Zircon	3488	Anhedral	Felsic Minerals	None	Irregular zoning and cracks around edges, zone of modeling and contains some pits	73x45
2524	Zircon	5393	Anhedral	Felsic Minerals	Shocked?	Polycrystaline grain, possibly altered granular texture	94x50
2943	Zircon	2811	Euhedral	Felsic Minerals (near sulphide)	None	Zoned, cracked edges	66x40
8108	Zircon	5783	Anhedral	Felsic Minerals	None	Irregular zoned, cracked edges, contains pits	82x77
12033	Zircon	5942	Anhedral	In contact with sulphide	None	Irregular zoning and cracks around edges, zone of modeling, contains pits	150x50
12938	Zircon	3703	Subhedral	Felsic Minerals	None	Slight zoning, cracks around the edges, crack through the grain, contains pits	70x57
14111	Zircon	5142	Euhedral	Felsic Minerals	None	Concentric zoning, cracked throughout, some modelled areas	91x59

Feature #	Type	Area (μm²)	Morphology	Surrounding Phases	Level of Shock	Comments	Size (~l by w μm)
Average Zircon		*4248*	*50% Anhedral* *30% Subhedral* *20% Euhedral*	80% Felsic Minerals 20% Near Sulphide	*None*	*90% are cracked* *90% are have irregular zoning* *70% contain pits* *40% are Mottled*	89x52
				W1B(2)			
2134	Baddeleyite	16	Anhedral	Felsic Minerals	None	Featureless	4x2
2404	Baddeleyite	16	Prismatic	Felsic Minerals	None	Featureless	5x1.5
Average Baddeleyite		*16*		*Felsic Minerals*	*None*	*Featureless*	*4.5x1.75*
83	Monazite	294	Anhedral	Felsic Minerals	None	Many unconnected grains	32x16
1151	Monazite	42	Anhedral	Felsic Minerals	None	Contains pits	6x1.5
1152	Monazite	49	Anhedral	Felsic Minerals	None	Irregular edges, contains pits	6x6
1364	Monazite	137	Anhedral	Felsic Minerals	None	Irregular edges, contains pits, multiple grains	
4096	Monazite	284	Anhedral	Felsic Minerals	None	Small discontinuous grains in a digested pod	27x15
5132	Monazite	188	Anhedral	Felsic Minerals	None	Contains pits	15x7
5530	Monazite	214	Anhedral	Felsic Minerals	None	Small discontinuous grains in a digested pod	14x14
Average Monazite		*173*	*Anhedral*	*Felsic Minerals*	*None*	*57% Contain pits* *43% Are made up of discontinuous grains*	*17x10*
601	Zircon	9837	Anhedral	Felsic Minerals	None	Irregular zoning, contains cracks and pits	120x100
999	Zircon	4041	Anhedral	Felsic Minerals	None	Has irregular zoning, cracks, and irregular edges	89x44
1648	Zircon	6742	Anhedral	Felsic Minerals	None	Has zoning, semi-polycrystalline, some Mottled textures and pits.	100x50
1973	Zircon	7758	Anhedral	Felsic Minerals (near sulphide)	None	Has irregular zoning, Mottled textures and some cracks and pits	150x53
2938	Zircon	2973	Subhedral	Felsic Minerals (near sulphide)	None	Has packages of polycrystalline areas, cracks, pits and small remnants of concentric zoning	60x55
3084	Zircon	3524	Euhedral	Felsic Minerals	None	Slight remnants of concentric zoning, cracks and pits	67x50
3090	Zircon	2507	Euhedral	Felsic Minerals	None	Core and rim, cracked, slight remnant of concentric zoning	60x49
3094	Zircon	4851	Anhedral	Felsic Minerals	None	Multiple disconnected grains, Mottled textures	

Feature #	Type	Area (μm^2)	Morphology	Surrounding Phases	Level of Shock	Comments	Size (~l by w µm)
5747	Zircon	1257	Anhedral	Felsic Minerals	None	Multiple cracks, slight remnant of concentric zoning, Mottled texture and one large pit	81x37
5750	Zircon	4059	Subhedral	Felsic Minerals	None	Multiple cracks, Mottled texture	67x67
Average Zircon		*4755*	*60% Anhedral* *20% Subhedral* *20% Euhedral*	*Felsic Minerals*	*None*	*90% are cracked* *80% are have irregular zoning* *60% contain pits* *50% are Mottled* *30% Are made up of discontinuous grains*	*88x56*
W1C(1)							
47	Monazite	97	Anhedral	Felsic Minerals	None	Small discontinuous grains, found in a pit	40x20
1434	Monazite	154	Anhedral	Felsic Minerals	None	Multiple small cracks	25x5
2731	Monazite	49	Anhedral	Mafic Inclusion	None	Very tiny, Mottled textures	5x4
3429	Monazite	47	Subhedral	Mafic Inclusion	None	Small grain, two pits, striations in a fan like array	4x4
5420	Monazite	84	Anhedral	Mafic Inclusion	None	Irregular edges, multiple pits	11x4
Average Monazite		*86*	*80% Anhedral* *20% Subhedral*	*60% Mafic Inclusion* *40% Felsic Minerals*	*None*	*60% contain pits* *20% are cracked* *20% are Mottled* *20% Are made up of discontinuous grains*	*17x7*
129	Zircon	2636	Anhedral	Felsic Minerals	None	Semi-polycrystalline texture, multiple small pits	87x31
188	Zircon	1064	Anhedral	Felsic Minerals	None	Small pits, Mottled internal texture	45x22
491	Zircon	1282	Subhedral	Felsic Minerals	None	Cracked edges, slightly Mottled internal texture, contains pits	60x19
678	Zircon	595	Anhedral	Contact (matrix and inclusion)	None	Large cracks though grain, small cracks around edges, one large inclusion	37x26
921	Zircon	504	Subhedral	Mafic Inclusion	None	Slight zoning, large cracks through grains	22x20
1035	Zircon	685	Subhedral	Mafic Inclusion	None	Zoning near the edge, small pits and cracks	32x18
1253	Zircon	484	Subhedral	Mafic Inclusion	None	Core with Mottled texture, cracked but featureless rim.	30x18
2457	Zircon	472	Subhedral	Mafic Inclusion	None	Core with Mottled texture, cracked but featureless rim, slight zoning on edge, pit in the middle	20x19

Feature #	Type	Area (μm^2)	Morphology	Surrounding Phases	Level of Shock	Comments	Size (~l by w μm)
4442	Zircon	1083	Subhedral	Mafic Inclusion	None	Slight concentric zoning around edges, multiple cracks, contains small pits	45x22
5006	Zircon	463	Subhedral	Mafic Inclusion	None	Core with slight Mottled textures, cracked featureless rims	24x18
Average Zircon		*927*	*70% Subhedral* *30% Anhedral*	*60% Mafic Inclusion* *30% Felsic Minerals* *10% At Contact*	*None*	*70% are cracked* *60% contain pits* *50% are Mottled* *30% are have zoning* *30% Have a visible core* *10% Are somewhat granular* *10% Contain inclusions*	*40x21*
				RX187408			
32921	Baddeleyite	281	Anhedral		None	Contains small cracks	20x3
33483	Baddeleyite	127	Subhedral		None	Featureless	5x2
38122	Baddeleyite	81	Anhedral		None	Contains small cracks	3x1
39014	Baddeleyite	94	Anhedral		None	Contains cracks	7x2
40435	Baddeleyite	108	Anhedral		None	Contains small pits along edges	9x2
Average Baddeleyite		*138*	*80% Anhedral* *20% Subhedral*		*None*	*60% are cracked* *20% contain pits* *20% Featureless*	*9x2*
12371	Zircon	947	Anhedral		None	Contains inclusions	350x25
20540	Zircon	4842	Anhedral		None	Contains cracks and pits	93x36
30395	Zircon	1049	Anhedral		None	Contains cracks and pits	53x23
38345	Zircon	2063	Anhedral		None	Contains cracks	53x26
41096	Zircon	5872	Anhedral		None	Contains cracks and pits	130x40
41136	Zircon	3252	Subhedral		None	Contains cracks	67x50
41139	Zircon	2170	Anhedral		None	Contains two cracks and two pits	72x39
41289	Zircon	257	Euhedral		None	Contains cracks and pits	75x56
40163	Zircon	2411	Anhedral		None	Contains cracks	94x25
Average Zircon		*2540*	*78% Anhedral* *11% Subhedral* *11% Euhedral*		*None*	*89% are cracked* *56% contain pits* *11% Contain inclusions*	*110x36*

Feature #	Type	Area (μm^2)	Morphology	Surrounding Phases	Level of Shock	Comments	Size (~l by w µm)
21566	Zirconalite	441	Subhedral		None	Contains cracks and pits	36x8
21671	Zirconalite	298	Subhedral		None	Contains pits	79x4
Average Zirconalite		*370*	*Subhedral*		*None*	*100% contain pits* *50% are cracked*	*56x6*
15032	Zircon and Zironalite	2424	Subhedral		None	Contains cracks and pits	100x22
31541	Zirconalite and Baddeleyite	298	Subhedral		None	Cracked	105x5
25159	Zirconalite, Baddeleyite and zircon	361	Anhedral		None	Featureless	15x12

Appendix F-3: Vredefort Accessory Phase Plates

Note all the images shown in this appendix are BSE images.

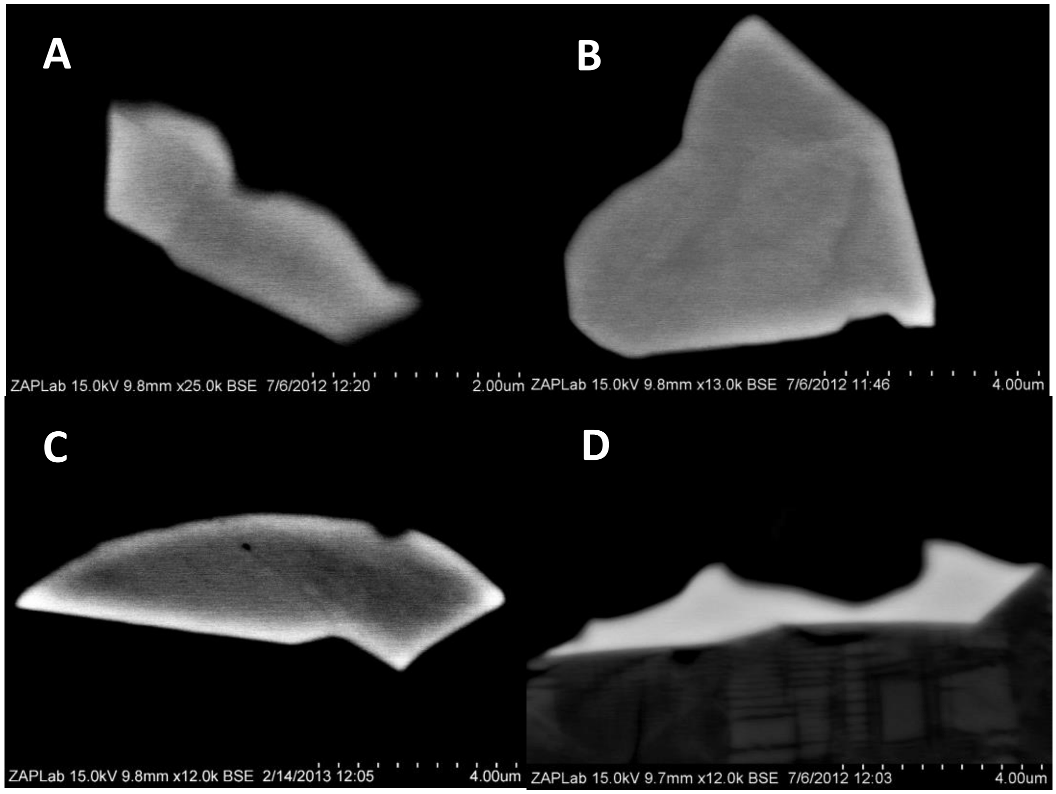

Figure F-3-1: Gabbronorite baddeleyites. A: B565 from sample V234, B: 1121 from sample V234, C: B4959 from sample V246, and D: B247 from sample V234. The baddeleyites appear to be internally featureless with anhedral to subhedral morphologies.

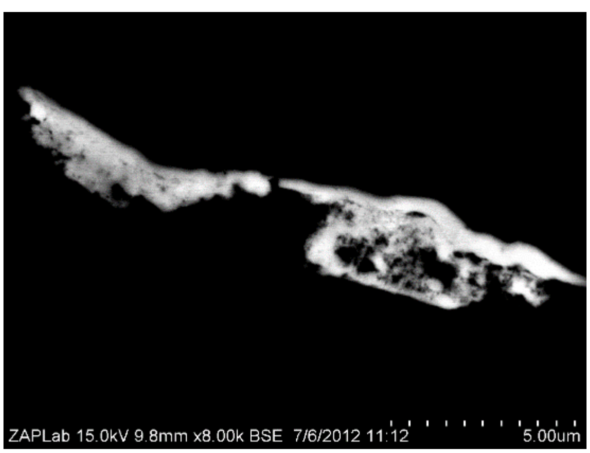

Figure F-3-2: Gabbronorite anhedral monazite grain M1143, from sample V234.

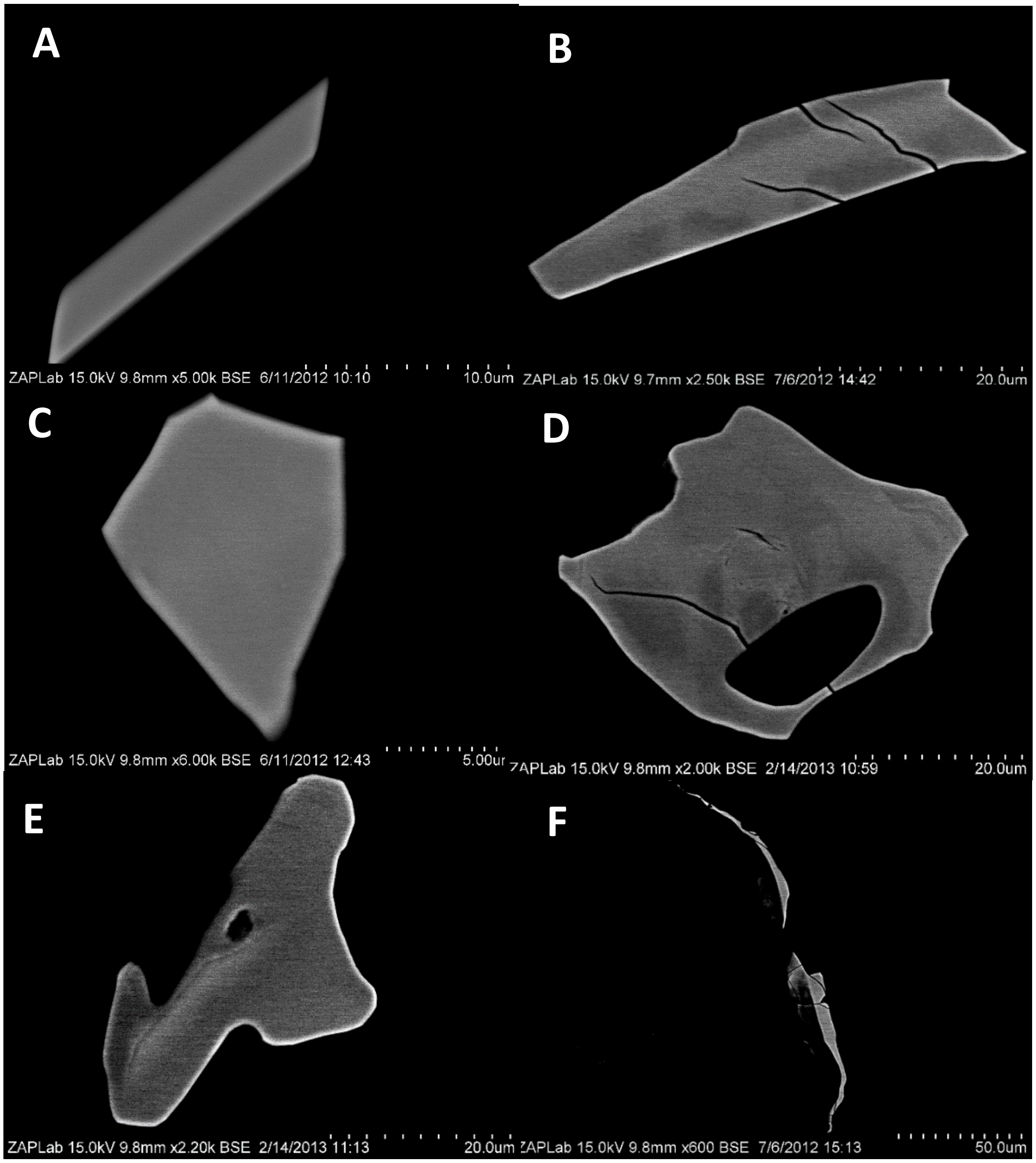

Figure F-3-3: Gabbronorite Zirccons. A: Z37 from sample 235B, B: Z211 from sample V234, C: Z3311 from sample V235B, D: Z5226 from sample V246, E: Z4624 from sample V246, and F:Z869 from sample V234. The most dominant internal features are cracks and pits and the morphologies range from euhedral, as shown in the prismatic grain in image A to anhedral and stringer-like as shown in image F.

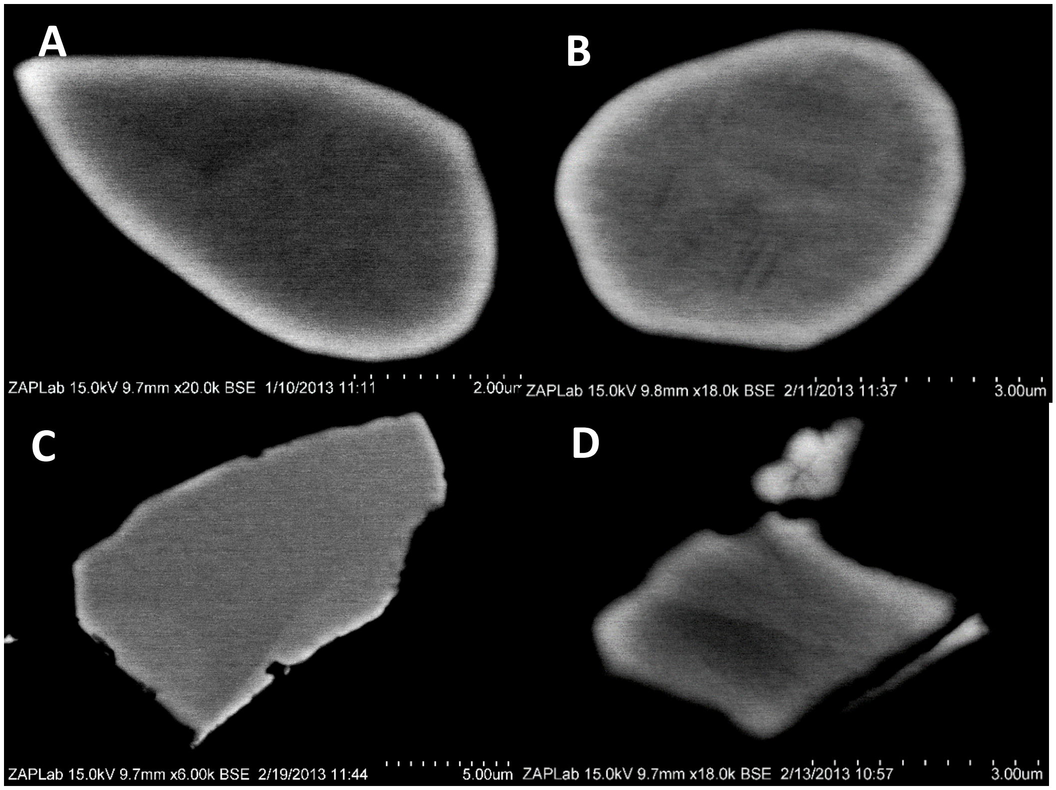

Figure F-3-4: ILG Baddeleyite**.** A: B:31 from sample V238, B: B1699 from sample V234-2 C: B6652 from sample V262 and D: B4837 from sample V238. The grains are internally featureless and have subhedral to anhedral morphologies.

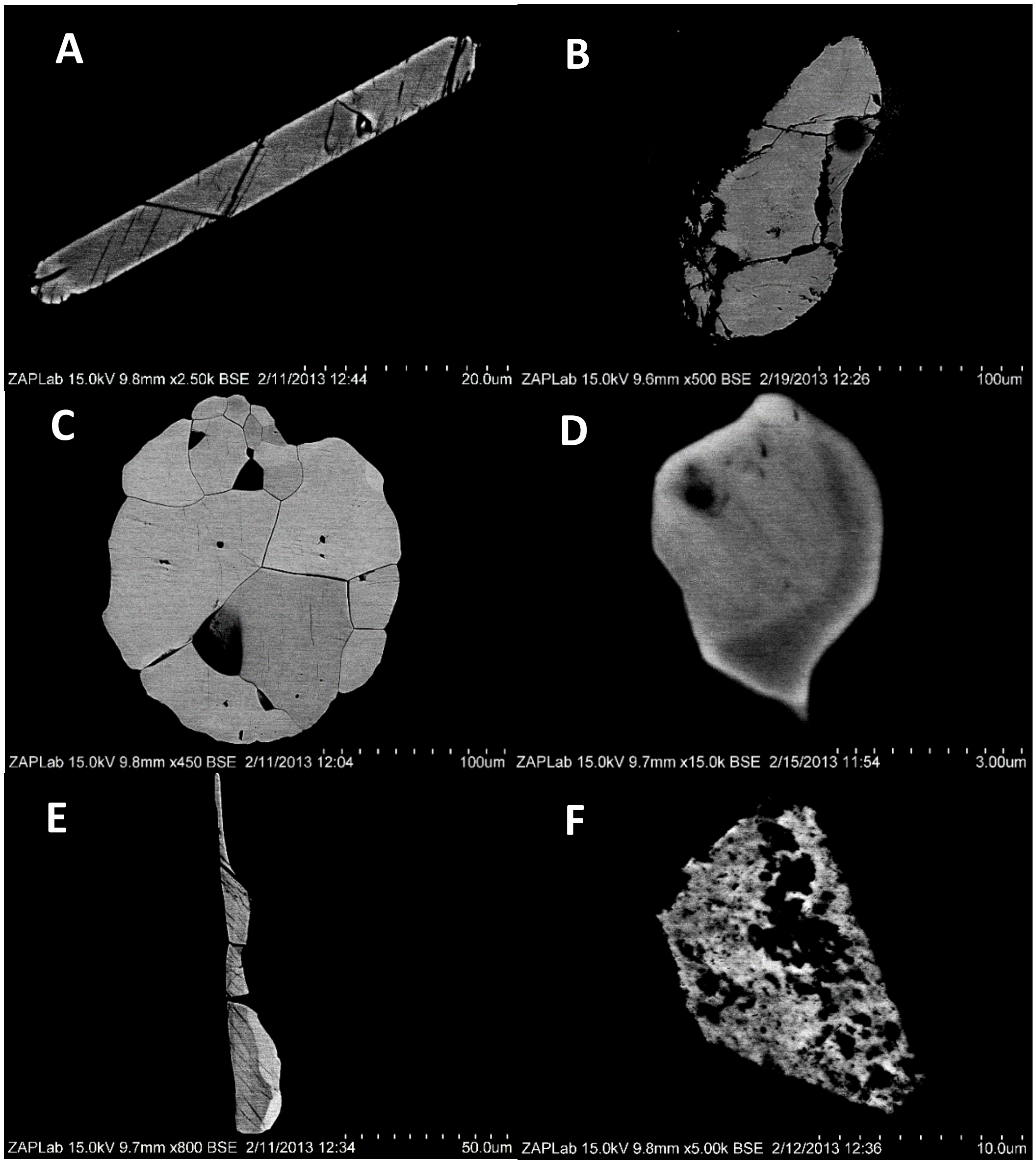

Figure F-3-5: ILG Monazite**.** A: M2379 from sample V234-2, B: M14831 from sample V262 C: M1051 from sample V234-2 D: M84 from sample V252, E: M1680 from sample V234-2, and F: M2254 from sample V245. There are a wide variety of internal features and grain morphologies in the monazites found in the ILG. The grain in image C is an excellent example of a recrystallized grain. Note the extreamly small size of the nearly featureless grain in image D.

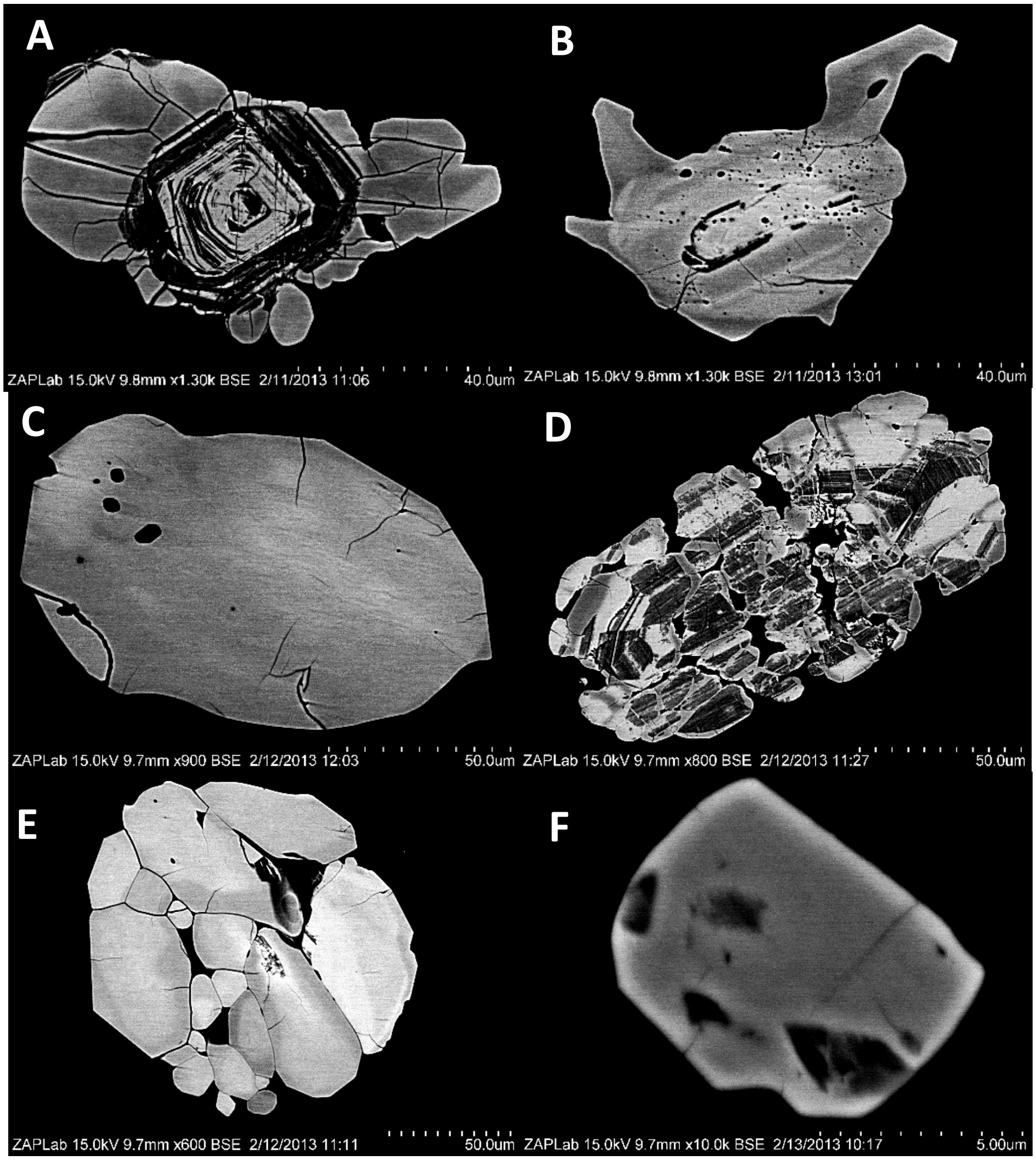

Figure F-3-6: ILG Zircons. A: Z58 from sample V234-2, B: Z2719 from sampleV234-2, C: Z2011 from sample V245 D: Z2250 from sample V245, E: Z2520 from sample V245 and F: Z972 from sample V238. The zircon grains like the monazite grains seen in the ILG have a wide variety of internal features and morphologes range from subhedral (image F) to anhedral (image B). Note the partial recrystallization of the grainin image D verses the complete recrystallization in the grain in image E.

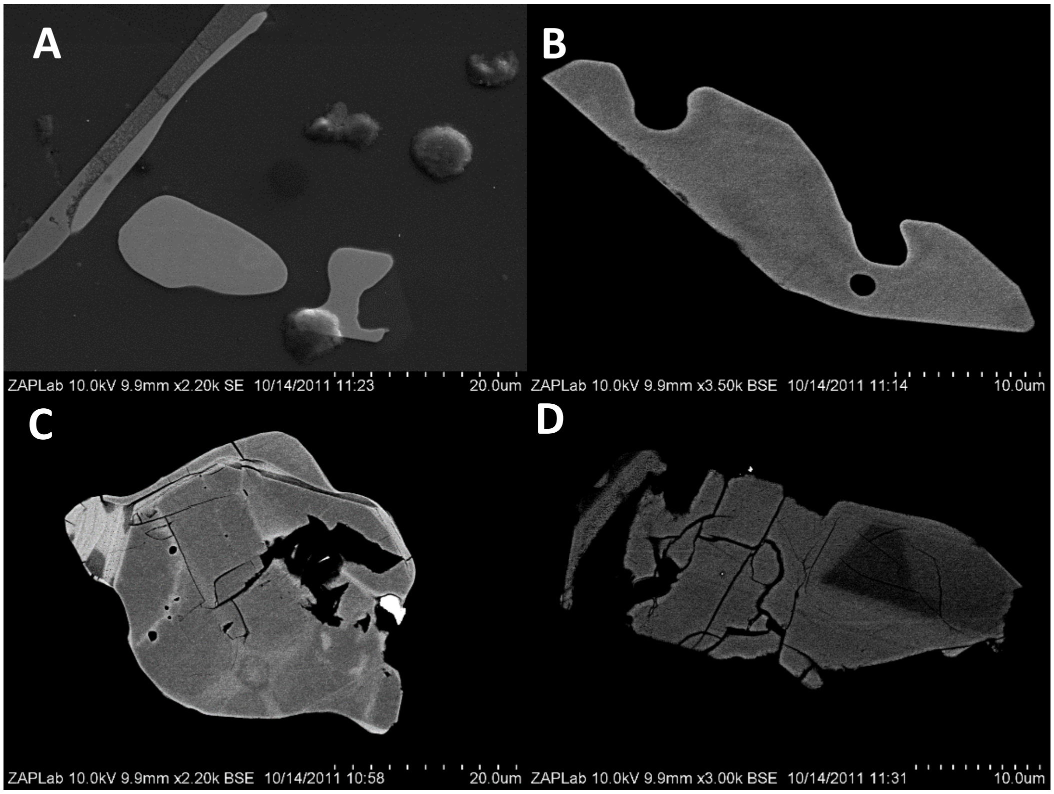

Figure F-3-7: Transition zone zircon: These grains are from sample V249, which contains both the gabbronorite and inclusions of the ILG. A: Z211, B: 373, C: 469, and D: 499 show the variety of morphologies and internal textures seen in the sample that contains both rock types.

Vita

Name:	Carmela-Lisa Cupelli
Post-secondary Education and Degrees:	The University of Western Ontario London, Ontario, Canada 2009- To be completed 2016 PhD.
	The University of Western Ontario London, Ontario, Canada 2003-2008 B.Sc.
Honors and Awards	Robert and Ruth Lumsden Graduate Award in Earth Science 2009-2012 & 2014-2015
	J. P. Bickell Foundation Scholarship 2008
	Dean's Honor List 2008
	Honour W Award 2006
	Common Wealth Award 2003
Related Work Experience	Assistant Geologist Tri Origin Exploration June 2016
	Teaching Assistant The University of Western Ontario 2008-2013
	Field Geologist Vale Inco Lonmin JV Summer 2008
	Geological Assistant Inco Exploration 2006-2007
Internal Reports	Old Mine Plans to Wire Frames Using AutoCAD and Datamine Inco 2007

Publications

Cupelli, C.L., Moser, D.E., Barker, I.R., Darling, J.R., Bowman, J.R., and Dhuime, B. (2014). Discovery of mafic impact melt in the center of the Vredefort dome: Archetype for continental residua of early Earth cratering? Geology, v.42, 5, p.403-406.

Antonenko, I., Osinski, G.R., Battler, M., Beauchamp, M., **Cupelli, L.,** Chanou, A., Francis, R., Mader, M.M., Marion, C., McCullough, E., Pickersgill, A.E., Preston, L.J., Shankar, B., Unrau, T., Veillette, D. (2013). Issues of Geologically-Focused Situational Awareness in Robotic Planetary Missions: Lessons from an Analogue Mission at Mistastin Lake Impact Structure, Labrador, Canada. Advances in Space Research, v.52, p.272-284.

Moser, D.E., **Cupelli, C.L.,** Barker, I.R., Flowers, R.M., Bowman, J.R., Wooden, J., and Hart. J.R. (2011). New Zircon Shock Phenomenon and their use for Dating and Reconstruction of Large Impact Structures Revealed by Electron Nanobeam (EBSD, CL, EDS), and Isotopic U-Pb, and (U-Th)/He Analysis of the Vredefort dome. Canadian Journal of Earth Science, V4, 8, p.117-139.

Conference Presentations

Cupelli, C.L., Moser, D.E., Barker, I.R., Darling, J.R., Bowman, J.R., Wooden, J., Dhuime, B. (2013) Discovery of Mafic Impact Melt in the Central Uplift of the Vredefort Basin. Large Meteorite Impacts and Planetary Evolution V., Sudbury, Canada, August 5-8 (3096).

Moser, D.E., Barker, I.R., Tait, K.T., Darling, J.R., Chamberlain, K.R., Schmitt, A.K., **Cupelli, C. L.,** Reinhard, D.A., Olson, D., Clifton, P.H., Larson, D.J., Gault, B., Bugnet, M. (2013) Atomic Records of Inner Solar System Impact Processes from U-Pb Dating Phases. Large Meteorite Impacts and Planetary Evolution V., Sudbury, Canada, August 5-8 (3104).

Cupelli, C. L., Moser, D.E., Barker, I.R., Darling, J., Bowman, J.R., Wooden, J., Hart, R. (2012) Zircon-based identification of mafic impact melt bodies at the center of the Vredefort dome–remnants of the lost melt sheet. Lunar and Planetary Science Conference, The Woodlands, Texas, March 18-23 (2402).

Marion, C.L., Osinski, G.R., Abou-Aly, S., Antonenko, I., Barfoot, T., Barry, N., Bassi, A., Battler, M., Beauchamp, M., Bondy, M., Blain, S., Capitan, R., Cloutis, E., **Cupelli, L.,** Chanou, A., Clayton, J., Daly, M., Dong, H., Ferrière, L., Flemming, R., Flynn, L., Francis, R., Furgale, P., Gammell, J., Garbino, A., Ghafoor, N., Grieve, R.A.F., Hodges, K., Hussein, M., Jasiobedzki, P., Jolliff, B.L., Kerrigan, M.C., Lambert, A., Leung, K., Mader, M.M., McCullough, E., McManus, C., Moores, J., Ng, H.K. Otto, C., Ozaruk, A., Pickersgill, A. E., Pontefract, A., Preston, L.J., Redman, D., Sapers, H., Shankar, B., Shaver, C., Singleton, A., Souders, K., Sten-ning, B., Stooke, P., Sylvester, P., J. Tripp, J., Tornabene, L.L., Unrau,T., Veillette, D., Young, K., Zanetti, M. (2012) A Series of Robotic and Human Analogue Missions in Support of Lunar Sample Return. Lunar and Planetary Science Conference, The Woodlands, Texas, March 18-23 (2333).

Antonenko, I., Mader, M.M., Osinski, G.R., Battler, M., Beauchamp, M., **Cupelli, L.,** Chanou, A., Francis, R., Marion, C., McCullough, E., Pickersgill, A., Preston, L., Shankar, B., Unrau, T. and Veillette, D., Geo-focused situational awareness in robotic planetary missions: Lessons from an analogue mission at Mistastin Lake impact structure, Labrador, Canada, *GAC-MAC Joint Annual Meeting: Ottawa 2011*, Abstract #372, 2011.

Mader, M.M., Antonenko, I., Osinski, G.R., Marion, C.L., Beauchamp, M., Battler, M., Chanou, A., **Cupelli, L.**, Francis, R., McCullough, E., Pickersgill, A., Preston, L., Shankar, B., Unrau, T., and Veillette, D., Integrated planetary operations at the Mistastin Lake lunar analogue site, Labrador, Canada: Recommendations for future lunar missions, *GAC-MAC Joint Annual Meeting: Ottawa 2011*, Abstract #558, 2011.

Antonenko, I., Mader, M.M., Osinski, G.R., Battler, M., Beauchamp, M., **Cupelli, L.**, Chanou, A., Francis, R., Marion, C., McCullough, E., Pickersgill, A., Preston, L., Shankar, B., Unrau, T., Veillette, D. (2011) Issues of Geo-Focused Situational Awareness in Robotic Planetary Missions: Lessons from an Analogue Mission at Mistastin Lake Impact Structure, Labrador, Canada. Lunar and Planetary Science Conference, The Woodlands, Texas, March 7-11 (2594).

Mader, M.M., Antonenko, I., Osinski, G.R., Battler, M., Beauchamp, M., **Cupelli, L.**, Chanou, A., Francis, R., Marion, C., McCullough, E., A., Preston, L., Shankar, B., Unrau, T., Veillette, D. (2011) Optimizing Lunar Sample Return: Lessons Learned from a Robotic Precursor Lunar Analogue Mission at the Mistastin Impact Sturcture, Labrador, Canada. Lunar and Planetary Science Conference, The Woodlands, Texas, March 7-11 (5038).

Marion, C., Osinski, G.R., Antonenko, I., Barfoot, T., Battler, M., Beauchamp M., Cloutis, E., **Cupelli, L.**, Chanou, A., Daly, M., Ferrière, L., Flemming, R., Francis, R., Ghafoor, N., Grieve, R.A.F., Hodges, K., Hussain, M. Jolliff, B.L., Mader, M.M., McCullough, E., Otto, C., Preston, L., Redman, D., Shankar, B. Singleton, A., Stooke, P., Sylvester, P., Tornabene, L.L., Unrau, T., and Veillette, D. A Lunar Analogue Mission: Sample Return to the South Pole-Aitken Basin. Lunar and Planetary Science Conference, The Woodlands, Texas, March 7-11 (2515).

Moser, D.E., **Cupelli, C.L.**, Barker, I.R., Flowers, R.M., Bowman, J.R., Wooden, J., and Hart, R. (2011) New Zircon Shock Phenomenon for Dating and Reconstruction of Large Impact Basins Revealed by Electron Nanobeam (EBSD, CL, EDS), U-Pb, and (U-Th)/He Isotopic Analysis of the Vredefort dome. Lunar and Planetary Science Conference, The Woodlands, Texas, March 7-11 (2462).

Shankar, B., Antonenko, I., Osinski, G.R., Mader, M.M., Preston, L., Battler, M., Beauchamp, M., Chanou, A., **Cupelli, L.**, Francis, R., Marion, C., McCullough, E., Pickersgill1, A., Unrau, T., and Veillette, D. (2011) Lunar Analogue Mission: Overview of the Site Selection Process at Mistastin Lake Impact Structure, Labrador Canada. Lunar and Planetary Science Conference, The Woodlands, Texas, March 7-11 (2594).

Cupelli, L. and Moser, D. (2009) Colour SEM-CL Investigation of Zircon Crystallization in the Central Uplift of the Vredefort Impact Basin, South Africa. American Geophysical Union Spring Meeting, Toronto, Ontario, May 24-27 (GA31B-06).